Microseismic and Real-time Imaging of Fractures and Microfractures in Barre Granite and Opalinus Clayshale

by

Bing Qiuyi Li

B.ASc. Mineral Engineering
University of Toronto, 2013

S.M. Civil and Environmental Engineering
Massachusetts Institute of Technology, 2015

Submitted to the Department of Civil and Environmental Engineering in Partial Fulfilment of the Requirements for the Degree of

Doctor of Philosophy

at the

Massachusetts Institute of Technology

June 2019

Signature redacted

Signature of Author _____

Department of Civil and Environmental Engineering
17th of May, 2019

Signature redacted

Certified by _____

Herbert Einstein
Professor of Civil and Environmental Engineering
Thesis Supervisor

Signature redacted

Accepted by _____

Heidi Nepf
Donald and Martha Harleman Professor
Chair, Departmental Committee for Graduate Students

Microseismic and Real-time Imaging of Fractures and Microfractures in Barre Granite and Opalinus Clayshale

by

Bing Qiuyi Li

Submitted to the Department of Civil and Environmental Engineering
on the 17th of May, 2019, in Partial Fulfilment of the
Requirements for the Degree of
Doctor of Philosophy in Civil Engineering

Abstract

The goal of the work is to better understand field microseismicity through laboratory experiments. Currently, industry practice consists of detecting activity using monitoring stations located around the volume of interest, and subsequently using the data to infer characteristics such as location, magnitude and mechanism of the corresponding microseismic sources. With this approach it is difficult, given the generally great depths of the microseismic activity, to verify characteristics such as the extent, orientation and mechanism of the fracturing activity. Our goal in the laboratory is to address this knowledge gap by imaging the initiation and propagation of hydraulic fractures in real time, and compare these data to the microseisms emitted during the experiment. Experiments are conducted on Barre Granite, a coarse-grained crystalline rock similar to that often found in enhanced geothermal systems, and Opalinus clayshale, a fine-grained sedimentary rock analogous to shales found in unconventional oil and gas reservoirs. These materials are first tested in a four-point beam-bending setup to generate baseline results under dry conditions, and then hydraulically fractured to compare their behaviour under conditions similar to those in the field.

We find that differences between granite and shale behaviour can be attributed to at least two factors. Firstly, the grain size affects the size of the process zone ahead of the fracture tip, which results in a significantly larger zone in granite. Secondly, the shale exhibits more velocity strengthening material while granite is a velocity weakening material, i.e. slip in granite tends to nucleate along single small asperities while slip in shale tends to occur along larger contact areas. As a result, macro-scale tensile fractures in granite are composed of hundreds of micrometre- to millimetre-scale en-echelon shear microcracks that then coalesce with tensile microcracks. This mechanism tends to generate more seismic activity than in shale, where tensile microcracks on the order of tens of micrometres are created directly. The magnitude of seismicity is quantified in this thesis by normalised radiated seismic energy, which we find in shale is approximately 2-5 % of that in granite. We also find that fluid pressure has a significant effect on seismic activity, and hypothesise that increased loading rate leads to increased inertia in the material ahead of the crack tip, which results in increased fracture complexity. This may result in increased seismic activity due to the increased total accumulated fracture length over which seismic slip may occur.

Thesis Supervisor: Herbert H. Einstein
Title: Professor of Civil and Environmental Engineering

Acknowledgements

"It's the job that's never started as takes longest to finish." (Tolkien, 1954)

If I had my way, I would wake up every day at noon, sit around drinking tea and ultimately get no work done. Clearly, that has not entirely been the case. After all, this 500 page brick can't *entirely* be nonsense, can it? The African proverb "It takes a village to raise a child" seems appropriate here. After all, a mere six years ago I may have been the laziest, ignorant, and most petulant child this institution has ever seen, but now I'd like to think I have become ..... well ever so slightly less lazy, ignorant, and petulant. **And**, if I don't say so myself, I think I've also become just a tad more caring, and a smidge less thoughtless. This transformation, of course, is owed exclusively to my wonderful village of support, consisting of people that have known and cared for me since I was a itty-bitty poop-spewing, snot-emitting, pee-leaking infant, all the way to that guy I met a month ago, to whom I say hi to in the hallway, but whose name I still don't know (and am too embarrassed to ask). Thank you all dearly, you have made this godforsaken (but nonetheless *lovely!*) institution one of the greatest learning opportunities in my life.

Specifically, I would like to thank my family for having my best interest at heart all these years, my friends for putting up with me and my eccentricities, and my lab mates for our endless discussions on life, the universe, Joe coffee and DOTA 2 (occasionally rocks and fractures get brought up). Thanks of course go to Professors H.H. Einstein, J.T. Germaine, G.A. Prieto, B. Evans, and E. Kausel for being the fountains of knowledge and insight that they are. Additionally, I would like to thank Total S.A. for sponsoring my work, the frisbee crew for the excuse (as if we needed one) to run around on Killian court like idiots, and the SEA lunch bunch for all the delicious ('cmon, it's not *THAT* bad!) dimsum we've shared. Finally, to the wisest squid of them all: You're the best, thank you for walking into my life, and for believing in me. Love you to Pluto's moon and back.

Contents

1 Concerning Rocks **28**
1.1 Objective 28
1.2 Thesis Organisation 29

2 Background and Methodology **31**
2.1 Acoustic Emissions 31
2.1.1 Overview 31
2.1.2 Acquisition Equipment and Analytical Techniques 32
2.1.2.1 Sensors 33
2.1.2.2 Pre-amplifiers 35
2.1.2.3 Data Acquisition System 35
2.1.3 Velocity Measurements 35
2.1.4 Calibration to Moment Magnitude Scale 36
2.1.5 First Arrival Picking 38
2.1.6 Hypocenter Location Inversion 40
2.1.7 Seismic Source Mechanism Inversion 42
2.1.8 Seismic Efficiency 45
2.2 Digital Image Correlation 46
2.2.1 DIC noise quantification 47
2.2.2 Zone of Large Strain Ahead of the Crack Tip 53
2.3 Previous Studies 53
2.3.1 Laboratory Studies 54
2.3.1.1 The Effect of Pore Pressure on Hydraulic Fracture Growth: An Experimental Study (AlTammar et al., 2018) 54
2.3.1.2 Opening and mixed mode fracture processes in a quasi-brittle material via digital imaging (Lin et al., 2014) 56
2.3.1.3 Direct observations of damage during unconfined brittle failure of Carrara marble (Tal et al., 2016) 60
2.3.1.4 Fracture Toughness Measurements and Acoustic Emission Activity in Brittle Rocks (Nasseri et al., 2006) 63
2.3.1.5 Rate Dependence of Acoustic Emissions Generated during Shear of Simulated Fault Gouge (Mair et al, 2007) 67
2.3.1.6 Effect of grain size on fractal structure of acoustic emission hypocenter distribution in granitic rock (Kusunose et al., 1991) 70

2.3.1.7 Effects of grain size on the initiation and propagation thresholds of stress-induced brittle fractures (Eberhardt et al., 1999) 73
2.3.1.8 Hydraulic fracture energy budget: Insights from the laboratory (Goodfellow et al., 2015) 75
2.3.1.9 Rock fabric influence on hydraulic fracture propagation (Stanchits et al., 2015) 78
2.3.1.10 Frictional properties of shale reservoir rocks (Kohli and Zoback, 2013) 80
2.3.1.11 Mechanical properties of shale-gas reservoir rocks — Part 2: Ductile creep, brittle strength, and their relation to the elastic modulus (Sone and Zoback, 2013) 82
2.3.2 Field Studies 84
2.3.2.1 Non-double-couple mechanisms of microearthquakes induced by hydraulic fracturing (Sileny et al., 2009) 84
2.3.2.2 On the mechanisms of shale microfracture propagation (Padin et al., 2014) 88
2.3.2.3 Natural fractures in shale: A review and observations (Gale et al., 2014) 91
2.3.3 Summary of Literature Review 93

3 Tensile Fracturing in Granite **94**
3.1 Experimental Setup 94
3.1.1 Physical Setup 94
3.1.2 Camera Setup 95
3.1.3 Repeatability 97
3.2 Load-displacement behaviour 98
3.3 General comparison of strain and AE observations 100
3.3.1 Strain observations 100
3.3.2 AE observations 101
3.4 209 s to 309 s: Process zone development 105
3.4.1 Strain observations 105
3.4.2 AE observations 107
3.4.3 Comparison of AE and visual data between 209 s and 309 s 109
3.5 309 s to the end of the experiment: Crack propagation 111
3.5.1 Strain observations 111
3.5.2 AE observations 113
3.5.3 Comparison of AE and visual observations 114
3.6 Displacement vectors over time 117
3.7 Summary and conclusions 120

4 Tensile Fracture in Shale **122**
4.1 Load-Displacement 122
4.2 Acoustic Emissions 124
4.3 DIC results 127
4.4 Comparison of AE and crack extent 132

4.5 Summary and conclusions . . . 133

5 Hydraulic Fracturing of Barre Granite 134
5.1 Physical Setup . . . 134
5.2 Results . . . 138
5.2.1 Rate of AE events over time . . . 138
5.2.2 Amplitude of AE over time . . . 140
5.2.3 Focal Mechanisms . . . 142
5.2.4 Hypocenter Location Analysis . . . 144
5.2.5 Spatio-temporal Analysis . . . 148
5.2.5.1 30-VL5-INC5-C . . . 148
5.2.5.2 2a-30-0-VL0-C . . . 152
5.2.5.3 2a-30-120-VL0-B . . . 155
5.2.5.4 Spatio-temporal Distribution of Focal Mechanisms . . . 158
5.3 Discussion . . . 160
5.3.1 Stress state . . . 160
5.3.2 Time-to-Failure analysis . . . 162
5.4 Summary and Conclusions . . . 163

6 Hydraulic Fracturing of Shale 166
6.1 Experimental Procedure and Setup . . . 166
6.2 Pressure-Fracturing Results . . . 169
6.2.1 Fracture Progression . . . 169
6.2.2 Fracture speed . . . 171
6.2.3 Pressure-Time Results . . . 172
6.3 Acoustic Emissions (AE) Results . . . 174
6.3.1 AE Analysis Results . . . 174
6.3.2 Comparison of AE Data to Fracture Process . . . 176
6.4 Second Round of Tests . . . 178
6.5 Discussion and Conclusions . . . 180

7 Microseismicity and Real-time Visualisation of Microstructural Damage during Hydraulic Fracturing 181
7.1 Methodology . . . 181
7.1.1 Physical setup . . . 181
7.1.2 Imaging setup . . . 183
7.1.3 Acoustic Emissions setup . . . 186
7.2 Results . . . 186
7.2.1 Strain and displacement maps . . . 187
7.2.2 Opening displacement . . . 193
7.2.3 Statistical Distribution of strains . . . 194
7.2.4 Displacement and AE activity over time . . . 196
7.2.5 AE hypocenter locations . . . 200
7.3 Scaling . . . 203
7.4 Conclusions . . . 204

8 Energy Budget **205**
8.1 Tests considered . . . 205
8.2 Radiated seismic energy E_R . . . 207
8.2.1 Attenuation . . . 209
8.3 External mechanical work done $\tilde{E}$ . . . 215
8.4 Discussion and Conclusions . . . 217

9 Summary, Discussion, and Conclusions **219**

Bibliography **224**

A AE setup details **235**
A.1 Foreword . . . 235
A.2 Connecting AE equipment . . . 235
A.3 AEwin settings for acquiring data . . . 240
A.4 Analysing AE data . . . 248
A.5 MATLAB codes . . . 249
A.5.1 Ball drop magnitude calibration . . . 249
A.6 Glaser sensors . . . 249
A.7 Parametric connector box . . . 251

B Other tests **256**
B.1 Notched Brazilian Test on Opalinus . . . 256
B.2 HF on small specimen . . . 258

C Detailed analysis of granite hydraulic fracture tests **260**

List of Figures

2.1 Schematic of specimen and AE setup. Microcracks in the rock radiate microseismic waves in the form of elastic waves, which are converted to voltages by the piezoelectric sensors. The sensor voltages are amplified by the pre-amplifiers, and then digitised and recorded by the data acquisition system. 33

2.2 Sensor sensitivity on the y-axis plotted over frequency on the x-axis. D/A curve shows the sensitivity of a Nano30 sensor. B/A curve shows the sensitivity of a Glaser-type sensor (McLaskey and Glaser, 2012). To calculate B/A and D/A, sensors are attached to a steel block, on which a glass capillary tube is loaded until breakage. The waveforms (in units of volts) corresponding to the tube breakage are recorded, and expressed in the frequency domain using a Fourier transform. The known theoretical displacement for tube breakage at each sensor location is also expressed in the frequency domain using a Fourier transform, and the amplitude of the recorded waveform is element-wise divided by the amplitude of the theoretical displacement in the frequency domain. A relatively flat sensitivity curve such as B/A indicates that the voltage is a constant multiplier of the displacement across a wide range of frequencies, and so the displacement at any sensor can simply be calculated by multiplying the voltage by a constant value. However, an irregular curve such as D/A indicates that the voltage-displacement relationship depends on the frequency of the displacement, and so more sophisticated calibrations are required to calculate the displacements given a voltage waveform. 34

2.3 (a) Spectra of the instrument-apparatus response and three AE events seen during the four point bending experiment. The notation is the same as that used by McLaskey et al. (2015). The AE magnitudes were M_w = -6.63, -7.56 and -8.08. f_c is the corner frequency of the AE events. (b) For these three AE events, a linear relation was found between M_w and its first motion amplitude. From Li and Einstein (2017). 37

2.4 Magnitude-frequency distribution plot for all events in the four point bending experiment, based on the calibration shown in Figure 2.3. From Li and Einstein (2017). 38

2.5 a) Waveform data over 0.46 s period immediately prior to failure. b) Close-up of red box in subfigure a, with automatic picks shown in red circles. c) Segmented AIC values for the waveform data shown in subfigure b. Notable peaks in AIC value shown with triangles, while red circles denote false detections. From Li, Goncalves da Silva and Einstein, 2019). 39

2.6 Example of first arrival amplitude 40

2.7 Schematic of hypocenter location inversion. Black refers to sensor locations, red to the source location, green to the travel path and associated travel times t_i, and blue to the facing direction of each sensor. 41

2.8 Algorithm used to calculate hypocenter locations for AE events and constrain location accuracy. From Li, Goncalves da Silva and Einstein, 2019) 42

2.9 Schematic of force pairs that form the moment tensor. From Shearer (2009). 43

2.10 Explanation of the decomposition of the moment tensor. 44

2.11 a) Illustration of moment tensor decomposition. Adapted from Grosse and Ohtsu (2008). b) Diamond CLVD-ISO plot illustrating AE event classification used in this study. After Vavryčuk (2015). 45

2.12 Illustration of process to calculate displacement map. 46

2.13 Schematic of the DIC subset including a portion of a crack. DIC results will average effect of the crack over the entire subset. 47

2.14 Contour plot of opening displacement (mm) between images taken 2 seconds apart using different subset radii. Standard deviation of the displacement map is given in each figure heading. From Li and Einstein (2017). 49

2.15 Contour plot of ε_{yy} calculated from the displacement data shown in Figure 2.14. Standard deviation of the strain maps are given in the figure headings. Li and Einstein (2017). 50

2.16 Contour plot of ε_{xx} for images exhibiting significant process zone development. (Left) Data plotted with strain contours from -0.01 to +0.01. (Right) Same data with strain contours from -1E-3 to +1E-3 to highlight the extent of the process zone. It can be seen that the width of apparent process zone exceeds the diameter of the DIC calculation. Li and Einstein (2017). 51

2.17 Opening displacement and ε_{xx} for images taken 2 seconds apart for the micro-camera. Standard deviation of the strain maps are given in the figure headings. Li and Einstein (2017). 52

2.18 Schematic of fracture cell (AlTammar et al., 2018). 54

2.19 A series of contour maps showing Tresca strain calculated from digital image correlation applied to hydraulic fracture test 9, where far field stress = 0.34 MPa is applied and held constant in the x-direction. Then, all holes are saturated at a constant fluid pressure of 0.28 MPa for 80 minutes, at which time fluid pressure in the bottom right hole is increased to 1.03 MPa for 2 minutes, and finally fluid pressure in the center hole was increased until fracturing occurred at 2.37 MPa. Each subfigure shows the strain at an unspecified time, and no colourbar is provided in the original journal article. From AlTammar et al., 2018. 55

2.20 (a) Loading geometry and observation region (dashed lines) on the specimen surface used in the Lin et al. (2014) study. (b) Typical digital image where the rock is speckled and the notch is on the bottom left. 57

2.21 Displacement contour maps at 80-70% of post peak load. Left two plots show horizontal displacement, right two plots show vertical displacement. The load platen is in line with the notch in the top two plots (See Fig. 2.20), which creates zero eccentricity, while the load platen is offset from the notch in the bottom two plots, resulting in a beam with 11.4 % eccentricity (See Fig. 2.20). The authors identify cohesive zones (CZ, referred to as process zone in this work) and slip zones (SZ, referred to as "behind the crack tip" in this work) based on shape of the displacement contours. From Lin et al. (2014). 58

2.22 To create this plot, the authors considered the final crack path shown in Figure 2.21a, and selected query points along the crack at which the x displacement on either side of the crack was sampled over time. The y axis of this plot shows the distance from the notch tip to each query point, and the x axis shows the magnitude of displacement at that query point. Each coloured line represents an increment in time. Each query point is sampled on either side of the crack, and the displacement on the left side of the crack is plotted on the left side of this graph, and a similar treatment was afforded to the right side of the crack. The subtraction between the left and right side of the same increment in time gives the total opening displacement of the crack at that time. From Lin et al. (2014). 59

2.23 Photograph showing imaging and loading devices used by Tal et al. (2016). 61

2.24 a) Stress-strain curve obtained from setup shown in Figure 2.23. b) Each row shows an image captured at the stress-strain state shown with the green circles in subfigure a, overlaid with a contour plot of strains ε_{xx}, ε_{yy} and ε_{xy} for the first, second and third columns respectively. From Tal et al. (2016). 62

2.25 3-D block diagram showing location of CCNBD specimens prepared along each plane with respect to microcrack orientations in Barre granite; rose diagrams show the alignment of microcracks for each plane. From Nasseri et al. (2006). 64

2.26 Crack propagation in Barre granite with existing microcracks. The close-up image shows the rough and segmented morphology of the fracture surface. Left shows the test in which the crack propagated perpendicularly to microcracks, while right shows test parallel to microcracks. From Nasseri et al. (2006). 64

2.27 x-axis shows time, y axis shows a) relative proportion of AE focal mechanisms, b) AE hits and the load curve. Crack propagation begins at 568 s. From Nasseri et al. (2006). 65

2.28 (Left) Microcrack density and orientation (rose diagram) in fracture process zone and far-field area near notch A. Inset delineates the width of FPZ as derived from the superimposed AE events. From Nasseri et al. (2006). 66

2.29 Relation of AE events distribution to that of microcrack density (determined visually based on Figure 2.28) as a function of distance from the fracture plane. Rose diagrams on the right indicate the angular statistical distribution of microcrack orientations. From Nasseri et al. (2006). 66

2.30 Photo of double direct shear experimental setup used by Mair et al. (2007). 68

2.31 x-axis shows the velocities at which the granular materials were sheared. y-axis shows (a) mean number of AE per second during each test and (b) mean number of AE per μm of displacement during each test. In all cases, the number of AE per second increases with velocity. In all cases,the number of AE per μm of displacement decreases with increasing velocity. The absolute number of hits and rate of change varies between the two materials. The lines are hand drawn to highlight the main trends of the materials. From Mair et al. (2007). 69

2.32 Schematic diagram of monitoring system. Acoustic emissions (AE) were detected by 20 piezoelectric sensors (Labelled PZT) of 2 MHz resonant frequency, and the waveform data were fed into transient recorders with a 20 MHz alternating - direct current converter. The wave data were then transmitted to a hard disk through a minicomputer. Electric pulse signals (using the pulse generator) were intermittently fed into four piezoelectric sensors (labelled a, b, c and 20) to produce elastic P-waves during the experiment, and variation of the axial and the radial velocities were monitored. Six pairs of strain gauges were attached to the surface of the sample to monitor local surface strain in the axial and circumferential directions. The strain and stress data were recorded by a personal computer during the experiment. From Kusunose et al. (1991). 71

2.33 a) Map of AE hypocenters for Inada (top) and Osima (bottom) granodiorites. The hypocenters are plotted for the events that occurred at axial stress below 80% of the failure strength. In this stress range 885 and 2365 events were located, with an accuracy of 2 mm, for Inada and Oshima granodiorites, respectively. b) Correlation integral (C(r)) vs. lag distance (r) for Inada and Oshima granodiorites. The Oshima granodiorite data fall on a straight line. This shows that the AE hypocenter distribution of Oshima granodiorite has a single fractal structure. In contrast, the Inada granodiorite data fall on two straight lines; the fractal dimension for the distance range longer than the grain size is 2.4 and that for the shorter range is 2.0. From Kusunose et al. (1991). 72

2.34 x-axis shows axial stress during each experiment. y-axis shows AE energy release rate, normalised per MPa of axial load. Top, middle, bottom show plots of granodiorite, grey granite, and pegmatite respectively. Red dotted line represents the maximum energy rate during each test. From Eberhardt et al. (1999). 74

2.35 (a) Laboratory hydraulic fracture apparatus. Experiment SR4 (σ_1 = 30 MPa, σ_3 = 10 MPa). (b,e) μCT fracture surface projected on the σ_1–σ_3 plane. (c) AE event location projected on the σ_1–σ_3 plane, and (d) μCT fracture surface projected on the σ_1–σ_1 plane. From Goodfellow et al. (2015). 76

2.36 (a) x-axis shows injection energy (work done by injection of fracturing fluid at flow rate Q and pressure P) plotted against radiated seismic energy on y-axis. Reference lines correspond to the seismic injection efficiency ($E_R/E_{injection}$) in percentages. (b) x-axis shows total injected volume plotted against seismic moment of the largest seismic event on the y-axis. From Goodfellow et al. (2015). 77

2.37 Photographs of smaller specimen before (a) and after the test (b); photograph of opened bedding plane (c); 3D rendering of AE events (spheres) and post-test epoxy distribution (light-red surfaces)(d). From Stanchits et al. (2015). 79

2.38 Larger specimen: (a) 3D rendering of AE events (spheres) combined with hydraulic fracture (red surface) and mineralized fracture (green surface) surfaces; (b) photograph of the fractured block cut into 8-in cubes; (c) maximum bead size from analysis of microphotographs of the fracture surfaces. From Stanchits et al. (2015). 79

2.39 Friction experiment sample assembly inside triaxial pressure vessel used by Kohli and Zoback (2013) to test frictional properties of various shale rocks. 81

2.40 Friction coefficient (black symbols) and (a - b) (grey symbols) as functions of clay and organic content at 10 MPa normal stress for all samples in the study. Values of (a - b) are obtained from averaging the results of all velocity steps within a single experiment. Error bars represent the maximum, (a - b)(+), and minimum, (a - b)(-), values of (a - b) observed in each experiment. From Kohli and Zoback (2013). . . . 81

2.41 a) Ultimate strength for each specimen plotted as a function of the confining pressure. b) For each specimen, the ultimate strength was resolved onto the specimen failure surface as shear and normal traction. c-d) Unconfined compressive strength (UCS) was inferred from the y-intercept of each line in subfigure (a). e-f) Internal friction angle was calculated from the slope of each line in subfigure (a) and assuming a linear Coulomb failure criterion. g-h) The residual sliding friction coefficient was calculated from subfigure (b), again assuming a linear Coulomb failure criterion. From Sone and Zoback (2013). 83

2.42 Illustration of hydraulic fracture imaging geometry in the Cotton Valley experiment (inset, dark dot on the sketch of Texas). Black heavy lines indicate monitoring wells 1 and 2 (full squares mark positions of the geophones used in this study), gray heavy line indicates treatment well. Hypocenters of selected microearthquakes in groups G1–G4 and R are marked by circles. Grey arrows at the bottom of the model indicate direction of maximum horizontal stress. Distance is in meters. Note that detected events mostly occur between 2750 m and 2850 m elevation. From Sileny et al. (2009). 85

2.43 Seismicity observed during hydrofracturing (top) map view and (bottom) vertical cross section, together with composite mechanisms displayed as 3-D wire frame plots of P radiation patterns (compressions, red; dilatations, blue) for selected events in groups G1–G4 and individual mechanisms for events R(2) and R(5). Hypocenter locations of the five groups are represented by the color-coded dots: G1, black; G2, green; G3, blue; G4, cyan; R, red. The microearthquakes, for which we determined mechanisms, are numbered. Position of the injection well marked by blue square in map view and blue squares in depth section. Direction of maximum horizontal stress is indicated by gray arrows. Black quadrilaterals and arrows on each focal mechanism indicate approximate directions of forces corresponding to focal mechanisms. From Sileny et al. (2009). 87

2.44 On the left, distribution of cumulative moment versus depth for lower and upper Eagle Ford treatments. Note that regardless of the vertical placement of the perforations, most cumulative moment is occurring at the upper Eagle Ford while the lower Eagle Ford seems not to generate microseismicity. The same is occurring at the Vaca Muerta formation (on the right), where events from stages 1 and 2 are migrated upwards from the perforations, which are placed at the lower member of the Vaca Muerta. The plots show that few microseismic events occur in the TOC rich strata in both the Eagle Ford and Vaca Muerta formations. From Padin et al. (2014). 89

2.45 Microseismic monitoring of two horizontal wells fractured at the Eagle Ford. At the bottom of the figure, the "least active" vs the "most active" microseismic stages are shown. At the top, post frac results are shown for two different wells. Note that events with magnitudes less than -2 are located within the lower Eagle Ford. From Padin et al. (2014). 90

2.46 Contribution to oil production of the perforation stages in the Vaca Muerta well 1. From Padin et al. (2014). 90

2.47 Host rock compositional variation. Variable mineral composition fields of Barnett, Eagle Ford Formation (EF), and clay-rich mudrock (Md) (modified from Passey et al., 2010), Monterey Formation (from Isaacs, 1981) and Marcellus Formation (drawn from data in Pommer, 2013). Sealed, open, and fracture resistant axes are our interpretation of the tendencies that these compositional variations represent for fracture attributes. End members in the compositional field are interpreted as propensity to fracture or resist fracture (clay poor versus clay rich), propensity for fracture wall rocks to resist cementation or bridge (quartz rich), and propensity for fractures to seal with calcite (calcite rich). Qtz = quartz; fsp = feldspar. 92

3.1 Specimen geometry and AE sensor locations. S refers to PAC Micro30S sensors, and G refers to a Glaser-type sensor. Boxes denote locations of the loading platens. Units in mm. 95

3.2 (a) Reference image for the front camera, corresponding to a field of view (FOV) of around 5 x 7.5 cm. (b) Reference image for the back camera, corresponding to a FOV of around 2.95 x 4.425 mm. 96

3.3 (a) Load-displacement data for the three experiments. Drops in load during the initial elastic region are points in time where the loading was paused to refocus the cameras. (b) Crack mouth opening displacement over time for all three experiments, with a nominal rate of 0.0127 mm/min. 98

3.4 (a) Crosshead load and displacement over time. (b) Same data expressed as load-displacement to identify key stages of behaviour: 'a' linear load-displacement behaviour indicating elastic deformation. 'b' Vertical load appears to increase in 3 distinct non-linear steps, indicating the material is no longer deforming elastically. 'c' The load decreases while the crosshead maintains its position, indicating that the fracture is steadily propagating. The transition points are indicated in the red circles. 99

3.5 Machine input work, calculated from the integral of Figure 3.4b. The three stages of deformation are also highlighted here. The behaviour transitions from 'a' to 'b' at around 210 s, and from 'b' to 'c' at around 310 s. 99
3.6 (a) Opening strain from macro-DIC at key points in time. (b) Points in time indicated on the energy-time curve. Dotted purple line indicates semi-elliptic bulb of strain. 101
3.7 (a) AE events for entire experiment, coloured by time. Arrow indicates a specific zone in the AE cloud where there appears to be no events. (b) AE events with Mw > -7.4, coloured by magnitude. Black circles indicate events occurring along possible grain boundaries or zone of no events. 102
3.8 (a) Detailed photo of the crack surface, large quartz grain shown in red. Scale in cm. White flat surface is the pre-cut notch. (b) Curvature in the crack path due to the quartz grain. 103
3.9 Magnitude-frequency distribution of AE events. x-axis is the magnitude of events, and y-axis is the cumulative number of events, similar to a cumulative density function. (a) Each curve shows the magnitude-frequency distribution for AE events occurring over a given time interval. (b) Each curve shows the magnitude-frequency distribution for AE events occurring over a given range of distances from the notch tip. A shallower slope (lower b-value) represents a time window or distance range where relatively more large magnitude events occurred than small magnitude events, and a curve with a higher frequency (higher on the y-axis) represents more total events occurred within a given time window or distance range. 104
3.10 AE hit rate over the course of the experiment. Figure 3.5 is superimposed for reference. 105
3.11 ε_{xx} and ε_{xy} from micro-DIC at 253, 275 and 297 s of the experiment. The times correspond to approximately 90%, 95% and 100% of peak load respectively. The black bar in each figure schematically indicates approximate location of notch tip. Zone a: Initial portion of the crack, which appears to be purely tensile given that ε_{xy} indicates very little strain. Zone b: Ensuing en-echelon crack, which clearly shows step-like structure particularly in the ε_{xy} plot. 106
3.12 Source locations for events occurring between 0 and 300 s in the experiment. Colour shows time of occurrence. Clusters a and b each seem to occur closely in time in a linear pattern 108
3.13 (a) Microcrack orientation and location for tensile events occurring between 0 and 300 seconds. (b) Orientation and location of shear conjugate planes. Colour indicates magnitude. 108
3.14 Detailed view of ε_{xy} at 300 s of the experiment. Black crosses indicate query points used for Figure 3.15. Point 1 is the lowermost point, and point 7 is the uppermost. 110
3.15 Evolution of (a) ε_{xx} and (b) ε_{xy} over time (taken at 2 s intervals) at the query points specified in Figure 3.14. Query point 1 is the lowest point, and point 7 is the uppermost point. Histogram shows the AE hit rate over the same period. 110
3.16 (a) ε_{xx} and (b) ε_{xy} on the macro-DIC over the course of the experiment. Red and white arrows indicate the best qualitative estimate of the extent of the process zone and crack respectively. 112

3.17 ε_{xx} and ε_{xy} over time, taken at 20 s intervals. Rightmost image (c) shows locations of query points. The strains at query points 1, 2 and 3 appear to be anomalous towards the end of the experiment, which may be due to very large crack opening since the employed DIC algorithm does not account for discontinuities. 113
3.18 (a) Location of all AE events occurring after 300 s. (b) Microcrack orientation and location for tensile events with Mw > -7.5. (c) Orientation and location of shear conjugate planes. Colour indicates magnitude. 114
3.19 a) Displacement contour plot at 1000 s, on which we chose query points (crosses) based on a contour line of constant displacement that best estimated the location of the crack. Dotted purple lines demonstrate how the query points in this subfigure are related to the x-axis in the bottom subfigure. b) Strain data (y-axis) shown as a function of distance from notch tip on the x-axis and time in the colour scheme. Each line represents the state of strain at a given time. Dashed black line at y = 0.03 shows the calibrated strain value, which was used to calculate the crack extent. 115
3.20 Distance from the notch tip for AE events, DIC process zone (red line) and DIC crack extent (brown line). Left image shows the density of the location of AE events as binned in the figure. Middle image is coloured by magnitude, right image by contribution of shear ratio as per the moment tensor decomposition, where 0 indicates no shear and 1 indicates a pure double-couple mechanism. 116
3.21 Displacement vectors superimposed onto contour maps of ε_1 and γ_{max} for the macro-DIC results. Red dotted lines indicate development of a wedge-shaped envelope representing the zone of influence of the crack. 118
3.22 Displacement vectors superimposed onto contour maps of ε_1 and γ_{max} for the micro-DIC results. Red dotted lines indicate development of a wedge-shaped envelope representing the zone of influence of the crack. 119
3.23 (Left) Distribution of principal strains over the entire micro-DIC image at time of maximum load. Positive strain is tension. (Right) Scatter plot of $\varepsilon_1 - \varepsilon_3$ for each pixel of strain data. 120

4.1 Map of the Mont Terri underground laboratory showing location of boring cores including the BMA-2 cores used in this thesis. 123
4.2 Load-displacement data over time for the shale and granite beam bending experiments. Note that the timescale for the granite beam has been offset from the original data so that the beginning of loading matches the shale beam. 124
4.3 a) AE hypocenter locations over time for entire test, where colour indicates source time b) tensile event location and microcrack orientation, where colour represents magnitude c) shear event location and conjugate plane orientation, where colour represents magnitude. 125
4.4 Hypocenter locations of AE events over time. Colour represents the time within the range specified in each subfigure heading, size represents magnitude, and symbol represents the focal mechanism. 126
4.5 AE hit rate over the course of the experiment. Machine work over time is superimposed for reference. 126
4.6 Displacement vectors superimposed onto contour maps of ε_1 and γ_{max} for the macro-DIC results. 128

4.7 Displacement vectors superimposed onto contour maps of ε_1 and γ_{max} for the micro-DIC results. 129
4.8 Contour map of horizontal displacement u at various stages during the test. White dotted line indicates two crack paths. 129
4.9 Contour map of ε_{xx} for a) shale and b) granite at approximately the time of peak load. Upper limit of the color scale is set at the 90th percentile of strain. Opalinus strain measurement is resolved to 0.26 %, with a spatial resolution of 292 μm. Granite strain measurement is resolved to 0.15 %, with a spatial resolution of 172 μm. 130
4.10 Contour map of ε_{xy} for a) shale and b) granite at approximately 100 seconds after peak load. Black arrows indicate en-echelon cracks. 131
4.11 (Left) Distribution of principal strains over the entire micro-DIC image at time of maximum load. Positive strain is tension. (Right) Scatter plot of $\varepsilon_1 - \varepsilon_3$ for each pixel of strain data. 132
4.12 Scatter plot shows the distance from the notch tip to each AE event over time on the x-axis, line plots show the extent of the process zone and crack as measured by the DIC. 133

5.1 a) Schematic of the specimen setup including L-β-α naming convention and boundary conditions for tests used in this paper. VL0 refers to experiments with 0 MPa of applied vertical stress, VL5 with 5 MPa of vertical stress. INC5 indicates that the fluid pressure in increased in 5 MPa increments. For example, the specimen above is 2a-30-30-VL5, indicating a 30 degree inclination of the flaws (β) and 30 degrees between the flaws (bridging angle α), and 5 MPa of vertical stress. b) Notation denoting regions surrounding the pre-cut flaws. 135
5.2 a) Front and b) oblique view of the pressurisation device used in hydraulic fracturing tests; c) schematic showing the different parts of the device. (From Goncalves da Silva et al, 2015) 136
5.3 a) Overall view and b) schematic of the test setup used in the hydraulic fracturing tests. (After Goncalves da Silva et al. 2015) 137
5.4 Water pressure (red) and rate of AE hits (black) over time for each test. Arrows and black boxes indicate phenomena commented on in the text. Green line indicates the time at which white patching is first visually observed during the experiment. . 139
5.5 Water pressure (blue line) and AE amplitude (scatter data) over time. Green line indicates the time at which white patching was first detected visually. 141
5.6 Relative cumulative proportion of DC (red), CLVD (green) and ISO (red) during the last seconds of each test. Black dashed circles indicate significant numbers of implosive NDC events during and after crack propagation, and purple circles indicate periods of cyclic explosive and implosive NDC events. Crack initiation occurs approximately where the curves flatten out towards the end of the experiment. Note that cumulative proportion of CLVD and ISO can decrease over time since implosion/crack closure events count negatively towards the cumulative proportion whereas explosion/tensile cracks count positively. 143

5.7 Hypocenter locations for each test. The magnitude of the event is shown by the size of the data point. Dark grey lines indicate the cracks, and light grey areas indicate white-patching. The symbols indicate whether the event can be classified as double couple (x), explosive non double couple (Δ), or implosive non double couple (o), and colour represents time, where red is the latest event and blue the earliest. . . . 147
5.8 Test 30-VL5-INC5-C (a) Crack sequence shown in alphabetical order. (T) denotes the cracks open in tension, and subscripts refer to crack type as defined in Wong and Einstein (2009). Black lines denote cracks and grey areas indicate white patching. (b) Pressure-time plot for the experiment. Black squares indicate times used in Figure 5.9. 149
5.9 Temporal evolution of AE hypocenters for test 30-VL5-INC5-C. DC events refer to those with higher double couple, or shear content, explosive NDC (non double-couple) to those with lower DC and positive ISO and CLVD components, and implosive NDC to those with lower DC and negative ISO and CLVD. Colour is used to show time, and size indicates magnitude. Visual observations of the white patching (in grey) and cracking extent (in black) are overlaid where applicable. . . 150
5.10 SEM image taken near the flaw tip of test 2a-30-0-VL5-A showing a series of connected en-echelon microcracks, such as the one highlighted in the orange circles. From Goncalves da Silva (2016). 151
5.11 (a) Crack sequence shown in alphabetical order. (T) denotes the cracks open in tension, and subscripts refer to crack type as defined in Wong and Einstein (2009). Black lines denote cracks and grey areas indicate white patching. Black circle indicates location where crack C coalesces with the left flaw (b) Pressure-time plot for the experiment. Black squares indicate times used in Figure 5.12. 153
5.12 Temporal evolution of AE hypocenters. DC events refer to those with higher double couple, or shear content, explosive NDC (non double-couple) to those with lower DC and positive ISO and CLVD components, and implosive NDC to those with lower DC and negative ISO and CLVD. Colour is used to show time, and size indicates magnitude. Visual observations of the white patching (in grey) and cracking extent (in black) are overlaid where applicable. 154
5.13 (a) Crack sequence shown in alphabetical order. (T) denotes the cracks open in tension, and subscripts refer to crack type as defined in Wong and Einstein (2009). Black lines denote cracks and grey areas indicate white patching. (b) Pressure-time plot for the experiment. Black squares indicate times used in Figure 5.14. 156
5.14 Temporal evolution of AE hypocenters. DC events refer to those with higher double couple, or shear content, explosive NDC (non double-couple) to those with lower DC and positive ISO and CLVD components, and implosive NDC to those with lower DC and negative ISO and CLVD. Colour is used to show time, and size indicates magnitude. Visual observations of the white patching (in grey) and cracking extent (in black) are overlaid where applicable. 157
5.15 Zoomed photo of the bottom flaw of test 2a-30-120-VL0-B and the area below and to the left of it, overlaid by AE events occurring throughout the test. Colour refers to time where red is the latest, crosses refer to DC dominated events, triangles to explosive NDC events and circles to implosive NDC events. The size of the symbols represents the magnitude of the events. 159

5.16 a) Maximum principal stress (tension positive) around the inner left flaw tip of 2a-30-30 geometry for different ratio of water pressure to vertical load (WP/VL). b) Same plot for maximum shear stress. From Goncalves da Silva and Einstein (2014). 161
5.17 Cumulative Benioff strain energy data and AMR fit for a) 2a-30-0-VL5-C and b) 2a-30-90-VL5-C tests. Green line and arrow indicates end of linear energy accumulation. 163

6.1 Schematic of the experimental setup used in this study. The specimen was loaded to a constant axial and lateral load, and then fluid was injected into a pre-cut flaw. The fractures were observed using a high-speed camera, a high-resolution camera and an acoustic emission system. The fluid pressures were measured in the pressure volume actuator and internally in the flaw. b) Photo of the experimental setup used in this study. 167
6.2 Specimen and flaw pressurization device configuration. (a) Schematic of the specimen and pre-cut flaw dimensions, horizontal bedding planes. (b) Schematic of the flaw pressurization device with a 1.5 in [3.81 cm] square seal. (c) Photo of the flaw pressurization device. 168
6.3 Specimens tested in this study. Constant axial (4.5 MPa) and lateral (1 MPa) external stresses were applied. Hydraulic oil was injected at different rates. Four specimens were tested each with a different injection rate. 169
6.4 Fracture progression and pressure-time curves for the test with 0.0807 ml/s injection rate. The PVA pressure was measured at the pump and the internal pressure was measured directly in the flaw. A decrease in the slope of the internal pressure versus time curve was observed at the first fracture initiation and a drop in the internal pressure were observed when fractures reached the seal boundary. 170
6.5 Fracture patterns for different injection rates. The fractures are labeled alphabetically in chronological order. The fractures are usually tensile, however, some sliding was observed in fracture B of the specimen with Q = 0.0807 mL/s. 171
6.6 Fracture speeds observed in this study. Shown are the speeds of the fractures over time, starting at each fracture's initiation time. Specimens tested with higher injection rates showed higher fracture speeds and higher fracture acceleration (slope). The number of fractures for each injection rate was different (See Figure 6.5). . . . 172
6.7 Evolution of flaw pressure over time for the four injection rates tested measured with a transducer inside the pressurized flaw. 173
6.8 Summary of the pressure results for the different injection rates. Increases in maximum pump (PVA)- and internal flaw pressures were observed at high injection rates. The fracture initiation pressure was approximately the same for all injection rates. 173
6.9 AE event locations and orientations for each test. Crosses indicate conjugate shear planes for shear events; the single lines indicate opening direction of non-DC events. Thick black line is the flaw. 175
6.10 Spectra for largest event seen at each injection rate. 175
6.11 Pressure and AE amplitude data for the four injection rate experiments. 177
6.12 Power spectra of AE1 and AE2 (Refer to Figure 6.11). 178
6.13 Internal flaw pressure over time for the second round of tests. 179

6.14 Fracture pattern and maximum internal flaw pressure during second round of injection rate tests. 179
6.15 Location of AE events detected during second round of injection rate tests. 180

7.1 Specimen dimensions in mm and AE sensor locations for a) granite and b) shale. AE sensor locations shown in blue, and dashed lines show nominal bedding plane orientation in the shale. 182
7.2 (a) Image of experimental setup including high speed camera, enclosure, load frame and pre-amplifiers. b) Schematic and image of fluid injection enclosure used on granite specimens (from Gonçalves da Silva and Einstein (2018)). c) Schematic and image of fluid injection enclosure used on shale specimens (from Morgan et al. (2017)) 182
7.3 Image of shale specimen with speckling. Inset shows high speed video frame of speckled region. 184
7.4 Images of the bare rock used in each test, at 5X magnification. 185
7.5 Pressure and AE amplitude over time for each test. Dashed orange and green lines respectively denote beginning and end points for t_{norm} scheme used in subsequent analysis, where $t_{norm} = 0$ is the start of injection, and $t_{norm} = 1$ is the time of highest AE rate. 187
7.6 Maximum (ε_1) and shear strain (γ_{max}) contours at various stages during granite 0.39 mL/s test. Arrows show displacement field, with rigid body translation subtracted such that the mean displacement of the entire area is zero. Red circles indicate en-echelon cracks. 188
7.7 Maximum (ε_1) and shear strain (γ_{max}) contours at various stages during granite 0.019 mL/s test. Arrows show displacement field, with rigid body translation subtracted such that the mean displacement of the entire area is zero. Red circles indicate locations of fracture branching. 189
7.8 ε_1 and shear strain γ_{max} contours at various stages during Opalinus 0.39 mL/s test. Arrows show displacement field, with rigid body translation subtracted such that the mean displacement of the entire area is zero. Red dashed line indicates wedge of opening displacement. 191
7.9 ε_1 and shear strain γ_max contours at various stages during Opalinus 0.019 mL/s test. Arrows show displacement field, with rigid body translation subtracted such that the mean displacement of the entire area is zero. Dashed lines A and B indicate narrow zone of non-horizontal displacement. 192
7.10 Illustration of plumose fracture, from Cobain et al. (2015). 192
7.11 a) Schematic of opening displacement. Displacement is calculated across the crack 1 mm from the notch tip. b) Opening displacement over pressure. c) Opening displacement over normalised time, where t = 0 is the start of injection, and t = 1 is the time of maximum AE amplitude. Green circles indicate the time in each test where the displacement begins to behave inelastically. 194
7.12 Histogram of principal strains for (Left) Granite 0.39 mL/s and (Right) Granite 0.019 mL/s, based on the entire micro-DIC image at $t_{norm} = 1$. 195
7.13 Histogram of principal strains for (Left) Opalinus 0.39 mL/s and (Right) Opalinus 0.019 mL/s, based on the entire micro-DIC image at $t_{norm} = 1$. 195

7.14 Histogram of (left) minimum (ε_3), (middle) volumetric (ε_v), and (right) maximum (ε_1) strain for each test, alongside beam bending data from chapters 3 and 4. Note that the magnitude of probability density and the variance are dependent on the quality of the speckling, where the quality was lowest for the Opalinus beam bending test, and highest for the Opalinus 0.019 mL/s and granite beam bending tests. . 196
7.15 Scatter plot of $\varepsilon_1 - \varepsilon_3$ for each pixel of strain data from all 4 HF tests. 196
7.16 a) Plot of normal and shear displacements across the microcrack at 3 points along the microcrack. This is plotted alongside the rate of acoustic emission hits during the test. Top x-axis shows real time axis in seconds, bottom x-axis shows t_{norm}. b)Image showing the 3 points along the microcrack, at which normal and shear displacements are calculated in a). Blue arrows show the direction along which shear and normal displacements are resolved. a) and b) show the Granite 0.39 mL/s test, and c) and d) show the Granite 0.019 mL/s test. Erroneous data points in c) around $t_{norm} = 0.945$ (shown in orange circle) likely correspond to external factors such as a bubble. 198
7.17 a) Plot of normal and shear displacements across the microcrack at 3 points along the microcrack. This is plotted alongside the rate of acoustic emission hits during the test. Top x-axis shows real time axis in seconds, bottom x-axis shows t_{norm}. b) Image showing the 3 points along the microcrack, at which normal and shear displacements are calculated in a). Blue arrows show the direction along which shear and normal displacements are resolved. a) and b) show the Opalinus 0.39 mL/s test, and c) and d) show the Opalinus 0.019 mL/s test. 199
7.18 AE hypocenter locations for all four tests. 201
7.19 Relative proportion of double couple couple dominated (> 50%), explosive non double couple, and implosive non double couple events (Hudson et al., 1989) captured during the four experiments. 201
7.20 Evolution of AE hypocenter locations over time. The catalogue of events is divided into 6 equal-sized bins, each represented in a single frame. (Left) Granite 0.39 mL/s test, (Right) Granite 0.019 mL/s test. Bold subtitle in each subplot indicates t_{norm}. Size of scatter point indicates magnitude, colour indicates time. 202
7.21 Evolution of AE hypocenter locations over time. The catalogue of events is divided into 6 equal-sized bins, each represented in a single frame. (Left) Opalinus 0.39 mL/s test, (Right) Opalinus 0.019 mL/s test. Bold subtitle in each subplot indicates t_{norm}. Size of scatter point indicates magnitude, colour indicates time. 202

8.1 Final crack pattern of a) granite a-30-30 uniaxial compression test, and b) Opalinus intact compression test. 206
8.2 (Left) Load-displacement data over time for granite a-30-30 uniaxial compression test, and Opalinus intact compression test. (Right) Load-displacement data over time for granite and shale beam bending tests. 206
8.3 Gutenberg-Richter plots for all experiments. 208
8.4 Table 8.1 in graphical format. 208
8.5 a) Unfiltered small amplitude waveform from 0.019 mL/s Opalinus test. b) - e) Waveform filtered at indicated frequency bands. f) Moving average RMS envelope of each frequency filtered wave. 210

8.6 Same as Figure 8.5, but for a large amplitude waveform. 211
8.7 Waveform envelopes for all events detected at channel 5 during 0.019 mL/s Opalinus clayshale experiment, presented for each frequency band. Dotted red line shows slope estimating $-\frac{\pi f}{Q_c}$. 212
8.8 Waveform envelopes for all events detected at channel 5 during 0.019 mL/s granite experiment, presented for each frequency band. Dotted red line shows slope estimating $-\frac{\pi f}{Q_c}$. 214
8.9 Pressure-volume data for HF setup with and without the enclosure and granite specimen. 216
8.10 a) Load-displacement data from beam bending experiments, b) Load-displacement data from uniaxial compression experiments, c) Pressure over time from hydraulic fracturing experiments. 216
8.11 Table 8.4 in graphical format. 216
8.12 Bar chart summarising the radiated seismic energy per unit work for various tests on Barre Granite and Opalinus Clayshale. 218

A.1 Springs are inserted into each opening in the platen, so that the sensors press against the specimen. 236
A.2 Sensors go on top of the spring, and honey acts as couplant between rock and sensor. 236
A.3 Platens, with sensors in them, go around the specimen, and are temporarily held together with elastic bands. this entire assembly will go into the loading machine and/or hydraulic fracture enclosure. 237
A.4 Sensors connect to pre-amps, be sure to connect wires as shown here. 20dB for granite, 60dB for shale. 238
A.5 BNC cables connect pre-amplifiers to data acquisition system. Parametric box also connectors to back to DAQ PC. 239
A.6 To calibrate for moment magnitudes, set up all sensors, place 10cm straw vertically near center of specimen, drop ball in the straw and record the waveform. Repeat 10 or so times. 240
A.7 Settings for measuring wave velocity. Select output file (boxed in magenta) to determine file location. 241
A.8 Schematic of shale specimen, bedding planes in dashed lines. V1 and V2 refer to velocities across and along bedding planes respectively. 242
A.9 Screenshot of settings to use in AE channel setup tab. Please ensure "Global waveform enable" is ticked to save waveforms. 243
A.10 Illustration of a test where channel 1 is recording ambient noise, as seen by the disproportional number hits on channel 1 (Top figure, blue dotted box), and the consistent hits occurring over time (Bottom figure, blue dotted box). 244
A.11 Settings for pre-amplifiers. Purple box is the setting for Glaser sensor/pre-amps. Use same settings as channels 1-7 if PAC sensors/pre-amps are used. 244
A.12 Settings used for waveforms. Sample rate of 5 million samples per second (MSPS), pre-trigger of 256 us and file length of 15k (15000) have been empirically determined to be the most that the system can handle for long periods of time (Li et al., 2015). 245
A.13 Settings used for timing. Only HLT and max duration matter here. 246

A.14 Settings for parametrics window. 246
A.15 Settings for second parametrics window. Gain is set to x100 on channel 1 as the pressure transducer, which has a small range, is on this channel. 247
A.16 Settings for filtering AE data within the PAC software. Usually used when a few channels capture noise (channel is constantly triggered, see Figure A.10), resulting in very large files. In this case, it is easiest to filter that channel by amplitude. . . . 248
A.17 Settings for exporting wavesforms to .csv files to be read into MATLAB. 248
A.18 Photograph of Glaser sensor and accompanying pre-amplifier. 250
A.19 To use the Glaser sensor with the PAC PCI-2 acquisition card, please change the position of the bridge on the acquisition card as shown in the red box in the inset. . 251
A.20 Wiring of the parametric adapter box to use outside sensors (LVDT, pressure, load, high speed trigger) to be saved into the AE data acquisition. This is important when the outside data need to be synchronised to the AE. 252
A.21 Detailed wiring diagram of the parametric adapter box. 253
A.22 List of pins on the parametric adapter box. Refer to Figure A.21 for the wiring diagram. 254
A.23 Photo of the parametric adapter box. Wiring and pins are listed in previous 2 figures. 254

B.1 Photograph of fractured notch Brazilian test on Opalinus clayshale. 256
B.2 Strain maps of fractured notch Brazilian test on Opalinus clayshale. Significant bedding plane compression can be seen in the axial strain. 257
B.3 AE and DIC strain over time of fractured notch Brazilian test on Opalinus clayshale. We can see that the AE events relate mostly to the end of the test, when the crack initiates and propagates. 258
B.4 a) Photograph of small shale HF specimen, b) photograph of the setup, c) pressure-time curves of the large and small specimen tests, d) sample AE waveform showing that the amplitude of displacement is larger than the voltage range of the acquisition system, and so many more smaller amplitude events should be detected if they were produced. 259

List of Tables

2.1 Chronological list of AE workflow. Description column briefly outlines what occurs at each step; Outputs column describes which steps are required for subsequent steps; and Scientific Results column specifies types of raw data obtained at each step, which have scientific value in understanding the behaviour of the rock, and thus may be found in scientific documents. 32

2.2 Table outlining the measurement errors associated with displacement and strain data calculated using DIC presented throughout this thesis. Measurement precision refers to numerical resolution of the measurement, and is presented as the standard deviation of the displacement or strain map between two consecutive frames at the beginning of the test. Effectively, we have applied the analysis shown in Figures 2.14 to 2.17 to all tests. Spatial resolution is also presented, because measurements from the DIC method are averaged over a search area (Figure 2.12), and so the displacement or strain at any location is smoothed by nearby datapoints. The displacement radius is the subset radius described in Figure 2.12, and the strain radius is the area over which the displacement gradients are calculated. 48

2.3 Average elastic constants for the 240 m level URL samples (standard deviation in parentheses). From Eberhardt et al. (1999). 73

2.4 Average crack thresholds for the 240 m level URL samples (standard deviation in parentheses). From Eberhardt et al. (1999). 75

2.5 Investigated Events With the Percentage of the Isotropic Component, Double Couple, and Compensated Linear Vector Dipole[a]. From Sileny et al. (2009). 86

4.1 Predicted plastic zone size for Opalinus clayshale and Barre granite using literature material properties and Irwin's equation (1958). 128

5.1 Summary of test data from the hydraulic fracture stimulation stage of the experimental series. The focal mechanisms are the cumulative proportion excluding the initial vertical loading stage. Note that the absolute value of all the focal mechanism proportions sum to 100%, but –CLVD and –ISO are expressed as negative proportions in this study. 144

5.2 Summary of accelerated moment release (AMR) model applied to AE results. RMSE column indicates goodness of fit between the model and experimental data. 162

5.3 Summary table showing a) whether there all regions of AE activity correspond to visual damage, b) the reverse situation, i.e. whether all regions with visual damage correspond to AE activity, c) whether the point of crack initiation (first crack to form) corresponds to a high concentration of AE hypocenters, d) whether there were multiple clusters of hypocenters i.e. whether one could have made a unique prediction on the point of crack initiation. 164

6.1 AE event locations and orientations for the 0.39025 mL/s injection rate experiment. Crosses indicate conjugate shear planes for shear events; the single lines indicate opening direction of non-DC events. Thick black line is the flaw. 174

7.1 Table showing medians of histograms shown in Figure 7.14 194
7.2 Table summarising scaling relationships. 203

8.1 Summary of seismic energy calculation for each experiment. 207
8.2 Summary of calculated Q for Opalinus clayshale per channel, per frequency band. . 209
8.3 Summary of calculated Q for granite per channel, per frequency band. 213
8.4 External mechanical work done by the injection fluid or loading machine during each experiment. 215
8.5 Table summarising seismic kinetics and kinematics of various tests. $E_R/\tilde{E}$ is calculated from Tables 8.1 and 8.4, and the focal mechanism proportions are taken from previous chapters. 217

Chapter 1

Concerning Rocks

"It's a dangerous business, Frodo, going out your door... You step into the Road, and if you don't keep your feet, there is no knowing where you might be swept off to."

This thesis is largely concerned with rocks, and from its pages a reader may discover much of their character and a little of their history. Further information will also be found in selected manuscripts, listed in the bibliography, that have already been published. Those tales were derived from individual journeys of shale, of granite, of microseims, and of imaging. Many, however, may wish to know more about these remarkable processes as a comprehensive story. For these readers, this thesis should satisfy that burning curiosity. Now then, enough faffing about. I've had my fun. On with the show.

1.1 Objective

Broadly speaking, the goal of the work is to enhance the understanding of microseismicity in the field through laboratory experiments. Currently, the state of the art in field microseismicity (Viegas et al., 2015)(Vermylen and Zoback, 2011) consists of detecting activity using monitoring stations located around the volume of interest, and subsequently using the data to infer characteristics such as location, magnitude and mechanism of the corresponding microseismic sources. With this approach it is difficult, given the generally great depths of the microseismic activity, to verify characteristics such as the extent, orientation and mechanism of the fracturing activity.

In this context, there are two main advantages to laboratory studies of microseisms, henceforth termed acoustic emissions (AE): firstly, the fracture mechanism can be controlled through careful selection of the specimen geometry and loading conditions. This should remove the confounding factor of complex fracture systems that exist in the field. Secondly, the recorded microseismic data can be compared to other sources of information that are not available in the field, such as stress-strain, cracking and water pressure (for failure through hydraulic fracturing). Extensive literature is available on laboratory AE studies (e.g. Ohno et al. (2014); Lockner et al. (1991); Graham et al. (2010)), but most appear to lack corresponding analysis of rock fracturing. Given that the rock mechanics group at MIT has significant expertise in visual analysis of crack-initiation, -propagation, -coalescence there is potential to apply the study of rock fracture to microseismic monitoring.

Specifically, substantial work has been done in the group on visually distinguishing tensile from shear fracturing by the naked eye (Wong and Einstein, 2009a), as well as on process zone development (white patching) (Morgan et al., 2013; Wong and Einstein, 2009a,b) in crystalline materials and marble. There is significant potential to compare these visual observations with detected acoustic emissions. Additionally, a relatively new technology called digital image correlation (Blaber et al., 2015), which can determine displacement and hence strain fields on the specimen, may prove to be an excellent complement to the existing, mostly qualitative, analysis techniques (Lin et al., 2014). In particular, the DIC method can be applied on both a macro- (~cm) as well as a micro- (~sub mm) scale to gain an understanding at different scales.

Given the recent interest in hydraulic fracturing of organic-bearing materials for the oil and gas extraction (Maxwell and Cipolla, 2011), this thesis work additionally focusses on comparing visual and microseismic data in the context of shale fracture processes. This material poses a significant technical challenge, and thus opportunity, given that it tends to be more anisotropic and heterogeneous than the granite, marble and gypsums materials studied previously. Thus, the goals of this thesis are twofold: (1) to study the extent to which acoustic emissions reflect rock fracture initiation and propagation processes observed through imaging, and (2) to compare how these relationships differ from a brittle, crystalline, (mostly) isotropic Granite and a ductile-brittle, sedimentary, highly anisotropic Opalinus Clayshale.

1.2 Thesis Organisation

The mighty tales of this journey are arranged thusly:

1. *Chapter one: Concerning Rocks* is where you, dear reader, are now.
2. *Chapter two: Background and Methodology* first describes the theory and laboratory implementation of acoustic emissions, digital image correlation, and rock fracture. The chapter then summarises relevant previous studies, with a focus on granite and shale.
3. *Chapter three: Tensile Fracture in Granite* describes a series of four point beam bending tests on Barre granite, which was instrumented with AE, Macro-DIC and Micro-DIC in addition to traditional data outputs such as load and displacement. This chapter overlaps significantly with Li and Einstein (2017).
4. *Chapter four: Tensile Fracture in Shale* describes a series of four point beam bending tests on Opalinus clayshale, which was instrumented with AE, Macro-DIC and Micro-DIC in addition to traditional data outputs such as load and displacement.
5. *Chapter five: Hydraulic Fracturing of Granite* describes a series of hydraulic fracturing experiments on Barre granite, which was instrumented with AE, and qualitative high-speed and high-resolution image analysis in addition to traditional data outputs. This chapter overlaps significantly with Li et al. (2019).
6. *Chapter six: Hydraulic Fracturing of Shale* describes a series of hydraulic fracturing experiments on Opalinus clayshale for four injection rates in which AE and qualitative high-speed and high-resolution image data were recorded and analysed in addition to traditional data outputs. This chapter overlaps significantly with Morgan et al. (2017).

7. *Chapter seven: Comparison between hydraulic fracturing in Granite and Shale* describes a series of hydraulic fracturing experiments on Barre Granite and Opalinus clayshale for two injection rates, in which AE and micro-high-speed-DIC were recorded and analysed in addition to traditional data outputs. This chapter overlaps significantly with Li and Einstein (2020).

8. *Chapter eight: Seismic efficiencies* considers the magnitude of AE energy released in all the previously presented experiments, and attempts to establish general principles for different loading conditions and rocks.

9. *Chapter nine: Summary and Conclusions* finishes this wonderful journey with a *wizz!*, *bang!* and *how-do-you-do* to top it all off. Thank you for your attention.

Chapter 2

Background and Methodology

"Some who have read the book, or at any rate have reviewed it, have found it boring, absurd, or contemptible, and I have no cause to complain, since I have similar opinions of their works, or of the kinds of writing that they evidently prefer."

2.1 Acoustic Emissions

2.1.1 Overview

The earliest recorded (Drouillard 1996) observation of acoustic emissions (AE) was in Arabian alchemist Geber's work in the 8th century . He noticed that during smelting, tin would produce a "harsh sound" that later became known as tin cry and that iron would "sound much" during forging. It is possible these sounds would have been noticed as early as the Bronze age (around 3500 B.C.), when man first learned to smelt tin. Other metals such as cadmium, magnesium and zinc were also noted to produce audible acoustic emissions by the mid-19th century. By the 1930s a number of studies established a clear correlation between mechanical twinning in metals and audible sounds whose frequency depended on the geometry of the specimen.

In parallel, advances in technology for measurements of high frequency, small amplitude oscillations allowed one to study acoustic emissions. These included the acoustic horn in the 17th century, the stethoscope in 1816, and the development of electro-mechanical devices in the early 20th century that facilitated conversion from mechanical motion to an electrical signal. One of the pioneers of the field was Josef Kaiser, who performed a number of tensile tests on metal alloys in the late 1940s and 1950s at the Technische Hochschule Munchen in Germany (Tensi 2004). He studied the variation of amplitude and frequency in relation to the stress-strain curve, and one of the most notable observations was the phenomenon that the production of acoustic emissions were irreversible, much like plastic strain. This implies that fewer emissions are observed until the historical maximum stress of a material is reached, and is now known as the Kaiser effect.

We should also consider the relation between AE and seismology, the study of earthquakes. The latter is concerned with the acquisition and analysis of elastic waves that are propagated through the Earth and detected at some distance from the source (Grosse and Ohtsu 2008). This is entirely analogous to acoustic emissions, where sensors gather information regarding elastic waves gen-

Table 2.1: Chronological list of AE workflow. Description column briefly outlines what occurs at each step; Outputs column describes which steps are required for subsequent steps; and Scientific Results column specifies types of raw data obtained at each step, which have scientific value in understanding the behaviour of the rock, and thus may be found in scientific documents.

	Description	Outputs to Subsequent Steps	Scientific Results
Velocity measurement	Calculate pulse travel time between known sensor-receiver pairs.	Velocity used in hypocenter location inversion.	Seismic (ultrasonic) velocity
Magnitude calibration	Calibrate recorded voltages to absolute earthquake magnitude.	Magnitudes required to calculate seismic energy released by focal mechanism.	Calibration curve relating signal amplitude to seismic moment magnitude
Data acquisition	Acquisition and digitisation of motion detected at sensors.	Waveforms used in all subsequent steps.	Magnitude, frequency, hit counts, raw digital waveforms
Arrival time picking	Determine times at which each waveform first diverges from noise band.	Arrival times used in hypocenter location inversion. Waveform amplitude at arrival times used in focal mechanism inversion.	
Hypocenter location	Invert for best fit point in space from which an event originated	Hypocenter locations used in focal mechanism inversion.	Hypocenter locations, event counts
Focal mechanism	Invert for best fit moment tensor to describe each event's first arrival amplitudes		Normal and slip vectors, proportion of double-couple, and non-double couple components

erated from energy released at depth. The main difference between the two fields lies in scale. Where earthquakes occur kilometres within the Earth, acoustic emissions (also sometimes termed nanoseismicity by some researchers) operate at most on the decimetre scale, and are much smaller in magnitude and higher in frequency (Yoshimitsu et al., 2014) than that observed in seismology, as a result of the self-similarity property of earthquakes (Shearer, 2009; Goodfellow et al., 2015). These factors require acoustic emissions equipment to have higher voltage sensitivity and resolution to be able to observe smaller events, as well as operate at higher sampling rates to be able to capture the higher frequency events. Microseismicity lies between the seismic and acoustic emission scale, and generally refers to seismic data captured from the intermediate (up to 100's of metres) scale. These are of interest to industrial and civil engineering projects such as hydraulic fracturing, enhanced geothermal systems, and carbon dioxide sequestration. Further historical details and theoretical treatment can be found in books such as Shearer (2009) and Grosse and Ohtsu (2008).

2.1.2 Acquisition Equipment and Analytical Techniques

The general workflow used by the seismic, microseismic, and nanoseismic communities are quite similar, and can be summarised in Table 2.1 below. This section provides a general outline on each step, then describes the specific AE equipment and setup used in this thesis (shown schematically in Figure 2.1, and provides some theoretical background and technical details on various AE analytical techniques.

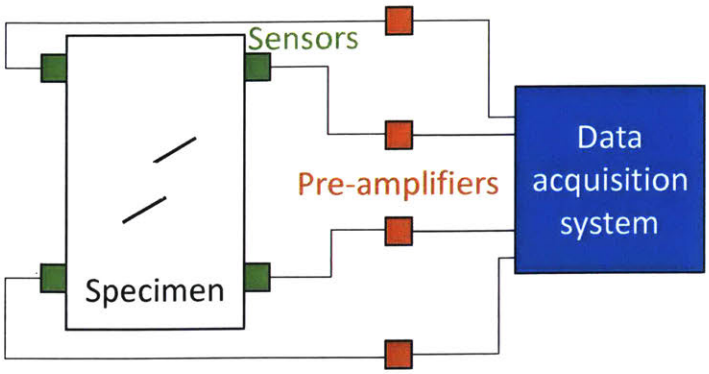

Figure 2.1: Schematic of specimen and AE setup. Microcracks in the rock radiate microseismic waves in the form of elastic waves, which are converted to voltages by the piezoelectric sensors. The sensor voltages are amplified by the pre-amplifiers, and then digitised and recorded by the data acquisition system.

2.1.2.1 Sensors

The digital signal recorded by the acquisition system is the mathematical convolution of the displacement at the source with wave propagation effects in the rock, and with the measurement instrument's response function (McLaskey and Glaser, 2012). At the acoustic emission scale, the sensor has the largest effect on the instrument response, as the commonly-used small piezoceramic elements result in a highly non-linear response function (see line D/A in Figure 2.2). This means that the voltage produced by the sensor is highly sensitive to the frequency of the displacement at the sensor face, and so the voltage output by the sensor is not proportional to displacement, velocity, nor acceleration, but rather a more complicated response depending on the frequency of the excitation. The Micro30S sensors (Mistras, 2015) used in the majority of this work, which are similar to the Nano30 sensors shown in Figure 2.2, suffer from this limitation, with peak sensitivity of -67 dB at 180 kHz and greater than -80 dB sensitivity between 80 and 350 kHz. A few products, such as the Glaser-type sensors, are available with a relatively flat frequency response (See Figure 2.2), but are larger, more expensive, and more difficult to mount due to the sensors' point contact with the rock. Sensor calibration for magnitudes is described in Section 2.1.4.

Sensors in this work are mounted to the specimen with 0.002" 3M VHB acrylic double-sided tape for the granite hydraulic fracturing and beam bending tests, and with a spring loaded platen with honey as couplant in the Opalinus clayshale and micro-high-speed-DIC tests. The spring loaded platens with honey couplant were developed during the course of the thesis work, and is intended to supersede the double sided tape where the experimental setup permits it.

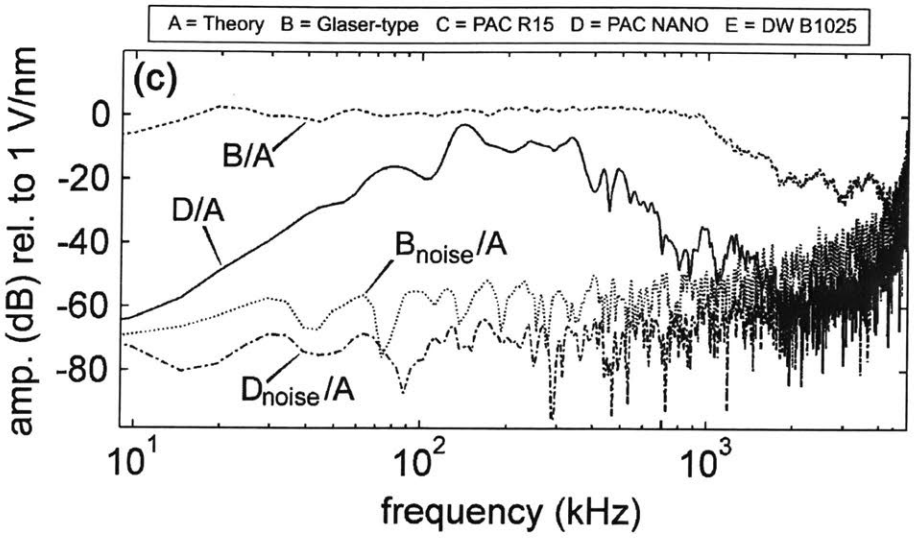

Figure 2.2: Sensor sensitivity on the y-axis plotted over frequency on the x-axis. D/A curve shows the sensitivity of a Nano30 sensor. B/A curve shows the sensitivity of a Glaser-type sensor (McLaskey and Glaser, 2012). To calculate B/A and D/A, sensors are attached to a steel block, on which a glass capillary tube is loaded until breakage. The waveforms (in units of volts) corresponding to the tube breakage are recorded, and expressed in the frequency domain using a Fourier transform. The known theoretical displacement for tube breakage at each sensor location is also expressed in the frequency domain using a Fourier transform, and the amplitude of the recorded waveform is element-wise divided by the amplitude of the theoretical displacement in the frequency domain. A relatively flat sensitivity curve such as B/A indicates that the voltage is a constant multiplier of the displacement across a wide range of frequencies, and so the displacement at any sensor can simply be calculated by multiplying the voltage by a constant value. However, an irregular curve such as D/A indicates that the voltage-displacement relationship depends on the frequency of the displacement, and so more sophisticated calibrations are required to calculate the displacements given a voltage waveform.

2.1.2.2 Pre-amplifiers

Pre-amplifiers are included between the sensor and the acquisition system in order to increase the signal voltage, and thus improve the signal to noise ratio. In this work, the 2/4/6 pre-amplifier from Physical Acoustics Corporation is used, with a 20 dB setting used in granite studies, and 60 dB setting used in Opalinus studies. Do note that this pre-amplifier requires 28V on the outside BNC (Bayonet Neill–Concelman) ring on the data acquisition side, and outputs 28V on the outside ring on the sensor side. Decibels are an expression of signal amplitude, calculated as:

$$dB = 20log(V(\mu V)) \; - \; Amplification \tag{2.1}$$

Where $V(\mu V)$ is voltage in microvolts, and amplification is 20/40/60 dB in this work. We can then see that 20/40/60 dB corresponds to 10/100/1000X amplification.

2.1.2.3 Data Acquisition System

Four PCI-2 data acquisition cards from Physical Acoustics Corporation (PAC) were used in this thesis work. The main parameters in the software were set at 5 MHz, with a file length of 15360 datapoints, maximum duration of 3 ms, and 350 μs hit lockout time to minimise dead time between recordings (More settings and configurations can be found in Appendix A). The final configuration is capable of capturing approximately 84% of all data when triggered continuously. A i7-4790k CPU, 16 GB of DDR3 RAM, and 5400 rpm hard drive was found to be sufficient to support this acquisition system, while the original Core2duo system provided by PAC was not. More details can be found in Li et al. (2015) and Li (2015).

2.1.3 Velocity Measurements

A seismic event is a localised rapid displacement that occurs along a pre-existing plane of weakness, which, as examples, may be a fault at a seismic scale, a bedding plane at a microseismic scale, or a grain boundary at the nanoseismic (AE) scale. This rapid displacement propagates through the rock medium as elastic waves, among which compressional (P) and shear (S) waves are known as the body waves. The velocity at which these waves propagate are, under simplified conditions, expressed as a function of the rock's (or indeed any material's) mechanical properties, as shown in Equation 2.2.

$$\begin{aligned} v_P &= \sqrt{\frac{E(1-\nu)}{\rho(1+\nu)(1-2\nu)}} \\ v_S &= \sqrt{\frac{G}{\rho}} \end{aligned} \tag{2.2}$$

Where E is Young's modulus, G is shear modulus, ν is Poisson's ratio, ρ is density. From a scientific perspective, monitoring these ultrasonic velocities can be used to detect changes in the rock properties, such as damage which tends to decrease the velocity (Sayers and Kachanov, 1995), fluid saturation which tends to increase the velocity (Nur and Simmons, 1969), or confining stress which tends to increase the velocity (Khaksar et al., 1999).

From a practical perspective, the wave velocity is required to invert for the hypocenter location of the seismic event (See section 2.1.6). At the nano- and micro-seismic scale, a homogeneous velocity is sufficient, but at the seismic scale the velocity varies significantly with depth, and so a ray-tracing method should be incorporated along with a heterogeneous velocity model. Additionally, note that a transversely anisotropic velocity model with different velocities along and across bedding planes is generally required in shale. In this work an elliptical distribution is assumed for angles between $v_{parallel}$ and $v_{perpendicular}$.

In this work, the auto sensor test (AST) function in the PAC software (See Appendix A) is used to measure velocities once sensors are attached. The function outputs a text file with travel time between pairs of sensors, and velocity is calculated as distance/time. For shale, it is generally good practice to record the velocity parallel and perpendicular to the bedding plane orientation (See Appendix A).

2.1.4 Calibration to Moment Magnitude Scale

Given the convolutional effects of the wave propagation medium (in this case rock) and instrument response discussed in the previous section, it is necessary to implement a calibration scheme to relate the digital voltages of the waveforms to magnitudes that are relatable to field seismic and microseismic work. In this thesis, we use an empirical calibration method developed by McLaskey et al. (2015), which relates an AE event to moment magnitude (M_w), a parameter commonly used in seismology that describes the total energy transformed during an earthquake (Shearer, 2009). The basis of the method is that the entire system (rock specimen, sensors, preamplifiers, acquisition system) is grouped into a single experimental transfer function that describes how a source (for example, the contact force of a ball drop) is transformed into a recorded electrical signal. This transfer function is determined by dropping a steel ball onto the rock specimen and recording the waveform, which is then divided by its theoretical Hertzian contact function (Equation 2.3) in the frequency domain.

$$\begin{aligned} f(t) &= F_{max} sin(\pi t/t_c)^{3/2} \quad 0 \leq \mid t \mid \leq t_c \\ f(t) &= 0 \quad otherwise \end{aligned} \tag{2.3}$$

Where F_{max} is the maximum force exerted by the ball, and t_c is the time the ball spends in contact with the rock.

As an example, the transfer function for our experiment is shown as the blue curve in Figure 2.3a for a 1.58 mm steel ball using the same notation as McLaskey et al. (2015). Then, the ratio is determined between this transfer function and that of an AE event, and this ratio is taken to be proportional to its moment magnitude M_0 (Equation 2.4).

$$M_0 = \Delta p C_{F\dot{M}} \frac{S^{int}(f)}{\hat{\Psi}^{ext}(f)} \tag{2.4}$$

Where Δp is the ball's momentum loss upon impacting the rock, $C_{F\dot{M}}$ is approximated as $(v_P + v_S)$, $S^{int}(f)$ is the recorded AE waveform transformed into the frequency domain (e.g. purple, red, yellow curves in Figure 2.3), and $\hat{\Psi}^{ext}(f)$ is the recorded waveform of the ball drop divided by the theoretical Hertzian function in the frequency domain (See blue curve in Figure 2.3).

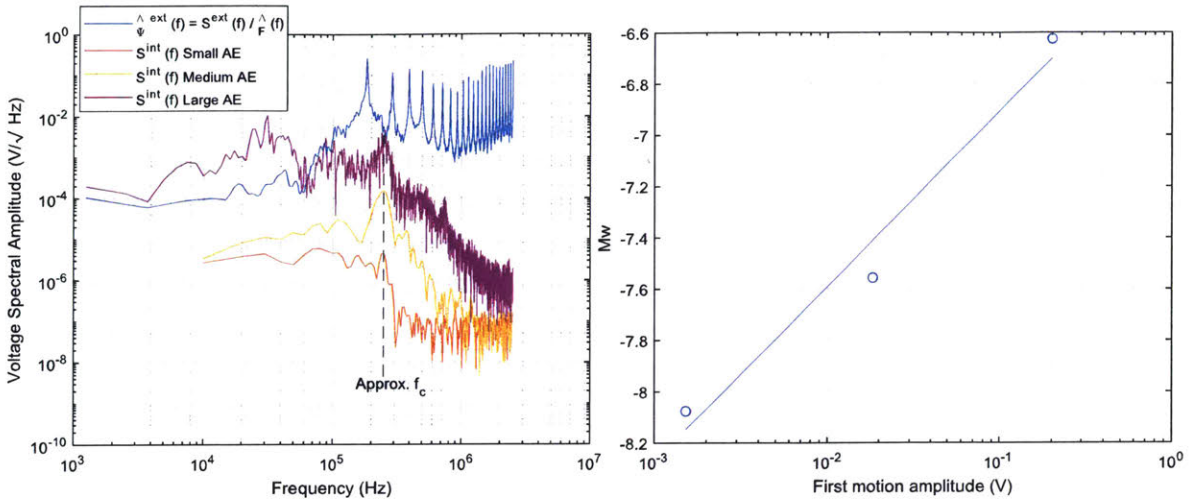

Figure 2.3: (a) Spectra of the instrument-apparatus response and three AE events seen during the four point bending experiment. The notation is the same as that used by McLaskey et al. (2015). The AE magnitudes were M_w = -6.63, -7.56 and -8.08. f_c is the corner frequency of the AE events. (b) For these three AE events, a linear relation was found between M_w and its first motion amplitude. From Li and Einstein (2017).

This calibration was performed for 3 AE events (shown as the red, yellow and purple curves in Figure 2.3a with different amplitudes to capture a range of behaviours, so that the relation between the voltage and M_w can be generalised for the entire catalogue of AE events. In this case, the calculated M_w values were -6.63, -7.56 and -8.08, and it was found that there is a loglinear relation between an event's M_w and its first motion amplitude (Figure 2.3b). This relation was assumed to be correct for the entire experiment since the 3 selected AE events span the range of amplitudes seen in the experiment. Thus, it was applied to the first motion amplitude of all events to calculate its respective M_w. The results are plotted as a cumulative histogram (similar to a grain size distribution), traditionally known as a magnitude-frequency distribution plot (Gutenberg and Richter, 1954), shown in Figure 2.4. It can be seen that the events in the experiment span from M_w = -8 to -6.3, supporting the original notion that the three hand-picked events cover the range of events recorded during the experiment.

As seen in Figure 2.4, the events from the experiment roughly follow the expected quasi-linear relation between magnitude and frequency distribution, with a slight increase in slope (known as b-value in seismology) towards the higher magnitudes. The M_w values range from -6 to -10, which overlap with but are on average smaller than other experiments in granite such as those by Yoshimitsu et al. (2014), where the events tend to cluster between M_w of -5 to -7. The larger AE events also lie in the same range as described in McLaskey et al. (2015), who calibrated two AE events to $M_w = -6.4$ and -7.2. The ball calibration procedure is programmed in the *BallDropCaib.m* code.

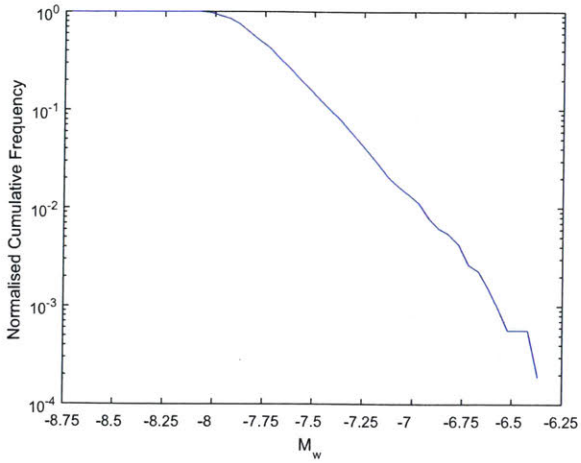

Figure 2.4: Magnitude-frequency distribution plot for all events in the four point bending experiment, based on the calibration shown in Figure 2.3. From Li and Einstein (2017).

2.1.5 First Arrival Picking

Given a raw waveform such as shown in Figure 2.5a, it is necessary to develop an algorithm to detect the onset times where the signal diverges from the noise band, such as shown with the red circles in Figure 2.5b.

The picker implemented in this work achieves this by dividing the entire waveform recording into shorter segments, and picks within these segments. One such segment is shown in Figure 2.5c. The Akaike information criterion (AIC) value (Equation 2.5 (Akaike, 1974)) was then calculated for each segment, which is the AIC value plotted in Figure 2.5c.

$$AIC(t_w) = (t_w - t_0).log(var(R_w(t_0, t_w))) + (T_w - t_{w+1}).log(var((R_w(t_{w+1}, T_w))) \quad (2.5)$$

Where w is each data point of the waveform, t_w is the time at data point w, t_0 is the time at the start of the waveform, $var(R_w(t_0, t_w))$ is the variance of all the voltages from t_0 to t_w, T_w is the time of the last data point, $var(R_w(t_{w+1}, T_w))$ is the variance of all the voltages from t_{w+1} to T_w. In each segment, we then take peaks in the AIC value above a certain height as candidates for a first arrival times (Inverted triangles in Figure 2.5c).

However, this can result in false detections from the signal tail, as seen at 2056.4422s and 2056.4437s (Red circles) in Figure 2.5c. To resolve this issue, the algorithm only takes the arrivals where the signal amplitude as measured by the root mean squared is larger after the arrival than before i.e. we only take arrival picks where the signal is noisier after the arrival than before the arrival. We empirically determined that a time segment length of 0.4 ms with 30% overlap to be appropriate parameters for the tested materials and loading conditions. A minimum AIC peak of $4 \times 10^{-5} s.log(V^2)$ is used in granite, and $5 \times 10^{-5} s.log(V^2)$ is used in shale.

First arrival amplitudes are also determined in this step. The algorithm starts at the picked arrival time, and traverses forward in time until the signal changes sign i.e. reaches the end of that half-wave. The algorithm then considers the maximum (or minimum for a negative half-wave)

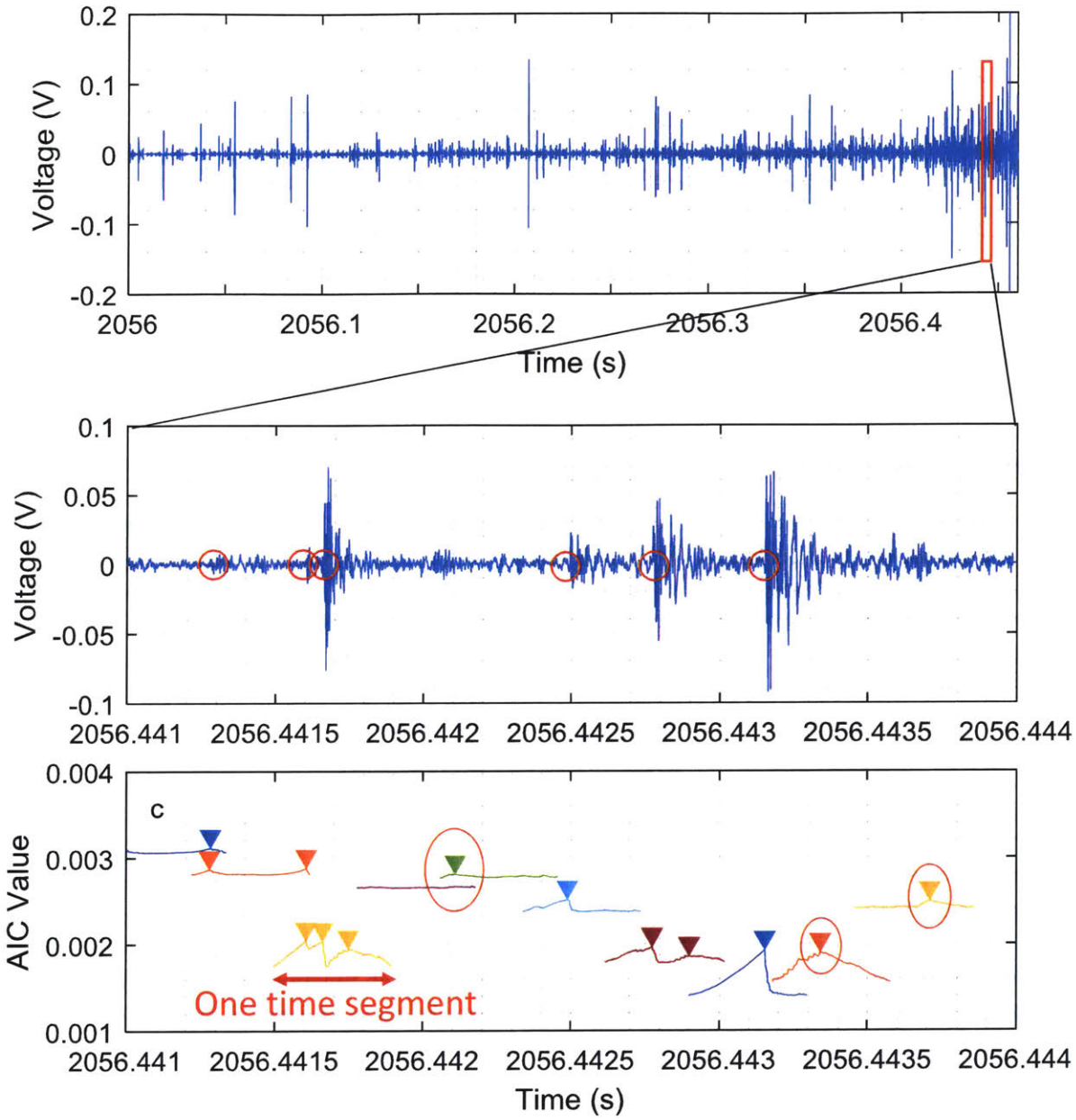

Figure 2.5: a) Waveform data over 0.46 s period immediately prior to failure. b) Close-up of red box in subfigure a, with automatic picks shown in red circles. c) Segmented AIC values for the waveform data shown in subfigure b. Notable peaks in AIC value shown with triangles, while red circles denote false detections. From Li, Goncalves da Silva and Einstein, 2019).

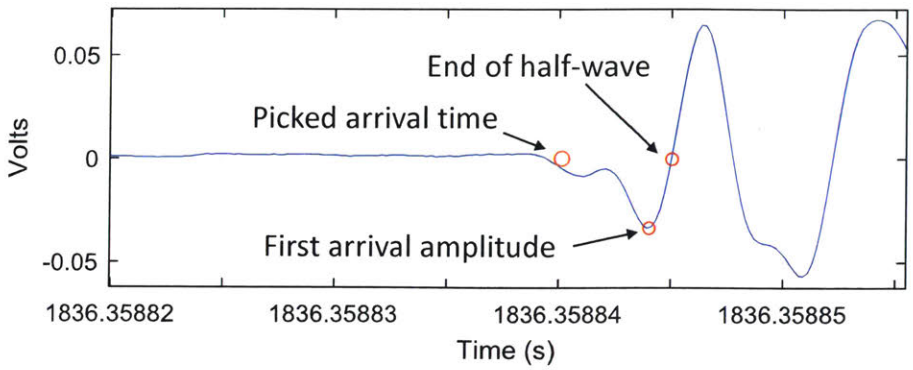

Figure 2.6: Example of first arrival amplitude

voltage within the traversed half-wave as the corresponding first arrival amplitude. An example is given in Figure 2.6. First arrival picking is encoded in the *arrivalPicker.m* code.

2.1.6 Hypocenter Location Inversion

Localisation is the process of inferring the location and time of an acoustic emission event given a set of arrival times detected by the sensor array. This is schematically represented in Figure 2.7, where an acoustic emission is emitted and each sensor detects a waveform after some t_i. The difference between arrival times of different sensors can then be used to predict the location of the source.

This can be expressed mathematically as searching for the position in space that minimises a residual function such as shown in Equation 2.6 (Shearer, 2009).

$$\varepsilon = \sum_{i=1}^{n} \left| t_i - \frac{\sqrt{(x_a - x_i)^2 + (y_a - y_i)^2}}{v} \right| \tag{2.6}$$

Where t_i is the arrival time at channel i, n is the number of channels, x_a and y_a are the assumed co-ordinates of the source, x_i and y_i are the co-ordinates of the sensor, and v is the velocity.

The spatial co-ordinate (x_a, y_a) that produces the smallest ε is the best guess for the source location. This optimisation is implemented using the fminsearch function in MATLAB. In order to constrain the location accuracy, we implement the logic shown in Figure 2.8 to iteratively remove channels with error larger than 1 to 5 mm for granite and 1 cm for Opalinus clayshale. Localisation is encoded in the $tradLoc2_2.m$ and *tradLocAniso.m* codes.

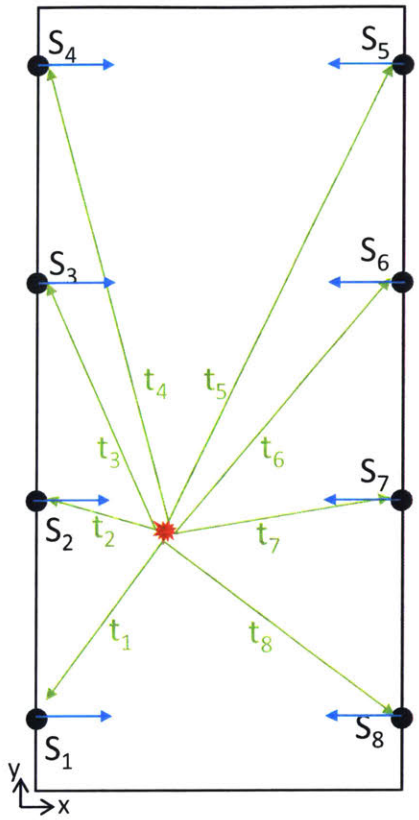

Figure 2.7: Schematic of hypocenter location inversion. Black refers to sensor locations, red to the source location, green to the travel path and associated travel times t_i, and blue to the facing direction of each sensor.

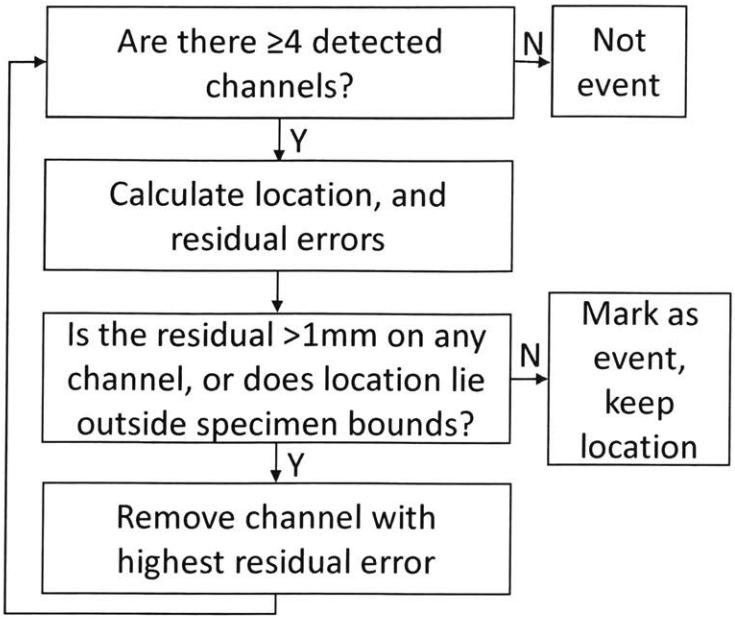

Figure 2.8: Algorithm used to calculate hypocenter locations for AE events and constrain location accuracy. From Li, Goncalves da Silva and Einstein, 2019)

2.1.7 Seismic Source Mechanism Inversion

The premise behind source mechanism inversion is that given only displacements observed at arbitrary locations x and times t, we can deduce some information about an assumed point force f at origin location x_0 and time t_0 that caused the displacements (Shearer, 2009). This can be expressed as:

$$u_i(x,t) = G_{ij}(x,t;x_0,t_0) f_j(x_0,t_0) \tag{2.7}$$

Where u is the observed displacement, G is the Green's function describing wave propagation within the given medium and boundary conditions, and f is the force applied at the source. The Green's function of the Earth is incredibly complex, and for the scale of micro- and nanoseismic events is generally simplified to an elastic half-space, resulting in the following form (Ohtsu, 2000):

$$A(x) = C_s \frac{R_e}{R} r r^T M \tag{2.8}$$

Where $A(x)$ are the first arrival amplitudes observed at the sensor array, C_s is the sensor coupling coefficient, R is the distance between the source and the sensor, r is the vector describing the displacement between the source and the sensor, and R_e is the half space reflection coefficient expressed as:

$$R_e = \frac{2k^2 a(k^2 - 2(1-a^2))}{(k^2 - 2(1-a^2))^2 + 4a(1-a^2)\sqrt{k^2 - 1 + a^2}} \tag{2.9}$$

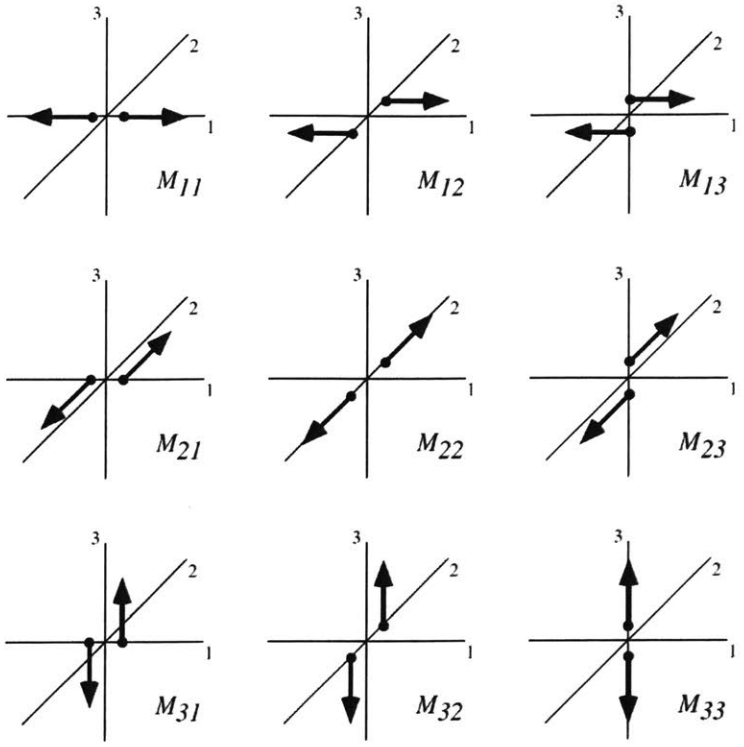

Figure 2.9: Schematic of force pairs that form the moment tensor. From Shearer (2009).

Where $k = V_P/V_S$, and a is the dot product of the vector r from Equation 2.8 and the facing direction of the sensor. The M term in Equation 2.8 is the representation of the forces occurring at the source, and is generally represented as pairs of forces applied along spatial axis i, offset in spatial axis j. There are nine such force pairs in 3D space, creating a 3x3 matrix known as the moment tensor illustrated in Figure 2.9. For example, the forces in the M_{12} term are applied in the 1 direction, and offset in the 2 direction to create a moment. To conserve angular momentum, the tensor is symmetric, i.e. $M_{12} = M_{21}$. Given that a 2D plane stress assumption is taken for the majority of experiments shown in this thesis, we additionally make the assumption that $M_{12} = M_{23} = 0$, and $M_{33} = \nu(M_{11} + M_{22})$, where ν is the Poisson's ratio.

This moment tensor can be decomposed to provide information on both the kinetics and kinematics of the source, however in this work the moment tensor is only used for the kinematics since the method described in Section 2.1.4 provides the moment magnitude of each event, which is sufficient for the kinetics since it allows us to compare our magnitudes to field studies. The first kinematics result is the orientation of the fault on which the slip occurred, and the direction of this slip. This is expressed mathematically as (Vavrycuk, 2011):

$$\begin{aligned} n &= \sqrt{\frac{M_1 - M_2}{M_1 - M_3}} e_1 + \sqrt{\frac{M_3 - M_2}{M_3 - M_1}} e_3 \\ s &= \sqrt{\frac{M_1 - M_2}{M_1 - M_3}} e_1 - \sqrt{\frac{M_3 - M_2}{M_3 - M_1}} e_3 \end{aligned} \tag{2.10}$$

Where n is the normal vector to the fault; s is the slip vector; M_1, M_2, M_3 are the largest,

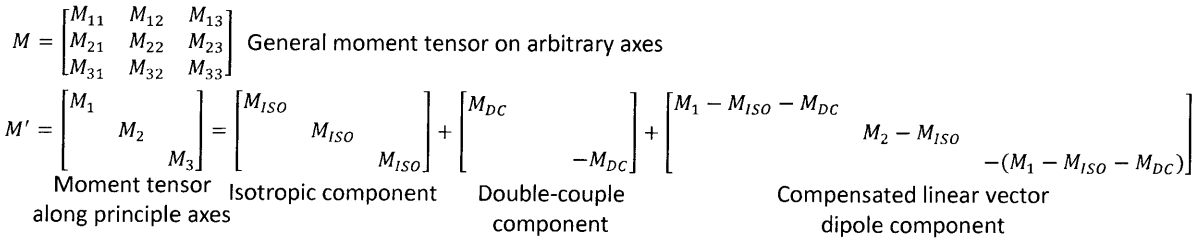

Figure 2.10: Explanation of the decomposition of the moment tensor.

intermediate, and smallest eigenvalues of the moment tensor respectively; and e_1 and e_3 are the eigenvectors corresponding to M_1 and M_3 respectively. One significant limitation of this method is that the normal vector is interchangeable with the slip vector due to the force pair assumption. For example, one cannot determine whether a vertically dipping fault strikes N-S or E-W. Algorithms such as Lund and Slunga (1999), Vavrycuk (2014) and Li and Du (2019) have attempted to address this ambiguity by considering a Coulomb failure envelope for both fault plane-slip vector pairs, and considering the pair closer to the failure envelope as the correct option. However these algorithms rely on a significant number of assumptions and require a large number of events that slip under the same stress state.

The second kinematics result is the source type, namely the relative proportion of isotropic (ISO), double-couple (DC), and compensated linear vector dipole (CLVD) components. The DC component represents the proportion of the moment tensor that represents strike-slip movement along the fault, the isotropic component represents the relative magnitude of volume expansion determined from the trace of the tensor, and the CLVD is a numerical artefact to maintain static equilibrium. These are illustrated in Figure 2.10 can be calculated from the moment tensor using the following formulation (Vavrycuk, 2015):

$$\begin{bmatrix} C_{ISO} \\ C_{CLVD} \\ C_{DC} \end{bmatrix} = \frac{1}{2M} \begin{bmatrix} M_1 + M_2 + M_3 \\ M_1 + M_3 - 2M_2 \\ M_1 - M_3 - |M_1 + M_3 - 2M_2| \end{bmatrix} \qquad (2.11)$$
$$where \quad M = \frac{1}{2}(|M_1 + M_2 + M_3| + M_1 - M_3)$$

Where M_1, M_2, M_3 are the eigenvalues as previously defined. In this formulation, the CLVD and isotropic components can be negative or positive, representing implosion and explosion respectively. Physically, this can be illustrated in Figure 2.11, where we see that an event with a large DC component represents an event with mostly slip along the fault, negative CLVD as collapse of a fault, positive CLVD as a tensile crack (i.e. a directional volume change), positive ISO as an explosion (i.e. an isotropic volume change), and negative ISO as an implosion.

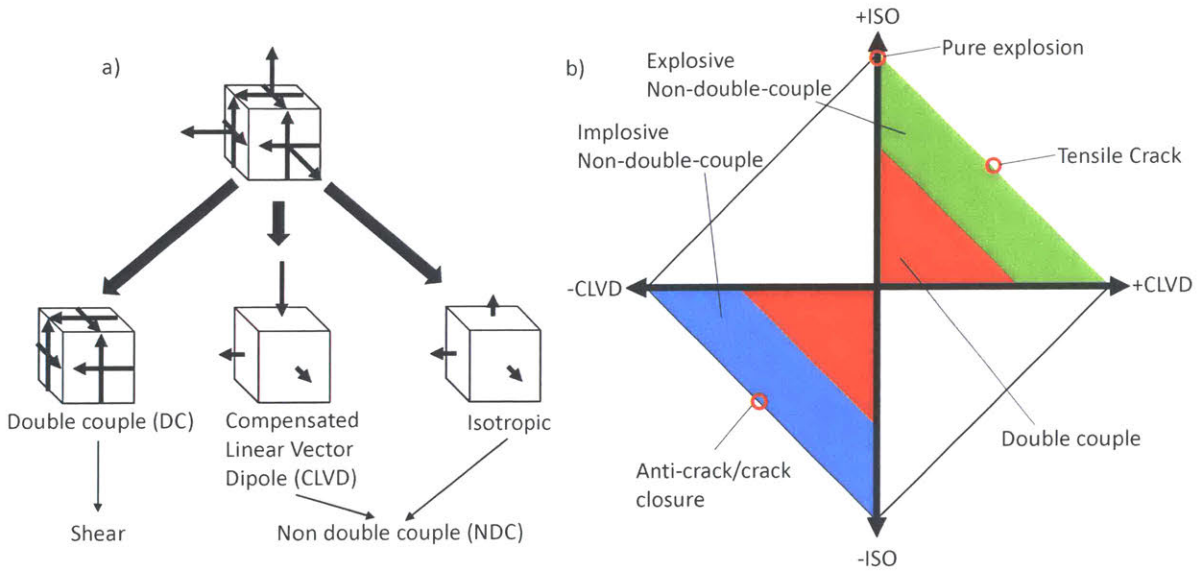

Figure 2.11: a) Illustration of moment tensor decomposition. Adapted from Grosse and Ohtsu (2008). b) Diamond CLVD-ISO plot illustrating AE event classification used in this study. After Vavryčuk (2015).

2.1.8 Seismic Efficiency

The seismic efficiency of an earthquake is defined as the fraction of total energy released by the earthquake (E) that is radiated as seismic waves (radiated seismic energy E_R):

$$\eta = \frac{E_R}{E} \tag{2.12}$$

Radiated seismic energy is generally considered to be $10^{-4}\%$ to $10^{-2}\%$ of the M_0 of an earthquake Shearer (2009), and can also be estimated from the total M_0 of all microseismic events produced during an experiment in the laboratory, as shown by Goodfellow et al. (2015). This is further described in Section 2.3.1.8.

The total energy released is strictly calculated as $E = \frac{1}{2}(\sigma_1 + \sigma_2)DA$, where σ_1 is the stress on the fault before the earthquake, σ_2 is the stress on the fault after an earthquake, D is the displacement along the fault, and A is the area over which slippage occurred. In reality, these parameters are very difficult to accurately measure.

In the laboratory, one can approximate the energy inputs and outputs of the experimental setup as follows:

$$\tilde{E} = E_R + E_{process\,zone} + E_{fracture} + losses \tag{2.13}$$

Where $\tilde{E}$ is the work done by external sources such as the loading machine or pump, E_R is energy radiated as seismic waves, $E_{processzone}$ is the energy dissipated in the process zone through friction and creation of microcracks, $E_{fracture}$ is the energy required to create the new fractures, and $losses$ captures other sources of energy dissipation. This formulation is not rigorous, but following Goodfellow et al. (2015), we only consider the ratio $\frac{E_R}{\tilde{E}}$, denoted seismic energy budget, and consider this to be analogous to the seismic efficiency.

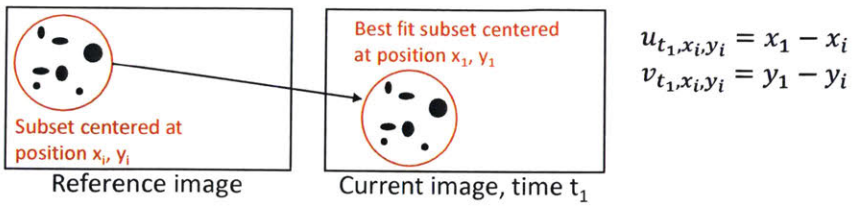

Figure 2.12: Illustration of process to calculate displacement map.

2.2 Digital Image Correlation

Digital image correlation is a class of methods to extract displacement fields from a series of images. This is calculated by comparing the location of a unique pixel pattern across images. The Ncorr code (Blaber et al., 2015) is used in the majority of this work. The code performs correlation, based on subset deformation, where for each subset in the reference image a best fit subset is found in the current image. The difference, in the x and y directions between the current and reference subsets are considered to be the u and v displacements, i.e. displacements in the x and y directions respectively. Given that an image is divided into a large number of subsets, a displacement field can then be generated for each current image. This is illustrated schematically in Figure 2.12, where we see that a subset (the red circle) is considered in the reference image, and the subset radius where the pattern most resembles that seen in the reference image is found in the current image. The difference in the position of the center of this subset is the displacement. This is calculated for each pixel (one can also calculate at each nth pixel by applying a subset spacing) to generate a displacement map. The reference image is compared to each current image independently, to generate a series of displacement maps.

The displacements can then be transformed into strain fields ε_{xx}, ε_{xy} and ε_{xy} as specified in Equation 2.14, and these strain fields can be used to better understand the process zones and cracks created during loading.

$$\begin{aligned} \varepsilon_{xx} &= \frac{1}{2}(2\frac{\partial u}{\partial x} + (\frac{\partial u}{\partial x})^2 + (\frac{\partial v}{\partial x})^2 \\ \varepsilon_{xy} &= \frac{1}{2}(\frac{\partial u}{\partial y} + \frac{\partial v}{\partial x} + \frac{\partial u \partial u}{\partial x \partial y} + \frac{\partial v \partial v}{\partial x \partial y}) \\ \varepsilon_{yy} &= \frac{1}{2}(2\frac{\partial v}{\partial y} + (\frac{\partial u}{\partial y})^2 + (\frac{\partial v}{\partial y})^2 \end{aligned} \tag{2.14}$$

The code has been shown to work well for geotechnical materials (Zhang et al., 2016; Stanier et al., 2015; Li and Einstein, 2017), and a similar approach has been used successfully on the micro-scale in marble (Tal et al., 2016). For the purposes of this thesis ε_{xx} is considered as opening or tensile strain, given that it corresponds to the primary tensile stress induced by the boundary conditions. Similarly, ε_{xy} is considered to be the shear strain given that it is oriented 45 degrees to the primary tensile stress field, and is required in addition to ε_{xx} in order to fully understand the Mohr's strain circle. Note that a positive ε_{xy} describes a motion where the "top" half of the fracture moves "leftwards" while a negative ε_{xy} describes the reverse situation. The full strain state is considered because this and other studies (Morgan et al.,2013; Goncalves da Silva et al., 2016) have noted en-echelon cracking even in a generally tensile stress state.

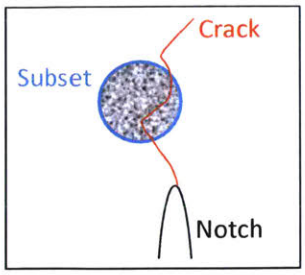

Figure 2.13: Schematic of the DIC subset including a portion of a crack. DIC results will average effect of the crack over the entire subset.

One of the main limitations of DIC is that the displacement and strain calculations assume a continuous medium and thus cannot account for discontinuities, which is precisely the definition of a crack. Blaber et al., (2015) provide a solution to this by allowing the subset to be truncated at the crack. However, this method requires the crack geometry to be precisely known. In the experimental setups of this thesis, the crack opening was small enough such that the overlying paint did not separate, and so this solution could not be applied since the exact crack geometry could not be identified. As a result, areas immediately near the crack may not describe the strain experienced by the material if the pixels are within the zone of influence of a crack, as illustrated in Figure 2.13. To mitigate this, we have chosen the subset radius (blue circle in Figure 2.13) to be as small as possible (generally 10-15 pixels for macro-DIC, and 15-30 pixels for micro-DIC) to minimise the pixels over which the discontinuity affects the results. Similarly, the strain search radius is kept small at around 2-3 pixels to minimise the zone of influence of the crack. The drawback of the small subset radius is that it tends to increase the noise observed in the DIC results. A quantitative treatment of this source of error is presented in Section 2.2.1.

Nevertheless we present most of our visually observed data and interpretations in the form of strains as opposed to displacements since it more clearly illustrates the extent and nature of the process zone both at the micro- and macro- scale. This is also justified given that there is generally a gradual transition from the process zone to the existence of a crack.

In this work we refer to macro-DIC as captured from images at smaller than 1X magnification, and micro-DIC as captured from images at approximately than 5X magnification.

2.2.1 DIC noise quantification

In order to understand the level of background noise in the current implementation of the DIC method, two images captured two seconds apart during the elastic deformation stage were chosen since the amount of displacement is minimal and it is assumed that the majority of the calculated displacement can be attributed to noise. DIC was applied between these two images, and the opening displacement is shown in Figure 2.14. The ε_{xx}, which was calculated from the displacements, is shown in Figure 2.15. These are shown at subset radii of 15, 30 and 60 pixels, where 15 was the radius used in this study. The larger radii produce data that are less noisy since they are averaged over a wider area.

Figure 2.14 shows that for the displacement data, the noise in general increases as the subset radius shrinks. Specifically, it is observed that much of the noise occurs in the form of zones of

	Measurement precision		Spatial resolution	
Test	Displacement standard deviation (μm)	Strain standard deviation	Displacement radius (μm)	Strain radius (μm)
Granite FPB macro	75.5	0.15%	143.0	171.6
Granite FPB micro	3.7	2.69%	17.1	20.5
Opalinus FPB macro	3.0	0.26%	97.2	291.7
Opalinus FPB micro	1.2	2.09%	25.5	42.4
GR HF 0.39 mL/s	0.3	0.47%	82.2	104.1
GR HF 0.019 mL/s	0.4	1.17%	82.0	103.9
OPA HF 0.39 mL/s	0.4	0.99%	82.2	104.1
OPA HF 0.019 mL/s	0.2	0.32%	81.8	103.7

Table 2.2: Table outlining the measurement errors associated with displacement and strain data calculated using DIC presented throughout this thesis. Measurement precision refers to numerical resolution of the measurement, and is presented as the standard deviation of the displacement or strain map between two consecutive frames at the beginning of the test. Effectively, we have applied the analysis shown in Figures 2.14 to 2.17 to all tests. Spatial resolution is also presented, because measurements from the DIC method are averaged over a search area (Figure 2.12), and so the displacement or strain at any location is smoothed by nearby datapoints. The displacement radius is the subset radius described in Figure 2.12, and the strain radius is the area over which the displacement gradients are calculated.

zero displacement, which is particularly notable for the data calculated from a radius of 15 pixels. This may be attributed to the speckle pattern, which due to its random nature contains larger areas that are entirely white or black, and so using a smaller radius causes the displacement calculated from these monochromatic zones to be zero. However, it can be seen that overall the magnitudes and trends in the displacement are consistent between the 15 pixel radius used in this study and the larger radii. In terms of the strain shown in Figure 2.15, it appears that a doubling of the radius results in approximately three times reduction of the standard deviation in the strain, which was true for the increase from 15 to 30 pixels, and 30 to 60 pixels. This implies that the error decreases linearly from a 15 pixel radius to a 60 pixel radius, and so there is no optimum point at which a larger radius provides marginal benefits to noise reduction. As a result, the smallest radius of 15 pixels was chosen since this minimises the area over which the crack discontinuity affects the displacement and strain data. As shown in Figure 2.16, the noise is still small enough such that it does not significantly inhibit the ability to discern process zone features and extent. We suggest that areas within this 15 pixel radius, along with areas exhibiting strains above a threshold opening strain of 3% are likely those affected by the discontinuity of the crack. However, it is important to note that the focus of this paper is on the shape, extent, and features of the process zone as opposed to the specific magnitude of the strains.

A similar quantification of noise is shown for the micro-DIC in Figure 2.17, where we chose the smallest subset radius from which displacement could be reliably calculated. The noise is larger in the micro-DIC than the macro-DIC due to the 25 μm spacing on the mesh, which has a larger spacing between features than the optimal 3x3 pixel/speckle size in the current state of practice. This regular mesh configuration is less accurate than speckling since the pattern is not unique. It was not possible to use a smaller mesh as they are very easy to tear as the spacing becomes smaller.

The above approach is applied to all the DIC results presented in this thesis, and listed in Table 2.2.

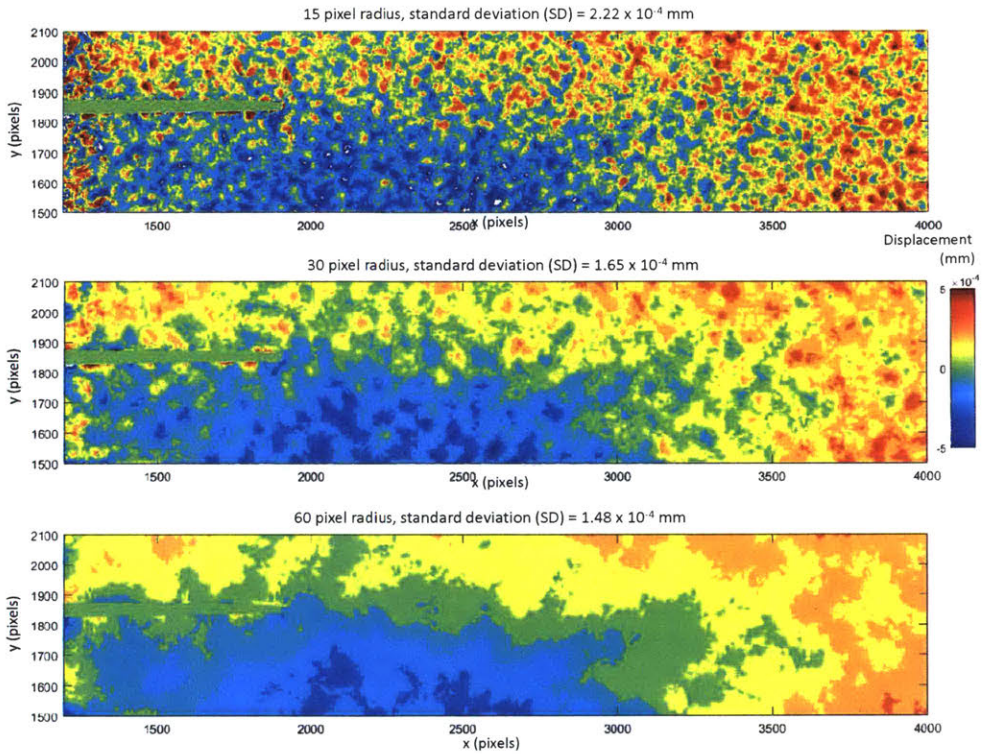

Figure 2.14: Contour plot of opening displacement (mm) between images taken 2 seconds apart using different subset radii. Standard deviation of the displacement map is given in each figure heading. From Li and Einstein (2017).

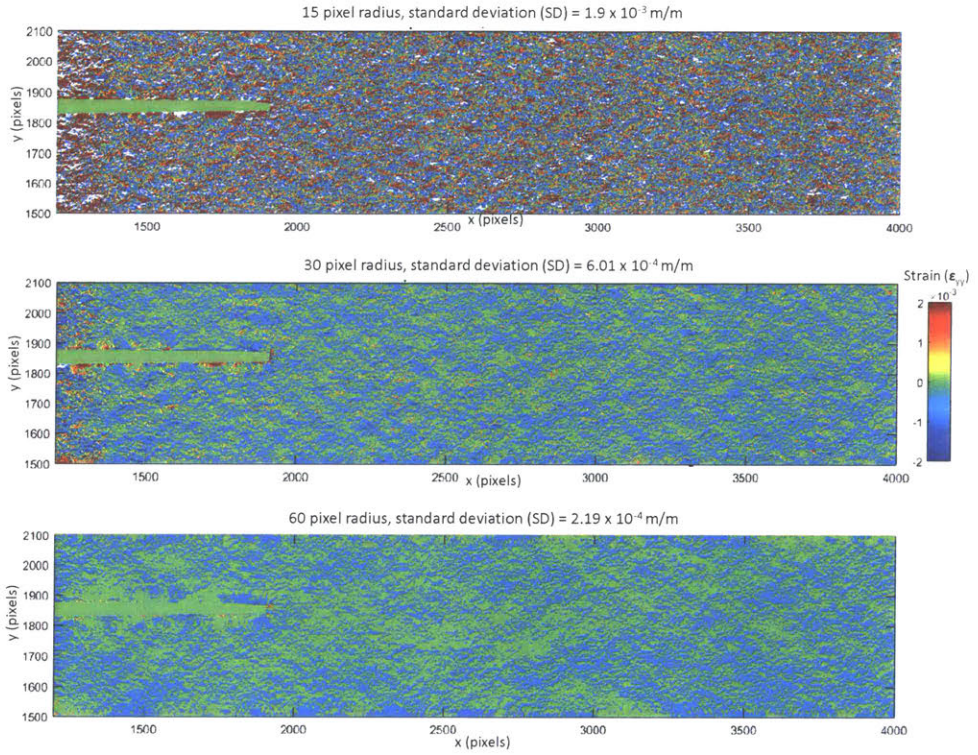

Figure 2.15: Contour plot of ε_{yy} calculated from the displacement data shown in Figure 2.14. Standard deviation of the strain maps are given in the figure headings. Li and Einstein (2017).

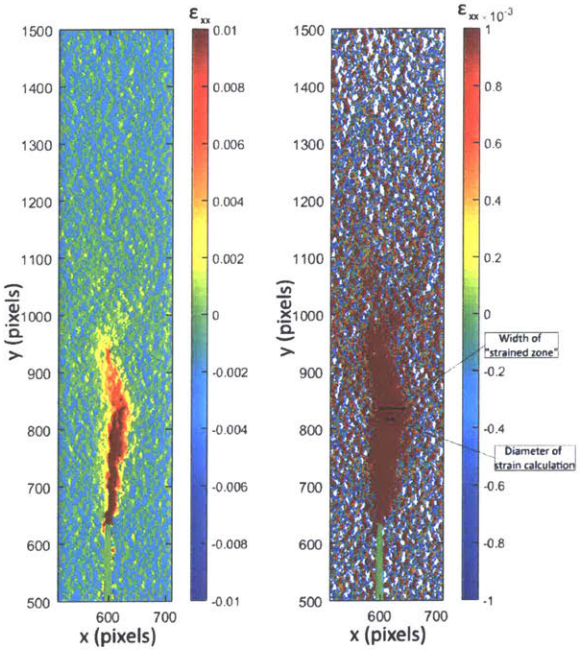

Figure 2.16: Contour plot of ε_{xx} for images exhibiting significant process zone development. (Left) Data plotted with strain contours from -0.01 to +0.01. (Right) Same data with strain contours from -1E-3 to +1E-3 to highlight the extent of the process zone. It can be seen that the width of apparent process zone exceeds the diameter of the DIC calculation. Li and Einstein (2017).

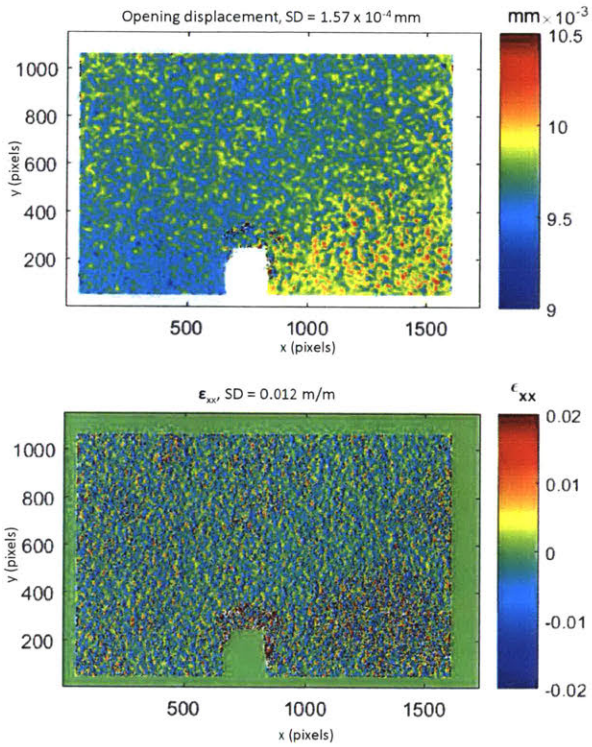

Figure 2.17: Opening displacement and ε_{xx} for images taken 2 seconds apart for the micro-camera. Standard deviation of the strain maps are given in the figure headings. Li and Einstein (2017).

2.2.2 Zone of Large Strain Ahead of the Crack Tip

Given that the imaging and DIC methods are applied in many cases to understand the development of the crack and the highly strained (and by association highly stressed) zone ahead of the crack tip, it is important to first define this zone. In the literature, the concept has been referred to as the process zone (Botvina and Korunsky, 2005; Neimitz et al., 1987), the inelastic zone (Labuz et al., 1987; Brock et al., 1985)), the cohesive zone (Park and Paulino, 2011; Broek, 1982; Lin et al., 2014; Neimitz et al., 1987), the plastic zone (Broek, 1982; Botvina and Korunsky, 2005), and the damage zone (Labuz et al., 1987; Botvina and Korunsky, 2005), among other terms. We suggest that these terms, especially in the context of an experimental study, are not significantly different.

Neimitz et al. (1987) describe the process zone as: "the notion of the process zone (PZ) is broadly used in fracture mechanics. It consists of a small region surrounding the crack tip. It is a controlling factor for the onset of instability as well as for crack growth. Its size and shape depends on the nature of the material and the level of loading. It has different features for brittle, ductile or environmental fracture. Usually, continuum mechanics arguments are applied outside of this zone, while a distribution of "cohesive" forces is postulated in its interior." That is, we may regard the process zone as the zone within which linear elastic fracture mechanics does not apply, as the stress cannot be inifinitely high at the crack tip. Similarly, the inelastic zone was defined by Brock et al., (1985) as "distributions of screw dislocations, and one such distribution growing from a crack edge prior to crack propagation is considered." That is, some area ahead of the crack tip where the material does not behave elastically as defects have formed at the molecular level.

The plastic zone is defined by Broek (1982) as "According to the elastic stress field solutions discussed in the previous chapter a stress singularity exists at the tip of an elastic crack. In practice; materials (especially metals) tend to exhibit a yield stress, above which they deform plastically." This is a rigorous definition and is useful for numerical models, as one can define a threshold stress value beyond which the material behaviour is considered to yield, and thus can be included within the plastic zone.

The cohesive zone is another model first proposed by Dugdale (1960), and is described by Park and Paulino (2011) as "Cohesive interactions approximate progressive nonlinear fracture behavior, named as the cohesive zone model. Cohesive interactions are generally a function of displacement jump (or separation). If the displacement jump is greater than a characteristic length (dn), complete failure occurs (i.e., no loadbearing capacity)." This model conceptualises the process zone as some area where there is a discontinuity in displacement, i.e. the material is opening on either side of the pre-crack, but that there are some cohesive forces between the sides of the pre-crack which eventually vanish to zero at the crack tip, defined by some value of opening. In this work, we denote this zone as the inelastic or process zone, as they appear to be most general and fitting for an experimental study since we do not assume any conceptual model for the behaviour.

2.3 Previous Studies

This section presents data from existing studies that provide insight on fracture processes. As described in Chapter 1, we are most interested in hydraulic fracturing, and within this topic concerned with (1) the extent to which microseismic data are representative of the underlying hydraulic fracture processes, and (2) how these phenomena differ between a brittle, coarse grained, granite and

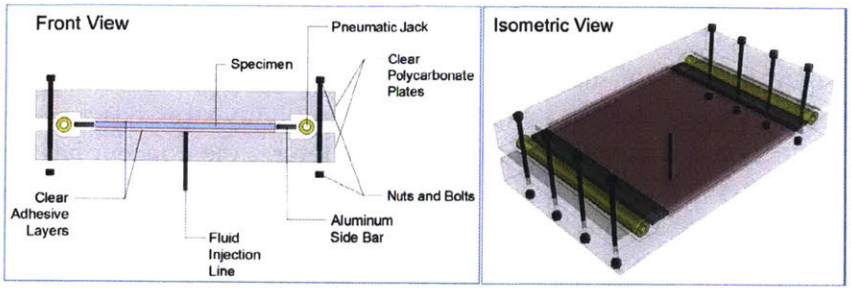

Figure 2.18: Schematic of fracture cell (AlTammar et al., 2018).

a ductile, fine grained, Opalinus clayshale.

2.3.1 Laboratory Studies

2.3.1.1 The Effect of Pore Pressure on Hydraulic Fracture Growth: An Experimental Study (AlTammar et al., 2018)

In this study, the authors present results from a series of tests where 5.1 mm thick plaster-talc specimens with various borehole configurations were uniaxially loaded, sealed within a polycarbonate enclosure, and glycerin was injected until hydraulic fractures were created. The experimental setup can be seen in Figure 2.18. The specimen was speckled with paint, and images taken at 30 fps were used to calculate displacement and strain fields using Ncorr (Blaber et al., 2015).

The authors present results from 13 tests, the most interesting of which is shown in the Tresca strain plots over time in Figure 2.19. In this test, fluid pressure in the bottom right hole is held at 1.03 MPa while the other three outer holes are held at 0.28 MPa, and fluid pressure in the center hole is increased until hydraulic fractures propagate to the edges of the specimen. We see that the fracture initiates in the x-direction, i.e. it ignores the bottom right borehole, but over time the fracture bifurcates and one branch propagates towards the bottom right hole as a series of en-echelon fractures. Once this secondary fracture fully connects to the bottom right hole, the fracture again bifurcates, and the new branch propagates away from the bottom right hole, presumably as a result of the fluid pressure in the bottom right hole increasing as a result of its direct connection to the higher pressure in the center hole. From this study, we learn that the DIC tool is powerful for analysing development of hydraulic fractures, and also that the direction of fracture propagation is quite sensitive to regions of higher or lower pressure, and may bifurcate when these regions of higher or lower pressure change. Do note, however, that the study does not address the issue that strain, defined only on a continuous medium, is here defined across a crack, which is by definition a discontinuity.

From the other tests, the authors overall conclude that regions of high pore pressure affect the propagation of hydraulic fractures; that breakdown pressures were lower when adjacent holes were also pressurised; and that closely spaced injection ports tend to result in multiple fractures that propagated along σ_1. The study also highlights the potential of the DIC method to easily identify the growth of hydraulic fractures over time in a laboratory setting. The authors do not, however, take advantage of the quantitative nature of the DIC data as we do in this thesis.

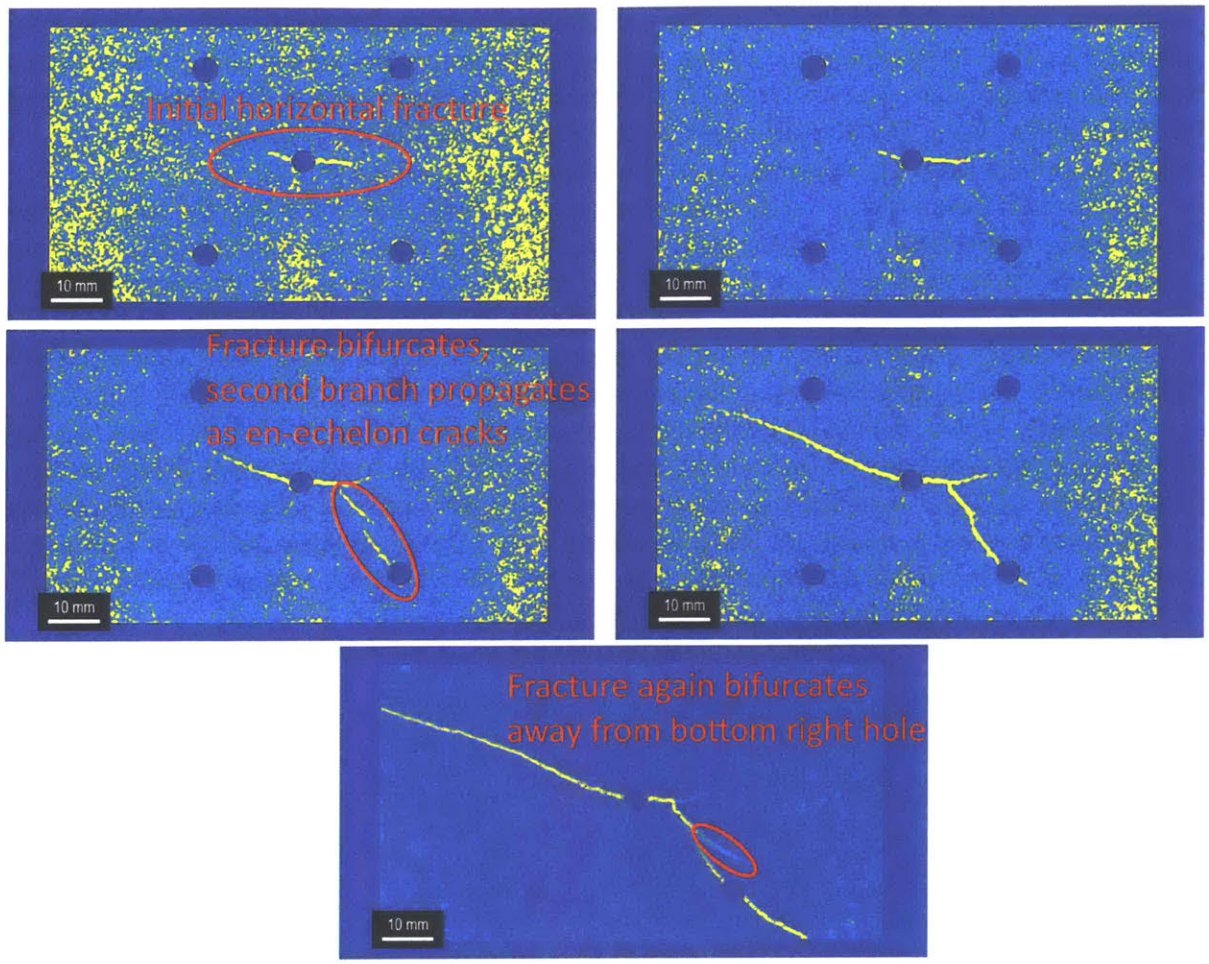

Figure 2.19: A series of contour maps showing Tresca strain calculated from digital image correlation applied to hydraulic fracture test 9, where far field stress = 0.34 MPa is applied and held constant in the x-direction. Then, all holes are saturated at a constant fluid pressure of 0.28 MPa for 80 minutes, at which time fluid pressure in the bottom right hole is increased to 1.03 MPa for 2 minutes, and finally fluid pressure in the center hole was increased until fracturing occurred at 2.37 MPa. Each subfigure shows the strain at an unspecified time, and no colourbar is provided in the original journal article. From AlTammar et al., 2018.

2.3.1.2 Opening and mixed mode fracture processes in a quasi-brittle material via digital imaging (Lin et al., 2014)

In this study, the authors conduct a series of three point beam bending tests on Berea sandstone, where the position of the notch is offset from the axis of the loading platen to generate both shear and tensile stresses at the notch tip. This offset was different in each experiment to vary the relative magnitude of shear and tensile stress. The experiments were conducted in crack mouth opening displacement (CMOD) control so that the tensile fracture propagates slowly over a time period of over 500 seconds, and were instrumented with load, displacement, and high resolution imaging, with the goal of using DIC to observe the effect of the the ratio of stress intensity factors ($\frac{K_I}{K_{II}}$) on the displacement field. The specimen is shown schematically in Figure 2.20.

Figure 2.21 shows that the DIC method is capable of identifying the tip of a cohesive zone (CZ), which in this thesis we call the process zone. They also identify a slip zone (SZ), where the crack is fully debonded, that can be identified by tightly spaced opening displacement contours. Figure 2.21 also shows that the displacement is almost entirely opening even for the beam with 11.4 % eccentricity. The authors also select query points along the crack, which allows them to quantitatively evaluate the opening of the crack in space and time as shown in Figure 2.22.

This study served as inspiration for the work presented in Chapters 3 and 4, where we take advantage of the quantitative nature of DIC and compare DIC data to AE captured during the same test. The use of CMOD control also allows us to fully capture the time behaviour of the fracture, which is not possible in traditional brittle fracturing tests since the fractures initiate and propagate rapidly over the period of microseconds. We also take the additional step of evaluating strains, which are not considered in the Lin et al. (2014) study.

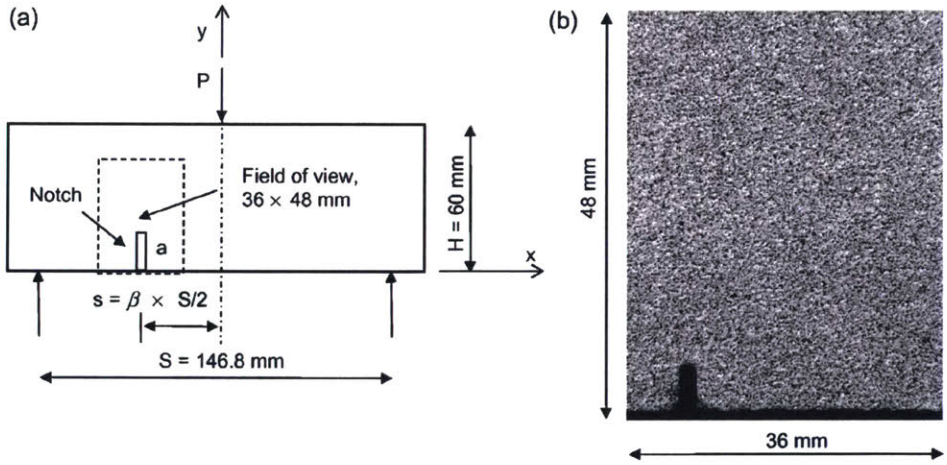

Figure 2.20: (a) Loading geometry and observation region (dashed lines) on the specimen surface used in the Lin et al. (2014) study. (b) Typical digital image where the rock is speckled and the notch is on the bottom left.

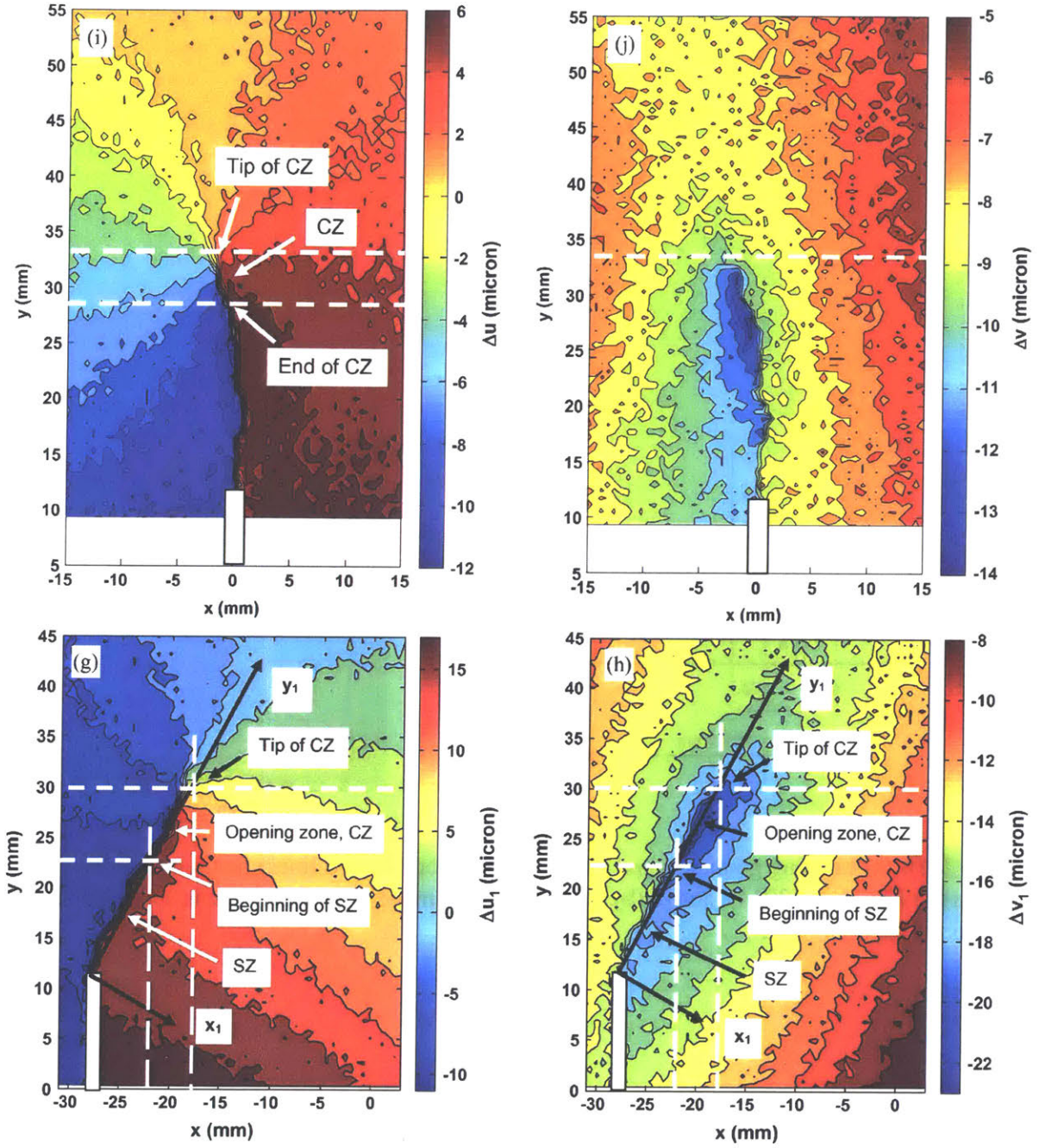

Figure 2.21: Displacement contour maps at 80-70% of post peak load. Left two plots show horizontal displacement, right two plots show vertical displacement. The load platen is in line with the notch in the top two plots (See Fig. 2.20), which creates zero eccentricity, while the load platen is offset from the notch in the bottom two plots, resulting in a beam with 11.4 % eccentricity (See Fig. 2.20). The authors identify cohesive zones (CZ, referred to as process zone in this work) and slip zones (SZ, referred to as "behind the crack tip" in this work) based on shape of the displacement contours. From Lin et al. (2014).

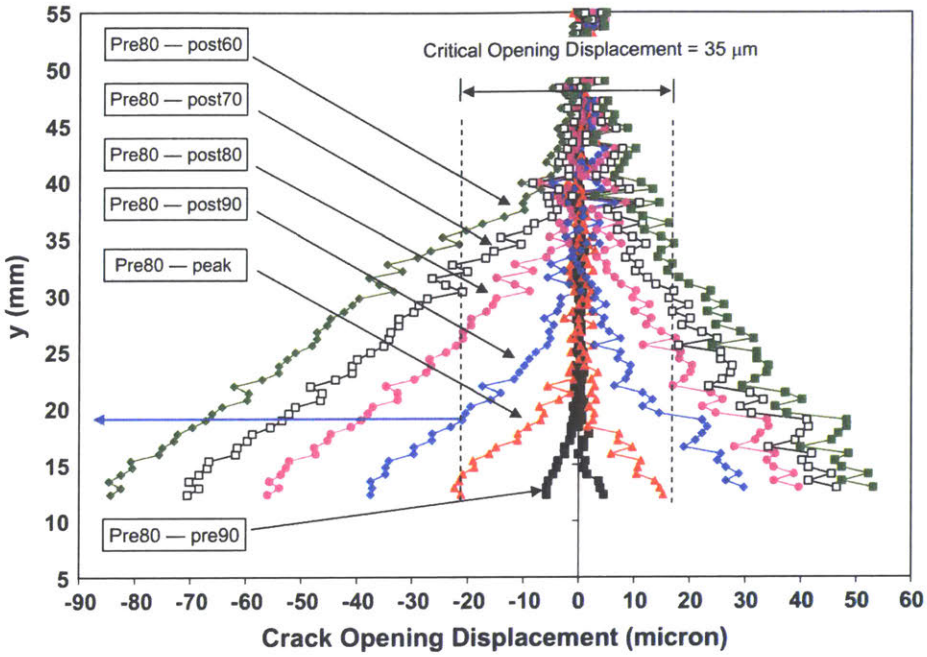

Figure 2.22: To create this plot, the authors considered the final crack path shown in Figure 2.21a, and selected query points along the crack at which the x displacement on either side of the crack was sampled over time. The y axis of this plot shows the distance from the notch tip to each query point, and the x axis shows the magnitude of displacement at that query point. Each coloured line represents an increment in time. Each query point is sampled on either side of the crack, and the displacement on the left side of the crack is plotted on the left side of this graph, and a similar treatment was afforded to the right side of the crack. The subtraction between the left and right side of the same increment in time gives the total opening displacement of the crack at that time. From Lin et al. (2014).

2.3.1.3 Direct observations of damage during unconfined brittle failure of Carrara marble (Tal et al., 2016)

The authors conduct a series of uniaxial compression tests at a displacement rate of 0.5 $\mu m/s$ on 12 mm x 12 mm x 5 mm specimens of Carrara marble at varying temperatures. They then coat a 1.16 mm x 0.85 mm area in the middle of the specimen (See Figure 2.23) with a carbon vacuum-sputter on a 2000 wires/inch mesh to create a regular grid on the face of the specimen. Images were then taken throughout the experiment, and were analysed by DIC obtain strain maps over time.

Figure 2.24a shows the stress-strain curve for a specimen tested at 105 ^{o}C, which is labelled with frames 1-6 at which the strains are shown in Figure 2.24b. We can see that the development of significant strains begin after frame 2, which is when the stress-strain curve begins to show ínelastic deformation. Significant localised strains continue to develop as the experiment continues.

Overall, this study introduced the concept of utilising DIC at a microscopic scale to study the development of microfractures in real time throughout an experiment, given that the microseismic events detected throughout an experiment tend to also be on the microscopic to nanoscopic length scale. The micro-DIC results presented in Chapters 3, 4 and 7 were inspired by this study. Note that in our results the micro-DIC data are located at the tip of a pre-cut notch in order to control the location of fracture initiation, whereas in this study the window of observation was simply located in the center of an intact specimen.

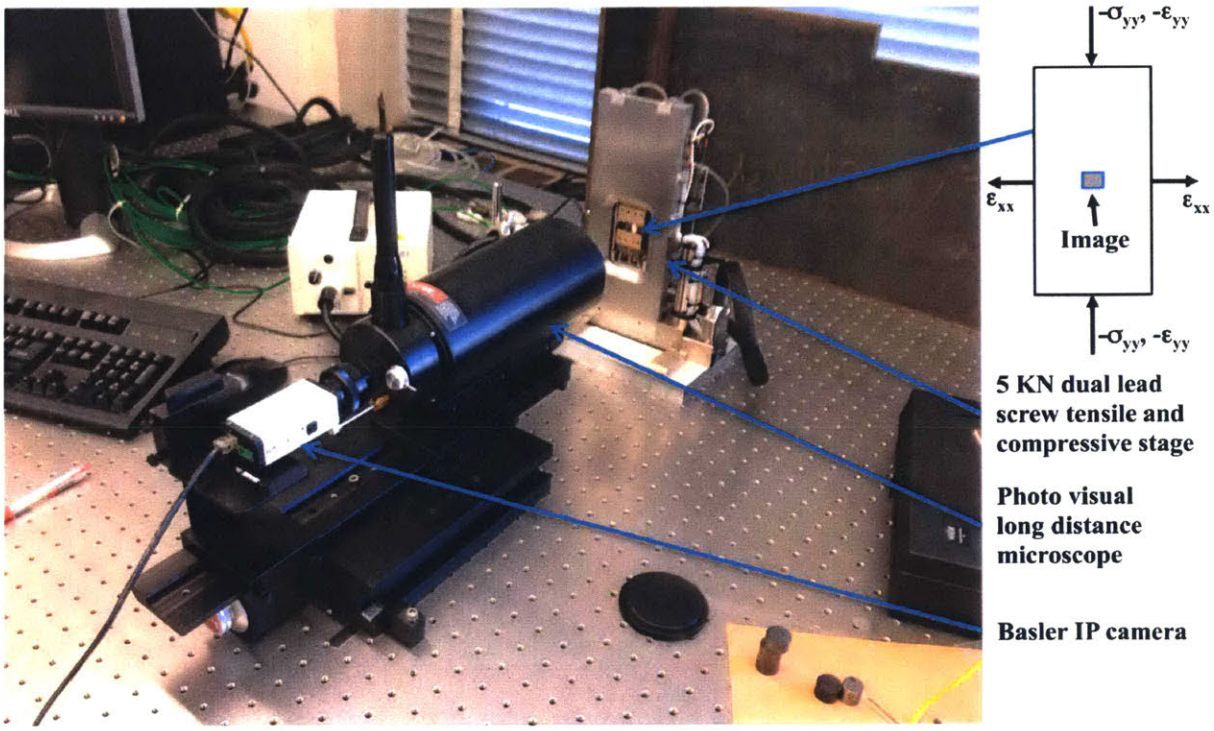

Figure 2.23: Photograph showing imaging and loading devices used by Tal et al. (2016).

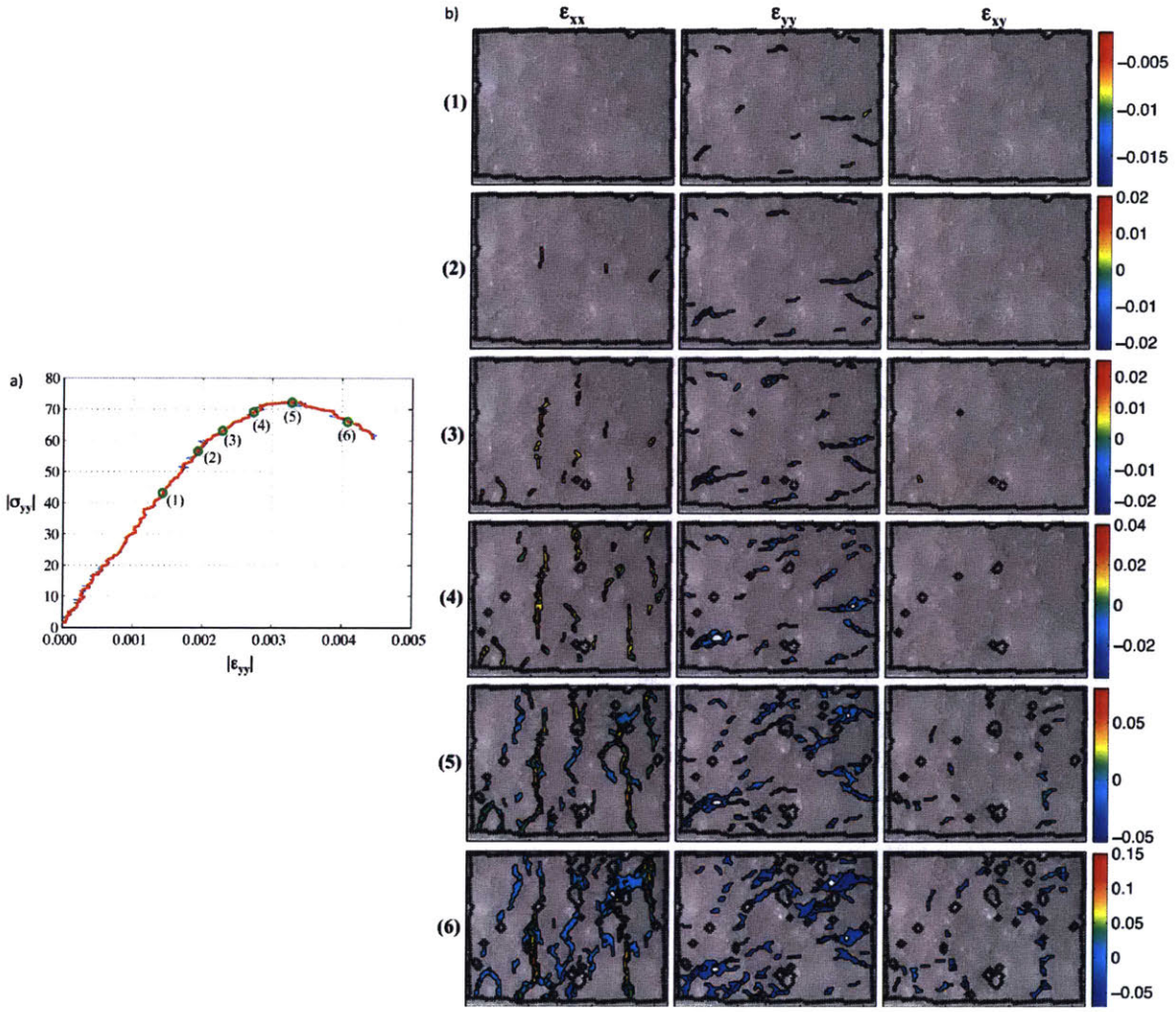

Figure 2.24: a) Stress-strain curve obtained from setup shown in Figure 2.23. b) Each row shows an image captured at the stress-strain state shown with the green circles in subfigure a, overlaid with a contour plot of strains ε_{xx}, ε_{yy} and ε_{xy} for the first, second and third columns respectively. From Tal et al. (2016).

2.3.1.4 Fracture Toughness Measurements and Acoustic Emission Activity in Brittle Rocks (Nasseri et al., 2006)

In this laboratory study, chevron cracked notched Brazilian disc (CCNBD) tests were performed on specimens of Barre and Lac du Bonnet granite. For each material, P-wave velocities were first measured along three orthogonal directions, and the directions with intermediate, slowest and fastest velocities assigned as x, y, z axes respectively. Thin sections were then prepared normal to each axis, and CCNBD specimens prepared with the notch aligned in six directions corresponding to K_{xy}, K_{yx}, K_{xz}, K_{zx}, K_{yz}, K_{zy} (See Figure 2.25).

It was found that the Mode I fracture toughness K_{1C} varied between 1.14 and 1.89 $MPa.m^{0.5}$ for Barre granite, where the toughness was highest perpendicular to the direction of pre-existing microcracks, and lowest along pre-existing microcracks. Microstructural imaging using dye penetration, X-ray, SEM and TEM methods showed increased segmentation, roughness and creation of wing cracks when the fracture propagated perpendicular to the microcrack orientation (See Figure 2.26).

AE data were also captured for the Lac du Bonnet granite, and showed that the peak AE rate occurs approximately three seconds prior to the drop in load. The authors also note that events were initially mostly tensile type, and shear events became more common as the specimen approached failure (See Figure 2.27).

The authors also compared the AE hypocenter locations to the imaged microcracks, and found that the spatial concentration of AE matched well to the spatial concentration of microcracks along the path of the crack, as seen in Figure 2.28.

Overall, the study highlights the importance of pre-existing rock fabric on crack initiation and propagation, and that the spatial distribution of AE hypocenters show a 1:1 spatial correlation to the qualitatively and visually observed microcrack damage.

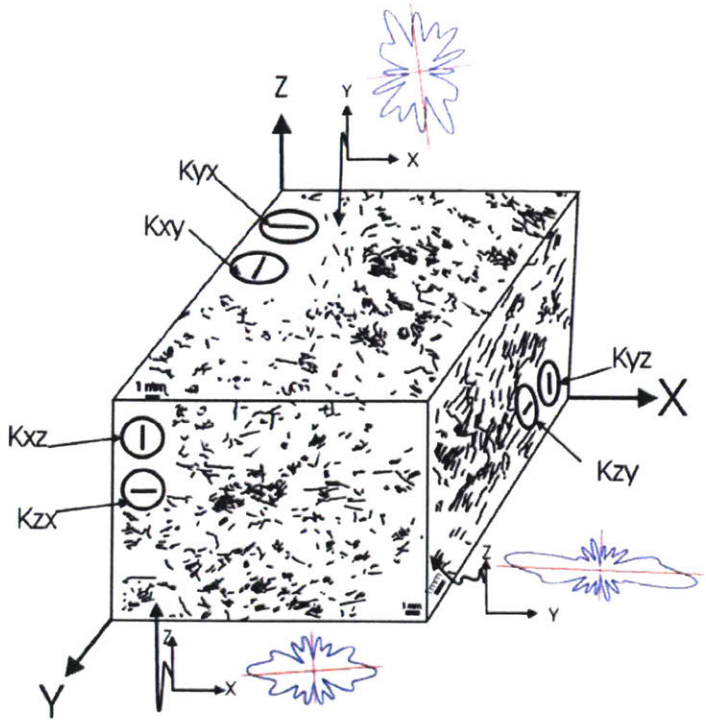

Figure 2.25: 3-D block diagram showing location of CCNBD specimens prepared along each plane with respect to microcrack orientations in Barre granite; rose diagrams show the alignment of microcracks for each plane. From Nasseri et al. (2006).

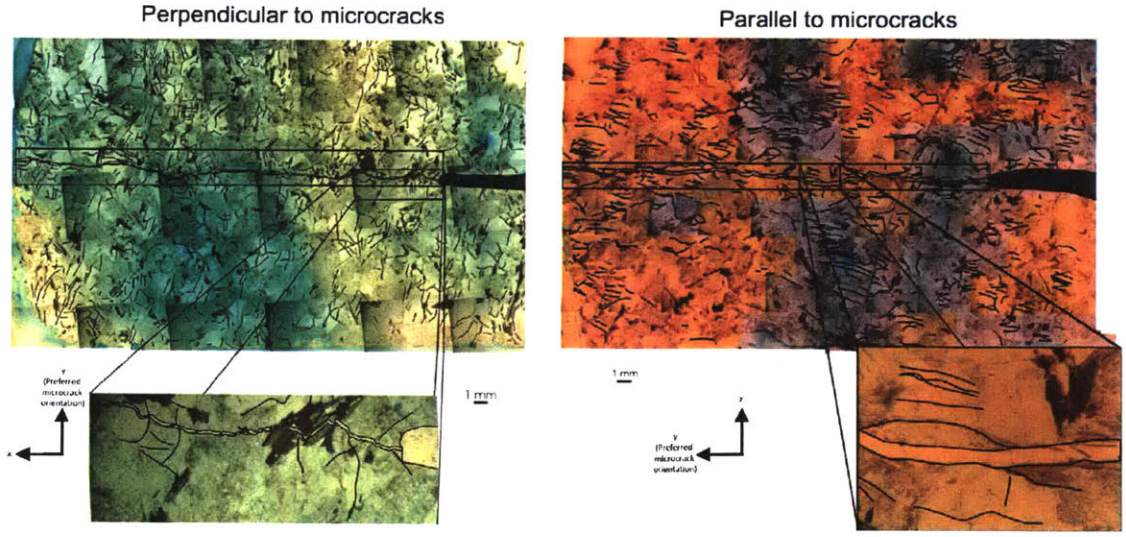

Figure 2.26: Crack propagation in Barre granite with existing microcracks. The close-up image shows the rough and segmented morphology of the fracture surface. Left shows the test in which the crack propagated perpendicularly to microcracks, while right shows test parallel to microcracks. From Nasseri et al. (2006).

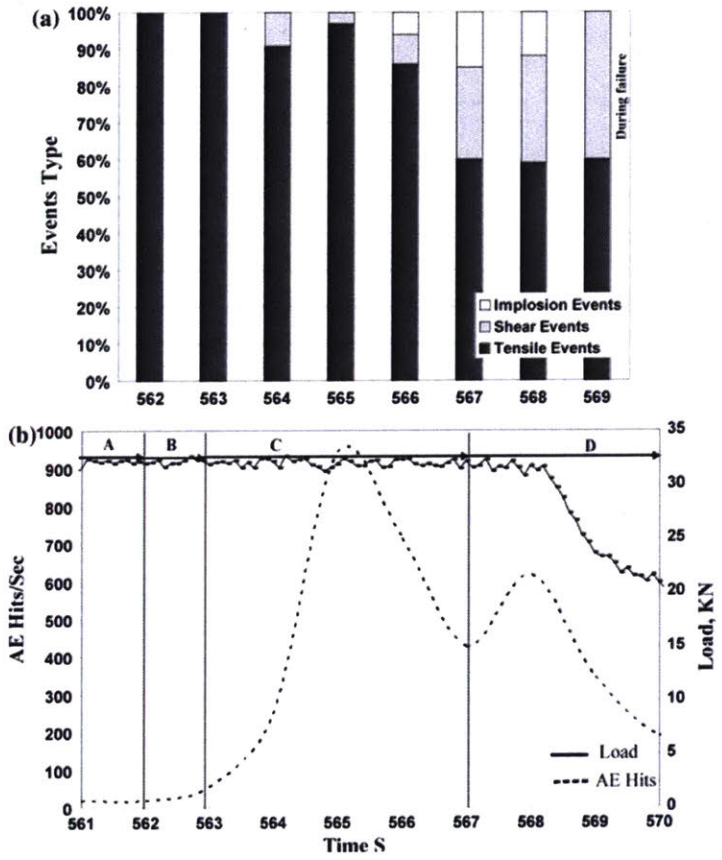

Figure 2.27: x-axis shows time, y axis shows a) relative proportion of AE focal mechanisms, b) AE hits and the load curve. Crack propagation begins at 568 s. From Nasseri et al. (2006).

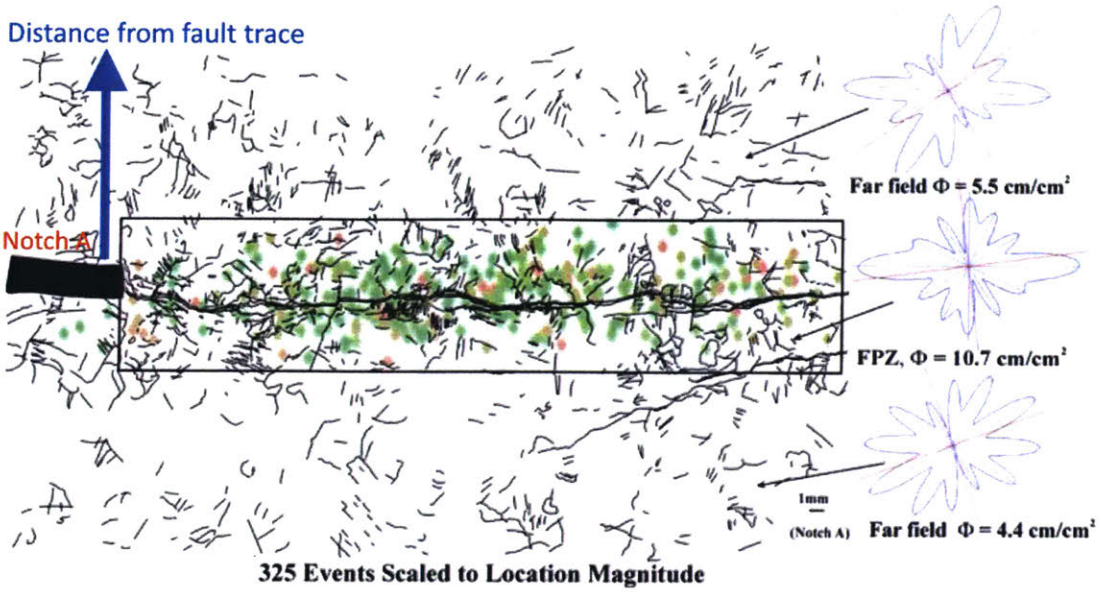

Figure 2.28: (Left) Microcrack density and orientation (rose diagram) in fracture process zone and far-field area near notch A. Inset delineates the width of FPZ as derived from the superimposed AE events. From Nasseri et al. (2006).

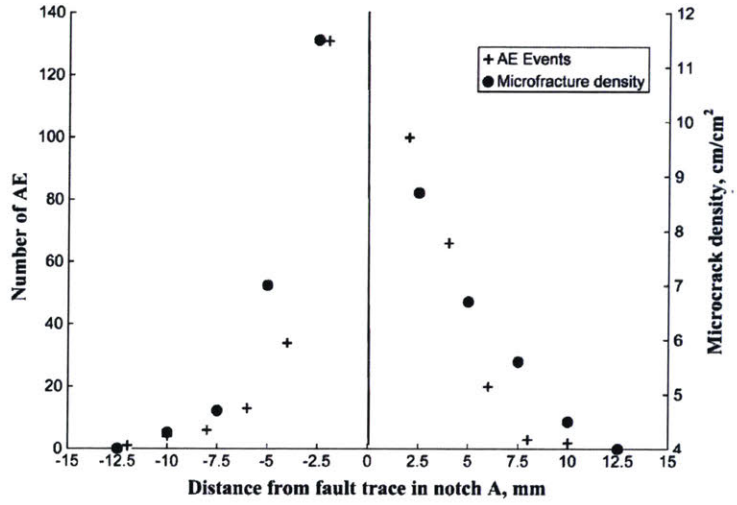

Figure 2.29: Relation of AE events distribution to that of microcrack density (determined visually based on Figure 2.28) as a function of distance from the fracture plane. Rose diagrams on the right indicate the angular statistical distribution of microcrack orientations. From Nasseri et al. (2006).

2.3.1.5 Rate Dependence of Acoustic Emissions Generated during Shear of Simulated Fault Gouge (Mair et al, 2007)

In this study, the authors use a double direct shear apparatus on Ottawa sand and soda lime glass spheres at various normal stresses and shear velocities. The setup is shown in Figure 2.30. The experiments were instrumented with acoustic emission sensors, with a primary focus on determining the mean number of AE per second to understand the effect of shear velocity on the rate of seismic energy release.

The results are best summarised in Figure 2.31. We see that the mean number of AE per second increases with increasing shear velocity, but that the shearing process is in fact more seismically efficient at slower shear velocities when considering the number of AE per micron of slip. Interestingly, we also see that the spherical glass beads produce more AE than the angular Ottawa sand at the slip velocities tested. This study, then, establishes a relationship between seismic efficiency and shear velocity that will also be studied in this thesis when we indirectly vary the slip rate along mineral grains as we vary the rate of injection in a series of hydraulic fracturing tests in Chapters 6 and 7.

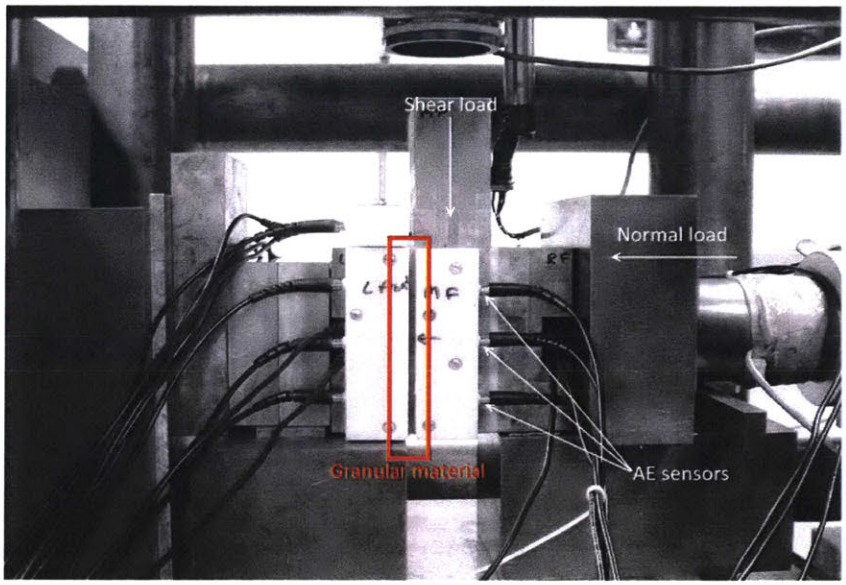

Figure 2.30: Photo of double direct shear experimental setup used by Mair et al. (2007).

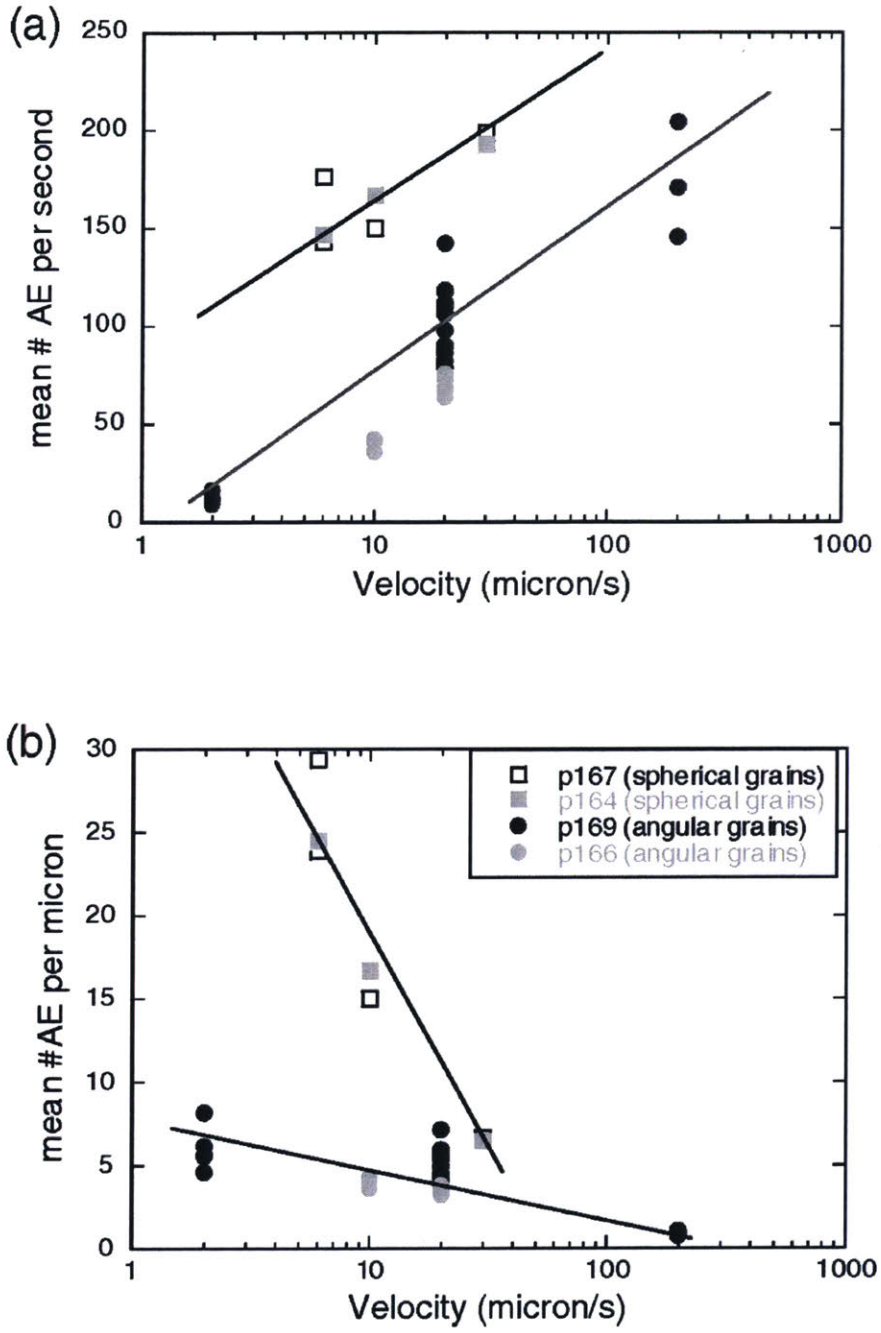

Figure 2.31: x-axis shows the velocities at which the granular materials were sheared. y-axis shows (a) mean number of AE per second during each test and (b) mean number of AE per μm of displacement during each test. In all cases, the number of AE per second increases with velocity. In all cases,the number of AE per μm of displacement decreases with increasing velocity. The absolute number of hits and rate of change varies between the two materials. The lines are hand drawn to highlight the main trends of the materials. From Mair et al. (2007).

2.3.1.6 Effect of grain size on fractal structure of acoustic emission hypocenter distribution in granitic rock (Kusunose et al., 1991)

In this study, the authors triaxially loaded Inada and Osima granodiorites to failure to determine the difference in AE response between these rocks. They share similar mineral compositions, but differ primarily in grain size: the Inada granodiorite grains range between 3 to 10 mm, while the Osima granodiorites range between 1 to 2 mm. Cylindrical specimens (100 mm height, 50 mm diameter), were held under a confining pressure of 50 MPa and axial stress was increased to failure. The setup is shown schematically in Figure 2.32.

Figure 2.33a shows that in general, the fine grained Osima granodiorite produced a higher number of AE with tighter clustering around the center of the specimen, whereas the AE from the Inada granodiorite were fewer and appear almost uniformly distributed across the specimen. Figure 2.33b, which shows the correlation integral vs lag distance of the AE hypocenters, suggests that the coarse grained Inada granodiorite exhibits a fractal dimension of 2.0 for length scales below the mean grain size, and fractal dimension 2.4 at lengths greater than the grain size. Conversely, the Oshima granodiorite exhibits the same D = 2.7 fractal dimension at all measured lengths, although note that the 1 mm grain size is less than the smallest correlation length of 2 mm. We learn from this paper that a) fine grained rocks appear to be more seismically productive, and b) that in the coarse grained rock there appears to be more AE events related to intragranular microcracks than intergranular microcracks. This study is relevant to the present work as it suggests that the grain size has an effect on the seismic activity generated during the creation of shear fractures.

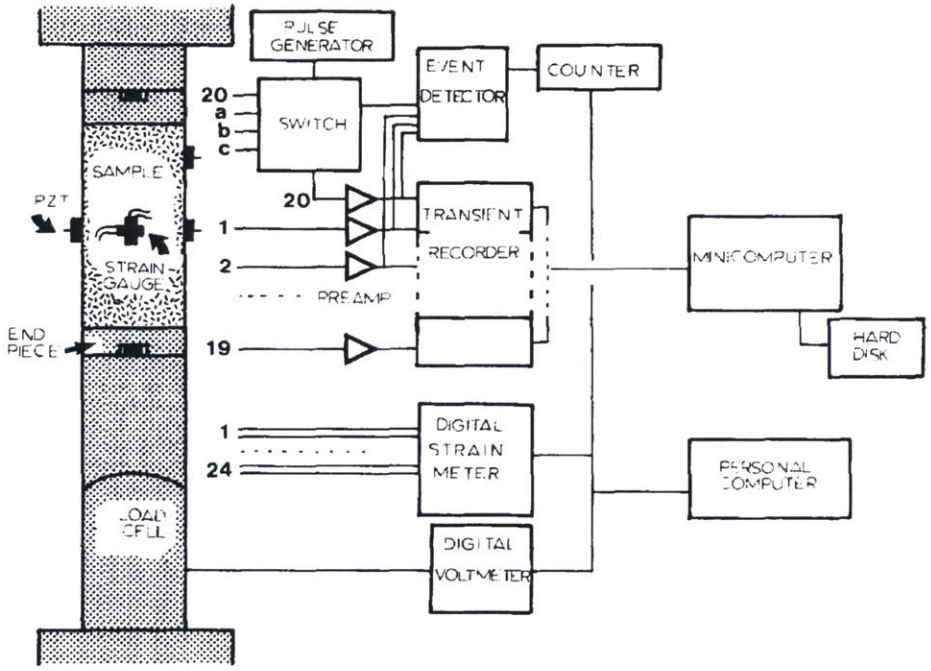

Figure 2.32: Schematic diagram of monitoring system. Acoustic emissions (AE) were detected by 20 piezoelectric sensors (Labelled PZT) of 2 MHz resonant frequency, and the waveform data were fed into transient recorders with a 20 MHz alternating - direct current converter. The wave data were then transmitted to a hard disk through a minicomputer. Electric pulse signals (using the pulse generator) were intermittently fed into four piezoelectric sensors (labelled a, b, c and 20) to produce elastic P-waves during the experiment, and variation of the axial and the radial velocities were monitored. Six pairs of strain gauges were attached to the surface of the sample to monitor local surface strain in the axial and circumferential directions. The strain and stress data were recorded by a personal computer during the experiment. From Kusunose et al. (1991).

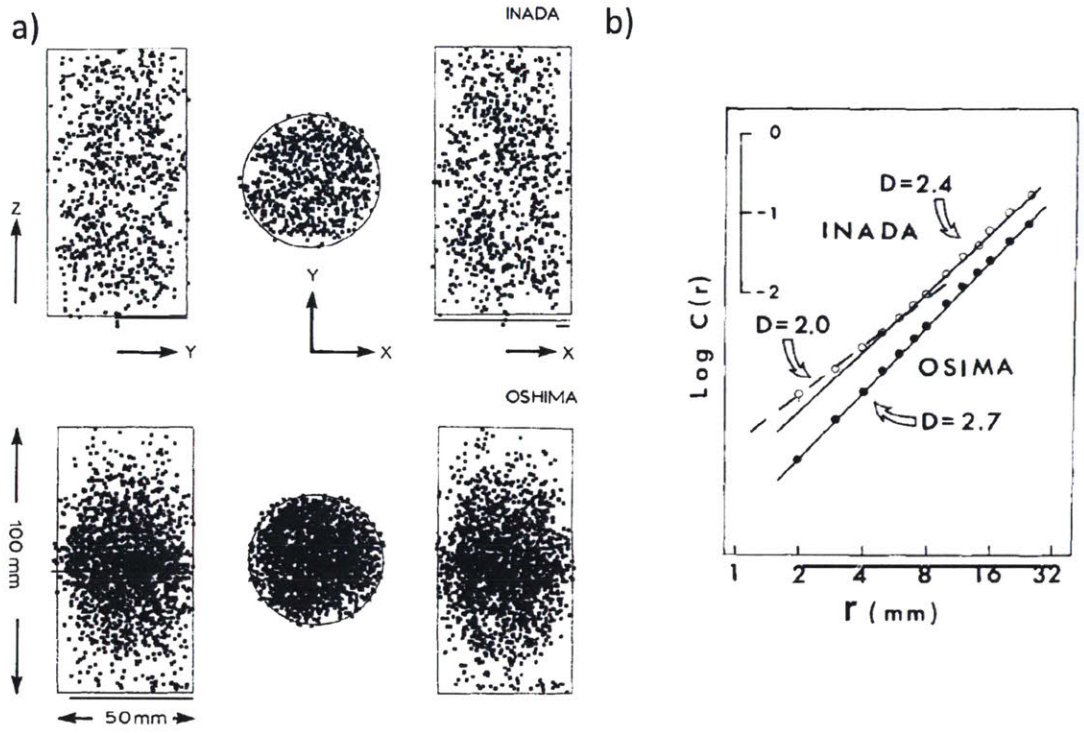

Figure 2.33: a) Map of AE hypocenters for Inada (top) and Osima (bottom) granodiorites. The hypocenters are plotted for the events that occurred at axial stress below 80% of the failure strength. In this stress range 885 and 2365 events were located, with an accuracy of 2 mm, for Inada and Oshima granodiorites, respectively. b) Correlation integral (C(r)) vs. lag distance (r) for Inada and Oshima granodiorites. The Oshima granodiorite data fall on a straight line. This shows that the AE hypocenter distribution of Oshima granodiorite has a single fractal structure. In contrast, the Inada granodiorite data fall on two straight lines; the fractal dimension for the distance range longer than the grain size is 2.4 and that for the shorter range is 2.0. From Kusunose et al. (1991).

2.3.1.7 Effects of grain size on the initiation and propagation thresholds of stress-induced brittle fractures (Eberhardt et al., 1999)

In this study, the authors conduct similar experiments to those described in Kusunose et al. (1991), using three rocks with similar mineralogy but varying grain size: a grey granite, a granodiorite, and a pegmatitic granite with mean grain sizes of 3 mm, 1 mm, and 20 mm respectively. In this study, cylindrical specimens (61 mm diameter, 137 mm height) were instrumented with strain gauges and AE, then uniaxially loaded to failure at a rate of 0.25 MPa/s. The results are best summarised in Tables 2.3 and 2.4, and Figure 2.34.

In terms of mechanical properties, we see that the rocks become increasingly stiff with decreasing grain size, and that the crack coalescence and crack damage stresses are higher for smaller grain size while crack closure and crack initiation stress stress appear relatively invariant with respect to grain size. The authors suggest that microcrack closure and initiation processes are dependent more on the grain mineralogy than grain size, since they saw that cracks tended to initiate from feldspar and quartz grains in all tests. They suggest that the effect of grain size on crack coalescence and damage may be explained by a model similar to that shown earlier in this thesis by Nasseri et al. (2006), whereby microcracks along a long grain are generally colinear along the grain boundary, thus less energy is required to connect these microcracks. Conversely, in a fine grained rock the microcracks tend to be randomly oriented along separate grain boundaries, resulting in more energy required to connect these microcracks. Regarding AE, Figure 2.34 shows that the maximum energy rate of the grey granite is higher than the granodiorite by 20 dB/MPa (about 10X), and the pegmatite is higher than the grey granite by 31 dB/MPa (about 35X). This observation contradicts the results seen by Kusunose et al. (1991), who, as previously described, observed more AE in the fine grained granodiorite specimen. Note, however, that that Kusunose et al. (1991) study did not report amplitudes, and so the results are not directly comparable to this study.

The finding that increasing grain size correlates to increased seismic activity, and lower crack coalescence and crack damage stresses is relevant to this thesis as Barre granite and Opalinus clayshale, the two materials explored in this thesis, have significantly different grain sizes which contributes to the discrepancies in their behaviour.

Table 2.3: Average elastic constants for the 240 m level URL samples (standard deviation in parentheses). From Eberhardt et al. (1999).

Material parameter	Granodiorite (1 mm grain size)	Grey granite (3 mm grain size)	Pegmatite (20 mm grain size)
Samples tested	5	5	5
Young's modulus, E_{avg} (GPa)	67.2 ($\pm$3.5)	63.8 ($\pm$2.2)	60.1 ($\pm$1.7)
Tangent modulus, E_T (GPa)	69.4 ($\pm$1.3)	60.3 ($\pm$1.1)	57.7 ($\pm$3.0)
Secant modulus, E_S (GPa)	66.8 ($\pm$0.9)	49.7 ($\pm$1.9)	51.6 ($\pm$2.0)
Poisson's ratio, ν_{avg}	0.30 ($\pm$0.03)	0.33 ($\pm$0.04)	0.29 ($\pm$0.07)

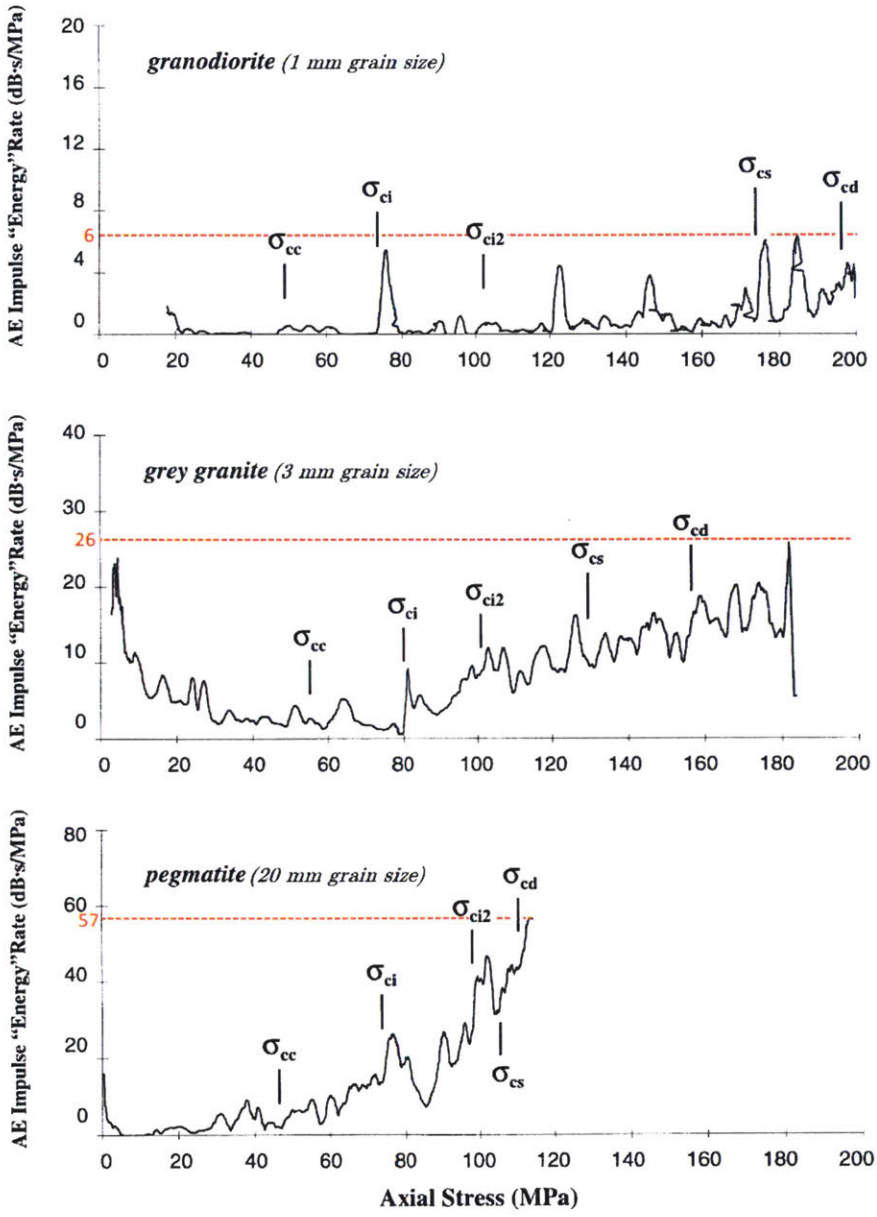

Figure 2.34: x-axis shows axial stress during each experiment. y-axis shows AE energy release rate, normalised per MPa of axial load. Top, middle, bottom show plots of granodiorite, grey granite, and pegmatite respectively. Red dotted line represents the maximum energy rate during each test. From Eberhardt et al. (1999).

Table 2.4: Average crack thresholds for the 240 m level URL samples (standard deviation in parentheses). From Eberhardt et al. (1999).

Strength parameter	Granodiorite (1 mm grain size)	Grey granite (3 mm grain size)	Pegmatite (20 mm grain size)
Number of tests	5	5	5
Crack closure, σ_{cc} (MPa)	45.6 ($\pm$3.4)	55.6 ($\pm$1.5)	45.2 ($\pm$2.7)
Crack initiation, σ_{ci} (MPa)	79.6 ($\pm$2.7)	79.6 ($\pm$2.3)	72.0 ($\pm$5.9)
Secondary cracking, σ_{ci2} (MPa)	102.8 ($\pm$4.5)	102.8 ($\pm$4.3)	96.0 ($\pm$4.4)
Crack coalescence, σ_{cs} (MPa)	164.7 ($\pm$9.0)	127.6 ($\pm$14.2)	104.8 ($\pm$6.4)
Crack damage, σ_{cd} (MPa)	194.0 ($\pm$2.8)	147.4 ($\pm$9.1)	113.2 ($\pm$6.8)

2.3.1.8 Hydraulic fracture energy budget: Insights from the laboratory (Goodfellow et al., 2015)

In this study, the authors present results from a series of triaxial experiments on Westerly granite, where various confining and axial stress states are held constant and the rock is hydraulically fractured by injection of distilled water into a pre-drilled, packered borehole, as seen in Figure 2.35. In each experiment, the cell pressure was larger than the axial stress so that the fracture initiated and propagated perpendicular to the axial direction. The experiment was instrumented with a linear variable differential transformer (LVDT), a pressure transducer, and AE sensors. The goal of the experiment was to compare the energy supplied by the fluid injection to the energy released as seismic waves, and thus gain some insights into the seismicity of the hydraulic fracturing process.

One main takeaway is their methodology for calculating radiated seismic energy (E_R) from moment magnitude (M_0). Radiated seismic energy "represents the seismic energy that would propagate to the far field in a whole space with no attenuation" (Shearer, 2009). They suggest that an upper bound can be calculated from an empirical relationship proposed for large earthquakes by Kanamori (1978):

$$\begin{aligned} log_{10}(E_R) &= 1.5M_w + 4.8 \\ M_w &= \frac{2}{3}[log_{10}M_0 - 9.1] \end{aligned} \tag{2.15}$$

This empirical relation was calibrated for large earthquakes, where the apparent stress on the fault (See Section 2.1.8) ranged from 1 to 5 MPa. To calculate the lower bound estimate of the radiated seismic energy, the authors assumed a much smaller apparent stress of 0.01 MPa, which has been found to be appropriate for laboratory-scale tests (Goodfellow and Young, 2014). They then apply a scaling methodology proposed by Wyss and Brune (1968) to estimate the radiated seismic energy. The authors found the lower and upper bound differ by almost exactly 2 orders of magnitude (100X), and so as a reasonable estimate we use the geometric mean of 10X, i.e. $log_{10}(10E_R) = 1.5M_w + 4.8$ in the remainder of this work.

The main finding of this study is shown in Figure 2.36, which shows the injection energy, seismic energy, and injection volume for their laboratory experiments alongside literature data on various hydraulic fracture operations in the field. We see in Figure 2.36a that the seismic efficiency of hydraulic fracturing varies between 1E-3% to 1E-9% for both field and lab scale hydraulic fracturing, and it appears from Figure 2.36b that hydraulic fracture operations tend to be lower seismic moment release for any given injected volume than other activities such as EGS and

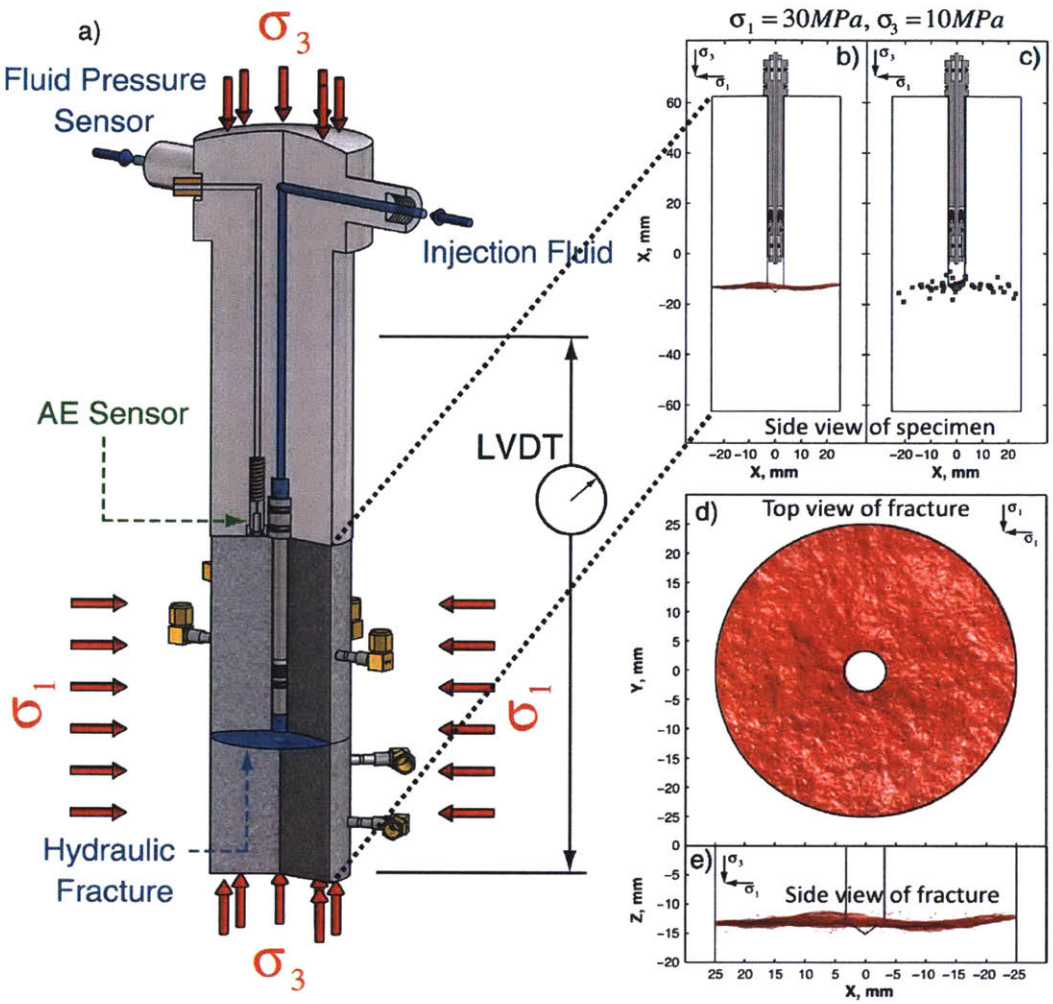

Figure 2.35: (a) Laboratory hydraulic fracture apparatus. Experiment SR4 (σ_1 = 30 MPa, σ_3 = 10 MPa). (b,e) μCT fracture surface projected on the σ_1–σ_3 plane. (c) AE event location projected on the σ_1–σ_3 plane, and (d) μCT fracture surface projected on the σ_1–σ_1 plane. From Goodfellow et al. (2015).

wastewater disposal. The authors calculate injection energies in the range of 10 - 20 J, which is a good basis of comparison to some work in this thesis.

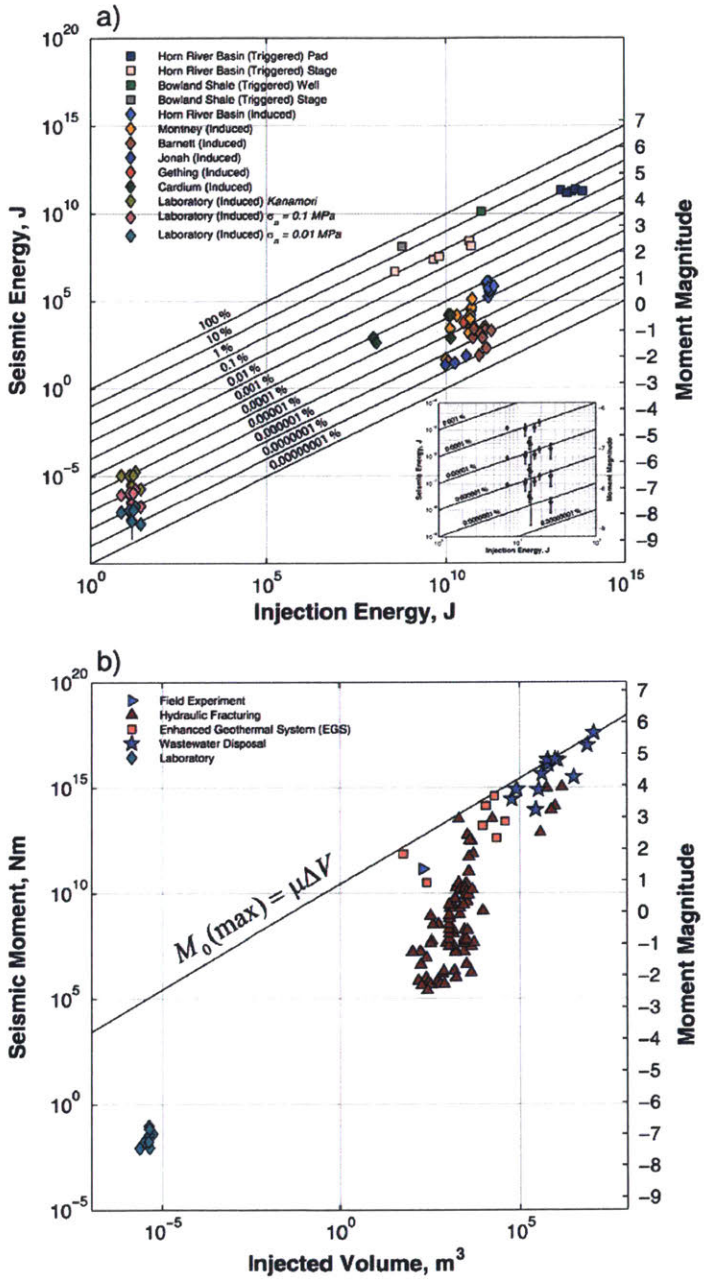

Figure 2.36: (a) x-axis shows injection energy (work done by injection of fracturing fluid at flow rate Q and pressure P) plotted against radiated seismic energy on y-axis. Reference lines correspond to the seismic injection efficiency ($E_R/E_{injection}$) in percentages. (b) x-axis shows total injected volume plotted against seismic moment of the largest seismic event on the y-axis. From Goodfellow et al. (2015).

2.3.1.9 Rock fabric influence on hydraulic fracture propagation (Stanchits et al., 2015)

In this poorly documented but interesting study, the authors present the results of experiments on two specimens of Niobrara tight shale: a 229 x 229 x 381 mm block (Figure 2.37) and a 711 x 711 x 914 mm block (Figure 2.38. These blocks were drilled with a 25.4 mm and a 95 mm diameter borehole respectively. Both boreholes were drilled along a bedding plane, and aligned with σ_3 in the smaller specimen and 40 degrees from σ_3 in the larger specimen. The blocks were loaded polyaxially to $\sigma_v = 2500$ psi, $\sigma_H = 2100$ psi, $\sigma_h = 1700$ psi, then hydraulic fractures were created by injection of fluid. For the smaller specimen, epoxy was used as the injection fluid, and then the far-field stresses were held for 12 hours after creation of hydraulic fractures to allow the epoxy to cure, after which the distribution of epoxy was observed post-mortem. For the larger specimen, silicon oil mixed with plastic particles was injected, and the specimen was again opened post mortem to observe the distribution of these plastic particles. The experiment was instrumented with fluid volume and pressure, load and displacement in each loading direction, and 38 AE sensors for the smaller block and 62 sensors for the larger block, achieving an estimate location error within 6 mm using an anisotropic heterogeneous velocity model.

The results are summarised in Figures 2.37 and 2.38. We see that in general, the main hydraulic fracture plane is almost exactly perpendicular to σ_h, with the exception of a branch near the top of the smaller specimen where the HF propagated a short distance along a bedding plane. In terms of AE, the hypocenter locations generally follow the geometry of the newly created hydraulic fracture, and appear to migrate away from the borehole in time. Interestingly, few AE events were located on the opening along the pre-existing bedding plane. This study is one of the few studies that directly compare AE results to visual evaluation of the creation of hydraulic fractures, although note that in this study the visual data are only taken at the end of the test, while in this thesis the image data are collected throughout the experiment.

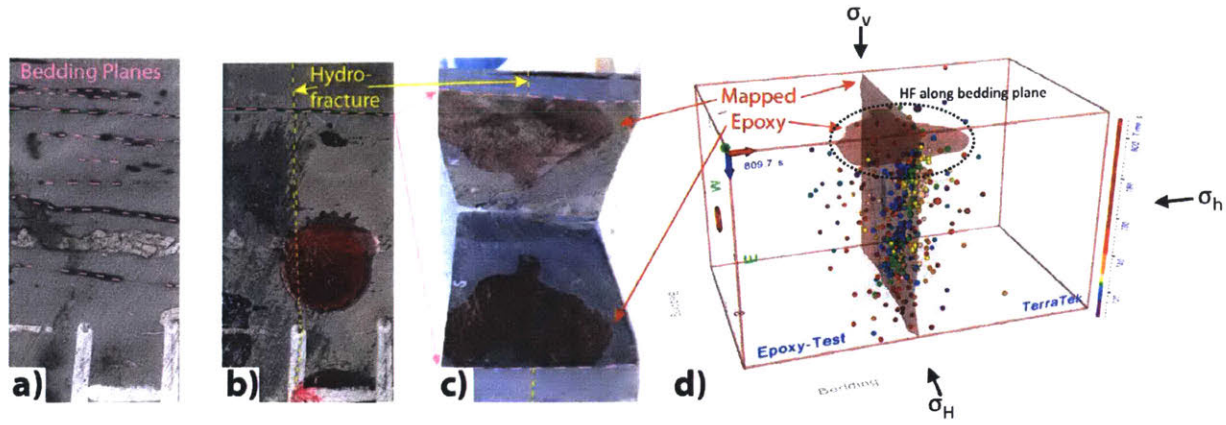

Figure 2.37: Photographs of smaller specimen before (a) and after the test (b); photograph of opened bedding plane (c); 3D rendering of AE events (spheres) and post-test epoxy distribution (light-red surfaces)(d). From Stanchits et al. (2015).

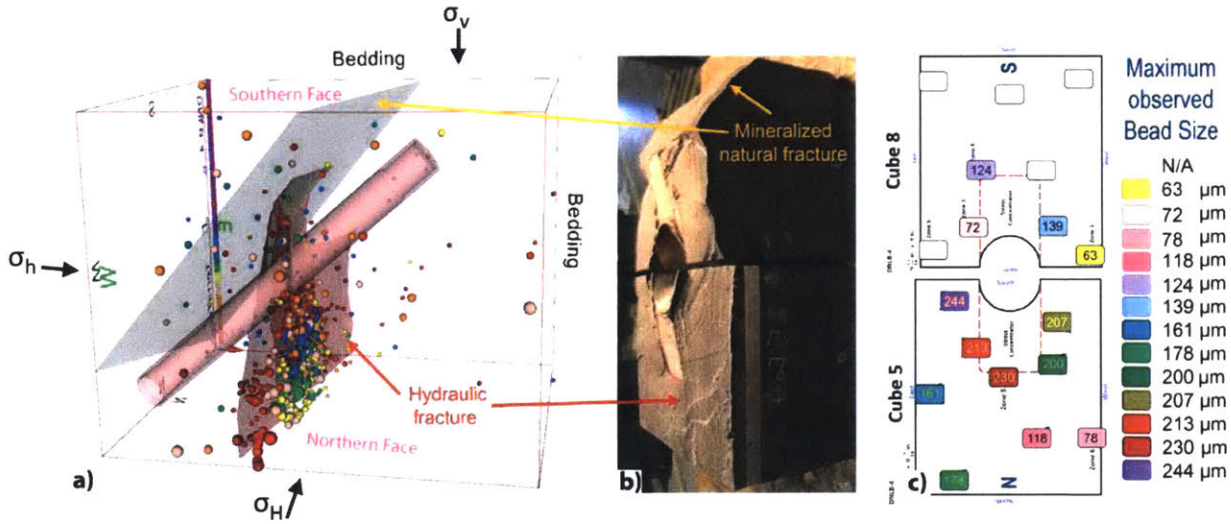

Figure 2.38: Larger specimen: (a) 3D rendering of AE events (spheres) combined with hydraulic fracture (red surface) and mineralized fracture (green surface) surfaces; (b) photograph of the fractured block cut into 8-in cubes; (c) maximum bead size from analysis of microphotographs of the fracture surfaces. From Stanchits et al. (2015).

2.3.1.10 Frictional properties of shale reservoir rocks (Kohli and Zoback, 2013)

In this study, the authors tested the frictional properties of reconstituted paste synthesised from crushed shale rocks originating from the Barnett, Haynesville and Eagleford formations. To determine the frictional properties, 2 mm of paste was emplaced between two forcing blocks at 30 degrees from vertical within a triaxial cell (See Figure 2.39), with 30 MPa of confining pressure. The gouge layer was then sheared at 0.1, 1.0 and 10 μms^{-1} at 10, 20 and 30 MPa of normal stress. The study also considers the different shales in the context of rate state friction theory (Dieterich, 1979; Ruina, 1983), which describes how the dynamic friction coefficient of a fault is dependent on the shear velocity. In this theory, the (a-b) parameter describes whether a fault is slip-weakening or slip-strengthening, i.e. whether the friction coefficient decreases or increases with increasing slip velocity. A negative (a-b) indicates slip-weakening behaviour, which releases accumulated strain in rapid bursts arising from a localised rupture. This is generally considered as the mechanism for a typical seismic event. Conversely, faults with positive (a-b) release strain energy in a slow ductile fashion, which is generally not detected through conventional methods such as geophones.

A key finding from this study is shown in Figure 2.40, where we see that the friction coefficient decreases approximately linearly with increasing clay + total organic content (TOC). We also see that the (a-b) parameter is relatively constant between -0.002 to -0.003 for shales with less than 30% TOC + clay, beyond which the (a-b) increases linearly with increasing TOC + clay. As a result, this study suggests that shale rocks with higher TOC + clay content will tend to exhibit positive (a-b) and will thus be more aseismic, i.e. produce less seismic energy, given strain sources ranging in scale from far field tectonic stress for earthquakes, to locally elevated pore pressures resulting from hydraulic fracturing operations. This finding is important to this thesis as it touches upon the effect that relatively ductile clay minerals and organic content have on seismicity, although this study is based on sliding along a fault, as opposed to our focus on the creation of hydraulic fractures.

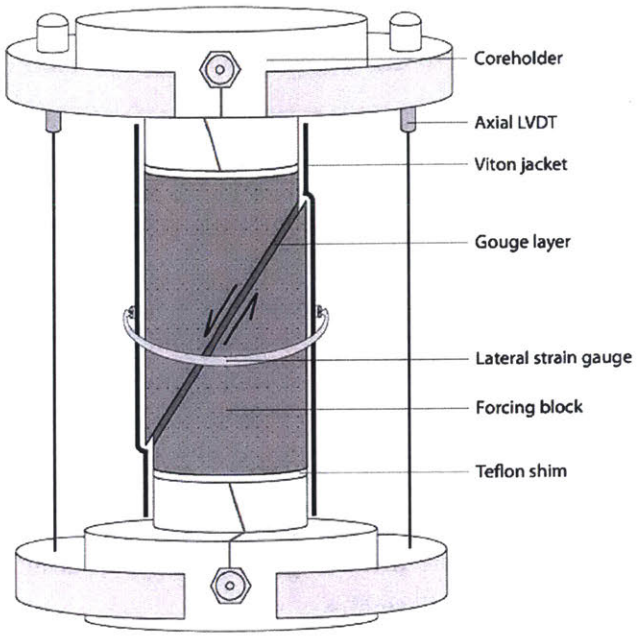

Figure 2.39: Friction experiment sample assembly inside triaxial pressure vessel used by Kohli and Zoback (2013) to test frictional properties of various shale rocks.

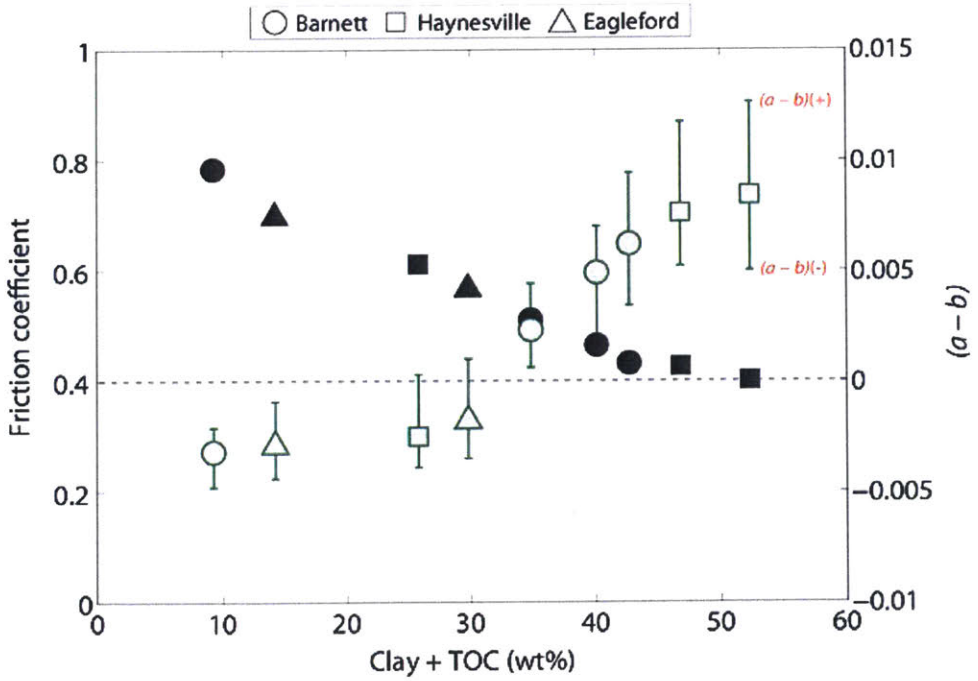

Figure 2.40: Friction coefficient (black symbols) and (a - b) (grey symbols) as functions of clay and organic content at 10 MPa normal stress for all samples in the study. Values of (a - b) are obtained from averaging the results of all velocity steps within a single experiment. Error bars represent the maximum, (a - b)(+), and minimum, (a - b)(-), values of (a - b) observed in each experiment. From Kohli and Zoback (2013).

2.3.1.11 Mechanical properties of shale-gas reservoir rocks — Part 2: Ductile creep, brittle strength, and their relation to the elastic modulus (Sone and Zoback, 2013)

This study characterises the same shale rock samples as the study by Kohli and Zoback (2013), from the perspective of creep, Young's modulus, brittle strength, and residual strength. 1 inch diameter intact specimens were tested in a triaxial cell with no pore pressure; the specimens were first loaded to a given hydrostatic pressure (10, 20, 30, 40, or 60 MPa), then the axial load was increased until specimen failure.

The strength parameters are of particular interest in this thesis, and these results are best summarised in Figure 2.41. The unconfined compressive strength (UCS) is negatively correlated with clay+kerogen content, and positively correlated to Young's modulus, which suggests that increasing clay+kerogen content is negatively correlated to both UCS and Young's modulus. There does not appear to be strong correlation between friction coefficients and clay+kerogen content (Figures 2.41e and g), which contrasts Figure 2.40 by Kohli and Zoback (2013), where the friction coefficient definitively decreased with increasing clay+TOC content. This may be attributed to the difference in experimental setup, where this study was performed in intact specimens, and Kohli and Zoback simulated shear along a fault gouge.

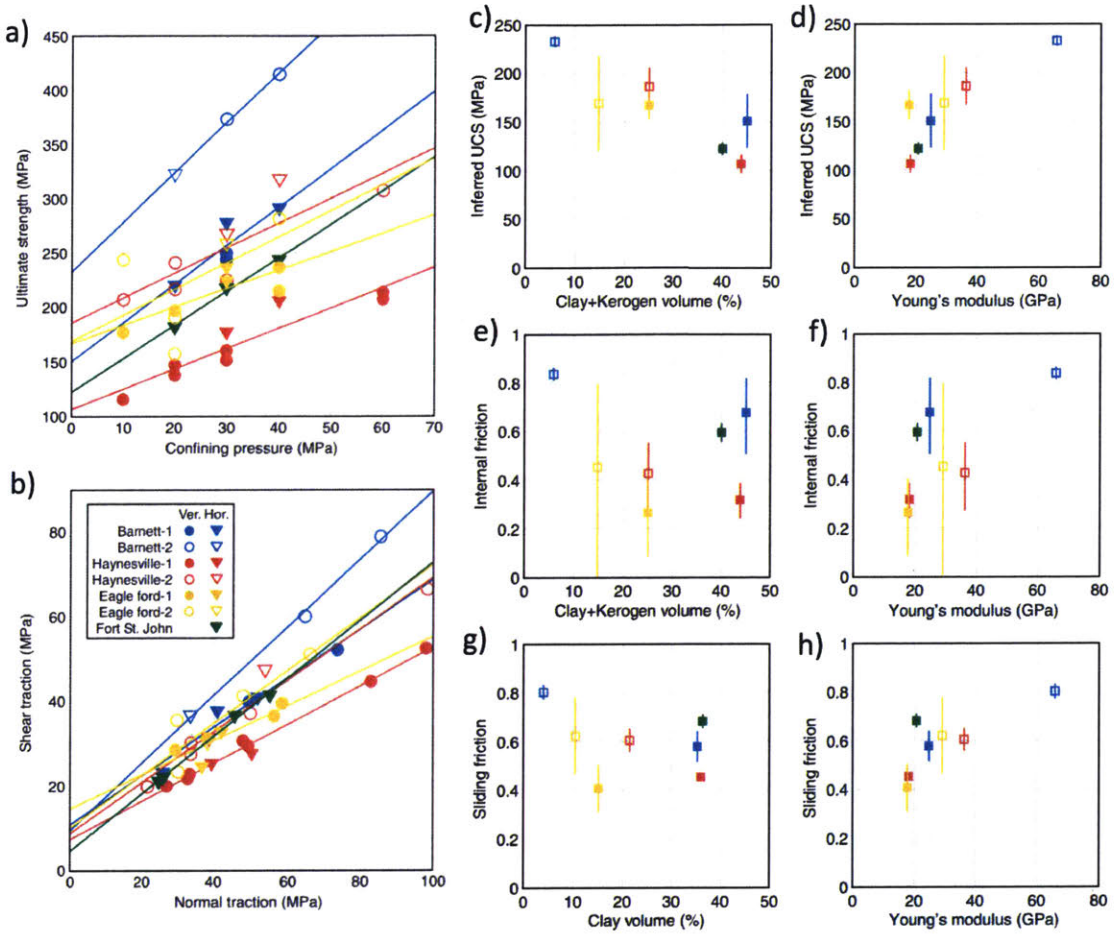

Figure 2.41: a) Ultimate strength for each specimen plotted as a function of the confining pressure. b) For each specimen, the ultimate strength was resolved onto the specimen failure surface as shear and normal traction. c-d) Unconfined compressive strength (UCS) was inferred from the y-intercept of each line in subfigure (a). e-f) Internal friction angle was calculated from the slope of each line in subfigure (a) and assuming a linear Coulomb failure criterion. g-h) The residual sliding friction coefficient was calculated from subfigure (b), again assuming a linear Coulomb failure criterion. From Sone and Zoback (2013).

2.3.2 Field Studies

2.3.2.1 Non-double-couple mechanisms of microearthquakes induced by hydraulic fracturing (Sileny et al., 2009)

In this study, the authors invert the full moment tensor from a database of microseismic waveforms acquired from six unconventional oil and gas hydraulic fracture treatments in the Cotton valley gas field in east Texas, USA. The reservoir rock consists of low permeability sands interbedded with shales. The waveforms are captured from eight stations along two vertical downhole three-component geophone arrays. 700 events were localised, and assigned groups G1-G4 or R. The layout of the operation is shown in Figure 2.42.

Table 2.5 shows that the the proportion of double couple ranges from approximately 15% to 45%, which indicates that volume change (ISO) or crack opening (CLVD) is a significant proportion of all underlying focal mechanism. This is likely attributed to the presence of elevated pore pressures from fluid injection at the treatment well. Interestingly, group R events all exhibit negative ISO, suggesting that crack closure is a significant mechanism in that region.

Figure 2.43 shows the composite focal mechanism of each group in map and side views. Dots indicate hypocenter locations, and are coloured by group. Red/blue wireframes represent the mean focal mechanism (Recall Section 2.1.7) for each group. We can see that the poles for the tensile crack/opening mechanism of G1-G3 are all approximately aligned along the same direction, approximately perpendicular to σ_{Hmax}. This suggests that the events represent fractures opening along σ_{hmin}. Conversely, the poles of the closure events of group R are aligned along the direction of σ_{Hmax}, suggesting these events represent fractures closing due to the maximum stress. Interestingly, the locations of group R events (red) are clustered linearly, which suggests they occurred along a natural joint whose strike is parallel to σ_H. However, the focal mechanism of R(2) and R(3) indicate crack closure along planes oriented normal to the strike of the natural joint, which indicates that the joint may in fact be composed of small fractures aligned perpendicular to the overall joint orientation.

Overall, this paper presents an interesting case study which shows that hydraulic fracturing operations appear to create a significant amount of non double couple focal mechanisms, and that these are generally explained by the stress state, although their spatial distribution may be attributed to local geologic features such as faults.

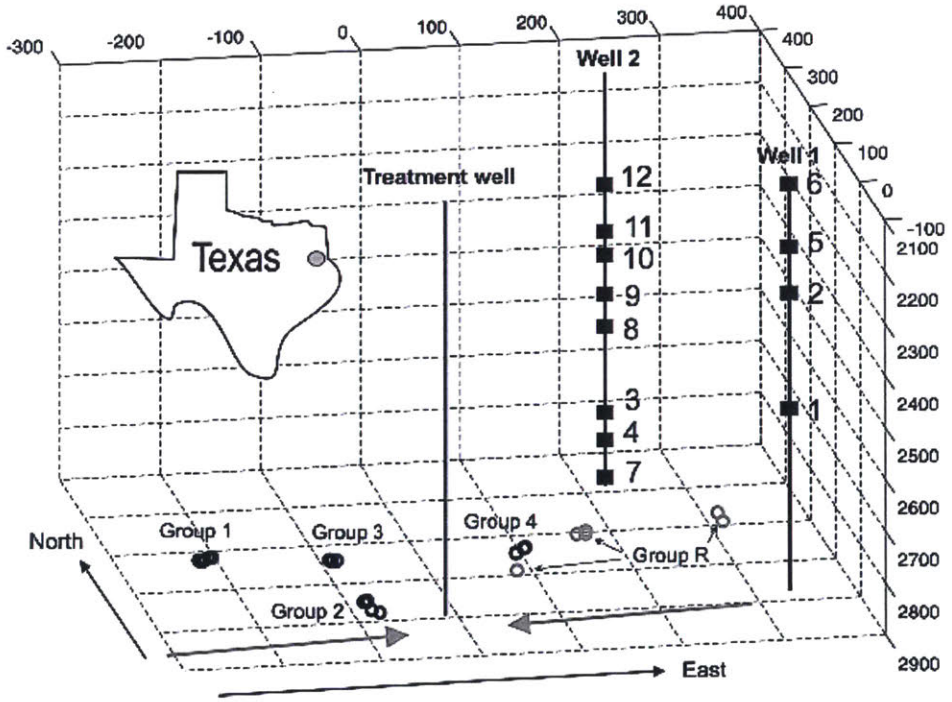

Figure 2.42: Illustration of hydraulic fracture imaging geometry in the Cotton Valley experiment (inset, dark dot on the sketch of Texas). Black heavy lines indicate monitoring wells 1 and 2 (full squares mark positions of the geophones used in this study), gray heavy line indicates treatment well. Hypocenters of selected microearthquakes in groups G1–G4 and R are marked by circles. Grey arrows at the bottom of the model indicate direction of maximum horizontal stress. Distance is in meters. Note that detected events mostly occur between 2750 m and 2850 m elevation. From Sileny et al. (2009).

Table 2.5: Investigated Events With the Percentage of the Isotropic Component, Double Couple, and Compensated Linear Vector Dipole[a]. From Sileny et al. (2009).

		No Attenuation			$Q_P = 30$, $Q_S = 50$		
Event	Moment (N m)	ISO	DC	CLVD T/P	ISO	DC	CLVD T/P
			Group G1				
1	0.13561×10^8	+31.0	29.8	39.2 T	+24.5	48.6	26.9 T
3	0.11602×10^8	+33.3	27.8	38.9 T	+27.1	44.5	28.5 T
4	0.60329×10^7	+2.2	17.5	80.3 T	+3.0	29.7	67.3 T
8	0.49590×10^7	+30.3	22.7	47.0 T	+22.0	39.6	38.4 T
10	0.47097×10^7	−43.3	26.3	30.5 T	−35.5	44.8	19.7 T
Composite		+27.7	26.4	45.9 T	+20.9	43.9	35.2 T
			Group G2				
1	0.19048×10^9	+30.2	16.1	53.7 T	+30.9	16.4	52.7 T
3	0.32007×10^8	−31.7	34.1	34.2 T	−16.3	41.8	41.9 T
4	0.28336×10^8	+25.9	14.2	59.9 T	+25.5	23.4	51.1 T
6	0.21386×10^8	+5.2	48.3	46.5 T	+5.2	48.3	46.5 T
8	0.15526×10^8	+21.0	20.1	58.9 T	+29.2	17.4	53.4 T
Composite		+27.0	16.7	56.3 T	+28.4	14.9	56.7 T
			Group G3				
1	0.17126×10^8	−8.7	6.6	84.7 T	−0.8	10.9	88.3 T
2	0.15211×10^8	+4.7	3.4	91.8 T	+9.3	8.8	81.9 T
4	0.11430×10^8	−4.7	13.5	81.9 T	+5.3	21.4	73.3 T
5	0.97501×10^7	+31.4	13.0	55.5 T	+29.8	18.7	51.5 T
9	0.54714×10^7	−82.0	3.2	14.8 T	−68.9	4.6	26.5 T
Composite		−5.3	8.7	85.9 T	+1.5	15.0	83.6 T
			Group G4				
1	0.10332×10^8	+46.8	34.8	18.5 P	+62.4	25.9	11.7 P
2	0.93847×10^7	+33.5	37.9	28.6 P	+54.0	30.5	15.5 P
3	0.83578×10^7	+51.5	26.4	22.1 P	+64.7	20.4	14.9 P
6	0.72974×10^7	+40.4	45.3	14.3 P	+57.5	38.0	4.6 P
8	0.68752×10^7	+52.1	36.2	11.7 P	+65.9	32.5	1.7 P
Composite		+45.2	35.1	19.7 P	+61.4	27.6	11.0 P
			Group R				
2	0.68964×10^7	−34.0	49.9	16.1 P	−36.0	41.2	22.9 T
5	0.28848×10^7	−42.8	28.5	28.7 P	−49.3	50.1	0.7 P
7	0.26910×10^7	−60.9	28.0	11.1 P	−57.9	21.0	21.1 T
8	0.26655×10^7	−39.0	33.1	27.8 P	−42.9	47.3	9.7 T

[a]Moments of investigated events are by J. T. Rutledge (personal communication, 2006). ISO, isotropic component; DC, double-couple; and CLVD, compensated linear vector dipole. Positive/negative sign of ISO means explosion/implosion; T or P with CLVD marks alignment of the major dipole. Moment tensor calculated for a medium without attenuation and with $Q_P = 30$ and $Q_S = 50$.

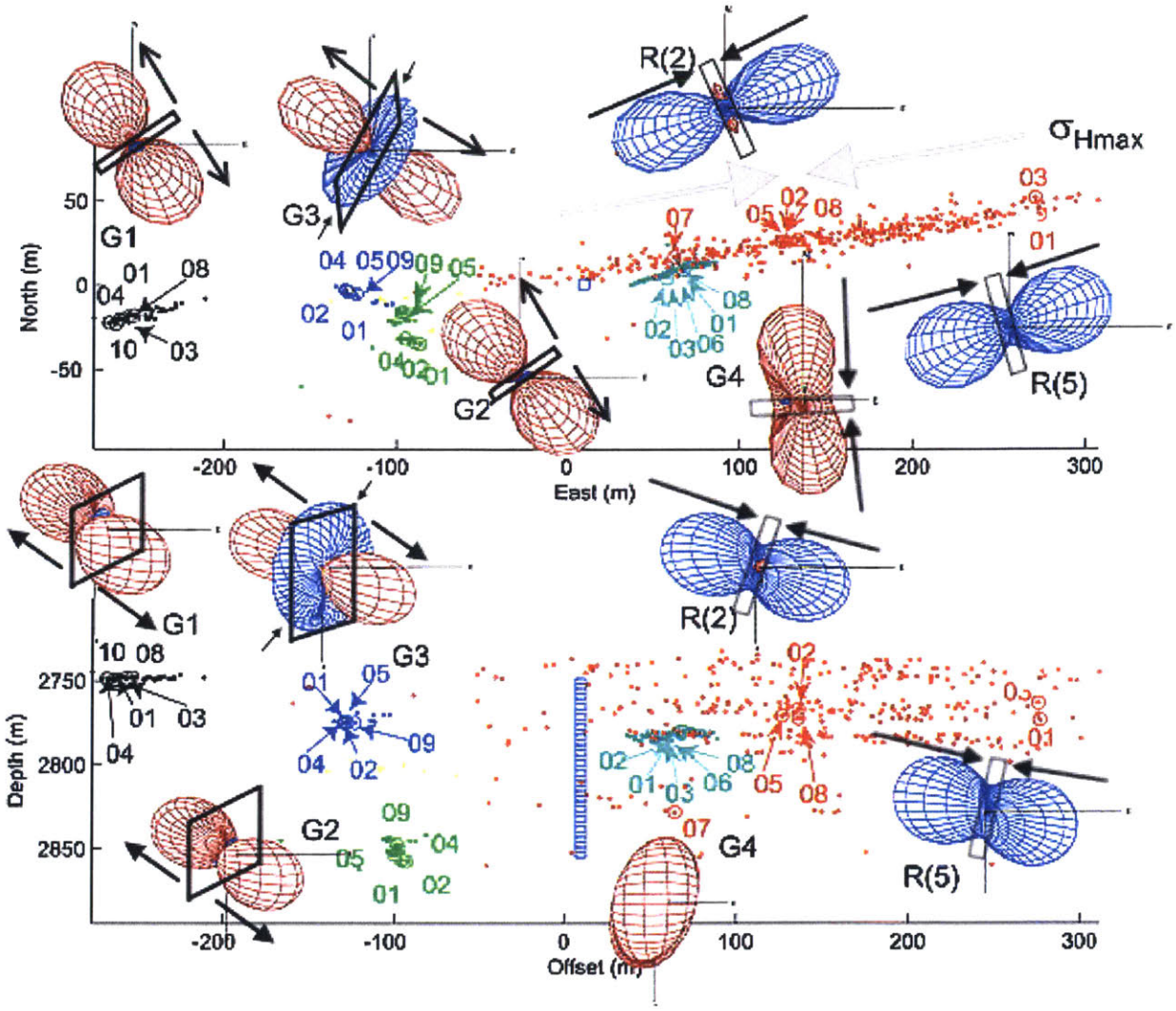

Figure 2.43: Seismicity observed during hydrofracturing (top) map view and (bottom) vertical cross section, together with composite mechanisms displayed as 3-D wire frame plots of P radiation patterns (compressions, red; dilatations, blue) for selected events in groups G1–G4 and individual mechanisms for events R(2) and R(5). Hypocenter locations of the five groups are represented by the color-coded dots: G1, black; G2, green; G3, blue; G4, cyan; R, red. The microearthquakes, for which we determined mechanisms, are numbered. Position of the injection well marked by blue square in map view and blue squares in depth section. Direction of maximum horizontal stress is indicated by gray arrows. Black quadrilaterals and arrows on each focal mechanism indicate approximate directions of forces corresponding to focal mechanisms. From Sileny et al. (2009).

2.3.2.2 On the mechanisms of shale microfracture propagation (Padin et al., 2014)

In this study, the authors present, analyse and discuss a comprehensive dataset from two unconventional oil and gas plays: one in the Vaca Muerta formation in Argentina, and the other in the Eagle Ford formation in Texas, USA. The datasets for both include qualitative assessment of total organic content (TOC), borehole log data including pore and in-situ stresses, Young's modulus, as well as localised microseismic events. The data are generally poorly presented, but the authors' main interpretations appear to stem from interpretations of Figures 2.44, 2.45 and 2.46.

There appear to be three parts to the study's assertions:

1. TOC content correlates positively with aseismicity. This is supported by the observation, seen in Figure 2.44a, which shows that the lower Eagle Ford region, which has the highest TOC, accounts for very minimal seismic energy compared to the upper Eagle Ford region. Figures 2.44b similarly shows that very few microseismic events are located towards the bottom of the lower Vaca Muerta formation, where the perforations (typically steel balls fired with explosive charges to initiate hydraulic fractures) are located and the TOC content is also highest. The authors highlight that the higher TOC content regions in Vaca Muerta correspond to high pore pressure, higher material anisotropy, lower elastic modulus, and high σ_{Hmax}. Similarly, they describe the spatial distribution of microseismic events in Figure 2.45, and state that the magnitudes in the Lower Eagle Ford are lower than the strata surrounding the lower Eagle Ford, even though the perforations are made in the lower Eagle Ford. The current author agrees with this assertion, which is also supported by the Kohli and Zoback (2013) study.

2. Creation of hydraulic fractures is more aseismic than slip along natural fractures because the creation of hydraulic fractures is a slow process, as was suggested by Maxwell and Cipolla (2011). This is supported by the data in Figure 2.46, which shows that hydrocarbon production in the high TOC strata increases with time as the hydraulic fractures slowly propagate with time, whereas production from the lower TOC strata peak early and decrease with time as no new fractures are created or stimulated. The current author disagrees partly with this assertion in that while shear slip does appear more seismic than the creation of HF, the creation of HF is not necessarily a slow process, as seen by studies such as Morgan et al. (2017) and Morgan and Einstein (2017), where we see that both shear and hydraulic fractures propagate slower in shale compared to brittle materials such as granite (Morgan et al., 2013).

3. Assertions 1 and 2 above lead the authors to the conclusion that higher TOC causes aseismicity because the fracture mechanism transitions from fault slip (mode II) to creation of hydraulic fractures (mode I). Specifically, the high TOC rocks tend to exhibit slow, tensile hydraulic fractures due to the ductility of the materials. Conversely, more brittle materials fracture by shear or mixed-mode mechanisms that are faster. However, the current author believes there is insufficient evidence to support this claim that slower fractures are more mode I dominated.

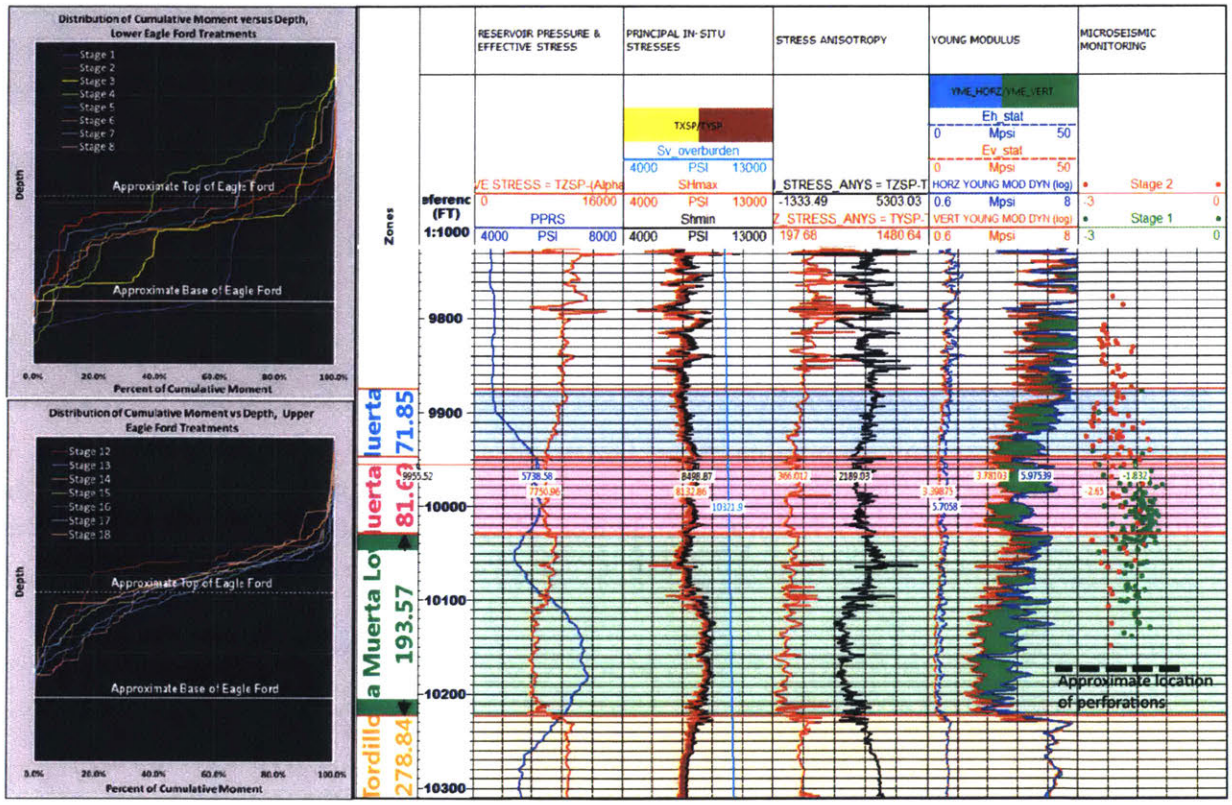

Figure 2.44: On the left, distribution of cumulative moment versus depth for lower and upper Eagle Ford treatments. Note that regardless of the vertical placement of the perforations, most cumulative moment is occurring at the upper Eagle Ford while the lower Eagle Ford seems not to generate microseismicity. The same is occurring at the Vaca Muerta formation (on the right), where events from stages 1 and 2 are migrated upwards from the perforations, which are placed at the lower member of the Vaca Muerta. The plots show that few microseismic events occur in the TOC rich strata in both the Eagle Ford and Vaca Muerta formations. From Padin et al. (2014).

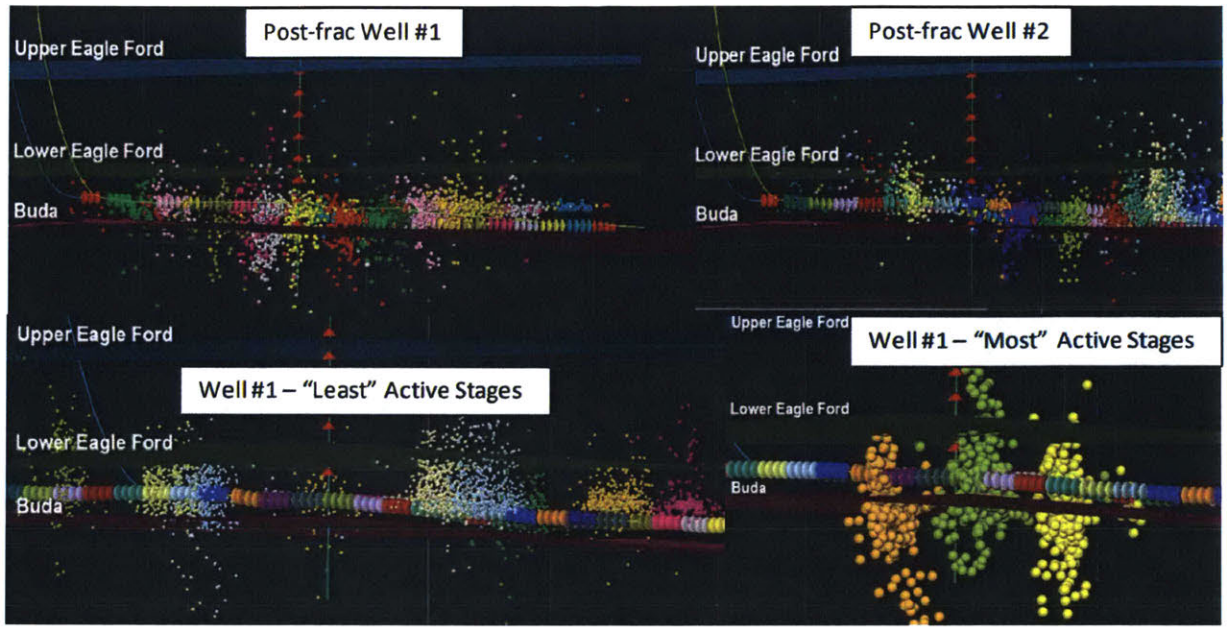

Figure 2.45: Microseismic monitoring of two horizontal wells fractured at the Eagle Ford. At the bottom of the figure, the "least active" vs the "most active" microseismic stages are shown. At the top, post frac results are shown for two different wells. Note that events with magnitudes less than -2 are located within the lower Eagle Ford. From Padin et al. (2014).

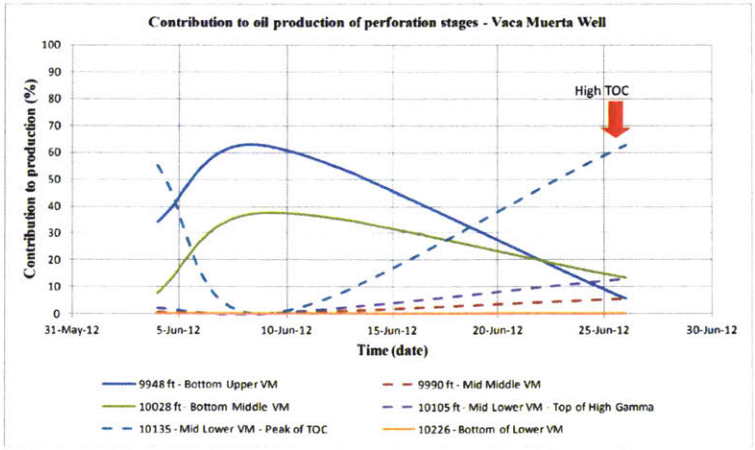

Figure 2.46: Contribution to oil production of the perforation stages in the Vaca Muerta well 1. From Padin et al. (2014).

2.3.2.3 Natural fractures in shale: A review and observations (Gale et al., 2014)

In this paper, the authors present a comprehensive literature review along with new data on shear and tensile fractures in shale, including discussions on fracture density, aperture, dimensions, orientation, and cementation. The data are primarily viewed from the perspective of the oil and gas industry, with a specific focus on enhancing permeability for oil and gas production from unconventional (hydraulic fracturing) treatments. The data are primarily drawn from core and outcrop samples.

Regarding the effect of clay and organic content, they establish that higher clay or organic content in shales generally leads to lower strength and elastic modulus, with a tendency towards shear failure than tensile failure. Their literature review also found that shales generally exhibit "far lower fracture abundance or no fractures", and they describe a specific field observation by Ferrill et al. (2012) where a fracture in chalk terminates at the shale stratum. The distinction is also made, as seen in Figure 2.47, that clay and organic shales tend to exhibit ductile behaviour through creep, that silica-rich shales tend to exhibit greater brittleness, and that carbonate shales tend to exhibit sealed fractures. However, the authors then appear (and themselves admit) to an apparent contradiction that "clay- and organic- rich layers sometimes contain many fractures...high organic content locally corresponds to closely spaced natural fractures". They posit that this may partly attributed to changes during burial, where initially ductile shales become increasingly brittle through diagenesis and overpressure (Nygard et al, 2006). In summary, this study provides many interesting pieces of information that may shed light on the differences between fracture processes in granite and shale discussed in this thesis.

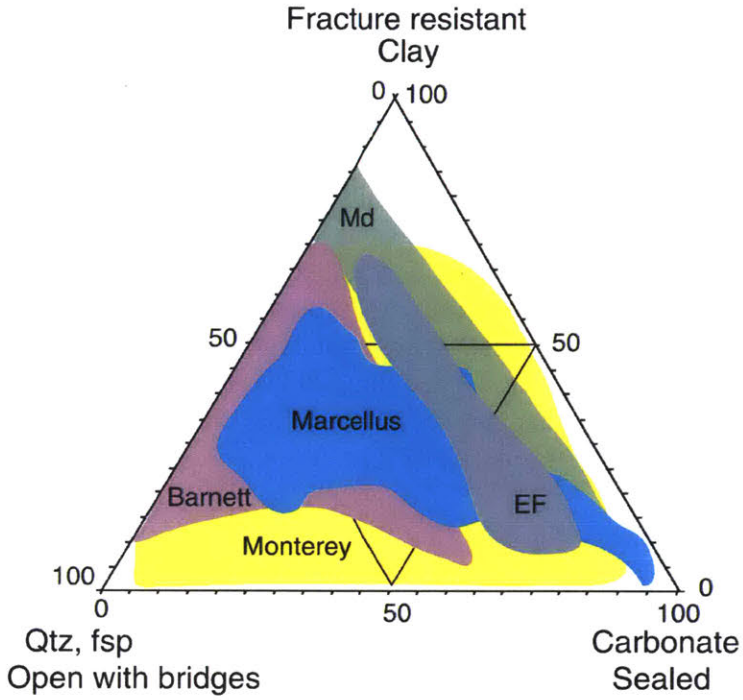

Figure 2.47: Host rock compositional variation. Variable mineral composition fields of Barnett, Eagle Ford Formation (EF), and clay-rich mudrock (Md) (modified from Passey et al., 2010), Monterey Formation (from Isaacs, 1981) and Marcellus Formation (drawn from data in Pommer, 2013). Sealed, open, and fracture resistant axes are our interpretation of the tendencies that these compositional variations represent for fracture attributes. End members in the compositional field are interpreted as propensity to fracture or resist fracture (clay poor versus clay rich), propensity for fracture wall rocks to resist cementation or bridge (quartz rich), and propensity for fractures to seal with calcite (calcite rich). Qtz = quartz; fsp = feldspar.

2.3.3 Summary of Literature Review

Recall that the goal of this thesis is to study (1) the relationship between the creation of hydraulic fractures and the microseismicity generated during this process, and (2) how this relationship differs between granite and shale materials. To that end, the results presented in this section can be summarised as follows:

- The digital image correlation (DIC) technique can serve as a powerful tool to quantitatively identify and evaluate the growth of both dry and hydraulic fractures. In the studied literature there were no significant attempts to address the discontinuity in the displacement/strain field across a crack. There also do not appear to be studies in rock where DIC was applied to high-speed imaging to quantify crack growth. DIC was also used on microscope images to quantify the development of shear cracks during a uniaxial compression test on intact Carrara marble, which we adopt in work presented in this thesis.

- Acoustic emissions acquired during laboratory rock fracture experiments show that the spatial distribution of events correspond nearly 1:1 with the spatial distribution of microcracks observed using microscopy, and hydraulic fractures that were mapped post-experiment. Regarding grain size, two studies appear to be contradictory on whether increasing grain size affects the seismicity of the creation of shear fractures. Regarding mineralogy, it appears that increasing clay+organic content correlates to decreasing seismicity during shear along a fault. Regarding the rate of shear across a simulated fault, we find that decreasing shear rate is associated with an increased number ofobserved acoustic emissions per millimetre of displacement. We also see that considering the energy budget between the work done by the injection fluid during hydraulic fracturing and the energy radiated as seismic waves can be an effective tool to compare laboratory and field processes. The energy budget method will be applied in this thesis to compare different fracturing mechanisms (dry vs. wet, tensile vs. shear) and to compare between granite and shale.

- The beam bending test methodology, when conducted under crack mouth opening displacement control, serves as a simple benchmark method of generating a tensile fracture that propagates slowly, so that the AE are dispersed in time and can be easily analysed. Similarly, visual data can be captured using a time-lapse on a high resolution camera with a frame-rate on the order of seconds, which allows for more detailed analysis than image data from a low resolution, high speed camera.

- Field studies shows that microseisms related to hydraulic fracturing have a significant non-double couple component, which can be compared to our laboratory studies. Analysis of fractures and microfractures in the field also suggest that clay and organic content are related to seismic activity, and that the characteristics of microfractures in more ductile shales appear to be markedly different from more brittle rocks such as granite.

Chapter 3

Tensile Fracturing in Granite

"You may learn something, and whether what you see be fair or evil, that may be profitable, and yet it may not. Seeing is both good and perilous."

In this series of tests, a granite specimen was subjected to four point bending to generate tensile stresses, which result in the formation of a process zone consisting of microcracks, which then coalesce and develop into a crack. This process was forced to occur slowly under crack mouth opening control, such that different observation methods could be used to describe the cracking process. This experimental setup is chosen because the slow fracture process serves as a benchmark for the faster and more complex fracture processes presented in later chapters. Specifically, these observations are 1) Load-displacement behaviour, 2) Strains observed on the surface of the specimen and interpreted by DIC and 3) Acoustic emissions. The results section will first present the load-displacement data, which are then compared to the corresponding visual and acoustic emissions data.

3.1 Experimental Setup

3.1.1 Physical Setup

The specimen (dimensions 241.3 x 51 x 25.4 mm) was set up as shown in Figure 3.1. The material was Barre Granite from Vermont. The top loading platens were not spaced as per ASTM standards, to accommodate the dimensions of our loading machine, which are acceptable given that the absolute value of the ultimate load was not of interest. The used spacing was adequate to generate a repeatable stable stress condition. An extensometer was attached to the notch opening, and the experiment was operated under Crack Mouth Opening Displacement (CMOD) control at a constant rate of 0.0127 mm/min (see Figure 3.3b).

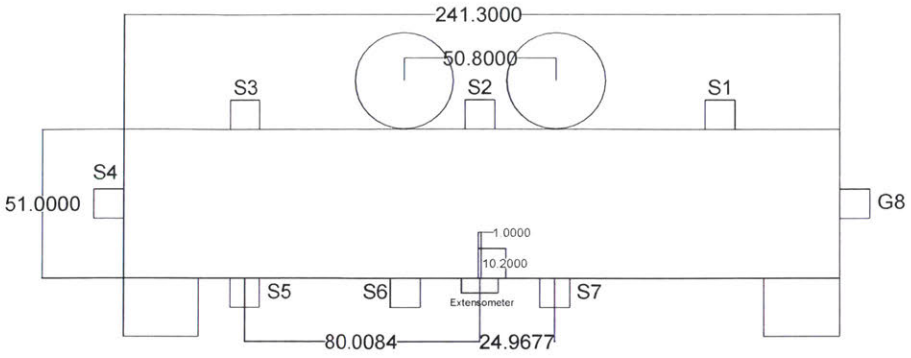

Figure 3.1: Specimen geometry and AE sensor locations. S refers to PAC Micro30S sensors, and G refers to a Glaser-type sensor. Boxes denote locations of the loading platens. Units in mm.

3.1.2 Camera Setup

The experiment was instrumented with two cameras. On the front face, a Canon 6D was used with a Tokina 100mm f/2.8 ATX M100 lens at a distance of around 40 cm such that the field of view was approximately 7.5 cm x 10 cm. On the back face, we used a Canon SL1 with a 65mm MP-E macro lens at 5X such that the field of view was approximately 2.95 mm x 3.93 mm. For surface preparation, the side facing the front camera was painted with a white acrylic paint background with black paint sputtered at around 0.1 to 1 mm speckle size. The back side was painted with the same white acrylic background paint, then polished to 10 μm grit with alumina powder and sputtered with carbon black on a 1000 Nickel mesh to create a grid pattern with approximately 25 μm spacing. Figure 3.2 shows photos of the prepared specimen. For simplicity, analyses of images from the front camera will be referred to as "macro-images" or "macro-DIC" and likewise back camera images and analyses as "micro-images" and "micro-DIC". The macro-DIC is performed with reference to time 143 s, and the micro-DIC is referenced to time 147 s.

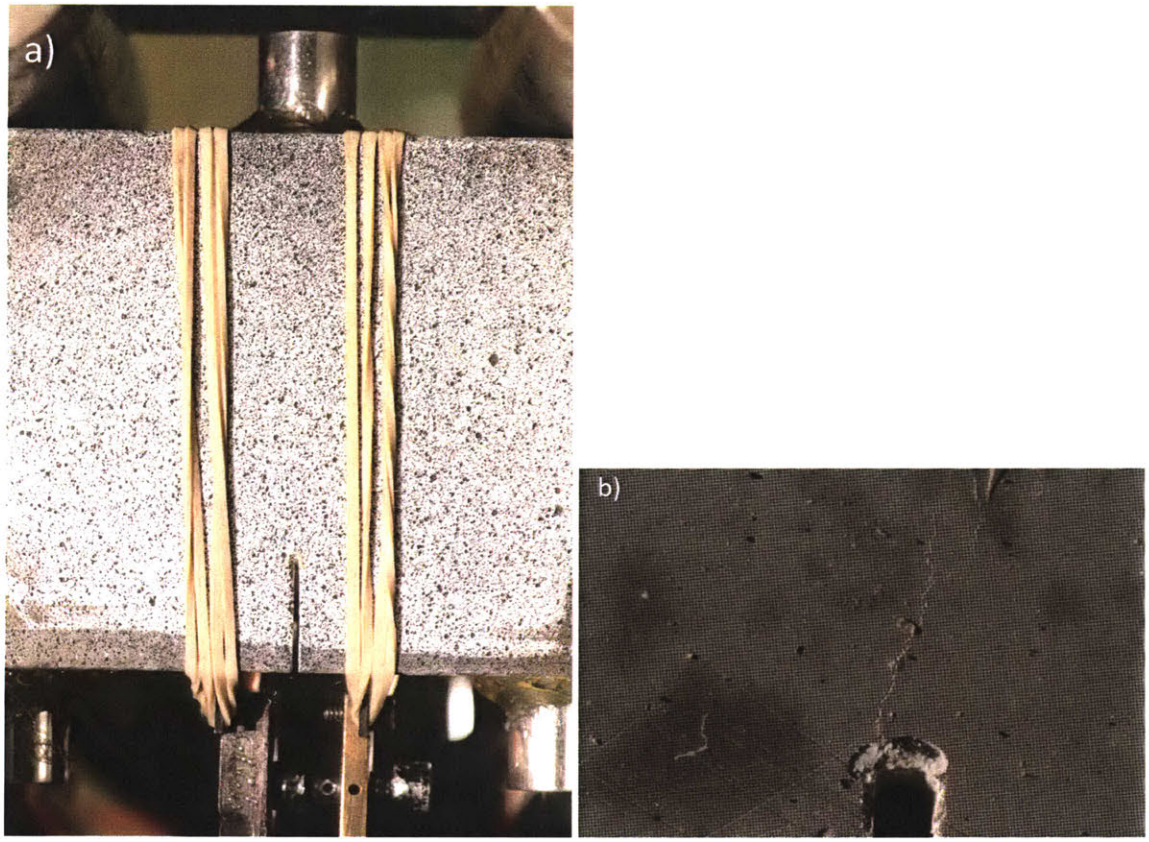

Figure 3.2: (a) Reference image for the front camera, corresponding to a field of view (FOV) of around 5 x 7.5 cm. (b) Reference image for the back camera, corresponding to a FOV of around 2.95 x 4.425 mm.

3.1.3 Repeatability

To ensure that the results are consistent, two repeats (i.e. three tests in total) of the same experiment were performed. The load-displacement graphs are shown in Figure 3.3a. The drop in load close to the end of the elastic region are due to refocusing of the cameras. During the pause the position of the crosshead was held constant, but the machine software is such that no data are acquired when the experiment was paused. When the machine is restarted the load drops for the duration of 2-4 data points (0.01 s data acquisition interval). This is unfortunately unavoidable since the specimen expands in the depth dimension due to the Poisson effect such that the micro-camera requires refocusing at the end of the initial loading phase. This must be done manually since autofocus in unreliable in this setup. The peak loads and crosshead displacement are similar for the three experiments; the elastic phase (linear region of the force-displacement plot) has slightly different slopes while the inelastic phase (post-linear region of the force-displacement plot) follows a different path in each experiment. These differences may be attributed to heterogeneities within the granite specimens. Note that all three experiments transition from the linear region at approximately 2.3 x 10-4 m of crosshead displacement and appear to show some stick-slip behaviour during the inelastic and cracking phase in that the load is constant for a period of time before increasing and decreasing rapidly. Since the load-displacement behaviour was reasonably similar and the AE and DIC trends were similar in all experiments, the discussion of results will be focused on the first experiment.

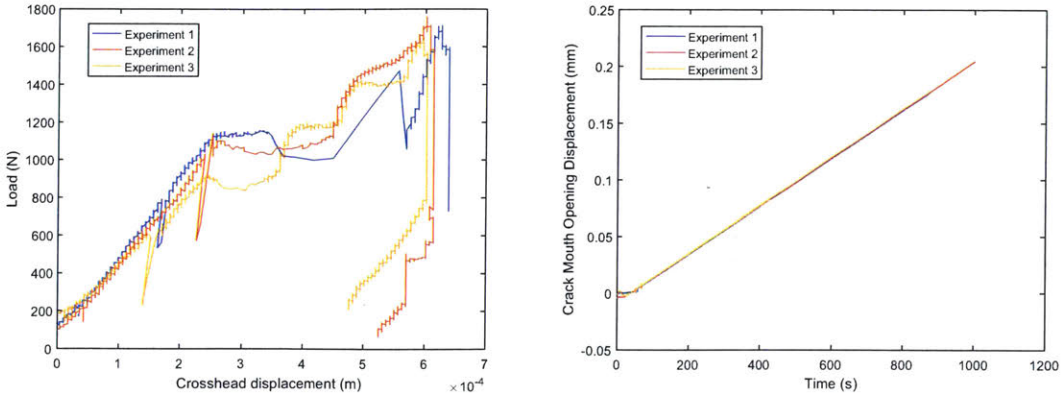

Figure 3.3: (a) Load-displacement data for the three experiments. Drops in load during the initial elastic region are points in time where the loading was paused to refocus the cameras. (b) Crack mouth opening displacement over time for all three experiments, with a nominal rate of 0.0127 mm/min.

3.2 Load-displacement behaviour

Figure 3.4 shows the load-displacement data for the first experiment, and it can be seen in Figure 3.4b that the loading curve consists of three main stages: an initial linear phase ('a'), followed by a non-linear period of increasing load ('b'), and finally a monotonically decreasing load while the crosshead is held constant ('c'). The load-displacement curve can be integrated to produce the machine input energy, as shown in Figure 3.5. Note that the maximum machine energy input is around 0.7 J.

Figures 3.4 and 3.5 indicate three distinct stages which can be interpreted as 'a' elastic deformation, 'b' process zone development and 'c' crack initiation and propagation, where crack initiation is considered to be the first time a new traction free surface is created, and crack propagation refers to the continued creation of such traction free surfaces. Both the load-displacement and energy-time data support this interpretation, which also correspond to the stages outlined in Eberhardt et al. (1999), although we have chosen to interpret their crack initiation and stable crack growth stage as the development of the process zone. These stages are now used as the basis of comparison for the visual and AE observations. Note that although a crack initiates and propagates in stage 'c', a process zone continues to develop ahead of the propagating crack tip.

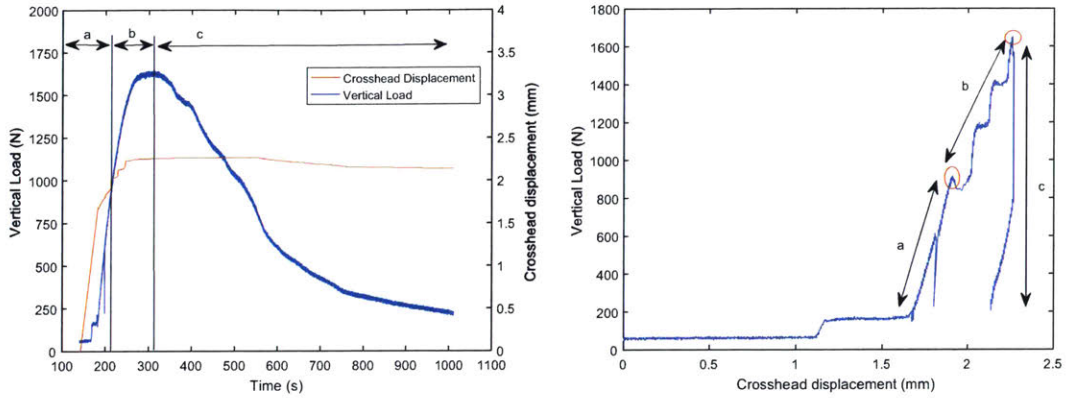

Figure 3.4: (a) Crosshead load and displacement over time. (b) Same data expressed as load-displacement to identify key stages of behaviour: 'a' linear load-displacement behaviour indicating elastic deformation. 'b' Vertical load appears to increase in 3 distinct non-linear steps, indicating the material is no longer deforming elastically. 'c' The load decreases while the crosshead maintains its position, indicating that the fracture is steadily propagating. The transition points are indicated in the red circles.

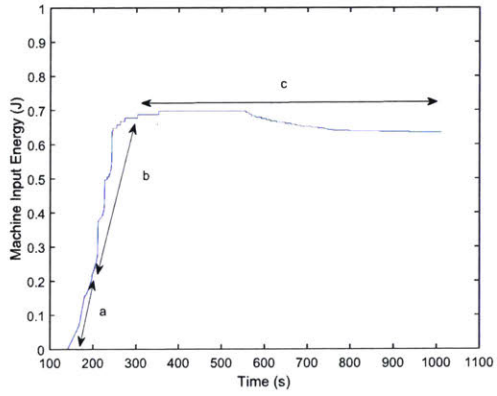

Figure 3.5: Machine input work, calculated from the integral of Figure 3.4b. The three stages of deformation are also highlighted here. The behaviour transitions from 'a' to 'b' at around 210 s, and from 'b' to 'c' at around 310 s.

3.3 General comparison of strain and AE observations

These comparisons will first be done for the entire experiment to evaluate general trends in behaviour, and then specifically for stages 'b' and 'c' of the load-displacement curve.

3.3.1 Strain observations

Figure 3.6 shows the macro-DIC opening strain at key points in time corresponding to the load-displacement curve (Fig. 3.4a), to determine the extent of damage that can be visually observed on the specimen. Note that some of the strains are calculated across discontinuities.

Figure 3.6 shows that at time 209 s, very little deformation can be seen given the noise threshold of the DIC method. This is to be expected as the load-displacement curve indicates that the behaviour is elastic until this point, and that the displacement is quite small. However by 259 s, there is a zone of significant opening strain extending around 2 mm from the notch tip. This again is consistent with the load curve, which shows a small amount of non-linear deformation by this time. By 309 s there is a large, 2-3 mm wide zone of deformation extending around 7 mm ahead of the notch tip. This zone of deformation then decreases in size by 549 s, likely caused by unloading of the rock at that location since the crack tip and its corresponding process zone move upwards as the crack propagates.

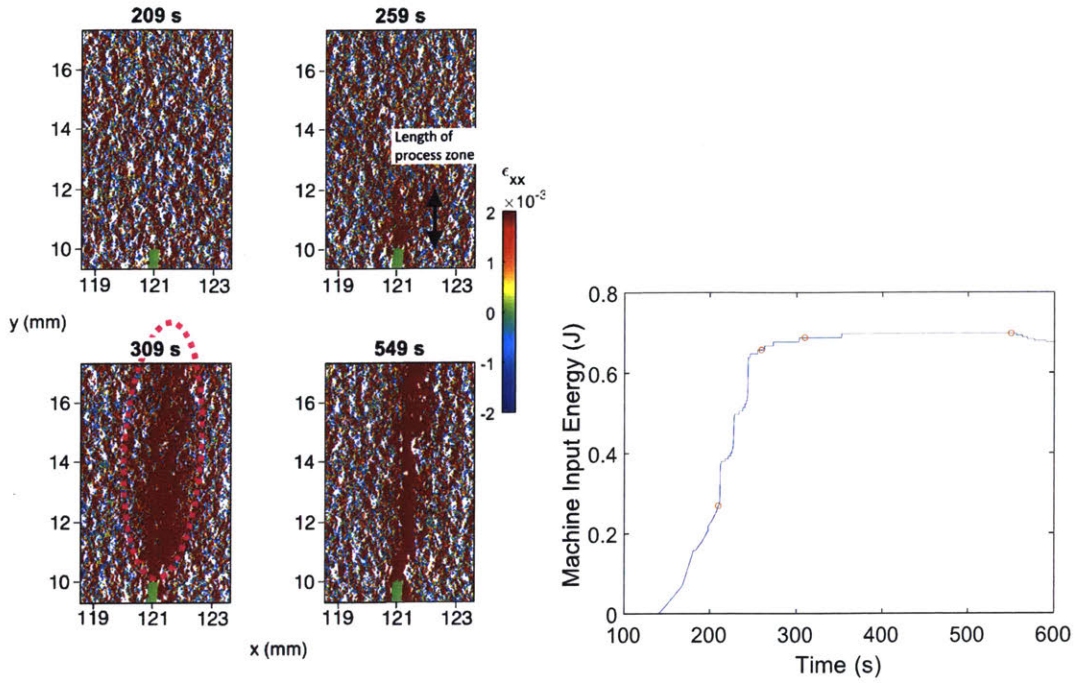

Figure 3.6: (a) Opening strain from macro-DIC at key points in time. (b) Points in time indicated on the energy-time curve. Dotted purple line indicates semi-elliptic bulb of strain.

3.3.2 AE observations

Figure 3.7a shows the location of AE events over the course of the experiment. There is significant scatter in the horizontal direction even with the imposed 1 mm accuracy for localisation, which implies that the approximately 10 mm wide scatter of event locations can be attributed to the formation of a process zone (Wong and Einstein, 2009) as cracking propagates through the specimen. This is significantly wider than the 2 mm process zone observed in the DIC. An explanation is that the AE may be sensitive to smaller perturbations. As expected, the AE locations shift upward as cracking propagates (See time scale in Figure 3.7a), but again there seems to be significant scatter in the vertical direction, highlighting the stochastic nature of AE events stemming from heterogeneities in the crystalline rock specimen. It is also notable that at around location (x = 120 mm, y = 23 mm) there is a small zone of approximately 1 mm in diameter that is lacking in AE events, indicating that there may be a particularly high strength mineral grain at that location.

Figure 3.7b shows the largest AE events, coloured by their magnitude. There appears to be wider scatter of locations near the notch tip, which may be due to a wider process zone prior to crack initiation and is consistent with Figure 3.6, which showed a large process zone near the notch tip. Overall, the large events shown in Figure 3.7b seem to occur closer to the crack path than Figure 3.7a, which shows all the events. This suggests that the larger events are more critical to the creation of the crack itself, whereas smaller events are more likely to be related to the continued development of the process zone ahead of the propagating crack tip. Interestingly, there appears to be a significant semicircular pattern in the event locations again at around (x = 120 mm, y = 23 mm), suggesting that the larger AE events may be preferentially occurring at grain boundaries.

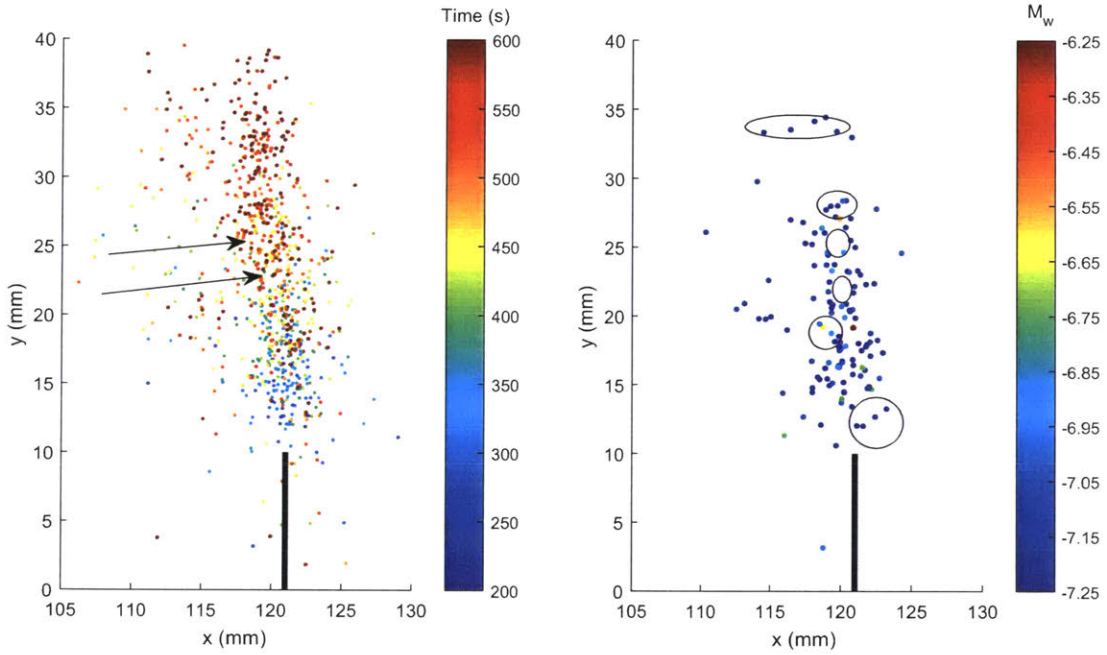

Figure 3.7: (a) AE events for entire experiment, coloured by time. Arrow indicates a specific zone in the AE cloud where there appears to be no events. (b) AE events with Mw $>$ -7.4, coloured by magnitude. Black circles indicate events occurring along possible grain boundaries or zone of no events.

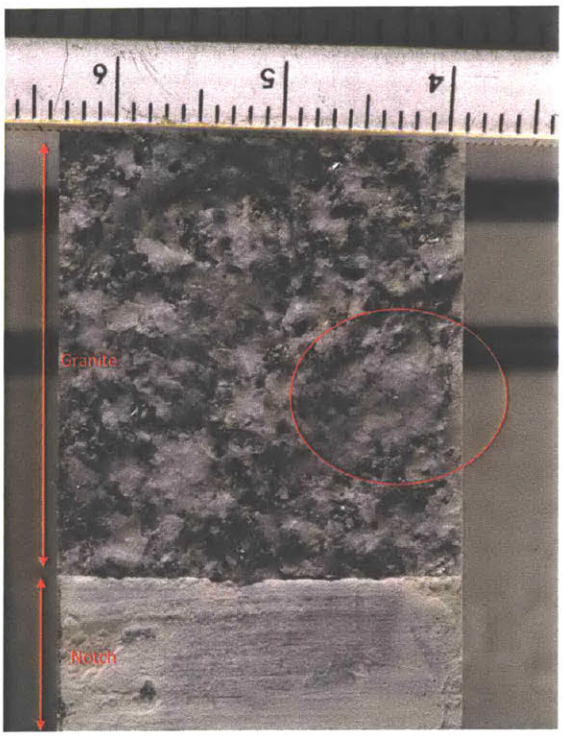

Figure 3.8: (a) Detailed photo of the crack surface, large quartz grain shown in red. Scale in cm. White flat surface is the pre-cut notch. (b) Curvature in the crack path due to the quartz grain.

This happens at other locations that are circled in Figure 3.7b, and is supported by visual inspection which showed, for example, that there was a large quartz grain (Fig. 3.8) approximately 10 mm from the notch tip. Overall, it appears that the AE locations correspond to the strain maps, both showing a larger scatter around the notch tip that may be associated with the initial process zone.

More information can be gained by considering details of the AE evolution over time and space. This is done in Figure 3.9, which shows the magnitude-frequency distribution of AE events, which shows the proportion of large compared to small events. Different curves show the b-value at various times and distance from the notch tip.

Figure 3.9a shows that the development of the process zone, which occurs between 200 and 300 s, contains the fewest and lowest magnitude events. This is consistent with the behaviour observed in the energy-time curve, which suggests that crack propagation is more energetic than process zone development. Interestingly, this time period has a shallower slope than the 300 - 400 s and 500 - 600 s period, indicating that small events comprise a lower proportion of events during this time. As expected, the time between 400 and 500 s contains the most and highest magnitude events, which is consistent since this is the period of greatest machine work (Figure 3.5). Figure 3.9b shows the b-value for events grouped according to their distance from the original notch tip. We can see that the highest concentration of events is at 5-15 mm from the tip, followed by those at 15-25 mm, then by those right at the notch tip. The 5-10 mm grouping has a similar total number of events as the 10-15 mm grouping, but the 5-10 mm grouping has more large magnitude events, indicating that crack initiation may be associated with the largest events given that this grouping is quite close to the notch tip. This is supported by the 0-5 mm grouping, which has a small total

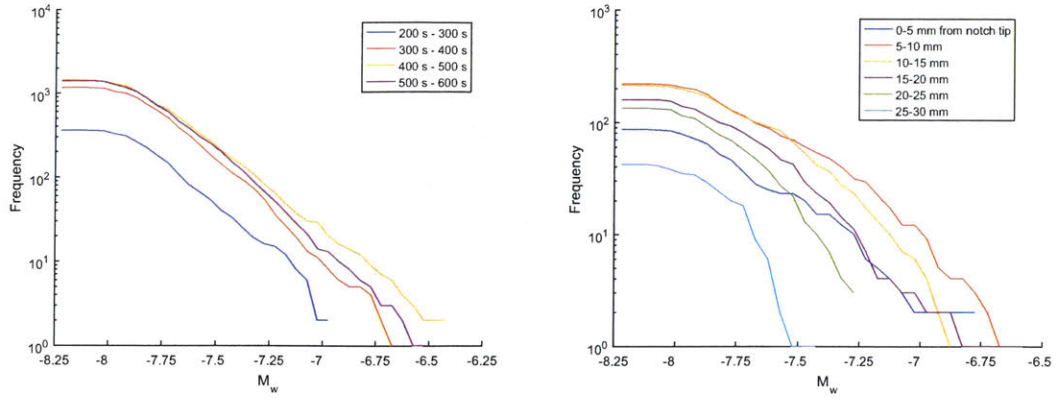

Figure 3.9: Magnitude-frequency distribution of AE events. x-axis is the magnitude of events, and y-axis is the cumulative number of events, similar to a cumulative density function. (a) Each curve shows the magnitude-frequency distribution for AE events occurring over a given time interval. (b) Each curve shows the magnitude-frequency distribution for AE events occurring over a given range of distances from the notch tip. A shallower slope (lower b-value) represents a time window or distance range where relatively more large magnitude events occurred than small magnitude events, and a curve with a higher frequency (higher on the y-axis) represents more total events occurred within a given time window or distance range.

number of events but also has a greater proportion of large magnitude events compared to the 10-25 mm groupings. In fact, one may conclude that the slope becomes steeper with distance from the notch tip, i.e. smaller events dominate with increasing distance from the notch tip.

Figure 3.10 shows the AE hit rate for the experiment, which increases linearly until approximately 340 s and maintains a steady rate until approximately 550 s, where it begins to decrease. This pattern appears to match well with the loading machine work shown in Figure 3.5, which is constant between 350 s and 550 s. There also appears to be more variance in the hit rate between 400 s and 600 s than in the previous 200 seconds, in that there are multiple large increases in activity even though the rate remains constant on average. This can be explained by stick-slip behaviour or small-scale heterogeneities of the material resulting in more emissions produced when the crack moves through a higher strength material. However, this is difficult to verify given that one cannot determine the extent of the crack at depth over time. Overall, it appears that the load-displacement, strain (DIC), and AE observations are reasonably consistent. Specifically, all three observations (Figures 3.4b, 3.6, and 3.7) show that stage b, which consists of process zone development, is associated with a wider bulb of lower energy activity near the notch tip. This is markedly different from stage c, which consists of crack propagation and appears to be higher energy and less spatially dispersed horizontally. For this reason, the two stages are now discussed separately in more detail.

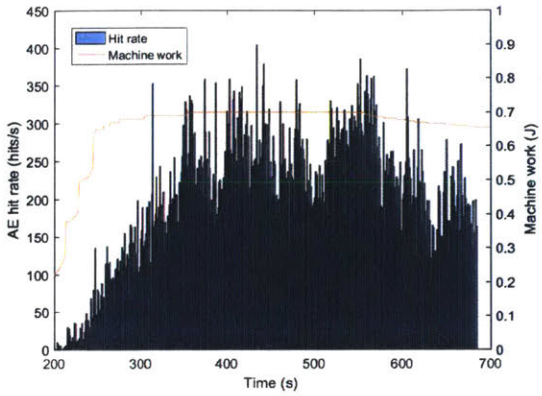

Figure 3.10: AE hit rate over the course of the experiment. Figure 3.5 is superimposed for reference.

3.4 209 s to 309 s: Process zone development

Between 209 s and 309 s (See stage b in Fig. 3.4), the machine load is monotonically increasing and the deformation is non-linear; the machine is constantly putting work into the system (Fig. 3.5).

3.4.1 Strain observations

Figure 3.11 shows the ε_{xx} and ε_{xy} strains from the micro-DIC at three different points in time. At 253 s, the microcracks have propagated to around 0.6 mm from the notch tip, which is a very small distance compared to the AE events (Figure 3.7), which reach up to 15 mm from the notch tip. One can also note that the first 0.5 mm of the microcracks initiate in tension given that at 253 s ε_{xx} shows significant opening strain but very little ε_{xy} contribution (zone a in Figure 3.11). After the initial 0.5 mm, it appears that the microcracks propagate as a series of en-echelon cracks (zone b in Fig. 3.11). These en-echelon microcracks occur at approximately 45 degrees to the tensile stress direction as expected, but there appears to be a preference for the SW-NE orientation, a trend that was also observed in the two repeat experiments and may be due to a bias in the loading machine. It is also interesting to note that at approximately 259 s the macro-DIC (Figure 3.6, black arrow) indicates a zone of increased strain that extends 2 mm from the notch tip, but the same time frame for the micro-DIC only indicates microcracking up to around 0.5 mm from the tip, and even at 275 s only extends approximately 1 mm from the notch tip. The much smaller extent of the strain-intense areas in the micro-DIC may be due to the small 3 mm field of view, such that general changes in strain seen in the macro-DIC fall into the background noise of the strain plots seen in Figure 3.11. As a result, the micro-DIC only highlights what may be referred to as linear white patching (Morgan et al., 2013; Wong and Einstein, 2009) i.e. the process zone visible by eye as a white line.

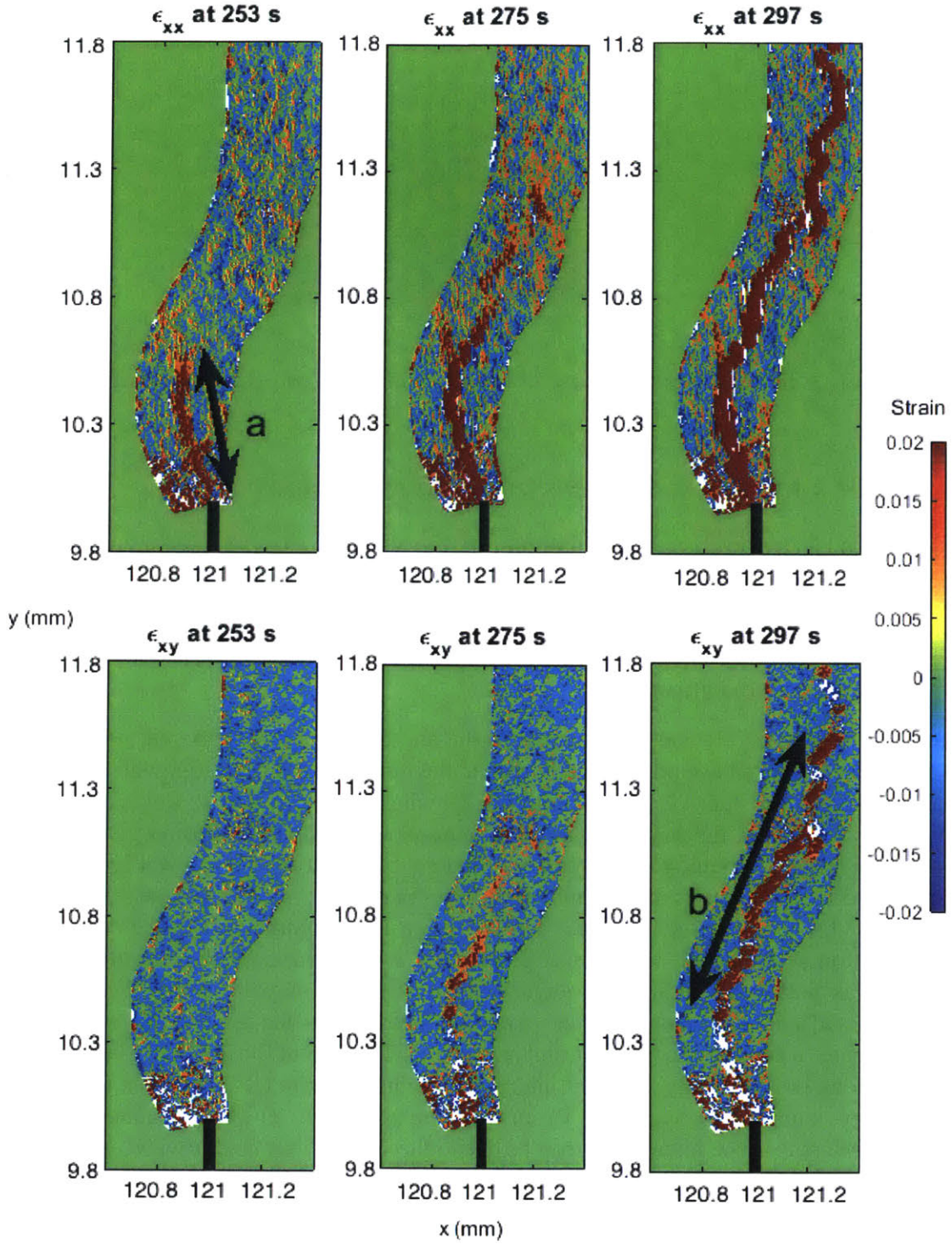

Figure 3.11: ε_{xx} and ε_{xy} from micro-DIC at 253, 275 and 297 s of the experiment. The times correspond to approximately 90%, 95% and 100% of peak load respectively. The black bar in each figure schematically indicates approximate location of notch tip. Zone a: Initial portion of the crack, which appears to be purely tensile given that ε_{xy} indicates very little strain. Zone b: Ensuing en-echelon crack, which clearly shows step-like structure particularly in the ε_{xy} plot.

3.4.2 AE observations

In terms of the AE data, the event locations shown in Figure 3.12 indicate that majority of events are dispersed, and cluster in an area around 10 mm from the tip of the notch. A vertical linear series of events appears to occur near the notch tip at around 250 s (Cluster a), and another linear cluster at around 270 s (Cluster b), indicating that there may have been concentrated microcracking at these locations. A look at the source mechanisms and magnitudes shown in Figure 3.13 indicates that the tensile events are much fewer and appear to occur somewhat away from the notch tip when compared to the shear events, which form the majority of the cluster immediately at the notch tip. As expected, the tensile microcracks are oriented along the orientation of the eventual crack, but the shear events appear to have a wide distribution of orientations. The magnitudes appear mostly to be quite small in this time period. Interestingly, the tensile events do not show the initial tensile portion noted as 'a' in Figure 3.11. This may be due to the small size of this tensile feature, such that it is not captured by the AE which averages behaviour across the specimen. Unfortunately, attempts to directly map the AE locations to observations in the micro-DIC were not successful, given that the location accuracy of the AE at 1 mm is considerably larger than the resolution of the micro-DIC at around 25 μm.

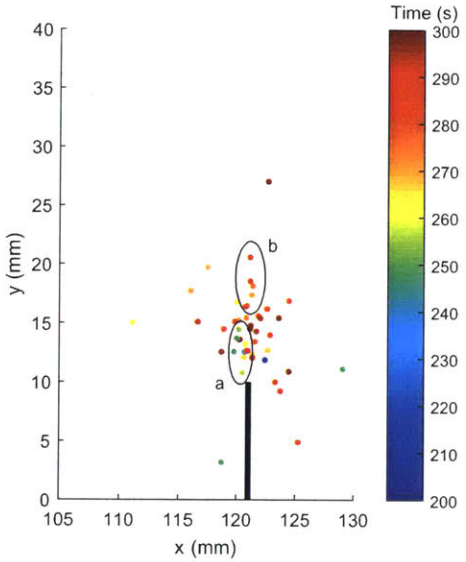

Figure 3.12: Source locations for events occurring between 0 and 300 s in the experiment. Colour shows time of occurrence. Clusters a and b each seem to occur closely in time in a linear pattern

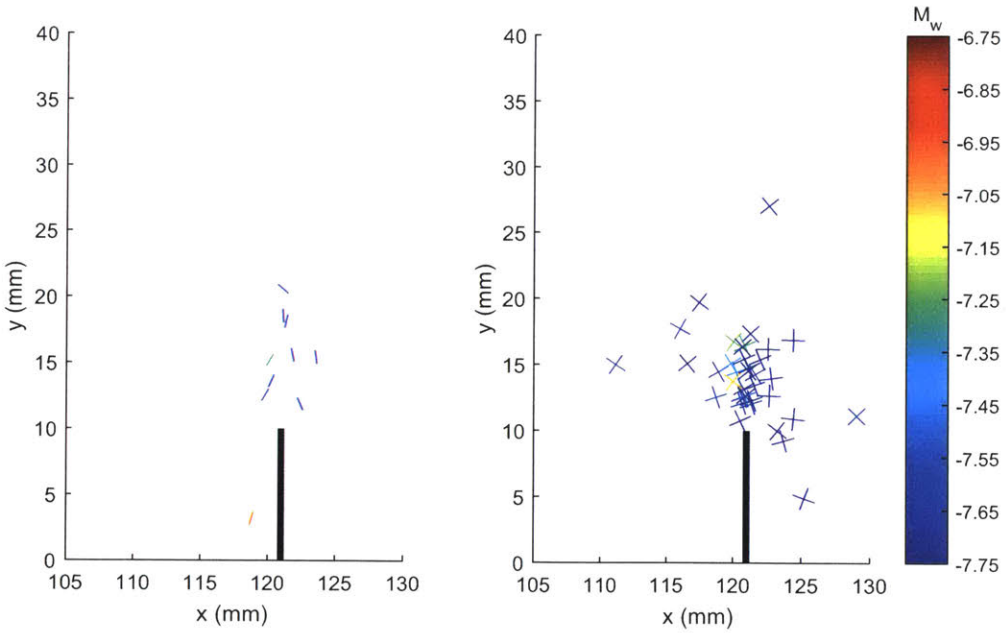

Figure 3.13: (a) Microcrack orientation and location for tensile events occurring between 0 and 300 seconds. (b) Orientation and location of shear conjugate planes. Colour indicates magnitude.

3.4.3 Comparison of AE and visual data between 209 s and 309 s

To relate the DIC and AE data, Figure 3.15 shows the evolution of the strains over time at specified query points. At point 1 (query points are shown in Figure 3.14), corresponding to the tensile zone noted previously, the rock has higher opening strain than elsewhere; it also begins to significantly open at around 260 s, approximately 10 seconds before the rock at other query points. It is also interesting to note that the remainder of the query points, though they are separated in space, all show very similar behaviour in that they begin to open around 270 s, albeit at slightly different rates. Given that a qualitative observation of Figure 3.11 shows that strains develop as early as approximately 250 s, this indicates that the early strains are quite small such that they fall within the noise band of the DIC analysis (the standard variability of strains seen between 240-260 s). As expected, ε_{xy} exhibits both positive and negative strains corresponding to the two possible orientations of the en-echelon cracks. However, it is notable that the positive (SW-NE) strains are approximately five times larger than the negative strains, which agrees with the general preference for the SW-NE direction noted earlier. There also appears to be some grouping of shear behaviour for the rock at separate locations, for example the behaviour at point 1 is similar to point 3; likewise points 4 and 6, 5 and 7 show similarity to each other. These points appear to develop strain at approximately the same rate, possibly suggesting that separate sections of the en-echelon cracks may be developing simultaneously. Overall, we conclude that microcrack initiation begins around 260 s, which corresponds to the middle of stage "b" on the load-time graph shown in Figure 3.4. The AE hit rate fluctuates significantly over the period of analysis, and one may argue the times of high AE activity are related to local minima or maxima in query point 1 of Figure 3.15a. However this relation would be tenuous at best since the DIC only samples the surface of the specimen, while AE data pertain to the entirety of the specimen.

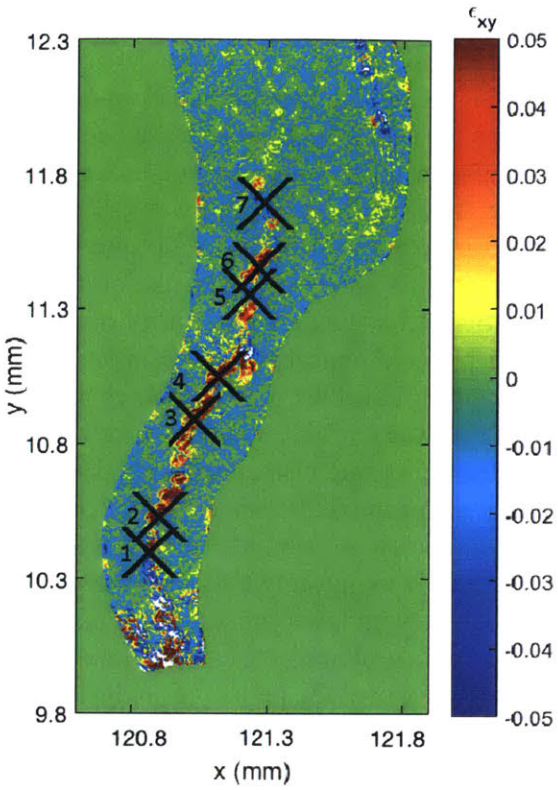

Figure 3.14: Detailed view of ε_{xy} at 300 s of the experiment. Black crosses indicate query points used for Figure 3.15. Point 1 is the lowermost point, and point 7 is the uppermost.

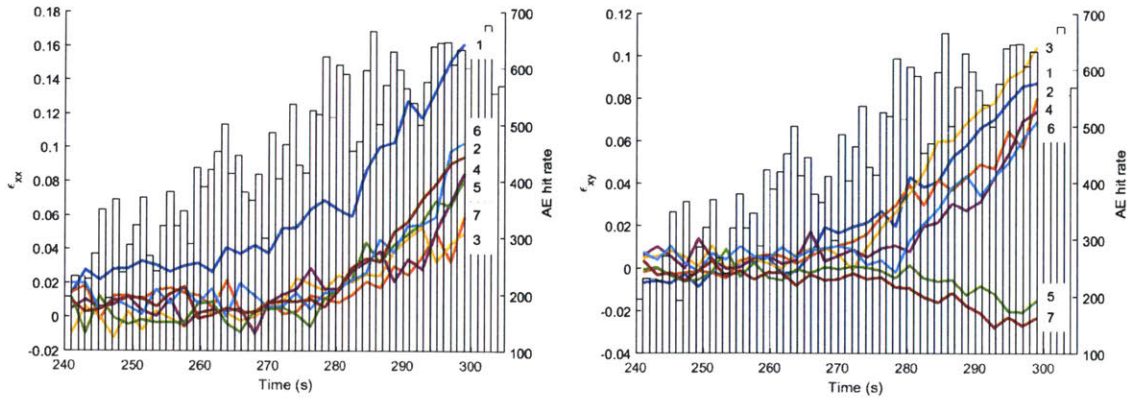

Figure 3.15: Evolution of (a) ε_{xx} and (b) ε_{xy} over time (taken at 2 s intervals) at the query points specified in Figure 3.14. Query point 1 is the lowest point, and point 7 is the uppermost point. Histogram shows the AE hit rate over the same period.

3.5 309 s to the end of the experiment: Crack propagation

Post-load-peak behaviour (stage c in Figure 3.4) generally consists of the continued growth of the crack, and is characterised by the further development of en-echelon cracks as shown in Figure 3.16.

3.5.1 Strain observations

As seen in Figure 3.16, the process zone appears to grow approximately linearly over time, as expected from the nature of CMOD control. It is also evident from the ε_{xy} plots that adjacent zones of positive and negative strain correspond to the development of en-echelon cracks.

Query points (Figure 3.17c) can again be considered for the DIC analysis, for which the strains over time are plotted as shown in Figures 3.17a and 3.17b. There appear to be some anomalies at later times for query points 1, 2 and 3 due to significant opening of the discontinuity, but overall the analysis shows a somewhat linear development of strain over time, with the query points furthest from the notch tip being the last to exhibit strains.

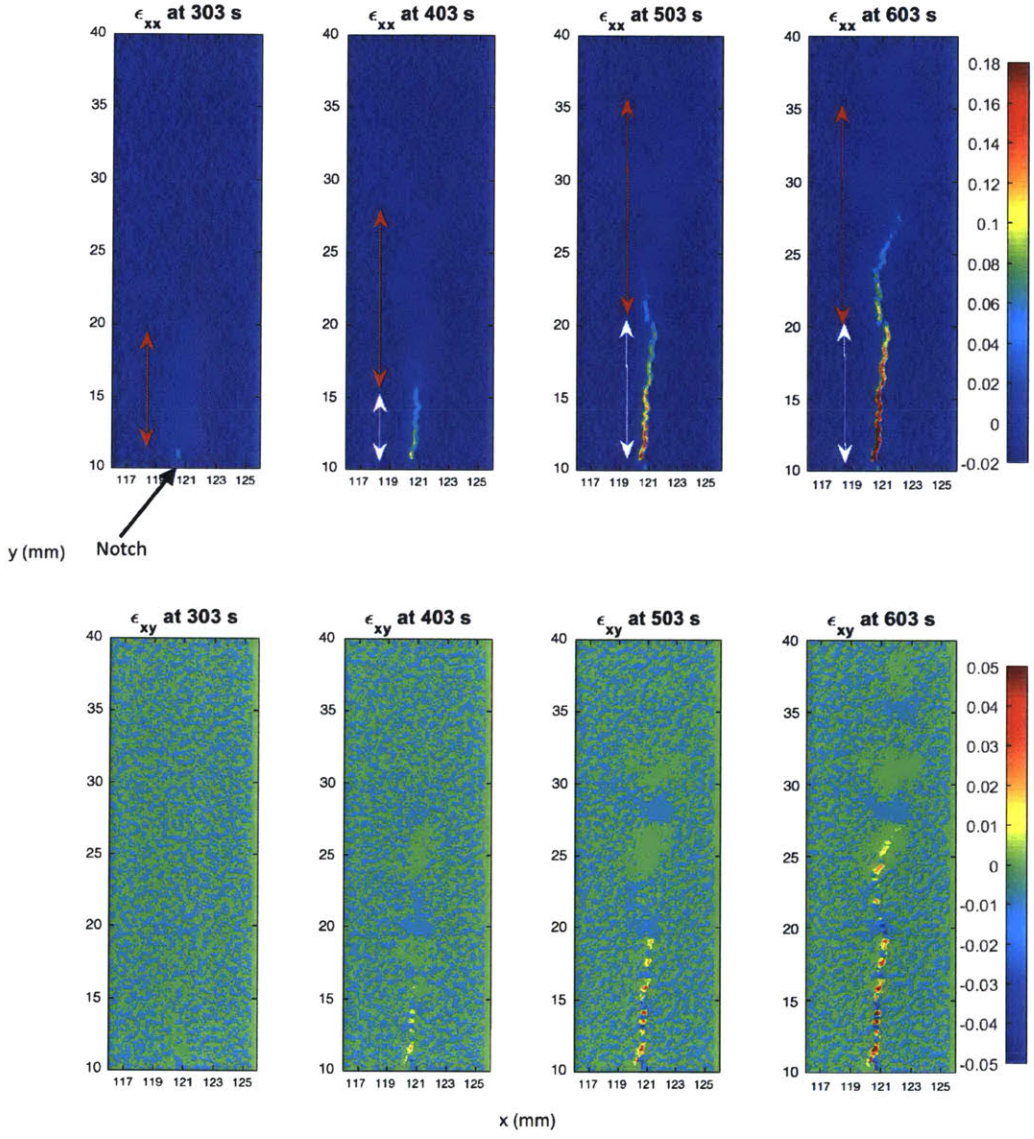

Figure 3.16: (a) ε_{xx} and (b) ε_{xy} on the macro-DIC over the course of the experiment. Red and white arrows indicate the best qualitative estimate of the extent of the process zone and crack respectively.

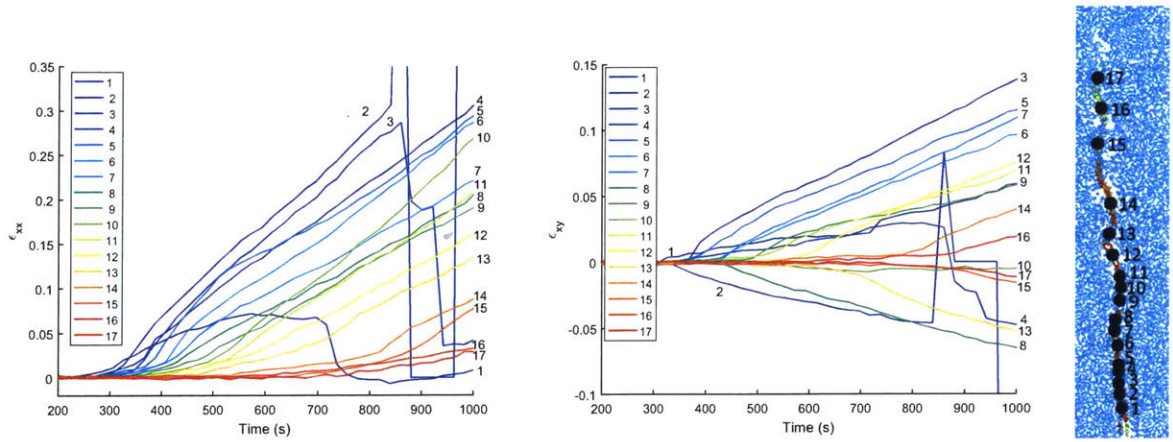

Figure 3.17: ε_{xx} and ε_{xy} over time, taken at 20 s intervals. Rightmost image (c) shows locations of query points. The strains at query points 1, 2 and 3 appear to be anomalous towards the end of the experiment, which may be due to very large crack opening since the employed DIC algorithm does not account for discontinuities.

3.5.2 AE observations

The AE events follow a general pattern with events moving upward with time as the crack propagates. **However, there is significant scatter in this trend, both in time and space. The tensile** microcracks are again oriented primarily vertically as expected since the crack propagates upwards, with the highest magnitude events occurring closest to the center of the cluster. The shear events are more numerous, and also appear more scattered than the tensile events, possibly due to shear occurring at multiple grain boundaries near the propagating crack while tensile events only occur at the crack itself. **However, the magnitudes do not appear to differ significantly between the** mechanisms.

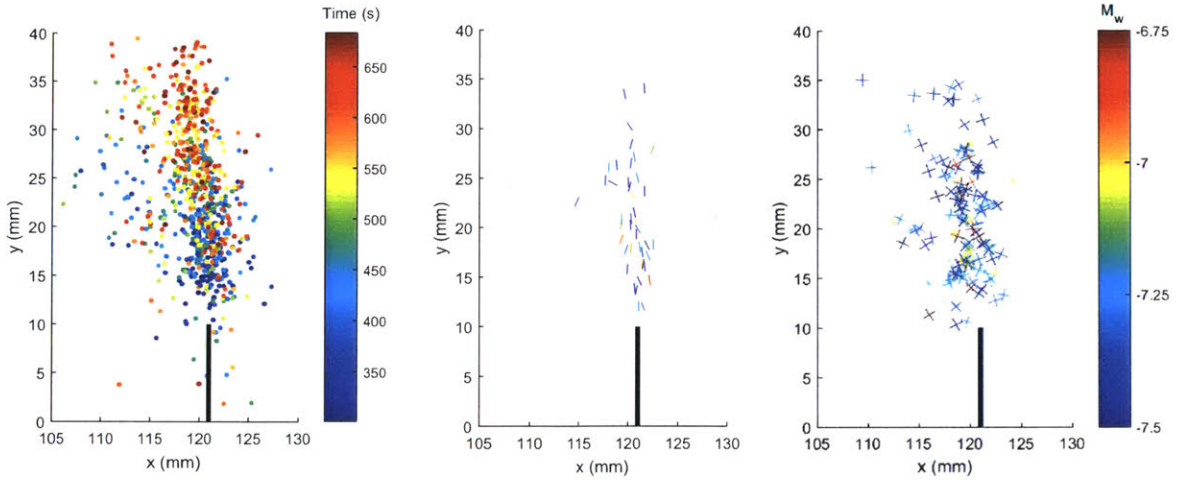

Figure 3.18: (a) Location of all AE events occurring after 300 s. (b) Microcrack orientation and location for tensile events with Mw > -7.5. (c) Orientation and location of shear conjugate planes. Colour indicates magnitude.

3.5.3 Comparison of AE and visual observations

Similar to the previous section, it is important to compare the strains from image analysis with the AE results for this time period. The extent of the process zone and the crack can be estimated from the ε_{xx} contours such as those shown in Figure 3.16. These were determined by considering a large number of query points (crosses) located along the crack, as estimated by a contour line of constant displacement in the opening displacement plot (Figure 3.19a). The ε_{xx} at these query points were then evaluated as a function of time and distance from the notch tip as shown in Figure 3.19b. The process zone was considered to have reached a query point if the strain exceeded the noise level at that point, which varied slightly between points but is generally less than 0.003. To determine the crack extent, the following was done: the load-displacement curve indicates that the crack initiates at approximately 309 s into the experiment. The strain at the tip of the notch at this time is approximately 0.03, or 3% in this experiment, as shown in Figure 3.19b. As a result, we consider 3% as the critical transition point from inelastic deformation to a crack, and use this value to track the propagation of the crack, i.e. if strain at a query point exceeds 3%, we consider the crack to have reached that query point. Note that although the crack initiation appears to be a distinct point in the load-displacement curve, the AE and DIC data do not suggest such a dramatic transition. As a matter of fact there is a gradual transition from the process zone to a fully cracked surface as multiple bonds with variable strength must be broken to create the free surface. The extent of the process zone and the crack can then be plotted alongside the distance from the notch tip of all AE events, as shown in Figure 3.20.

In Figure 3.20, the red line shows the furthest extent of the process zone that can be seen by the DIC. Similarly, the brown line is the best estimate of the distance of the crack tip from the original notch tip. As a result, the area between the two lines represents the range of the process zone length. Figure 3.20a shows that the highest spatio-temporal concentration of the AE events fall within the zone bounded by the two lines, particularly the high amplitude events (Figure 3.20b), but that there are some exceptions. The AE locations beyond the process zone determined by the

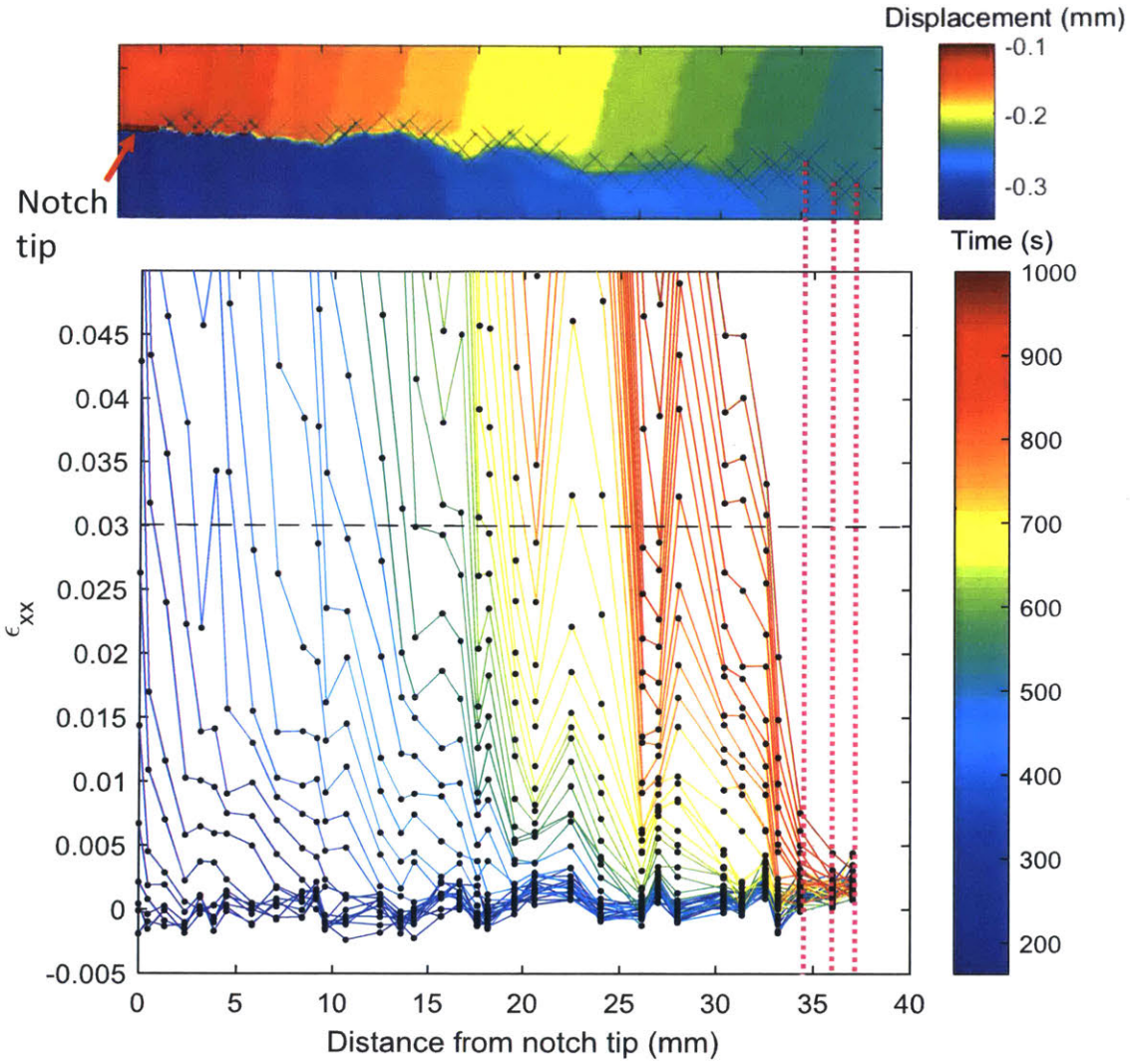

Figure 3.19: a) Displacement contour plot at 1000 s, on which we chose query points (crosses) based on a contour line of constant displacement that best estimated the location of the crack. Dotted purple lines demonstrate how the query points in this subfigure are related to the x-axis in the bottom subfigure. b) Strain data (y-axis) shown as a function of distance from notch tip on the x-axis and time in the colour scheme. Each line represents the state of strain at a given time. Dashed black line at y = 0.03 shows the calibrated strain value, which was used to calculate the crack extent.

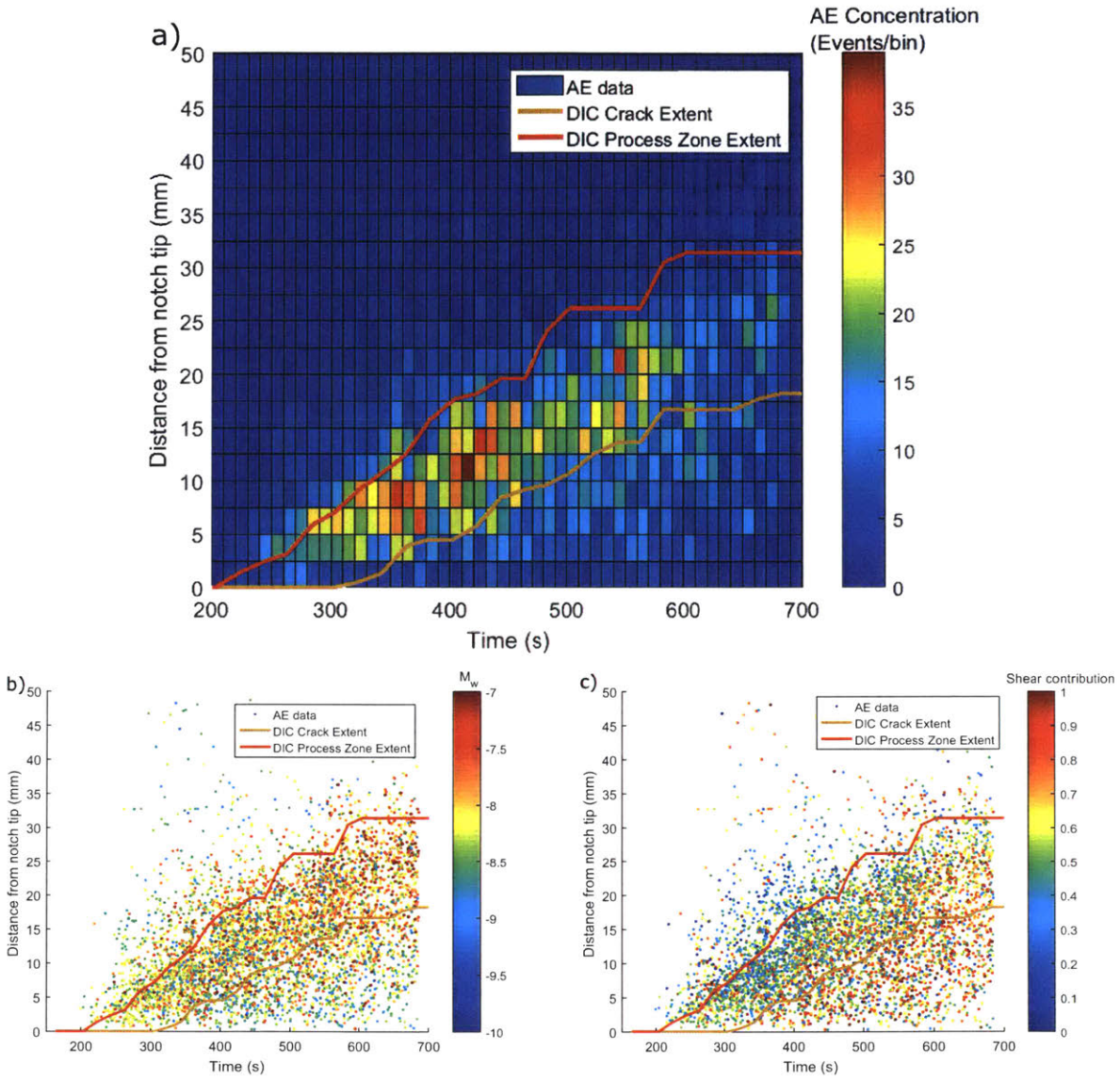

Figure 3.20: Distance from the notch tip for AE events, DIC process zone (red line) and DIC crack extent (brown line). Left image shows the density of the location of AE events as binned in the figure. Middle image is coloured by magnitude, right image by contribution of shear ratio as per the moment tensor decomposition, where 0 indicates no shear and 1 indicates a pure double-couple mechanism.

DIC may again suggest that the AE event locations are more sensitive to small strains than the DIC. AE events located within the crack extent may be explained by noting that Figure 3.20b shows that many of the events near to the notch tip seem to be high in shear. This may be occurring due to shearing along already open en-echelon cracks.

3.6 Displacement vectors over time

We can also consider the evolution of the displacement field over the course of the experiment, as shown in Figures 3.21 and 3.22. These vectors are all normalised to the same length regardless of the magnitude of displacement, and are plotted on contour maps of ε_1 and γ_{max} to see the extent of the process zone and the crack. In general, we can see that the macro-displacement is generally in the horizontal direction where the rock has cracked, and co-linear with the crack path ahead of the crack tip. Note that at t = 298.1 s, the displacement pattern is not significant, and appears to be reflecting minor eccentricity of the loading setup that are exaggerated since the vectors are all normalised to the same length. On a microscopic scale (Figure 3.22), we can see that the displacement field transitions from an initial random orientation to the nominal opening mode as the crack propagates. We find that at both scales, we can see the development of a wedge-shaped envelope representing the zone of influence of the crack, but that in the macro-DIC the vectors are co-linear with the crack path ahead of the envelope, while in the micro-DIC the vectors are generally randomly oriented ahead of the envelope.

We can also consider the statistical distribution of the principal strain components for the micro-DIC data, as shown in Figure 3.23a. We can see that in this case, ε_3 shows significant compressive strains despite the theoretically tensile stress field generated by the beam bending geometry. Figure 3.23b shows that both ε_1 and ε_3 exhibit significant noise, but there is no strong correlation between ε_1 and ε_3.

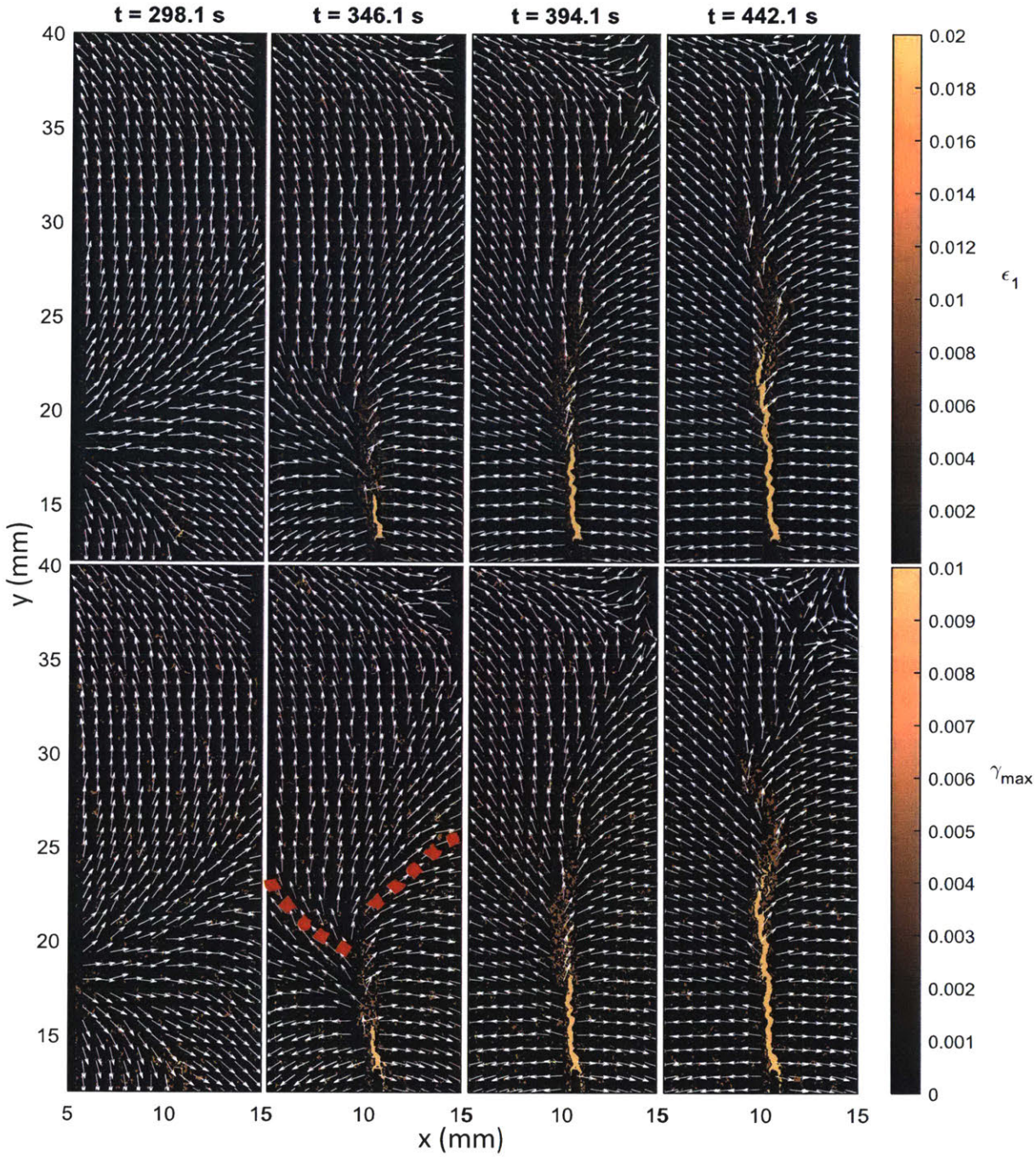

Figure 3.21: Displacement vectors superimposed onto contour maps of ε_1 and γ_{max} for the macro-DIC results. Red dotted lines indicate development of a wedge-shaped envelope representing the zone of influence of the crack.

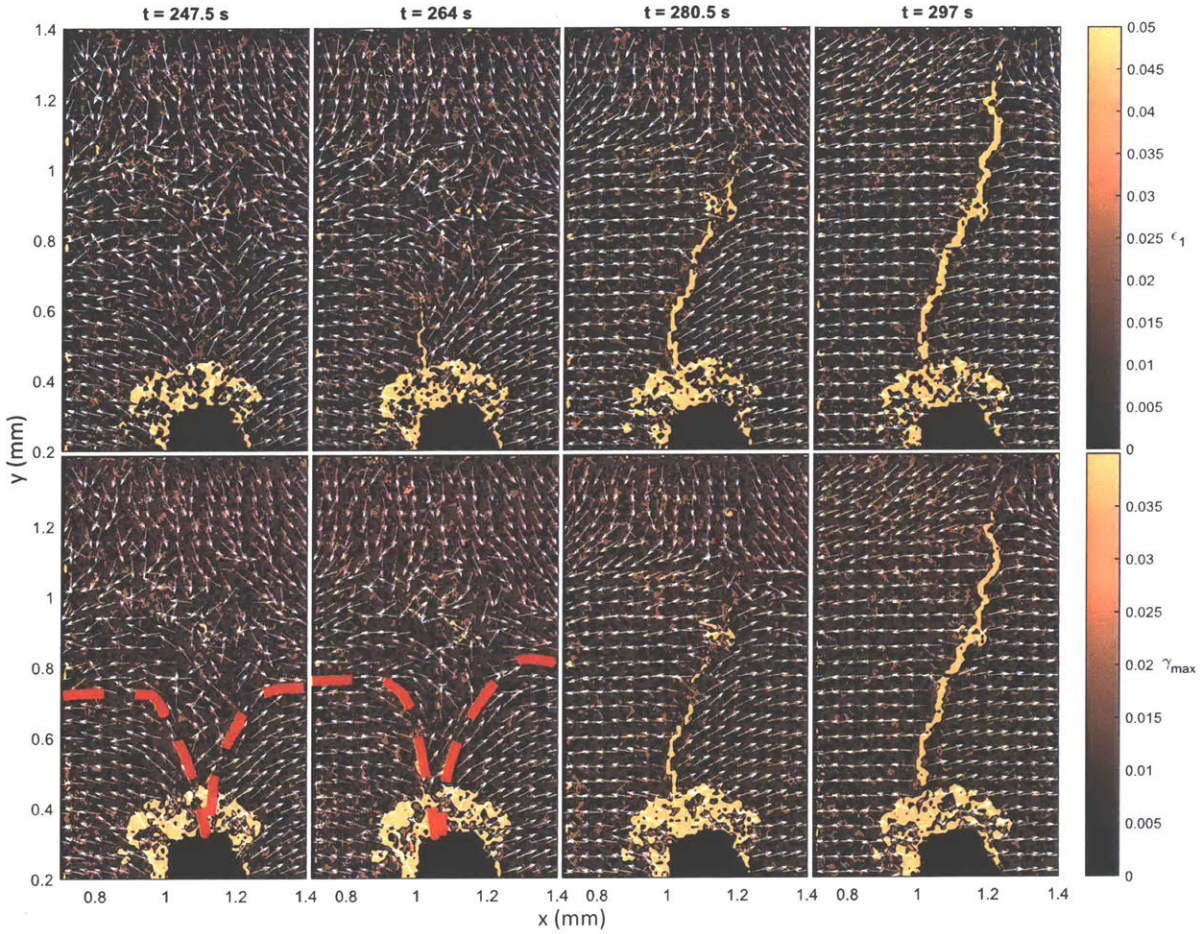

Figure 3.22: Displacement vectors superimposed onto contour maps of ε_1 and γ_{max} for the micro-DIC results. Red dotted lines indicate development of a wedge-shaped envelope representing the zone of influence of the crack.

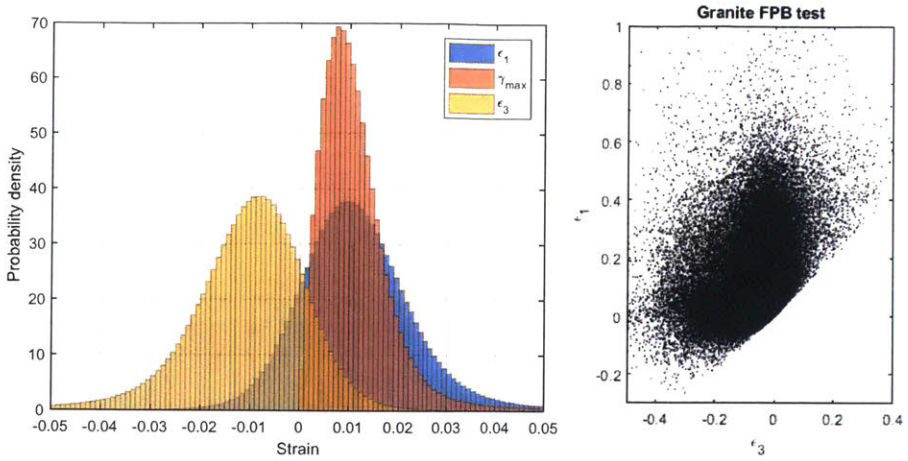

Figure 3.23: (Left) Distribution of principal strains over the entire micro-DIC image at time of maximum load. Positive strain is tension. (Right) Scatter plot of $\varepsilon_1 - \varepsilon_3$ for each pixel of strain data.

3.7 Summary and conclusions

Process zone development and crack propagation have been observed on a pre-notched four point bending experiment on granite. The experiment consisted of observations of load-displacement, strains on the specimen, and acoustic emissions, which were analysed and compared. The main results are summarised as follows:

- Calibration of AE events to moment magnitudes indicate that the events vary from Mw = -6.25 to -8.

- Load-displacement and corresponding energy-time data indicates three main stages of rock behaviour: 'a' Elastic deformation, 'b' formation of a process zone, and 'c' crack propagation. These stages appear to be relatively well related to changes in AE and DIC behaviour.

- Strain and AE observations over the course of the experiment show that during stage 'b', a wide bulb of lower energy activity develops around the tip of the pre-cut notch. During stage 'c', more energy is released and consumed in the propagation of the crack, together with less horizontal scatter of the AE event locations.

- During stage 'b', the formation of microcracks appears to initiate in tension, and then continue to appear as a series of en-echelon cracks in shear, which is supported by the focal mechanisms of AE events. The extent of these microcracks are on the sub-mm scale for this experiment, and are beyond the spatial resolution of acoustic emissions and macro-DIC, each of which show the process zone developing as a semi-elliptical bulb of strain (Figures 3.7 and 3.6).

- A consideration of the evolution of strains over time and space and the load-displacement data showed that at approximately 3% strain the process zone transitions into the crack front (See Figure 3.19).

- An estimate of the extent of the process zone and the crack itself from DIC data compared well with the extent of AE locations, although the AE cloud tended to be slightly larger than the DIC process zone. We can therefore conclude that the simultaneous observation of load-displacement, strain, and acoustic emissions and the relations between them provide a reasonably holistic picture of the development of the process zone and crack propagation. This is important as it will aid in the interpretation of other laboratory results and eventually field observations, where usually only one of these data types is available.

Chapter 4

Tensile Fracture in Shale

"Many are the strange chances of the world, and help oft shall come from the hands of the weak when the wise falter."

4.1 Load-Displacement

A similar beam bending setup to that described in Chapter 3 was used on specimens of BMA-2 Opalinus shale, where the bedding planes are oriented horizontally, i.e. the tensile fracture propagates perpendicular to the bedding planes. This relatively quartz-rich shale comes from the Mont Terri underground lab in Switzerland, located in the Jura mountains at a depth of approximately 200 m below the present surface. The mineralogy was analysed by James Hutton Limited using X-ray diffraction, who reported 47% quartz, 13.5 % calcite, 9.7 % kaolinite, and 16.2 % illite and illite/smectite.

The load-displacement data are shown in Figure 4.2. We see that the load and displacement show a similar pattern as the granite, where peak load occurs approximately 150 seconds after the start of the test, and the load then gradually decreases as the tensile crack propagates. The displacement is also similar in that the crosshead initially moves towards the specimen, and is then held relatively constant as the crack propagates. In terms of magnitude, the peak load of the shale is approximately half of that observed in granite. It is also notable that the load-displacement data do not exhibit the non-linear stage seen in the granite ('b' in Figure 4.2b), suggesting that there is less inelastic deformation prior to the initiation and propagation of shale tensile crack.

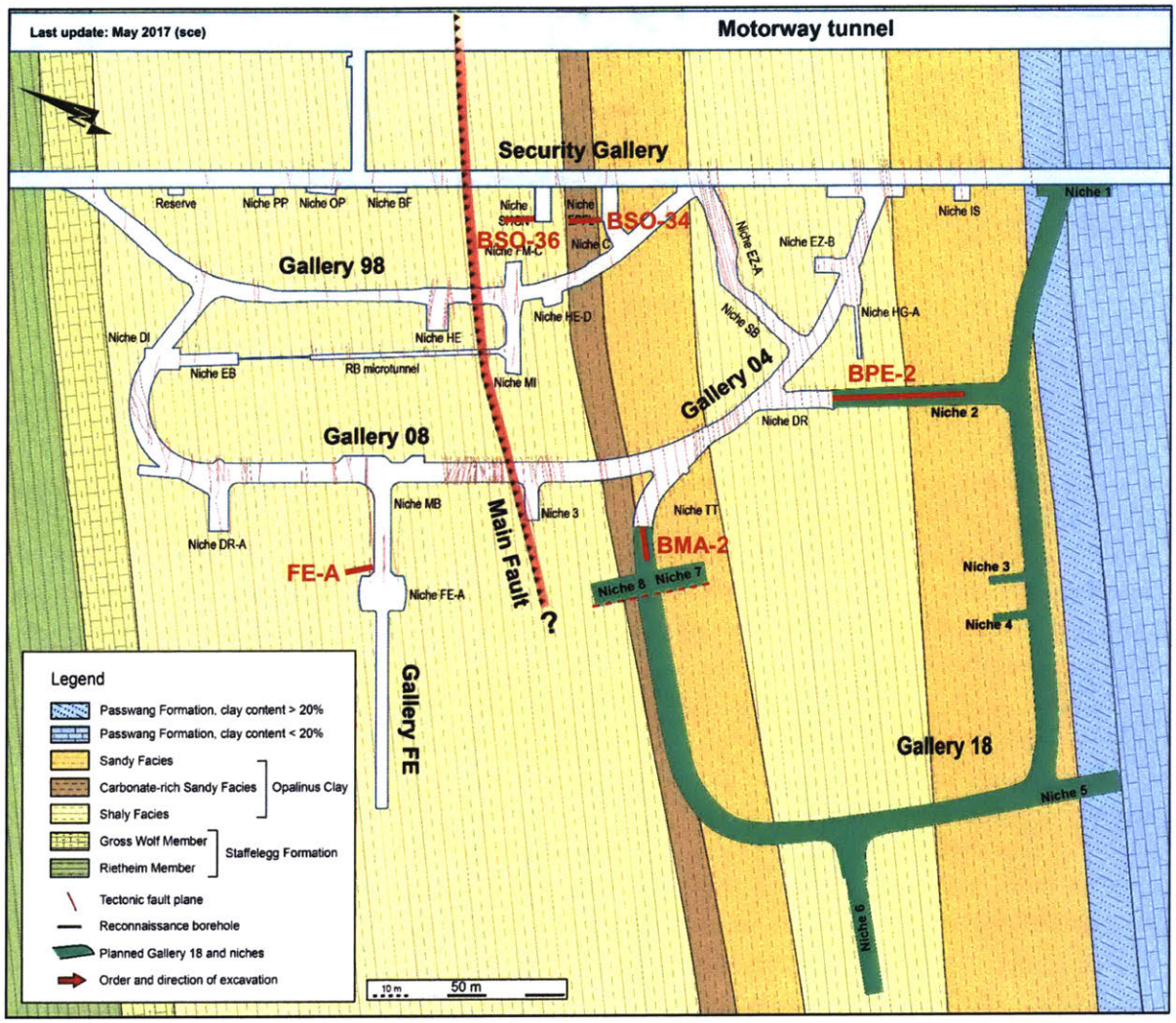

Figure 4.1: Map of the Mont Terri underground laboratory showing location of boring cores including the BMA-2 cores used in this thesis.

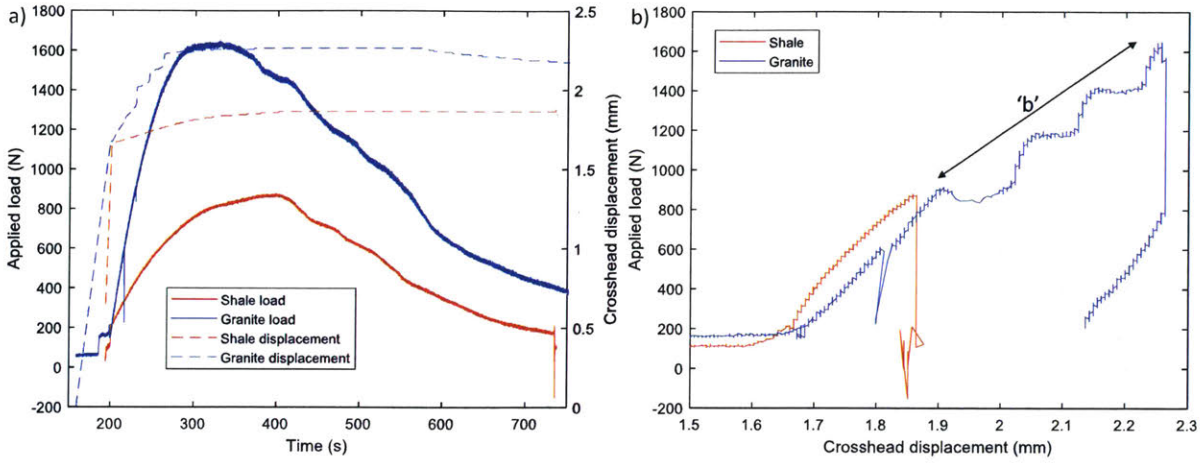

Figure 4.2: Load-displacement data over time for the shale and granite beam bending experiments. Note that the timescale for the granite beam has been offset from the original data so that the beginning of loading matches the shale beam.

4.2 Acoustic Emissions

The AE locations and focal mechanisms are shown in Figure 4.3. We can see that at around 200 s, some bedding plane movement occurred distally from the notch tip, likely as a result of specimen seating. A number of larger amplitude events also occur at around 400 s, which corresponds to peak load in Figure 4.2, and thus is likely indicate of crack initiation. After 400 s, the events do not exhibit any significant spatial clustering, suggesting that the continued propagation of the crack does not produce detectable AE events.

In terms of the focal mechanisms, we see that in shale the tensile events are oriented horizontally as opposed to vertically in the granite, suggesting that opening of horizontal bedding planes is a significant mechanism despite the overall stress field. The tensile events are also more horizontally scattered than the shear events, while the opposite trend was observed in the granite, i.e. tensile events showed less scattering and were closer to the path of the crack. We also see that in general, there are fewer AE events in the shale, and that these are smaller magnitude than seen in the granite.

We can also consider the development of AE over time in detail as shown in Figure 4.4. We see that the early bedding plane events identified in Figure 4.3a moved in an implosive mechanism, indicating that the bedding plane closed during initial seating loads. Towards the end of the 68.9 - 396.2 s time frame we also see a tightly grouped cluster of tensile events located near the notch tip. This spatial clustering prior to peak load (around 400 s) is consistent with the granite results, and likely corresponds to the development of a process zone ahead of the notch tip. However, we note that in this shale test these events are explosive NDC (tensile) in nature, while in the granite they occurred primarily in shear. Between 396.8 s to 485.32 s the events are more widely distributed in the y-direction, indicating the growth of the crack if we assume that the peak load corresponds to crack initiation like in the granite test. Unlike the previous time frame, we now also see some shear events, which likely corresponds to shearing along the newly created cracks. In the next two time frames (485.6 to 615.4 s), we mostly see mostly tensile events, although the location of AE

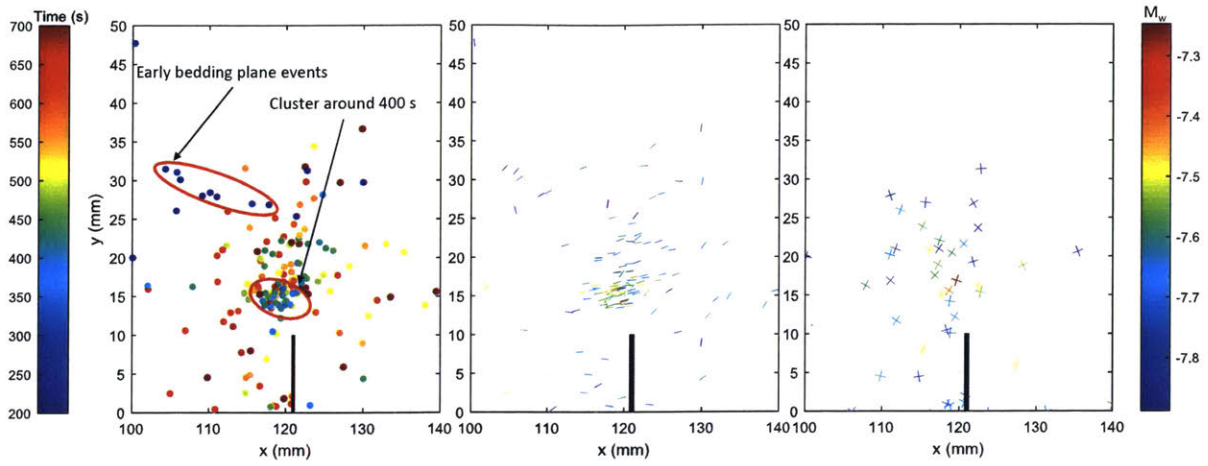

Figure 4.3: a) AE hypocenter locations over time for entire test, where colour indicates source time b) tensile event location and microcrack orientation, where colour represents magnitude c) shear event location and conjugate plane orientation, where colour represents magnitude.

events do not move up from the notch tip over time as in the granite test, which suggests that these AE events are not associated with the propagating crack tip.

The rate of events is presented in Figure 4.5. The trends are largely similar to the granite test, where the event rate increases with the amount of machine work, and is relatively constant while the crack propagates at constant machine work. We note that the AE event rate exhibits a large variance i.e. fluctuates significantly with time, which is consistent with the hit rate behaviour in the granite test. We attribute this to stick-slip behaviour or small scale heterogeneities along the crack path in the granite, which is also likely the case in a heterogeneous material such as Opalinus shale.

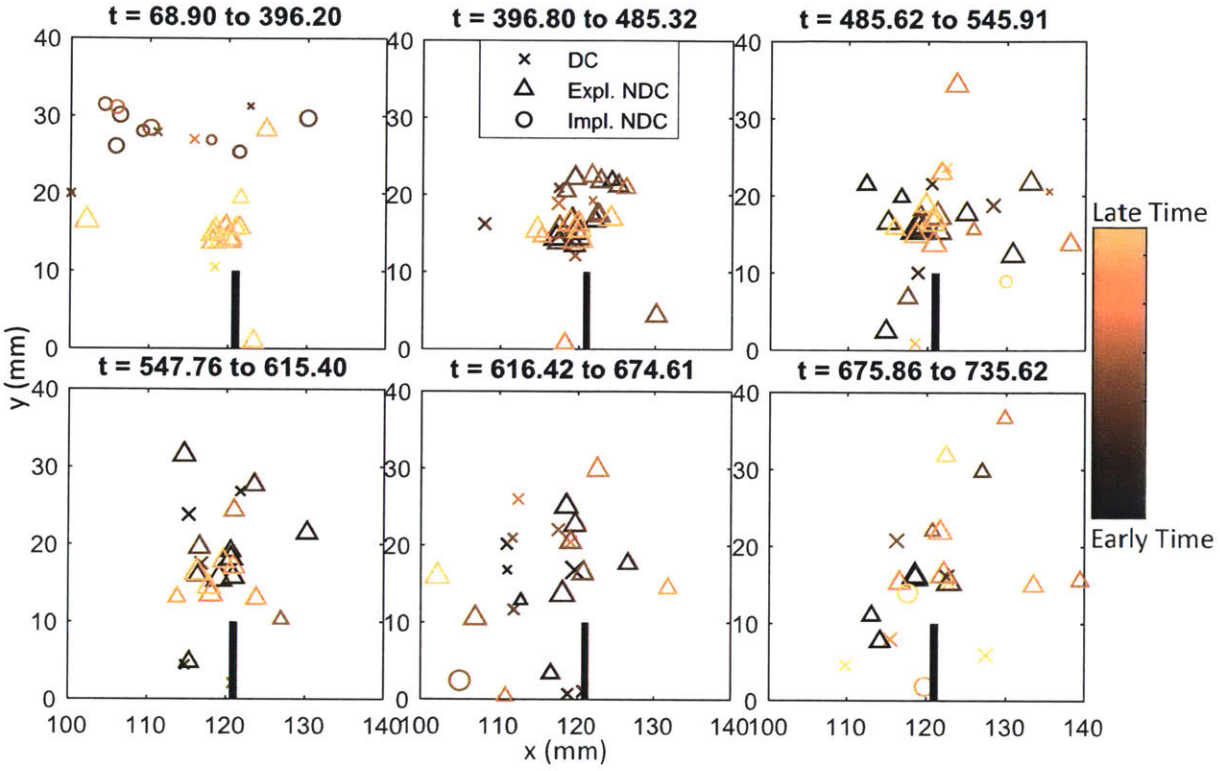

Figure 4.4: Hypocenter locations of AE events over time. Colour represents the time within the range specified in each subfigure heading, size represents magnitude, and symbol represents the focal mechanism.

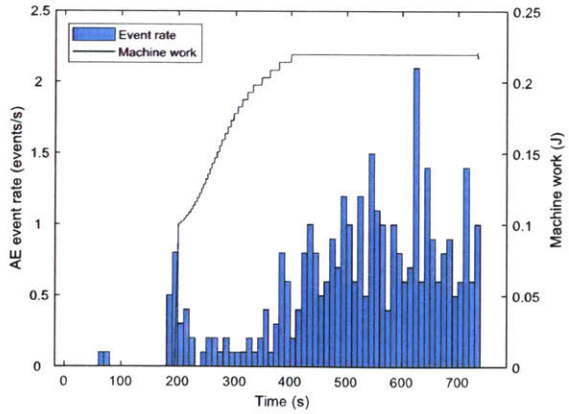

Figure 4.5: AE hit rate over the course of the experiment. Machine work over time is superimposed for reference.

4.3 DIC results

Strain and displacement maps over time are shown in Figures 4.6 and 4.7. We first note that the micro-DIC results in shale are noisier than the granite, as the speckling methodology used in granite requires water which is not possible in the shale. In terms of the macro-DIC, the displacement vectors ahead of the crack appear to be random ahead of the crack in shale, whereas in granite the displacement field appears to be relatively smooth even before significant cracking can be seen in the strain contours. This again supports the notion that the process zone in granite is larger than in the shale. In terms of the micro-DIC, the higher noise in the shale microDIC makes interpretation difficult, although it again appears that the displacement vector field is more random in the shale. The micro-DIC data also show that around 389 s (peak load occurs at 400 s), the microcracks have propagated beyond the extent of the observation window, which is similar to that seen in the granite.

Given the high level of noise in the micro-DIC strains, the data are also plotted as displacement contour maps shown in Figure 4.8. We can see that initially there appears to be a microcrack (white dotted lines) on the right that does not change in length throughout the test, while the microcrack on the left propagates over time. The right microcrack may either be an artefact from the scroll saw blade used to cut the notch (the granite specimen's notch was cut using waterjet), or a pre-existing microcrack.

We can also plot the macro-DIC strain contours for both granite and shale, as seen in Figure 4.9. It is evident that the process zone in granite is on the order of 2 mm in width, whereas the strain contour map in shale only highlights the crack itself. There are two explanations for the strain contour map in shale: either the process zone is smaller than the spatial resolution of the measurement, or the process zone is much larger than the window of observation for the DIC. We believe that it is more likely that the process zone is small, given two pieces of evidence. Firstly, if we make the assumption that the process zone is very large, there should nevertheless exist a falloff in strain magnitude away from the crack. The strain data in Figure 4.9 do not reflect this, and it is unlikely that the entire process zone strains less than the measurement precision of 0.26 % in the shale. Secondly, Wong and Einstein (2009) studied the development of microcracks in Carrara marble and moulded gypsum, and found that the zone of microcracking was significantly smaller in gypsum than in marble. While different materials are considered in this study, we do note the analogous situation that the grain size of marble is significantly larger than gypsum, and suggest that a similar difference exists between coarser grained granite and finer grained opalinus shale. This difference in the process zone size is likely the most significant contributor to the difference in AE behaviour between the two materials, and contradicts predictions made by linear elastic fracture mechanics, which predicts that the size of the inelastic zone (radius of plasticity) should be similar between granite and Opalinus shale (Table 4.1).

Figure 4.10 shows the comparison of ε_{xy} for both rocks approximately 100 seconds after peak load. We can see that the lengths of the en-echelon cracks are generally shorter in the granite than the shale, where the en-echelon cracks are up to 1.5 mm long. As per Chapter 3, the en-echelon cracks in granite are on the order of 10's of microns.

The distribution of strains is shown for the shale micro-DIC in Figure 4.11a. The distribution is generally similar to that seen in granite, where ε_3 is generally negative i.e. compressive. Figure 4.11b shows that there is significant data scatter owing to the low quality of the speckling used in this experiment.

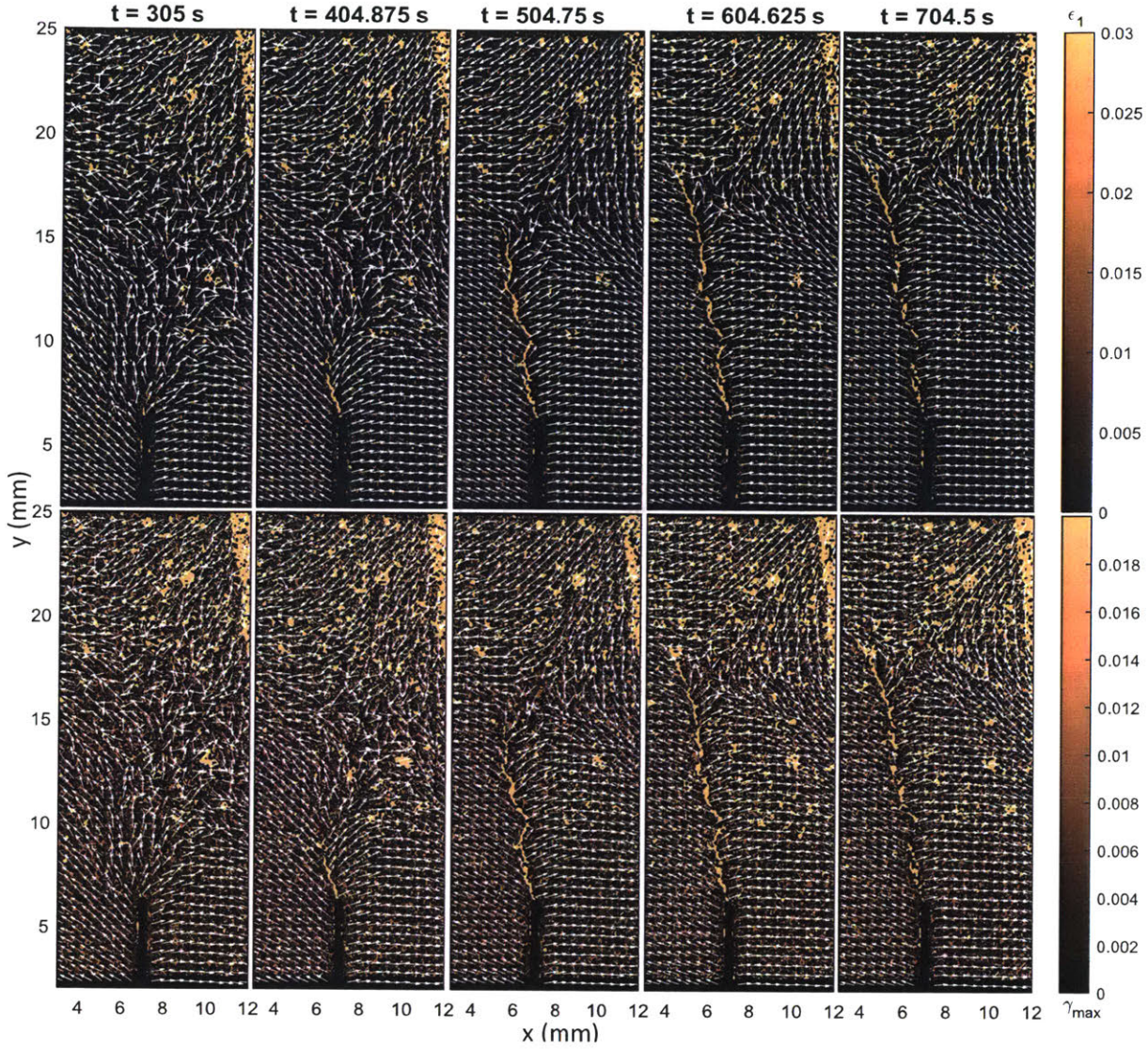

Figure 4.6: Displacement vectors superimposed onto contour maps of ε_1 and γ_{max} for the macro-DIC results.

Table 4.1: Predicted plastic zone size for Opalinus clayshale and Barre granite using literature material properties and Irwin's equation (1958).

Material	Mode I Fracture Toughness (K_I, MPa.m$^{0.5}$)	Tensile Yield Stress (σ_Y, MPa)	Radius of Plasticity $r_p = \frac{1}{\pi}\left(\frac{K_I}{\sigma_Y}\right)^2$ (mm)
Barre granite	2.00 (Wang and Hu, 2017)	9 (Wang and Hu, 2017)	15.7
Opalinus Clayshale	0.53 (Liu, 2015)	2 (Bossart and Thury, 2008)	22.4

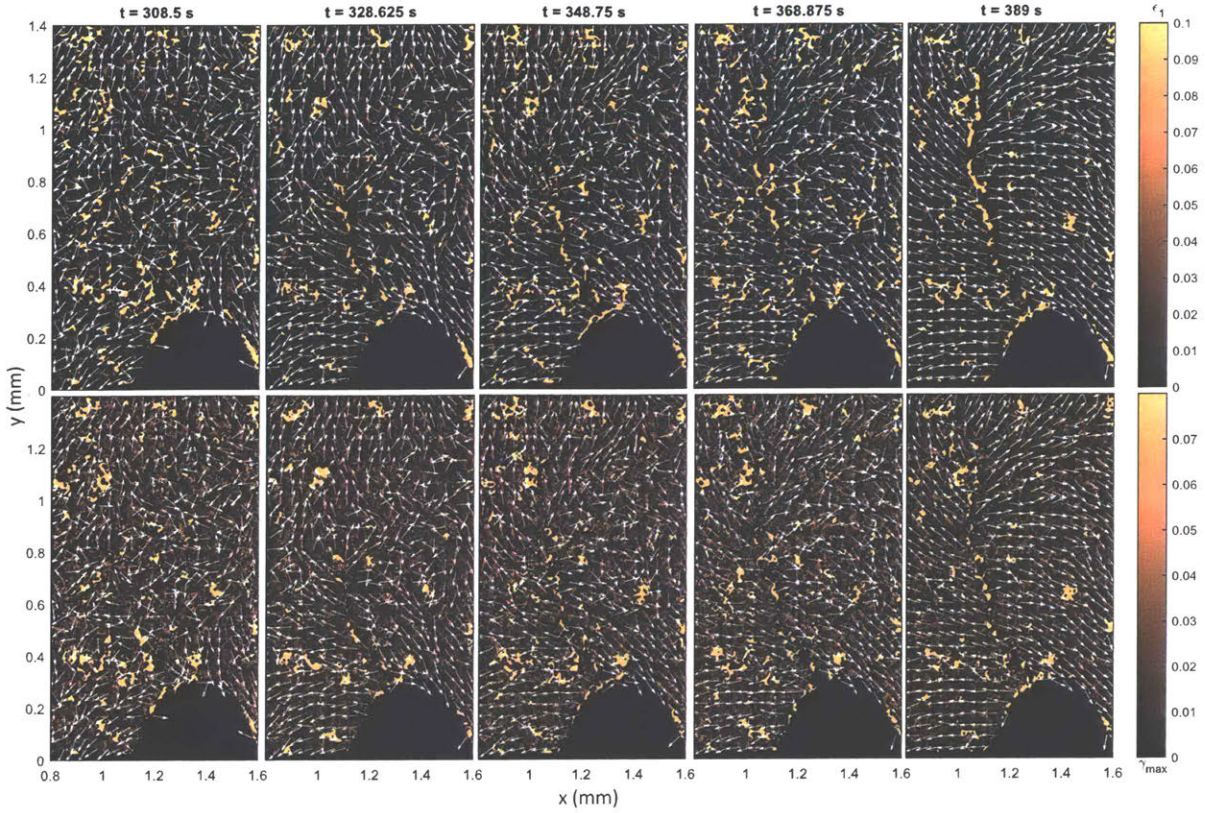

Figure 4.7: Displacement vectors superimposed onto contour maps of ε_1 and γ_{max} for the micro-DIC results.

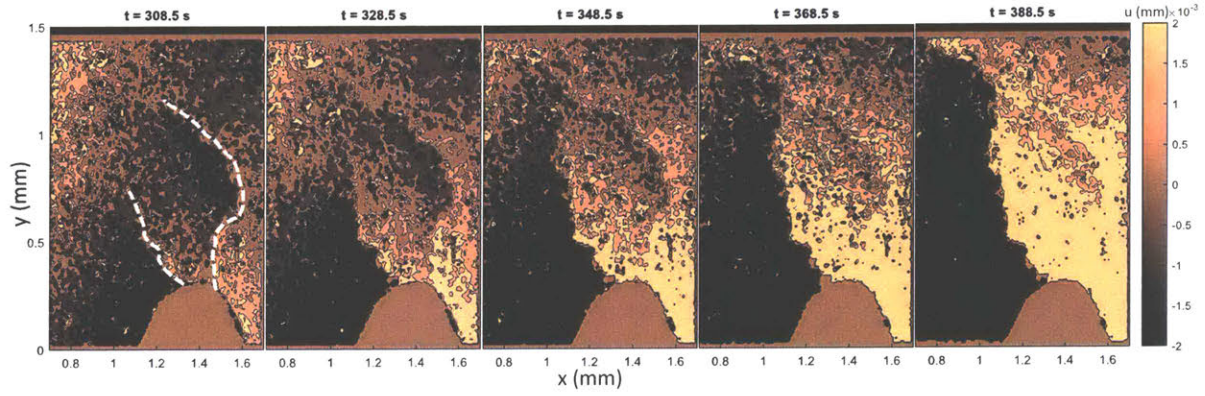

Figure 4.8: Contour map of horizontal displacement u at various stages during the test. White dotted line indicates two crack paths.

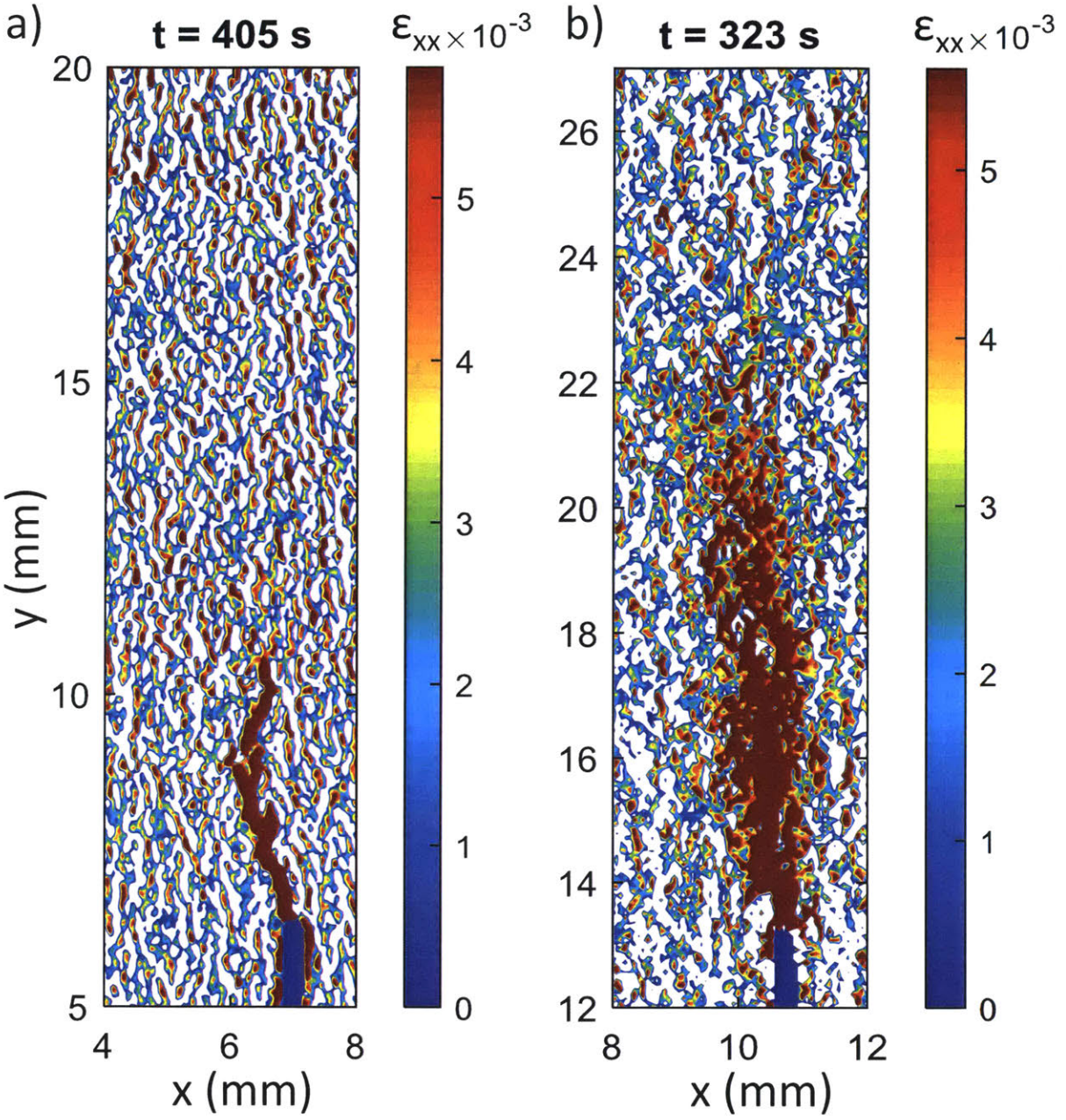

Figure 4.9: Contour map of ε_{xx} for a) shale and b) granite at approximately the time of peak load. Upper limit of the color scale is set at the 90th percentile of strain. Opalinus strain measurement is resolved to 0.26 %, with a spatial resolution of 292 μm. Granite strain measurement is resolved to 0.15 %, with a spatial resolution of 172 μm.

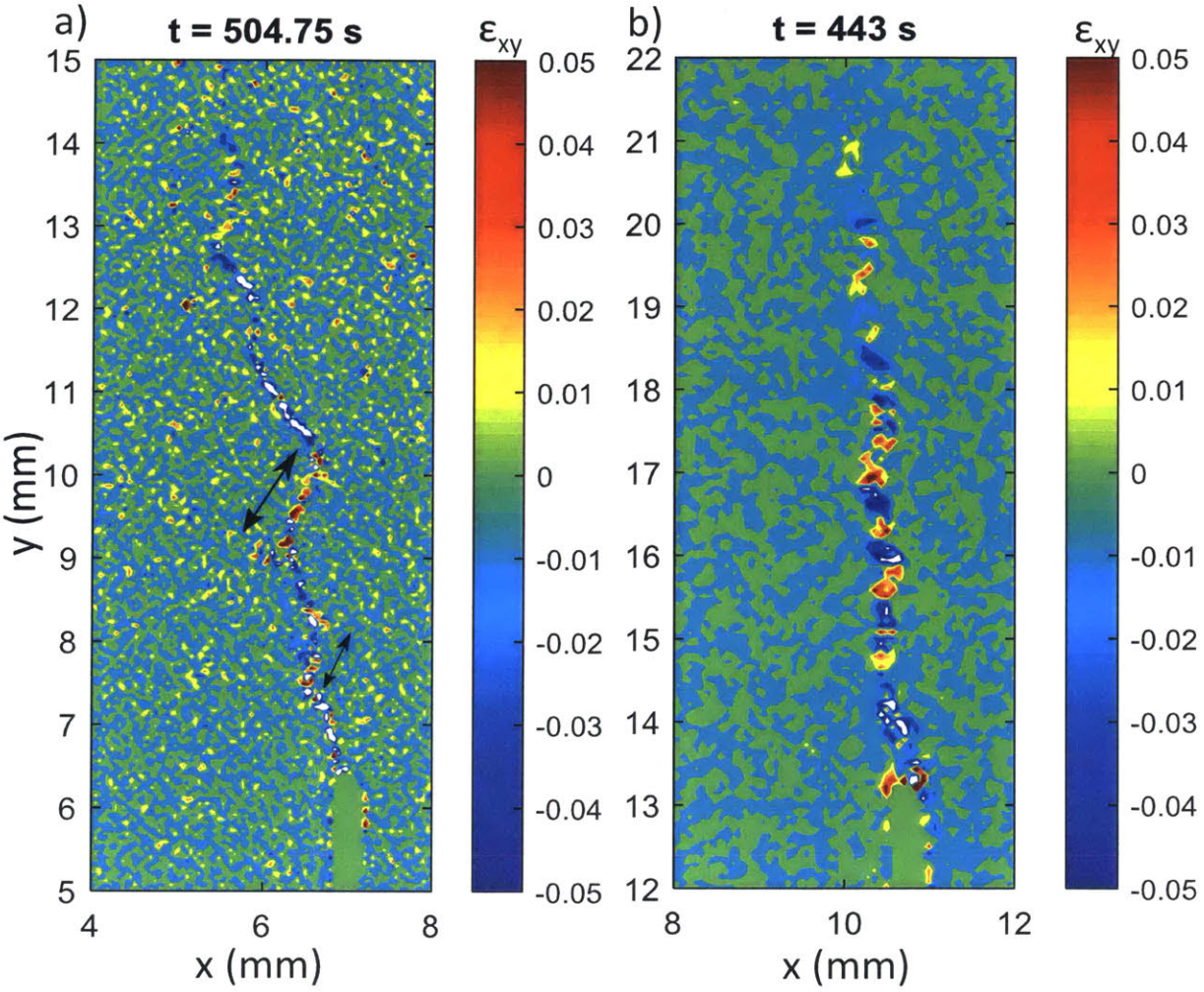

Figure 4.10: Contour map of ε_{xy} for a) shale and b) granite at approximately 100 seconds after peak load. Black arrows indicate en-echelon cracks.

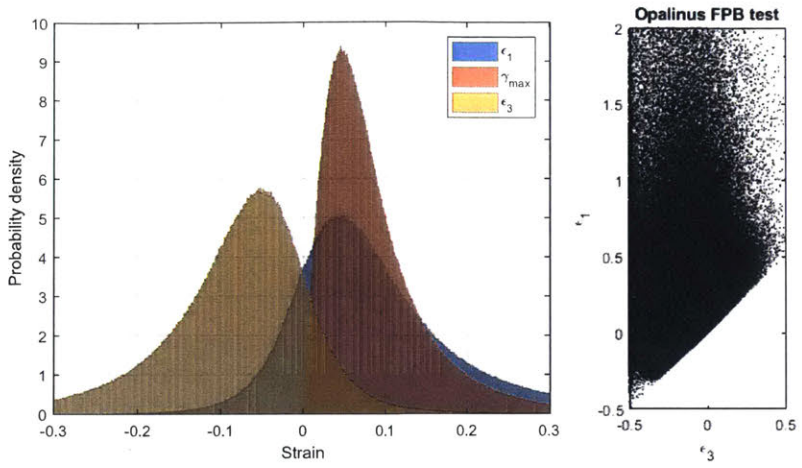

Figure 4.11: (Left) Distribution of principal strains over the entire micro-DIC image at time of maximum load. Positive strain is tension. (Right) Scatter plot of $\varepsilon_1 - \varepsilon_3$ for each pixel of strain data.

4.4 Comparison of AE and crack extent

Figure 4.12 is calculated in the same way as Figure 3.20, in order to analyse the relation between AE and crack propagation in the shale. As we can see and as discussed previously, the AE events' distance from the notch tip do not correlate to time, and therefore also do not strongly correlate to the propagation of the crack.

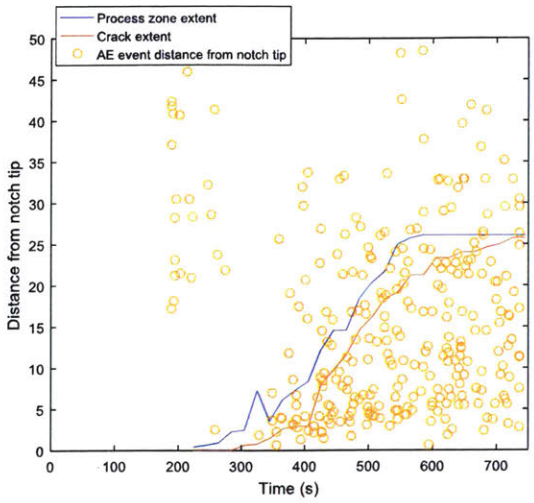

Figure 4.12: Scatter plot shows the distance from the notch tip to each AE event over time on the x-axis, line plots show the extent of the process zone and crack as measured by the DIC.

4.5 Summary and conclusions

- The small amount of non-linearity in the load-displacement plot (Figure 4.2) and the small zone of high strain seen in the macro-strain (Figure 4.9) suggest that the process zone is smaller in Opalinus clayshale than in granite, resulting in less inelastic deformation.

- The acoustic emissions magnitudes are generally smaller in magnitude and fewer in shale than in granite. Prior to peak load, the AE hypocenter locations were clustered close to the notch tip, but generally dispersed throughout crack propagation. This suggests that the creation of the initial process zone is seismically intensive, but the propagation of the crack is not.

- At the micro-DIC scale, it is possible that the granite tends to form more distinct en-echelon cracks than the shale. This is supported by the AE focal mechanisms, which show more double couple components in the granite. The AE focal mechanisms also showed that the tensile microcracks were oriented horizontally along the bedding planes, as opposed to the granite where they were oriented vertically along the overall direction of the crack.

Chapter 5

Hydraulic Fracturing of Barre Granite

"Home is behind, the world ahead, and there are many paths to tread through shadows to the edge of night, until the stars are all alight."

The objective of this study is to relate the AE produced during the hydraulic fracturing tests to the fracturing processes observed visually (Goncalves da Silva and Einstein, 2018). In order to achieve this objective, the amplitudes, rates, hypocenter locations and focal mechanisms of the AE were analyzed and interpreted at successive stages of crack development.

5.1 Physical Setup

The experimental setup is described in detail in other publications (Goncalves da Silva et al., 2015; Goncalves da Silva and Einstein 2018) and is summarised here. Specimens of Barre Granite are first cut to dimensions of 1" x 3" x 6", then the flaws are cut with a waterjet to geometries described in Figure 5.1.

The specimen is clamped inside the hydraulic fracturing device (Figure 5.2), which applies water pressure to the face of the specimen as well as inside the flaws (Figure 5.1 and 5.2), and is placed in the Baldwin load frame (Figure 5.3). A constant vertical stress of 0 or 5 MPa is then applied, and the specimen is finally hydraulically fractured by increasing water pressure in 0.5 MPa increments. The measurements in these tests are: AE, time-pressure data, high resolution images throughout the test, and high speed (14 000 fps) video taken in a 2-second window around fracture initiation.

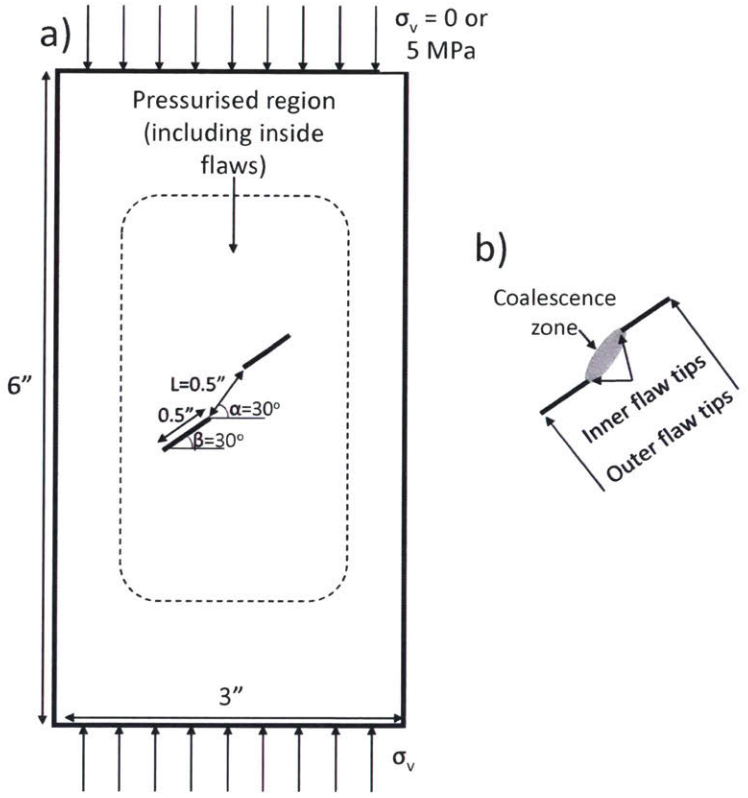

Figure 5.1: a) Schematic of the specimen setup including L-β-α naming convention and boundary conditions for tests used in this paper. VL0 refers to experiments with 0 MPa of applied vertical stress, VL5 with 5 MPa of vertical stress. INC5 indicates that the fluid pressure in increased in 5 MPa increments. For example, the specimen above is 2a-30-30-VL5, indicating a 30 degree inclination of the flaws (β) and 30 degrees between the flaws (bridging angle α), and 5 MPa of vertical stress. b) Notation denoting regions surrounding the pre-cut flaws.

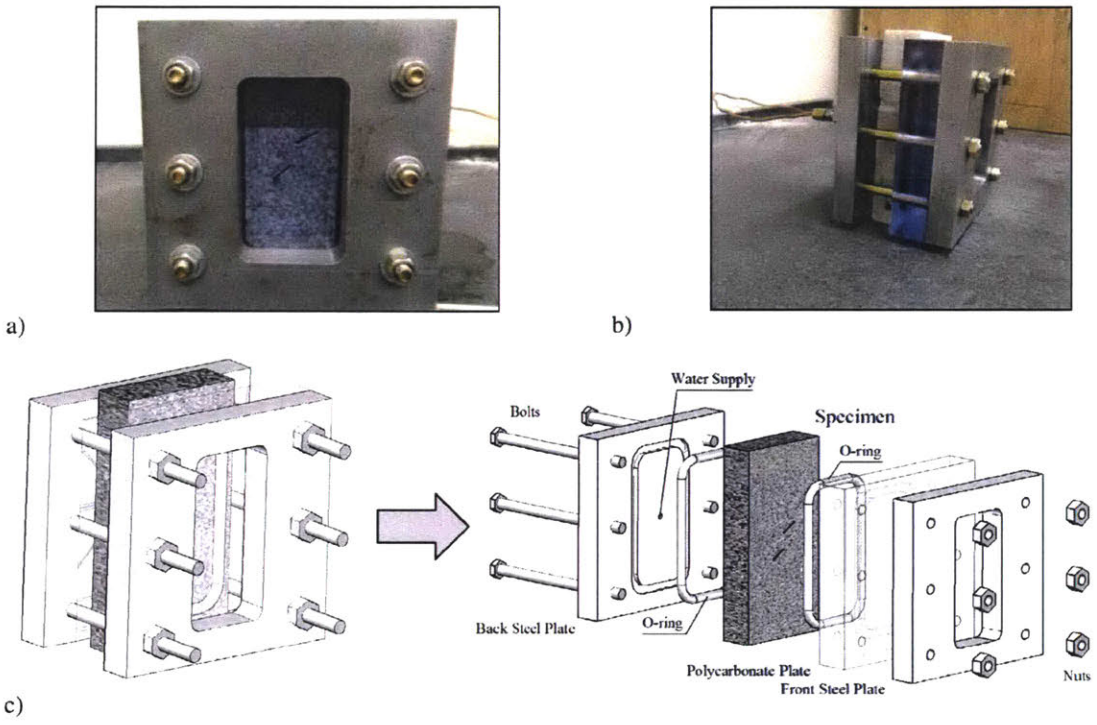

Figure 5.2: a) Front and b) oblique view of the pressurisation device used in hydraulic fracturing tests; c) schematic showing the different parts of the device. (From Goncalves da Silva et al, 2015)

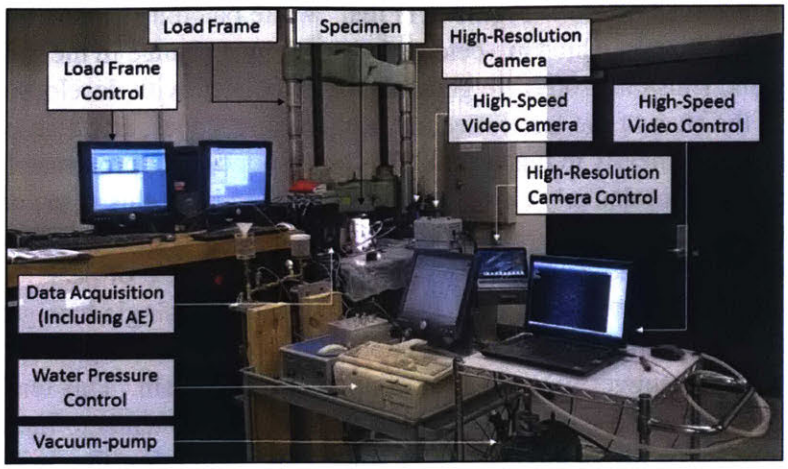

a)

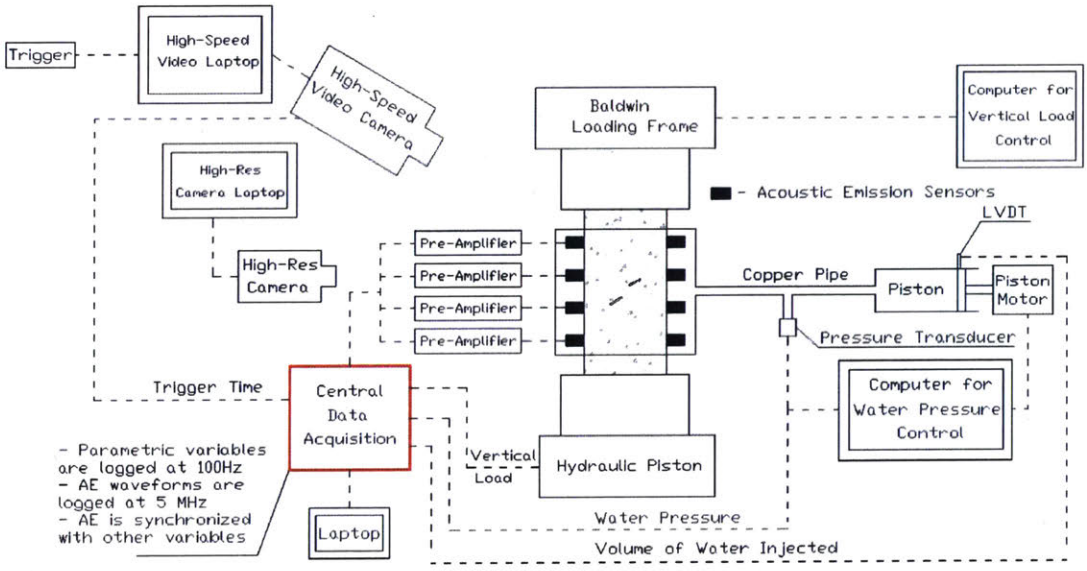

b)

Figure 5.3: a) Overall view and b) schematic of the test setup used in the hydraulic fracturing tests. (After Goncalves da Silva et al. 2015)

5.2 Results

5.2.1 Rate of AE events over time

Figure 5.4 shows the pressure-time data and the rate of AE hits (individual detections on any channel) for the 13 tests presented in this study (See Table 5.1), along with the time at which white patching is first observed. Recall (Figure 5.1) that "white patching" refers to zones consisting of microcracks (process zone), which are detected visually by a change in the refractive properties of the rock (Wong and Einstein, 2009). In general, AE associated with development of the hydraulic fracture begin at the start of the last or second last pressure stages, at which point the AE rate increases exponentially (linearly in log space). This corresponds to approximately 80% of maximum water pressure, which is relatively close to the peak driving load; this is in contrast to rock specimens brought to failure in compression (Yoshimitsu et al., 2014; Chang and Lee, 2004; Moradian et. al. 2016), where the AE begin to consistently occur at 25-50% of peak load. In some experiments, such as the 2a-30-0-VL0-C, 2a-30-120-VL5-B, and both single flaw geometries (See Table 5.1), the rate reaches another inflection whereupon the rate increases again (denoted as secondary rate in the Figure 5.4); suggesting the onset of another mechanism. This tended to occur around 90% of peak pressure. We also observe that the AE rate usually tends to increase in the pressure stage immediately following first detection of white patching (green line in Figures 5.4 and 5.5), suggesting that the white patching is well correlated to the onset of microseismic activity. Since the pressure was increased in 0.5 MPa steps, the rate of pressure application was not constant, and so fracturing occurred in some tests during an increase in pressure (e.g. 2a-30-30-VL5-C), while in other tests during a period of constant pressure (e.g. 2a-30-30-VL0-C). However, this does not appear to have a significant effect on this experimental series, since for all tests the AE hit rate appears to exhibit similar behaviour regardless of whether the pressure was static or increasing leading up to fracturing (see for example boxes in Figure 5.4 showing constant or rising pressure). Specifically, in each test the hit rate increases over approximately 5-10 seconds up to the time at which the pressure drops, which corresponds to fracture initiation (Li et al., 2015). However, the fact that we, in some cases, observe a hydraulic fracture developing at a constant water pressure indicates that there may be time dependent effects (Liu et al., 2001).

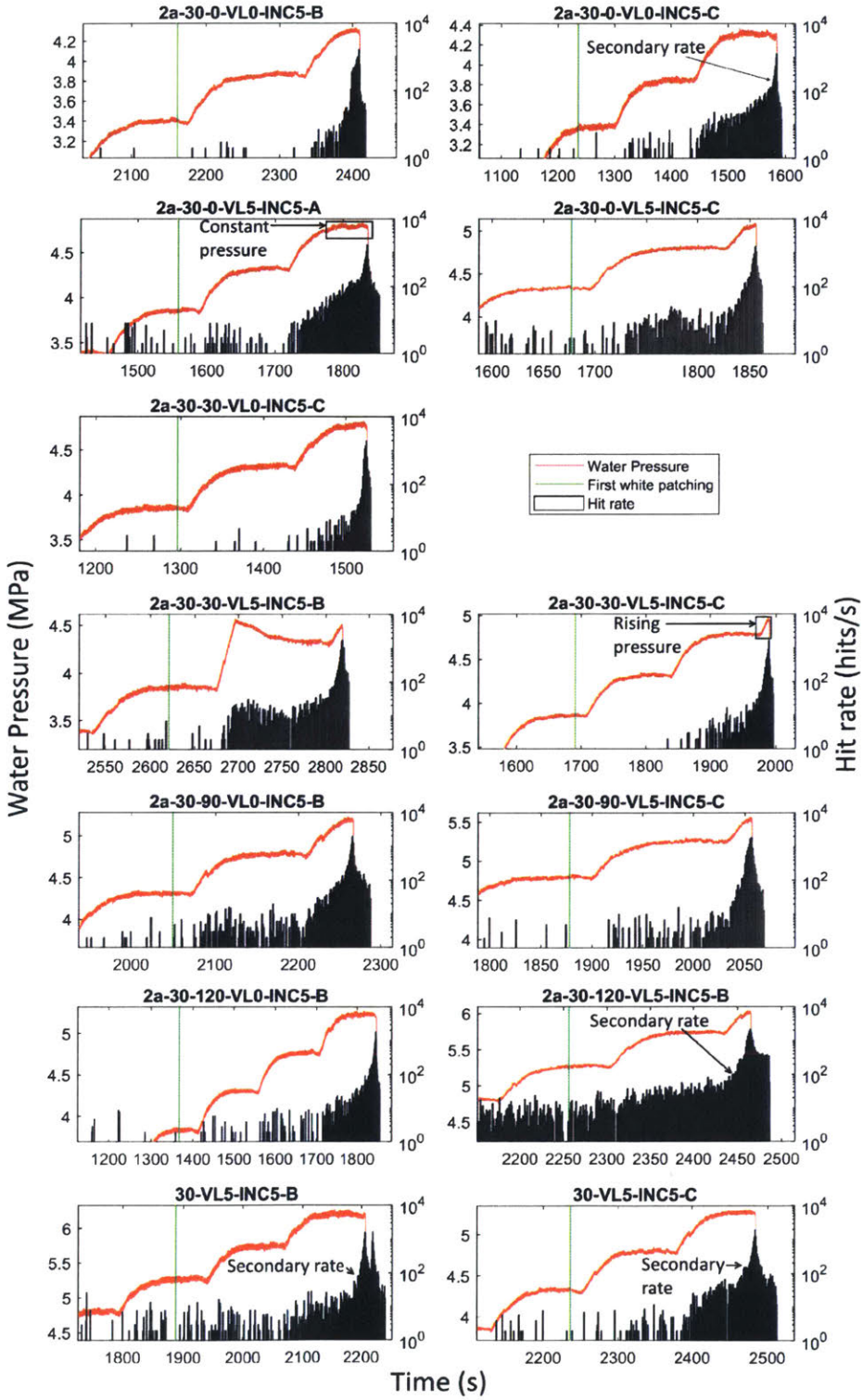

Figure 5.4: Water pressure (red) and rate of AE hits (black) over time for each test. Arrows and black boxes indicate phenomena commented on in the text. Green line indicates the time at which white patching is first visually observed during the experiment.

5.2.2 Amplitude of AE over time

Figure 5.5 shows the amplitude of AE hits that occur towards the end of each experiment. One can see that in most cases, peak amplitudes occur immediately before the drop in water pressure corresponding to the fracture initiation and propagation. We can also see that, in general, the average amplitude fluctuates significantly in the seconds immediately prior to fracture, as individual microseismic events reflect discrete microcracks that can be seen in the white patching discussed in the following sections. In general, the hit amplitude tends to follow a similar trend to the rate of AE hits shown in Figure 5.4, in that the average hit amplitude tends to increase along with the hit rate. While the AE amplitude and rate of hits reflect development of white patching in general, we can also consider the time at which visual white patching is first seen, as shown in the green line in Figures 5.4 and 5.5. This point in time does not appear to be closely related to a change in amplitude.

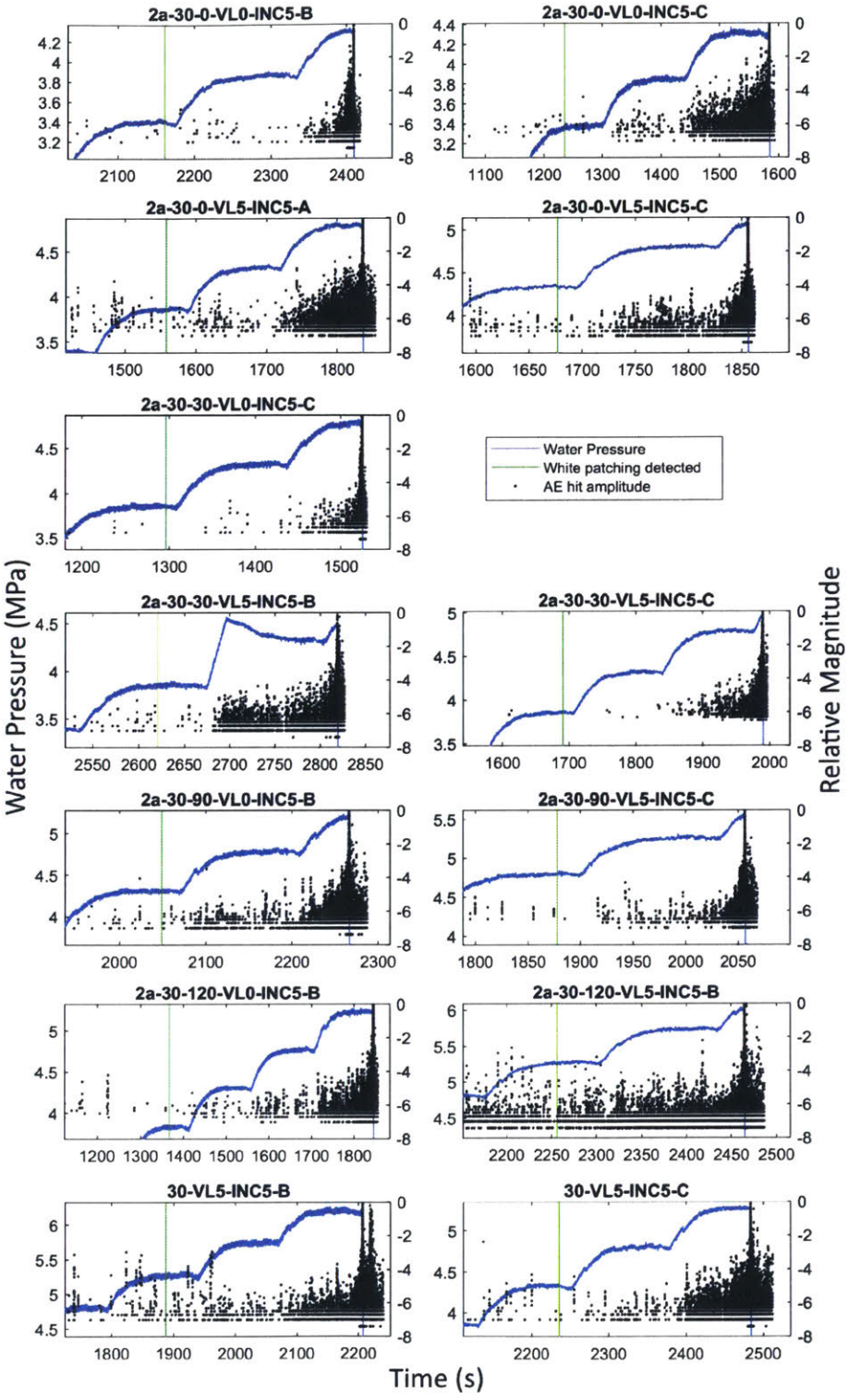

Figure 5.5: Water pressure (blue line) and AE amplitude (scatter data) over time. Green line indicates the time at which white patching was first detected visually.

5.2.3 Focal Mechanisms

General AE characteristics are listed in Table 5.1. The number of events generally increases with increasing bridging angle, and tests with a single flaw produced a larger number of events compared to the 2a-30-0 and 2a-30-30 geometries. Overall, the tests with the most events correspond to those with higher breakdown pressure, which intuitively makes sense given that higher pressure supplies a larger amount of energy to the system. However, there does not appear to be a significant difference between the number of events produced by tests confined by a vertical stress of 5 MPa as opposed to those at 0 MPa.

The focal mechanisms show that the events are primarily composed of double couple at around 55-60% cumulatively for all tests, followed by isotropic with a proportion of 30%. In all tests, explosion/tensile cracking was more dominant than implosion/anti-cracking, which makes sense given that the hydraulic fracture mechanism is associated with a tensile failure mode (Goncalves and Einstein, 2014). The proportion of DC appears to be relatively consistent amongst tests, with the exception of test 2a-30-120-VL5-B, which appears anomalous in that very few events were detected. Conversely, the proportion of +ISO and –ISO appears to be more variable, even between repeats of the same setup, as seen with the 2a-30-30-VL5 and single flaw results. This may suggest that the amount of volumetric expansion/compression is more closely tied to the specific microstructure around the crack path, where cracks that pass through grains may behave differently from cracks that propagate around grains (Morgan et al, 2013).

The time behaviour of the focal mechanisms is presented in Figure 5.6, which shows that in some tests a significant number of –ISO and –CLVD events occur during and immediately after fracture initiation and propagation (highlighted with black dashed circles in the Figure 5.6). Note that the high speed video shows that the hydraulic fractures initiate and propagate in a small time window when the curves in Figure 5.6 flatten towards the end of each test. These generally corresponded to tests with higher overall proportions of –ISO and –CLVD as seen in Table 5.1.

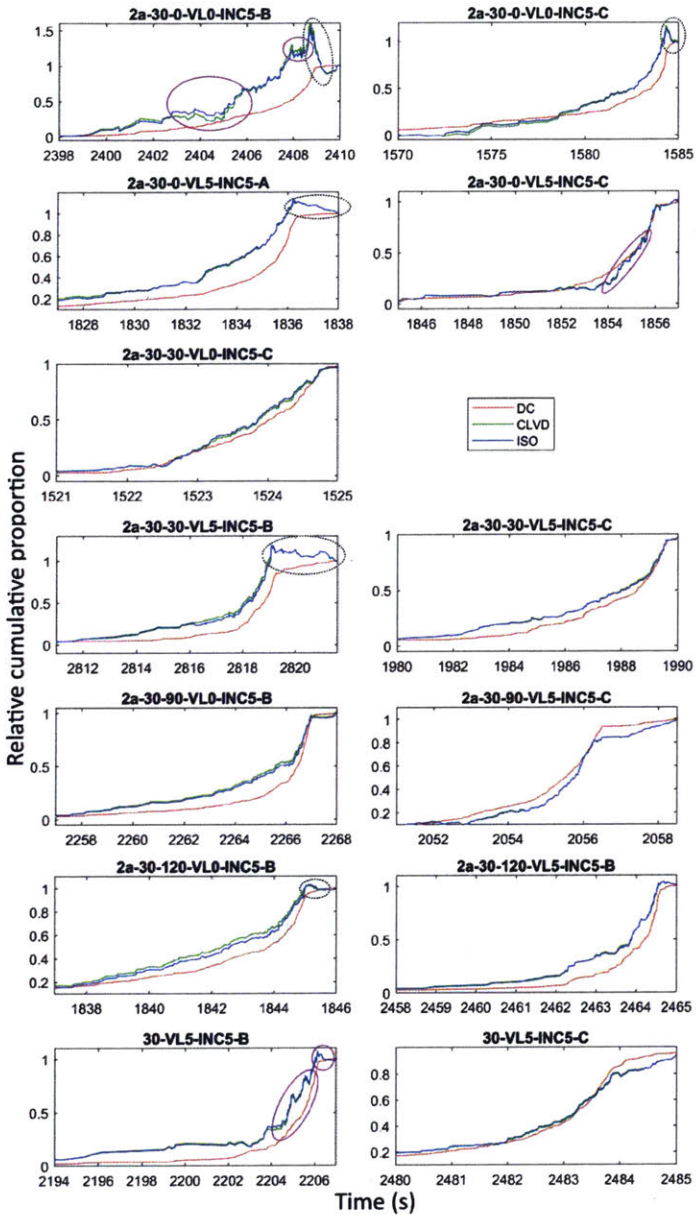

Figure 5.6: Relative cumulative proportion of DC (red), CLVD (green) and ISO (red) during the last seconds of each test. **Black dashed circles indicate significant numbers of implosive NDC events during and after crack propagation, and purple circles indicate periods of cyclic explosive and implosive NDC events. Crack initiation occurs approximately where the curves flatten out** towards the end of the experiment. Note that cumulative proportion of CLVD and ISO can decrease over time since implosion/crack closure events count negatively towards the cumulative proportion whereas explosion/tensile cracks count positively.

Table 5.1: Summary of test data from the hydraulic fracture stimulation stage of the experimental series. The focal mechanisms are the cumulative proportion excluding the initial vertical loading stage. Note that the absolute value of all the focal mechanism proportions sum to 100%, but –CLVD and –ISO are expressed as negative proportions in this study.

Specimen Name	Max Pressure (MPa)	Number of Events	DC (%)	+CLVD (%)	-CLVD (%)	+ISO (%)	-ISO (%)
2a-30-0-VL0-INC5-B	4.3	269	60.5	5.4	-3.7	18.3	-12.0
2a-30-0-VL0-INC5-C	4.3	247	59.4	6.9	-2.5	23.0	-8.2
2a-30-0-VL5-INC5-A	4.8	489	58.7	6.9	-2.6	23.1	-8.7
2a-30-0-VL5-INC5-C	5.1	281	60.5	6.0	-3.1	20.2	-10.2
2a-30-30-VL0-INC5-C	4.8	311	58.0	7.7	-1.8	26.7	-5.7
2a-30-30-VL5-INC5-B	4.5	291	56.9	6.5	-3.5	21.7	-11.5
2a-30-30-VL5-INC5-C	4.9	290	56.5	8.1	-1.9	27.2	-6.3
2a-30-90-VL0-INC5-B	5.2	408	57.2	7.5	-2.3	25.5	-7.5
2a-30-90-VL5-INC5-C	5.5	595	56.5	7.7	-2.4	25.3	-8.1
2a-30-120-VL0-INC5-B	5.2	545	60.7	6.5	-2.4	22.5	-7.9
2a-30-120-VL5-INC5-B	6.0	173	45.5	8.8	-3.6	30.7	-11.4
30-VL5-INC5-B (Single flaw)	6.2	367	54.4	5.6	-5.0	18.6	-16.4
30-VL5-INC5-C (Single flaw)	5.3	504	55.7	8.2	-2.1	27.1	-7.0

5.2.4 Hypocenter Location Analysis

The hypocenter locations are shown in Figure 5.7. In general, it appears that the hypocenters relate well to the visually observed crack path, where the hypocenters are spread over a width of 2-5 mm. It is also noted that the hypocenters in the higher bridging angle geometries (Figures 5.7h to 5.7k) are generally more scattered and difficult to interpret than for the lower bridging angle geometries. This may be caused by inaccuracies introduced by the analysis that may be attributed to the overlapping flaws, as the ray paths must travel around the flaws. Overlapping flaws may also generate a more complex stress field leading to a more complex velocity field that is difficult to capture with only eight sensors for velocity measurements. These factors can decrease the accuracy of the localisation procedure. Another factor may be that with the higher bridging angles the more complex stress field generates more possible points of failure, leading to more scattered hypocenters appearing outside of the cracks. We can make several qualitative observations based on the hypocenter data:

1. The highest concentration of hypocenters tends to be at the flaw tips, where the stress concentration is highest before crack initiation (see also Goncalves da Silva and Einstein, 2014).

2. Significant clustering can also be seen in the coalescence zone of some tests (Figures 5.7a, 5.7e and 5.7i), where a crack forms directly between the inner flaw tips (known as direct coalescence).

3. Tests where cracks emanate from each inner flaw tip and do not connect (Figure 5.7g) show few events in the zone directly between the flaws, which is expected given that no crack forms there. However, we note that cracks initiating from the inner flaw tips are usually associated with fewer hypocenters than those initiating from the outer flaw tips.

4. More events are seen in the center of the coalescence zone of the test shown in Figure 5.7i than the tests in Figures 5.7h, 5.7j and 5.7k, even though direct coalescence is observed in all

four cases. This may be explained when considering the specific crack paths: coalescence in Figure 5.7i occurs between the middle of the flaws, whereas the other three tests generally show coalescence between the flaw tips. This may be because less energy is required to initiate a crack from a flaw tip since the stress concentration is higher.

5. Many of the tests (Figures 5.7a, 5.7b, 5.7c and 5.7e) exhibit linear clusters of hypocenters even where no white patching nor cracking occurs. These appear to be more common for lower flaw angles, and are clustered perpendicularly to the flaw orientation.

6. The crack and hypocenter patterns for the single flaw geometries (Figures 5.7l and 5.7m) tend to be simpler than the double flaw geometries. It can be seen that in both cases the hypocenter locations migrate away from the flaw tips in time, and that the hypocenters most distant from the flaw tended to be NDC type focal mechanisms. Near the flaw tips, the focal mechanisms tended to be a combination of DC and NDC.

7. The focal mechanisms appear to cluster spatially by type of mechanism. For example in the test shown in Figure 5.7c, the area around the left outer flaw tip consists primarily of DC dominated events. Similarly in Figure 5.7g, we see that explosive NDC events occur closest to the outer left flaw tip, while most scattered events tend to be DC dominated.

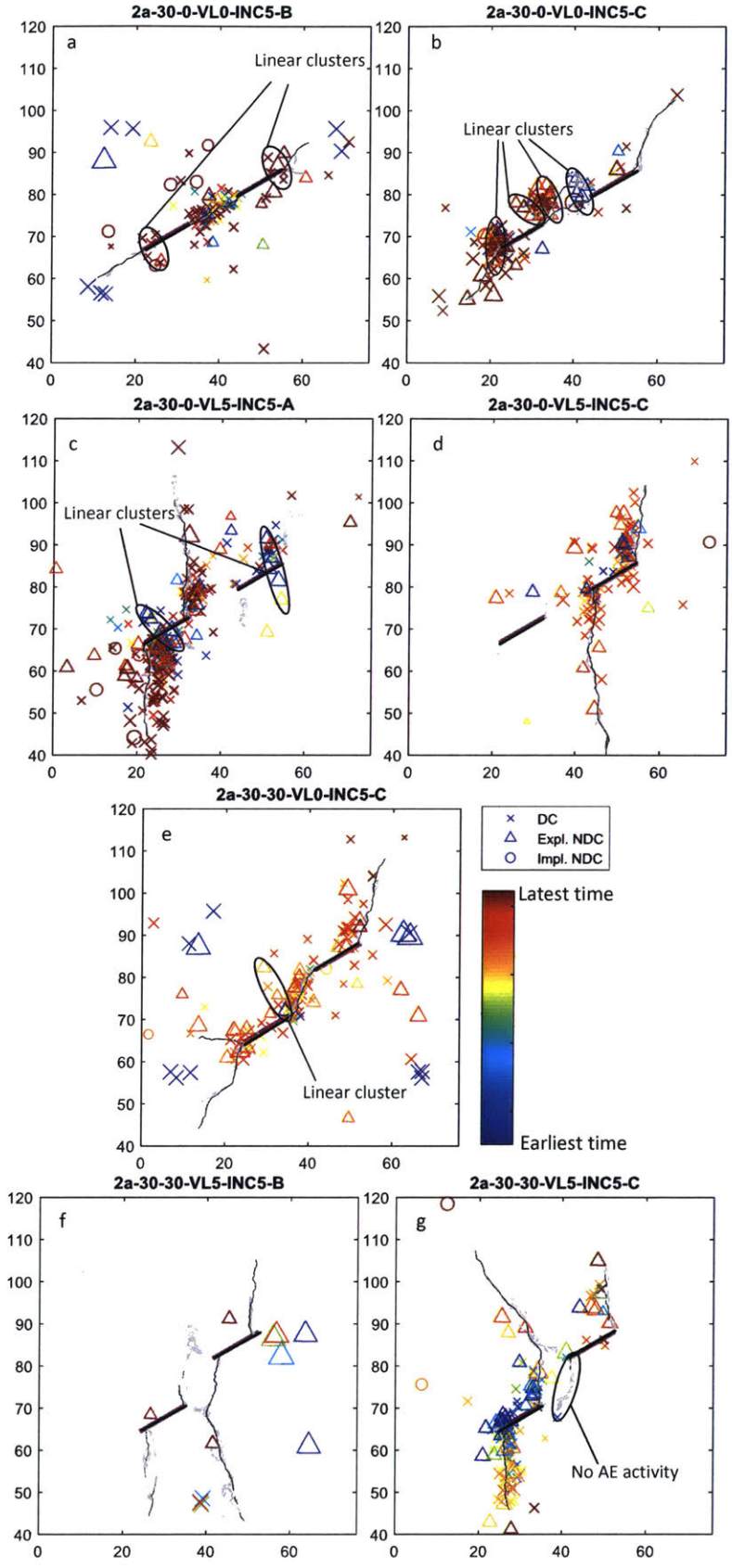
2a-30-0-VL0-INC5-B
a
Linear clusters
2a-30-0-VL0-INC5-C
b
Linear clusters
2a-30-0-VL5-INC5-A
c
Linear clusters
2a-30-0-VL5-INC5-C
d
2a-30-30-VL0-INC5-C
e
Linear cluster
DC
Expl. NDC
Impl. NDC
Latest time
Earliest time
2a-30-30-VL5-INC5-B
f
2a-30-30-VL5-INC5-C
g
No AE activity

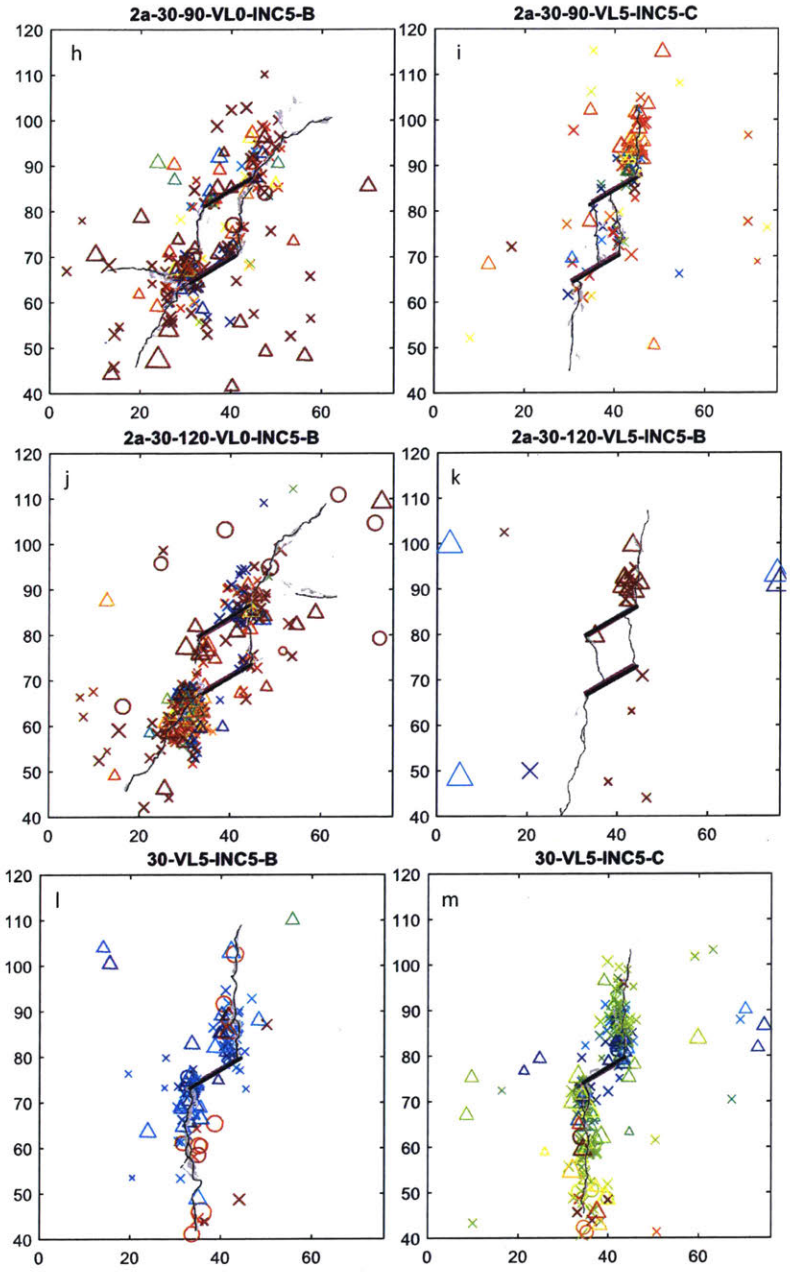

Figure 5.7: Hypocenter locations for each test. The magnitude of the event is shown by the size of the data point. Dark grey lines indicate the cracks, and light grey areas indicate white-patching. The symbols indicate whether the event can be classified as double couple (x), explosive non double couple (Δ), or implosive non double couple (o), and colour represents time, where red is the latest event and blue the earliest.

5.2.5 Spatio-temporal Analysis

This section presents the spatial-temporal development of AE hypocenters for tests 30-VL5-C, 2a-30-0-VL0-C, and 2a-30-120-VL0-B. The remaining analyses can be found in Appendix C. The hypocenter distributions for these tests are shown in Figures 5.7m, 5.7b and 5.7j; for spatio-temporal analysis, the AE events were ordered sequentially, and divided into six time segments each with equal number of AE events to qualitatively analyse their behaviour. Given that the event rate increases towards the end of the test, this means that the first segment may cover over 100s of the test, while the third frame may cover less than one second. These AE observations are also compared to the visually observed crack development. These three tests are chosen as they most clearly illustrate key findings from all the 13 tests.

5.2.5.1 30-VL5-INC5-C

We first present the analysis from a test with a single flaw (Figure 5.8), as this presents a simpler geometry and stress field, resulting in simpler crack patterns and straight ray paths for the AE signals. In this test, we observe a classic wing crack pattern, where crack A initiates from the left tip, then crack B from the right tip. Pressure increases until 2450s and fluctuates until 2484s, at which point the water pressure drops due to crack propagation.

As seen in figure 5.9, before 2472 s more AE hypocenters occur at the right tip than the left, and consist of a combination of all focal mechanisms. However, we note that the highest amplitude events at the right flaw tip are explosive NDC type, while the largest events at the left tip consist of mostly shear and implosive NDC. This indicates that the rock at the right tip is opening, which generates a compressive stress field at the left flaw tip. Visually at this time we only see small (2-3 mm) areas of white patching at each flaw tip. Between 2472.69 s and 2481.06 s, at the left flaw tip we see small shear events at the very tip, and some NDC events further from the flaw tip. On the right flaw tip we see many high amplitude explosive NDC events, with the highest amplitudes occurring in a zone approximately 5 mm above the flaw tip. A number of implosive NDC events also occur approximately 5 mm above the right flaw tip. Between 2481.08 s and 2482.73 s, the events occurring near the right flaw tip mostly consist of NDC events, where events occurring later in time are further from the flaw tip. This indicates growth of the zone of microcracking. Near the left flaw tip, we see mostly explosive NDC events. We suggest that this sudden shift in behaviour from DC dominated events in the previous frame to a number of high amplitude explosive NDC events indicates a coalescence of microcracks similar in nature to those described in Irwin (1958), and Wong and Einstein (2009b). This phenomenon is observed directly in limited cases in specimens used in the present study, through SEM imaging of areas exhibiting white patching. Figure 5.10 shows an example, where we see a series of connected en-echelon microcracks connecting into a larger crack feature emanating from a flaw tip. Between 2482.77 s and 2483.34 s, we see large explosive NDC events that occur near the furthest extent of the zone of previous AE hypocenters. We suggests this represents the continued growth of the zone of microcracking. Between 2483.35 s and 2483.66 s, we see that the majority of events occur below the left flaw tip. The majority of these are NDC events. This suggests the development and subsequent coalescence of microcracks from the left tip. Between 2483.66 s and 2484 s, many high amplitude events occur below the left and above the right flaw tips, and consist of a mix of focal mechanisms. This occurs approximately at the same time as macro-crack initiation and propagation, as shown in the figure.

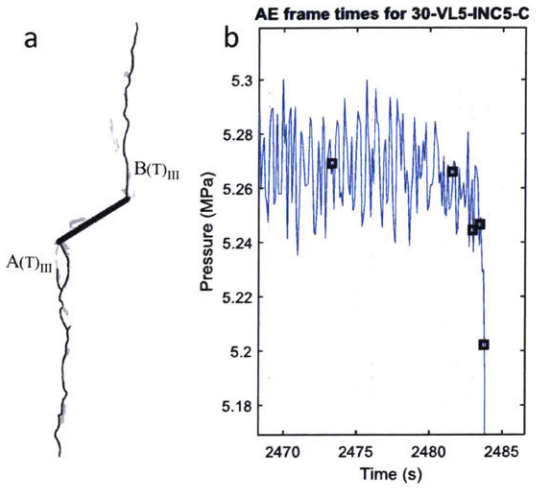

Figure 5.8: Test 30-VL5-INC5-C (a) Crack sequence shown in alphabetical order. (T) denotes the cracks open in tension, and subscripts refer to crack type as defined in Wong and Einstein (2009). Black lines denote cracks and grey areas indicate white patching. (b) Pressure-time plot for the experiment. Black squares indicate times used in Figure 5.9.

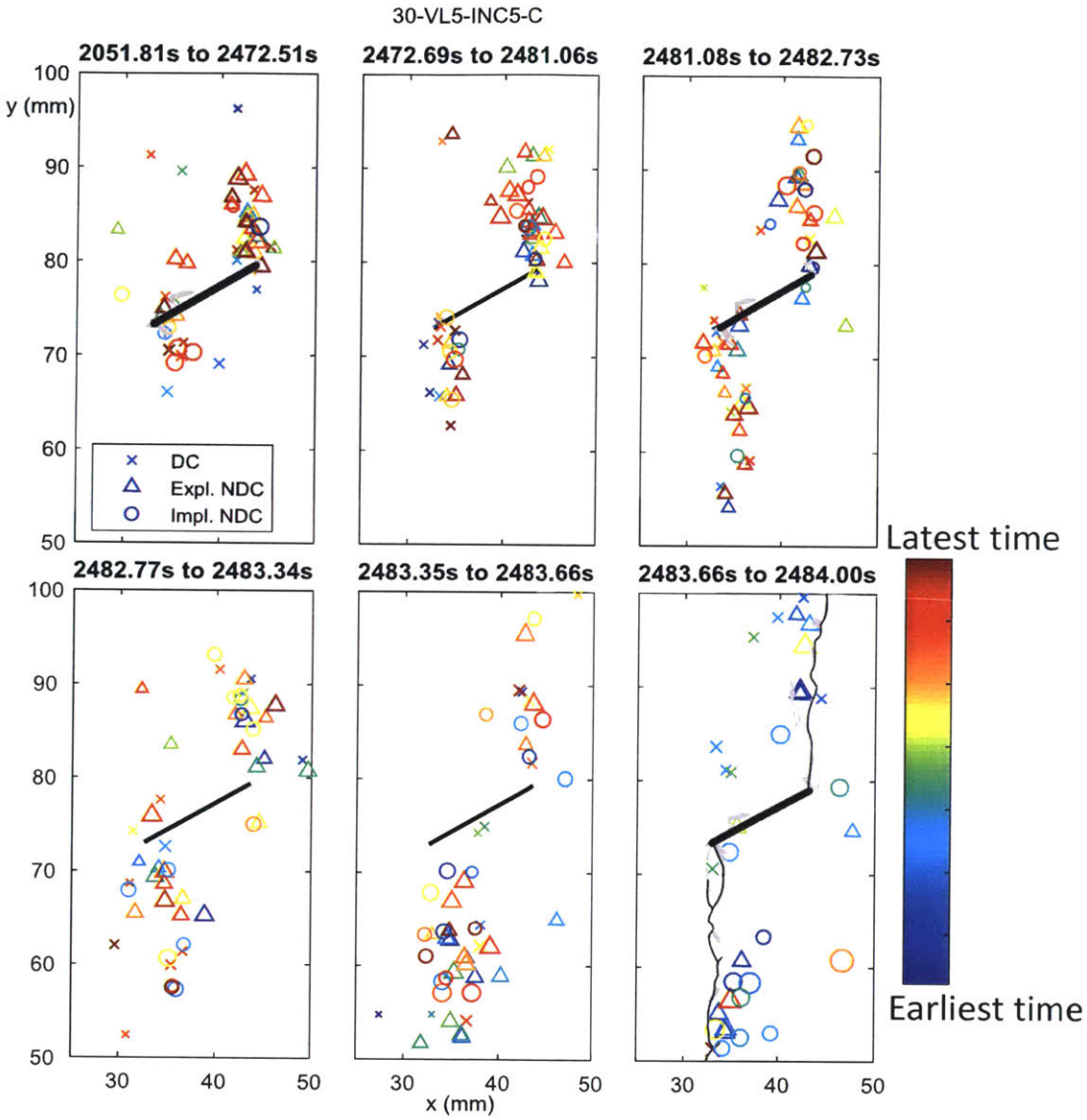

Figure 5.9: Temporal evolution of AE hypocenters for test 30-VL5-INC5-C. DC events refer to those with higher double couple, or shear content, explosive NDC (non double-couple) to those with lower DC and positive ISO and CLVD components, and implosive NDC to those with lower DC and negative ISO and CLVD. Colour is used to show time, and size indicates magnitude. Visual observations of the white patching (in grey) and cracking extent (in black) are overlaid where applicable.

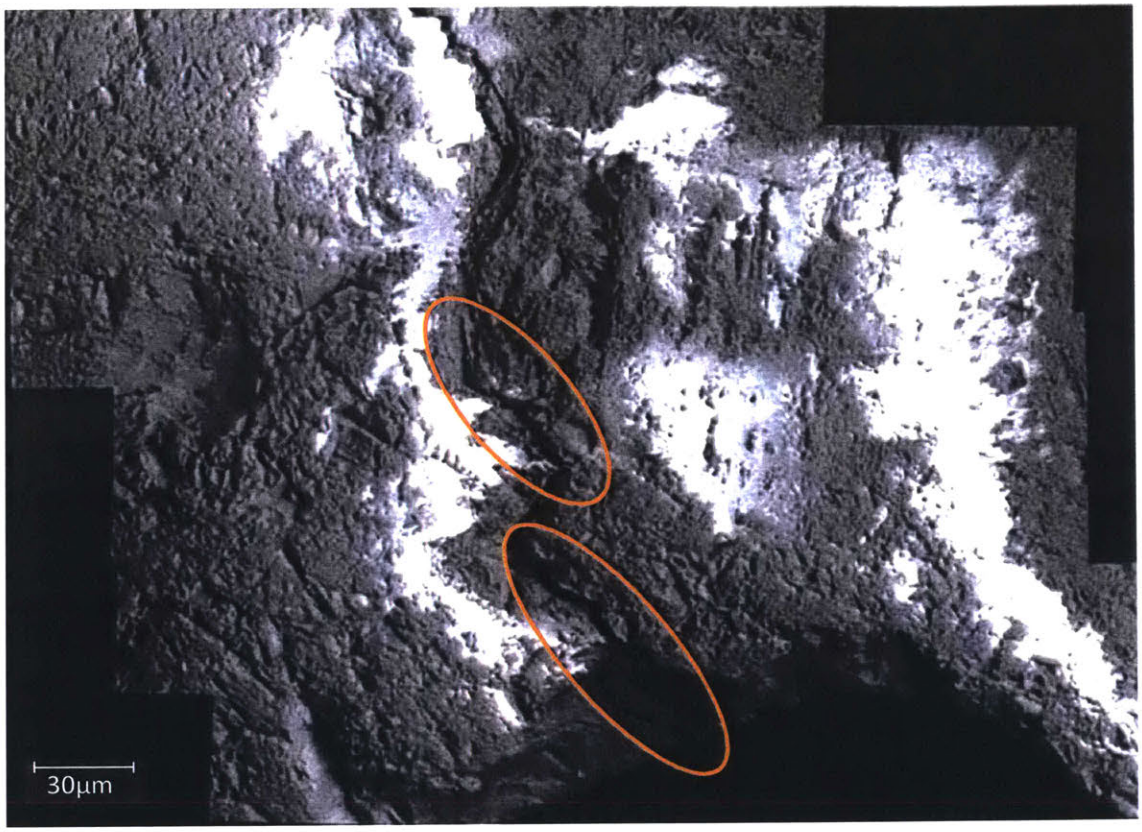

Figure 5.10: SEM image taken near the flaw tip of test 2a-30-0-VL5-A showing a series of connected en-echelon microcracks, such as the one highlighted in the orange circles. From Goncalves da Silva (2016).

5.2.5.2 2a-30-0-VL0-C

As seen in Figure 5.11, tensile crack A initiates first from the outer left flaw tip, followed by tensile crack B which does not coalesce (i.e. does not propagate to the inner right flaw tip) followed by propagation of tensile crack C, which then coalesces with the left flaw after the initiation of tensile crack D. Peak pressure occurs around 1569s, and a local minimum in pressure occurs around 1580s, a few seconds before pressure breakdown as seen in Figure 5.11.

In Figure 5.12, we can initially see a cluster of mostly explosive NDC events at the outer left flaw tip, and a cluster with mixed focal mechanisms at the inner flaw tips. Visually, there appears to be 2-3 mm of white patching at all flaw tips. Between 1553.79 s and 1574.13 s, the largest concentration of events continues at the outer left flaw tip, consisting of both explosive and implosive NDC focal mechanisms. A small number of events also occur at the inner left flaw tip, and consist of some DC events, which indicates opening at the outer left flaw tip. Between 1574.45 s and 1581.60 s a large number of DC events occur at the inner left flaw tip, while NDC events occur at the outer right flaw tip. The focal mechanisms are mixed at the outer left flaw tip. Between 1581.68 s and 1583.61 s, both explosive NDC and DC events occur at both tips of the left flaw, suggesting steady microcrack growth. Visually, the white patching extends by another 2-3 mm on both outer flaw tips. Between 1583.62 s and 1584.21 s, multiple large amplitude explosive NDC events occur near the outer left flaw tip. This may reflect sufficient opening around the flaw tip that fluid penetrates into the surrounding rock, as the spatial clustering of events is wider in this time frame than in previous frames. We also see a linear cluster at 45^o from the inner left flaw tip, which may indicate shear bands forming at an oblique angle along the final path of crack A. In the last frame the macro-cracks initiate and propagate, and are accompanied by AE events that are located along the cracks.

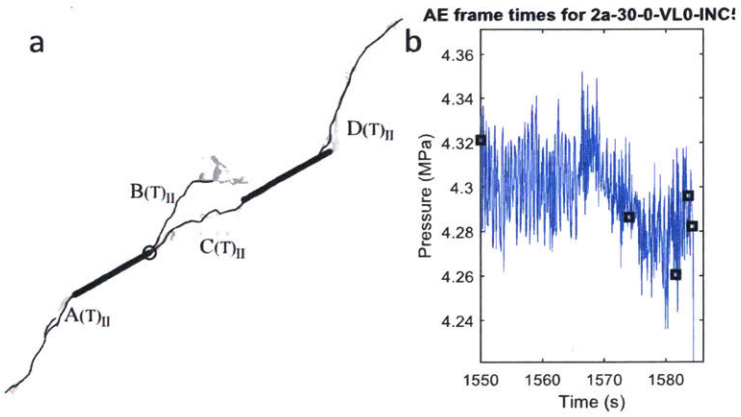

Figure 5.11: (a) Crack sequence shown in alphabetical order. (T) denotes the cracks open in tension, and subscripts refer to crack type as defined in Wong and Einstein (2009). Black lines denote cracks and grey areas indicate white patching. Black circle indicates location where crack C coalesces with the left flaw (b) Pressure-time plot for the experiment. Black squares indicate times used in Figure 5.12.

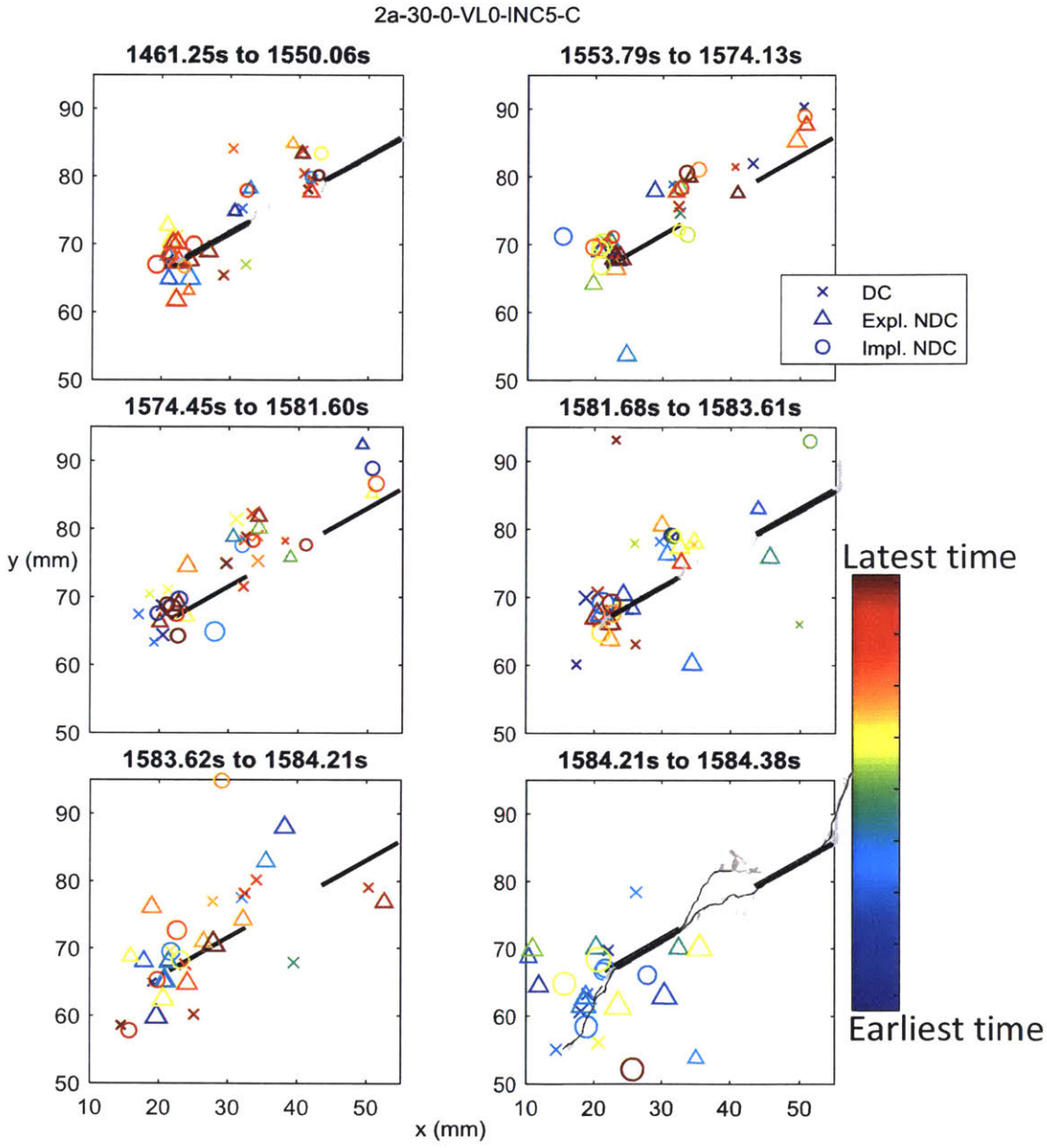

Figure 5.12: Temporal evolution of AE hypocenters. DC events refer to those with higher double couple, or shear content, explosive NDC (non double-couple) to those with lower DC and positive ISO and CLVD components, and implosive NDC to those with lower DC and negative ISO and CLVD. Colour is used to show time, and size indicates magnitude. Visual observations of the white patching (in grey) and cracking extent (in black) are overlaid where applicable.

5.2.5.3 2a-30-120-VL0-B

As shown in Figure 5.13, tensile crack A initiates from the bottom left flaw tip, then tensile crack B from the top right flaw tip. Tensile crack C then initiates from the top left flaw tip, but does not coalesce while tensile crack D initiates from the bottom right flaw tip, opens, and coalesces to the top right flaw tip. Water pressure fluctuates between 1800s and 1840s, at which point the water pressure begins to drop.

Figure 5.14 shows that up to 1831.45 s, visually there is 4-5 mm white patching at the top right flaw tip, and 2-3 mm of white patching on the other flaw tips. This corresponds well to the AE hypocenters, since we see that the earliest AE events occurred at the top right flaw tip. This is followed by a large number of NDC events immediately at the bottom left flaw tip and other NDC events at a distance up to 10 mm from the bottom left flaw tip. At this stage, the AE pattern appears to match well with the initiation points for cracks A and B. From 1831.54 s to 1839.88 s, the majority of AE events occur at the left tip of the bottom flaw, where the largest amplitude events occur as NDC type, suggesting the creation of major microcracks. Between 1839.96 s and 1842.83 s large DC and explosive NDC events continue to occur around the bottom left flaw tip, although the scatter of the hypocenter locations appear to be wider than in the previous time frame. A clear linear cluster of large explosive NDC events also occurs along the path of crack D, indicating that microcracks have created the white patching along crack D seen visually in the next frame. Between 1842.88 s and 1844.31 s the zone of hypocenter locations continues to grow, and consists largely of NDC events. We also see large amplitude explosive NDC events at all the flaw tips. This corresponds well to the visual observation that white patching has developed to 4-5 mm at all flaw tips. Between 1844.32 s and 1844.76 s the events near the flaw tips are primarily implosive NDC, while explosive NDC events occur further away from the flaw tips, indicating propagation of the microcracking front. In the last frame (1844.76 s to 1845.09 s) we can see that the crack has propagated, and that the accompanying AE events are primarily DC and appear to be closely aligned with the cracks A, B and C.

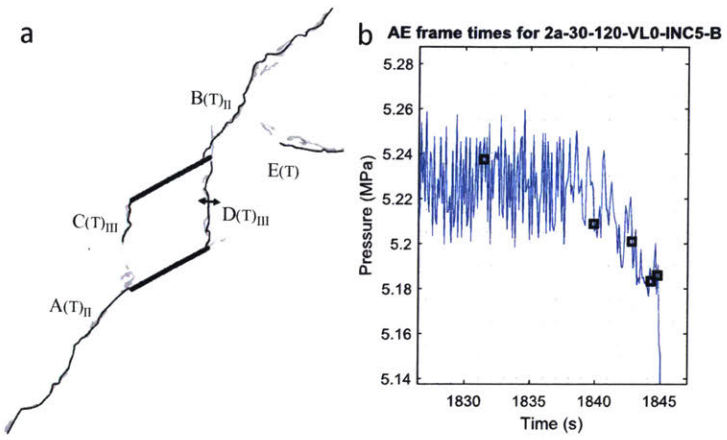

Figure 5.13: (a) Crack sequence shown in alphabetical order. (T) denotes the cracks open in tension, and subscripts refer to crack type as defined in Wong and Einstein (2009). Black lines denote cracks and grey areas indicate white patching. (b) Pressure-time plot for the experiment. Black squares indicate times used in Figure 5.14.

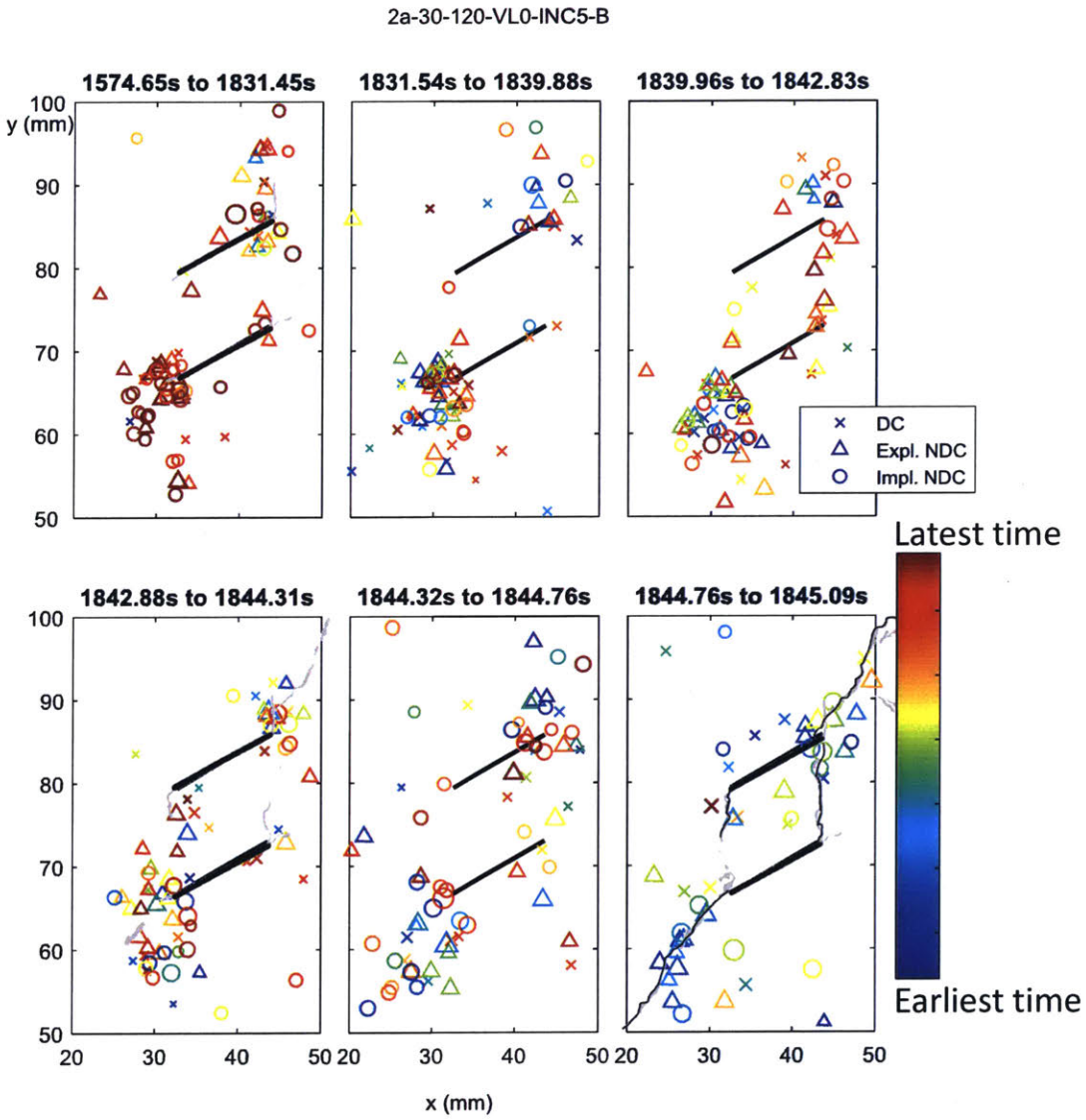

Figure 5.14: Temporal evolution of AE hypocenters. DC events refer to those with higher double couple, or shear content, explosive NDC (non double-couple) to those with lower DC and positive ISO and CLVD components, and implosive NDC to those with lower DC and negative ISO and CLVD. Colour is used to show time, and size indicates magnitude. Visual observations of the white patching (in grey) and cracking extent (in black) are overlaid where applicable.

5.2.5.4 Spatio-temporal Distribution of Focal Mechanisms

In all three tests described in this section, we observe phenomena in which focal mechanisms and hypocenter locations appear to be grouped in space over time. This can be seen at two scales: firstly at opposite ends of a flaw, where opening at one flaw tip generates a compressive stress field at the other flaw tip. For example, we note that in all three tests that if a large number of explosive NDC events occur at one flaw tip, we generally see more DC events at the other flaw tips.

Secondly, we see in test 2a-30-120-VL0-B that DC events tend to form linear clusters along grain boundaries, and explosive NDC events tend to exist outside of these clusters. This may be caused by tensile microcracks opening through a grain, while shear cracks occur along grain boundaries (Morgan and Einstein, 2013). This is shown in Figure 5.15, which is a photo of the bottom left flaw tip and the area below it, overlaid with AE events that occurred throughout the experiment.

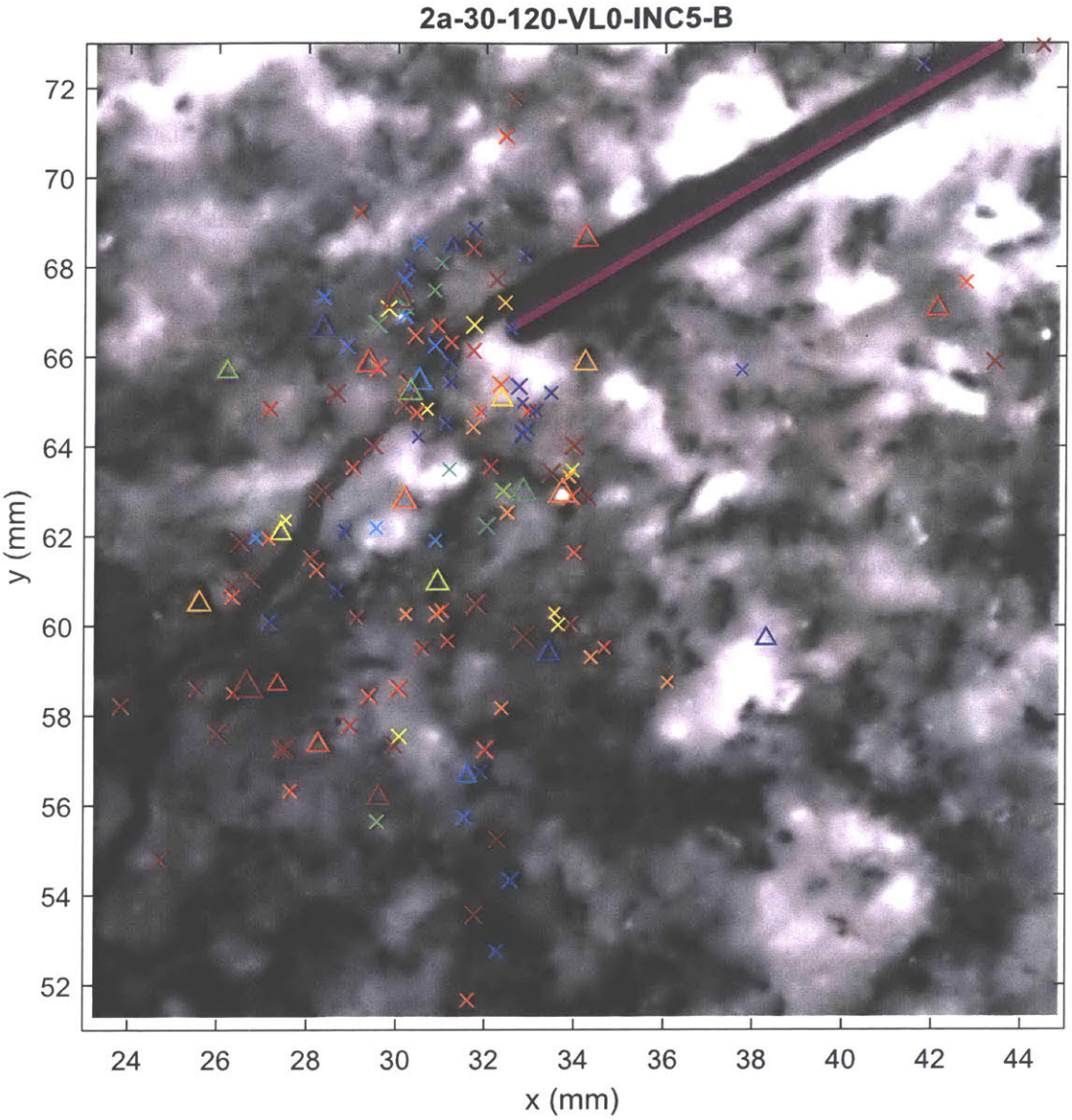

Figure 5.15: Zoomed photo of the bottom flaw of test 2a-30-120-VL0-B and the area below and to the left of it, overlaid by AE events occurring throughout the test. Colour refers to time where red is the latest, crosses refer to DC dominated events, triangles to explosive NDC events and circles to implosive NDC events. The size of the symbols represents the magnitude of the events.

5.3 Discussion

5.3.1 Stress state

The stress state of a 2a-30-30 geometry subjected to vertical load and water pressure is explored in depth by Gonçalves da Silva and Einstein (2014), and is summarised (See Figure 5.16) and used here as a basis for comparison to the AE results. We can see that the finite elements analysis shows that when a small vertical load is applied, i.e. WP/VL is high, tensile stresses tend to be higher than shear stresses between $\theta = \pm 30^o$, and shear stress is highest at approximately $\theta = \pm 70^o$. In the WP/VL = 1 case we can see that the top half of the flaw tip ($\theta = 0^o$ to -120^o) is in tension, while the bottom half ($\theta = 0^o$ to 120^o) is in compression. We can also see that for WP/VL = 1 the shear stresses are highest around $\theta = 0^o$, and generally higher above the flaw tip than below it.

To compare to the AE results, we can consider the location of AE events shown in Figure 5.7, and the relative proportion of focal mechanisms shown in Table 5.1. The distribution of focal mechanisms, where we saw that 50-60% of the radiation pattern could be explained by a double couple (shear) mechanism, correlate well to finite element model in that the magnitude of shear stresses are comparable to the tensile stresses. In terms of the AE hypocenter locations, Figure 5.7 shows that in general, cracks were more likely to initiate from the flaw tip i.e. $\theta \approx 0$ in 0 MPa vertical load tests (high WP/VL), where the finite element model shows tensile stress is close to zero and shear stress is maximum. On the other hand, cracks tended to initiate away from the flaw tip in 5 MPa vertical load tests (WP/VL ≈ 1) , where both principal and shear stresses are high.

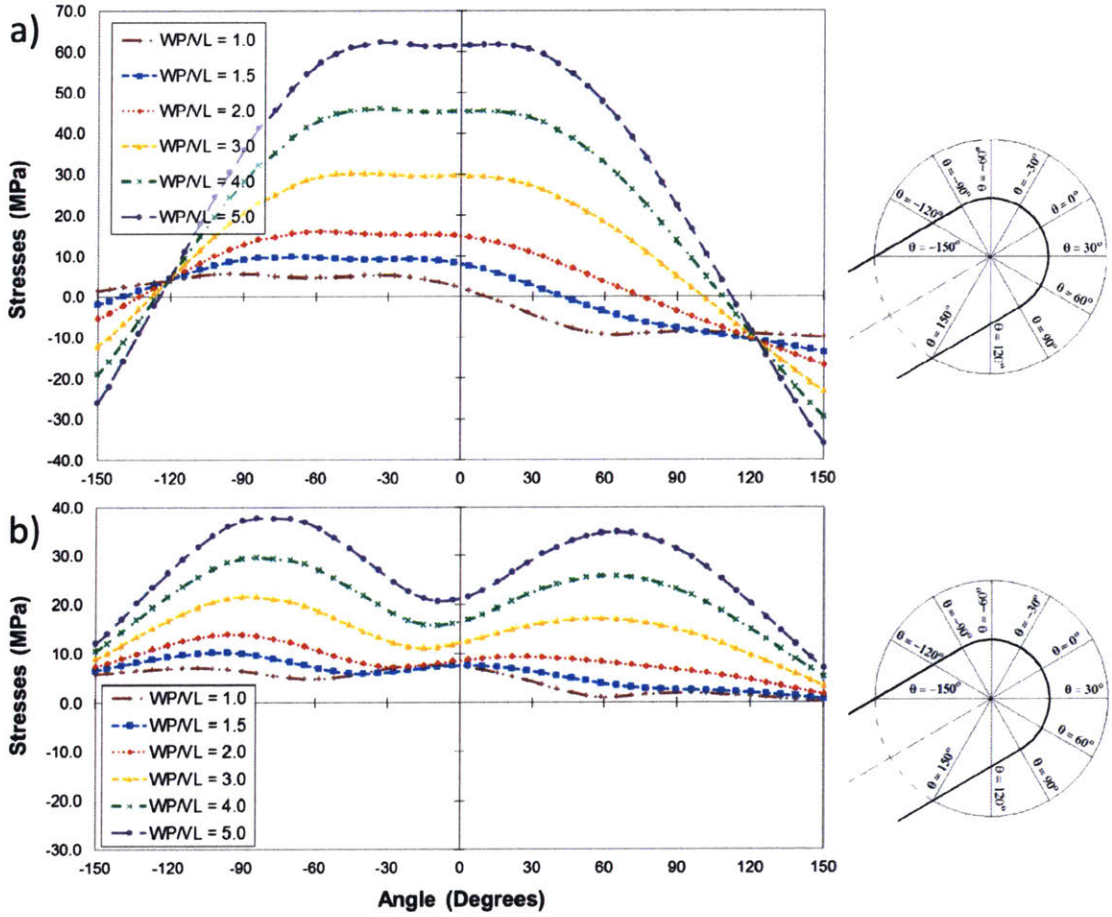

Figure 5.16: a) Maximum principal stress (tension positive) around the inner left flaw tip of 2a-30-30 geometry for different ratio of water pressure to vertical load (WP/VL). b) Same plot for maximum shear stress. From Goncalves da Silva and Einstein (2014).

5.3.2 Time-to-Failure analysis

In Figure 5.4, we saw that the AE hit rate tended to increase exponentially as the rock approached macro-crack initiation and propagation. This type of behaviour can be explained by a time-to-failure (Lei and Satoh, 2007; Bufe, Nishenko and Varnes 1994; Brehm and Braile, 1999) framework such as the accelerated moment release (AMR) model, which is summarised in Equation 5.1 below.

$$\Sigma E(t) = A + B(t_f - t)^m \tag{5.1}$$

Where $\Sigma E(t)$ is the cumulative Benioff strain energy (proportional to seismic wave energy) at time t calculated in relative terms by $E \propto 10^{0.75M}$ where M is the event magnitude, A is the cumulative Benioff strain at $t = t_f$, B is a fitting variable, and t_f is the time of failure, which in this work is taken as the time of macro-crack initiation. m is the second fitting variable which describes the rate of acceleration, and for natural earthquakes has been observed to be in the range of 0.2-0.3 (Lei and Satoh, 2007). Two sample fits are shown in Figure 5.17.

We can see that the 2a-30-0-VL5-C data can be well fit with the AMR model, but less so with the 2a-30-90-VL5-C test. This is likely due to the phenomenon, as noted in Section 3.1, that there appears to be two different stages of behaviour exhibited as the test approaches failure, where the first stage is characterised by linear energy accumulation, and then transitions to exponential energy accumulation, possibly when the microcracks begin to coalesce. This point in time is denoted by the green lines and arrows in Figure 5.17. Table 5.2 shows the results of AMR applied to all tests. In each test, the goodness of fit between the model and experimental data is expressed as the root mean squared error (RMSE). A, B and RMSE were not found to be significantly correlated to m. We can see that, in general, the m values span from 0.2 to 0.4, with a mean of 0.311. This lies reasonably close to the m = 0.2 to 0.3 specified by Lei and Ma (2014), and within the m = 0.13 to 0.47 suggested by Brehm and Braile (1999). This suggests that in the immediate seconds before macro-crack initiation, the energy accumulation characteristics of hydraulic fracturing is similar to that of natural earthquakes.

Table 5.2: Summary of accelerated moment release (AMR) model applied to AE results. RMSE column indicates goodness of fit between the model and experimental data.

Specimen name	m	B ($Nm^{0.5}s^{-1}$)	A ($Nm^{0.5}$)	RMSE ($Nm^{0.5}$)
2a-30-0-VL0-INC5-B	0.335	2.72E-05	1.06E-04	1.88E-06
2a-30-0-VL0-INC5-C	0.245	3.98E-05	9.59E-05	4.02E-06
2a-30-0-VL5-INC5-A	0.378	8.28E-05	4.04E-04	8.37E-06
2a-30-0-VL5-INC5-C	0.312	4.27E-05	1.59E-04	1.32E-06
2a-30-30-VL0-INC5-C	0.374	6.97E-05	1.78E-04	2.54E-06
2a-30-30-VL5-INC5-B	0.319	1.17E-05	6.32E-05	5.82E-07
2a-30-30-VL5-INC5-C	0.318	4.97E-05	1.30E-04	2.00E-06
2a-30-90-VL0-INC5-B	0.189	8.77E-05	1.50E-04	4.64E-06
2a-30-90-VL5-INC5-C	0.416	3.67E-05	9.84E-05	2.62E-06
2a-30-120-VL0-INC5-B	0.216	7.92E-05	1.68E-04	4.64E-06
2a-30-120-VL5-INC5-B	0.212	1.20E-05	6.92E-05	6.53E-07
30-VL5-INC5-B (Single flaw)	0.459	3.98E-05	1.40E-04	1.80E-06
30-VL5-INC5-C (Single flaw)	0.228	7.00E-05	1.73E-04	4.61E-06

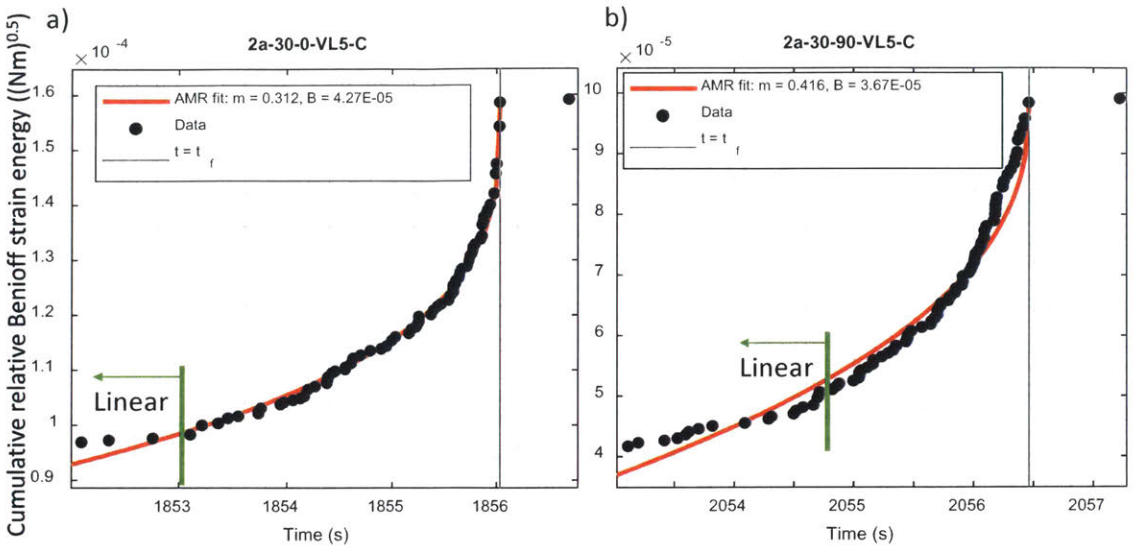

Figure 5.17: Cumulative Benioff strain energy data and AMR fit for a) 2a-30-0-VL5-C and b) 2a-30-90-VL5-C tests. Green line and arrow indicates end of linear energy accumulation.

5.4 Summary and Conclusions

We presented the acquisition, analysis and interpretation of acoustic emissions data from a series of laboratory hydraulic fracture experiments on granite. These data are related to corresponding visual observations made using high resolution and high speed imaging. This is summarised in Table 5.3, where we describe the similarity of the spatial distribution observed with the two methods, and assess the possibility of using AE as a predictor of the crack initiation point.

Overall, we see that for the majority of tests, there are areas of AE activity where we do not visually detected damage. This suggests that acoustic emissions monitoring is a more sensitive detector of microstructural damage than the visual method. Conversely, almost all areas where we visually detected damage corresponded to AE activity, which suggests that at least in this experimental setup the development of the process zone and crack development is seismic. We also determine that in most cases, the flaw tip from which the crack initiates corresponds to an area with a high concentration of AE hypocenters, such that one could predict it as an initiation point. However, we also note that, in general, the data often showed two or three flaw tips with significant hypocenter concentration, indicating that one would not be able to make a single prediction given AE data, but nevertheless narrow the possibilities to a few locations of crack initiation. The main results are summarised as follows:

- The rate of AE hits tends to be close to zero until 80% of the peak water pressure, at which point it increases exponentially. In some experiments, it was observed that there was a second inflection where the rate of AE accelerated, close to the time of failure.

- Analysis of the focal mechanisms revealed that, overall, approximately 55-60% of the radiation pattern could be explained by a double couple mechanism, while approximately 25-30% represent isotropic contributions. Explosive non-double-couple events tended to be more common than implosive non-double-couple events (i.e. more tension than compression) un-

Table 5.3: Summary table showing a) whether there all regions of AE activity correspond to visual damage, b) the reverse situation, i.e. whether all regions with visual damage correspond to AE activity, c) whether the point of crack initiation (first crack to form) corresponds to a high concentration of AE hypocenters, d) whether there were multiple clusters of hypocenters i.e. whether one could have made a unique prediction on the point of crack initiation.

	Are most cracks/white patching reflected by AE?	Do most AE hypocenters coincide with cracking/white patching?	Does point of crack initiation correspond to a concentration of AE?	Can one make a single prediction?
Co-planar				
2a-30-0-VL0-B	N	N	Y	N
2a-30-0-VL0-C	N	Y	Y	Y
2a-30-0-VL5-A	N	Y	Y	Y
2a-30-0-VL5-C	Y	Y	Y	N
Flat bridging angle				
2a-30-30-VL0-C	N	Y	N	N
2a-30-30-VL5-B	Y	N	Y	N
2a-30-30-VL5-C	Y	Y	Y	Y
Steep bridging angle				
2a-30-90-VL0-B	N	Y	Y	Y
2a-30-90-VL5-C	N	Y	Y	N
2a-30-120-VL0-B	N	N	Y	N
2a-30-120-VL5-B	N	Y	?	Y
Single Flaw				
30-VL5-B	Y	Y	Y	N
30-VL5-C	Y	Y	Y	N

til the end of the test, at which point a significant number of implosive events occur in some tests. These observations corresponded well with FEM modelling.

- Hypocenter locations of AE events generally correspond well to the cracks and white patching (zones of microcracks or process zone), with the highest concentration of hypocenters occurring at the flaw tips. In particular, the single flaw geometries showed the spatial growth of hypocenters away from the flaw tips over time

- Spatio-temporal analysis of the visual and AE data revealed behaviour where, initially, the focal mechanisms consist of mixed focal mechanism events until a point in time where many high amplitude explosive non-double-couple events occur over a short period of time. We suggest that the latter represents coalescence of microcracks and is a key pre-cursor to hydraulically induced cracking.

- The focal mechanisms can be spatially distinct, both at the length scale of the flaw, and on a grain scale. The first case arises from opening at one flaw tip generating a compressive stress at the other tip. The second case occurs when opening occurs on a grain boundary, causing shear on adjacent grains.

- Based on spatio-temporal analyses of all tests, we suggest that the visually observed microcracking tends to be related to damage, and that the AE, in general, could predict the point of crack initiation. However, this prediction may not be unique given that there are often two to three concentrations of AE hypocenters.

- Time-to-failure analysis showed a reasonably good fit to the exponential stage of AE energy accumulation, which occurs in the few seconds prior to macro-crack initiation and propagation.

We can therefore conclude that, in this material, under stress conditions where the failure is driven by fluid pressure with multiple points of crack initiation, the observed acoustic emissions present a reasonably complete picture of the areas of microcracking, and have a good potential to be used to predict the points of crack initiation and the final crack pattern.

Chapter 6

Hydraulic Fracturing of Shale

"Faithless is he that says farewell when the road darkens"

This chapter presents the results of an experimental study using a laboratory hydraulic fracturing setup that is capable of visually and acoustically observing the fracturing behaviour, while varying the injection rate across four experiments. Note that the Opalinus clayshale used in these tests was BSO-36, which contains 15.9 % quartz, 5.4 % calcite, 21.6 % kaolinite, and 45.4 % illite and illite/smectite.

6.1 Experimental Procedure and Setup

The four hydraulic fracturing tests were conducted on prismatic BSO-36 Opalinus shale specimens with a single pre-cut flaw (Figure 6.1). The tests were done in a biaxial load frame with a transparent clamp seal on the front and back faces (Refer to Figure 6.1). In addition, high speed- and high resolution cameras were used to capture the fracturing processes, with 1,000 frames per second (fps) at 2 Megapixels (MP) and 2 fps at 20 MP, respectively. Eight acoustic emission sensors, spring loaded in specialized loading platens, were used to monitor acoustic activity in the specimens. The flaw was pressured using a 15 MPa capacity pressure volume actuator (PVA), and the pressures were recorded in the actuator as well as directly inside the flaw.

The Opalinus shale specimens were dry cut from cores extracted from the Mont Terri Rock Laboratory in Switzerland [Refer to Morgan and Einstein (2014) for the cutting process]. The specimens were approximately 4in x 2in x1in [101mm x 50mm x 25mm] with a single vertical flaw of 0.33 in x 0.035 in [8.5mm x 0.9mm] (Figure 6.2a). The naturally occurring bedding planes were oriented horizontally. The pressure-sealing device consisted of two 1.5in x 1.5in [38mm x 38mm] polycarbonate seals, with an embedded silicon membrane, on the front and back faces of the specimen (Figure 6.2b and 6.2c). The 1.5 x 1.5 in polycarbonate seals were clamped to the specimen with a steel plate in the back and a thick polycarbonate plate the front via four bolts on the corners. Hydraulic oil (viscosity $\mu = 3.89cP$) was injected into the flaw using two 0.025in (0.64mm) diameter tubes, one in the front and one in the back.

The testing process was performed in the following order:

1. The platens are fitted onto the specimen with the spring-loaded acoustic sensors and the flaw pressurization device is assembled but not tightened.

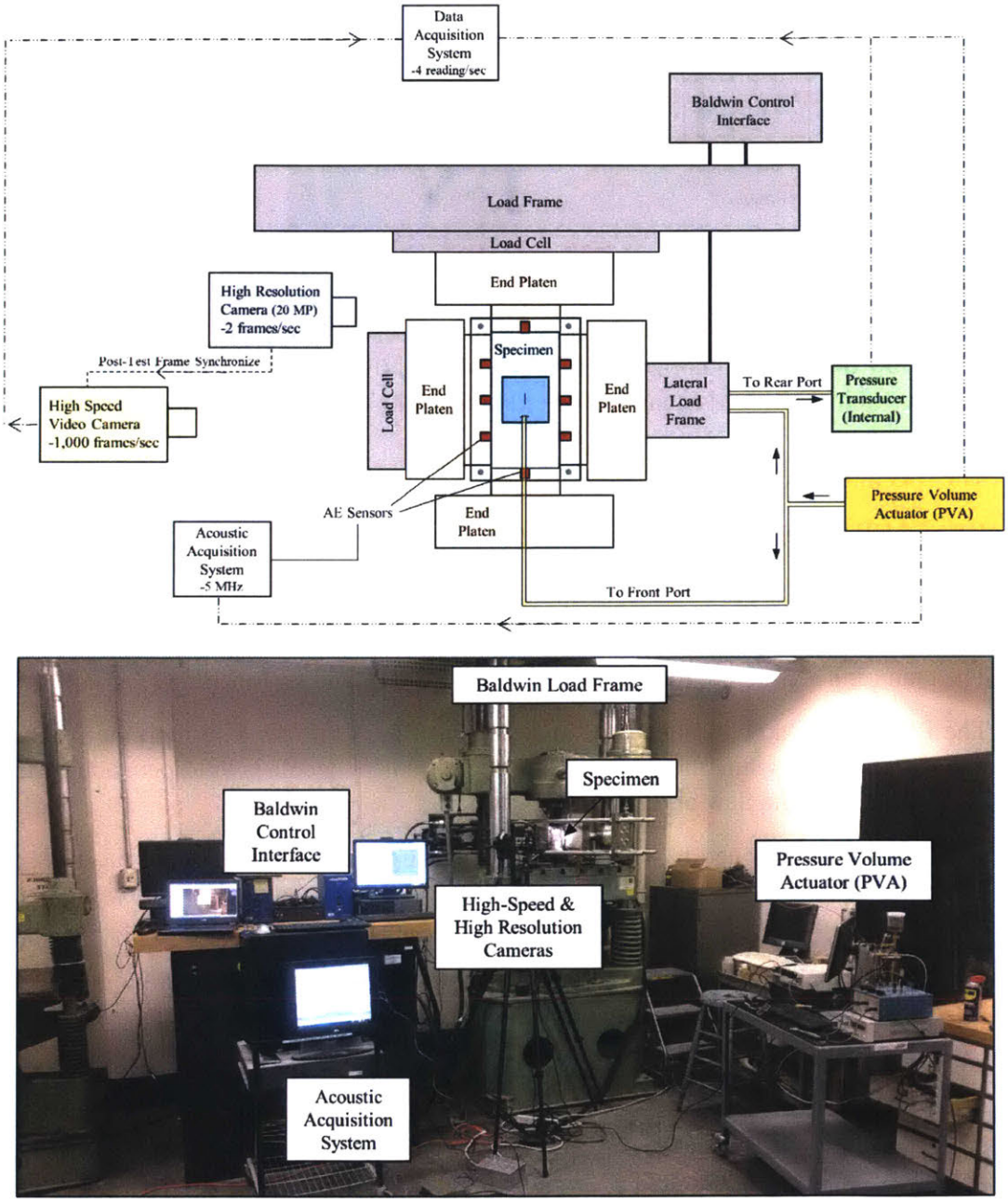

Figure 6.1: Schematic of the experimental setup used in this study. The specimen was loaded to a constant axial and lateral load, and then fluid was injected into a pre-cut flaw. The fractures were observed using a high-speed camera, a high-resolution camera and an acoustic emission system. The fluid pressures were measured in the pressure volume actuator and internally in the flaw. b) Photo of the experimental setup used in this study.

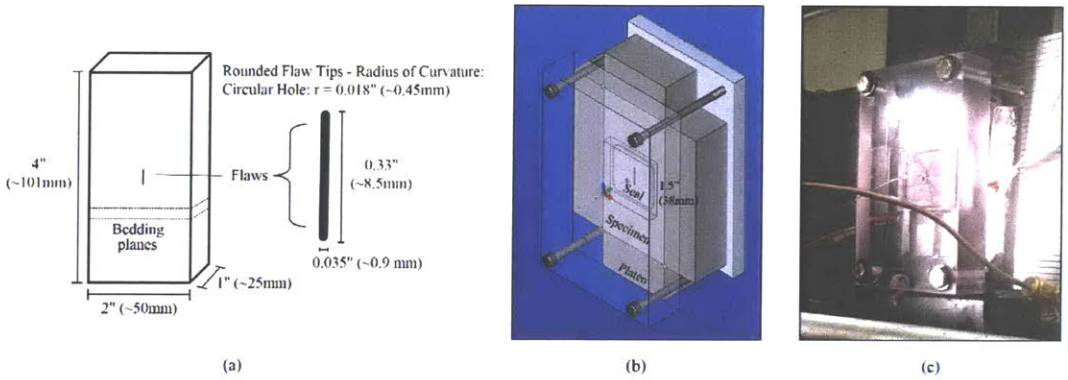

Figure 6.2: Specimen and flaw pressurization device configuration. (a) Schematic of the specimen and pre-cut flaw dimensions, horizontal bedding planes. (b) Schematic of the flaw pressurization device with a 1.5 in [3.81 cm] square seal. (c) Photo of the flaw pressurization device.

2. The specimen is put into the load frame.
3. HS and HR cameras are focused and activated
4. The specimen is subjected to the programmed biaxial loads (σ_1 and σ_3) which are held constant.
5. The clamping screws are torqued to apply $\sigma_2 = 2MPa$ and seal the flaw.
6. The PVA is activated to inject at a low flow rate (0.33 mL/min) through the front and rear injection needles, while the flaw pressure measurement needle is left open, acting as a bleed hole, to saturate the flaw and expel air.
7. Saturation is determined by observing a constant pressure reading from the PVA pressure transducer, at which point the PVA is deactivated while the internal flaw pressure transducer is attached to the flaw pressure measurement needle, closing the saturated system.
8. The test begins by reactivating the PVA to inject at the desired testing flow rate, in this case 1.33 mL/min to start pressurizing the flaw.
9. The HS camera is manually triggered once the specimen fractures concluding the test.

The order of these steps is important because they simulate bringing the rock to in-situ stress conditions, the saturation phase is analogous to drilling mud in the wellbore, and the pumping phase is follows what is done in field operations.

Four specimens were tested with different injection (flow) rates to investigate their effects on the fracturing behavior (Figure 6.3). The lateral and axial loads were held at a constant 4.5 MPa and 1 MPa, respectively. These stresses were chosen because they are below the fracture initiation stress for this flaw geometry observed in dry tests (without hydraulic fracture). The stresses were first applied isotropically to 1 MPa and then the axial load was increased to 4.5 MPa. The four injection rates used were 0.0059 mL/s, 0.0188 mL/s, 0.0807 mL/s, and 0.3903 mL/s. The uppermost and lowest injection rates were defined by the physical limits of the PVA used in this experimental setup.

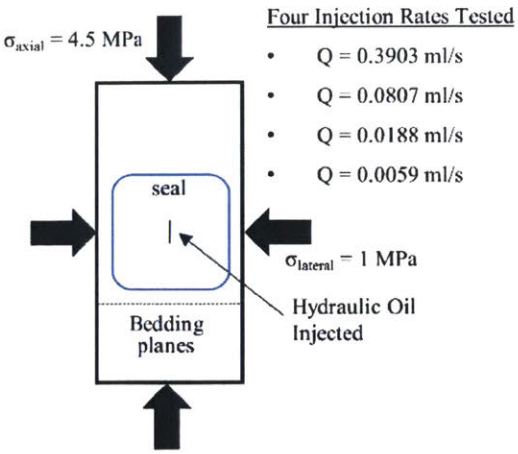

Figure 6.3: Specimens tested in this study. Constant axial (4.5 MPa) and lateral (1 MPa) external stresses were applied. Hydraulic oil was injected at different rates. Four specimens were tested each with a different injection rate.

6.2 Pressure-Fracturing Results

6.2.1 Fracture Progression

Figure 6.4 shows the progression of fractures over time, and how they relate to the pressure in the flaw and in the PVA pump for the test with the 0.0807 ml/s injection rate. Fractures initiated at the flaw tips and then propagated diagonally toward the edge of the seal. Often, fractures propagated along natural horizontal bedding planes (See fracture B in Figure 6.4). A decline in the slope of the internal pressure versus time curve occurred at the first fracture initiation, and the internal pressure dropped when fractures reached the seal boundary.

The observed fracture patterns for the different injection rates tested are shown in Figure 6.5. At lower injection rates (Q = 0.0059 mL, 0.0188 mL/s) the fracturing consisted of simply two fractures initiating at the flaw tips and then propagating up and down towards the direction of maximum principal stress. These fractures were not perfectly straight, alternating between following the bedding planes and cutting across the layers between the bedding planes. At high injection rates (Q = 0.0807 mL/s, 0.3903 mL/s) more fractures occurred (>3 fractures) and their location and their patterns became more complex. This included longer fractures along bedding planes and fractures that branched. Do note, however, that the these results from this set of experiments disagree with a second set of tests, as presented in Section 6.4.

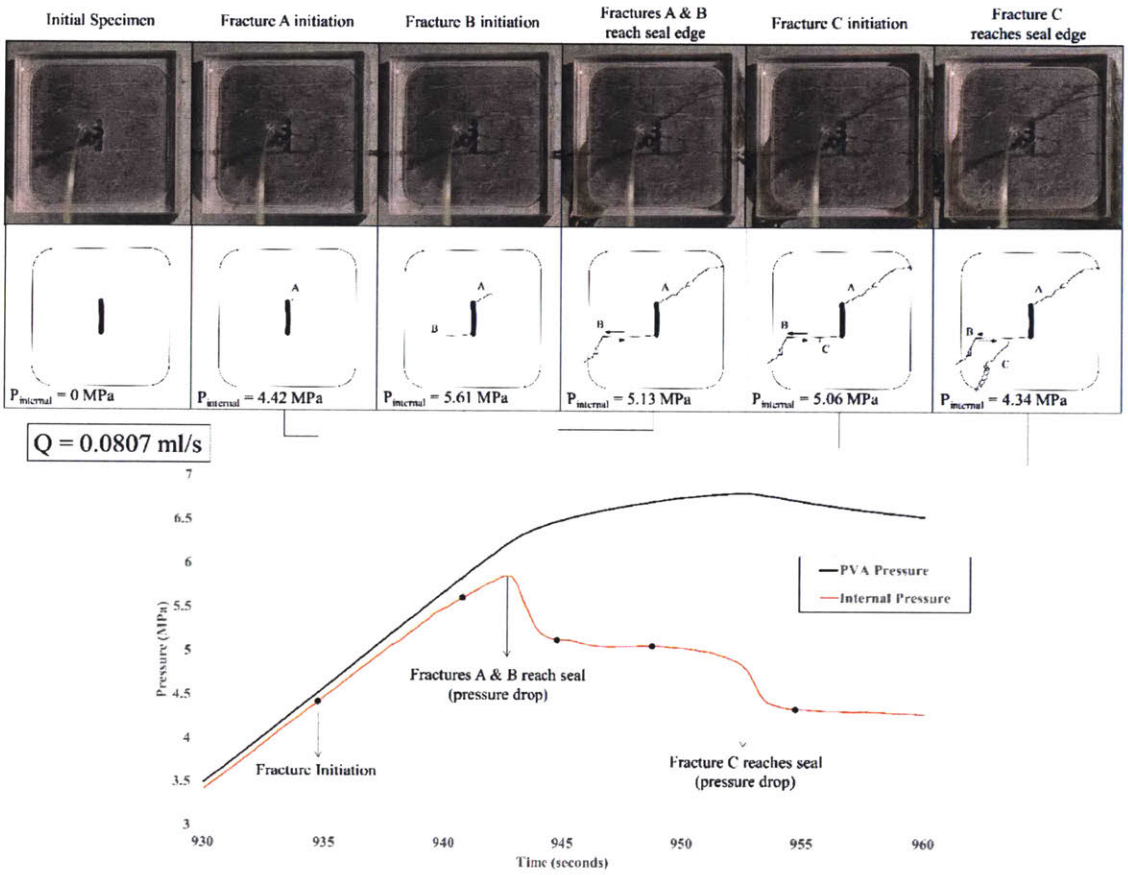

Figure 6.4: Fracture progression and pressure-time curves for the test with 0.0807 ml/s injection rate. The PVA pressure was measured at the pump and the internal pressure was measured directly in the flaw. A decrease in the slope of the internal pressure versus time curve was observed at the first fracture initiation and a drop in the internal pressure were observed when fractures reached the seal boundary.

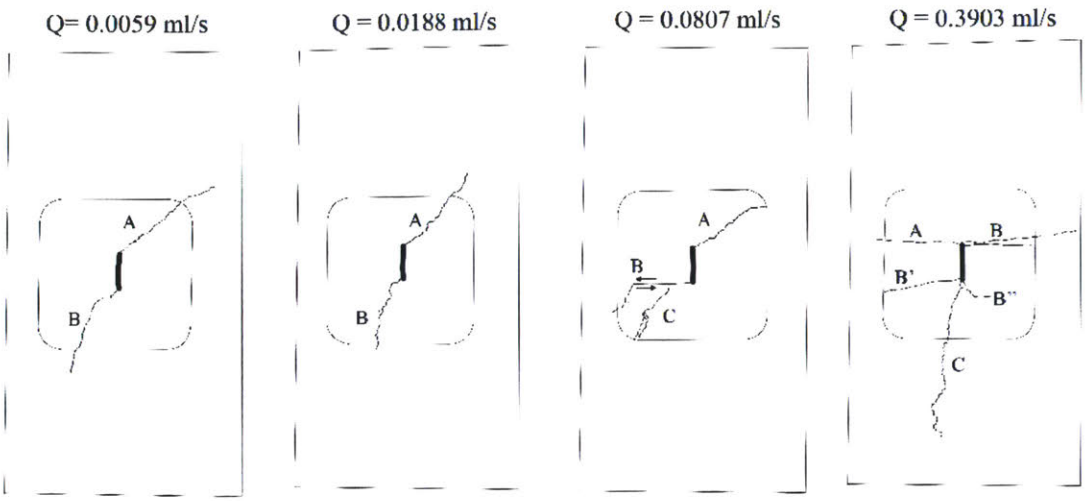

Figure 6.5: Fracture patterns for different injection rates. The fractures are labeled alphabetically in chronological order. The fractures are usually tensile, however, some sliding was observed in fracture B of the specimen with Q = 0.0807 mL/s.

6.2.2 Fracture speed

By using multiple images taken during the tests, and identifying the tip of each fracture as it propagated, the evolution of the fracture speed was determined for all fractures (Figure 6.6). In general, as the injection rate was increased the maximum fracture speed observed for the fractures also increased. Also, the specimens tested with higher injection rates showed higher fracturing accelerations (slopes in Figure 6.6). It should be noted that there was some variability in the fracture speed, as expected when using a natural rock, such as a faster propagating fracture for the slowest injection rate or a slowly propagating fracture at the highest injection rate (Refer to Figure 6.6). However, the general trend between higher injection rate and higher fracture speed appeared to hold.

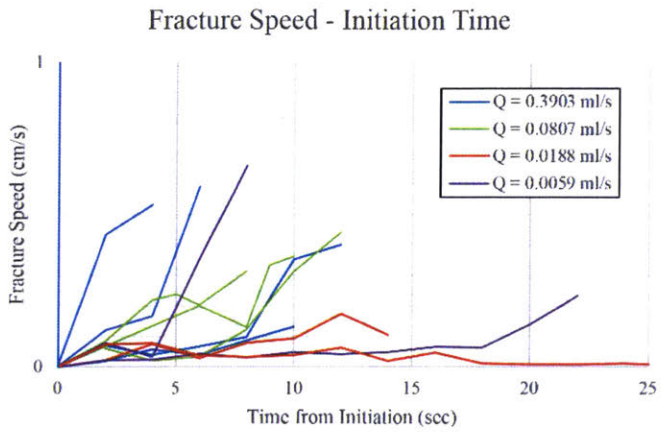

Figure 6.6: Fracture speeds observed in this study. Shown are the speeds of the fractures over time, starting at each fracture's initiation time. Specimens tested with higher injection rates showed higher fracture speeds and higher fracture acceleration (slope). The number of fractures for each injection rate was different (See Figure 6.5).

6.2.3 Pressure-Time Results

The effects of injection rate on the evolution of internal flaw pressure over time were also analyzed (Figure 6.7). This included fracture initiation, fractures propagating beyond the edge of the seal, and then constant pressure after the pump (injection) was stopped (Refer to Figure 6.7). Higher breakdown (maximum internal) pressures were observed for tests with higher injection rates. Interestingly, the residual internal pressure, i.e. the equilibrated pressure after the pump was stopped, was close to 1 MPa for all tests. This was the same stress level as the lateral stress and therefore may be considered as the equivalent of the "fracture closure stress" observed in the field.

For each test, the internal flaw pressure when fractures initiated, the maximum internal pressure and the maximum PVA pump pressure were determined (Figure 6.8). Significant increases in the maximum PVA and internal flaw pressures were observed at higher injection rates. Additionally, large deviations between the PVA and internal flaw pressures were observed as the injection rate increased. The internal flaw pressure at fracture initiation was reasonably similar for all injection rates and was approximately the same as the applied axial stress (4.5 MPa).

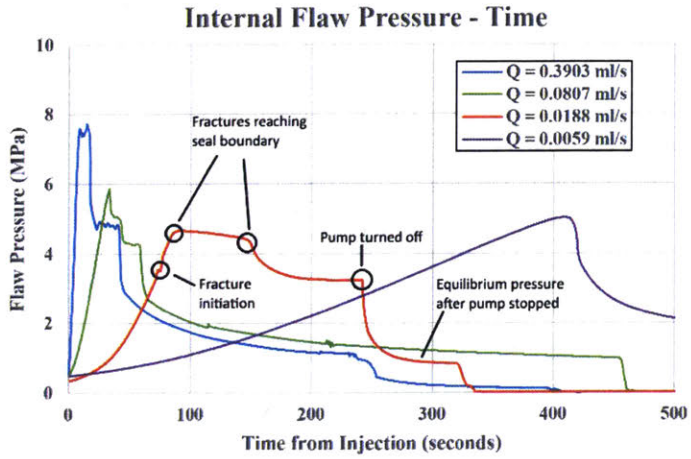

Figure 6.7: Evolution of flaw pressure over time for the four injection rates tested measured with a transducer inside the pressurized flaw.

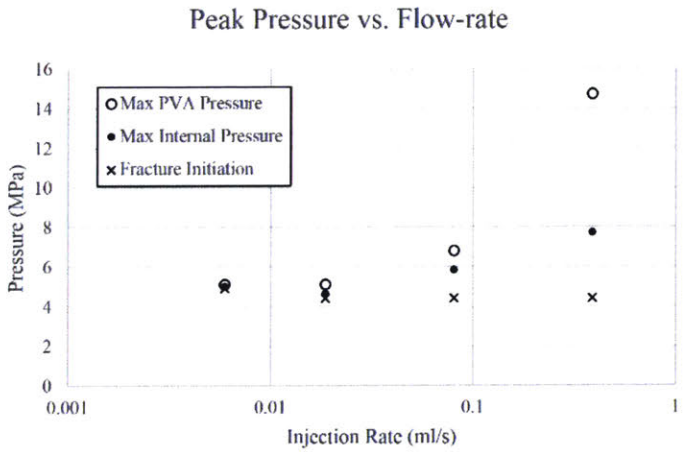

Figure 6.8: Summary of the pressure results for the different injection rates. Increases in maximum pump (PVA)- and internal flaw pressures were observed at high injection rates. The fracture initiation pressure was approximately the same for all injection rates.

6.3 Acoustic Emissions (AE) Results

AE event locations were calculated with an error tolerance of 1 cm using an anisotropic velocity model with 3000 m/s along bedding and 2500 m/s perpendicular to bedding. Moment tensor decomposition was done assuming an isotropic material.

6.3.1 AE Analysis Results

The AE equipment set-up was the same for all specimens; the number of events recorded varied significantly. Table 1 shows that the fastest injection rate produced the most AE events, followed by the slowest injection rate. The amplitudes appear to follow a similar trend. Applying moment tensor decomposition, it appears that the double-couple (DC) contribution is dominant for three out of four injection rates. It was also observed that the isotropic component was greater than the compensated linear vector dipole (CLVD) component. In general, the DC component decreases while the CLVD and isotropic components increase with increasing injection rate.

The AE event locations for the fastest injection rate are shown in Figure 6.9. It appears that the events initially occur closer to the center of the specimen, and then move away from the flaw tips with time. It also appears that the events closest to the initial flaw are closer to a horizontal orientation, suggesting that microcracking occurred preferentially along the bedding of the Opalinus shale.

Figure 6.10 shows the spectra for the largest AE event for each injection rate. The spectrum for each injection rate is the mean over all channels for that event, where each channel's spectrum is calculated over an 800 μs window centered on the first arrival. It appears that the fastest injection rate contains the highest power, particularly at lower frequencies, which indicates a larger fault area according to classic seismology theory, which states that the radius of a rupture is inversely proportional to its corner frequency (Shearer, 2009). However, this observation also appears to be true for the slowest injection rate, which also produced a larger number of AE events and contained an anomalously fast-growing fracture compared to the 0.01876 and 0.08065 mL/s experiments, as seen previously in section 3.2.

Table 6.1: AE event locations and orientations for the 0.39025 mL/s injection rate experiment. Crosses indicate conjugate shear planes for shear events; the single lines indicate opening direction of non-DC events. Thick black line is the flaw.

	0.00594 mL/s	0.01876 mL/s	0.08065 mL/s	0.39025 mL/s
Number of detected events	5	1	2	25
Average DC (Shear)	0.6493	0.5715	0.092	0.5506
Average CLVD (Deviatoric)	0.1336	0.1632	0.3459	0.1712
Average ISO (Isotropic)	0.2171	0.2653	0.5621	0.2782
Max amplitude (dB)	75	69	76	80

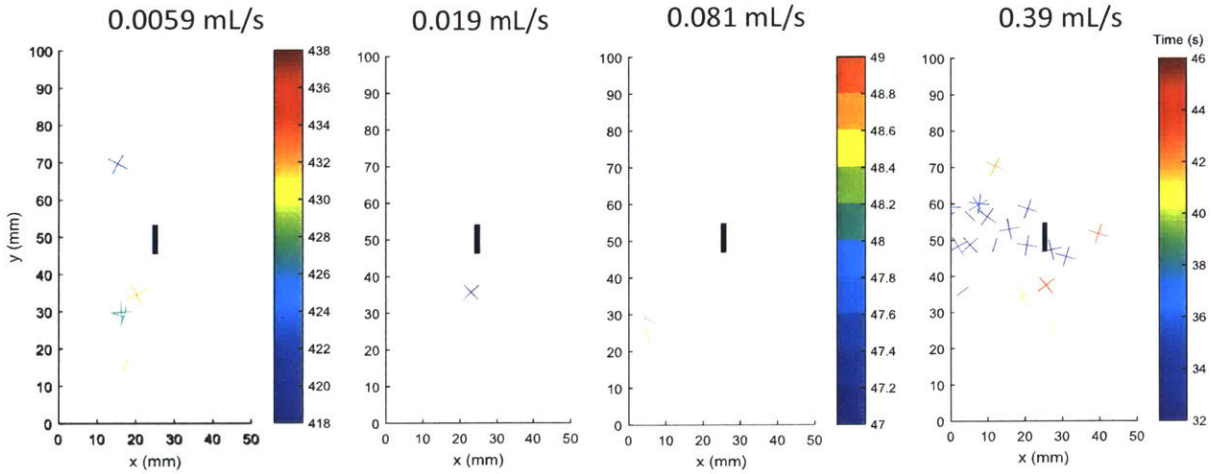

Figure 6.9: AE event locations and orientations for each test. Crosses indicate conjugate shear planes for shear events; the single lines indicate opening direction of non-DC events. Thick black line is the flaw.

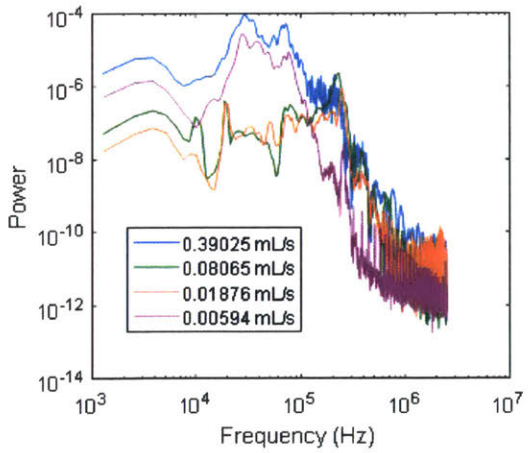

Figure 6.10: Spectra for largest event seen at each injection rate.

6.3.2 Comparison of AE Data to Fracture Process

Figure 6.11 shows AE amplitude and pressure over time for the different injection rates. In three of the four cases, the high amplitude events corresponded to peak PVA pressure. As seen in the previous section, this point in time corresponds to significant fracture propagation resulting in the fracture reaching the seal boundaries, such that the pressure drops significantly. This also implies that, in general, fracture initiation does not produce significant AE activity in some cases. The data were further analysed for the fastest injection rate, where three main AE events (AE1, AE2, AE3) were detected. The first event corresponds to fracture initiation of fracture B shown in Figure 6.5, along with significant process zone development of fractures B' and B". AE2 had a lower amplitude, and corresponds to the entire fracture initiation and propagation of fracture C. AE3 corresponds to continued propagation of existing fractures. It is interesting to note that AE1, which corresponds to a series of slower fractures, has more power at lower frequencies than AE2 (Figure 6.12), which is a fast fracture.

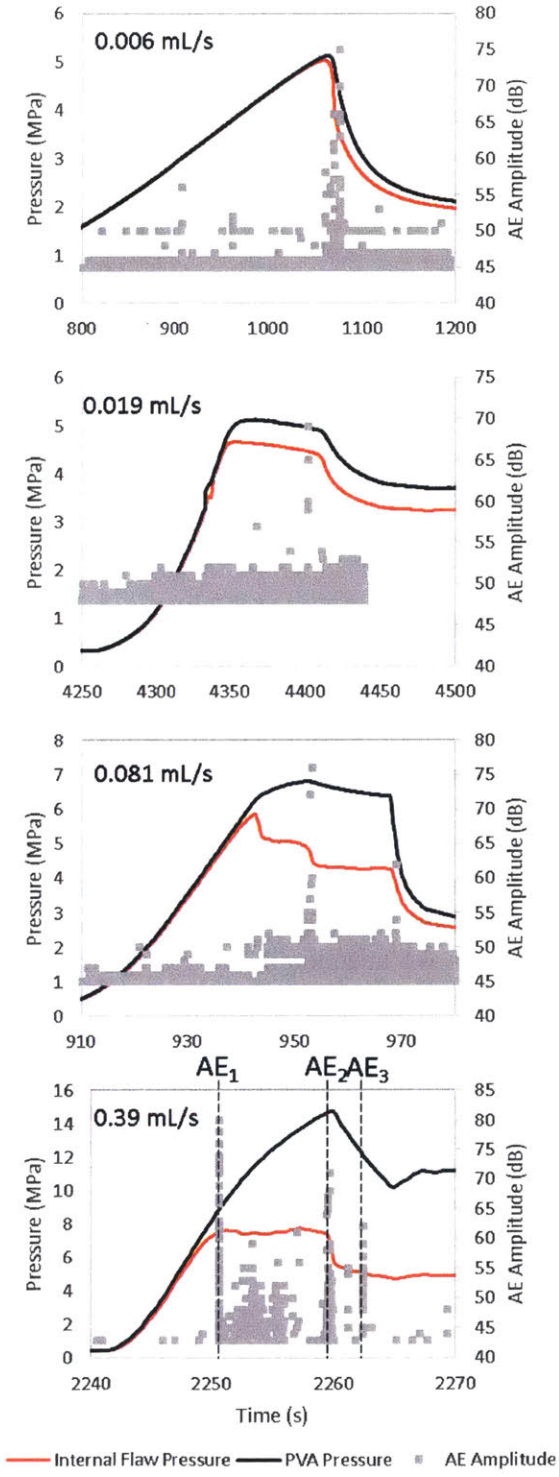

Figure 6.11: Pressure and AE amplitude data for the four injection rate experiments.

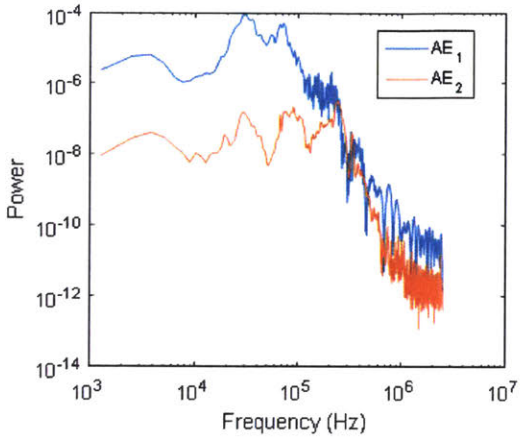

Figure 6.12: Power spectra of AE1 and AE2 (Refer to Figure 6.11).

6.4 Second Round of Tests

A second round of injection rate tests was conducted on BPE-2 using the same setup and injection rates. This material contains 33% quartz, 5.2 % calcite, 15.8 % kaolinite, and 32.1 % illite and illite/smectite. The results are summarised in Figures 6.13, 6.15, and 6.14. We can see that this test series again shows more AE are detected with increasing injection rate. The trend with maximum pressure is also consistent in that higher injection rates resulted in higher maximum pressures. However, it appears that in this series that the higher injection rate tends to result in a slightly less complex fracture network, which contradicts the results from the first series. Later results shown in Chapter 7 suggest that the results from this second series to be the case in general, i.e. that increasing injection rate results in less complex fractures. The differences may be due to sample-to-sample variation, as we anecdotally note that the high injection rate samples from the first round contained notable low-strength bedding planes. We also note that more AE were observed in general in the second round than the first round, which is likely related to the difference in mineralogy between the BSO-36 and BPE-2 shales (70.6% and 50.2% clay content respectively). This agrees with the study by Kohli and Zoback (2013), which suggested that shales with higher clay content are less prone to seismicity based on fault sliding tests.

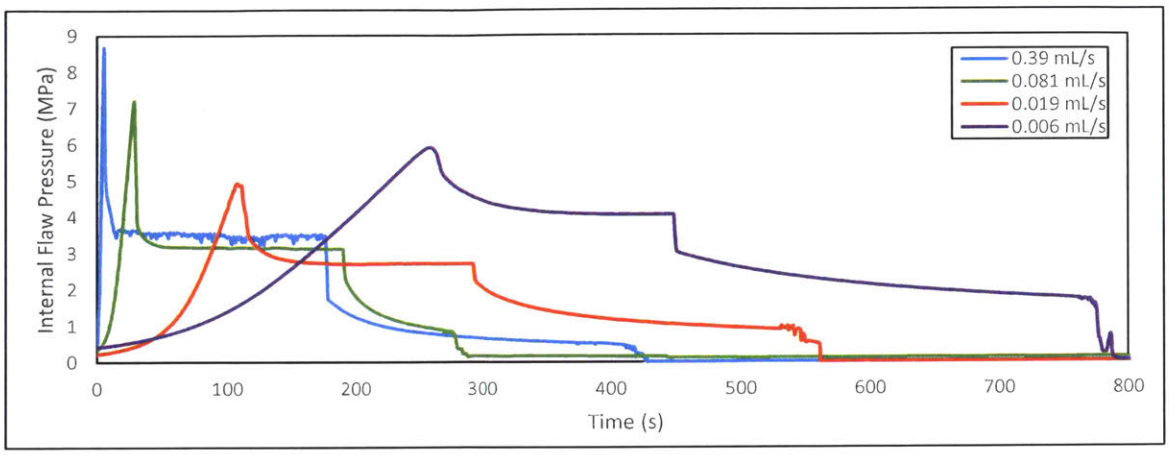

Figure 6.13: Internal flaw pressure over time for the second round of tests.

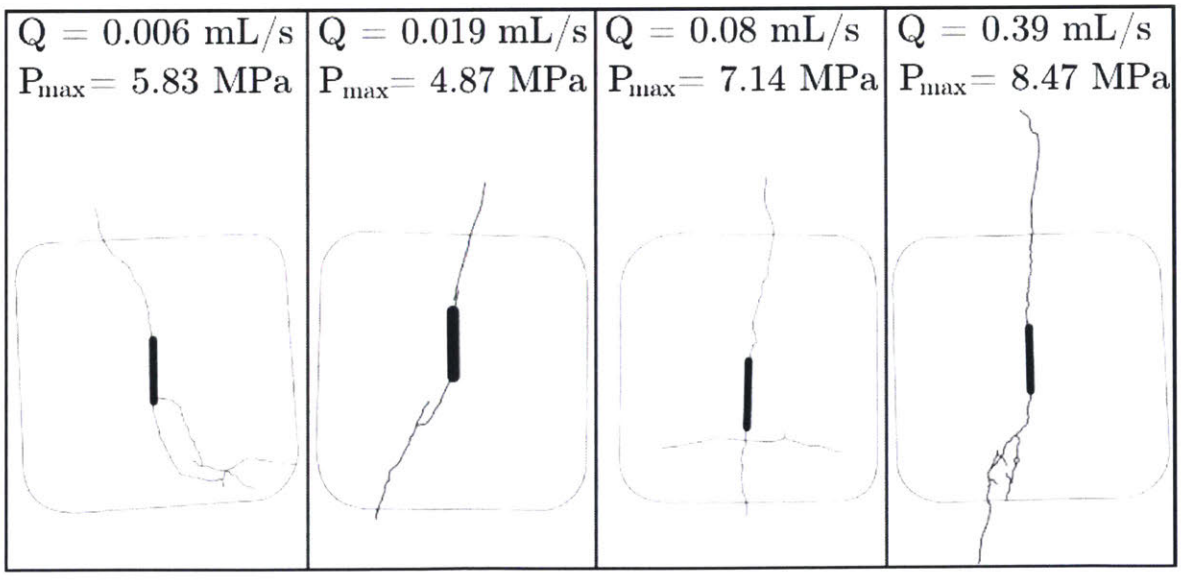

Figure 6.14: Fracture pattern and maximum internal flaw pressure during second round of injection rate tests.

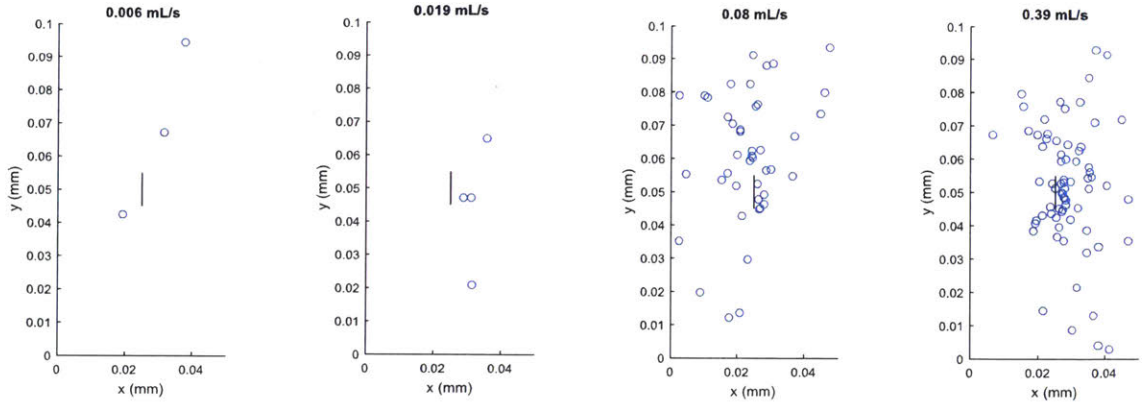

Figure 6.15: Location of AE events detected during second round of injection rate tests.

6.5 Discussion and Conclusions

This study investigated the effect of four different injection rates on prismatic Opalinus shale specimens with a pre-cut vertical flaw and constant external biaxial stresses. Given the set of injection rates and the fluid viscosity used in this study, the fracturing processes were in the toughness dominated regimes for all injection rates tested (as described by Bunger et al. (2005) and others). An injection fluid with a much higher viscosity would be needed in order to achieve a viscosity dominated fracturing regime.

Increasing the injection rate had a significant effect on the complexity and amount of fracturing that was observed. However, the two conducted test series showed contradicting results: the first series showed increasing complexity with increasing injection rate, and the second series showed the opposite trend. We suggest that this inconsistent is likely due to sample-to-sample variation.

Additionally, increasing the injection rate showed an increase in the maximum internal pressure (typically referred to as breakdown pressure). Other studies on the injection rate, such as Solberg et al., 1980, observed a log-linear relationship between injection rate and breakdown pressure. However, Barla et al. (1986) observed a relatively constant breakdown pressure at low pressurization rates and an increase in breakdown pressure at higher rates, similar to the present study. Note that the constant injection rate in this study is not strictly equivalent to the pressurization rate in the Barla et al. study, however, as seen in Figure 6.7, the pressure-time relation is relatively linear for all experiments and can be considered similar to a constant pressure rate experiment.

In terms of AE, it appears that the double couple (DC) component decreases as the injection rate increases, indicating a more expansive type of rupture with faster injection. An analysis of the AE event orientations showed that initially the events appear to be oriented with bedding, but evolve to become oriented diagonally to bedding over time. When comparing AE to the fracturing process, AE activity was generally not observed around the time of fracture initiation, but AE activity were observed when fractures reached the seal boundary. Additionally, the highest injection rate produces a much more micro seismically active fracture process than the lower injection rates. The two test series were conducted on shales with different clay contents, and we also note that seismicity is higher in the test series with lower clay content, which is consistent with previous studies based on a shearing mechanism.

Chapter 7

Microseismicity and Real-time Visualisation of Microstructural Damage during Hydraulic Fracturing

"I will take the Ring, though I do not know the way."

In this study, we hydraulically fracture granite and shale specimens at two injection rates each, and compare the magnitude-calibrated microseismicity with micro-DIC captured with a high speed camera. Different enclosure devices are used for the granite and shale as we were not able to design a single device capable of generally inducing hydraulic fractures in both materials. However, other experimental parameters such as load, injection rate, imaging and AE setup are kept the same in order to achieve test results that are comparable between materials.

7.1 Methodology

7.1.1 Physical setup

As shown in Figure 7.1, Barre granite specimens were cut to dimensions 152 x 76 x 25 mm, and a single vertical notch of length 12.7 mm was cut with a waterjet. The BMA-2 Opalinus shale (mineralogy is described in Chapter 4) specimens were cut to 102 x 51 x 25 mm, and a single vertical notch of length 8.5 mm was created by first drilling with a diamond bit, then cutting to the desired length with a steel blade. For each specimen, we intentionally create asymmetric flaw tips by piercing the rock at one end, and cutting directly to the other end. This creates a stress condition where the crack is more likely to initiate from the sharper (cut) edge. We then speckle at this sharper edge to consistently image the flaw tip at which crack initiation occurs.

In all tests, the specimens were initially loaded to 3.5 MPa in the axial direction, and then this load was maintained through the injection phase. For each material, a test was conducted at a nominal injection rate of 0.39 mL/s and 0.019 mL/s. The setup can be seen in Figure 7.2.

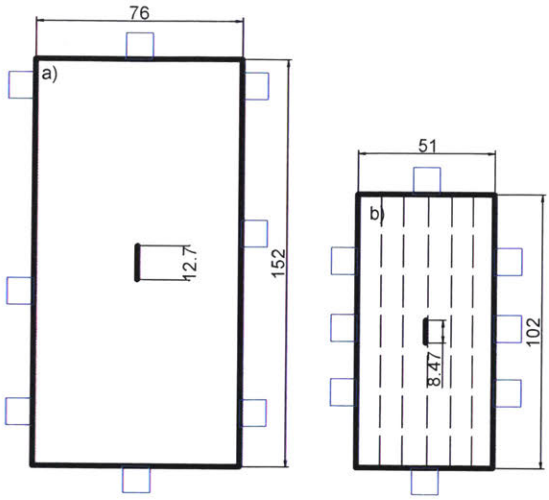

Figure 7.1: Specimen dimensions in mm and AE sensor locations for a) granite and b) shale. AE sensor locations shown in blue, and dashed lines show nominal bedding plane orientation in the shale.

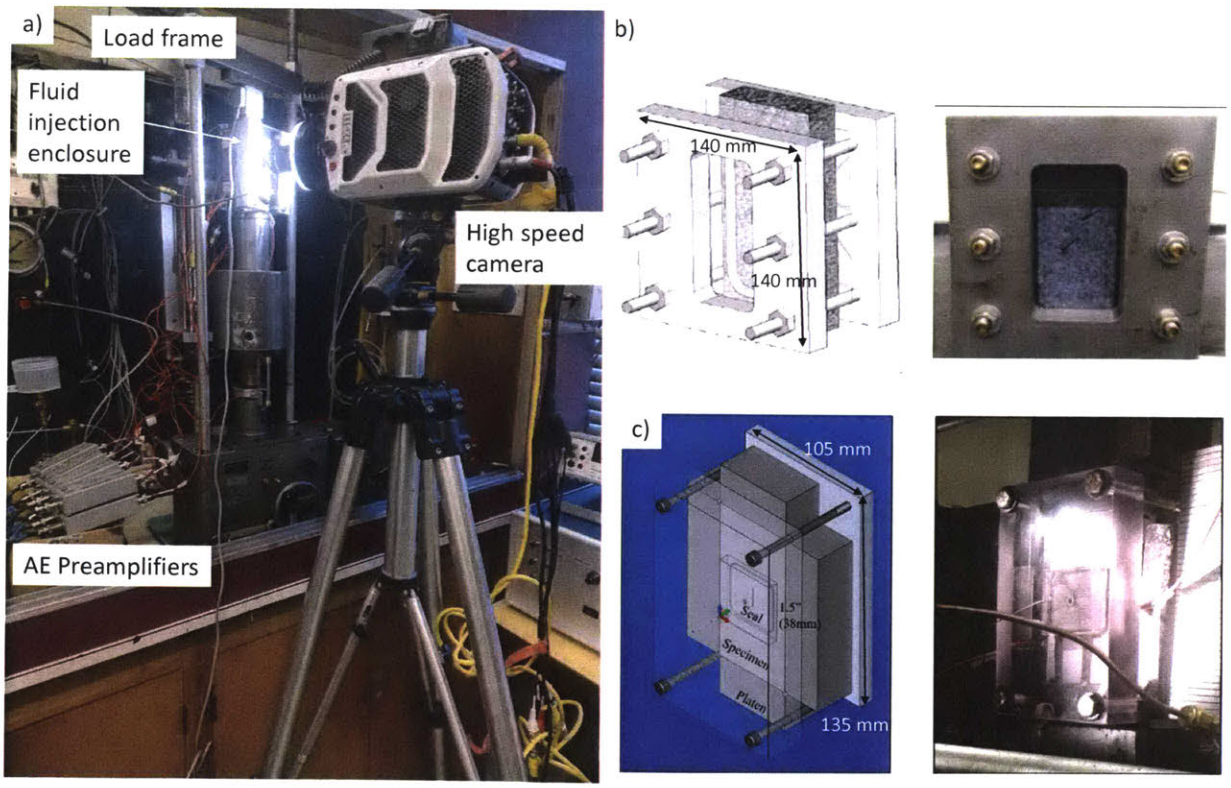

Figure 7.2: (a) Image of experimental setup including high speed camera, enclosure, load frame and pre-amplifiers. b) Schematic and image of fluid injection enclosure used on granite specimens (from Gonçalves da Silva and Einstein (2018)). c) Schematic and image of fluid injection enclosure used on shale specimens (from Morgan et al. (2017))

7.1.2 Imaging setup

The experiments were imaged with a Phantom v2511 high speed camera operating at 4000 fps for the 0.39 mL/s tests, and 600 fps for the 0.019 mL/s tests. The camera was coupled to a Laowa 25mm f/2.8 2.5-5X Ultra Macro lens at 5X, giving a field of view of approximately 7.2 x 4.5 mm (800 x 1280 pixels). The lens was directed to the area at the tip of the pre-cut notch, which was speckled by first painting a black base layer, and then lightly sprayed white paint, as seen in Figure 7.3. Image analysis was done in ncorr (Blaber et al., 2015) using a radius of 15 pixels for displacement, and radius of 2 pixels for strain. Figure 7.4 shows

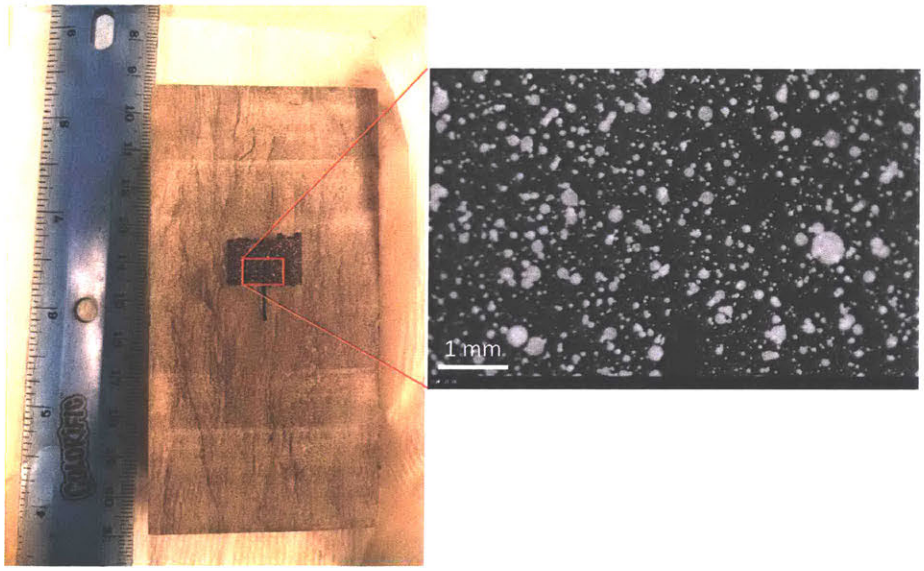

Figure 7.3: Image of shale specimen with speckling. Inset shows high speed video frame of speckled region.

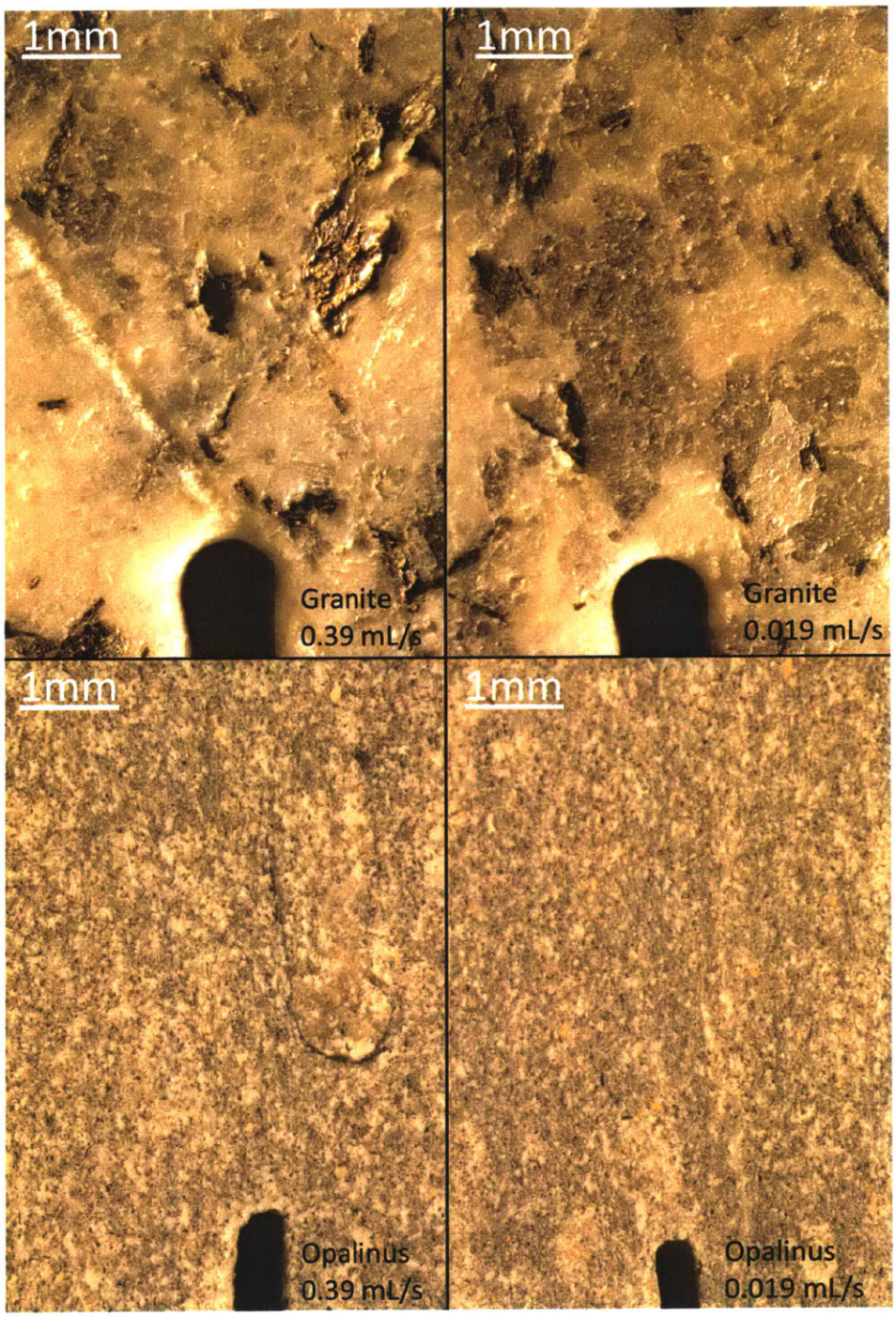

Figure 7.4: Images of the bare rock used in each test, at 5X magnification.

7.1.3 Acoustic Emissions setup

Each test was instrumented with eight Micro30S sensors from Physical Acoustic Corporation, sampled at 5 MHz using four PCI-2 data acquisition cards. The sensors were coupled with honey, and sensors in the load path were emplaced within an inset in the loading platens. Sensor locations are shown in Figure 7.1. 20dB and 60 dB of pre-amplification were used in the granite and shale tests respectively. Locations are calculated in granite using a P-wave velocity of 4500 m/s and error tolerance of 5 mm, and in Opalinus clayshale using an elliptical velocity distribution, with a P-wave velocity of 3500 m/s along the bedding plane, and 2000 m/s across bedding planes, to an error tolerance of 10 mm. More details of the AE setup can be found in Li and Einstein (2017).

7.2 Results

The results are first presented in terms of pressure and AE amplitude over time, as seen in Figure 7.5. First, we note that within the same material, a higher injection rate results in a higher maximum pressure. We also note that in general, maximum pressure was lower in Opalinus clayshale than in granite. In three of the four tests, we also note that peak AE rate corresponds to the maximum pressure, which suggests that the creation of the hydraulic fractures is most closely related to release of significant seismic energy. The exception, when only considering Figure 7.5, is the 0.39 mL/s Opalinus test, where peak AE rate occurs at approximately 7 MPa, while the maximum pressure during the test was 10 MPa. As will be seen in subsequent sections, this is likely due to cracks taking time to propagate to the seal boundaries, at which time the pressure drops.

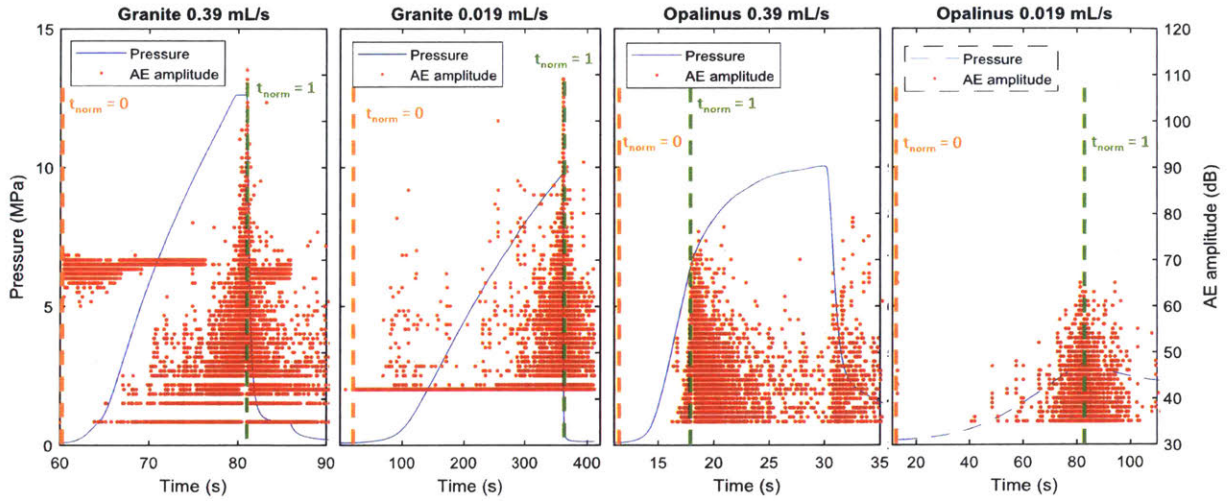

Figure 7.5: Pressure and AE amplitude over time for each test. Dashed orange and green lines respectively denote beginning and end points for t_{norm} scheme used in subsequent analysis, where $t_{norm} = 0$ is the start of injection, and $t_{norm} = 1$ is the time of highest AE rate.

7.2.1 Strain and displacement maps

Here, we present and describe the strain and displacement maps for each test over time, to gain a better understanding of the development of cracks seen at the 100 - 500μm scale, which we refer to as microcracks. This is shown for the two granite tests in Figures 7.6 and 7.7, where we can see that the cracks tend to form as a series of 2-3 en-echelon microcracks. We can also see that the area of significant strain is confined to the microcrack itself, as opposed to an area around the microcrack tips, as expected of a process zone. This supports the notion that in rocks the process zone is comprised of a series of small cracks. We also see that the values for γ_{max} are close to half of the values of ε_1, indicating that ε_3 are close to zero. Finally, we note that the fracture development appears to be more continuous in the 0.39 mL/s test, as the final crack patterns consists of a well connected series of 3 microcracks, whereas in the 0.019 mL/s the network appears to be somewhat more complex. For example, significant strain first shows at a distance from the flaw tip (circled in A in Figure 7.7), as opposed to right at the flaw tip as occurred at 0.39 mL/s. Additionally, there is a secondary microcrack branching off (circled as B) at approximately $x = 2.2mm, y = 0.7mm$, and a gap between microcracks (circled as C) at $x = 2.3mm, y = 1.3mm$. This indicates that there is a higher tendency for microcrack arrest in the lower injection rate test, which makes sense considering that in a lower injection rate setting there is more time for secondary effects such as fluid seepage and visoelasticity/viscoplasticity. The displacement vectors are not particularly telling in the granite tests, as the face of the rock is subject to fluid pressure and thus the vectors are dominated by the Poisson effect generated by this pressure, wherein the vectors spread outwards from the center of the specimen Gonçalves da Silva (2016). In contrast, a seal is directly applied to the face of the rock in the Opalinus setup, and so fluid pressure is only directly applied to the inside of the flaw.

The analogous figures are shown for the Opalinus clayshale tests in Figures 7.8 and 7.9. Here the time evolution of the displacement vectors are more interesting. In Figure 7.8 we can see that

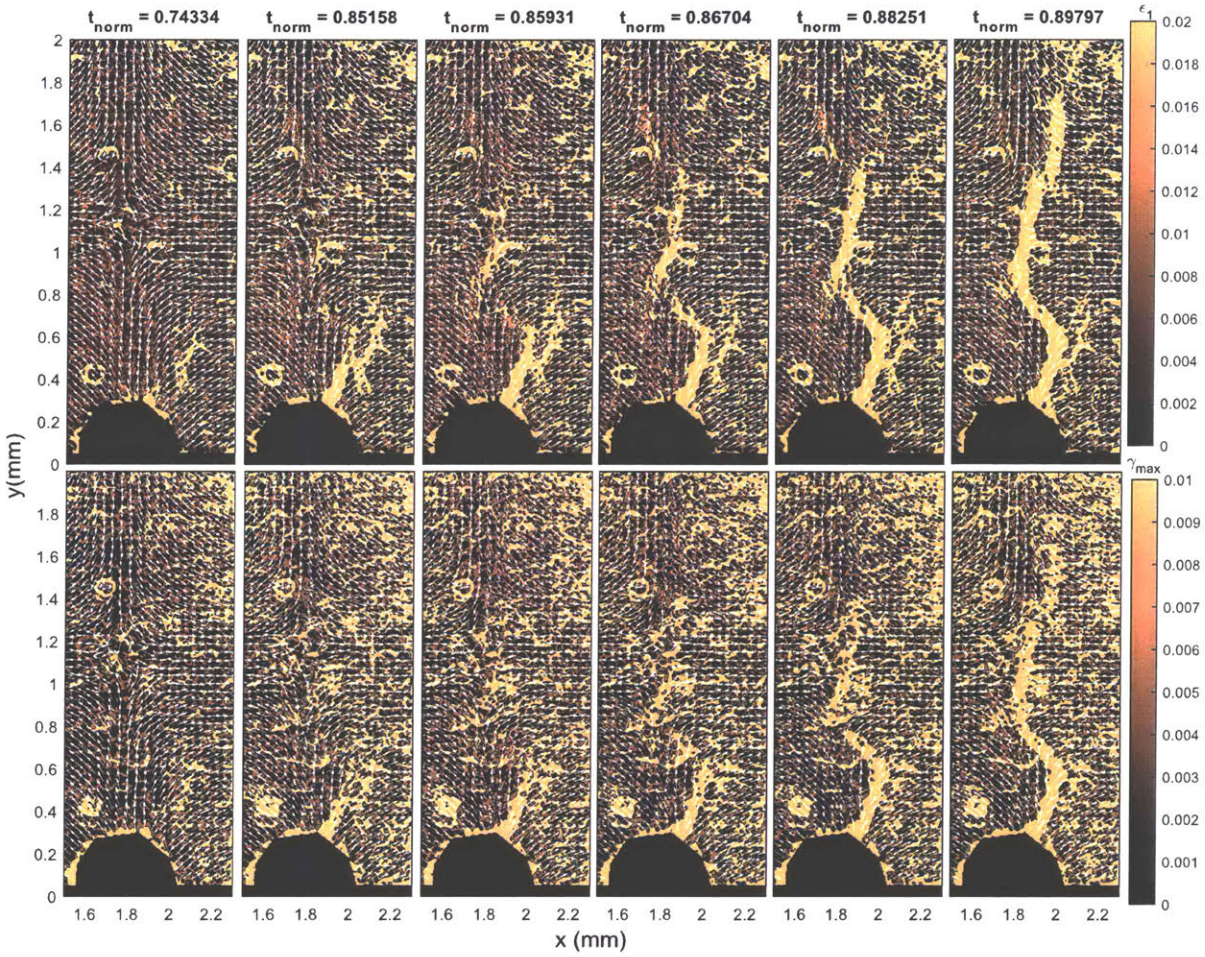

Figure 7.6: Maximum (ε_1) and shear strain (γ_{max}) contours at various stages during granite 0.39 mL/s test. Arrows show displacement field, with rigid body translation subtracted such that the mean displacement of the entire area is zero. Red circles indicate en-echelon cracks.

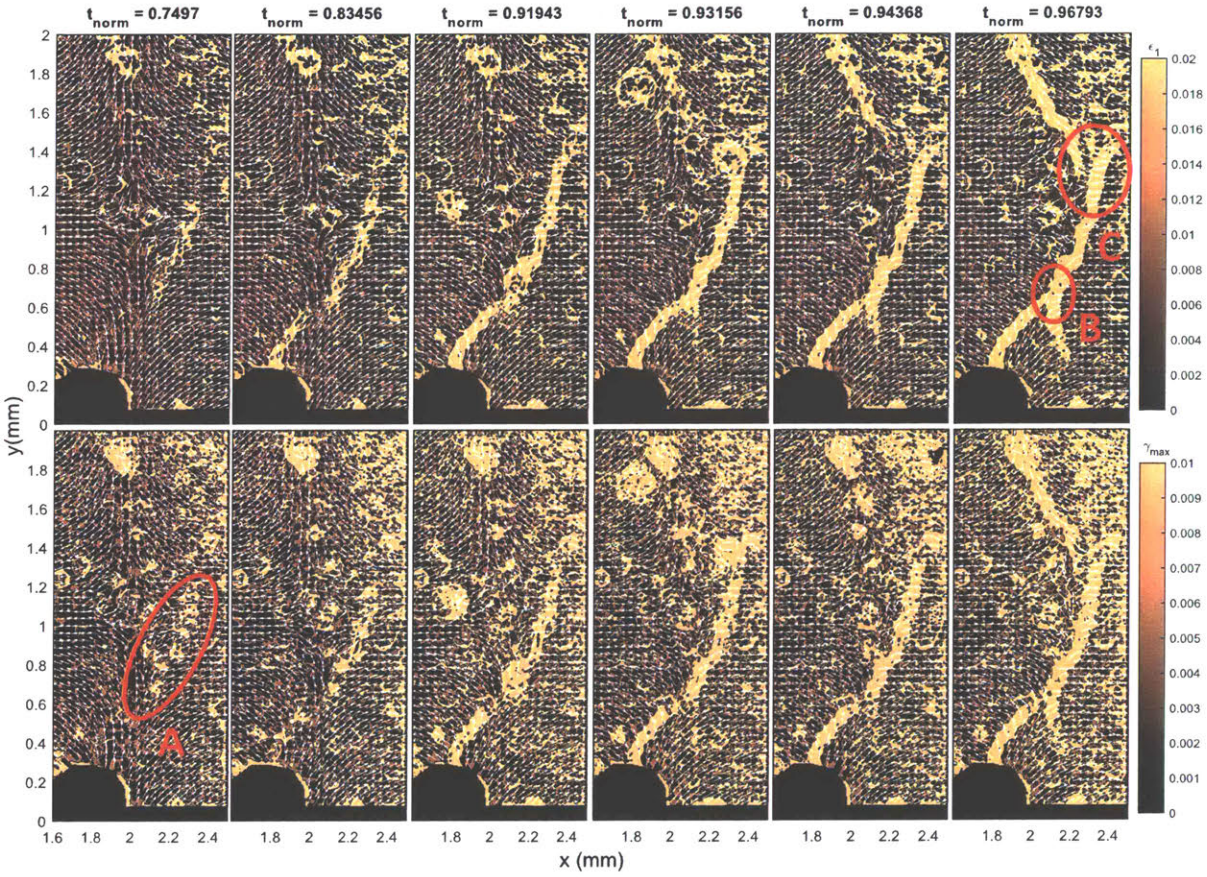

Figure 7.7: Maximum (ε_1) and shear strain (γ_{max}) contours at various stages during granite 0.019 mL/s test. Arrows show displacement field, with rigid body translation subtracted such that the mean displacement of the entire area is zero. Red circles indicate locations of fracture branching.

initially the vectors are mostly random except beside the notch, and that over time a wedge of opening displacement (shown in red dashed lines) emanates from the notch tip, and then moves upwards along with the microcrack tip. The behaviour at 0.019 mL/s, shown in Figure 7.9 is markedly different from the test at 0.39 mL/s. Initially at $t_{norm} = 0.66$, the displacement vectors look similar to the initial state of the 0.39 mL/s test, but by $t_{norm} = 0.95768$ we can see that the displacements are largely in the x direction, with the exception that there is a narrow zone of displacement along the eventual microcrack (shown in the red dashed lines labelled A in Figure 7.9. This somewhat represents plumose fracture patterns seen in nature, which are also indicative of tensile fracture 7.10. In subsequent frames we still see that the displacement vectors ahead of the zone of significant strain are much narrower (circled as B in Figure 7.9) and do not exhibit the same wedge shape seen in the 0.39 mL/s test. The lack of a "wedge" in the 0.019 mL/s tests suggests that the bedding plane opens ahead of the microcrack tip, whereas in the 0.39 mL/s test the bedding does not open ahead of the microcrack tip since the microcrack propagates at a much higher velocity. We also see a more complex microcrack network in the 0.019 mL/s test, with multiple bedding planes showing significant strain (circled as C in Figure 7.9), and the final pattern consisting of two offset microcracks.

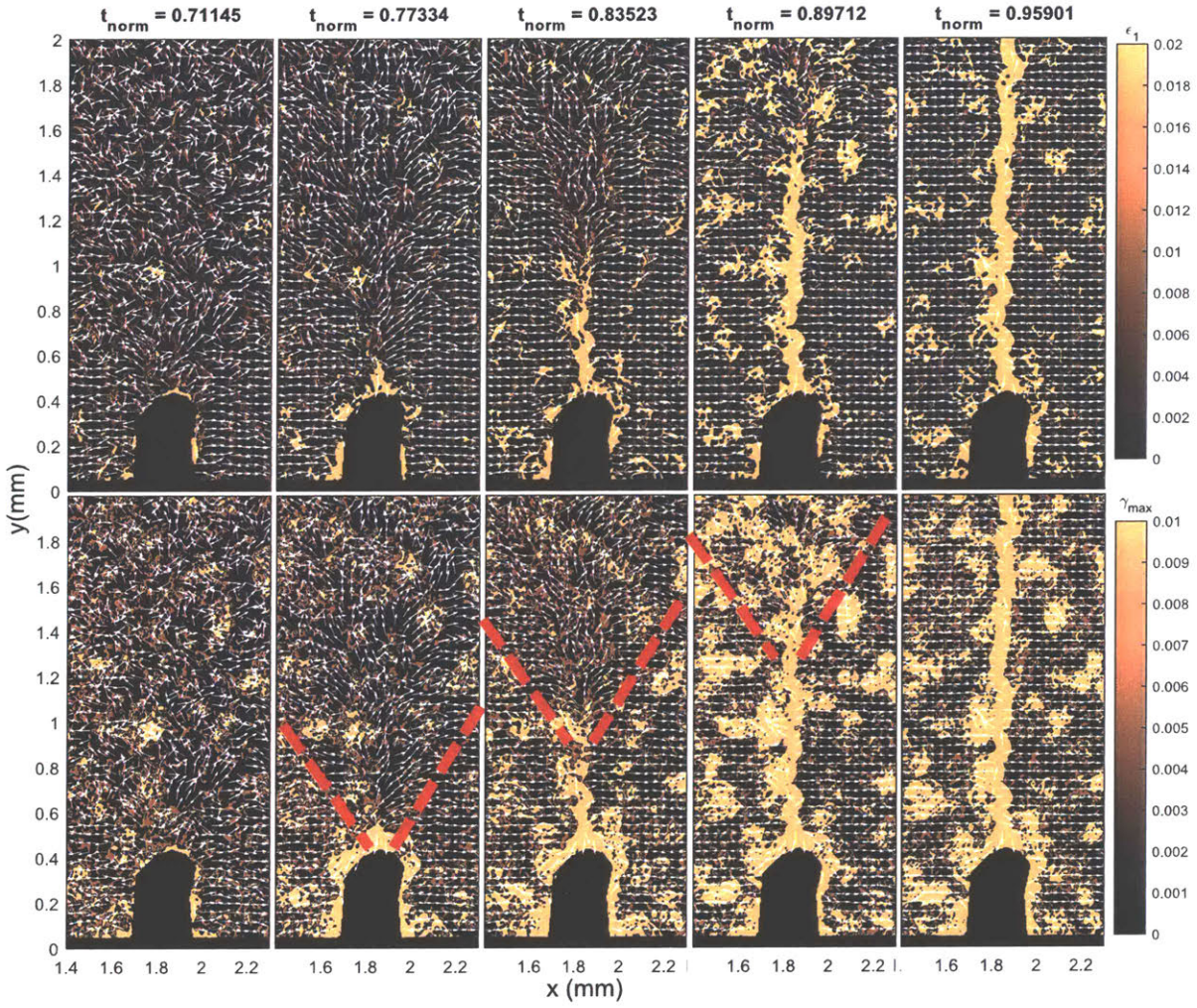

Figure 7.8: ε_1 and shear strain γ_{max} contours at various stages during Opalinus 0.39 mL/s test. Arrows show displacement field, with rigid body translation subtracted such that the mean displacement of the entire area is zero. Red dashed line indicates wedge of opening displacement.

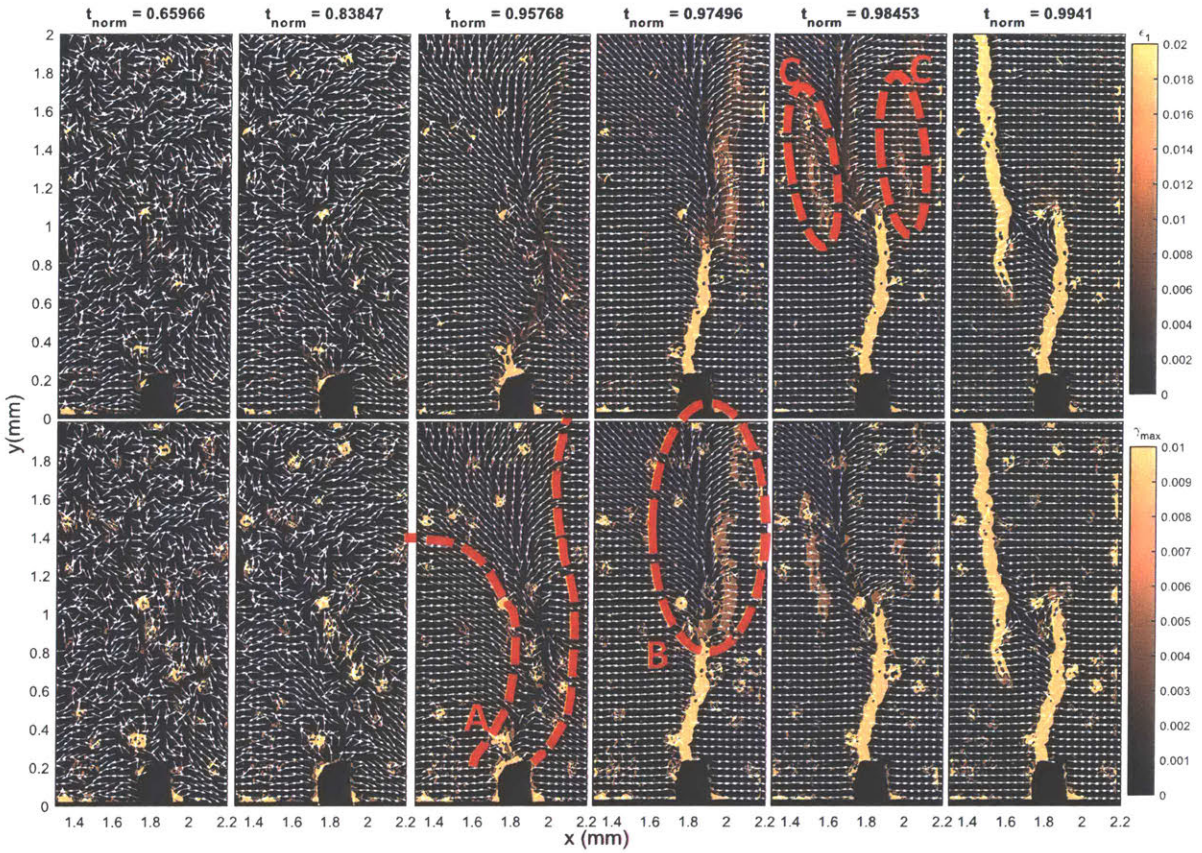

Figure 7.9: ε_1 and shear strain γ_max contours at various stages during Opalinus 0.019 mL/s test. Arrows show displacement field, with rigid body translation subtracted such that the mean displacement of the entire area is zero. Dashed lines A and B indicate narrow zone of non-horizontal displacement.

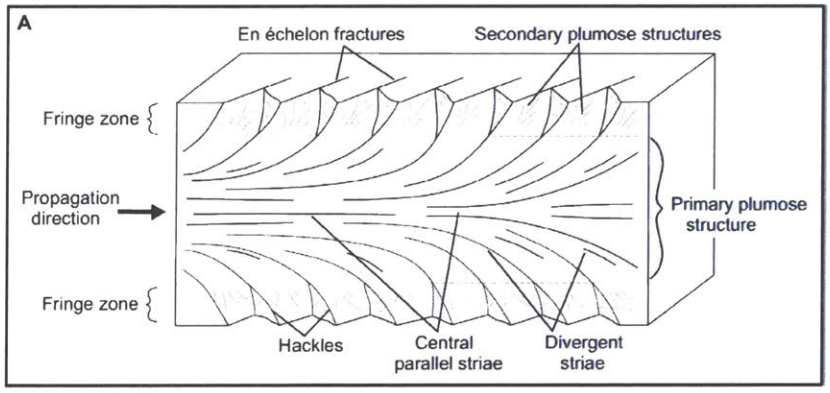

Figure 7.10: Illustration of plumose fracture, from Cobain et al. (2015).

7.2.2 Opening displacement

We can also plot the opening displacement of the crack, as shown in Figure 7.11. In Figure 7.11b we see that the higher injection rate results in higher maximum pressure in both rocks. It also appears that inelastic deformation occurs more gradually with higher injection rate for both rocks..

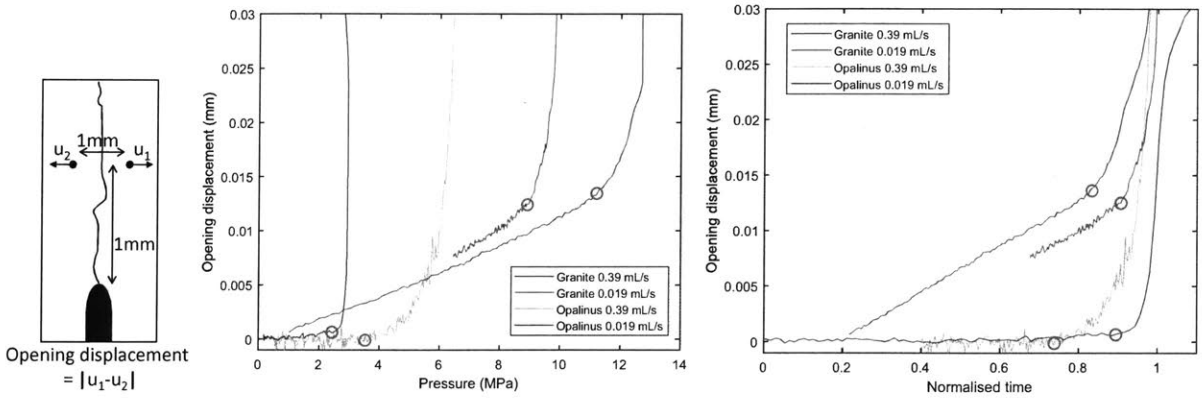

Figure 7.11: a) Schematic of opening displacement. Displacement is calculated across the crack 1 mm from the notch tip. b) Opening displacement over pressure. c) Opening displacement over normalised time, where t = 0 is the start of injection, and t = 1 is the time of maximum AE amplitude. Green circles indicate the time in each test where the displacement begins to behave inelastically.

7.2.3 Statistical Distribution of strains

Figures 7.12 and 7.13 show the histograms of principal strains, based on the entire high speed video frame such as shown in the inset of Figure 7.3. We note that the distribution of strains is generally similar between materials and injection, and is also comparable to the beam bending data shown in previous chapters in that the ε_3 values are compressive, ε_1 are tensile, and thus the Mohr's circle is almost centered at 0 stress. We may conclude, then, that in a general sense the state of strain at a notch or flaw tip does not differ significantly between materials or when comparing a dry to a wet tensile fracture.

In order to compare different tests in detail, we can consider $\varepsilon_v = \varepsilon_1 + \varepsilon_3$ for each test, and plot results for each test as shown in Figure 7.14 alongside ε_1 and ε_3. The medians are also summarised in Table 7.1. We can see that the Opalinus tests are closest to showing zero volume change for HF and beam bending, while the granite HF tests show slightly positive ε_v (volume expansion). We can see that the fast granite HF test shows marginally higher ε_v compared to the slow granite HF test, while this trend does not appear to be evident between the Opalinus HF tests. We also see that the granite beam bending tests showed a wider difference between the median ε_1 and ε_3 compared to the other tests, which indicates that the Mohr's circle is larger for that test.

To also gain an understanding of the state of strain at all points in the imaging window, Figure 7.15 shows a scatter plot of ε_1 vs. ε_3 for each pixel in the DIC analysis for each test. We can see

Table 7.1: Table showing medians of histograms shown in Figure 7.14

Material	Loading condition	ε_v	ε_3	ε_1
Barre granite	Four-point beam bending	0.0018	-0.0095	0.0111
Opalinus BMA-2	Four-point beam bending	0.0074	-0.0684	0.0727
Barre granite	Single flaw HF Q=0.39 mL/s	0.0158	-0.0222	0.0380
Barre granite	Single flaw HF Q=0.019 mL/s	0.0113	-0.0206	0.0322
Opalinus BMA-2	Single flaw HF Q=0.39 mL/s	0.0064	-0.0386	0.0443
Opalinus BMA-2	Single flaw HF Q=0.019 mL/s	0.0004	-0.0076	0.0078

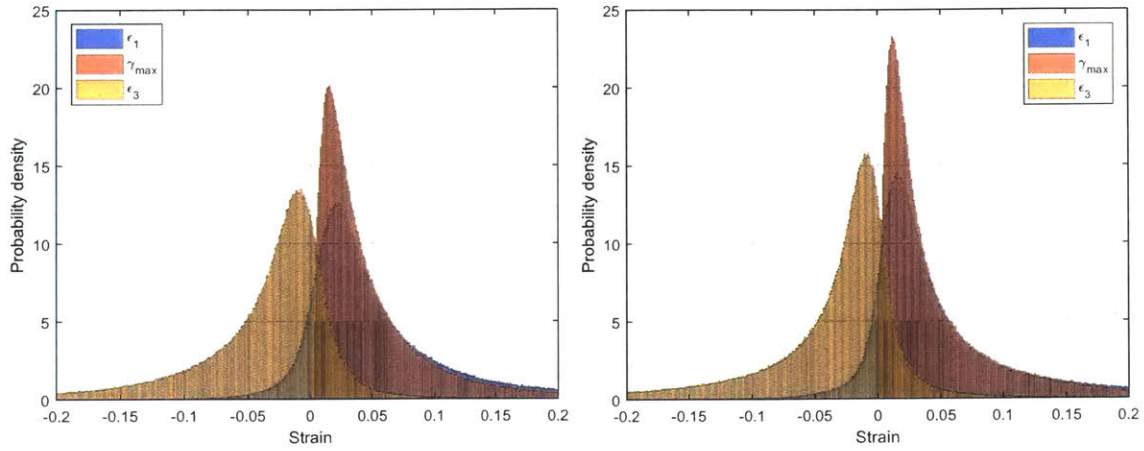

Figure 7.12: Histogram of principal strains for (Left) Granite 0.39 mL/s and (Right) Granite 0.019 mL/s, based on the entire micro-DIC image at $t_{norm} = 1$.

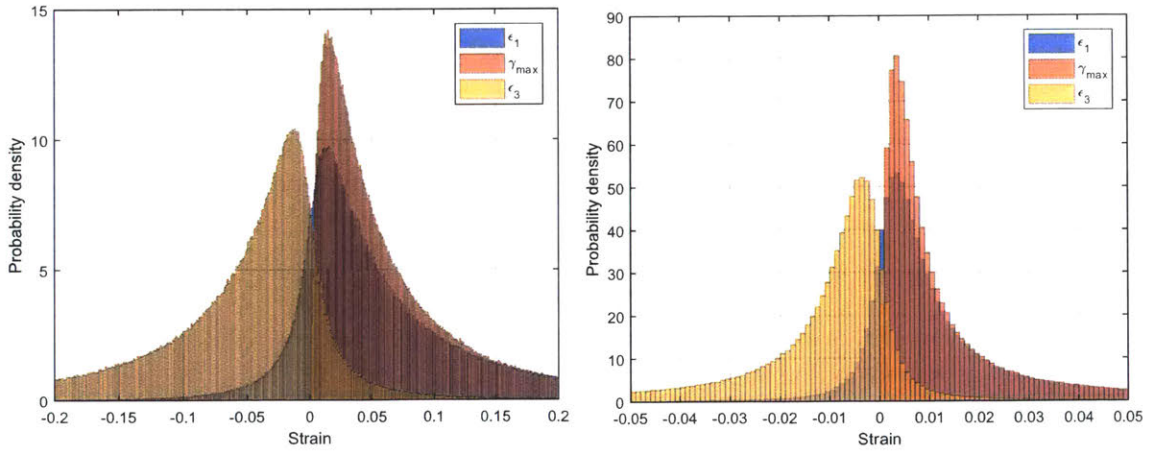

Figure 7.13: Histogram of principal strains for (Left) Opalinus 0.39 mL/s and (Right) Opalinus 0.019 mL/s, based on the entire micro-DIC image at $t_{norm} = 1$.

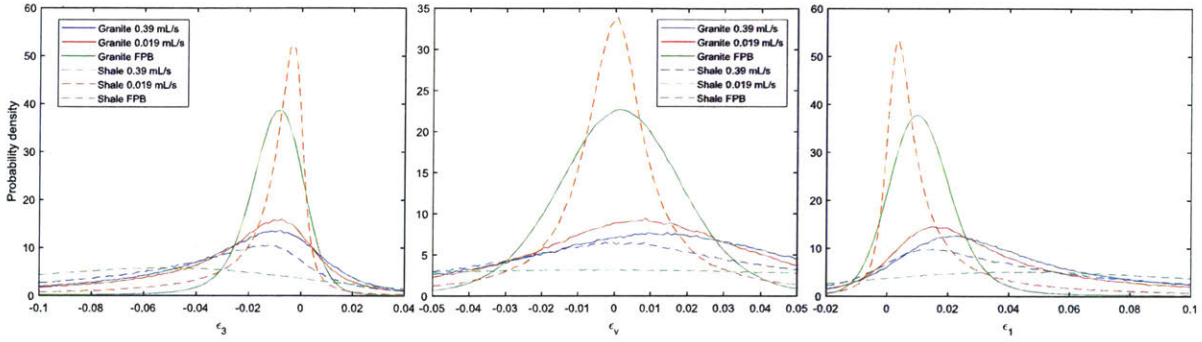

Figure 7.14: Histogram of (left) minimum (ε_3), (middle) volumetric (ε_v), and (right) maximum (ε_1) strain for each test, alongside beam bending data from chapters 3 and 4. Note that the magnitude of probability density and the variance are dependent on the quality of the speckling, where the quality was lowest for the Opalinus beam bending test, and highest for the Opalinus 0.019 mL/s and granite beam bending tests.

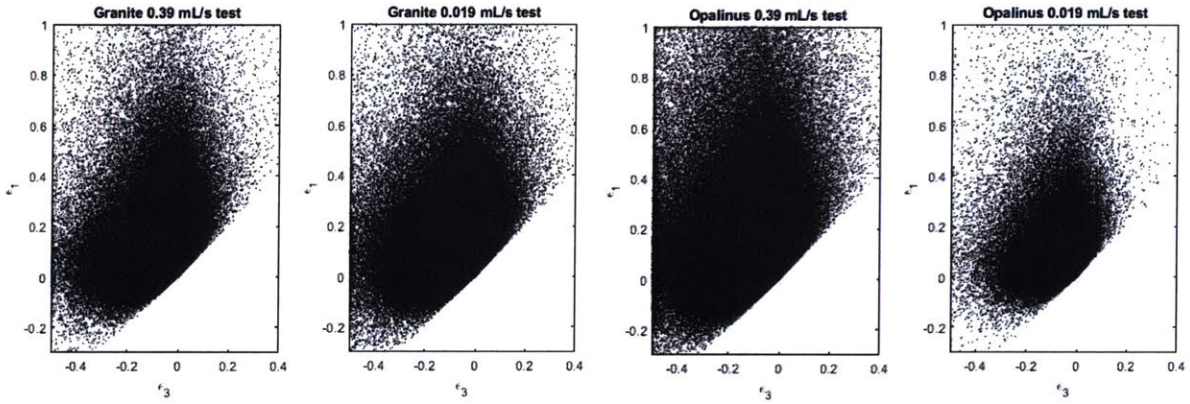

Figure 7.15: Scatter plot of $\varepsilon_1 - \varepsilon_3$ for each pixel of strain data from all 4 HF tests.

that in general, the principal strains are positively correlated (i.e. ε_1 increases with ε_3), although much wider scatter is observed in some tests, possibly due to the quality of the speckling pattern.

7.2.4 Displacement and AE activity over time

In this section, we present quantitative results regarding the shear and normal displacements across the microcrack at various points along the microcrack, as shown in Figures 7.16 and 7.17. These are presented alongside the rate of AE hits, to gain an understanding of the relationship between the displacements and AE activity. In the 0.39 mL/s granite test, we can see that initially the displacements are close to zero, and that there is an increase in the displacement rate at approximately $t_{norm} = 0.825$. We suggest that this represents a transition from elastic to inelastic deformation, as the timing corresponds well, albeit slightly later, to an increase in the rate of acoustic emissions. In the 0.019 mL/s test, this transition appears to be more gradual, and we see that the AE hit rate only increases after significant slip has occurred along multiple microcracks. We note that in the 0.39 mL/s test, the elevated AE rate occurs for approximately 4-5 seconds pre-peak, and that in

the 0.019 mL/s test the period of elevated AE occurs over approximately 3-4 seconds. Given that the peak rate of AE at both injection rates is in the range of 1800-2000 hits/s and that the period of elevated AE is also relatively similar, we suggest that the AE behaviour resulting from the initiation and propagation of a hydraulic fracture are similar despite the 20X difference in injection rate. This implies, at least in the context of this experimental setup, that the microcracks develop at a rate that is dependent on the injection rate (as seen in Figures 7.6 and 7.7), but that the process of macrocrack initiation and propagation, which corresponds to connection of these microcracks (see e.g. Ashby and Hallam (1986), Wong and Einstein (2009b)), does not depend on the injection rate.

In the shale, we first note that in all cases it appears that the normal displacements are larger than the shear, whereas in the granite this varied on a case-by-case basis. Secondly, we observe a phenomenon in the 0.019 mL/s test that the bedding plane at point 2 first closes in response to the opening at point 3. This reinforces the earlier notion that the lower injection rate results in opening of the bedding planes prior to the propagation of the microcrack. With regard to the AE rate, we can see that at both injection rates the AE tend to occur after the onset of inelastic deformation. It also appears that the AE rate is less intense and occurs over a longer period at the lower injection rate, which differs from the previously observed phenomenon in granite. This suggest that the microseismic properties of hydraulic fracture initiation and propagation, in the context of this experimental setup, depend on the injection rate for shale but not in granite. Do note, however, that the differences in the experimental setup between the granite and the shale, specifically the amount of fluid available to the fracture at the time of initiation, may also contribute to the differences in behaviour.

Overall, we also note that measurable inelastic deformation begins to occur around $t_{norm} = 0.95$ of peak fluid pressure at 0.039 mL/s in both granite and shale, while at 0.39 mL/s the damage begins to occur around $t_{norm} = 0.8$ to 0.85 in both granite and shale.

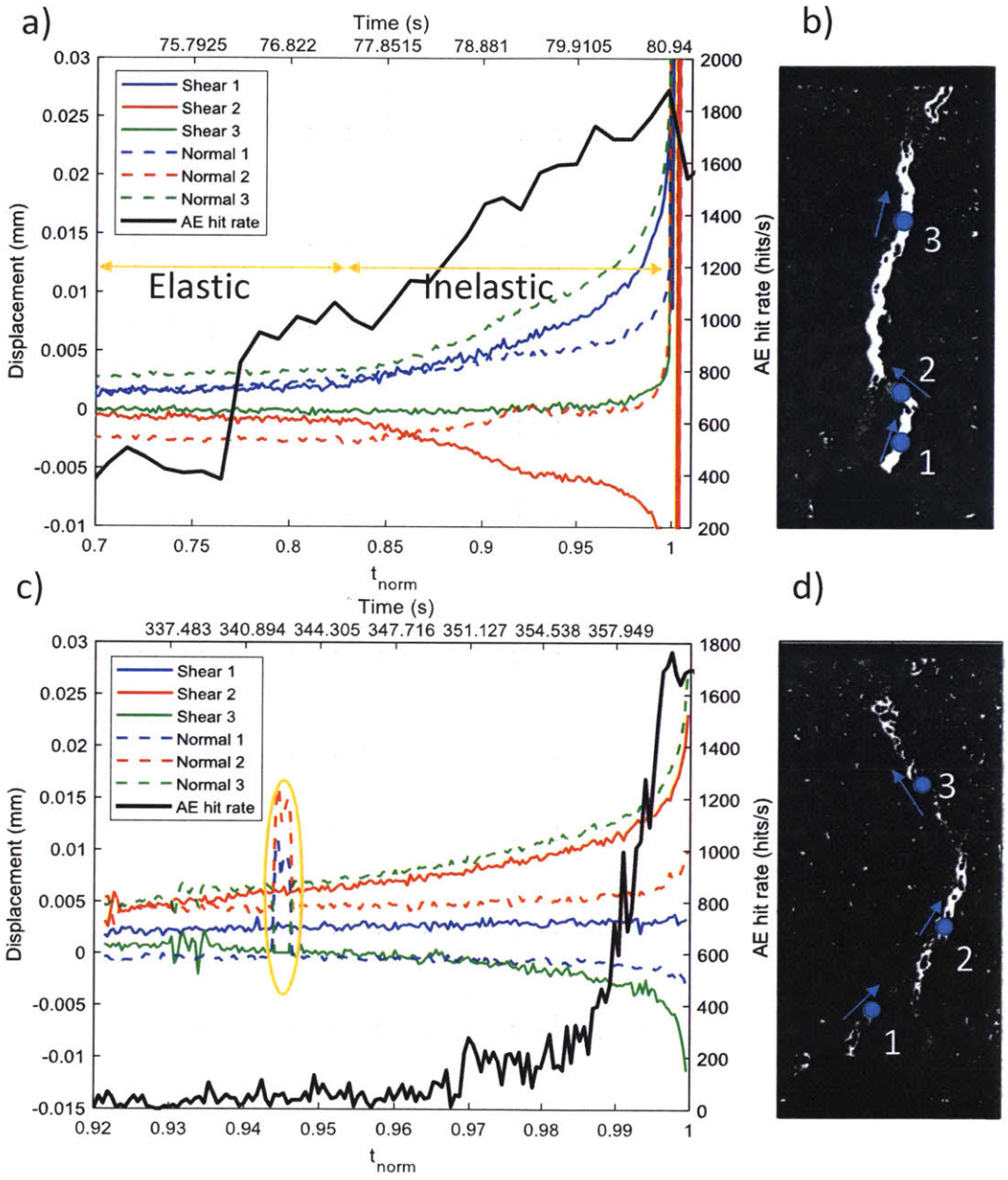

Figure 7.16: a) Plot of normal and shear displacements across the microcrack at 3 points along the microcrack. This is plotted alongside the rate of acoustic emission hits during the test. Top x-axis shows real time axis in seconds, bottom x-axis shows t_{norm}. b)Image showing the 3 points along the microcrack, at which normal and shear displacements are calculated in a). Blue arrows show the direction along which shear and normal displacements are resolved. a) and b) show the Granite 0.39 mL/s test, and c) and d) show the Granite 0.019 mL/s test. Erroneous data points in c) around $t_{norm} = 0.945$ (shown in orange circle) likely correspond to external factors such as a bubble.

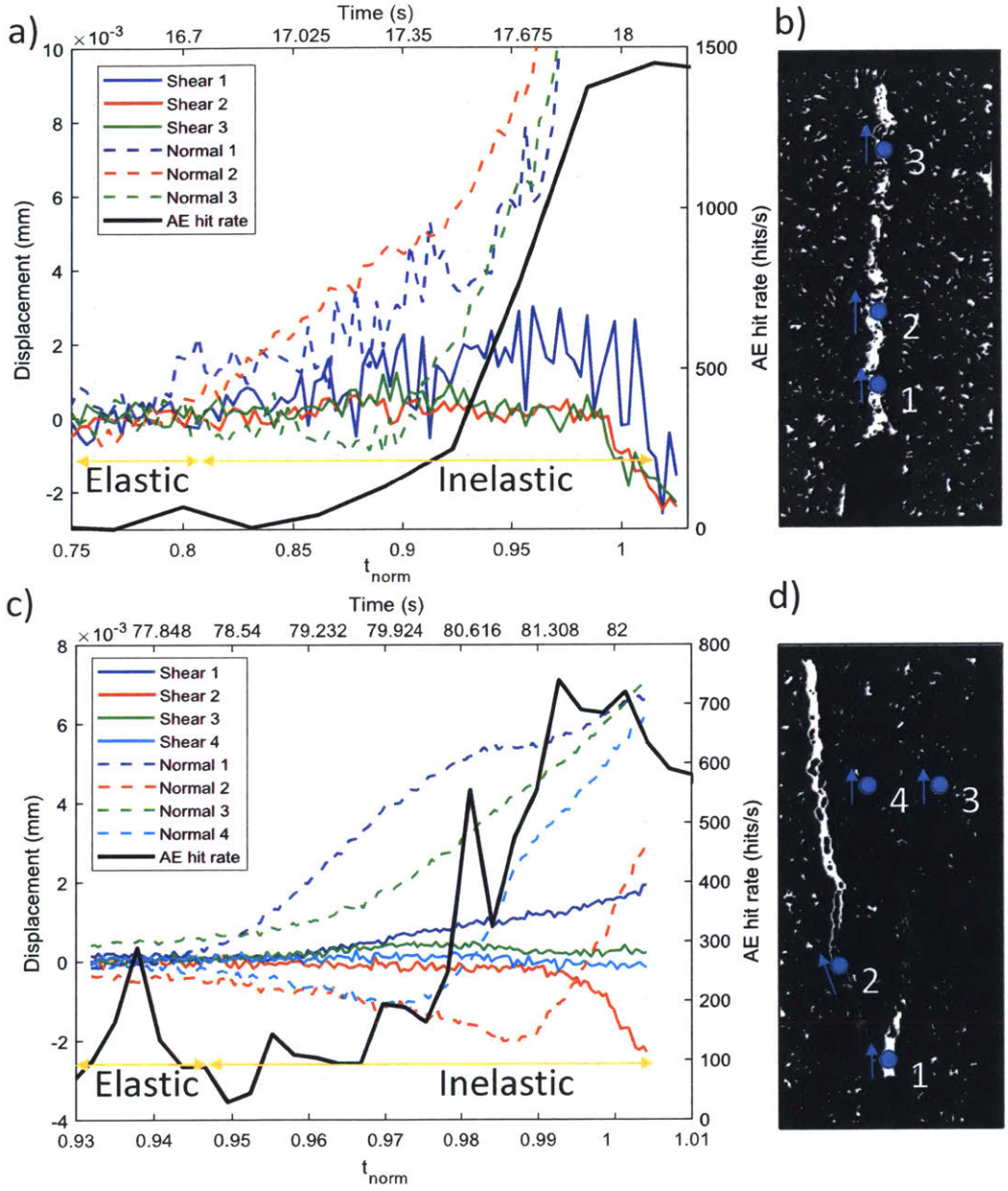

Figure 7.17: a) Plot of normal and shear displacements across the microcrack at 3 points along the microcrack. This is plotted alongside the rate of acoustic emission hits during the test. Top x-axis shows real time axis in seconds, bottom x-axis shows t_{norm}. b) Image showing the 3 points along the microcrack, at which normal and shear displacements are calculated in a). Blue arrows show the direction along which shear and normal displacements are resolved. a) and b) show the Opalinus 0.39 mL/s test, and c) and d) show the Opalinus 0.019 mL/s test.

7.2.5 AE hypocenter locations

AE hypocenter locations are shown in Figure 7.18. We see that in general, the hypocenters are more spread out in the granite than the Opalinus tests, which corresponds to the chapter 4, where we suggest that the process zone is larger in granite than in shale.

The relative proportions of focal mechanisms are also shown in Figure 7.19. We can see that in general, the faster injection results in a higher proportion of double couple events, and that there tend to be more implosion/compaction type events in the Opalinus than the granite tests. This corresponds well to Figures 7.9 and 7.17, which show that various bedding planes open and close as the microcracks propagate through the specimen. It also corresponds well to Figure 7.14, which shows that the granite tests exhibit larger volume expansion strains.

We can also consider the evolution of AE over time, as shown in Figures 7.20 and 7.21. We note throughout the 0.019 mL/s shale test the AE hypocenters tend to cluster near the flaw tip, whereas in the granite 0.019 mL/s test the cluster of AE events moves away from the flaw tip over time, which is consistent with the beam bending tests where we saw that AE events in the Opalinus beam tended to be clustered near the notch tip throughout the test. We also note that implosive NDC events are located close to the flaw tips throughout the test, which indicates that closure of microcracks and/or bedding planes is a major source of AE both before and after crack initiation, which agrees with the micro-DIC results shown in Figure 7.9. In the granite tests, we observe similar behaviour as seen in Chapter 5, where it appears that explosive NDC events are the primary microcracking mechanism throughout the experiment.

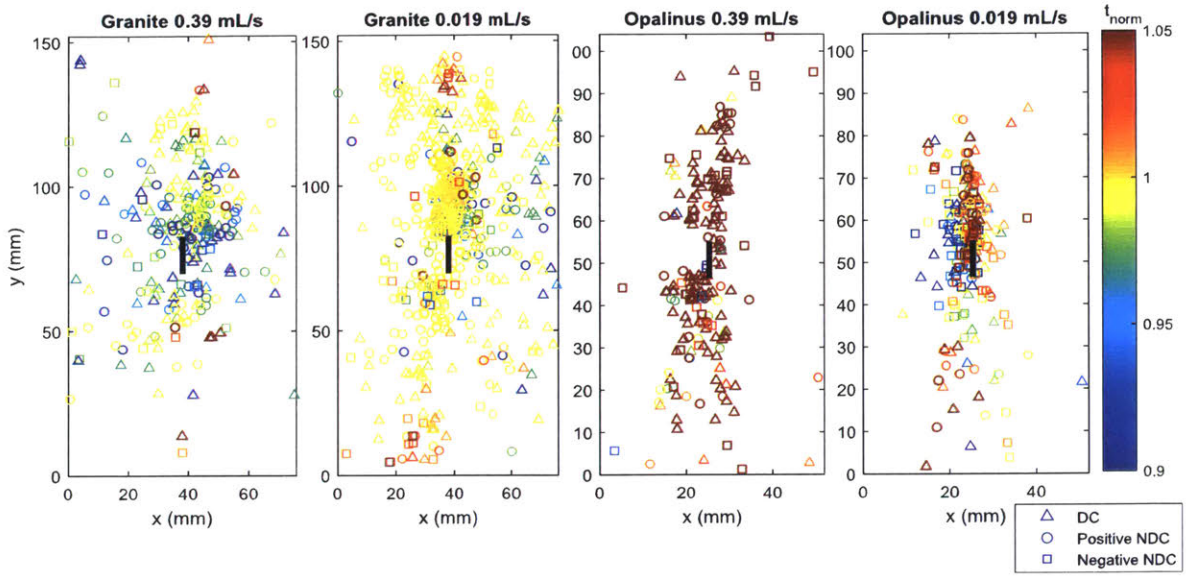

Figure 7.18: AE hypocenter locations for all four tests.

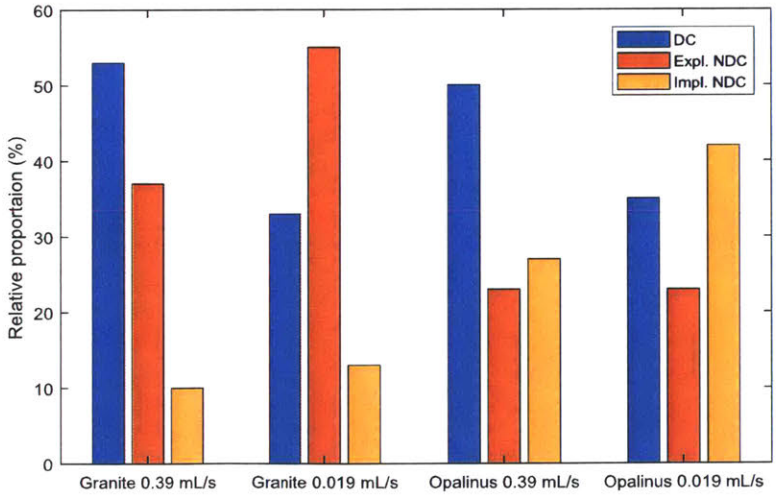

Figure 7.19: Relative proportion of double couple couple dominated ($> 50\%$), explosive non double couple, and implosive non double couple events (Hudson et al., 1989) captured during the four experiments.

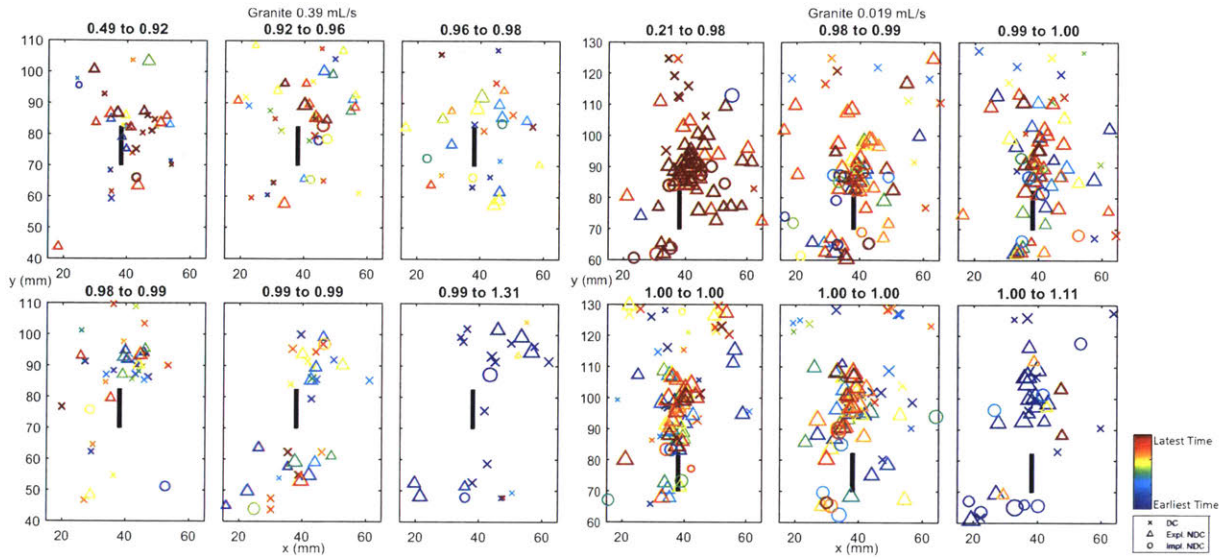

Figure 7.20: Evolution of AE hypocenter locations over time. The catalogue of events is divided into 6 equal-sized bins, each represented in a single frame. (Left) Granite 0.39 mL/s test, (Right) Granite 0.019 mL/s test. Bold subtitle in each subplot indicates t_{norm}. Size of scatter point indicates magnitude, colour indicates time.

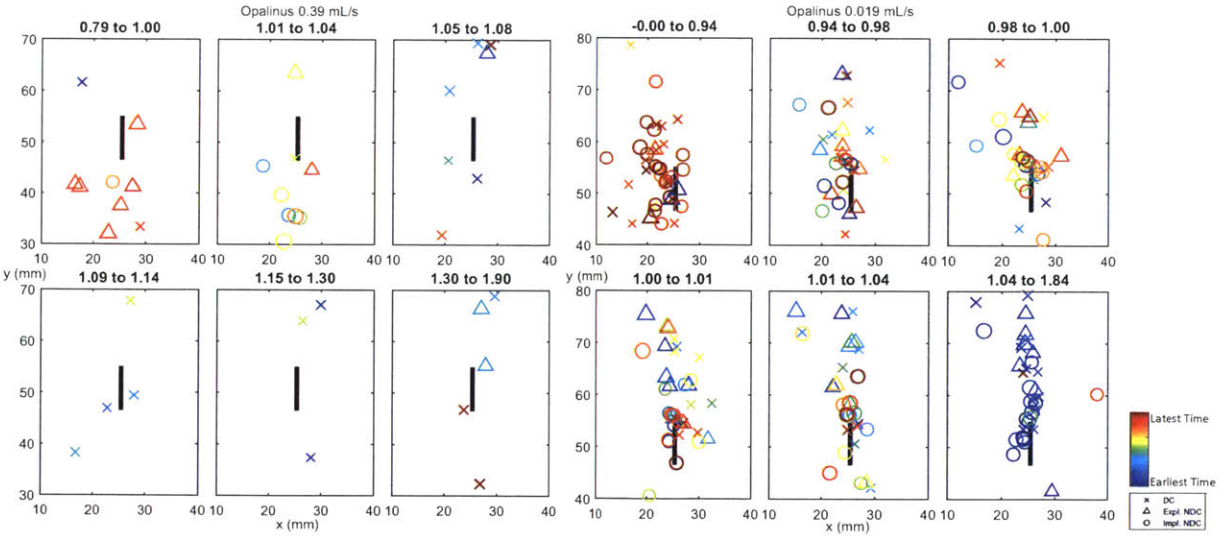

Figure 7.21: Evolution of AE hypocenter locations over time. The catalogue of events is divided into 6 equal-sized bins, each represented in a single frame. (Left) Opalinus 0.39 mL/s test, (Right) Opalinus 0.019 mL/s test. Bold subtitle in each subplot indicates t_{norm}. Size of scatter point indicates magnitude, colour indicates time.

7.3 Scaling

We calculate scaling parameters for the experiments presented in this chapter, in order to provide context in relation to field hydraulic fracture operations. We use the relationships proposed by Bunger et al. (2005), the results of which are presented in Table 7.2. We can see that in all cases, the ψ_1 parameter is less than 1, indicating that all the experiments are conducted within a toughness dominated regime. In order to transition to a viscous regime, a more viscous fluid and higher injection rate would be required, which are not possible in the present experimental setup.

Table 7.2: Table summarising scaling relationships.

Parameters		Shale	Granite
E (Pa)	Young's modulus	2.14×10^{9}	5.00×10^{10}
ν	Poisson ratio	2.50×10^{-1}	2.50×10^{-1}
E' (Pa)	Plane strain modulus	2.28×10^{9}	5.33×10^{10}
K_{1c} (Pa $m^{0.5}$)	Fracture toughness	5.00×10^{5}	2.00×10^{6}
K' (Pa $m^{0.5}$)	Modified fracture toughness	1.60×10^{6}	6.38×10^{6}
μ (Pa s)	Viscosity	3.89×10^{-3}	3.89×10^{-3}
μ' (Pa s)	Modified viscosity	4.67×10^{-2}	4.67×10^{-2}
C_l (m $s^{-0.5}$)	Leakoff	1.00×10^{-4}	1.00×10^{-4}
C' (m $s^{-0.5}$)	Modified leakoff	2.00×10^{-4}	2.00×10^{-4}
H (m)	Distance to boundary	5.00×10^{-2}	7.60×10^{-2}

	Shale		Granite	
Q	3.90×10^{-7}	1.90×10^{-8}	3.90×10^{-7}	1.90×10^{-8}
t_h (s)	1.00×10^{0}	2.06×10^{1}	4.89×10^{-1}	1.00×10^{1}
t_m (s)	1.15×10^{-8}	1.24×10^{-10}	3.46×10^{-5}	3.73×10^{-7}
ψ_1	1.15×10^{-8}	6.04×10^{-12}	7.09×10^{-5}	3.71×10^{-8}

7.4 Conclusions

- Lower injection rates tended to result in a more complex microfracture network, due to the increased number of arrested microcracks.
- Microcracks in granite tend to form as a series of oblique en-echelon cracks, whereas microfractures in opalinus tend to form directly along bedding plane boundaries. Specifically, in Opalinus all microcracks open in tension before shearing. In granite, the order of tension and shearing depends on the specific microcrack.
- Between 0.019 and 0.39 mL/s injection rates in the Opalinus, it appears that the behaviour transitions from bedding planes opening ahead of the microcrack tip to the bedding planes opening along with the microcrack tip.
- For the given experimental setup, inelastic deformation begins to occur around 95% of peak fluid pressure at 0.039 mL/s in both granite and shale, while at 0.39 mL/s the damage begins to occur around 80-85% of peak fluid pressure in both granite and shale.
- In all cases, the displacement field ahead of the crack tip tends to closely resemble a plumose fracture (See Figure 7.10), where the material immediately ahead of the crack tip displaces in the direction of the crack path, and there is a gradual transition on either side to a displacement field that is normal to the crack. This transition appears to within a smaller area for the Opalinus than the granite, suggesting that the process zone is smaller in Opalinus.
- Statistical analysis of the strain data suggest that the granite tests display more volumetric expansion than the shales.
- Generally the AE show many more implosive non-double-couple type events in the Opalinus tests than the granite. The AE hypocenters in Opalinus also tend to be much closer to the flaw tips compared to the granite, indicating a smaller process zone in the shale.
- We suggest that, within the injection rates tested, the microseismic behaviour of the initiation and propagation of a hydraulic fracture does not depend on the injection rate in granite, while this is not the case in Opalinus clayshale. The development of microcracks, however, depends on injection rate in all cases.

Chapter 8

Energy Budget

"The board is set, the pieces are moving. We come to it at last, the great battle of our time."

In order to compile and compare results from various experiments on different rocks and loading conditions, we calculate the energy budget in each experiment by considering the fraction of the work done by the loading machine or fluid injection ($\tilde{E}$) that is released as radiated seismic energy (E_R). The main goals are twofold: firstly, we would like to determine whether the difference in seismic energy between opalinus and granite are consistent across loading conditions. Secondly, we observe that hydraulic fracturing tends to produce fewer AE than beam bending or unaxial compression experiments, but would like to determine whether this is only proportionally lower as a result of the smaller work done by fluid injection compared to loading experiments.

8.1 Tests considered

We consider the four hydraulic fracturing tests discussed in Chapter 7, the beam bending tests on Barre granite (Chapter 3) and Opalinus clayshale (Chapter 4), and uniaxial compression tests on Opalinus clayshale and Barre granite that will be outlined in this section.

The uniaxial compression test on Barre granite was conducted on a 3 inch x 6 inch x 1 inch specimen, with a pre-cut a-30-30 flaw geometry (See chapter 5). The specimen was loaded to failure uniaxially in position control at a rate of 0.00254 mm/s (Figure 8.2) in a 200 000 lb capacity Baldwin loading machine, and the final crack pattern is shown in Figure 8.1a.

The uniaxial compression test on Opalinus clayshale was conducted on an intact 2 inch x 4 inch x 1 inch specimen, with vertical bedding planes i.e. in-plane with the loading direction. The experiment was conducted under load control at a rate of 82.56 N/s (Figure 8.2) in the 200 000 lb capacity Baldwin load frame, and the final crack pattern is shown in Figure 8.1b. We recognise that this specimen and loading condition was not identical to the granite experiment, but given the limited sample material we consider these differences to be minor compared to the differences between materials and between fracture mechanisms, i.e. compared to tensile fracture mechanisms.

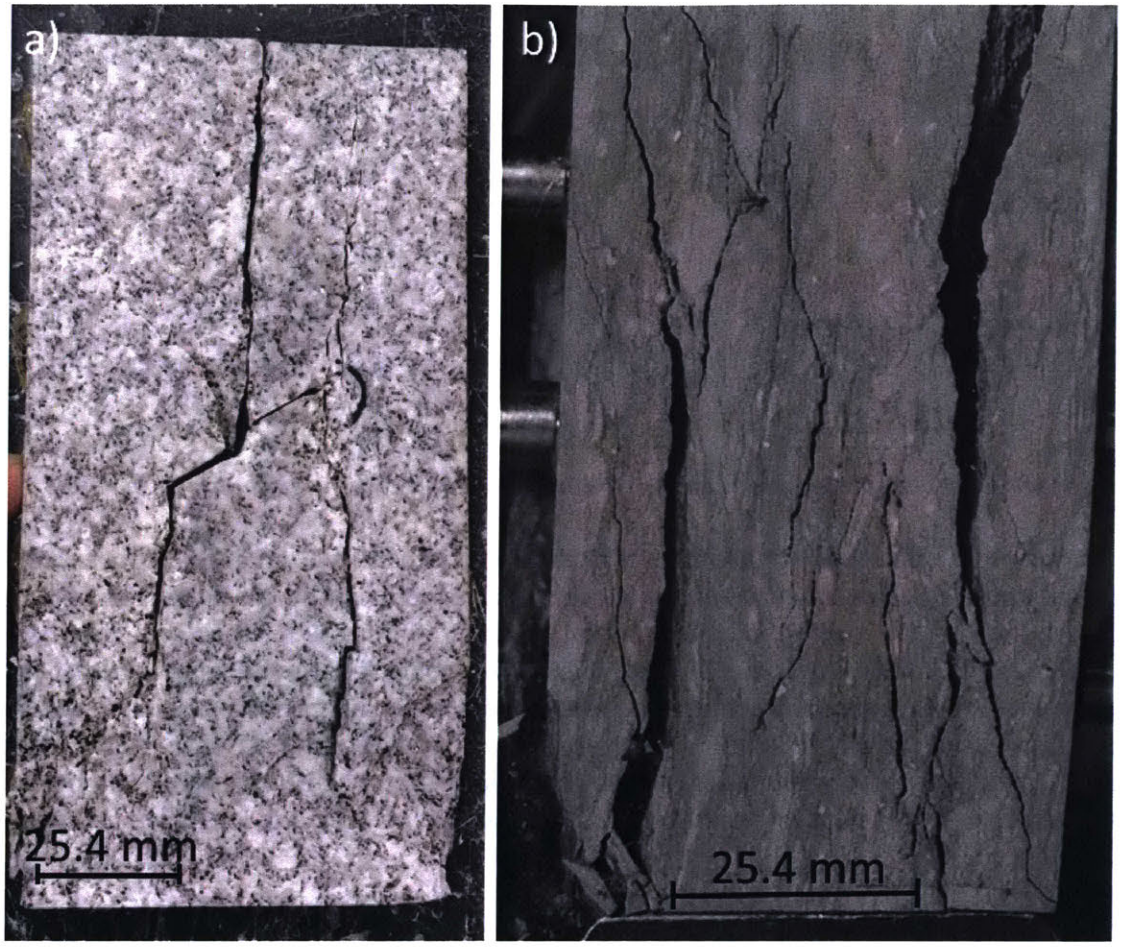

Figure 8.1: Final crack pattern of a) granite a-30-30 uniaxial compression test, and b) Opalinus intact compression test.

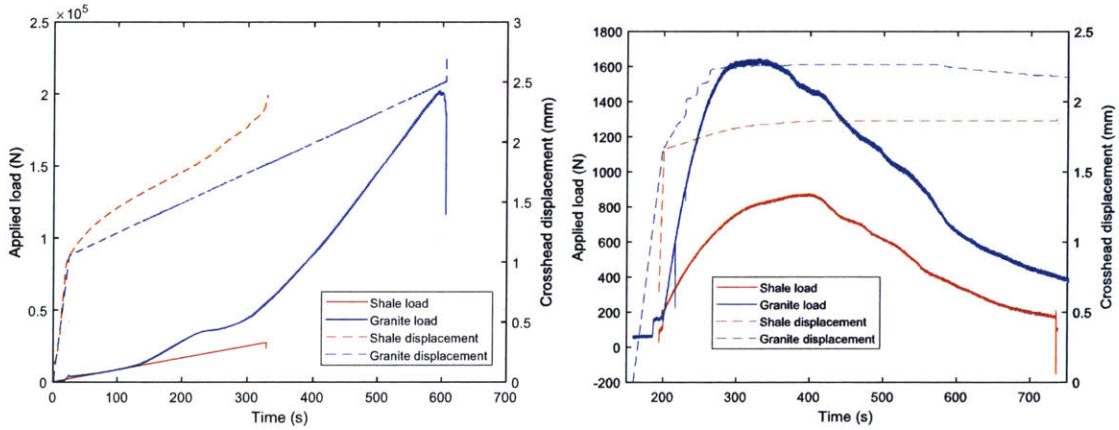

Figure 8.2: (Left) Load-displacement data over time for granite a-30-30 uniaxial compression test, and Opalinus intact compression test. (Right) Load-displacement data over time for granite and shale beam bending tests.

8.2 Radiated seismic energy E_R

The radiated seismic energy is estimated from each experiment by first calibrating all AE amplitudes to moment magnitudes as described in Section 2.1.4. The distribution of magnitudes in each experiment are summarised in the Gutenberg-Richter plots shown in Figure 8.3.

We then estimate total radiated seismic energy (E_R) by calculating the M_0 of each event detected during the test (only the injection stage is considered for HF tests), summing these M_0 to calculate the total transformed M_0, and estimating radiated seismic energy as described in Section 2.3.1.8:

$$\begin{aligned} log_{10}(10E_R) &= 1.5M_w + 4.8 \\ M_w &= \frac{2}{3}[log_{10}M_0 - 9.1] \\ \rightarrow \frac{E_R}{M_0} &= 5.01E-6 \end{aligned} \tag{8.1}$$

We note that this ratio for $\frac{E_R}{M_0}$ is similar to that observed in Shearer (2009) for earthquakes $M_w > 1$.

The results are shown in Table 8.1, and visualised in Figure 8.4. In general, the radiated seismic energy of the opalinus is two to three orders of magnitude smaller than the granite, and that the uniaxial compression tests radiate significantly more seismic energy than the other loading mechanisms.

Table 8.1: Summary of seismic energy calculation for each experiment.

Material	Loading condition	Total AE M_0 (Nm)	Radiated seismic energy E_R (J)
Barre granite	Four-point beam bending	1.96×10^{2}	9.84×10^{-4}
Opalinus BMA-2	Four-point beam bending	1.78×10^{0}	8.94×10^{-6}
Barre granite	a-30-30 uniaxial compression	3.87×10^{3}	1.94×10^{-2}
Opalinus BMA-2	Intact uniaxial compression	1.80×10^{1}	9.04×10^{-5}
Barre granite	Single flaw HF Q=0.39 mL/s	3.60×10^{0}	1.80×10^{-5}
Barre granite	Single flaw HF Q=0.019 mL/s	2.79×10^{1}	1.40×10^{-4}
Opalinus BMA-2	Single flaw HF Q=0.39 mL/s	2.10×10^{-1}	1.05×10^{-6}
Opalinus BMA-2	Single flaw HF Q=0.019 mL/s	1.43×10^{-1}	7.18×10^{-7}

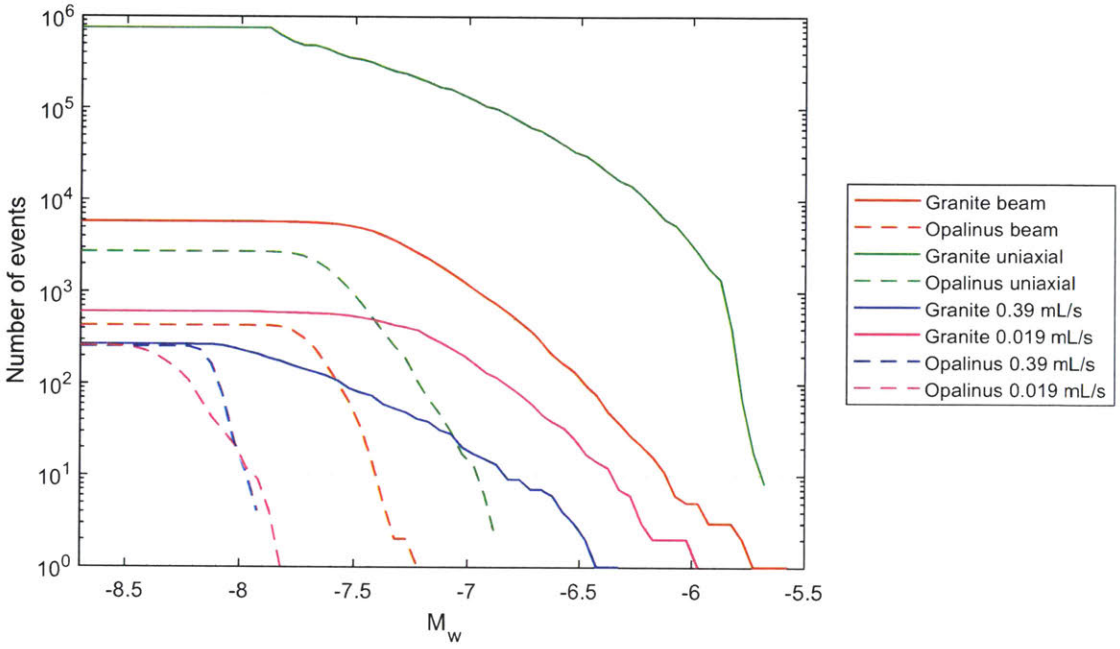

Figure 8.3: Gutenberg-Richter plots for all experiments.

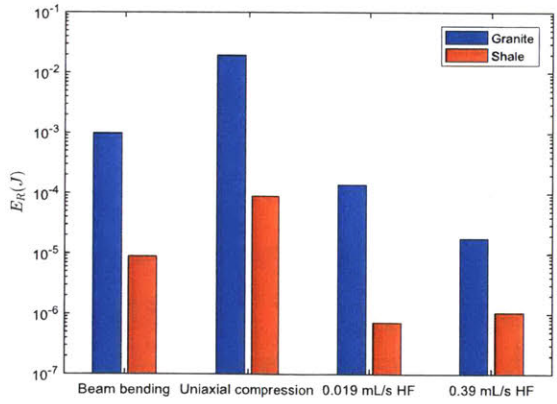

Figure 8.4: Table 8.1 in graphical format.

8.2.1 Attenuation

Amplitude attenuation is a concern for the estimation of radiated seismic energy from shale materials, as it has been shown in this thesis and other works (e.g. Moradian et al., 2015) that the quality factor, which is inversely proportional to amplitude attenuation, is significantly lower in shale than other rocks. In this section, we use the coda-decay method (Aki and Chouet, 1975) to estimate the quality factor Q from the waveforms acquired from the 0.019 mL/s Opalinus experiment, in order to estimate the effect of attenuation. The Q at a given frequency can be expressed as:

$$ln(A_c(f,t_c)\cdot t_c) = ln(I(f)A_0(f)) - \frac{\pi f}{Q_c}t_c \tag{8.2}$$

Where $A_c(f,t_c)$ is the amplitude in a given frequency band f and time after event origin time t_c, Q_c is the quality factor, and $ln(I(f)A_0(f))$ is a constant. If we plot $ln(A_c(f,t_c)t_c)$ vs. t_c, the slope is then equivalent to $-\frac{\pi f}{Q_c}$.

We first select a large and a small waveform, and filter by frequency bands 25 - 50 kHz, 50 - 100 kHz, 100 - 200 kHz, and 200 - 400 kHz using a 2-pole Butterworth filter, as shown in Figures 8.5 and 8.6. From these filtered plots, we select a window size of 20 μs by inspection, over which to calculate the moving average RMS for each frequency band, as shown in Figures 8.5f and 8.6f.

The moving average is calculated for every waveform acquired during the test, normalised by the corresponding first arrival amplitude, and presented on the same plot for each channel. As an example, the plot of channel 5 is shown in Figure 8.7. The slope, as denoted by the dotted red line, is approximated by visual inspection immediately after the maximum y-axis value, and is equivalent to $-\frac{\pi f}{Q_c}$. The calculated Q values are summarised in Table 8.2.

The calculated Q values are similar to those found in other lab studies on shale (Hu et al., 2018; Zhai et al., 2017; Deng et al., 2009). We can then use equation 8.3 to estimate the amplitude attenuation for our laboratory setting.

$$Attenuation\,factor = e^{\frac{-2\pi fx}{2cQ}} \tag{8.3}$$

Where we assume x, the distance from the source, to be 25.4 mm (the distance from the notch to the side of the specimen); c, the wave velocity, to be 3000 m/s. We consider the 100-200 kHz frequency band as this is the strongest (f = 150 kHz), at which the mean quality factor is Q = 8.4. The attenuation factor, then, is 0.63, i.e. the amplitude detected at the sensor is 63 % of

Q	Frequency (kHz)			
Channel	25 - 50	50 - 100	100 - 200	200 - 400
1		4.45	15.13	7.87
2		5.48	5.16	11.75
3		5.62	9.13	24.16
4		10.44	5.76	17.67
5	3.50	7.11	4.25	18.54
6				
7				
8		0.40	11.01	32.52
Average Q	3.50	5.58	8.41	18.75

Table 8.2: Summary of calculated Q for Opalinus clayshale per channel, per frequency band.

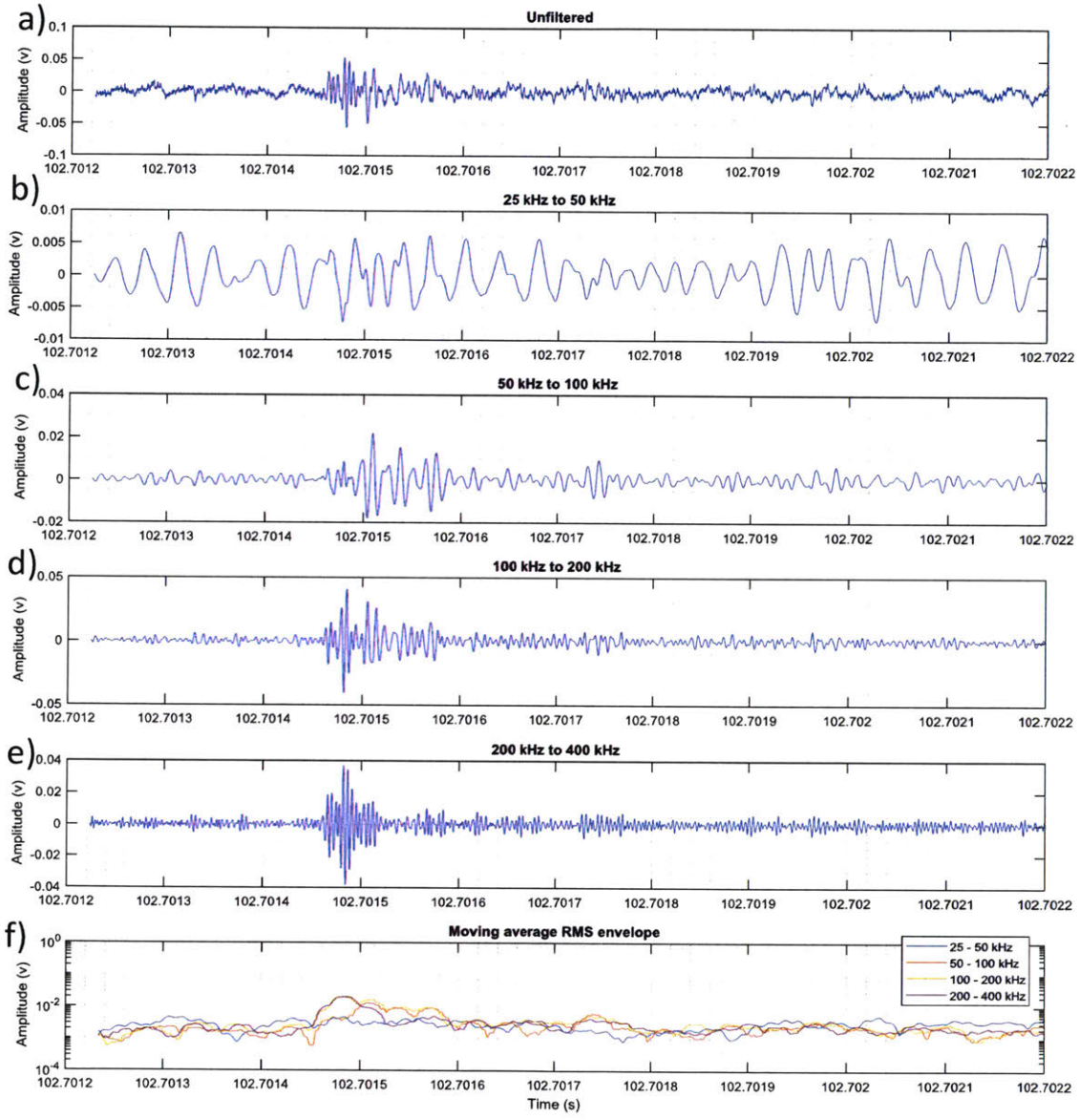

Figure 8.5: a) Unfiltered small amplitude waveform from 0.019 mL/s Opalinus test. b) - e) Waveform filtered at indicated frequency bands. f) Moving average RMS envelope of each frequency filtered wave.

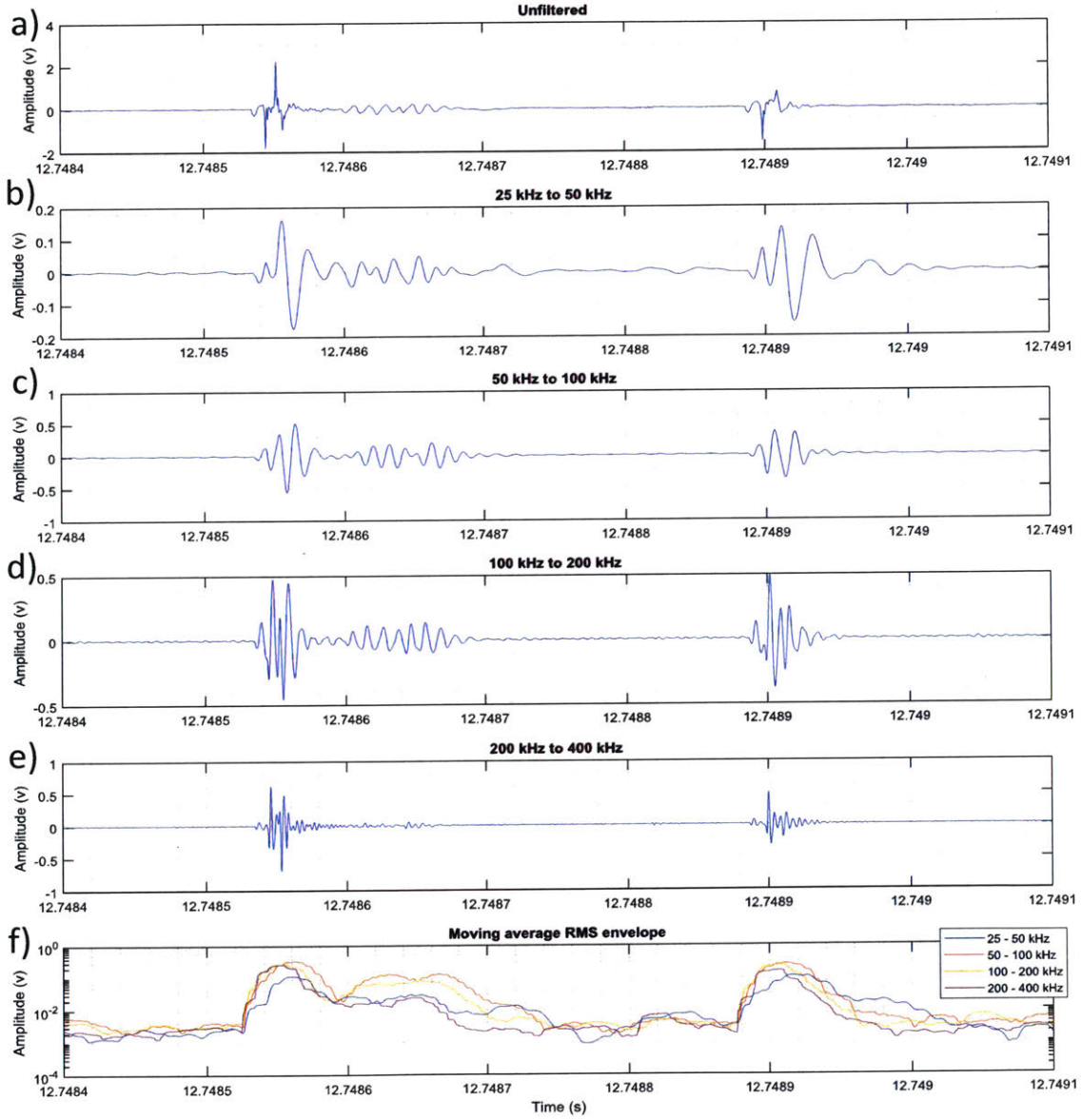

Figure 8.6: Same as Figure 8.5, but for a large amplitude waveform.

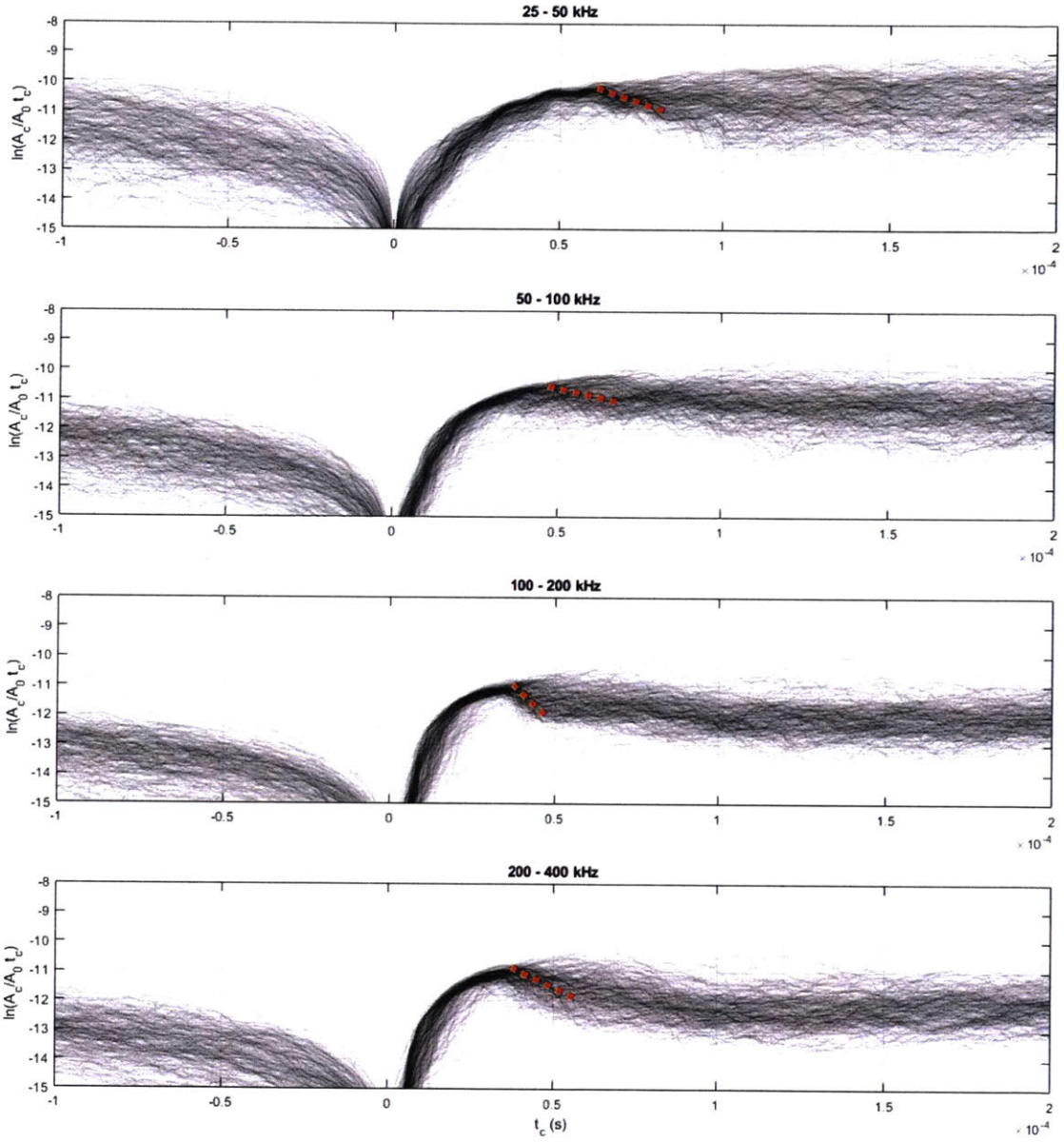

Figure 8.7: Waveform envelopes for all events detected at channel 5 during 0.019 mL/s Opalinus clayshale experiment, presented for each frequency band. Dotted red line shows slope estimating $-\frac{\pi f}{Q_c}$.

Q	Frequency (kHz)			
Channel	25 - 50	50 - 100	100 - 200	200 - 400
1	6.40	5.63	26.38	55.80
2				
3	14.35	13.01	21.84	23.82
4	6.34	12.40	16.23	34.63
5	4.52	35.67	4.62	17.92
6	18.72	7.85	16.66	67.02
7				
8	6.75	13.62	15.14	31.14
Average Q	9.51	14.70	16.81	38.39

Table 8.3: Summary of calculated Q for granite per channel, per frequency band.

the amplitude if the sensor was immediately at the source. This number is quite high, and so we can generally conclude that the effect of attenuation is not significant, thus not many events were undetected due to attenuation effects.

Similar analysis was conducted on the 0.019 mL/s granite HF experiment, and the results are shown in Figure 8.8 and Table 8.3. We can see that the quality factor for granite is generally twice that of shale, which results is slightly less attenuation. The mean quality factor of Q = 16.81 in the 100-200 kHz band resolves to an attenuation factor of 84 %, which is does not account for the order of magnitude in the difference in radiated seismic energy calculated in this chapter.

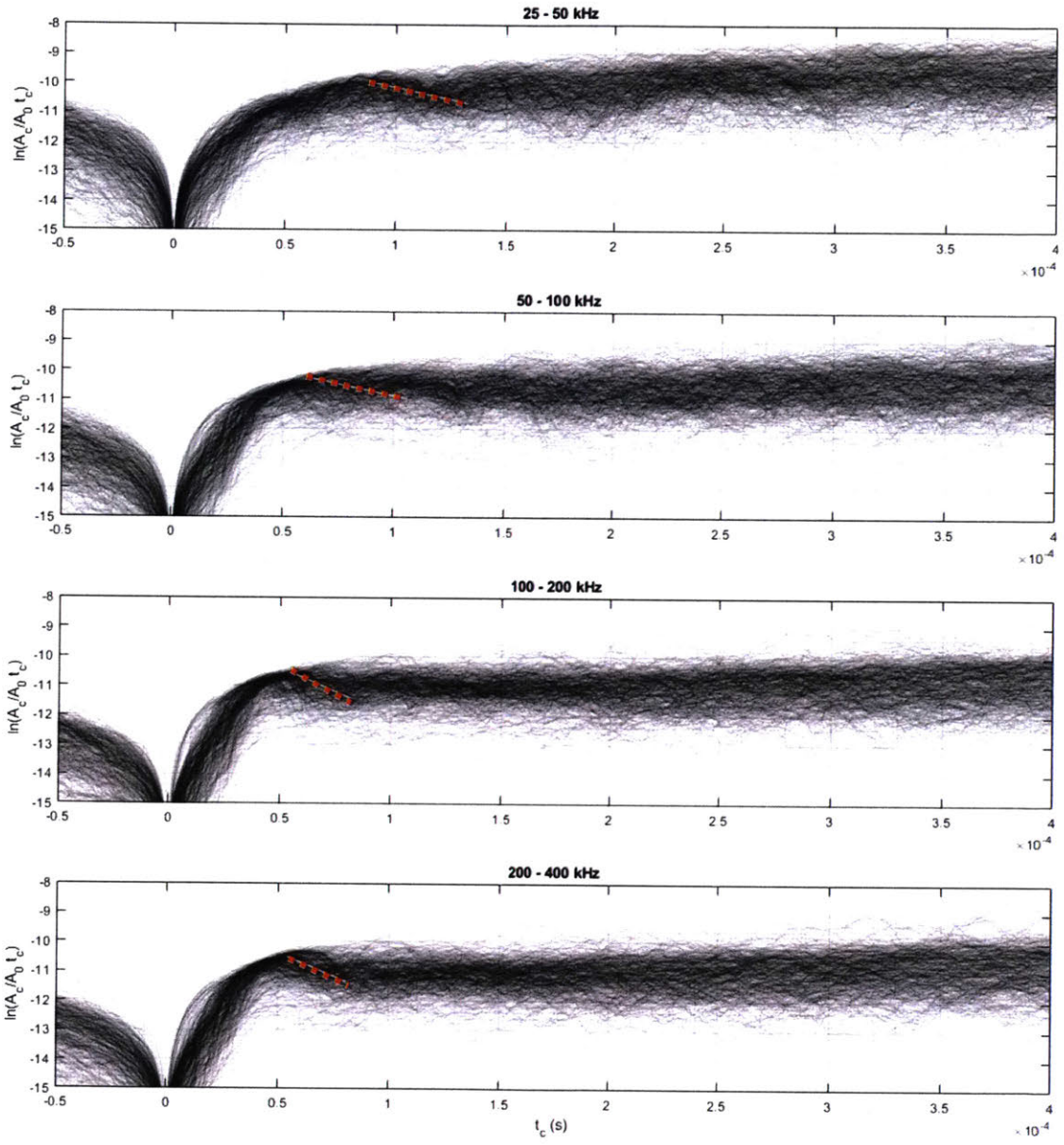

Figure 8.8: Waveform envelopes for all events detected at channel 5 during 0.019 mL/s granite experiment, presented for each frequency band. Dotted red line shows slope estimating $-\frac{\pi f}{Q_c}$.

8.3 External mechanical work done $\tilde{E}$

To calculate the work done by the loading machine during beam bending or uniaxial compression tests, we take the numerical integration of the load-displacement curves shown in Section 3.2, and take the maximum value of machine work over the course of the experiment.

For hydraulic fracturing experiments, we similarly numerically integrate the pressure-volume curve. However, in our setup the piping deforms significantly during an experiment, such that not all of the volume change at the pump is exerted on the rock specimen. To quantify this effect, we conducted a calibration test where the hydraulic fracturing enclosure was replaced by a stopper, and compare this to the pressure-volume curve from a calibration test with the enclosure and a granite specimen. The results are shown in Figure 8.9, where we see that the HF device with a granite specimen has a system compliance of 2.833 MPa/cm^3, i.e. 1 cm^3 of injected fluid increases fluid pressure by 2.83 MPa. When the HF enclosure is replaced by a stopper, the system compliance increases to 7.25 MPa/cm^3, i.e. 1 cm^3 increases pressure by 7.25 MPa. The difference between these compliances then, is the compliance of the HF enclosure, for which 1 cm^3 of fluid injection increases the pressure by 7.25 - 2.83 = 4.42 MPa. Using this calibration and assuming a linear pressure-volume curve, we can then estimate work done by the fluid as:

$$\tilde{E}_{fluid} = \frac{1}{4.42 \times 10^{12}\ Pa/m^3} \frac{1}{2} P_{max}^2 \tag{8.4}$$

The above methodologies are applied to the data shown in Figure 8.10, and the results are shown in Table 8.4 and visualised in Figure 8.11. The fluid injection energies are similar to those reported in Goodfellow et al. (2015), and we can see that the work done during the beam bending tests is an order of magnitude smaller than the hydraulic fracture tests, which are in turn an order of magnitude smaller than in the uniaxial compression tests.

Table 8.4: External mechanical work done by the injection fluid or loading machine during each experiment.

Material	Loading condition	Mechanical work $\tilde{E}$ (J)
Barre granite	Four-point beam bending	6.97×10^{-1}
Opalinus BMA-2	Four-point beam bending	2.19×10^{-1}
Barre granite	a-30-30 uniaxial compression	1.04×10^{2}
Opalinus BMA-2	Intact uniaxial compression	2.07×10^{1}
Barre granite	Single flaw HF Q=0.39 mL/s	1.77×10^{1}
Barre granite	Single flaw HF Q=0.019 mL/s	1.02×10^{1}
Opalinus BMA-2	Single flaw HF Q=0.39 mL/s	4.77×10^{0}
Opalinus BMA-2	Single flaw HF Q=0.019 mL/s	1.02×10^{0}

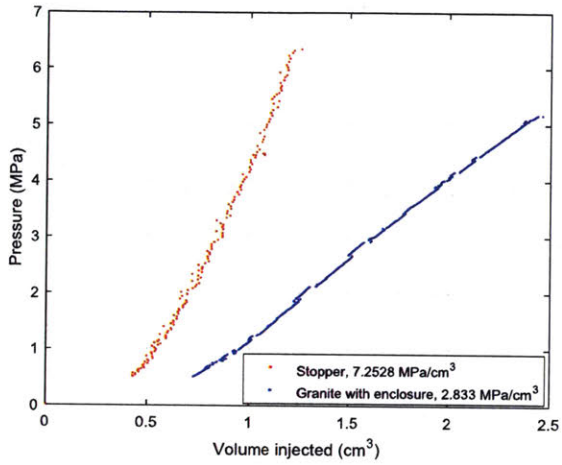

Figure 8.9: Pressure-volume data for HF setup with and without the enclosure and granite specimen.

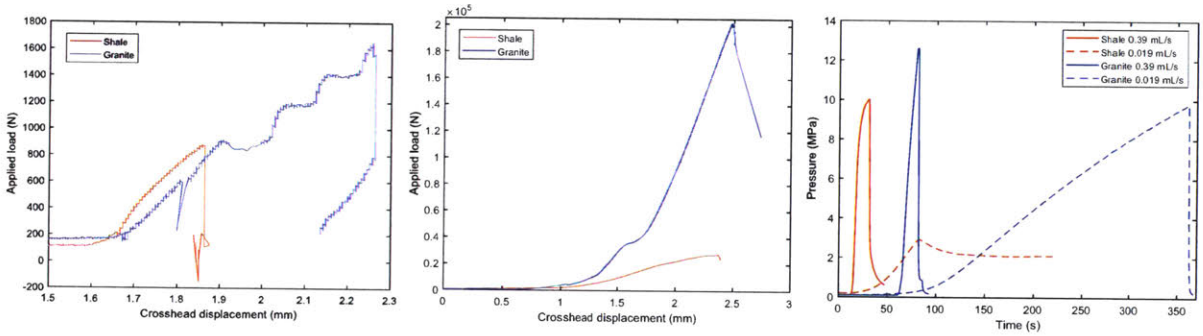

Figure 8.10: a) Load-displacement data from beam bending experiments, b) Load-displacement data from uniaxial compression experiments, c) Pressure over time from hydraulic fracturing experiments.

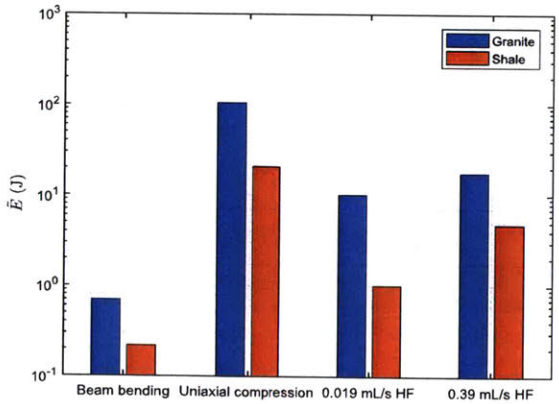

Figure 8.11: Table 8.4 in graphical format.

8.4 Discussion and Conclusions

The compiled results are shown in Table 8.5, and visualised in Figure 8.12. Firstly, we can see that for the beam bending, uniaxial compression, and low flow rate HF tests, the Opalinus seismic energy budget is 2-5% of the granite seismic energy budget, which suggests that this difference may be a material property that is independent of the loading condition. On the effect of the loading condition, we can see that the beam bending is the most efficient (highest $E_R/\tilde{E}$), followed by the uniaxial compression tests, then the slow HF tests, and that the fast HF tests are least efficient. If we consider the time scale over which each experiment occurs, this suggests that slower loading rates are more seismically efficient per unit energy, as was observed by Mair et al. (2007). Specifically, we suggest that the beam bending is more seismically efficient since the tensile fractures are generated slowly over a time period of hundreds of seconds, while the hydraulic fractures are formed within a few seconds even in the slower injection rate tests. We suggest that this rate dependency is related to the momentum of the material around the crack tip, where the loading mechanism supplies energy faster than the rate at which energy is dissipated at the tip. However, this raises an interesting dilemma, where we saw in Chapter 6 that only the fastest injection rate resulted in an detectable number of AE. We do note however that a more clay-rich shale was used in that series of tests, and so different mechanisms may be involved. We also note that the lower injection rate HF tests resulted in higher fracture complexity, which corresponds to higher seismic efficiency. Considering the focal mechanisms, we can also make some generalisations. Firstly, it appears that granite in general produces more double couple mechanisms than the shale, while the shale produces more negative volume change (-ISO) type focal mechanisms, indicating there is more shear in granite, and more grain closures in shales. This is supported by the imaging results from previous chapters, where we see that granite has a higher tendency to generate en-echelon shear cracks, and shale often exhibits closure along bedding planes. Secondly, we note that the proportion of volume expansion (+ISO) type mechanisms is relatively consistent between the two beam tests and the two uniaxial compression tests, indicating that the relative proportion of dilation is independent of the material in dry tests. However, we again note that the proportion of +ISO is consistent between injection rates but not materials in the hydraulic fracturing tests, where fluid penetration drives the development of fractures as opposed to boundary stress conditions. This can likely be attributed to the mechanism by which the hydraulic fractures were created in these tests: the hydraulic fractures in shale initiate and propagate along pre-existing bedding planes, which

Table 8.5: Table summarising seismic kinetics and kinematics of various tests. $E_R/\tilde{E}$ is calculated from Tables 8.1 and 8.4, and the focal mechanism proportions are taken from previous chapters.

Material	Loading condition	$E_R/\tilde{E}$	DC (%)	+ CLVD (%)	- CLVD (%)	+ ISO (%)	- ISO (%)
Barre granite	Four-point beam bending	1.41 x 10^{-3}	52.7	10.0	-1.1	32.7	-3.6
Opalinus BMA-2	Four-point beam bending	4.07 x 10^{-5}	42.1	10.3	-3.0	34.3	-10.4
Barre granite	a-30-30 uniaxial compression	1.87 x 10^{-4}	46.2	5.5	-6.7	18.5	-23.1
Opalinus BMA-2	Intact uniaxial compression	4.37 x 10^{-6}	46.8	4.5	-7.7	15.3	-25.7
Barre granite	Single flaw HF Q=0.39 mL/s	1.02 x 10^{-6}	52.1	8.2	-2.8	27.7	-9.3
Barre granite	Single flaw HF Q=0.019 mL/s	1.37 x 10^{-5}	46.8	9.8	-2.7	32.0	-8.8
Opalinus BMA-2	Single flaw HF Q=0.39 mL/s	2.21 x 10^{-7}	52.9	4.9	-6.2	15.8	-20.2
Opalinus BMA-2	Single flaw HF Q=0.019 mL/s	7.06 x 10^{-7}	36.9	5.1	-8.5	17.4	-32.2

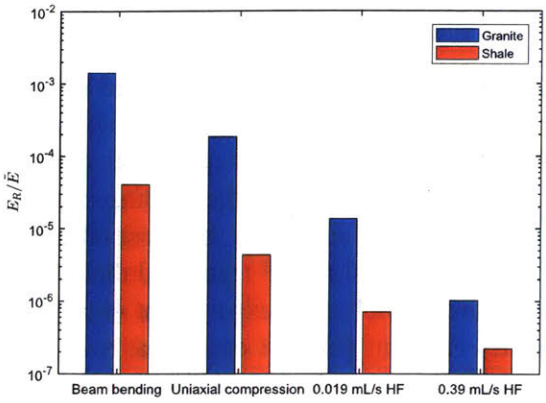

Figure 8.12: Bar chart summarising the radiated seismic energy per unit work for various tests on Barre Granite and Opalinus Clayshale.

requires less energy than in granite, where in some cases hydraulic fractures initiate and propagate through intact grains, since the en-echelon microcracks forming the process zone are not generally interconnected.

Chapter 9

Summary, Discussion, and Conclusions

Recall that the goal of this thesis is to study (1) the relationship between the creation of hydraulic fractures and the microseismicity generated during this process, and (2) how this relationship differs between granite and shale rocks.

The background chapter explores some existing literature on these topics. We firstly learn, based on a laboratory study where powdered shale is sheared in a triaxial cell, that shale materials tend to exhibit more velocity-strengthening behaviour with increasing clay and organic content. In the context of fractures, this suggests that fracture creation in shale will tend to be more aseismic, as microcracks will tend to decelerate after they initiate. We also find, based on a laboratory study where the authors shear a fault gouge composed of granular material, that decreasing shear rate is associated with an increased number of observed acoustic emissions per millimetre of displacement. The background chapter also outlines the various technologies associated with the acquisition and analysis of acoustic emissions and image data.

The thesis then describes four point beam bending tests in Barre Granite and Opalinus Clayshale, from which we conlude the following:

- At the micron scale, cracks in Barre granite tend to happen in shear as a series of en-echelon microcracks that coalesce via tensile cracks, while microcracks in Opalinus clayshale appear to form directly in tension. This is reflected in the microseismic focal mechanisms, which show that on average more double-couple type events occur in Barre granite than in the Opalinus clayshale.
- The process zone also appears to be significantly smaller in Opalinus clayshale than in Barre granite, as measured by both the acoustic emissions and image processing methods.
- The magnitude of microseismic events tend to be smaller in the shale than in the granite.

The thesis then describes hydraulic fracture experiments in both granite and shale, from which we conclude the following:

- Lower injection rates tended to create a more complex fracture network, due to the increased number of arrested microcracks.
- Again, we see that tensile cracking in Barre granite tend to happen in shear as a series of en-echelon microcracks that coalesce via tensile cracks, while microcracks in Opalinus clayshale appear to form directly in tension.

- The AE in shale show more implosive non-double-couple (compressional) events than in granite, which suggests that bedding plane compaction is a significant source of recorded AE in shale, but not granite.

- Inelastic deformation, as observed by AE and DIC, is first observed at a lower proportion of peak pressure in high injection rate tests than low injection rate tests.

We then estimate the radiated seismic energy and machine work done in each experiments, in order to quantitatively compare the different mechanisms and material behaviours. The results suggest the following:

- Fracture processes in Barre granite are more seismically efficient (more radiated seismic energy per unit work done by external forces) than Opalinus clayshale. This difference becomes more significant with increasing clay content in the shale. The Barre granite appears to be 20 to 50 times more seismically efficient than the BMA-2 Opalinus clayshale in beam bending, uniaxial compression, and hydraulic fracturing testing setups, as a result we suggest that this difference in seismic efficiency is a material parameter.

- Hydraulic fracturing is less seismically efficient than uniaxial compression tests, which are in turn less efficient than beam bending experiments. We suggest that this may be related to the momentum associated with the material ahead of the crack tip, since fractures propagate at different velocites in each test.

- Slower injection rates tended to result in higher seismic efficiency, although we note that no acoustic emissions may be detected at all when hydraulically fracturing shales with high clay content at a low injection rate.

Overall, we have covered a wide range of topics spanning rock physics, fracture mechanics, and seismology. Firstly, we will discuss the differences between shale and granite rocks. One conclusion is that the process zone in granite is significantly larger than in shale. A second conclusion that the radiated seismic energy from shale materials is lower than granite by approximately 20 times when normalised by the work done by the loading mechanism, and that this ratio is largely independent of the loading mechanism. From a fracture mechanics perspective, the difference in process zone size may be explained by the the stress-strain curves, which show more inelastic deformation in the granite than the shale, and it has been shown that materials which exhibit more inelastic deformation tend to exhibit larger process zones (Fakhimi and Tarokh, 2013). The difference in process zone size can also be explained from the perspective of grain size, since previous researchers such as Zietlow and Labuz (1998) have shown that the width of the process zone is linearly proportional to logarithm of the grain size. The difference in seismic energy may be attributed to the presence of clay minerals in the shale which tend to creep slowly rather than rapid catastrophic failure under load. For example, Kohli and Zoback (2013) showed that the (a-b) parameter of shales increases with clay content, i.e. that high clay shales tend to release accumulated strain by slow creep rather than a rapid nucleation mechanism. Intuitively, we presume this is because clay particles tend to be more ductile, and so will deform slowly and thus aseismically along large contact patches rather than by nucleation along a small contact patch. We also observe the same behaviour in this thesis, where hydraulic fracture experiments in a higher clay content shale

produced far fewer acoustic emissions than in a lower clay content shale. Micromechanically, we also find evidence that nucleation is more prevalent in the granite: the process zone in granite tends to form along localised en-echelon shear microcracks along specific grain boundaries, whereas in shale the fractures initiate and propagate directly in tension along bedding planes. This is supported by the focal mechanisms, which show that, on average, microseismic events in granite have a larger double couple component than in shale. On the bulk scale, we also see, for example as observed by Morgan (2015), that fractures created in uniaxial compression propagate far slower in shale than in granite, which again suggests velocity-strengthening behaviour observed from simulated fault gouge slip holds for the creation of new fractures. Specifically, fractures in shale will tend to propagate and arrest, denoted as stable cracking in fracture mechanics whereas cracking in granite tends to be unstable. However, there remains the apparent contradiction that the shale is composed of more ductile minerals, but exhibits less inelastic deformation than the granite at the bulk scale. We suggest that this contradiction occurs because the size of the process zone is a more significant factor than the ductility of individual grains, i.e. that there is a large zone of low inelastic strain in the granite, and a small zone of high inelastic strain in the shale. In the cases explored in this thesis, the overall "volume of inelastic strain", which one may conceptualise as the magnitude of strain integrated over the process zone, happens to be larger in granite, and so we see more inelastic deformation from the granite in the stress-strain curve. The difference in seismic energy between the two materials then, can be attributed to at least two underlying mechanisms: firstly, the process zone in shale is smaller, and so there is a smaller area from which seismic events may originate. This can be attributed to the shale's smaller grain size. Secondly, the clay minerals' in the shale tend to creep aseismically along a larger length scale rather than seismic rapid nucleation along smaller length scales.

We also suggest that the prevalence of shear microcracks in granite but not shale under a far field tensile stress state may be attributed to its rate-state behaviour. It is possible that shear cracks occur in granite (which exhibits rate-weakening behaviour) because any significant asperity can act as a local nucleation point, leading to rupture of a shear microcrack along obliquely oriented grain boundaries where shear stress is highest. Conversely in shale, slip will occur over a larger contact area, i.e. the magnitude of strain decreases more gradually with distance from the point of rupture than in granite. This larger contact area, combined with the smaller grain size in shale, may lead to the effect that the contact area in shale exists over multiple grains as opposed to a single asperity on a grain for granite. This makes it more likely for microcracks to initiate along a single grain boundary in granite, but across multiple grains in shale. It is then easier to initiate a generally optimally oriented tensile microcrack across multiple grains in shale, compared to individual grains in granite which are unlikely to be optimally oriented to the tensile stress field.

We can make some general comments on the differences between loading mechanisms. In this thesis, we present results from beam bending and hydraulic fracturing experiments in detail, and briefly discuss results from uniaxial compression tests. We find that the beam bending tests radiated the most seismic energy when normalised by external work done by the loading machine. The uniaxial compression tests radiated approximately ten times less normalised seismic energy than the beam bending tests, and the hydraulic fracture tests radiated the least normalised seismic energy, within which the low injection rate tests radiate more normalised energy than the high injection rate tests. There appear to be at least two factors affecting the normalised radiated seismic energy: the fluid pressure and the loading rate. Regarding fluid pressure, a recent study by Cappa et al (2019) found that increasing fluid pressure results in more aseismic slip and fracture opening,

i.e. we expect the seismic efficiency to be lower at higher fluid pressure. This is consistent with our finding that the higher injection rate tests radiate less normalised seismic energy than the lower injection rate tests, since higher injection rate also corresponds to higher maximum fluid pressure. We do not, however, observe more microcrack opening during the high injection rate tests, and so the underlying mechanism may instead be attributed to a lubrication effect of the fluid.

On the effect of loading rate, we first note from the hydraulic fracture tests that a lower injection rate results in a more complex fracture network. This may result from the difference in inertia in the material ahead of the crack tip. Assuming the stable cracking regime, lower inertia may result in the propagation of multiple fractures because once a crack propagates a small distance, the fluid pressure at the new crack tip is reduced and is thus lower than the pressure along the remainder of the crack, which allows new branches to form behind the crack tip. Conversely in the higher injection rate tests, the pressure increases more rapidly, and so there is more inertia ahead of the crack tip. This increases the probability that the initial crack will continue to propagate once it initiates, and so less branching and tortuosity is observed. It is possible that higher fracture complexity results in increased radiated seismic energy, as there is more fracture length over which seismicity can occur. The inertia-based argument can also explain the higher normalised radiated seismic energy in the beam bending setup as compared to all other test setups explored in this thesis. The beam bending tests were conducted under crack opening control such that the crack propagated slowly and stably over hundreds of seconds, and so the loading program is designed specifically to *minimise* inertia at the crack tip, which under our framework should maximise the normalised radiated seismic energy.

Ostensibly, this thesis set out to understand the relationship between what one can observe visually through imaging, and what can be observed aurally through microseismic monitoring. Unfortunately, like the proverbial six blind men and the elephant, this doctoral candidate has gleaned some meagre nuggets of truth, but overall come out more befuddled than when he began. This, however, should not be a cause for despair, after all Theodore Roosevelt once quipped that "Nothing in the world is worth having or worth doing unless it means effort, pain, difficulty". A career in research would not be interesting if the answers were so simple, and to look whimsically to the future, there are at minimum three additional Aristotelian senses to explore: taste (perhaps mineralogy), touch (mechanical properties), and smell (mass transfer). Worded perhaps more scientifically, the doctoral candidate recommends these following directions of study:

- Systematically investigate creation of "plumose" structures
- Systematically investigate why displacement vectors ahead of crack tip are co-linear with crack path
- Repeat injection rate tests in Chapter 7, as only one set of experiments was conducted for this thesis due to time constraints
- Repeat tests in this thesis with the bedding planes oriented perpendicular to the fracture path, to determine the effect of fracture propagation across alternating hard and soft layers
- Repeat tests in this thesis with different specimen dimensions, since sample size is known to affect the size of the observed process zone

- SEM and EDS imaging of Barre granite and BMA-2 Opalinus clayshale, to determine whether fractures preferentially propagate along certain minerals
- Different loading rates for beam and compression tests, to determine if the far-field loading rate has a similar effect as injection rate.
- Hydraulically fracture shales with different clay contents and develop a relationship between clay content and microseismicity, as this seems to be a critical parameter
- Estimate rate-and-state parameter (a-b) from shear rates than can be calculated from displacements shown in Figures 7.16 and 7.17, to see if results from Kohli and Zoback (2013) hold for the creation of new fractures
- Develop a hydraulic fracturing setup for (and test) higher viscosity fluids and injection rates to reach the "viscosity" regime in the Bunger scaling methodology
- Develop statistical models such as artificial neural networks to predict induced seismic sequences using existing microseismic data.
- Repeat HF tests with gases such as argon to determine if lower radiated seismic energy in HF is due to lubrication effect of the liquid.
- Consider whether the differences in injection rate arise from the differences in inertia of the material at the propagating crack tip.

'But,' said Opalinus, and tears started in his bedding planes, 'I thought you were going to enjoy the Microseismicity, too. For years and years, after all you have done.'

'So I thought too, once. But I have been too deeply hurt, Opalinus. I tried to save the Microseismicity, and it has been saved, but not for me. It must often be so, Opalinus, when things are in danger: some one has to give them up, lose them, so that others may keep them. But you are my heir: all that I had and might have had I leave to you. And also you have an acquisition system, and piezoelectric sensors; and Matlab-codes will come, and ball-drops, and image processing, and papers (oh so many papers!); and perhaps more that I cannot see. Your hands and your wits will be needed everywhere. You will be the Post-Doc, of course, as long as you want to be, and the most famous fractographer in history; and you will read things out of H. Einstein's notes, and keep alive the memory of the age that is gone. So that people will remember the Great Danger of a Doctorate and so love their beloved hairline all the more. And that will keep you as busy and as happy as anyone can be, as long as your part of the Story goes on.'

'Well, here at last, dear friends, on the shores of this defence comes the end of our thesis in Middle-Tech. Go in peace! I will not say: do not weep; for not all tears are an evil.' ✿

Bibliography

Akaike, H. (1974). Markovian representation of stochastic processes and its application to the analysis of autoregressive moving average processes. *Annals of the Institute of Statistical Mathematics*, 26(1):363–387.

Alam, S., Loukili, A., Grondin, F., and Roziere, E. (2015). Use of the digital image correlation and acoustic emission technique to study the effect of structural size on cracking of reinforced concrete. *Engineering Fracture Mechanics*, 143:17–31.

AlTammar, M. J., Sharma, Mukul, M., and Manchanda, R. (2018). The effect of pore pressure on hydraulic fracture growth: An experimental study. *Rock Mechanics and Rock Engineering*, 51:2709–2732.

Anders, M. H. and Laubach, Stephen E. abd Scholz, C. H. (2014). Microfractures: a review. *Journal of structural geology*, 69:377–394.

Ashby, M. and Hallam, S. (1986). The failure of brittle solids containing small cracks under compressive stress states. *Acta Metallurgica*, pages 497–510.

Asim, K., Martinez-Alvarez, F., Basit, A., and Iqbal, T. (2017). Earthquake magnitude prediction in hindukush region using machine learning techniques. *Natural Hazards*, 85:471–486.

ASTM C1161 (2013). *Standard Test Method for Flexural Strength of Advanced Ceramics at Ambient Temperature*. American Society for Testing and Materials (ASTM).

Backers, T., Stanchits, S., and Dresen, G. (2005). Tensile fracture propagation and acoustic emission activity in sandstone: The effect of loading rate. *International Journal of Rock Mechanics and Mining Sciences*, 42:1094–1101.

Bazant, Z. and Kazemi, M. (1990). Determination of fracture energy, process zone length and brittleness number from size effect, with application to rock and concrete. *International Journal of Fracture*, 44:111–131.

Bazant, Z. P. and Yu, Q. (2011). Size-effect testing of cohesive fracture parameters and nonuniqueness of work-of-fracture method. *Journal of engineering mechanics*, 137(8):580–588.

Benson, P. M., Thompson, B. D., Meredith, P. G., Vinciguerra, S., and Young, R. P. (2007). Imaging slow failure in triaxially deformed etna basalt using 3d acoustic-emission location and x-ray computed tomography. *Geophysical research letters*, 34:L03303.

Blaber, J., Adair, B., and A., A. (2015). Ncorr: Open-source 2d digital image correlation matlab software. *Experimental Mechanics*, 55:1105–1122.

Bossart, P. and Thury, M. (2008). Characteristics of the opalinus clay at mont terri. Technical report, Swiss Geological Survey.

Brace, W. and Bombolakis, E. (1963). A note on brittle crack growth in compression. *Journal of Geophysical Research*, pages 3709–3713.

Bredehoeft, J., Wolff, R., Keys, W., and Shuter, E. (1976). Hydraulic fracturing to determine the regional stress field, piceance basin, colorado. *Geological Society of America Bulletin*, 87:250–258.

Brehm, D. and Braile, L. (1999). Intermediate-term earthquake prediction using the modified time-to-failure method in southern california. *Bulletin of the Seismoiogical Society of America*, 89(1):275–293.

Broek, D. (1985). *Elementary engineering fracture mechanics*, chapter The crack tip plastic zone, pages 91–114. Springer.

Bufe, C., Nishenko, S., and Varnes, D. (1994). Seismicity trends and potential for large earthquakes in the alaska-aleutian region. *Pure and Applied Geophysics*, 142(1):83–99.

Bui, M., Adjiman, C. S., Bardow, A., Anthony, E. J., Boston, A., Brown, S., Fennell, P. S., Fuss, S., Galindo, A., Hackett, L. A., Hallett, J. P., Herzog, H. J., Jackson, G., Kemper, J., Krevor, S., Maitland, G. C., Matuszewski, M., Metcalfe, I. S., Petit, C., Puxty, G., Reimer, J., Reiner, D. M., Rubin, E. S., Scott, S. A., Shah, N., Smit, B., Trusler, J. P. M., Webley, P., Wilcox, J., and Mac Dowell, N. (2018). Carbon capture and storage (ccs): the way forward. *Energy Environ. Sci.*, 11:1062–1176.

Bunger, A., Kear, J., Dyskin, A., and Pasternak, E. (2014). Interpreting post-injection acoustic emission in laboratory hydraulic fracturing experiments. In *48th US Rock Mechanics/Geomechanics Symposium*, pages 119–122.

Bunger, A. P., Jeffrey, R. G., and Detournay, E. (2005). Application of scaling laws to laboratory-scale hydraulic fractures. In *40th US Rock Mechanics/Geomechanics Symposium*, number 05-818.

Cappa, F., Scuderi, M. M., Collettini, C., Guglielmi, Y., and Avouac, J.-P. (2019). Stabilization of fault slip by fluid injection in the laboratory and in situ. *Science Advances*, 5(3).

Chang, C., Zoback, M., and Khaksar, A. (2006). Empirical relations between rock strength and physical properties in sedimentary rocks. *Journal of Petroleum Science and Engineering*, 51(3-4):223–237.

Chang, S. and Lee, C. (2004). Estimation of cracking and damage mechanisms in rock under triaxial compression by moment tensor analysis of acoustic emission. *International Journal of Rock Mechanics and Mining Sciences*, 41:1069–1086.

Chen, C.-S., Pan, E., and Amadei, B. (1998). Fracture mechanics analysis of cracked discs of anisotropic rock using the boundary element method. *International Journal of Rock Mechanics and Mining Science*, pages 195–218.

Cobain, S., Peakall, J., and Hodgson, D. (2015). Indicators of propagation direction and relative depth in clastic injectites: Implications for laminar versus turbulent flow processes. *Geological Society of America Bulletin*, 127:1816–1830.

Collins, D. S., Pettitt, W. S., and Young, R. P. (2002). High-resolution mechanics of a microearthquake sequence. *Pure and Applied Geophysics*, 159:197–219.

de Pater, C., Cleary, M., Quinn, T., Barr, D., Johnson, D., and Weijers, L. (1994). Experimental verification of dimensional analysis for hydraulic fracturing. *SPE Production and Facilities*, 9(4):230–238.

Dend, J., Wang, S., and Han, D. (2009). The velocity and attenuation anisotropy of shale at ultrasonic frequency. *Journal of Geophysics and Engineering*, 8(269).

Denis du Peage, V. (2017). Exploring mechanisms leading to large induced seismic events during hydraulic stimulations in engineering geothermal systems (egs) and hydrocarbon extraction. Master's thesis, Ecole Polytechnique Federale de Lausanne.

Di Benedetti, M. and Nanni, A. (2014). Acoustic emission intensity analysis for in situ evaluation of reinforced conrete slabs. *Journal of materials in civil engineering*, 26:6–13.

Dieterich, J. H. (1979). Modeling of rock friction: 1 experimental results and constitutive equations. *Journal of Geophysical Research*, 84(B5):2161–2168.

Dresen, G., Stanchits, S., and Rybacki, E. (2010). Borehole breakout evolution through acoustic emission location analysis. *International Journal of Rock Mechanics and Mining Sciences*, pages 426–435.

Drouillard, T. F. (1996). A history of acoustic emission. *Journal of Acoustic Emission*, 14(1):1–34.

Dugdale, D. (1960). Yielding of steel sheets containing slits. *Journal of the Mechanics and Physics of Solids*, 8(2):100–104.

Eberhardt, E., Stead, D., and Stimpson, B. (1999a). Quantifying progressive pre-peak brittle fracture damage in rock during uniaxial compression. *International Journal of Rock Mechanics and Mining Sciences*, 36:361–380.

Eberhardt, E., Stimpson, B., and Stead, D. (1999b). Effect of grain size on the initiation and propagation thresholds of stress-induced brittle fractures. *Rock mechanics and rock engineering*, 32(2):81–99.

Fakhimi, A. and Tarokh, A. (2013). Process zone and size effect in fracture testing of rock. *International Journal of Rock Mechanics and Mining Sciences*, 60:95–102.

Ferrill, D., Morris, A., and McGinnis, R. (2012). Extensional fault-propagation folding in mechanically layered rocks: The case against the frictional drag mechanism. *Tectonophysics*, 576-577:78–85.

Fialko, Y. (2015). *Treatise on Geophysics*, chapter Fracture and Frictional Mechanics: Theory. Elsevier, 2 edition.

Fortin, J., Stanchits, S., Dresen, G., and Gueguen, Y. (2009). Acoustic emissions monitoring during inelastic deformation of porous sandstone: Comparison of three modes of deformation. *Pure and Applied Geophysics*, 166:823–841.

Frash, L. (2014). *Laboratory-scale study of hydraulic fracturing in geterogeneous media for enhanced geothermal systems and general well stimulation*. PhD thesis, Colorado School of Mines.

Gale, J. F., Laubach, S. E., Olsen, J. E., Eichhubl, P., and Fall, A. (2014). Natural fractures in shale: A review and new observations. *AAPG Bulletin*, 98(11):2165–2216.

Gonçalves da Silva, B. and Einstein, H. (2018). Physical processes involved in the laboratory hydraulic fracturing of granite: Visual observations and interpretation. *Engineering Fracture Mechanics*, 191:125–142.

Gonçalves da Silva, B. and Einstein, H. H. (2014). Finite element study of fracture initiation in flaws subject to internal fluid pressure and vertical stress. *International Journal of Solids and Structures*, pages 177–204.

Gonçalves da Silva, B., Li, B. Q., Moradian, Z., Germaine, J., and Einstein, H. H. (2015). Development of a test setup capable of producing hydraulic fracturing in the laboratory with image and acoustic emission monitoring. In *49th U.S. Rock Mechanics/Geomechanics Symposium*.

Gonçalves da Silva, B. M. (2016). *Fracturing processes and induced seismicity due to the hydraulic fracturing of rocks*. PhD thesis, Massachusetts Institute of Technology.

Goodfellow, S., Nasseri, M., Maxwell, S., and Young, R. (2015). Hydraulic fracture energy budget: Insights from the laboratory. *Geophysical research letters*, 42:3179–3187.

Goodfellow, S. and Young, R. (2014). A laboratory acoustic emission experiment under in situ conditions. *Geophysical research letters*, 41:3422–3430.

Graham, C., Stanchits, S., Main, I. G., and Dresen, G. (2010). Comparison of polarity and moment tensor inversion methods for source analysis of acoustic emission data. *International Journal of Rock Mechanics and Mining Sciences*, pages 161–169.

Grosse, C. U. and Ohtsu, M. (2008). *Acoustic Emission Testing*. Springer.

Gutenberg, B. and Richter, C. (1954). *Seismicity of the Earth*. Princeton Press, 2 edition.

Hill, D. P. and Prejean, S. G. (2006). *Earthquake Seismology*, chapter Dynamic Triggering.

Hoek, E. (1969). *Rock Mechanics in Engineering Practice*, chapter Brittle Failure of Rock. John Wiley and Sons.

Hoek, E. and Brown, E. (1997). Practical estimates of rock mass strength. *International Journal of Rock Mechanics and Mining Sciences*, 34(8):1165–1186.

Hu, J., Fu, L., Wei, W., and Zhang, Y. (2018). Stress-associated intrinsic and scattering attenuation from laboratory ultrasonic measurements on shales. *Pure and Applied Geophysics*, 175(3):929–962.

Hudson, J., Pearce, R., and Rogers, R. (1989). Source type plot for inversion of the moment tensor. *Journal of Geophysical Research*, 94:765–774.

Irwin, G. (1958). *Elasticity and Plasticity*, chapter Fracture. Springer.

Ishida, T. (2001). Acoustic emission monitoring of hydraulic fracturing in laboratory and field. *Construction and Building Materials*, pages 283–295.

Josh, M., Esteban, L., Delle Piane, C., Sarout, J., Dewhurst, D., and Clennell, M. (2012). Laboratory characterisation of shale properties. *Journal of Petroleum Science and Engineering*, pages 107–124.

Kanamori, H. (2004). Quantification of earthquakes. *Nature*, 271:411–414.

Kanamori, H. and Brodsky, E. E. (2004). The physics of earthquakes. *Reports on progress in physics*, 67(1):1429–1496.

Kao, H., Wang, K., Dragert, H., Kao, J. Y., and Rogers, G. (2010). Estimating seismic moment magnitude (m_w) of tremor bursts in northern cascadia: Implications for the "seismic efficiency" of episodic tremor and slip. *Geophysical research letters*, 37:L19306.

Ke, C., Chen, C., and Tu, C. (2008). Determination of fracture toughness of anisotropic rocks by boundary element method. *Rock mechanics and rock engineering*, 41(4):509–538.

Khaksar, A., Griffiths, C., and McCann, C. (1999). Compressional- and shear-wave velocities as a function of confining stress in dry sandstones. *Geophysical Prospecting*, 47(4):487–508.

Kohli, A. H. and Zoback, M. D. (2013). Frictional properties of shale reservoir rocks. *Journal of geophysical research: Solid Earth*, 118:1–17.

Korsunsky, A. and Botvina, L. (2005). Defect population statistics near and far from a critical event. In *11th International Conference on Fracture 2005*.

Kusunose, K., Lei, X., Nishizawa, O., and Satoh, T. (1991). Effect of grain size on fractal structure of acoustic emission hypocenter distribution in granitic rock. *Physics of the earth and planetary interiors*, 67:194–199.

Kwiatek, G. and Ben-Zion, Y. (2013). Assessment of p and s wave energy radiated from very small shear-tensile seismic events in a deep south african mine. *Journal of Geophysical research: Solid earth*, 118:3630–3641.

Labuz, J., Shah, S., and Dowding, C. (1987). The fracture process zone in granite: evidence and effect. *International Journal of Rock Mechanics and Mining Sciences and Geomechanics*, 24(4):235–246.

Lei, X. and Ma, S. (2014). Laboratory acoustic emission study for earthquake generation process. *Earthquake Science*, 27(6):627–646.

Lei, X. and Satoh, T. (2007). Indicators of critical point behavior prior to rock failure inferred from pre-failure damage. *Tectonophysics*, 431(1-4):97–111.

Li, B. Q. (2015). Acoustic emissions in hydraulic fracturing of barre granite. Master's thesis, Massachusetts Institute of Technology.

Li, B. Q. and Du, J. (2019). A methodology for unstructured damped stress inversion of microseismic focal mechanisms. *Geophysics*, pages XX–XX. In preparation.

Li, B. Q. and Einstein, H. H. (2017). Comparison of visual and acoustic emission observations in a four point bending experiment on barre granite. *Rock Mechanics and Rock Engineering*, 1:2277–2296.

Li, B. Q. and Einstein, H. H. (2020). Direct and microseismic observations of hydraulic fracturing in barre granite and opalinus clayshale. *XX*, pages XX–XX. In preparation.

Li, B. Q., Gonçalves da Silva, B. M., and Einstein, H. H. (2019). Laboratory hydraulic fracturing of granite: Acoustic emission observations and interpretation. *Engineering Fracture Mechanics*, pages XX–XX. In press.

Li, B. Q., Moradian, Z., Gon çalves da Silva, B., and Germaine, J. T. (2015). Observations of acoustic emissions in a hydraulically loaded granite specimen. In *49th U.S. Rock Mechanics/Geomechanics Symposium*.

Lin, Q., Huina, Y., Biolzi, L., and Labuz, J. F. (2014). Opening and mixed mode fracture processes in a quasi-brittle material via digital imaging. *Engineering Fracture Mechanics*, 131:176–193.

Lipton, Z. C., Berkowitz, J., and Elkan, C. (2015). A critical review of recurrent neural networks for sequence learning. *CoRR*.

Liu, Q., Xu, X., Tsutomo, Y., and Akio, C. (2001). Mechanical properties of tgp granite in dependence on temperature and time. In *ISRM International Symposium - 2nd Asian Rock Mechanics Symposium*, Beijing, China.

Liu, Y. (2015). Fracture toughness assessment of shales by nanoindentation. Master's thesis, University of Massachusetts, Amherst.

Lockner, D. A., J.D., B., Kuksenko, V., Ponomarev, A., and Sidorin, A. (1991). Quasi-static fault growth and shear fracture energy in granite. *Nature*, pages 39–42.

Ludovico-Marques, M., Chastre, C., and Vasconcelos, G. (2012). Modelling the compressive mechanical behaviour of granite and sandstone historical building stones. *Construction and Building Materials*, 28:372–381.

Lund, B. and Slunga, R. (1999). Stress tensor inversion using detailed microearthquake information and stability constraints: application to olfus in southwest iceland. *Journal of Geophysical Research: Solid Earth*, 104:14947–14964.

Maeda, N. (1985). A method for reading and checking phase times in autoprocessing system of seismic wave data. *Journal of the Seismological Society of Japan*, 38:365–379.

Mair, K., Marone, C., and Young, R. P. (2007). Rate dependence of acoustic emissions generated during shear of simulated fault gouge. *Bulletin of the seismological society of America*, 97(6):1841–1849.

Matsunaga, I., Kobayashi, H., Sasaki, S., and Ishida, T. (1993). Studying hydraulic fracturing mechanism by laboratory experiments with acoustic emission monitoring. *International Journal of Rock Mechanics and Mining Sciences and Geomechanics Abstracts*, 30(7):909–912.

Maxwell, S. and Cipolla, C. (2011). What does microseismicity tell us about hydraulic fracturing? In *SPE Annual Technical Conference 2011*.

Mayr, S., Stanchits, S., Langenbruch, C., Dresen, G., and Shapiro, S. (2011). Acoustic emission induced by pore-pressure changes in sandstone samples. *Geophysics*, 76:MA21–MA32.

McLaskey, G. C. and Glaser, S. D. (2010). Hertzian impact: Experimental study of the force pulse and resulting stress waves. *Journal of acoustical society of America*, 128(3):1087–1096.

McLaskey, G. C. and Glaser, S. D. (2012). Acoustic emission sensor calibration for absolute source measurements. *Journal of Nondestructive Evaluation*.

McLaskey, G. C., Lockner, D. A., Kilgore, B. D., and Beeler, N. M. (2015). A robust calibration technique for acoustic emission systems based on momentum transfer from a ball drop. *Bulletin of the Seismological Society of America*, 105:257–271.

Michael, A. J. (1984). Determination of stress from slip data: faults and folds. *Journal of geophysical research*, 89(B13):11517–11526.

Mistras (2015). Data sheet for micro30s. `http://www.physicalacoustics.com/content/literature/sensors/Model_Micro30S.pdf`.

Moradian, O., Li, B., Morgan, S., Goncalves da Silva, B., Germaine, J., and Einstein, H. (2015). Acoustic emission characteristics of shale. In *ISRM 2015 Proceedings*, Montreal, Canada.

Moradian, Z., Ballivy, G., Rivard, P., Gravel, C., and Rousseau, B. (2010). Evaluating damage during shear tests of rock joints using acoustic emissions. *International Journal of Rock Mechanics and Mining Sciences*, 1:590–598.

Moradian, Z., Einstein, H. H., and Ballivy, G. (2016). Detection of cracking levels in brittle rocks by parametric analysis of the acoustic emission signals. *Rock Mechanics and Rock Engineering*, 1:785–800.

Morgan, S. and Einstein, H. (2017). Cracking processes affected by bedding planes in opalinus shale with flaw pairs. *Engineering Fracture Mechanics*, 176:213–234.

Morgan, S., Johnson, C., and Einstein, H. (2013). Cracking processes in barre granite: fracture process zones and crack coalescence. *International Journal of Fracture*, 180:177–204.

Morgan, S. P. (2015). *An Experimental and Numerical Study on the Fracturing Processes in Opalinus Shale*. PhD thesis, Massachusetts Institute of Technology.

Morgan, S. P., Li, B. Q., and Einstein, H. H. (2017). Effect of injection rate on hydraulic fracturing of opalinus clay shale. In *ARMA 51st US Rock Mechanics / Geomechanics Symposium*, San Francisco.

Muller, G. and Dahm, T. (2000). Fracture morphology of tensile cracks and rupture velocity. *Journal of geophysical research*, 105(B1):723–738.

Nasseri, M., Mohanty, B., and Young, R. (2006). Fracture toughness measurements and acoustic emission activity in brittle rocks. *Pure and applied geophysics*, 163:917–945.

Neimitz, A. and Aifantis, E. C. (1987). On the size and shape of the process zone. *Engineering Fracture Mechanics*, 26(4):491–503.

Nemat-Nasser, S. and Horii, H. (1982). Compression-induced nonplanar crack extension with application to splitting, exfoliation, and rockburst. *Journal of Geophysical Research*, pages 6805–6821.

Nur, A. and Simmons, G. (1969). The effect of saturation on velocity in low porosity rocks. *Earth and Planetary Science Letters*, 7(2):183–193.

Nygard, R., Gutierrez, M., Bratli, R. K., and Hoeg, K. (2006). Brittle–ductile transition, shear failure and leakage in shales and mudrocks. *Marine and petroleum geology*, 23(2):201–212.

Ohno, K., Kimitaka, U., Atsushi, U., and Masayasu, O. (2014). Fracture process zone in notched concrete beam under three-point bending by acoustic emission. *Construction and Building Materials*, pages 139–145.

Ohtsu, M. (1995). Acoustic emission theory for moment tensor analysis. *Research in Nondestructive Evaluation*, 6(3):169–184.

Ohtsu, M. (2000). Moment tensor analysis of ae and sigma code. *Acoustic Emission-Beyond the Millennium*, pages 19–34.

Olson, J. E. (2004). Predicting fracture swarms — the influence of subcritical crack growth and the crack-tip process zone on joint spacing in rock. *Geological Society, London, Special Publications*, pages 73–88.

Padin, A., Tutuncu, A. N., and Sonnenberg, S. (2014). On the mechanisms of shale microfracture propagation. In *SPE Hydraulic Fracturing Technology Conference*.

Pais, J. C. and Harvey, J. T. (2012). *Four point bending*. CRC Press.

Park, K. and Paulino, G. H. (2011). Cohesive zone models: A critical review of traction-separation relationships across fracture surfaces. *Applied Mechanics Reviews*, 64(6):1–20.

Pellet, F. L. and Fabre, G. (2007). Damage evaluation with p-wave velocity measurements during uniaxial compression tests on argillaceous rocks. *International journal of geomechanics*, 7(6):431–436.

Perol, T., Gharbi, M., and Denolle, M. (2018). Convolutional neural network for earthquake detection and location. *Science advances*, 4(2).

Reasenberg, P. and Simpson, R. (1991). Response of regional seismicity to the static stress change produced by the loma-prieta earthquake. *Science*, 255:1687–1690.

Rouchier, S., Foray, G., Godin, N., Woloszyn, M., and Roux, J.-J. (2013). Damage monitoring in fibre reinforced mortar by combined digital image correlation and acoustic emission. *Construction and building materials*, 38:371–380.

Ruina, A. (1983). Slip instability and state variable friction laws. *Journal of Geophysical Research*, 88(B12):10359–10370.

Sarris, E. and Papanastasiou, P. (2011). The influence of the cohesive process zone in hydraulic fracturing modelling. *International Journal of Fracture*, 167(1):33–45.

Savic, M., Cockram, M., and Ziolkowski, A. (1993). Ultrasonic monitoring of hydraulic fracturing experiments. In *155th EAEG Meeting*.

Sayers, C. and Kachanov, M. (1995). Microcrack-induced elastic wave anisotropy of brittle rocks. *Journal of geophysical research: Solid Earth*, 100(B3):4149–4156.

Schmidhuber, J. (2015). Deep learning in neural networks: an overview. *Neural networks*, 61:85–117.

Scholz, C. (1998). Earthquakes and friction laws. *Nature*, 391:37–42.

Shearer, P. M. (2009). *Introduction to Seismology*. Cambridge University Press.

Sileny, J., Hill, D. P., Eisner, L., and Cornet, F. H. (2009). Non-double-couple mechanisms of microearthquakes induced by hydraulic fracturing. *Journal of geophysical research*, 114:B08307.

Simpson, D. W. (1976). Seismicity changes associated with reservoir loading. *Engineering Geology*, 10:123–150.

Sone, H. and Zoback, M. D. (2013). Mechanical properties of shale-gas reservoir rocks — part 2: Ductile creep, brittle strength, and their relation to the elastic modulus. *Geophysics*, 78(5):393–402.

Stanchits, S., Desroches, J., Burghardt, J., Surdi, A., and Whitney, N. (2015). Rock fabric influence on hydraulic fracture propagation. In *Proceedings of 77th EAGE Conference and Exhibition*.

Stanchits, S., Fortin, J., Gueguen, Y., and Dresen, G. (2009). Initiation and propagation of compaction bands in dry and wet bentheim sandstone. *Rock Physics and Natural Hazards*, pages 846–868.

Stanchits, S., Mayr, S., Shapiro, S., and Dresen, G. (2011). Fracturing of porous rock induced by fluid injection. *Tectonophysics*, pages 129–145.

Stanier, S., Blaber, J., Take, W., and White, D. (2015). Improved image-based deformation measurement for geotechnical applications. *Canadian Geotechnical Journal*, 53:727–739.

Stoeckhert, F., Molenda, M., Brenne, S., and Alber, M. (2015). Fracture propagation in sandstone and slate – laboratory experiments, acoustic emissions and fracture mechanics. *Journal of Rock Mechanics and Geotechnical Engineering*, pages 237–249.

Tal, Y., Evans, B., and Mok, U. (2016). Direct observations of damage during unconfined brittle failure of carrara marble. *Journal of Geophysical Research: Solid Earth*, 121:1584–1609.

Tensi, H. M. (2004). The kaiser-effect and its scientific background. *Journal of Acoustic Emission*, 22:S1–S16.

Topic, J., Bartos, J., Kopecky, L., Seps, K., Pros, Z., and Trejbal, J. (2016). Cement composite reinforced with synthetic fibers: Comparison of three-point and four-point bending test results. *Applied Mechanics and Materials*, 827:332–335.

van den Ende, M., Chen, J., Ampuero, J., and Niemeijer, A. (2018). A comparison between rate-and-state friction and microphysical models, based on numerical simulations of fault slip. *Tectonophysics*, 733:273–295.

Vavrycuk, V. (2011). Tensile earthquakes: theory, modelling, and inversion. *Journal of Geophysical research: Solid Earth*, 116:B12320.

Vavrycuk, V. (2014). Iterative joint inversion for stress and fault orientation from focal mechanisms. *Geophysical journal international*, 199:69–77.

Vavrycuk, V. (2015). Moment tensor decompositions revisited. *Journal of Seismology*, 19(1):231–252.

Vermylen, J. and Zoback, M. D. (2011). Hydraulic fracturing, microseismic magnitudes, and stress evolution in the barnett shale. In *SPE Hydraulic Fracturing Technology Conference*, The Woodlands, Texas, USA.

Viegas, G., Urbanic, T., Baig, A., and von Lunen, E. (2015). Rupture dynamics and source scaling relations of microseismic hydraulic fractures in shale reservoirs. In *13th ISRM International Congress of Rock Mechanics*.

Wang, Q., Guo, Y., Yu, L., and Li, P. (2017). Earthquake prediction based on spatio-temporal data mining: an lstm network approach. *IEEE Transactions on emerging topics in computing*.

Wang, Y., Fu, H., Liang, T., Wang, X., Liu, Y., Peng, Y., Yang, L., and Tian, Z. (2015). Large-scale physical simulation experiment research for hydraulic fracturing in shale. In *SPE Middle East Oil and Gas Show and Conference 2015*.

Wang, Y. and Hu, X. (2017). Determination of tensile strength and fracture toughness of granite using notched three-point-bend samples. *Rock Mechanics and Rock Engineering*, 50(1):17–28.

Warpinski, N., Mayerhofer, M., Agrawal, K., and Du, J. (2013). Hydraulic-fracture geomechanics and microseismic-source mechanisms. *SPE journal*, 18(4):766–780.

Warpinski, N., Wolhart, S., and Wright, C. (2004). Analysis and prediction of microseismicity induced by hydraulic fracturing. *SPE journal*, 9(1):24–33.

Weinberger, R. (1999). Initiation and growth of cracks during dessication of stratified muddy sediments. *Journal of structural geology*, 21:379–386.

Wong, L. and Einstein, H. (2009a). Crack coalescence in molded gypsum and carrara marble: part 1 - macroscopic observations and interpretation. *Rock mechanics and Rock Engineering*, 42:475–511.

Wong, L. and Einstein, H. (2009b). Crack coalescence in molded gypsum and carrara marble: Part 2—microscopic observations and interpretation. *Rock Mechanics and Rock Engineering*, pages 513–545.

Wyss, M. and Brune, J. (1968). Seismic moment, stress and source dimensions for earthquakes in the california-nevada region. *Journal of Geophysical research*, 73:4681–4694.

Yoshimitsu, N. and Kawakata, H. (2011). Temporal changes in the q of broadband p waves transmitting through a fracturing westerly granite sample under triaxial compressive conditions. *Bulletin of the Seismological Society of America*, 101:421–426.

Yoshimitsu, N., Kawakata, H., and Takahashi, N. (2014). Magnitude -7 level earthquakes: A new lower limitof self-similarity in seismic scaling relationships. *Geophysical Research Letters*, 41:4495–4502.

Zhai, H., Chang, X., Wang, Y., Xue, Z., Lei, X., and Zhang, Y. (2017). Sensitivity analysis of seismic velocity and attenuation variations for longmaxi shale during hydraulic fracturing testing in laboratory. *Energies*, 10(9).

Zhang, J., Peng, W., Liu, F., Zhang, H., and Li, Z. (2016). Monitoring rock failure processes using the hilbert–huang transform of acoustic emission signals. *Rock Mechanics and Rock Engineering*, 49:427–442.

Zietlow, W. and Labuz, J. (1998). Measurement of the intrinsic process zone in rock using acoustic emission. *International Journal of Rock Mechanics and Mining Sciences*, 35(3):291–299.

Appendix A

AE setup details

A.1 Foreword

Hello dear reader, welcome to my user guide on how to operate the PAC data acquisition device and analyse AE. First of all, I am sorry. You have been roped into a terribly tedious and unnecessarily complicated procedure. Humour aside, I would like to sincerely offer you a forewarning that this guide will be confusing on the first few readthroughs - many different steps come together to acquire, and then analyse AE. This guide is intended only to provide nitty-gritty details on how I did AE during my PhD thesis - it should be read with the AEwin software open, and a strong cup of tea by your side. It will be easiest if you flip back and forth between this guide and the software, trying out each step as outlined. I assume you already know generally what AE are, why we do it, and have a basic theoretical understanding of the workflow. If not, please read at minimum *Chapter 02: Background* in this thesis, and the excellent textbook *Acoustic Emission Testing* by Ohtsu and Grosse. This guide should also be supplemented by the user manual from the manufacturer.

Most importantly, please find the "For future kids" folder to get you started:

https://drive.google.com/drive/folders/1NRZiW9YIx-hYFtbOEIRwElYYyz0VqnQU

In this folder you will find this guide, the manufacturer user manual, the installation files for the AEwin software, *Acoustic Emission Testing* by Ohtsu and Grosse, an example file *base_layout.lay*, as well as a number of MATLAB files for AE analysis. You are a brave soul for undertaking this task. Good luck.

A.2 Connecting AE equipment

Figures in this section show how equipment is connected.

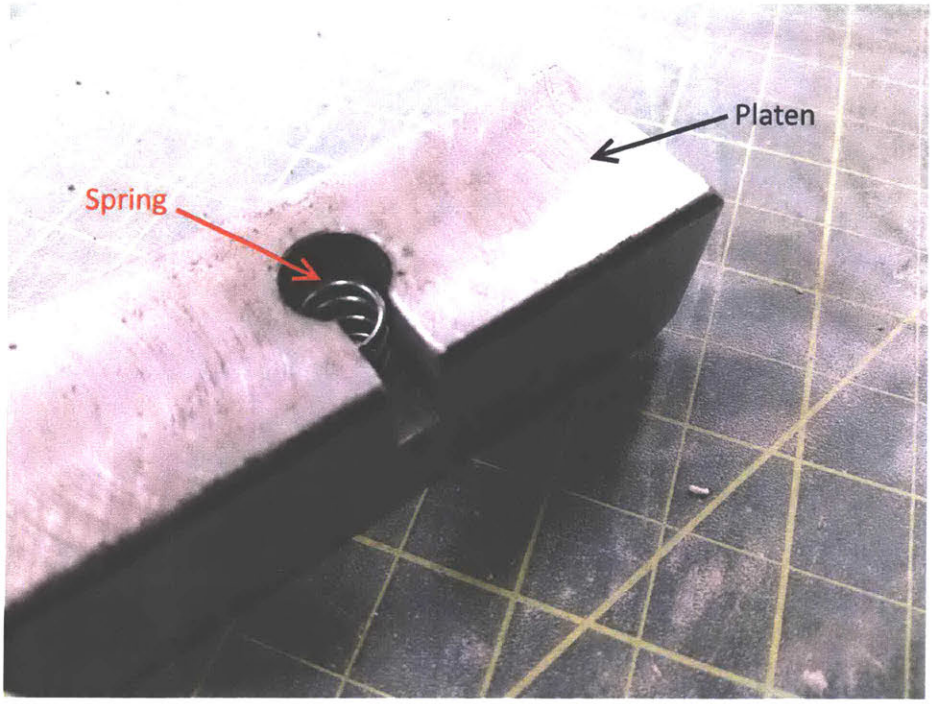

Figure A.1: Springs are inserted into each opening in the platen, so that the sensors press against the specimen.

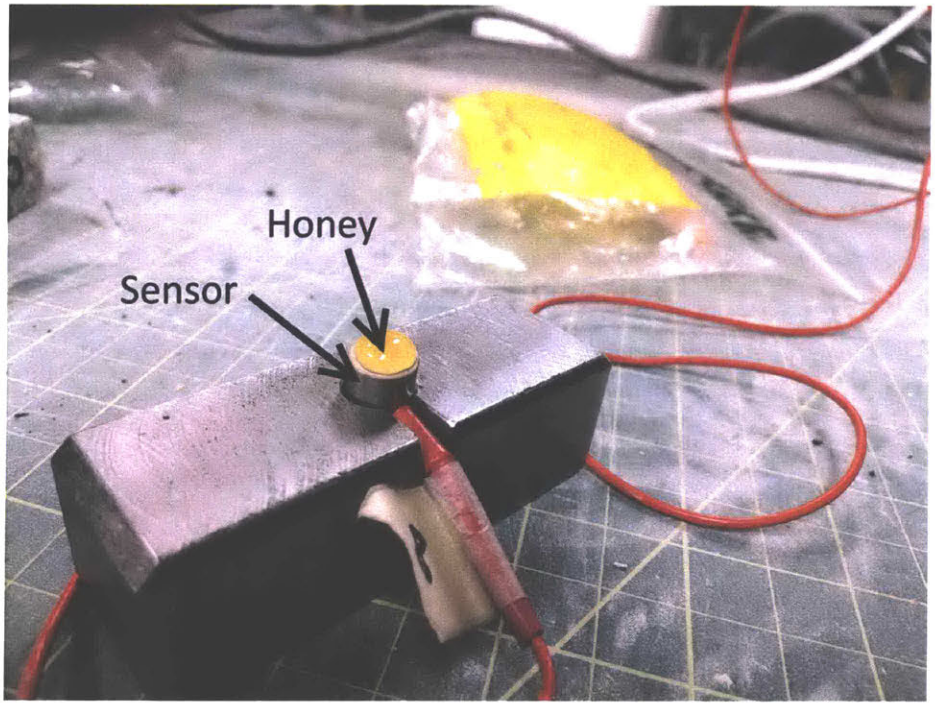

Figure A.2: Sensors go on top of the spring, and honey acts as couplant between rock and sensor.

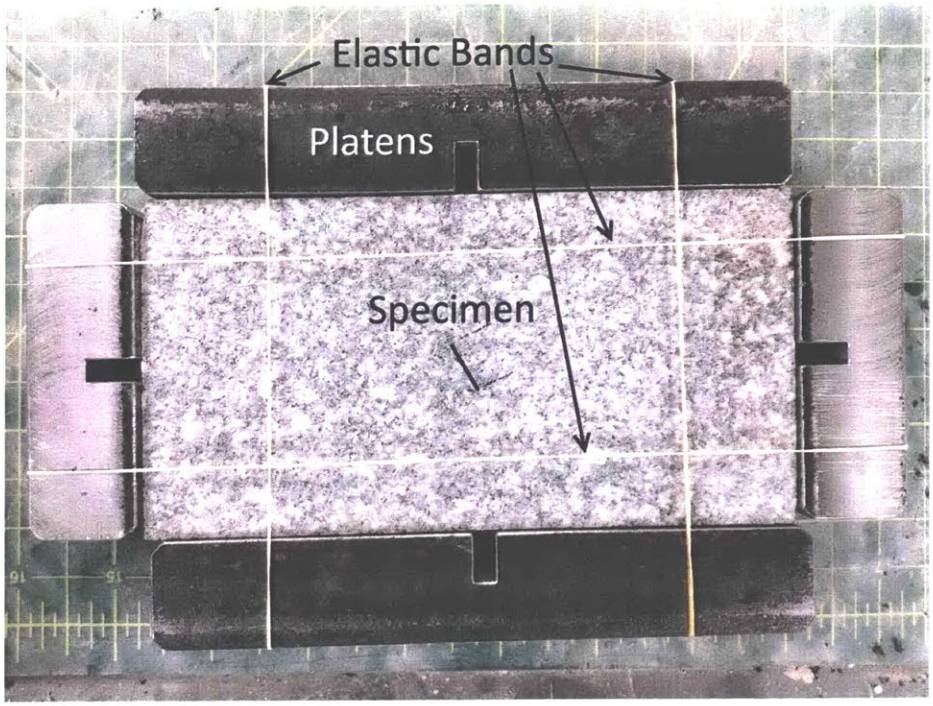

Figure A.3: Platens, with sensors in them, go around the specimen, and are temporarily held together with elastic bands. this entire assembly will go into the loading machine and/or hydraulic fracture enclosure.

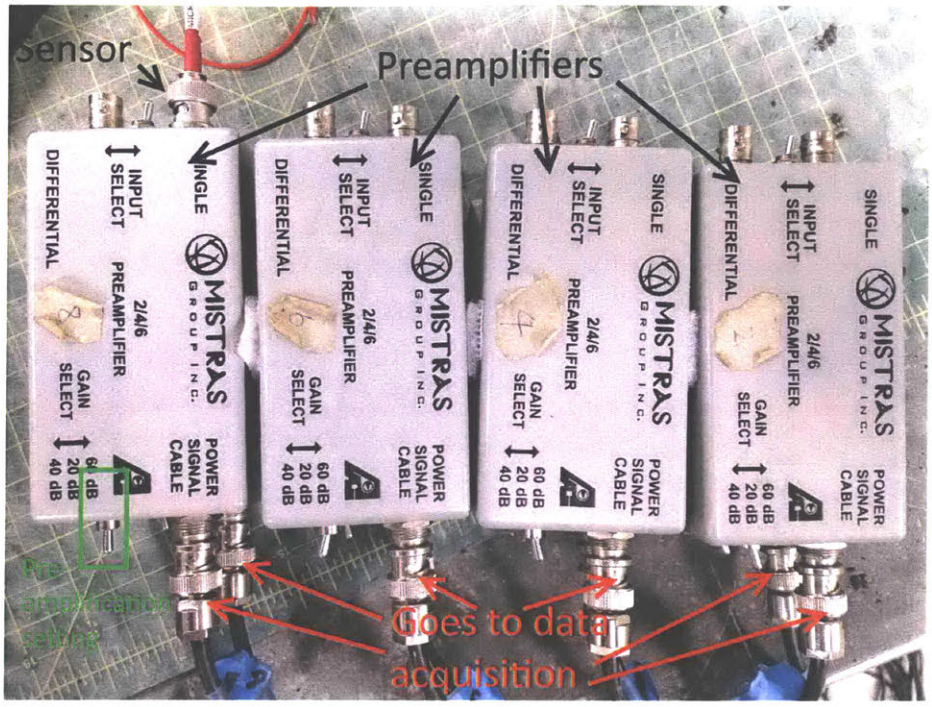

Figure A.4: Sensors connect to pre-amps, be sure to connect wires as shown here. 20dB for granite, 60dB for shale.

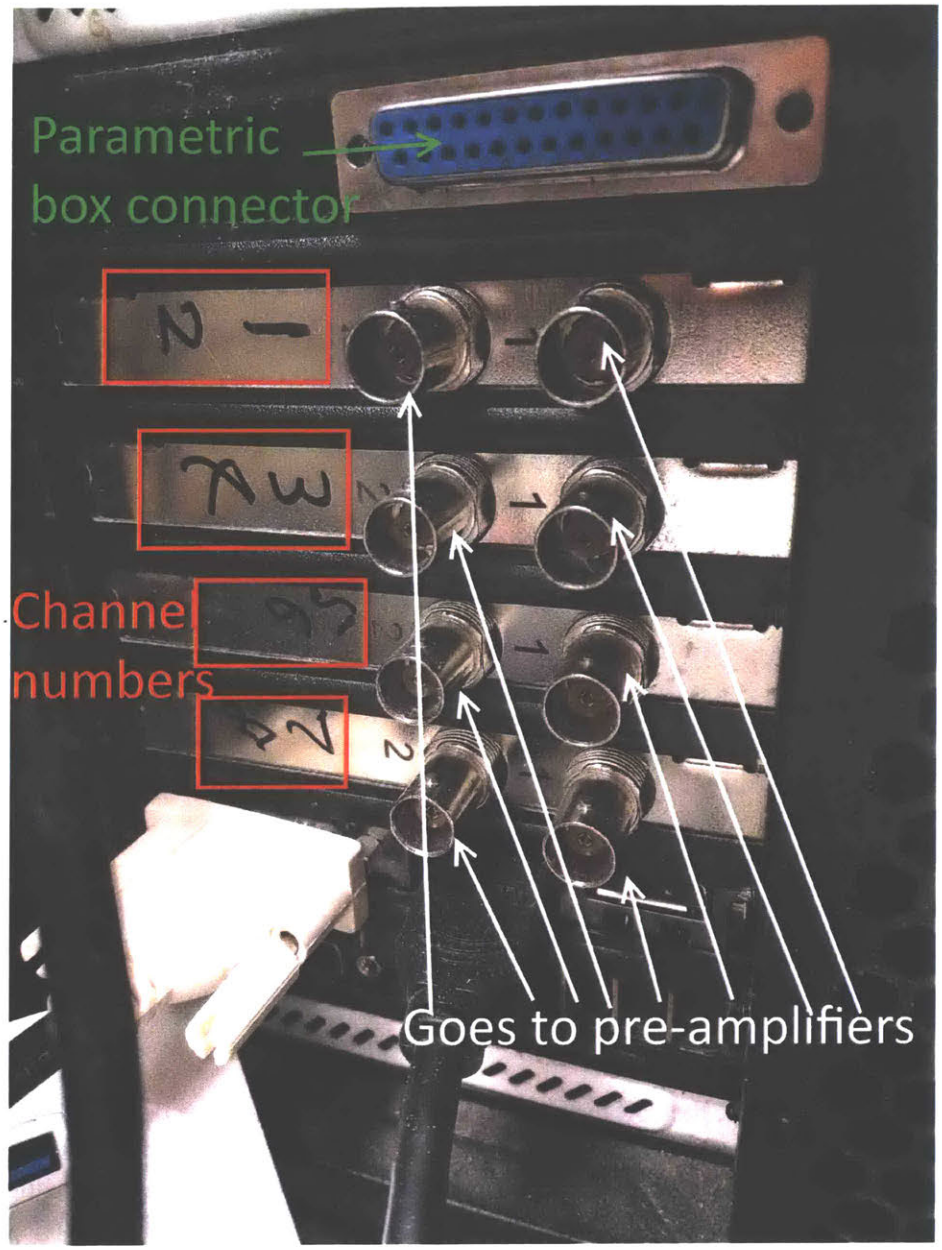

Figure A.5: BNC cables connect pre-amplifiers to data acquisition system. Parametric box also connectors to back to DAQ PC.

Figure A.6: To calibrate for moment magnitudes, set up all sensors, place 10cm straw vertically near center of specimen, drop ball in the straw and record the waveform. Repeat 10 or so times.

A.3 AEwin settings for acquiring data

Once the hardware is setup, the software must be configured to acquire data. All AE is acquired in the proprietary AEwin software, made by PAC, and data are stored in .dta files, which are also proprietary. Our goal is to only use AEwin to acquire data, and do everything else using MATLAB. Please pay careful attention to the screenshots in this guide, and to match the settings exactly.

The AEwin software can be found in the "For future kids" folder, in a subfolder called "AEwin software". Run setup.exe to install it. A blue USB key is required to run the AEwin software. One can begin acquiring data in AEwin by going to Acquire/Replay $->$ Acquire, which will create a .dta file that can be viewed by going to Acquire/Replay $->$ Replay. However, data acquisition should only start when the entire experiment is ready to go, and the settings are set correctly so that the only recorded waveforms correspond to the experiment itself. The settings are accessed at Acquisition setup $->$ AE hardware. If this is your first time, go to File $->$ Open layout and select the provided base_layout.lay file which has most of the common settings applied.

One of the first steps is to measure velocities. To do this, go to acquire $->$ AST, and select the output file location as shown below. For shale materials it is suggested to measure velocities along and across bedding planes as described in Figure A.8.

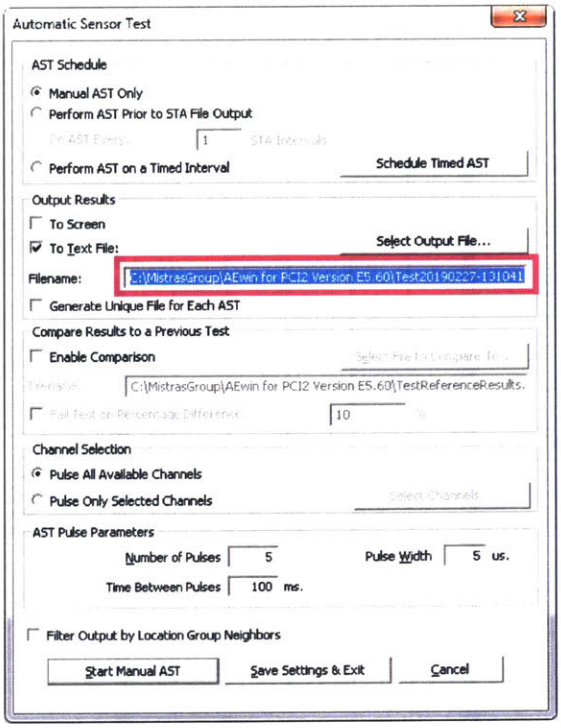

Figure A.7: Settings for measuring wave velocity. Select output file (boxed in magenta) to determine file location.

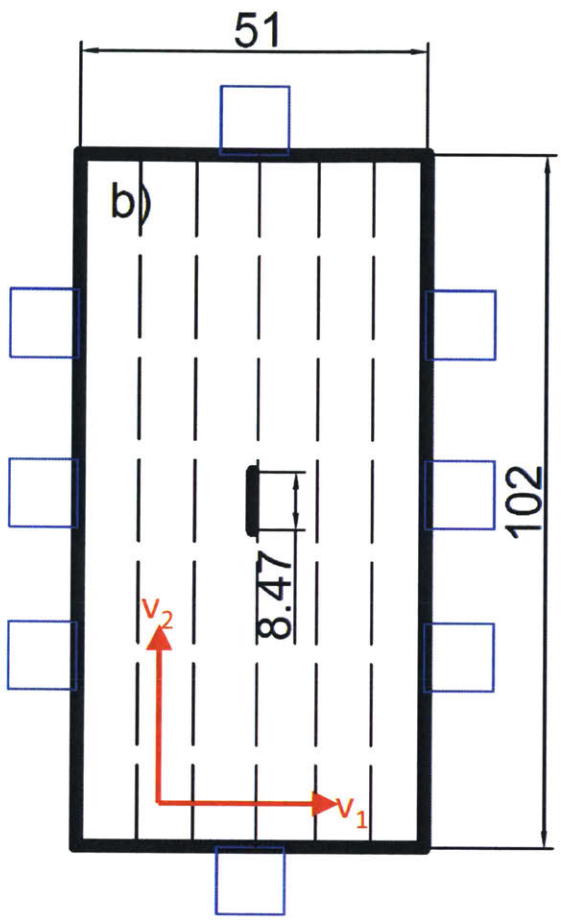

Figure A.8: Schematic of shale specimen, bedding planes in dashed lines. V1 and V2 refer to velocities across and along bedding planes respectively.

Figures A.9 to A.15 show settings to be used when acquiring AE data. Please replicate these settings exactly, except for settings in boxes which may need to be changed depending on the test.

Thresholds (Figure A.9) should be set to 40 dB by default, as this is generally above the typical electronic noise band. Adjust thresholds to higher levels if the following happens during a test.

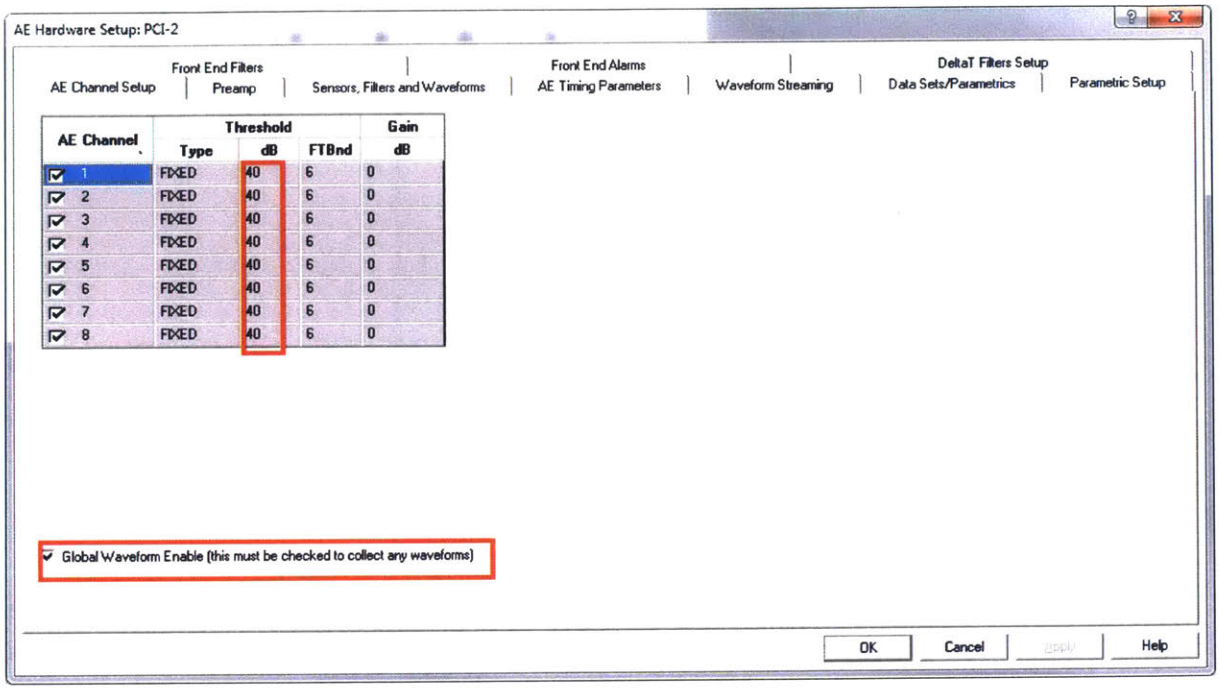

Figure A.9: Screenshot of settings to use in AE channel setup tab. Please ensure "Global waveform enable" is ticked to save waveforms.

Blue dotted line in "Amplitude vs time" plot (Figure A.10) indicates that at least one channel is always triggering, look at "hits vs channel" plot to see that channel 1 (blue dotted box) is the one constantly triggering, so adjust channel 1 threshold upwards. If the channel is left to trigger continuously, there will be lots of noise in the data, which is difficult to filter out and results in large files.

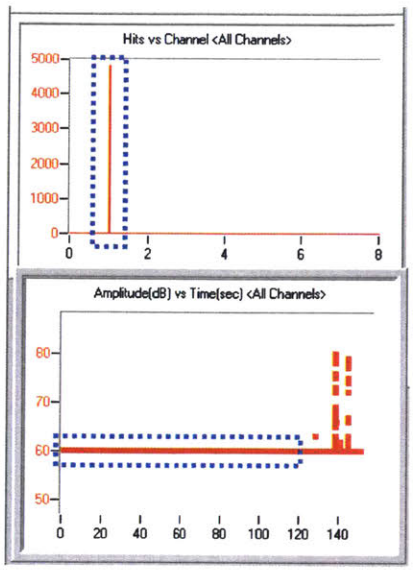

Figure A.10: Illustration of a test where channel 1 is recording ambient noise, as seen by the disproportional number hits on channel 1 (Top figure, blue dotted box), and the consistent hits occurring over time (Bottom figure, blue dotted box).

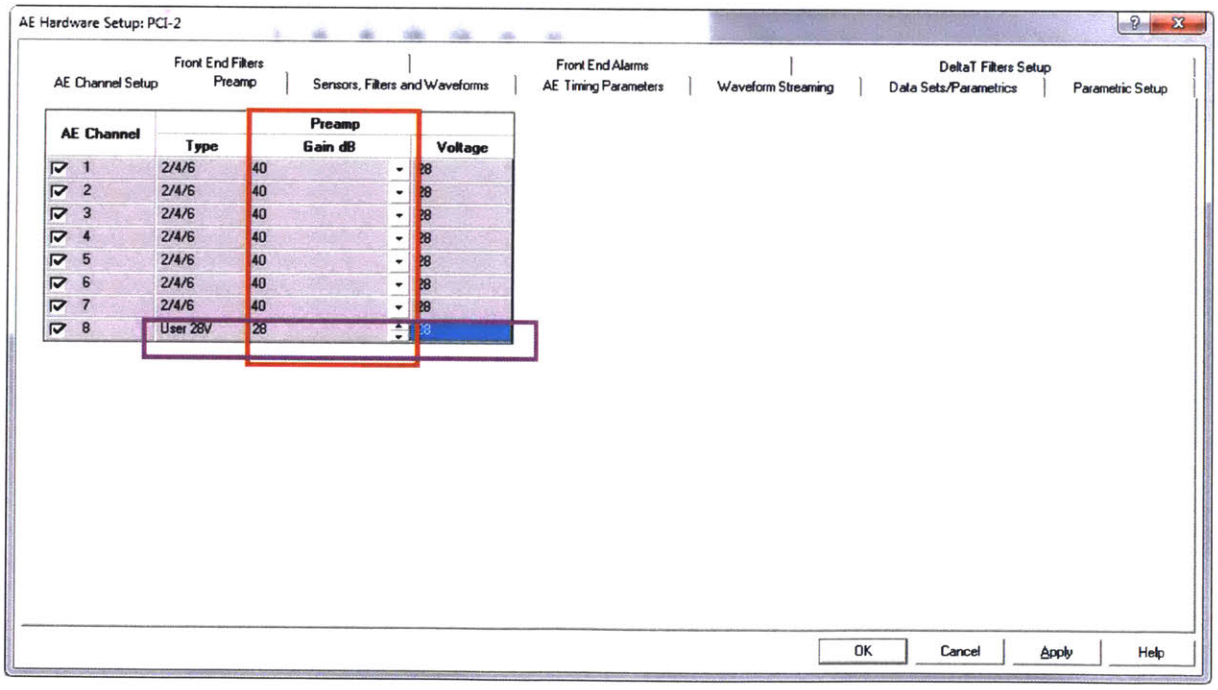

Figure A.11: Settings for pre-amplifiers. Purple box is the setting for Glaser sensor/pre-amps. Use same settings as channels 1-7 if PAC sensors/pre-amps are used.

Channel 8 (purple box) is for Glaser sensors (Section A.6), use same settings as channels 1-7 if using PAC sensors.

Figures A.12 and A.13 show settings that control how waveforms are saved. These do not need to be changed, the settings are chosen essentially to circumnavigate the inherent limitations of the acquisition system. Please refer to Li et al. (2015) and the PAC user manual for more information.

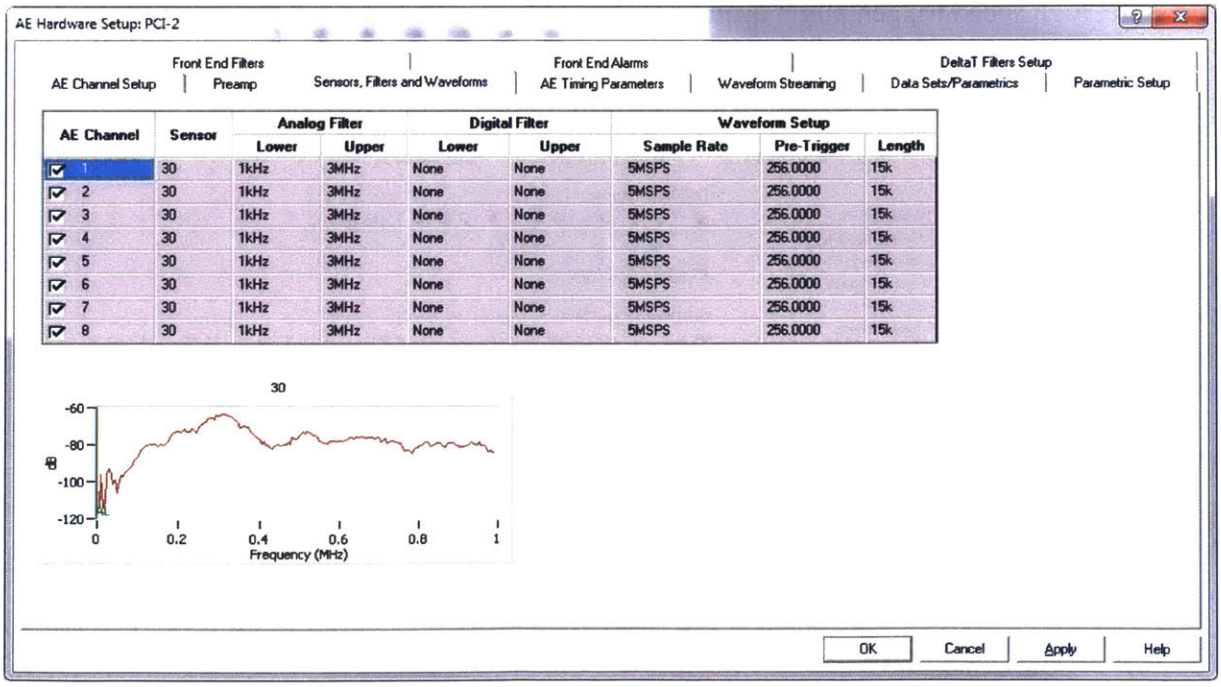

Figure A.12: Settings used for waveforms. Sample rate of 5 million samples per second (MSPS), pre-trigger of 256 us and file length of 15k (15000) have been empirically determined to be the most that the system can handle for long periods of time (Li et al., 2015).

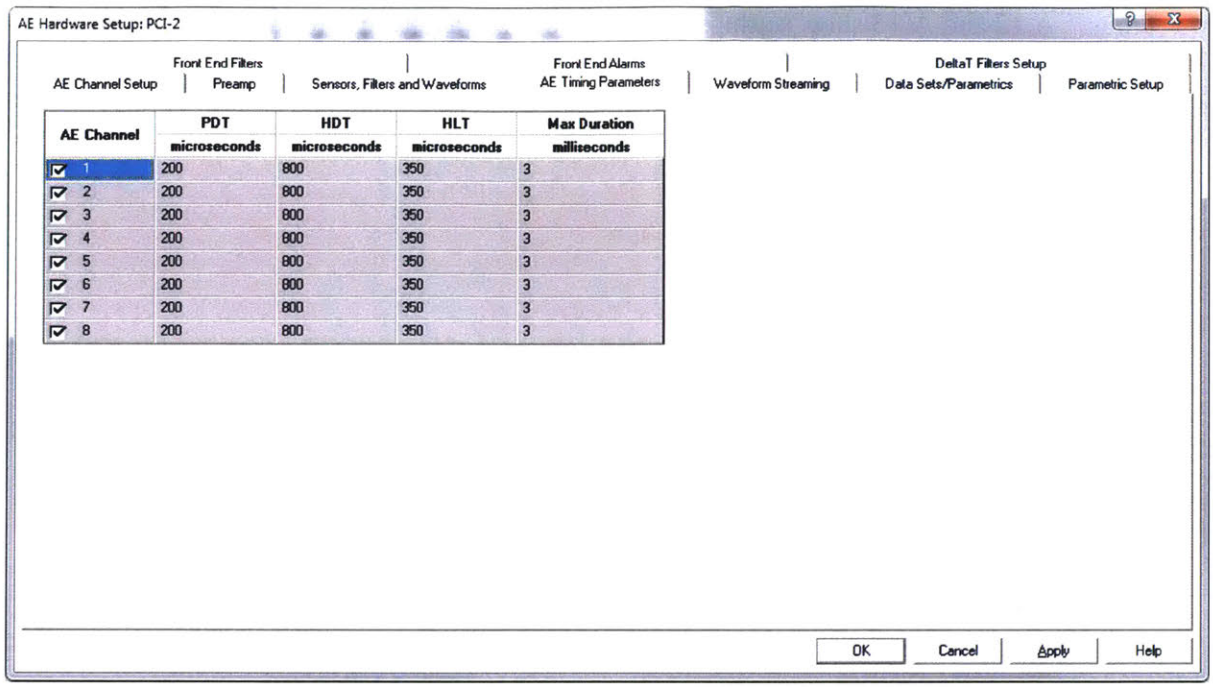

Figure A.13: Settings used for timing. Only HLT and max duration matter here.

Figures A.14 and A.15 show settings which control acquisition of external sensors such as pressure, high speed trigger, pump displacement, and load.

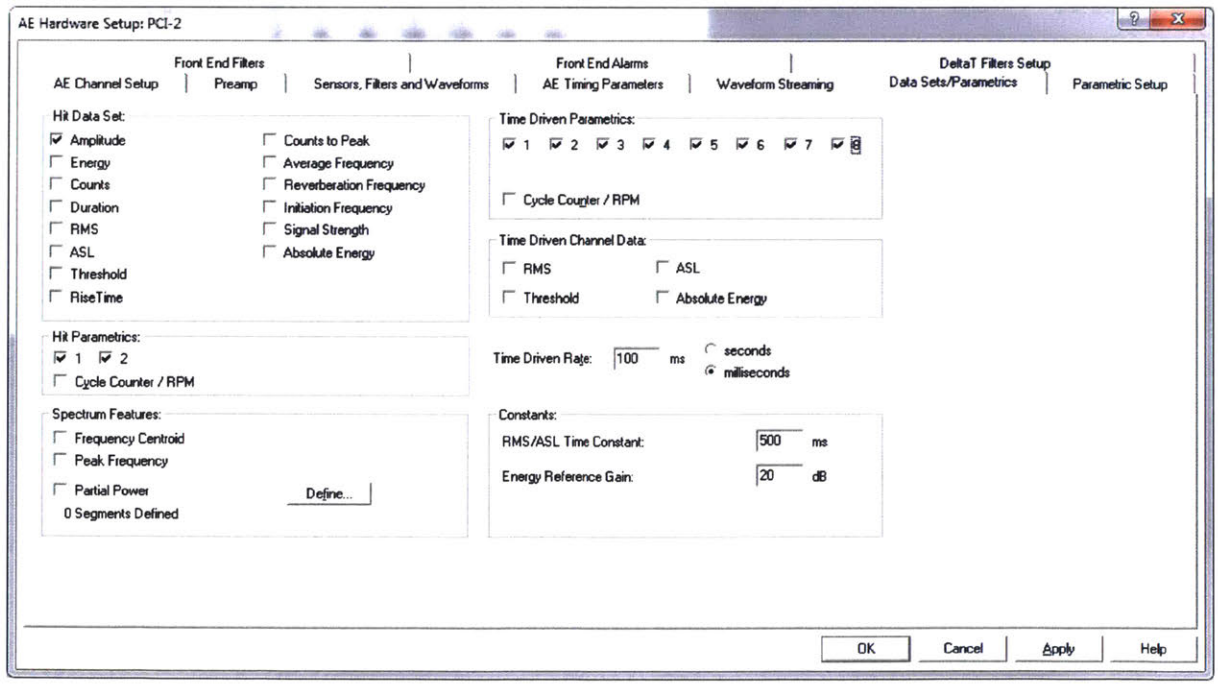

Figure A.14: Settings for parametrics window.

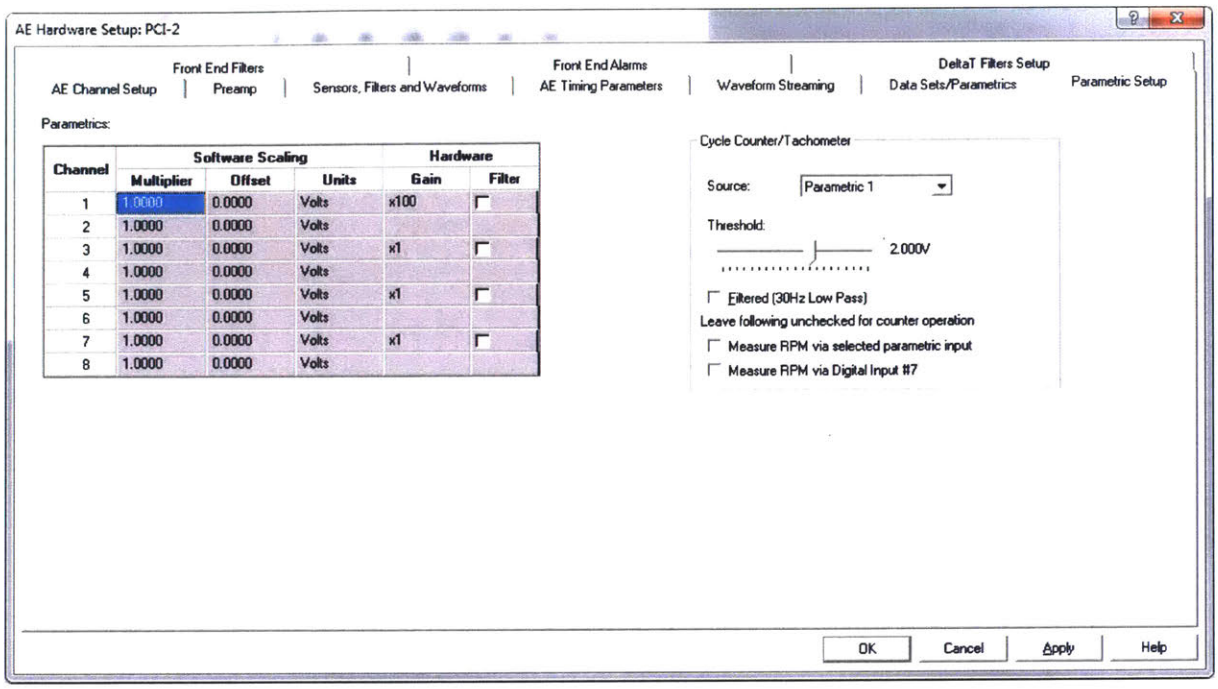

Figure A.15: Settings for second parametrics window. Gain is set to x100 on channel 1 as the pressure transducer, which has a small range, is on this channel.

Channel 1 gain is set to x100 for the pressure transducer which has a small voltage range, recorded voltages will be 100x higher than actual.

Sometimes, too much data are saved, for example when a channel is constantly triggered as in Figure A.10. In this case one can use a filter, for example removing all small amplitude events, or only select waveforms within a small time window. To filter hits by time, amplitude, etc, go to Utilities $->$ Data file filter. In the example below, only data between 50 to 100 dB in amplitude occurring between 150 to 250 seconds are included. Click run filter to use.

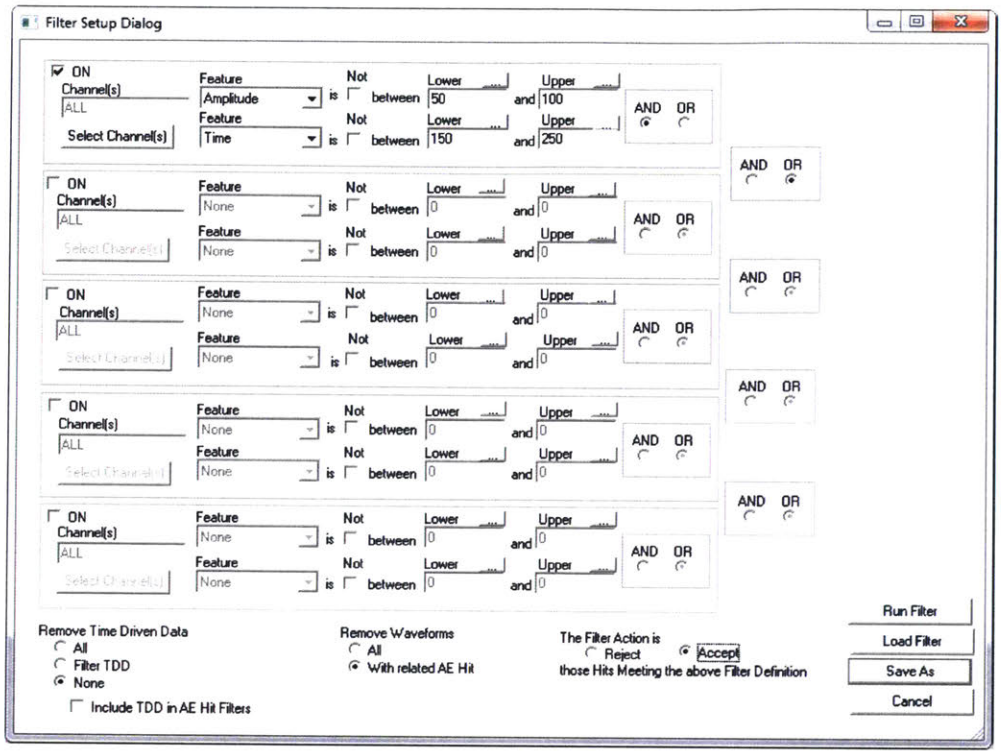

Figure A.16: Settings for filtering AE data within the PAC software. Usually used when a few channels capture noise (channel is constantly triggered, see Figure A.10), resulting in very large files. In this case, it is easiest to filter that channel by amplitude.

A.4 Analysing AE data

Once AE data are collected, one can then extract the data into a format that can be read externally, e.g. by MATLAB. To output the waveforms from AEwin (where they are contained in .dta files) to .csv files, go to Utilities $->$ ASCII waveforms, select the output folder and use the options below.

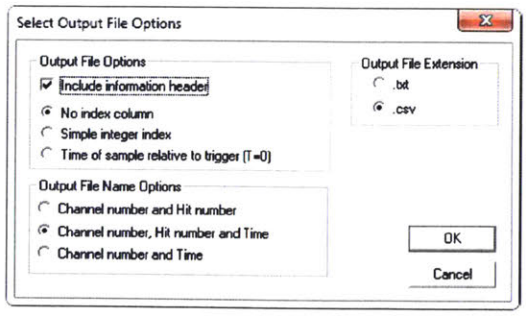

Figure A.17: Settings for exporting wavesforms to .csv files to be read into MATLAB.

Then run *One_lump_localise.m*, taking care to set the parameters accordingly.

A.5 MATLAB codes

Once AE data are extracted, a set of MATLAB codes are available to analyse the data. The *one_lump_localise.m* file contains code to first import AE waveforms generated by AEwin (Section A.4) into MATLAB, pick arrival times from these waveforms, locate AE events from these arrival times, and finally interpret moment tensors. Please note that many parameters are required for this process; these are specified in the beginning of the *one_lump_localise.m* file - be sure to correctly input each of these. Refer to Section 2.1.5 for the theoretical basis.

A.5.1 Ball drop magnitude calibration

ballDropCalib.m is for ball drop magnitude calibration. Users should already have recorded ball drop waveforms and performed the experiment using the same specific setup. Comments in the file should be sufficient to get started. Please refer to Section 2.1.4 for the theoretical basis of the calibration. Note: The calibration process is quite involved, please ensure you read the relevant literature before attempting.

A.6 Glaser sensors

The group has 1 Glaser-type sensor which has a flatter frequency response, making it easier to calibrate to actual displacement. Glaser sensors and pre-amps look like this:

Figure A.18: Photograph of Glaser sensor and accompanying pre-amplifier.

To use Glaser sensor with our PAC system, we need to change the pre-amp voltage from 0V to 28V like so:

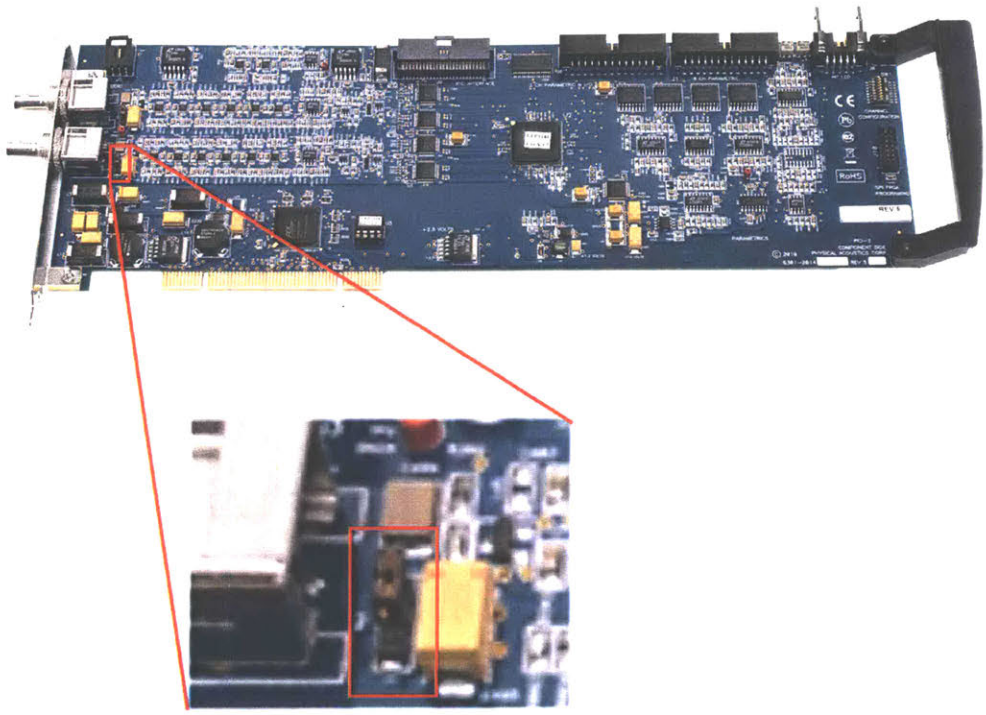

Figure A.19: To use the Glaser sensor with the PAC PCI-2 acquisition card, please change the position of the bridge on the acquisition card as shown in the red box in the inset.

The inset photo shows a connector that bridges pin 1 and pin 2 for PAC pre-amps (all the other cards will be like this). For glaser sensor/pre-amp, switch the connector to bridge pin 2 and pin 3.

A.7 Parametric connector box

This box is used to connect external channels such as pressure, high speed trigger, load to the AE system so that these are synchronised to the AE data. The *base_layout.lay* file is configured such that Channel 1 is pressure, channel 2 is high speed video, and the remaining channels can be allocated in any way.

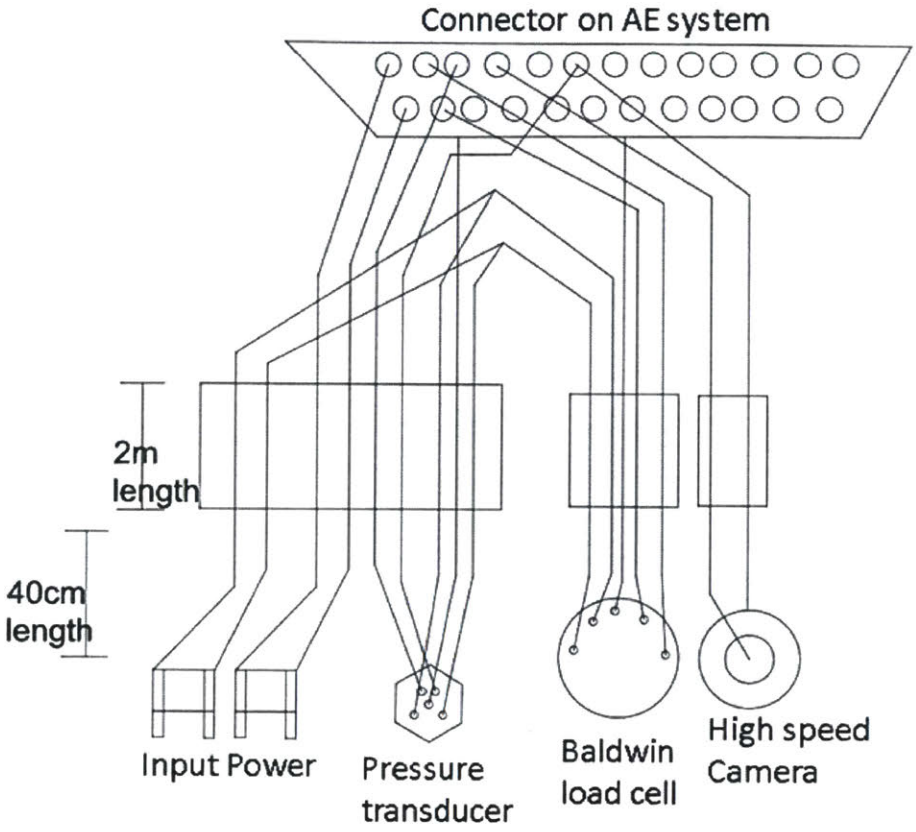

Figure A.20: Wiring of the parametric adapter box to use outside sensors (LVDT, pressure, load, high speed trigger) to be saved into the AE data acquisition. This is important when the outside data need to be synchronised to the AE.

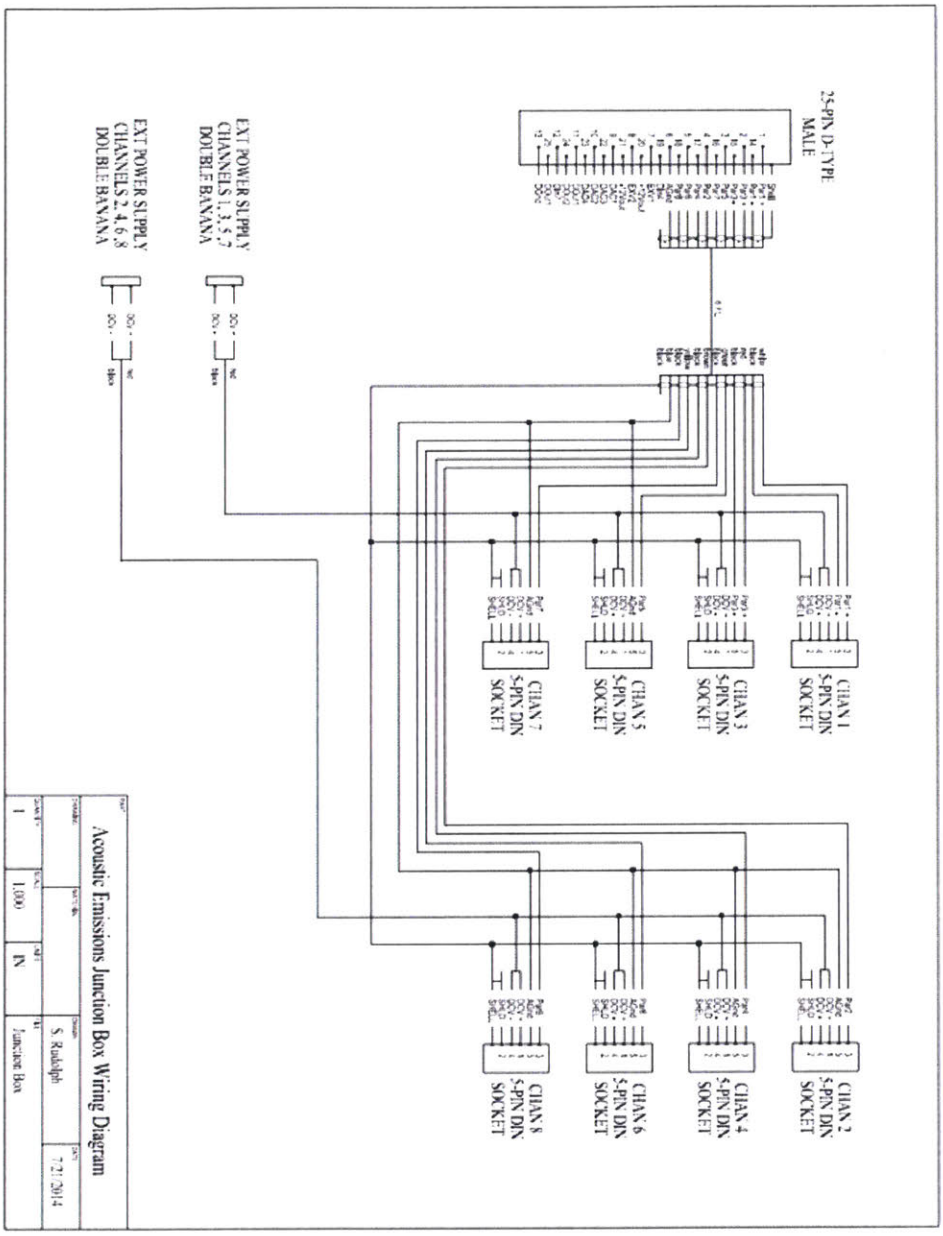

Figure A.21: Detailed wiring diagram of the parametric adapter box.

Pin #	Function	Description
1	+ Parametric #1 Input	+ Differential Input +/- 10 volts
2	+ Parametric #3 Input	+ Differential Input +/- 10 volts
3	Parametric #5 Input	Single Ended Input +/- 10 volts
4	Parametric #2 Input	Single Ended Input +/- 10 volts
5	Parametric #6 Input	Single Ended Input +/- 10 volts
6	Analog Ground	Analog Ground for Parametrics
7	EXEC_VOLTAGE1	
8	EXEC_VOLTAGE2	
9	RMS - DAC Out 1	RMS Analog Output
10	RMS - DAC Out 2	RMS Analog Output
11	Digital Output 1. **Alarm Warning Out**	Active High TTL Output
12	Digital Input 7	Spare TTL Level Input
13	Digital Ground	Digital Ground
14	- Parametric #1 Input	- Differential Input +/- 10 volts
15	- Parametric #3 Input	- Differential Input +/- 10 volts
16	Parametric #7 Input	Single Ended Input +/- 10 volts
17	Parametric #4 Input	Single Ended Input +/- 10 volts
18	Parametric #8 Input	Single Ended Input +/- 10 volts
19	Digital Input 4. Inhibit All AE Channels	Active Low TTL level input
20	+12 volt power out	+12 volt power out
21	- 12 volt power out	- 12 volt power out
22	RMS - DAC Out 3	RMS Analog Output
23	RMS - DAC Out 4	RMS Analog Output
24	Digital Output 2. **Alarm Trip Out**	Active High TTL Output
25	Digital Input 1. **Test Start Signal**	Active High TTL Input
26	N/C	N/C

Figure A.22: List of pins on the parametric adapter box. Refer to Figure A.21 for the wiring diagram.

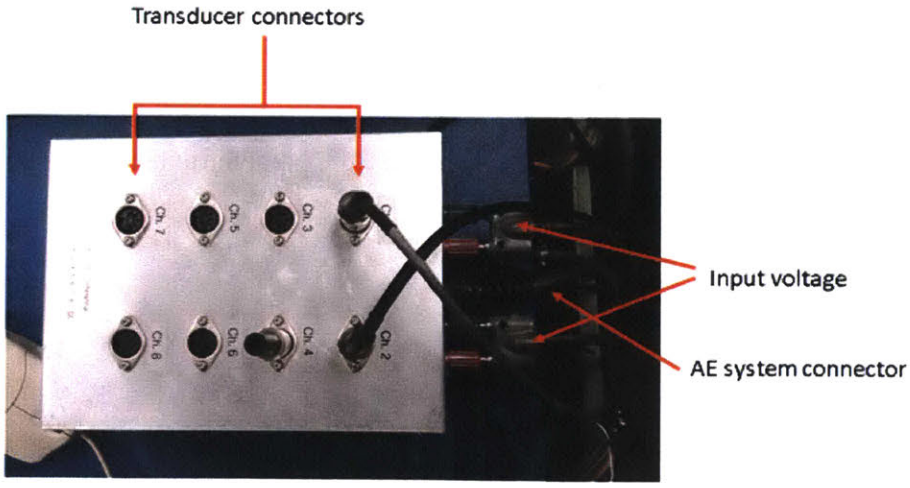

Figure A.23: Photo of the parametric adapter box. Wiring and pins are listed in previous 2 figures.

To get parametric data out of the AEwin file, go to Utilities $->$ ASCII output.

Appendix B

Other tests

B.1 Notched Brazilian Test on Opalinus

A test was conducted on a 3" diameter x 1" thickness pre-notched disk of Opalinus, results are shown in the following figures. The main conclusion is that very few AE events are detected in this test geometry.

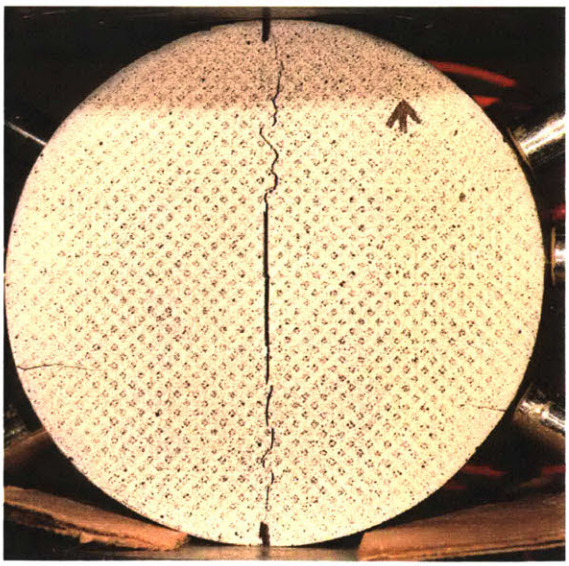

Figure B.1: Photograph of fractured notch Brazilian test on Opalinus clayshale.

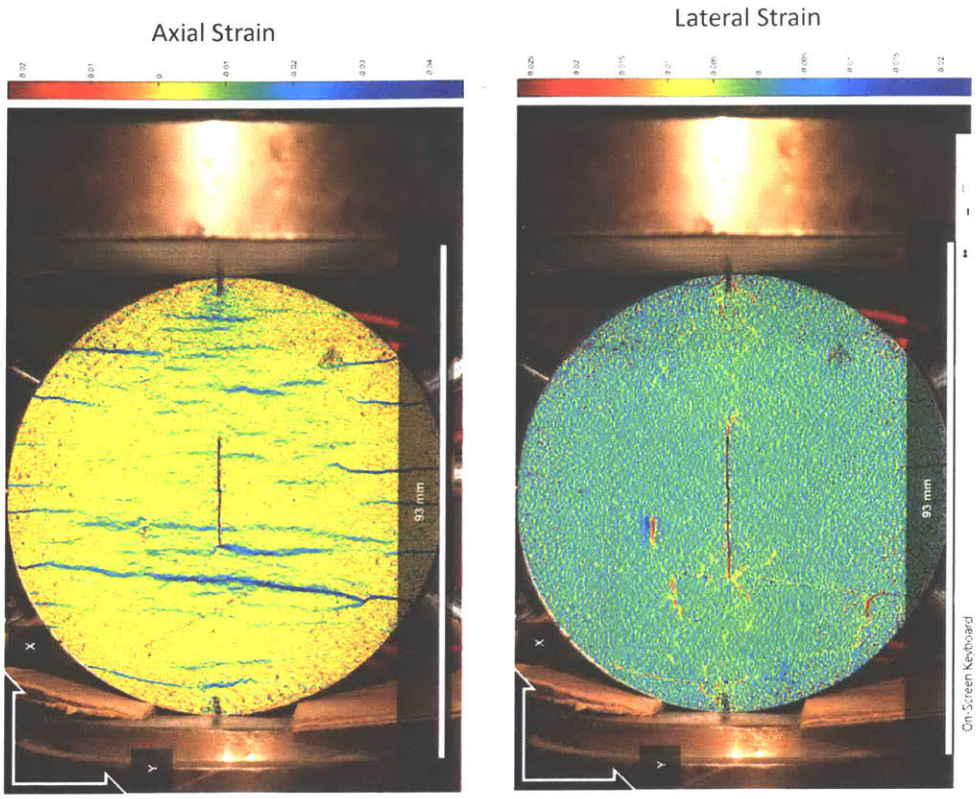

Figure B.2: Strain maps of fractured notch Brazilian test on Opalinus clayshale. Significant bedding plane compression can be seen in the axial strain.

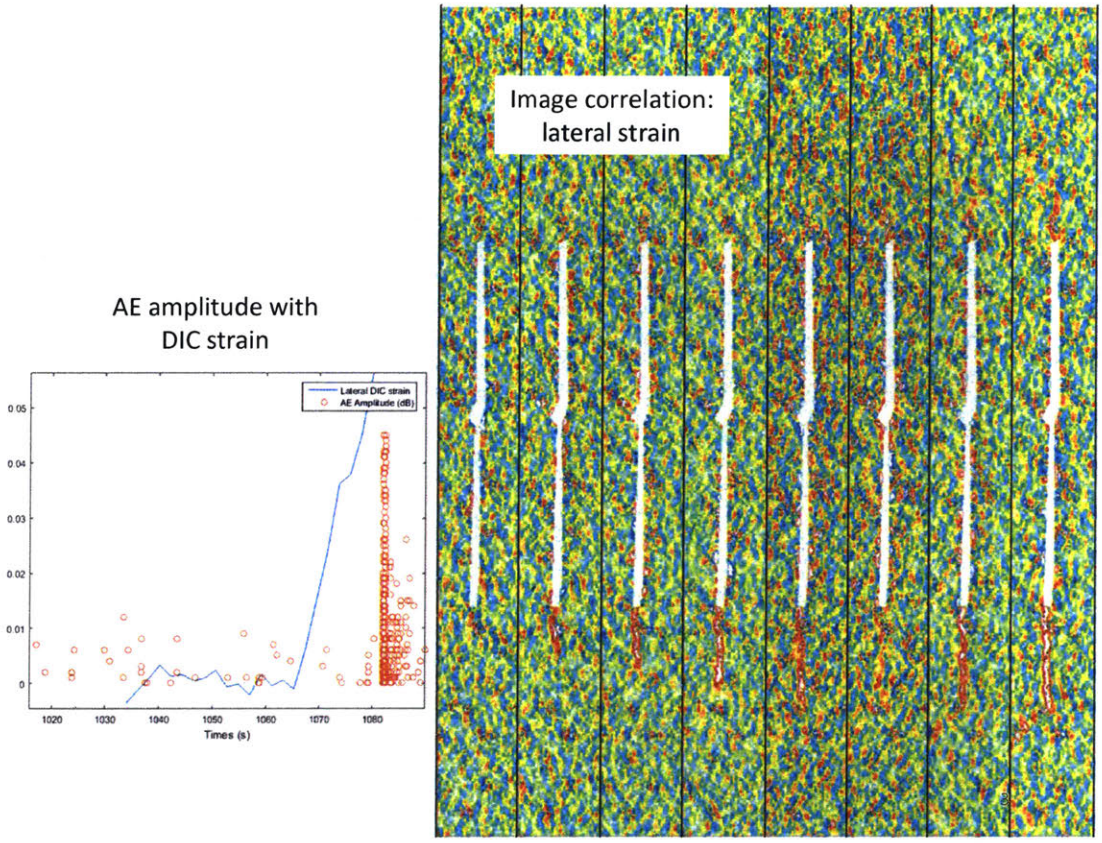

Figure B.3: AE and DIC strain over time of fractured notch Brazilian test on Opalinus clayshale. We can see that the AE events relate mostly to the end of the test, when the crack initiates and propagates.

B.2 HF on small specimen

A hydraulic fracturing test was done on a small 1.5 cm x 3 cm specimen of Opalinus clayshale to determine if the low number of detected AE events in the larger specimens were due to attenuation in the material. If attenuation is the cause of the low number of AE, then many more hits should be detected in the smaller specimen test since the distance between the crack and the sensor is smaller, and so attenuation is minimised. This was not the case, as the test showed that the number of detected hits was similar between the larger (140 hits detected) and smaller (130 hits detected) specimens, so we conclude that the low number of events is not due to attenuation. Details are provided below.

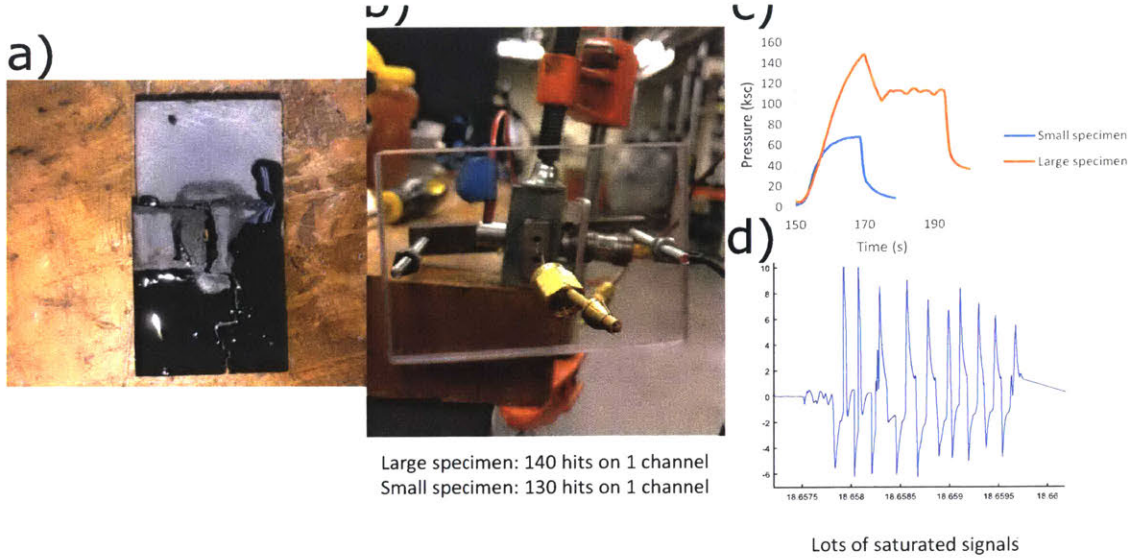

Figure B.4: a) Photograph of small shale HF specimen, b) photograph of the setup, c) pressure-time curves of the large and small specimen tests, d) sample AE waveform showing that the amplitude of displacement is larger than the voltage range of the acquisition system, and so many more smaller amplitude events should be detected if they were produced.

Appendix C

Detailed analysis of granite hydraulic fracture tests

AE hypocenter analysis for specimen 2a-30-0-VL0-B

Final crack geometry:

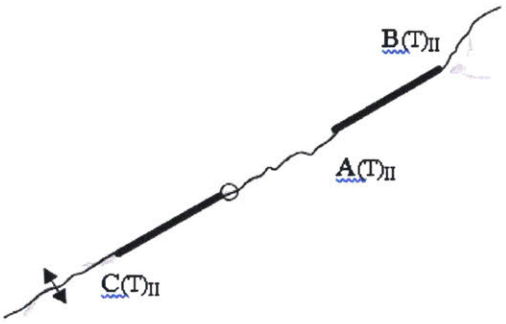

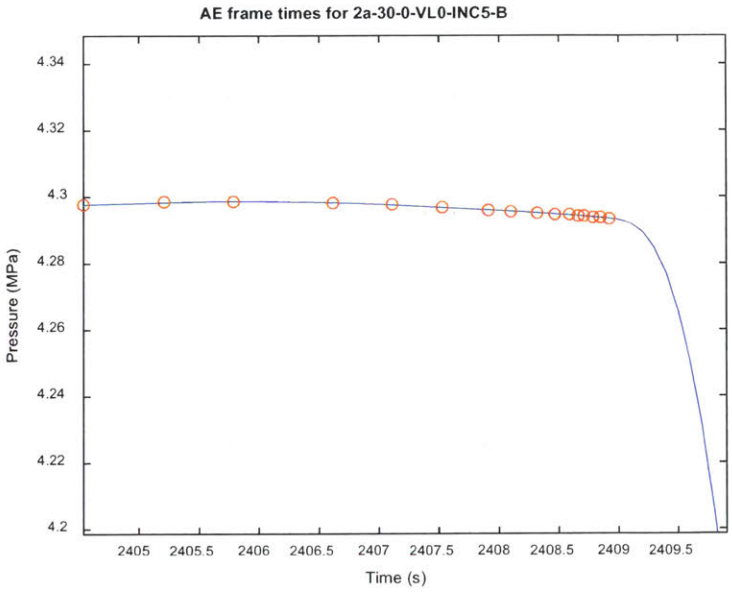

Crack initiates from inner tip of right flaw and coalesces directly, followed by opening of outer tip of the right flaw and finally the outer tip of the left flaw. Peak pressure occurs around 2406 s.

Development of AE locations are shown over the 20 frames presented in this analysis, where each frame shows 5% of the total number of events recorded during the test. This means that initially the frames will cover a long time period since few AE occurred at the beginning, while towards failure each frame will only cover fractions of a second since AE occur at a rapid rate.

Events with greater than 50% CLVD (compensated linear vector dipole) are considered shear type events and are marked with an 'x', while events with less than 50% CLVD are considered tensile and marked with 'o'. For those events detected by 4 sensors, it is not possible to invert the moment tensor and so these events are marked as undefined with '.'. The colour of an event indicates its relative magnitude, where red is the largest. Black ellipses are used to highlight areas of interest.

Where possible, AE frames are shown next to the appropriate analysis sketch from Bruno. However, these tend to be few in between and as discussed, the high speed frames tend to occur after the end of detectable AE events.

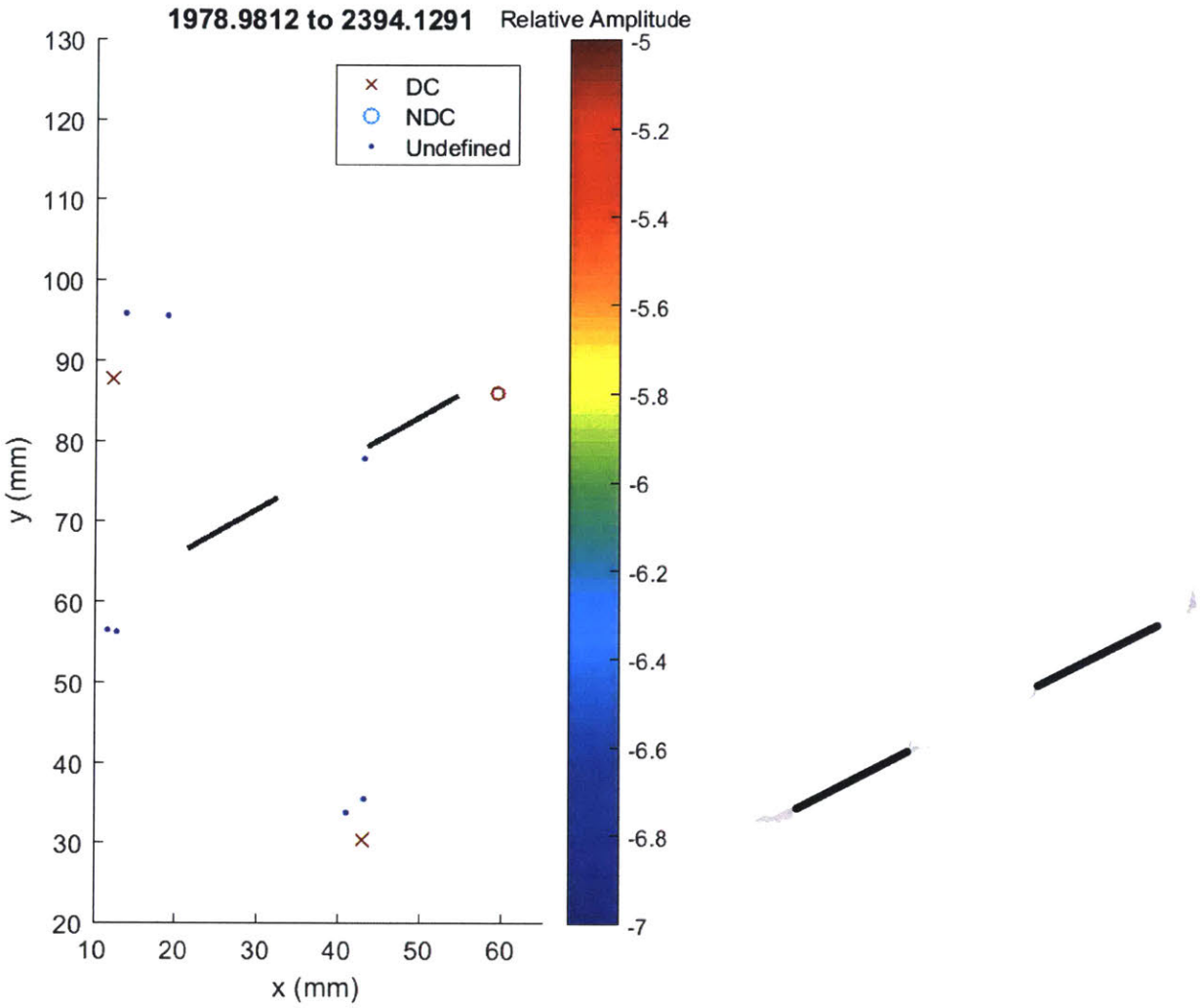

Early stages of the test covering approximately 400 seconds, AE locations are generally diffuse. Visually, white patching begins to occur at all flaw tips.

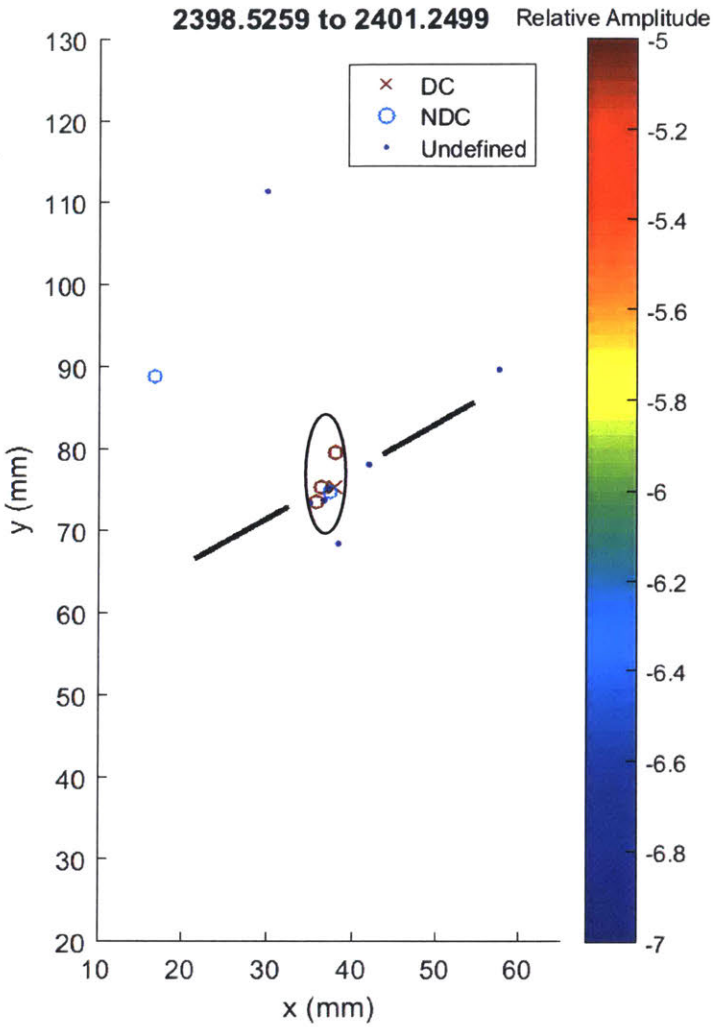

AE hypocenters cluster in coalescence zone. Four large amplitude events are detected: 1 shear, 3 tensile.

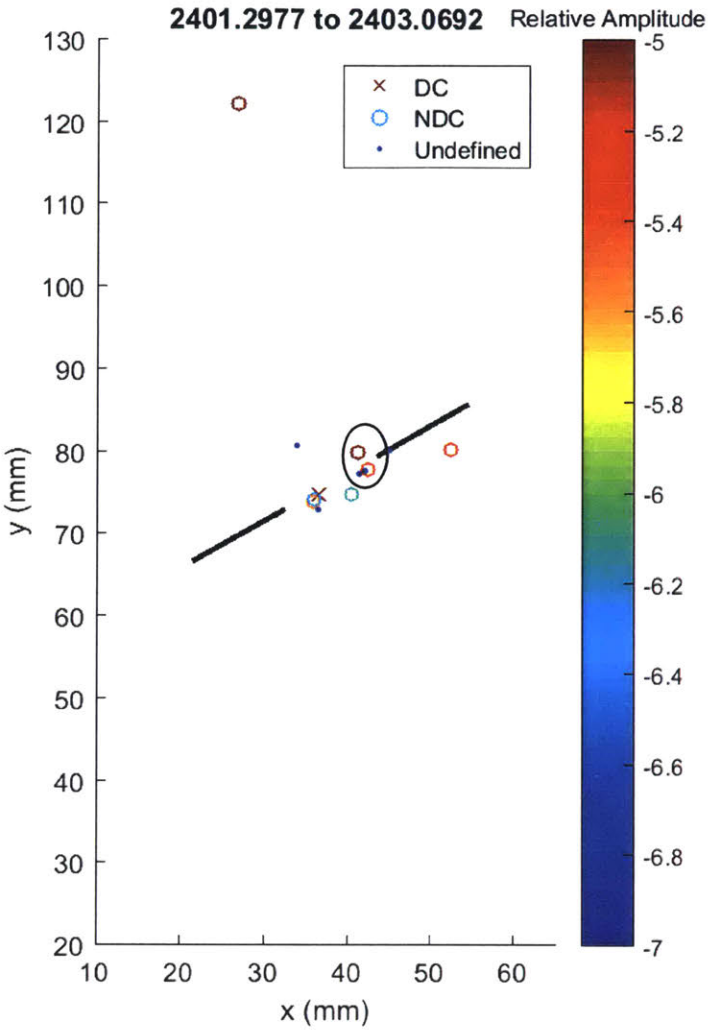

Continued AE concentration in coalescence zone. Large amplitude tensile events concentrated on right flaw, particularly at the inner tip.

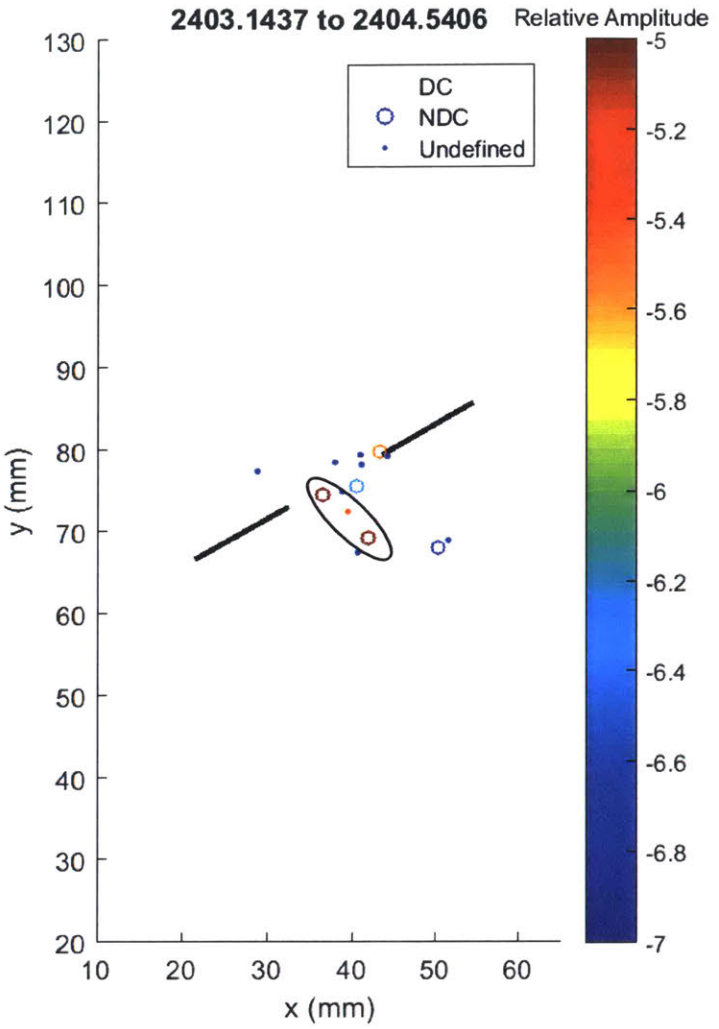

AE hypocenter locations spread out more vertically, and three large amplitude events form in the coalescence zone, normal to the flaw orientations. No shear events are detected.

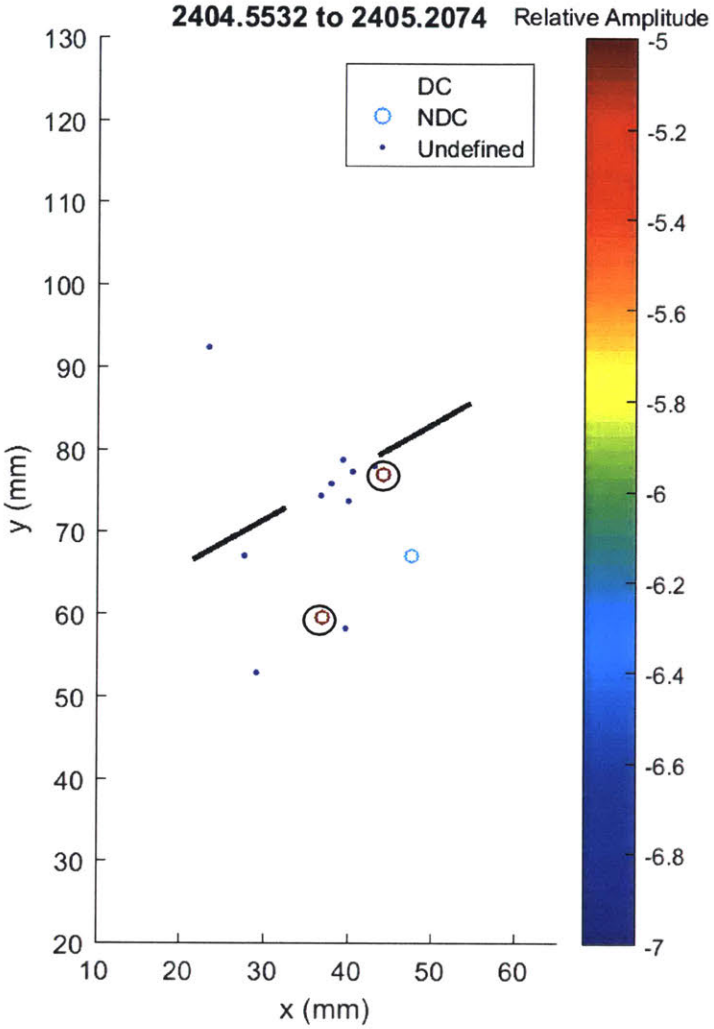

Undefined events mostly cluster in the coalescence zone, but again there is are 2 larger amplitude tensile events: one at the inner right flaw tip, and another below the flaws.

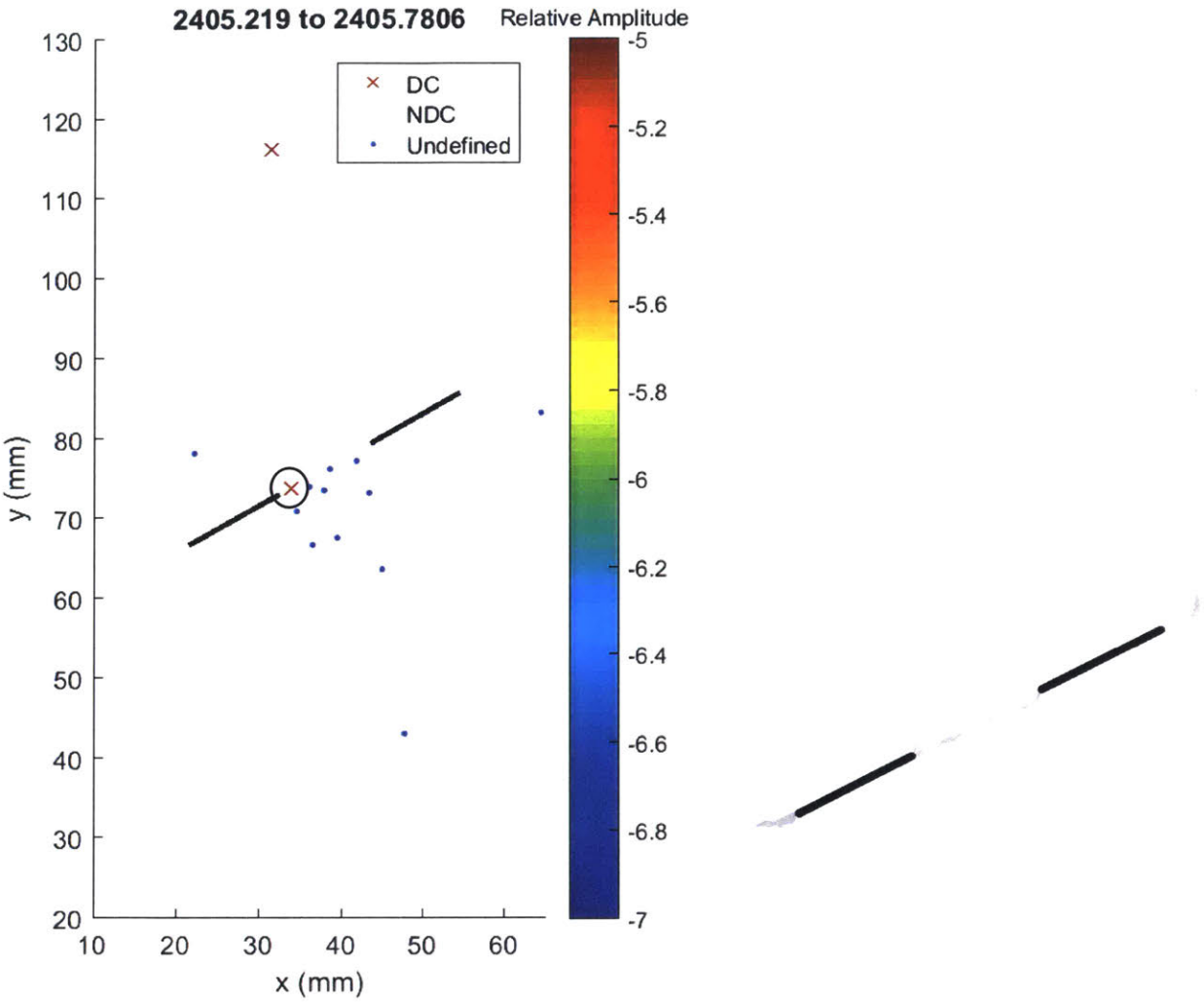

No tensile events in this time frame, but there is one large shear event on the left side of the coalescence zone and another shear event near the top O-ring. Visual analysis shows that there is some coalescence of white patching by this point in time.

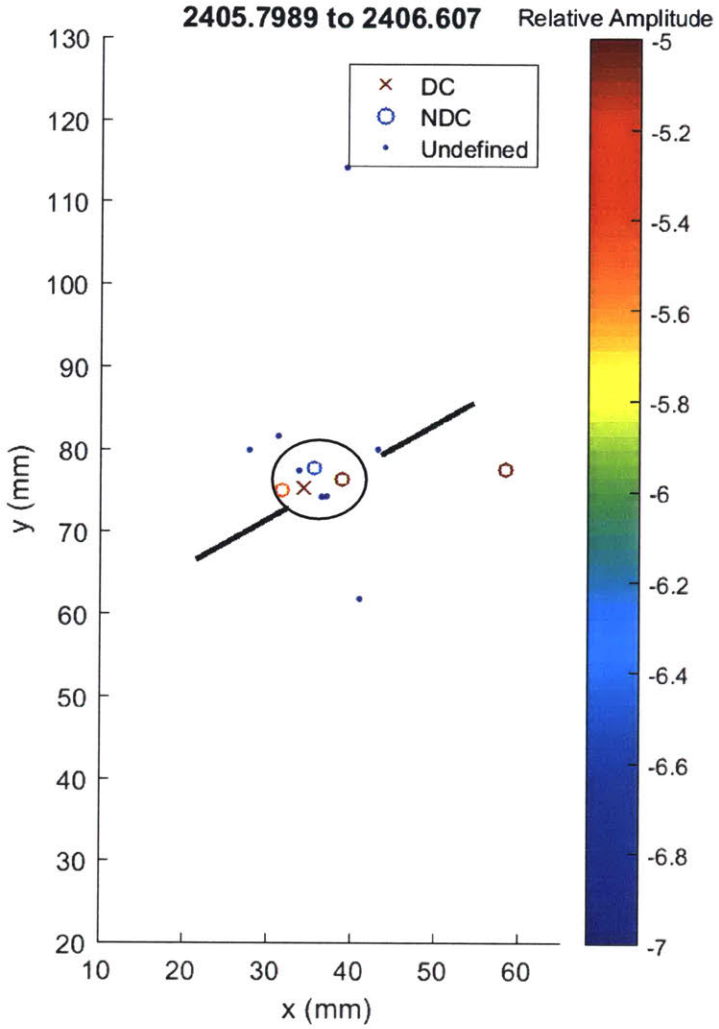

Majority of events occur at the inner tip of the left flaw. Of the large amplitude events at this location, 2 are tensile and one is shear. Peak pressure is reached around this time.

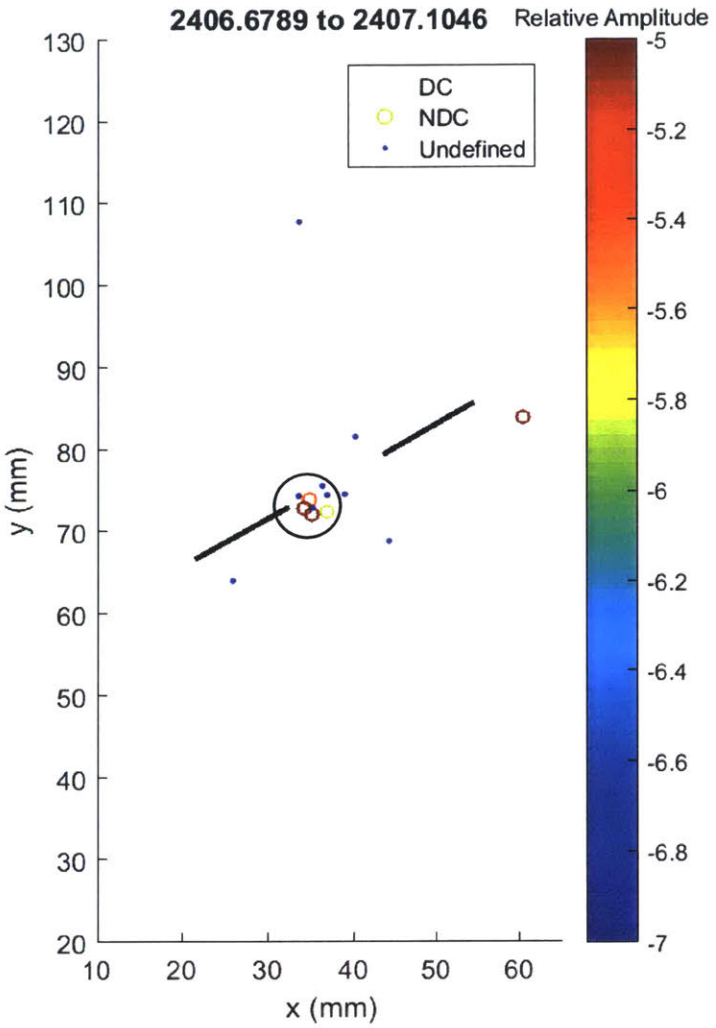

Events continue to cluster at the inner tip of the left flaw, and are still dominated by tensile type.

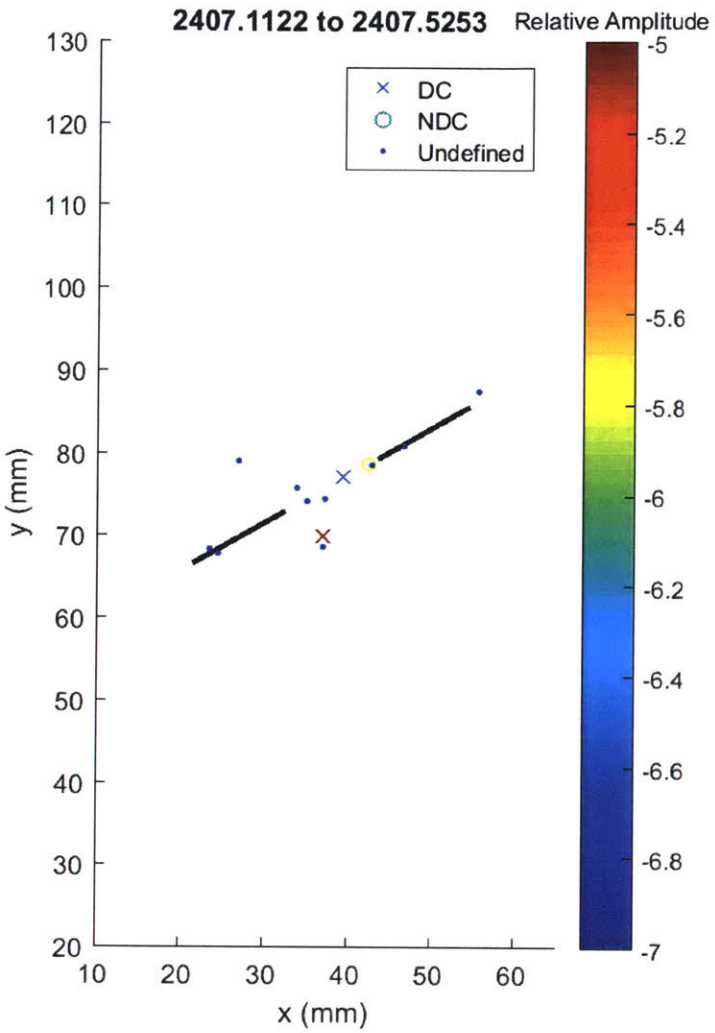

AE events migrate away from the left flaw, and occur generally in the coalescence zone. Both shear and tensile events occur.

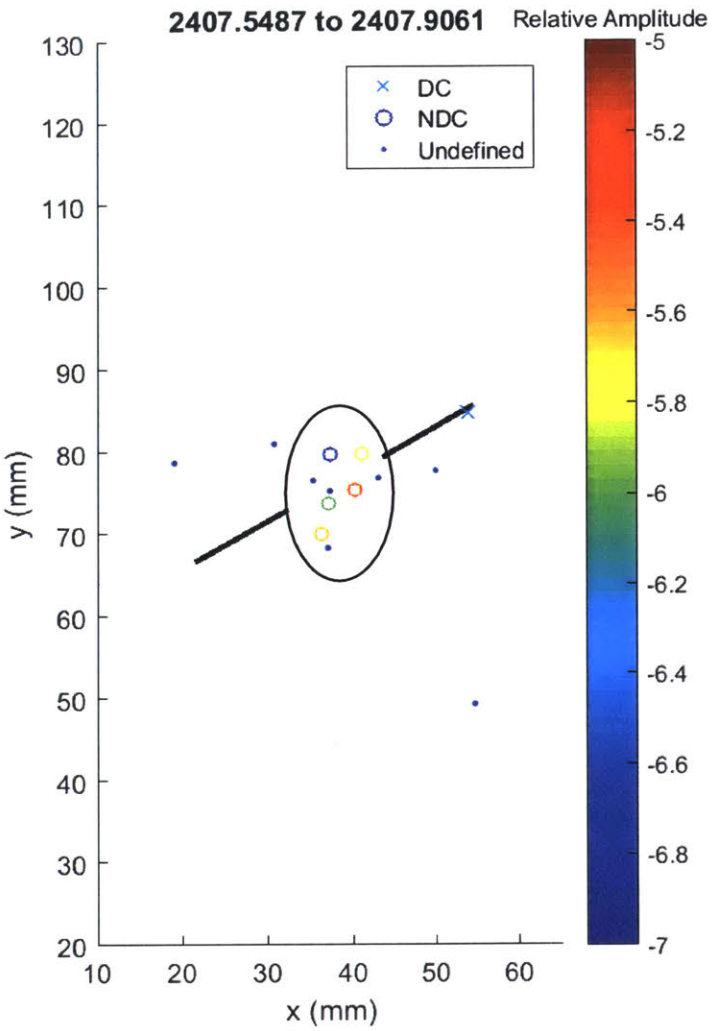

High concentration of tensile events occur in the middle of the coalescence zone. One smaller amplitude shear event occurs at the outer tip of the right flaw.

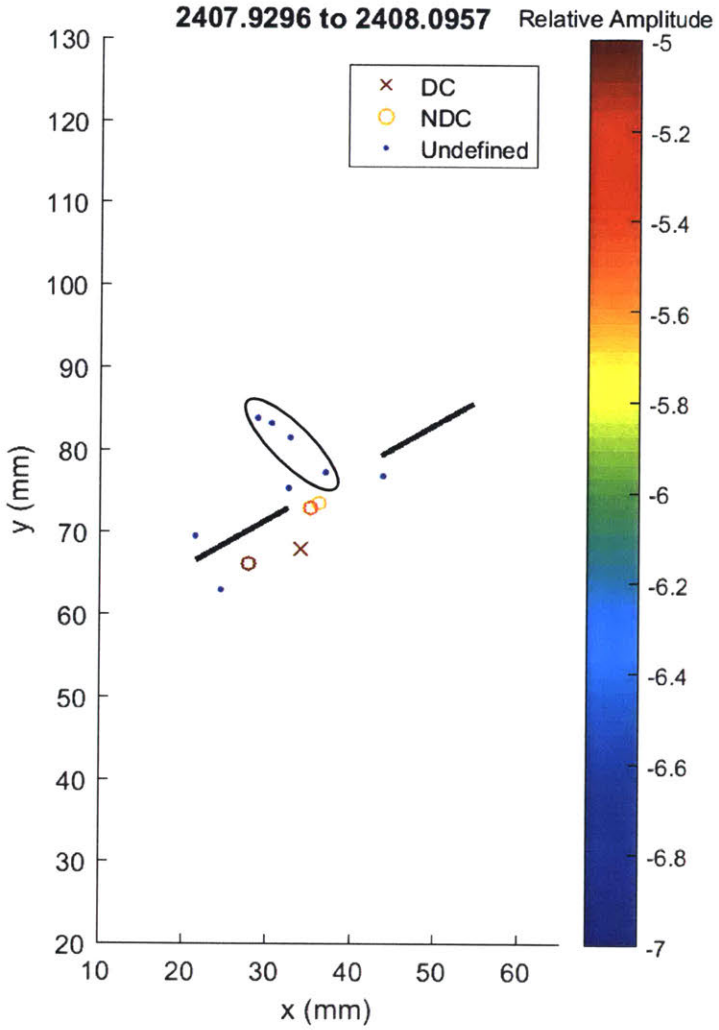

Undefined events appear to form a wing crack above the left flaw, while higher amplitude tensile and shear events occur around the left flaw.

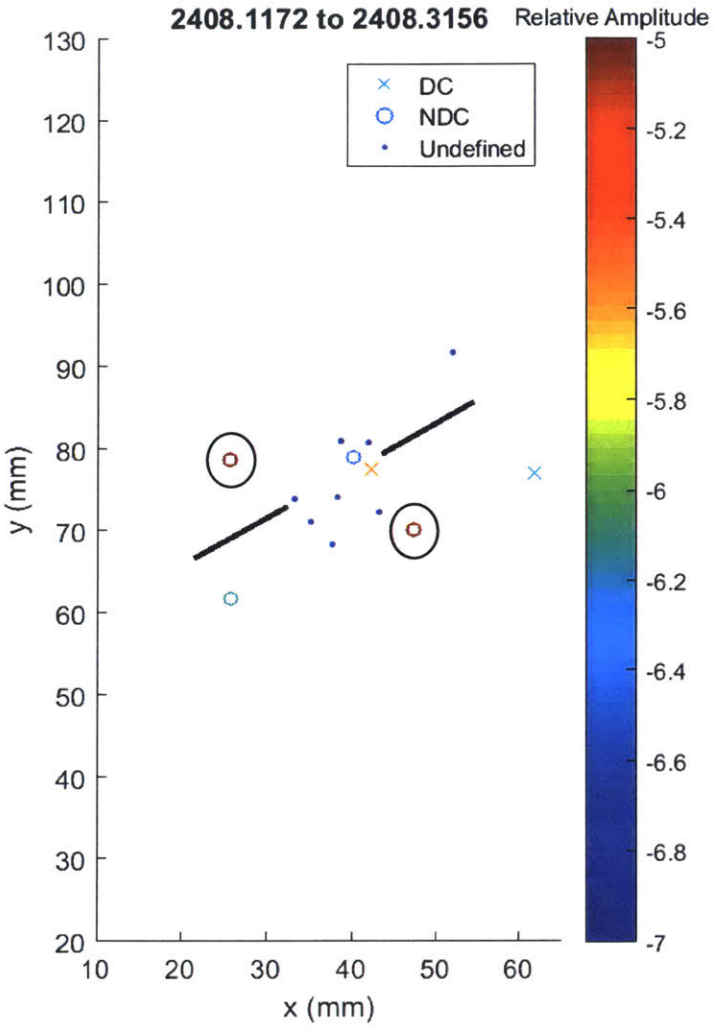

Undefined events continue to occur in the coalescence zone. Large amplitude tensile events occur at wing crack locations of both inner flaw tips.

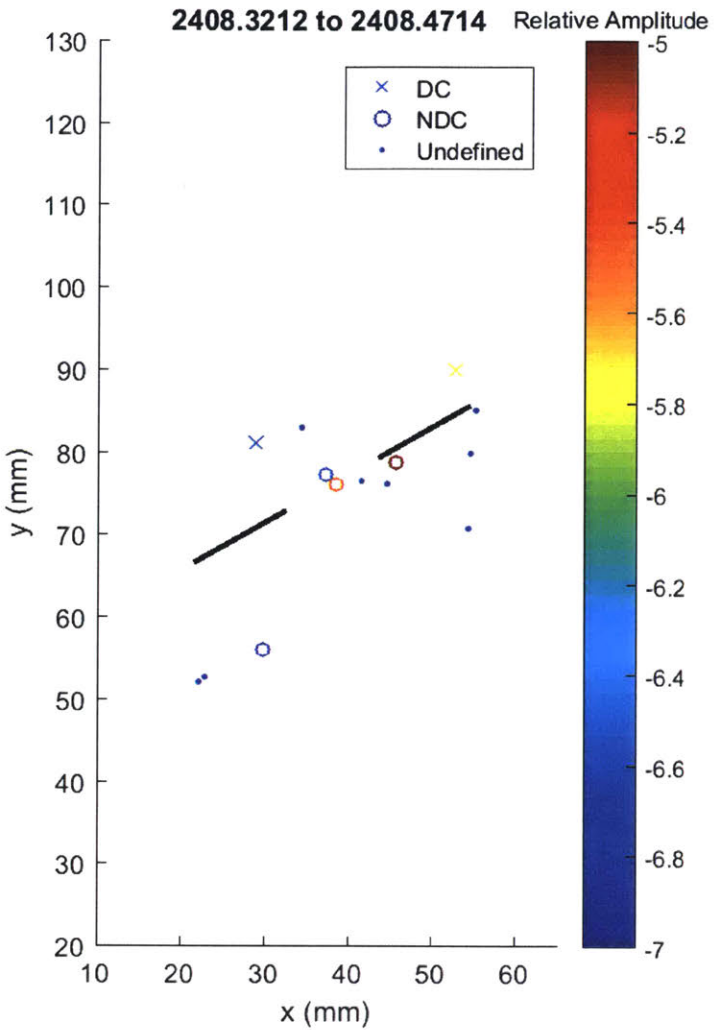

AE locations appear to be diffuse. High amplitude tensile events occur at inner tip of right flaw. Intermediate amplitude shear event occurs at outside tip of right flaw.

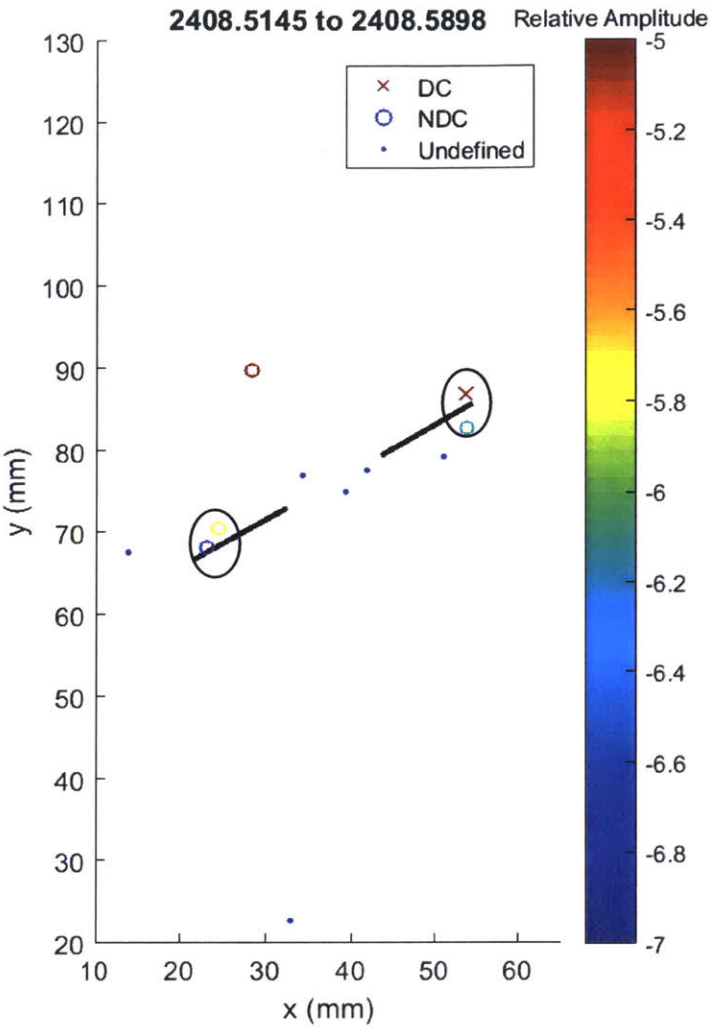

Shear and tensile events occur at both outer flaw tips.

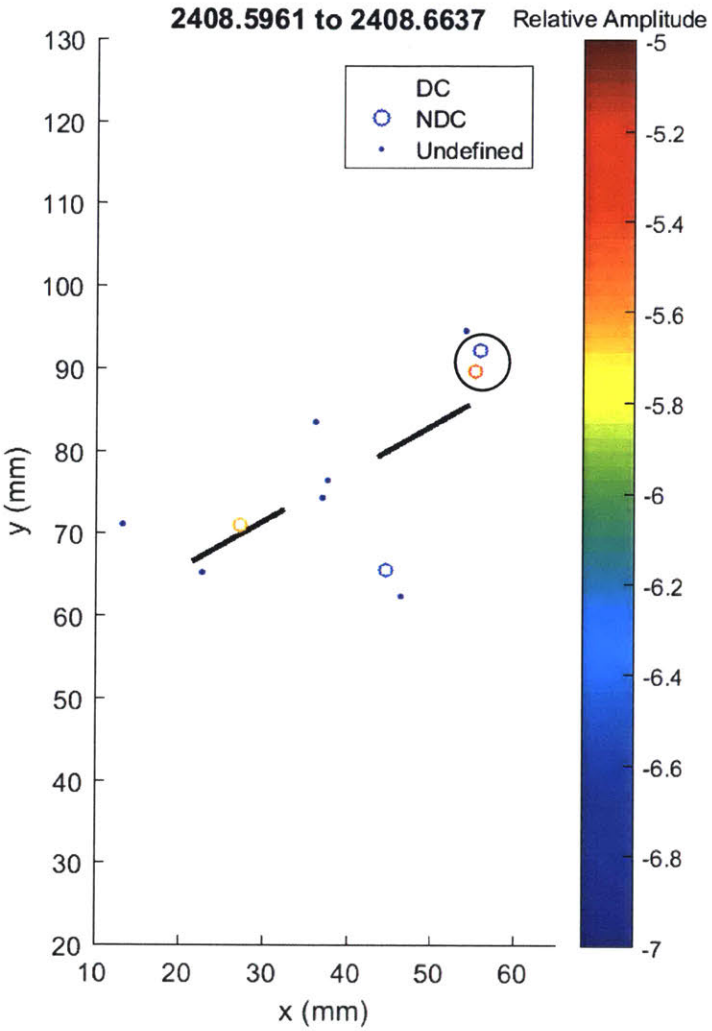

Tensile or undefined events occur, and mostly appear to be concentrated at right outer flaw tip.

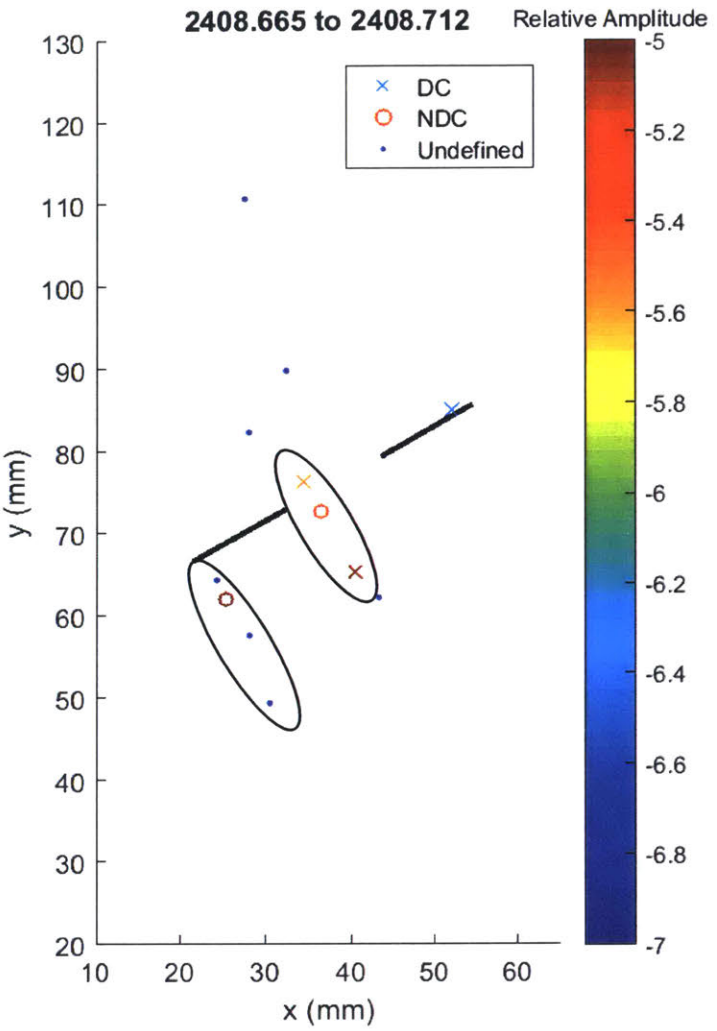

Higher amplitude events appear to be linearly clustered at wing/anti-wing crack locations of left flaw.

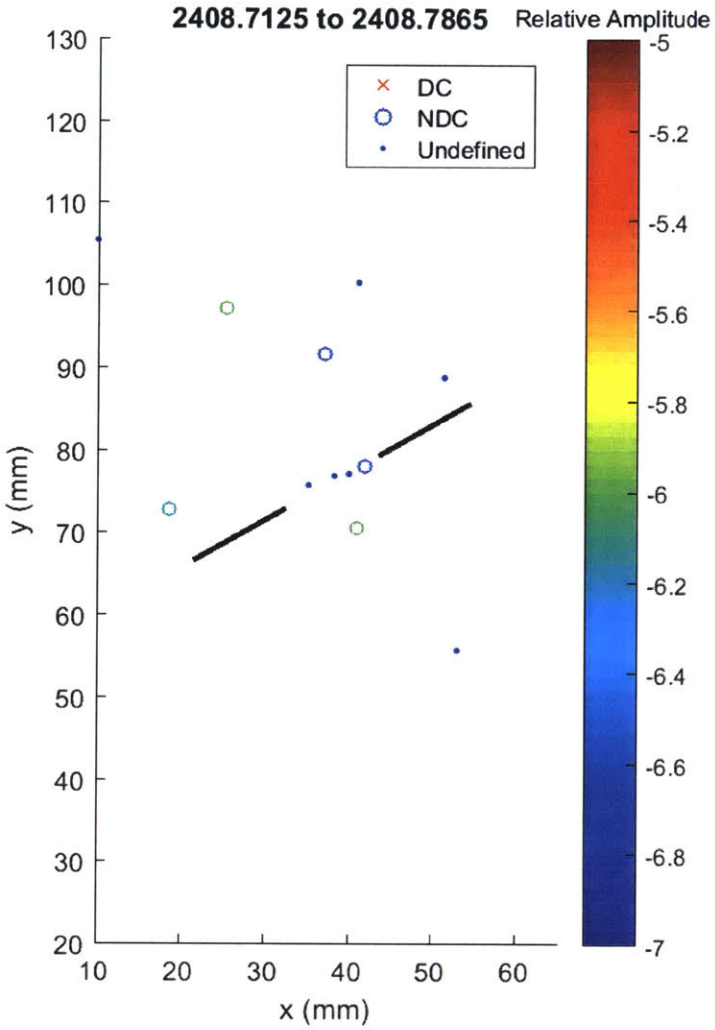

De-clustered low magnitude tensile events

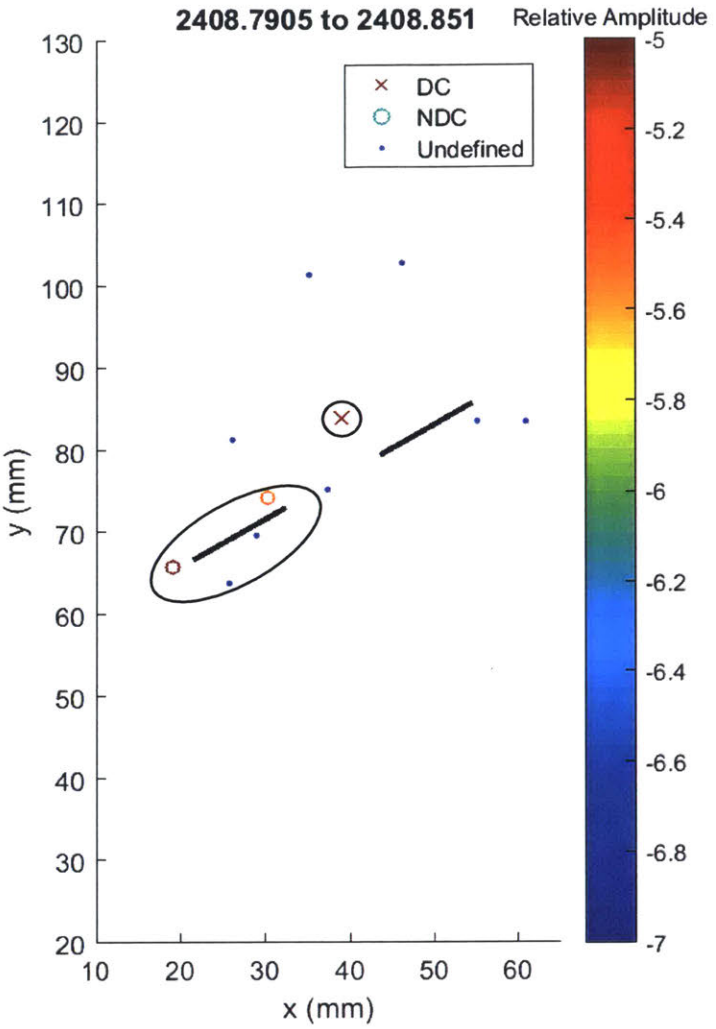

One high magnitude tensile event at each tip of left flaw, another shear event at inner tip of right flaw.

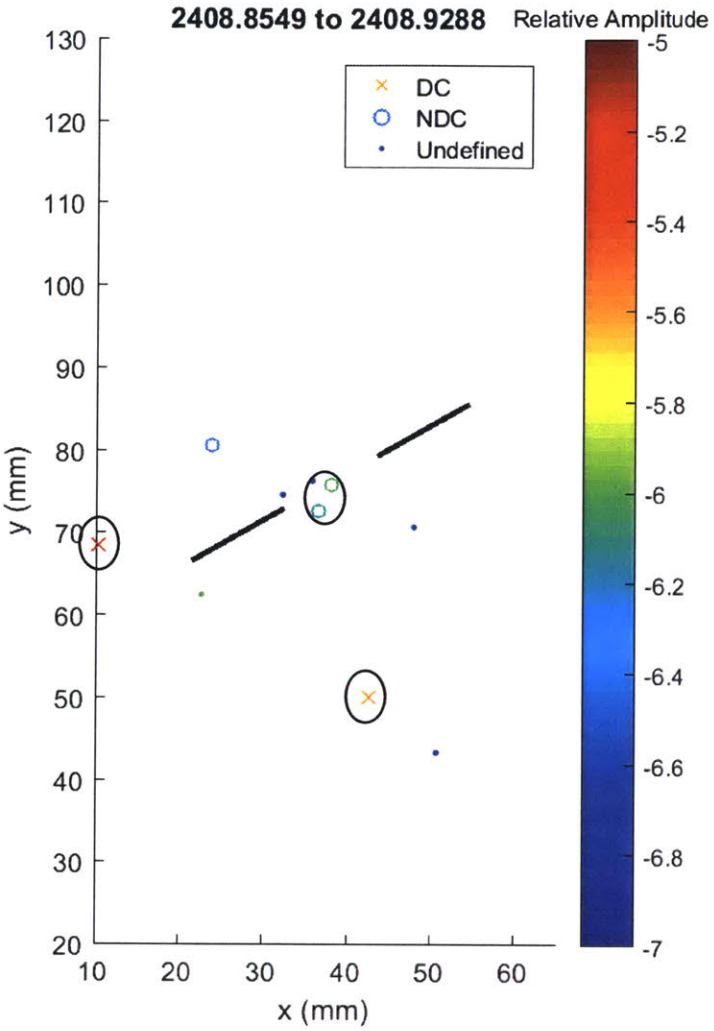

2 intermediate magnitude tensile events occur close to inner tip of left flaw. 2 higher magnitude shear events occur away from the flaw area.

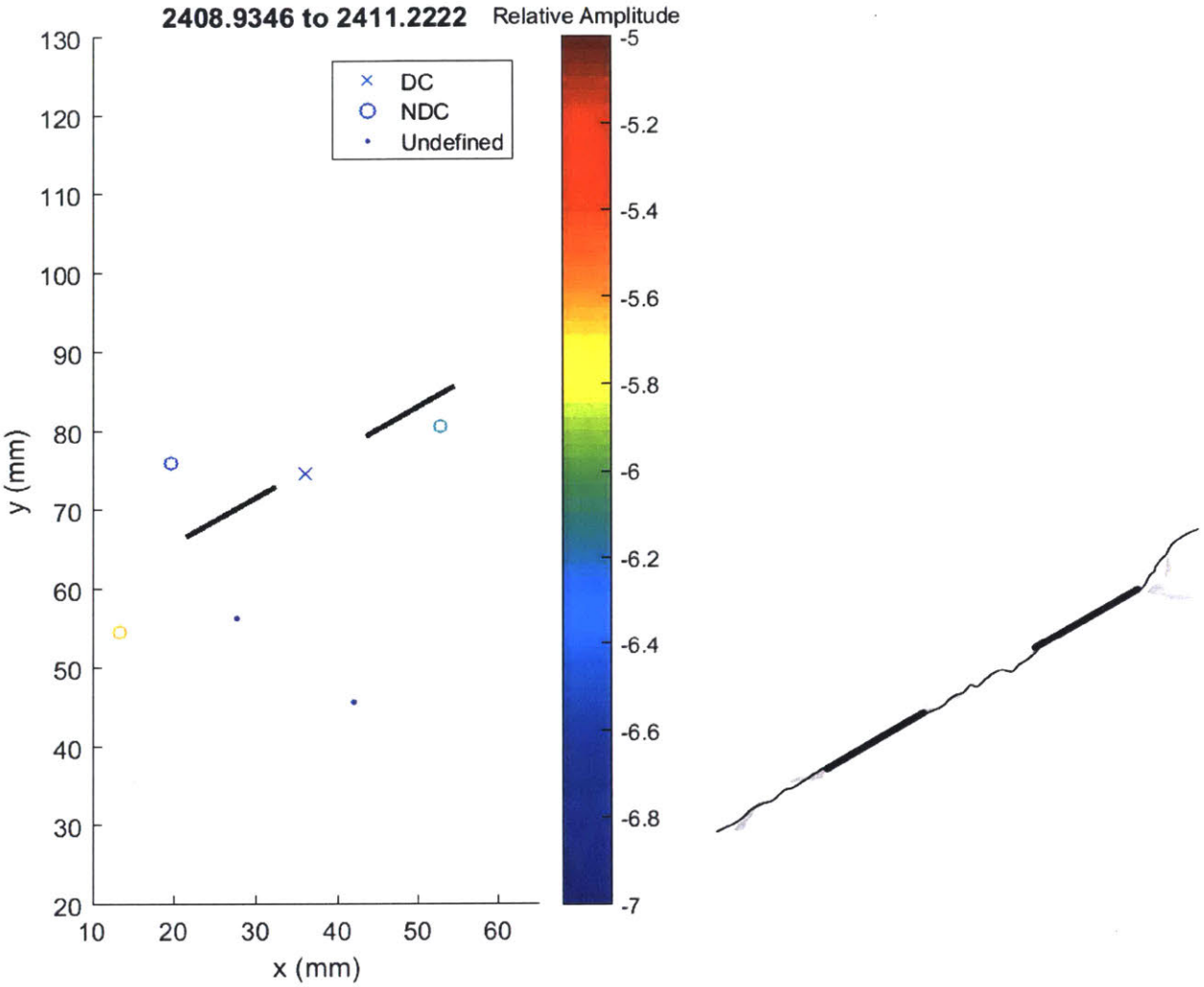

End of test. Diffuse AE locations. Majority of high speed video occurs during this last frame.

Summary

In general, there were many more tensile events than shear events. As discussed in previously, it is postulated that the lack of vertical axial stress in this test may allow more tensile events to occur, as grains do not need to slide past each other. A second observations is that the undefined events, which tended to be lower magnitude, are also more diffuse (spread out) than the larger magnitude events. This reflects the nature of the stress field, which is most intense at the flaw tips. In terms of timing, it appears that the hypocenters are initially located within the coalescence zone between the inner flaw tips, and then migrate outwards in time. At this point, some events appear to form linear patterns perpendicular to the flaw orientation, resembling wing/anti-wing cracks. In the last few frames, which correspond to fractions of seconds prior to visual crack initiation, it appears that the tensile events again cluster to all the flaw tips (including the outer tips), while shear events occur away from the flaws.

AE hypocenter analysis for specimen 2a-30-0-VL0-C

Final crack geometry:

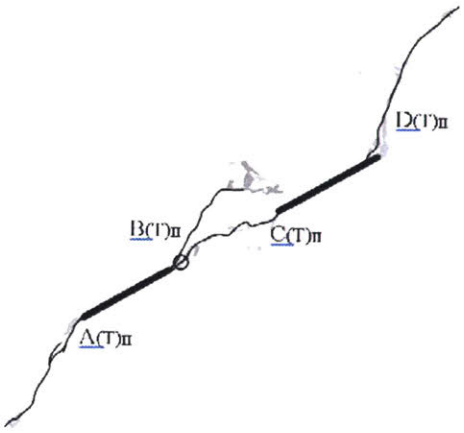

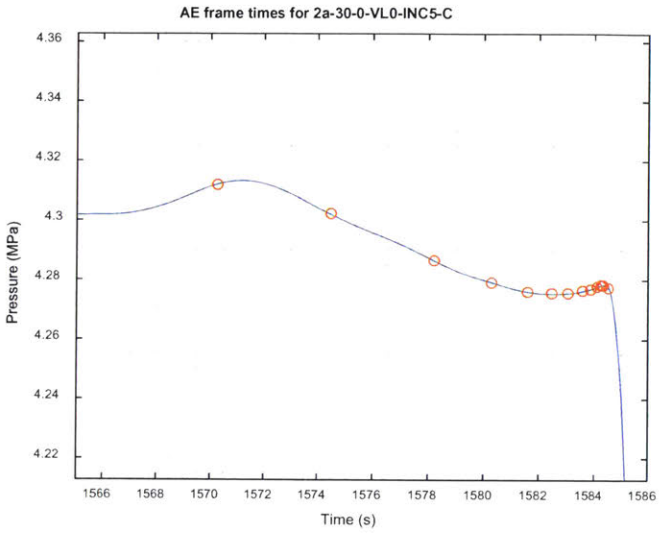

Crack initiates from outer tip of left flaw, followed by tensile crack B which does not coalesce followed by crack C, which does coalesce after the initiation of crack D. Peak pressure occurs around 1571 s, and a local minimum in pressure occurs around 1582.5 s a few seconds before pressure breakdown.

Development of AE locations are shown over the 20 frames presented in this analysis, where each frame shows 5% of the total number of events recorded during the test. This means that initially the frames will cover a long time period since few AE occurred at the beginning, while towards failure each frame will only cover fractions of a second since AE occur at a rapid rate.

Events with greater than 50% CLVD (compensated linear vector dipole) are considered shear type events and are marked with an 'x', while events with less than 50% CLVD are considered tensile and marked with 'o'. For those events detected by 4 sensors, it is not possible to invert the moment tensor and so these events are marked as undefined with '.'. The colour of an event indicates its relative magnitude, where red is the largest. Black ellipses are used to highlight areas of interest.

Where possible, AE frames are shown next to the appropriate analysis sketch from Bruno. However, these tend to be few in between and as discussed, the high speed frames tend to occur after the end of detectable AE events.

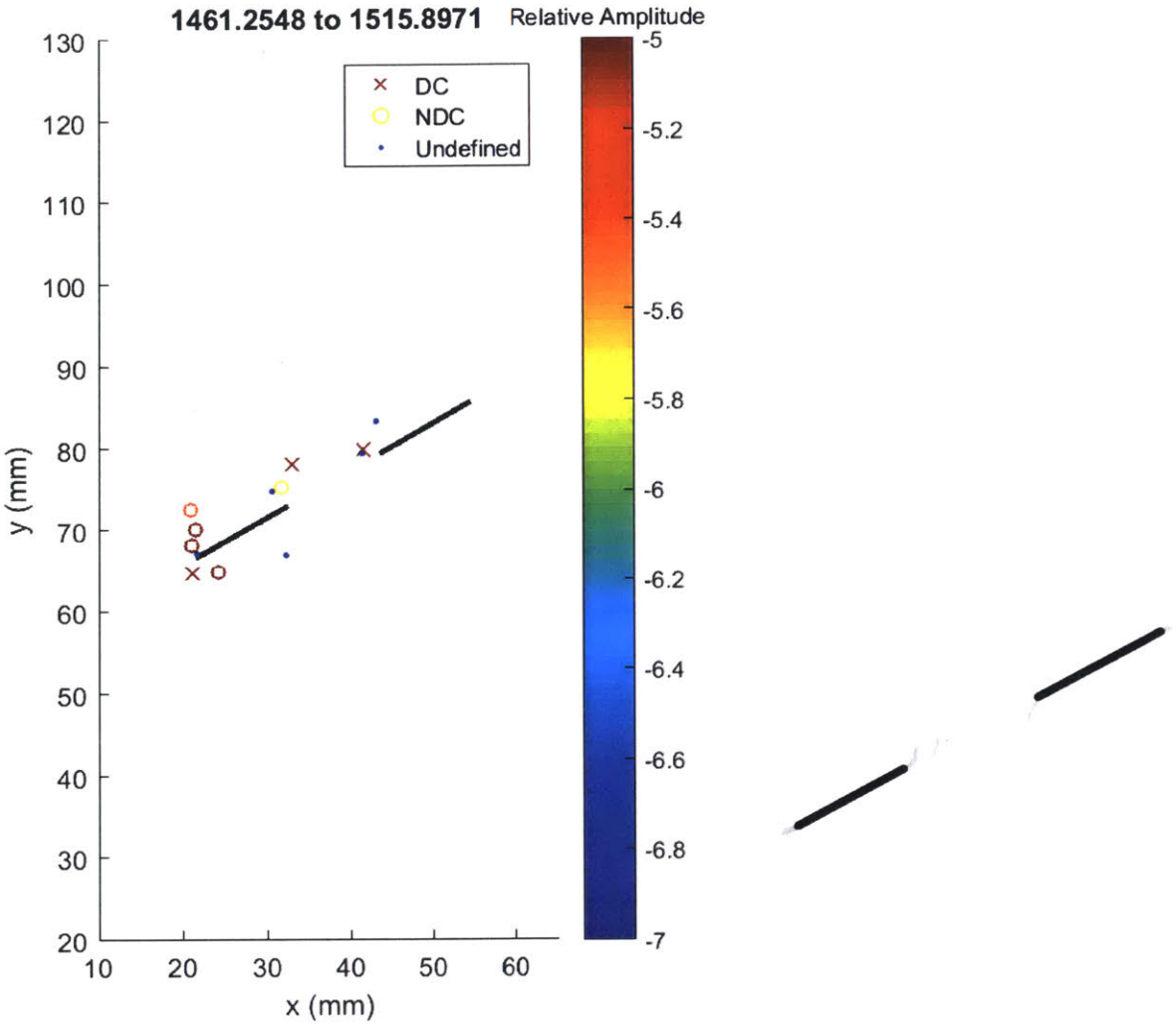

First 20 events which occur in preceding pressure stages over 50 seconds include large amplitude shear events at 3 of the flaw tips, and 4 tensile events forming an anti-wing crack at the outer tip of the left flaw, which is incidentally the first to initiate a crack later.

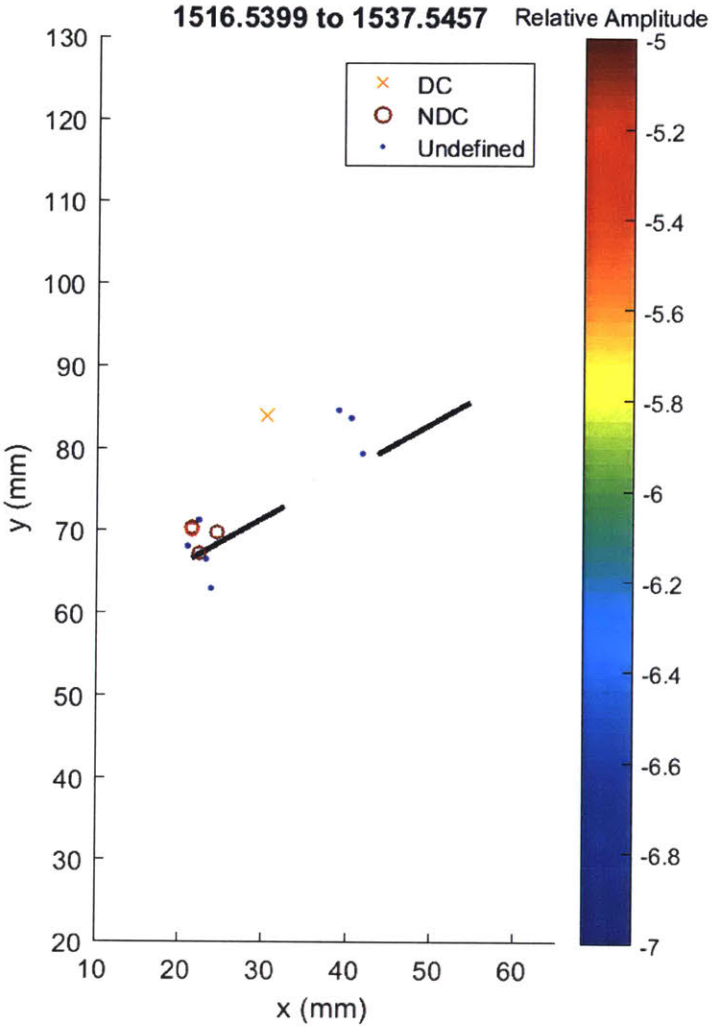

Small amplitude undefined events occur at anti-wing crack inner tip of right flaw, while high amplitude tensile events continue to cluster at outer tip of right flaw.

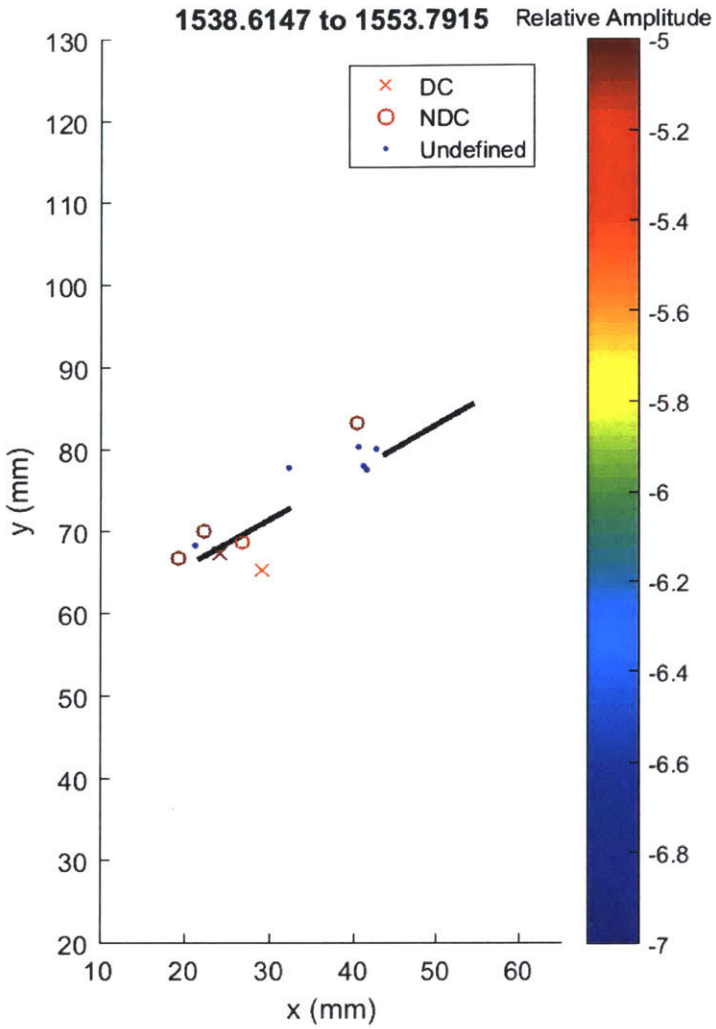

Largely the same pattern as the previous frame, except there are also shear events around the left flaw, and a single large tensile event at the inner tip of the right flaw.

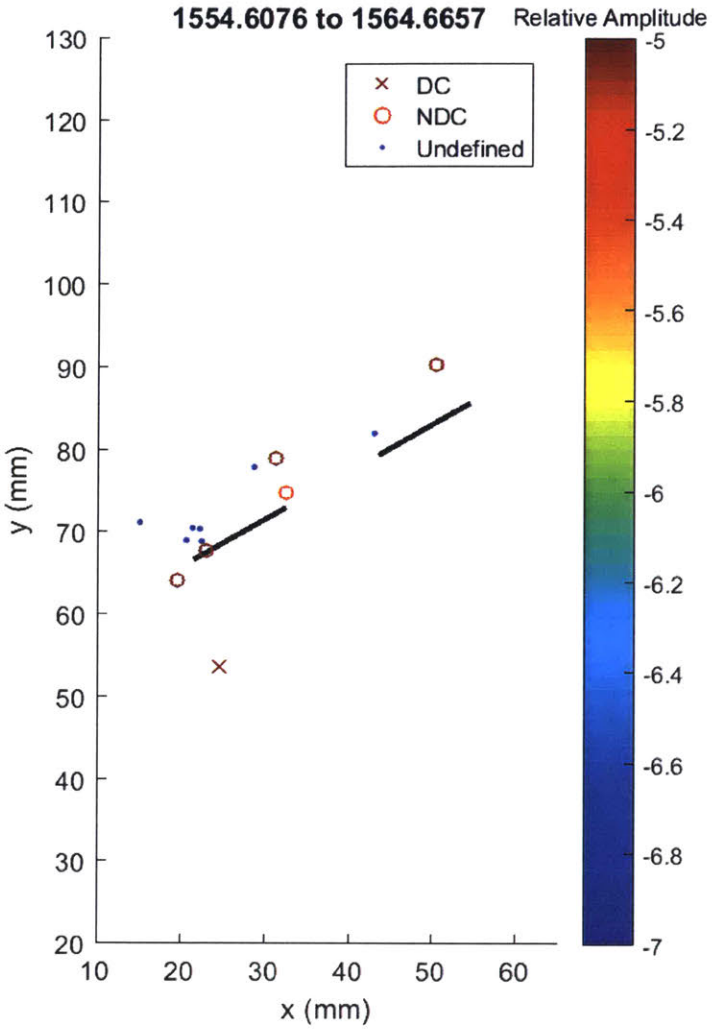

Tensile events form wing pattern shape on left flaw, significant low amplitude undefined events at outer tip of right flaw.

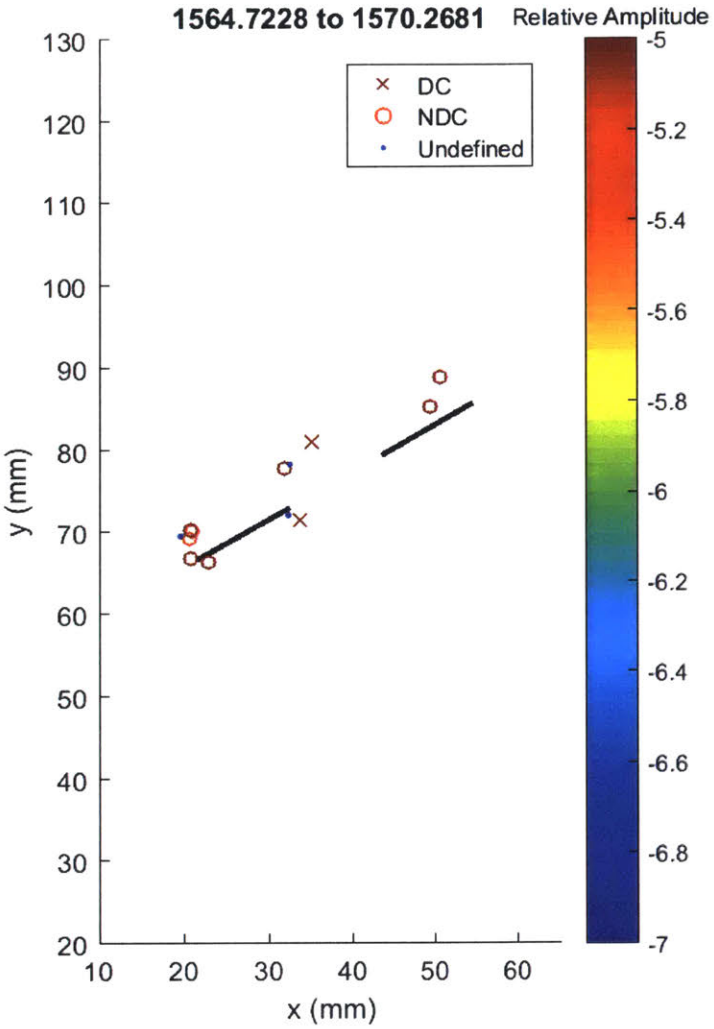

Dominated by high amplitude tensile events at both outer tips, and 2 shear events at inner tip of left flaw. Peak pressure occurs at this time.

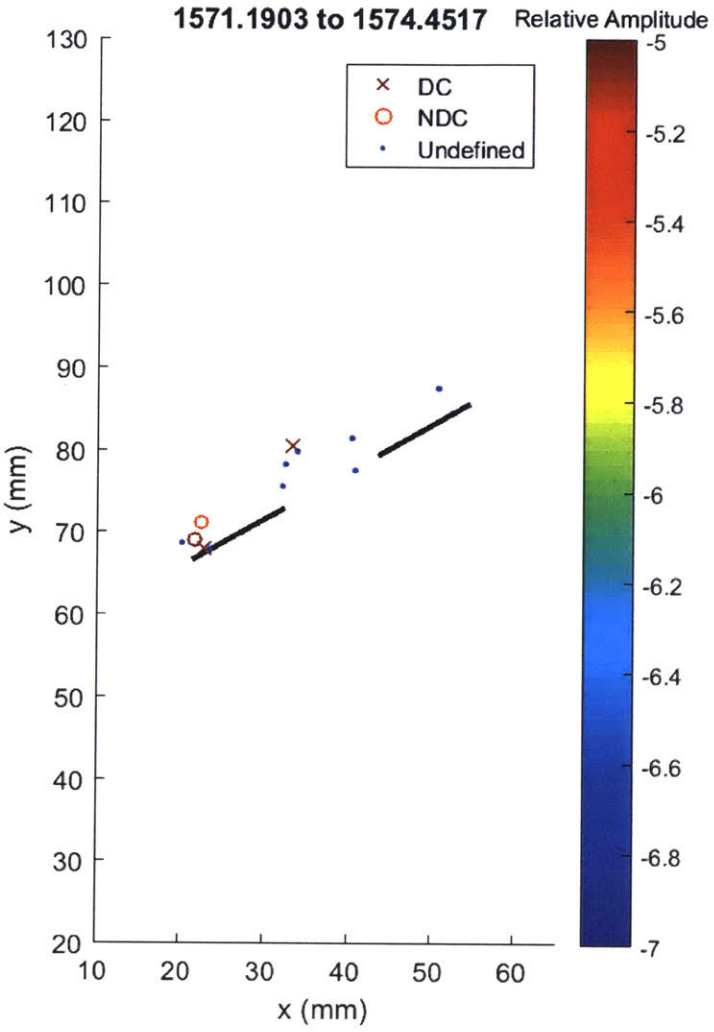

Continued high amplitude (1 shear, 2 tensile) activity at outer tip of right flaw, and undefined events forming wing crack patterns.

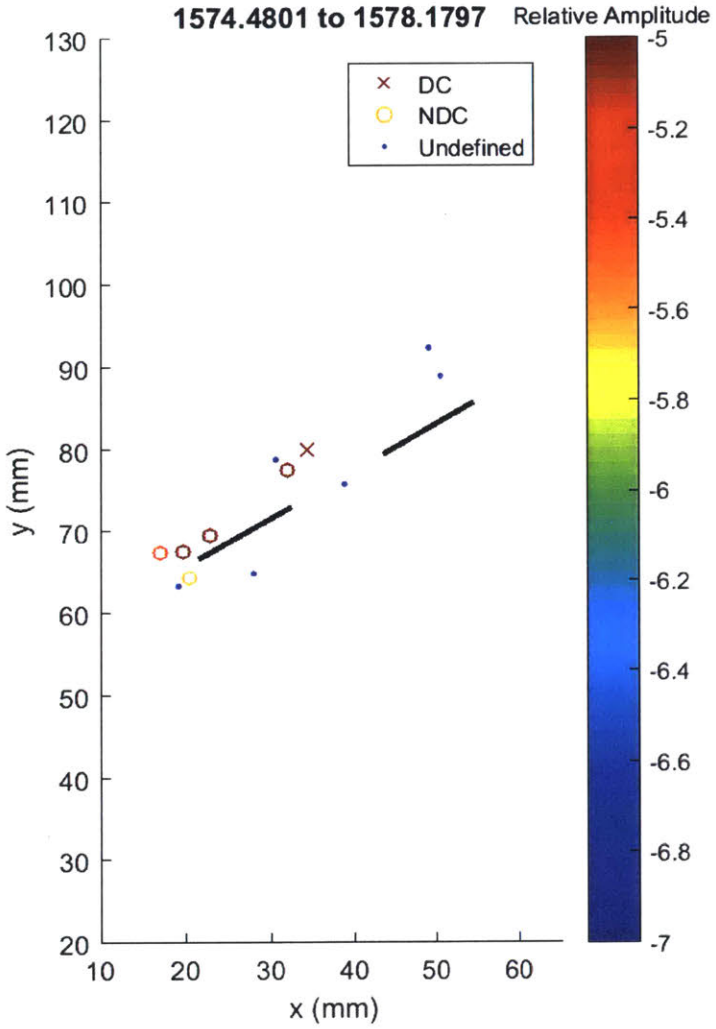

4 tensile events at outer tip of left flaw, 2 other high amplitude (1 shear 1 tensile) events at inner tip of same flaw. Right flaw only shows low amplitude events

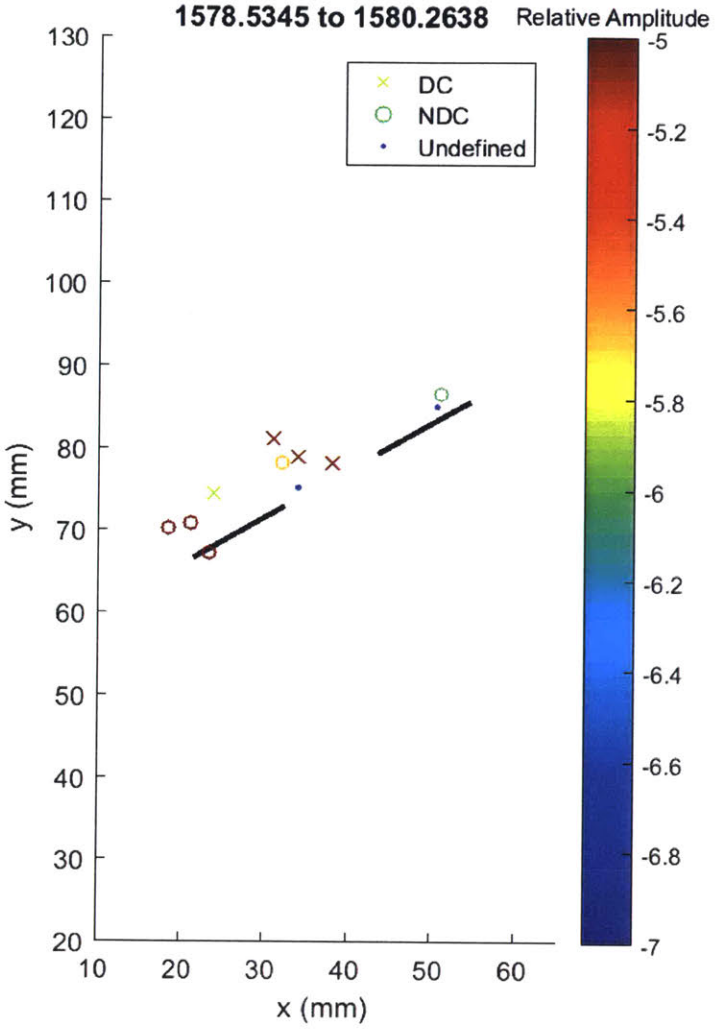

3 more tensile events at outer tip of left flaw, while 3 large shear events and 1 intermediate tensile event occurs in the coalescence zone. Could be related to the more complex fracture pattern (cracks B and C) in the same zone.

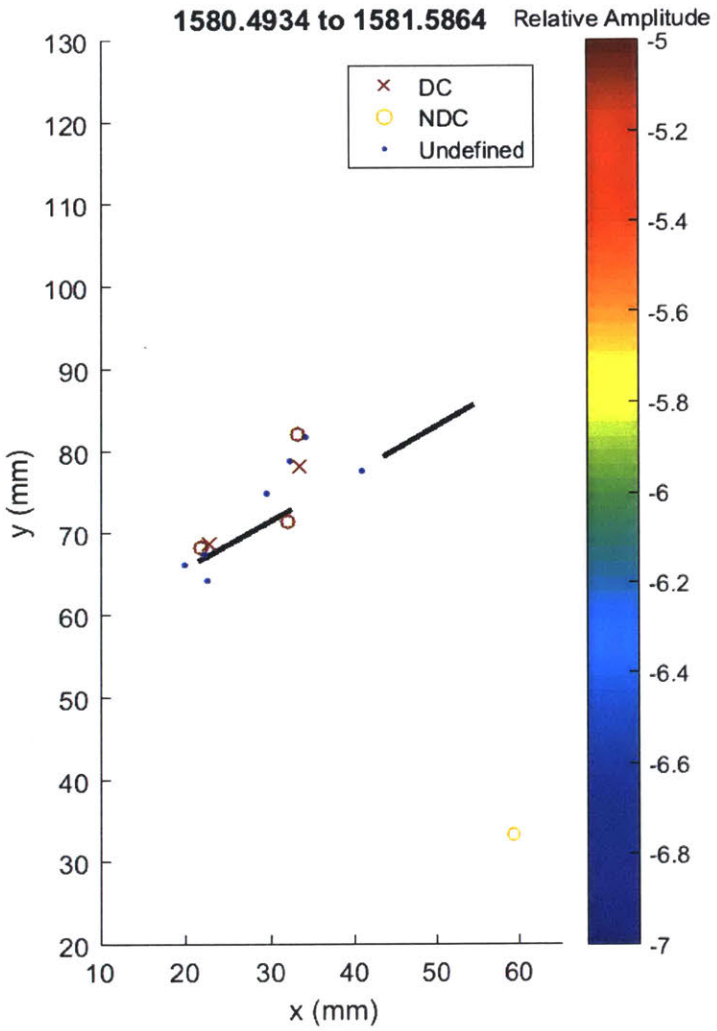

Large shear and tensile events at both tips of the left flaw.

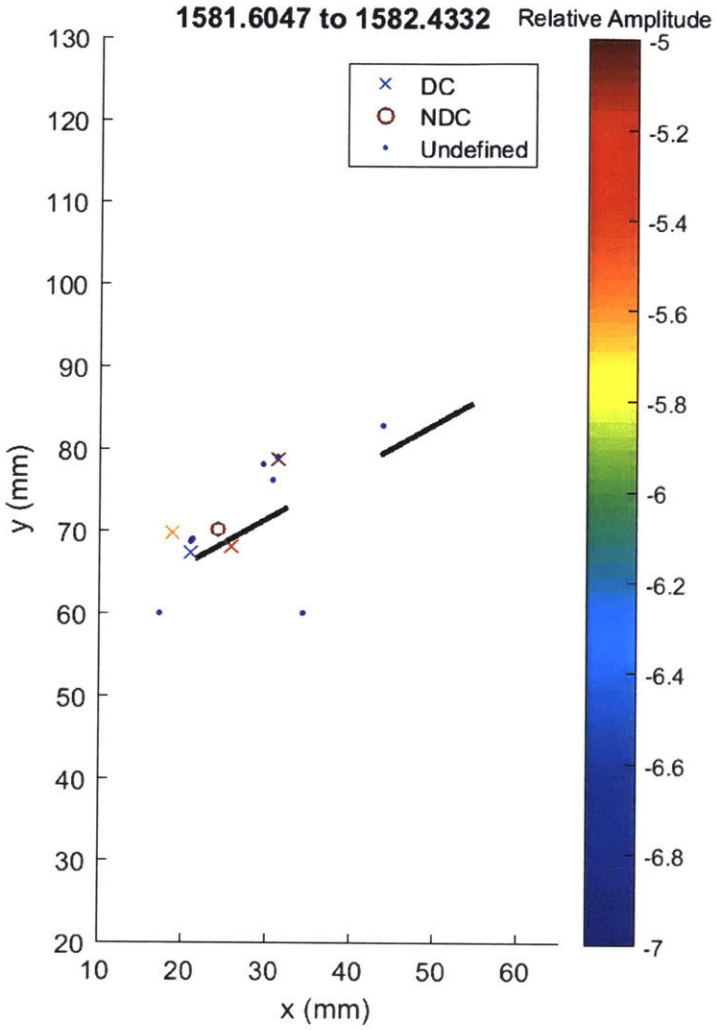

Events consists mostly of shear events at the outer tip of the left flaw. Local minimum in pressure is reached at this time.

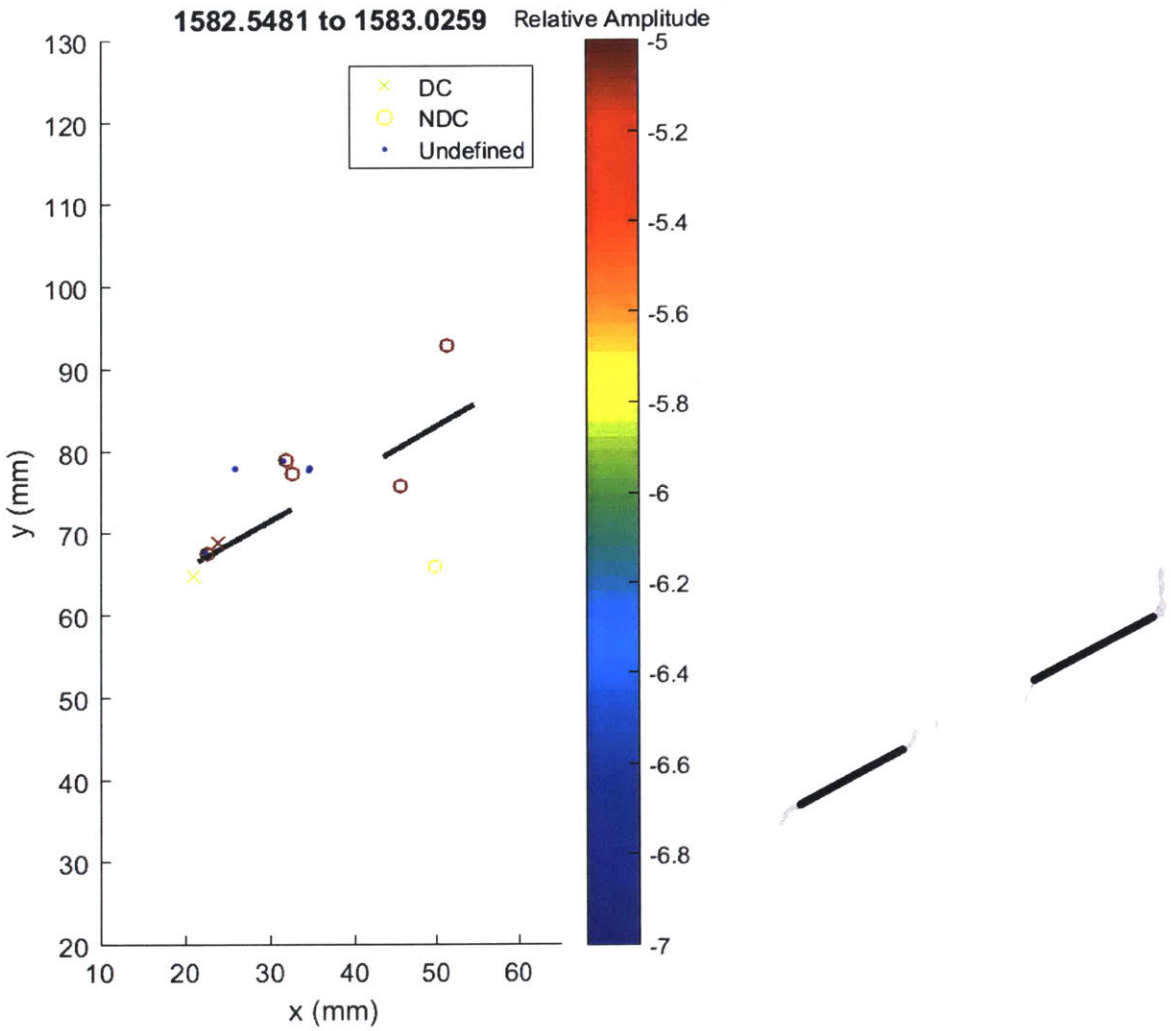

Tensile events occur at all flaw tips, and another 2 shear events occur at outer tip of left flaw.

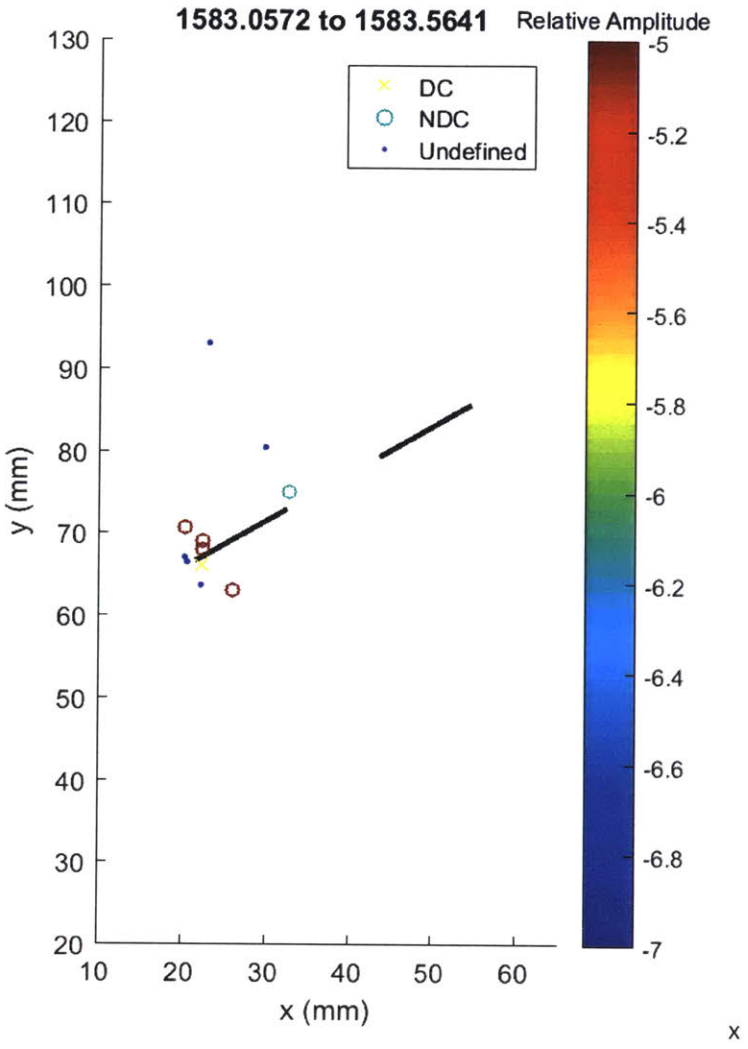

Tensile events concentrated at outer tip of left flaw in wing/anti-wing crack pattern.

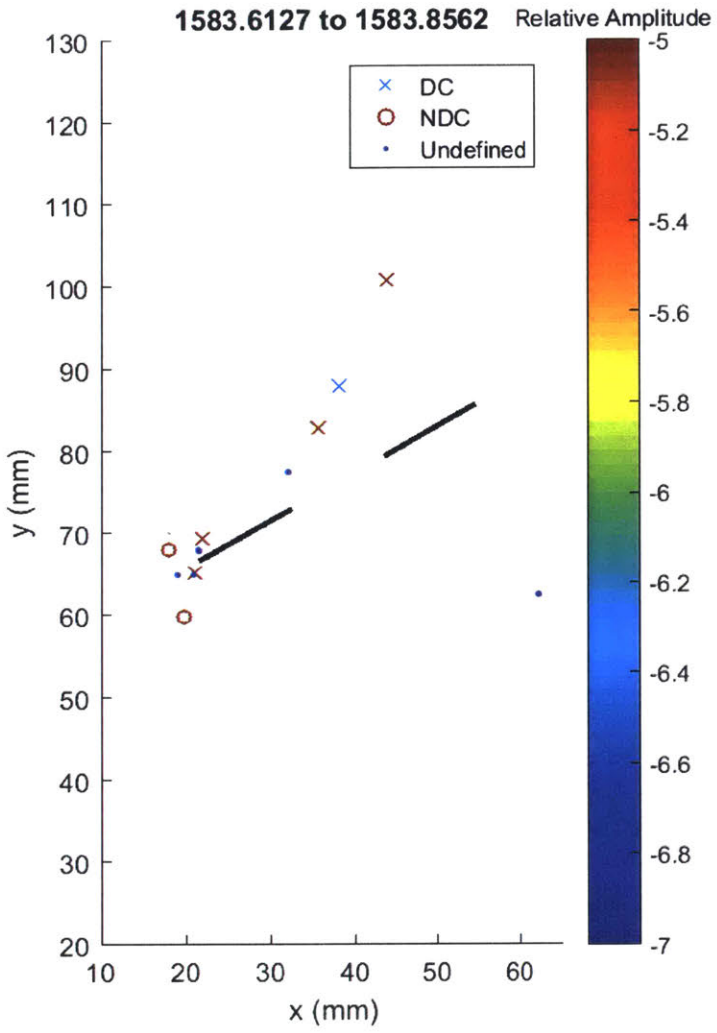

2 shear and 2 tensile events at outer tip of left flaw, and 3 linearly clustered shear events aligned with crack B.

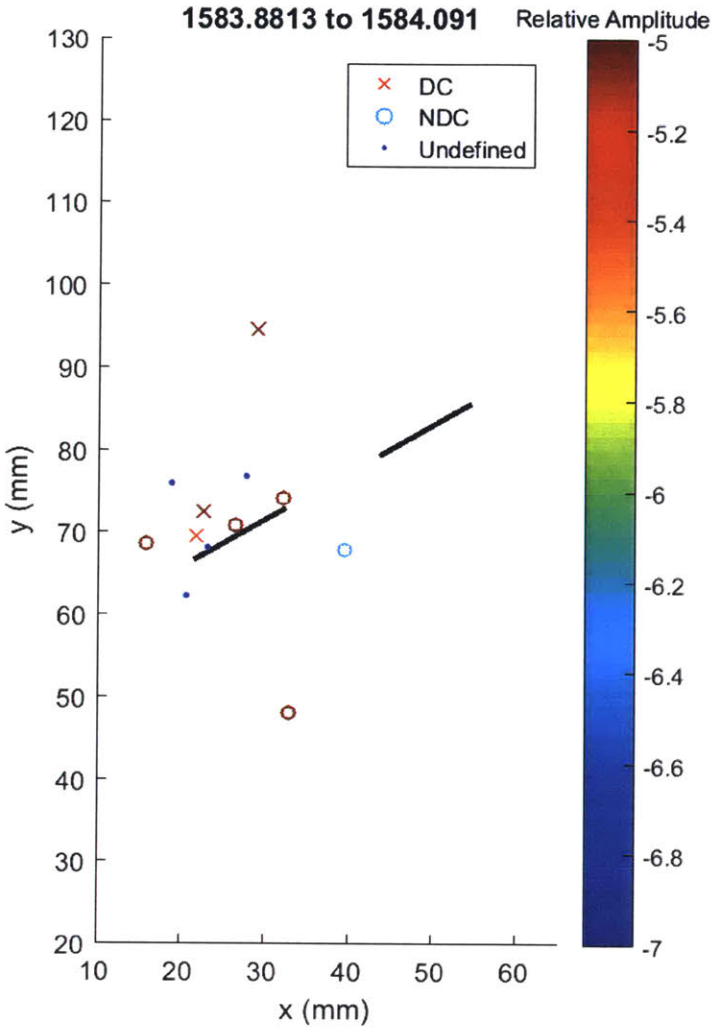

Large shear and tensile events around left flaw.

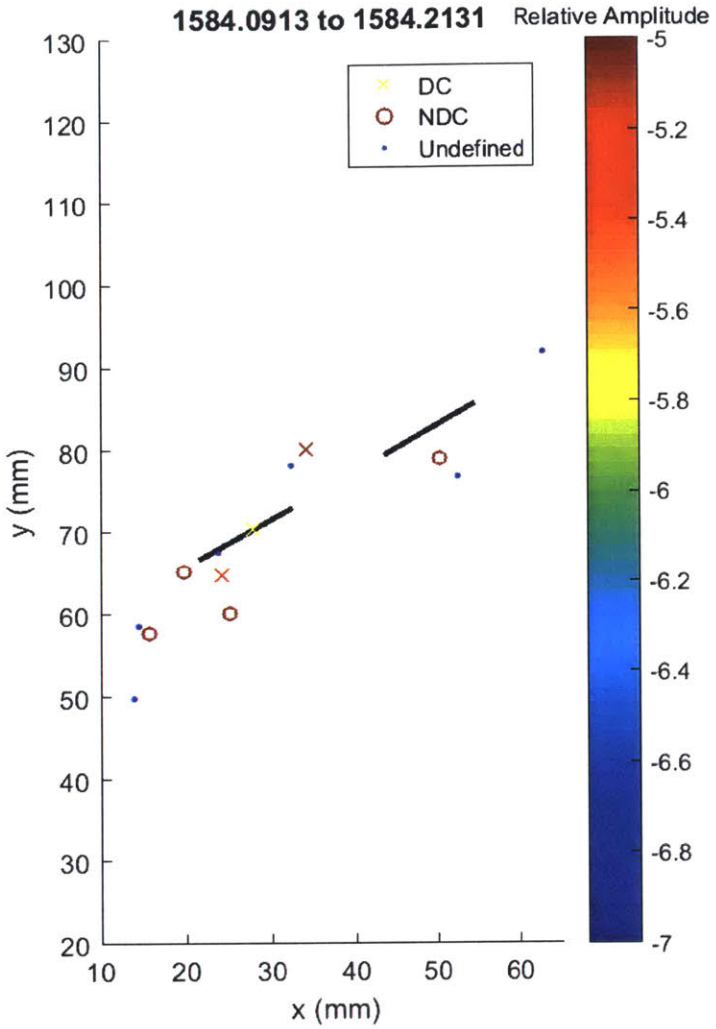

Events on both flaws, with higher concentration around outer tip of left flaw. Locations become more distributed.

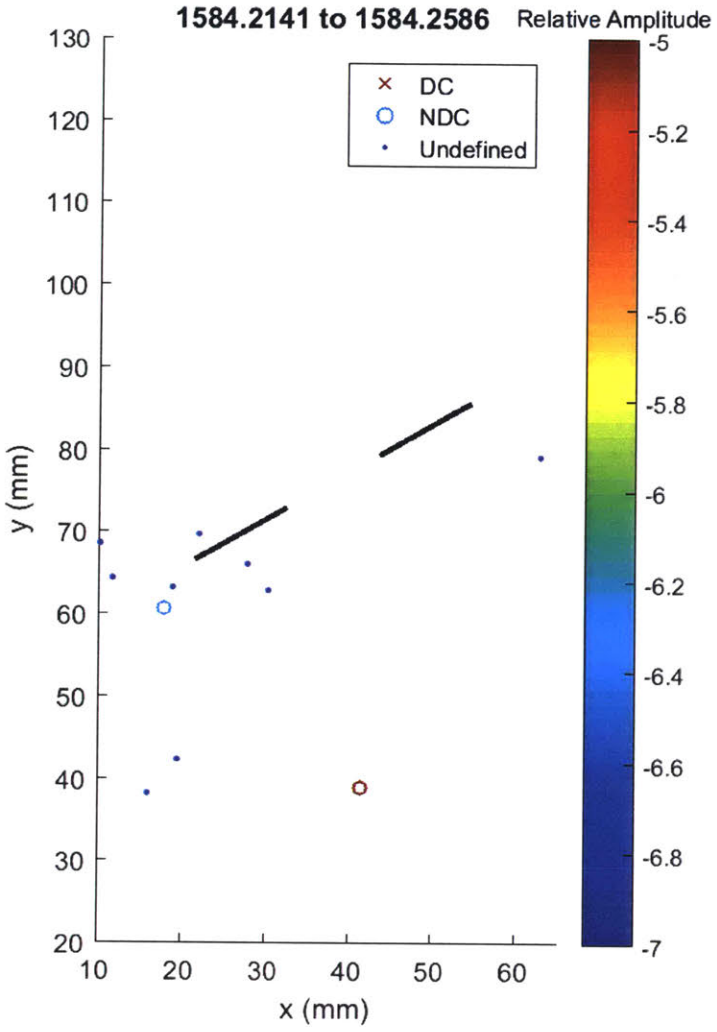

Many small amplitude, distributed events around left flaw.

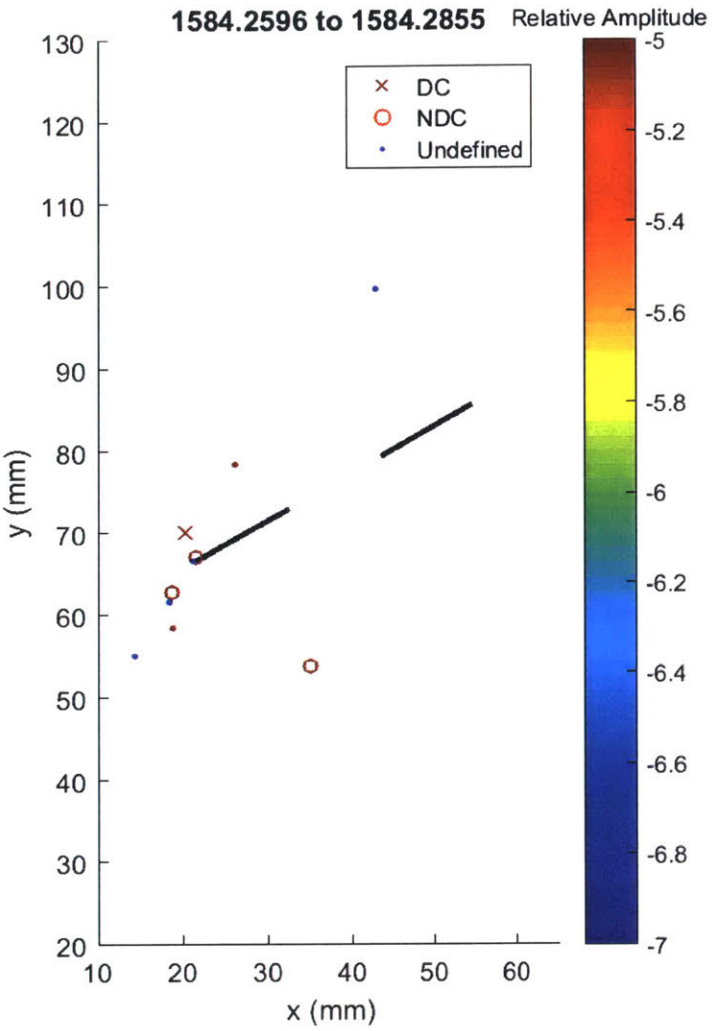

Large shear and tensile events at outer tip of left flaw.

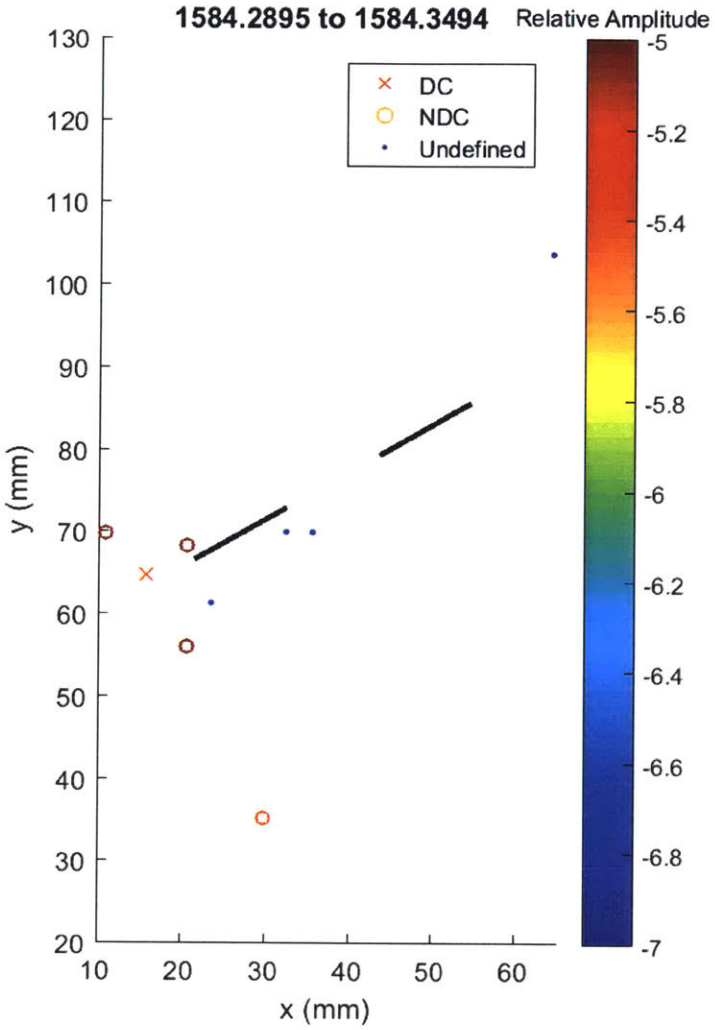

Same remarks as above.

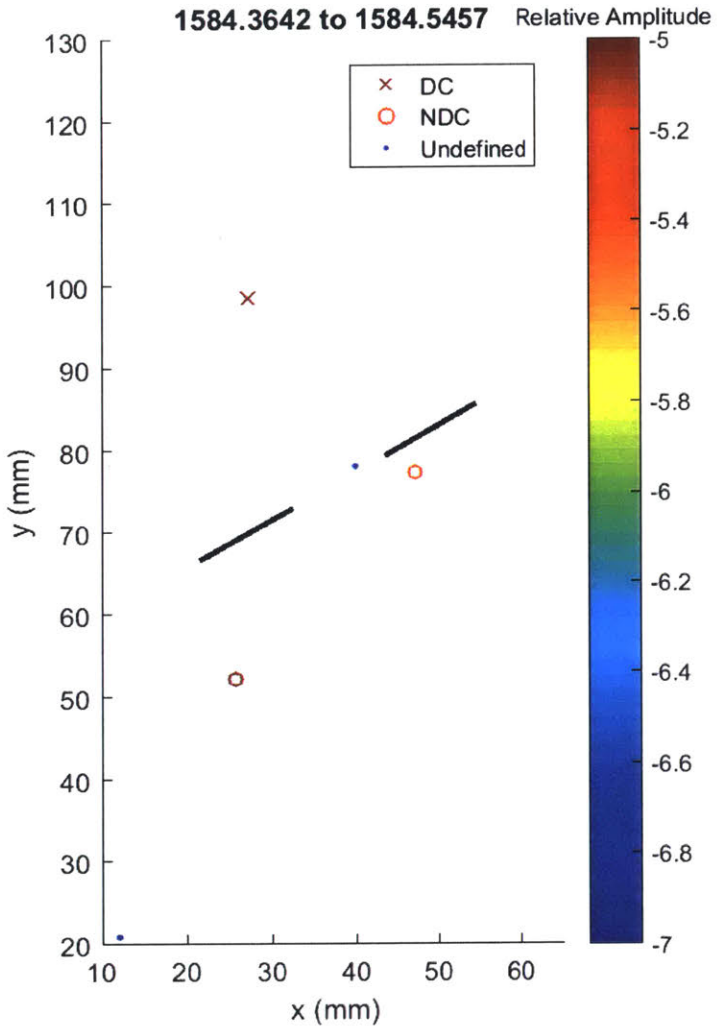

One large tensile events at inner tip of right flaw, other 2 large events away from flaw area.

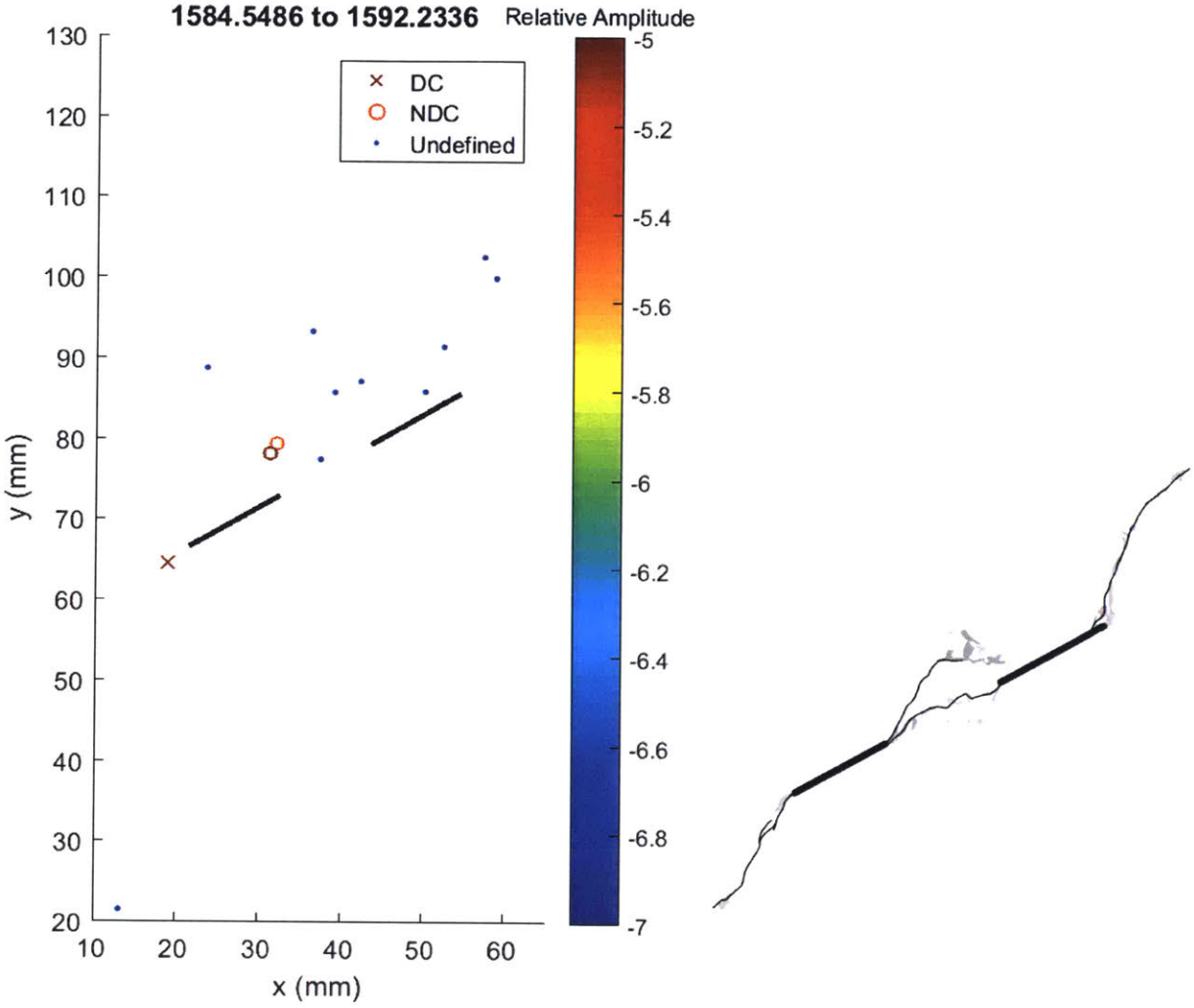

3 large events around left flaw, and small undefined events occur around right flaw.

Summary

High amplitude events are largely concentrated at the outer tip of the left flaw, which is where a crack first initiates. There is also significant activity around the inner tip of the left flaw, where the second crack initiates. Activity around the right flaw is generally dispersed, small amplitude, and occurs later in the test. There is significant linear clustering of events to form the wing/anti-wing crack patterns around the left flaw, particularly earlier in the test. These can occur for all types of events. Hypocenter locations appear to become more dispersed towards the end of the test.

AE hypocenter analysis for specimen 2a-30-0-VL5-A

Final crack geometry:

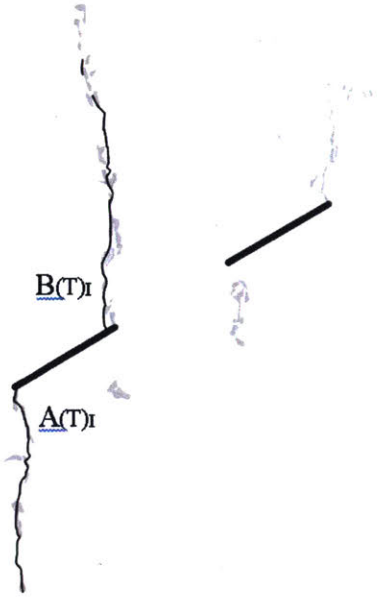

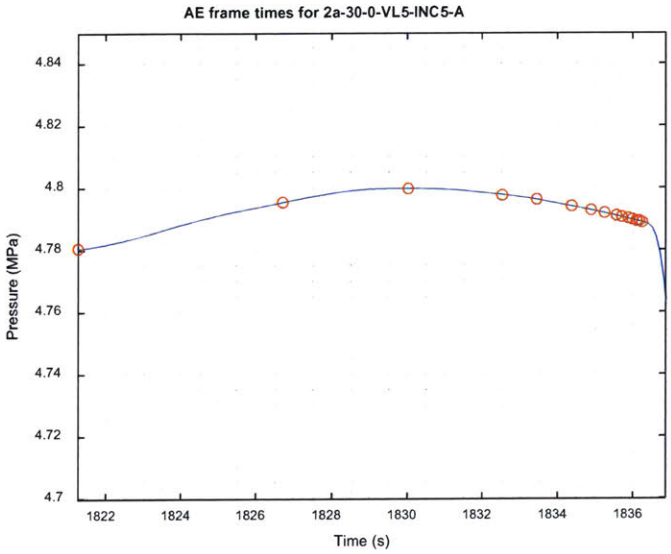

Crack initiates outer tip of left flaw, and a second crack initiates from the inner tip of the same flaw, forming a classic wing crack on the left flaw. No cracking observed on the right flaw, but white patching also exhibits a wing crack pattern. Peak pressure occurs around 1830 s.

Development of AE locations are shown over the 20 frames presented in this analysis, where each frame shows 5% of the total number of events recorded during the test. This means that initially the frames will cover a long time period since few AE occurred at the beginning, while towards failure each frame will only cover fractions of a second since AE occur at a rapid rate.

Events with greater than 50% CLVD (compensated linear vector dipole) are considered shear type events and are marked with an 'x', while events with less than 50% CLVD are considered tensile and marked with 'o'. For those events detected by 4 sensors, it is not possible to invert the moment tensor and so these events are marked as undefined with '.'. The colour of an event indicates its relative magnitude, where red is the largest. Black ellipses are used to highlight areas of interest.

Where possible, AE frames are shown next to the appropriate analysis sketch from Bruno. However, these tend to be few in between and as discussed, the high speed frames tend to occur after the end of detectable AE events.

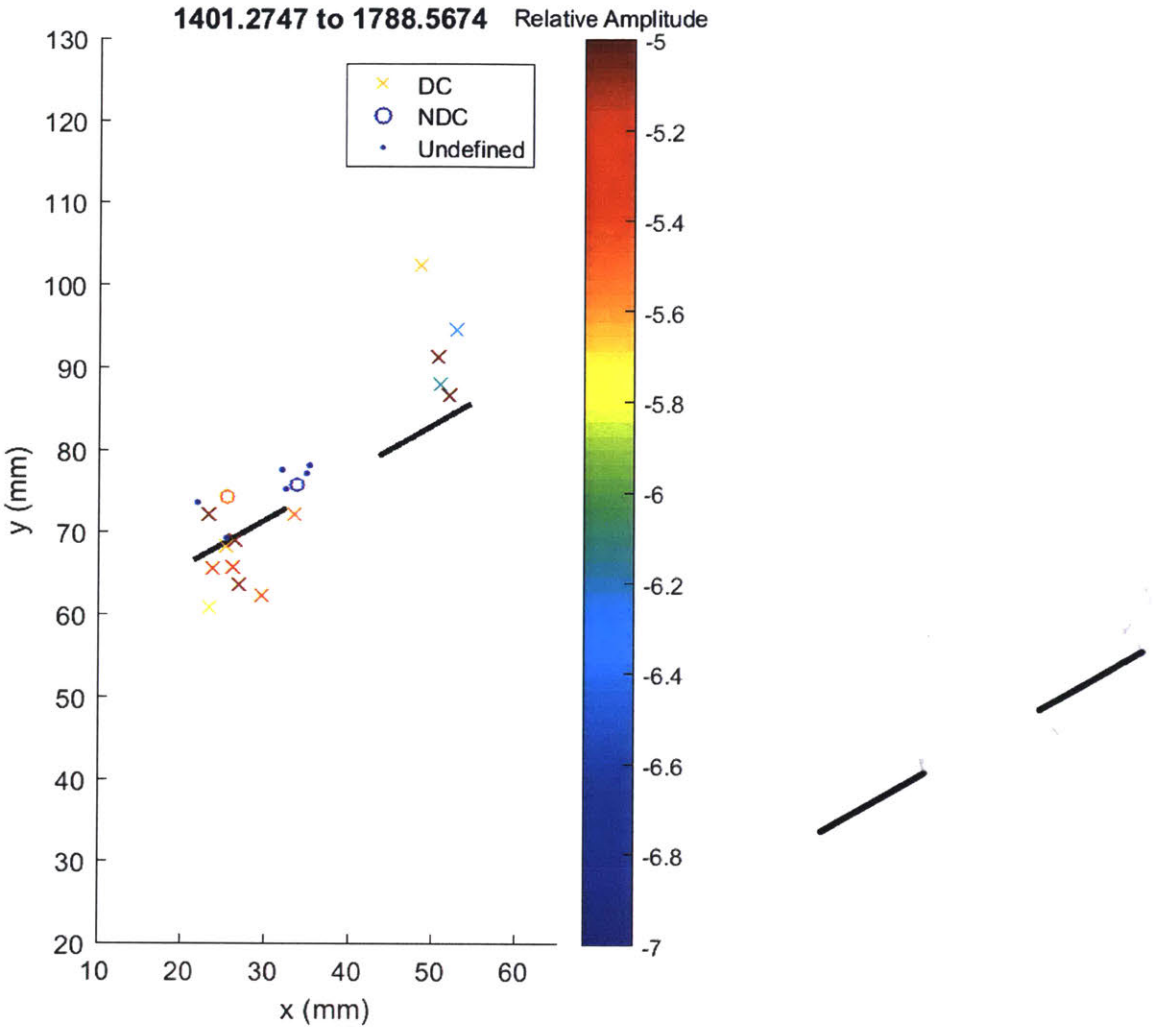

White patching occurs at inner tip of left flaw, and outer tip of right flaw. AE events occur at outer tip of both flaws, and a few at the inner tip of the left flaw. Most events are shear type, and the largest events occurred at the outer tip of the left flaw, despite no visual white patching occurring.

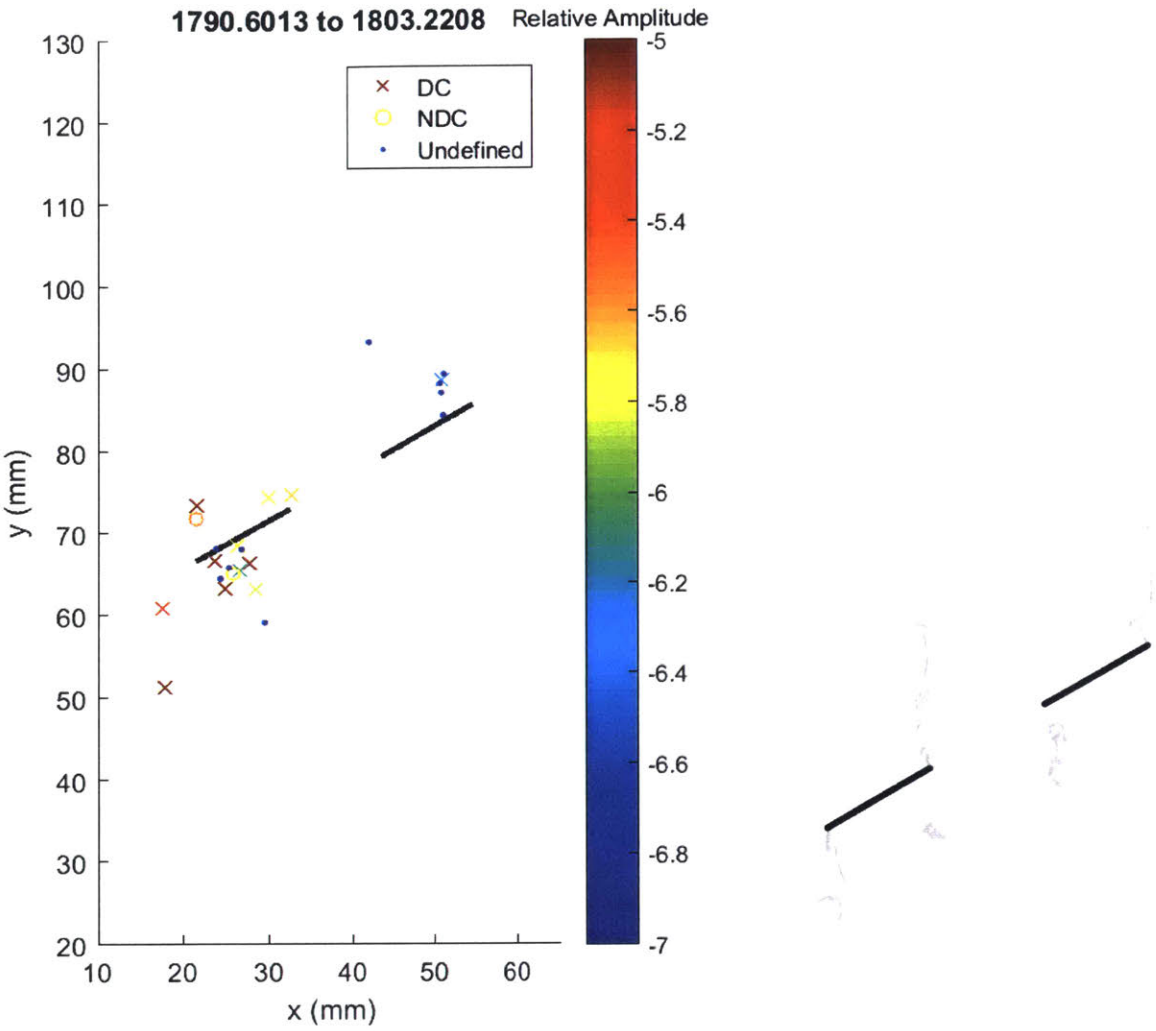

Significant development of wing crack shaped white patching on both flaws. Large amplitude AE events are clustered below the outer tip of the left flaw, which is the site on crack initiation. Low amplitude undefined events occur linearly at the outer tip of the right flaw. High amplitude events are mostly shear.

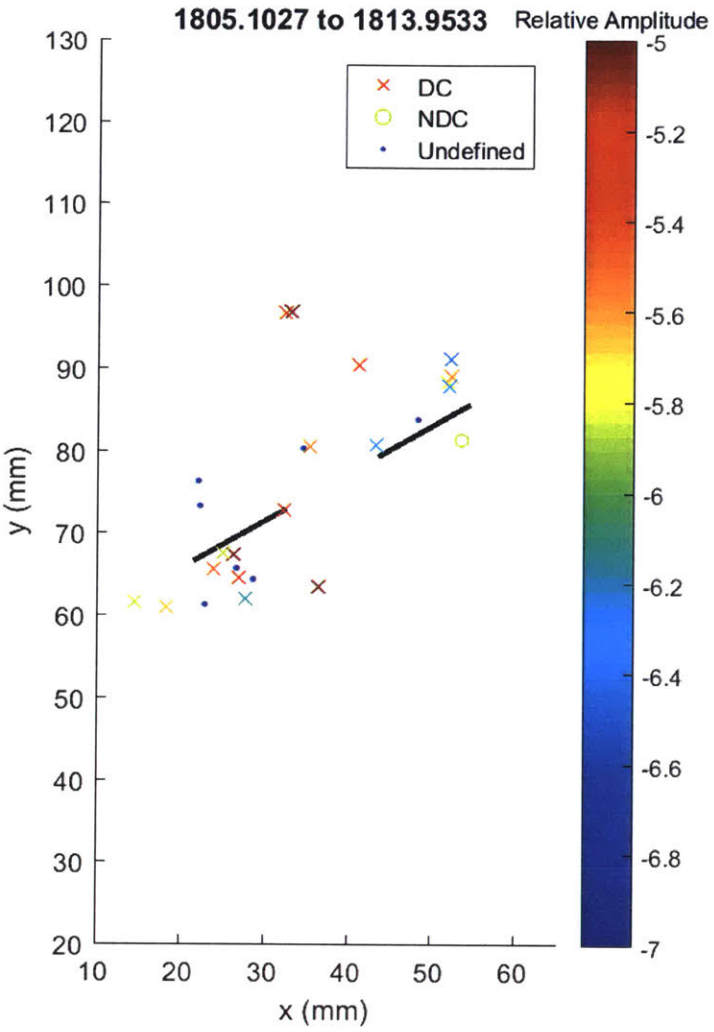

AE events continue to be mostly shear, and concentrated at the outer flaw tips. A few high amplitude events occur approximately 3cm above the inner tip of the left flaw.

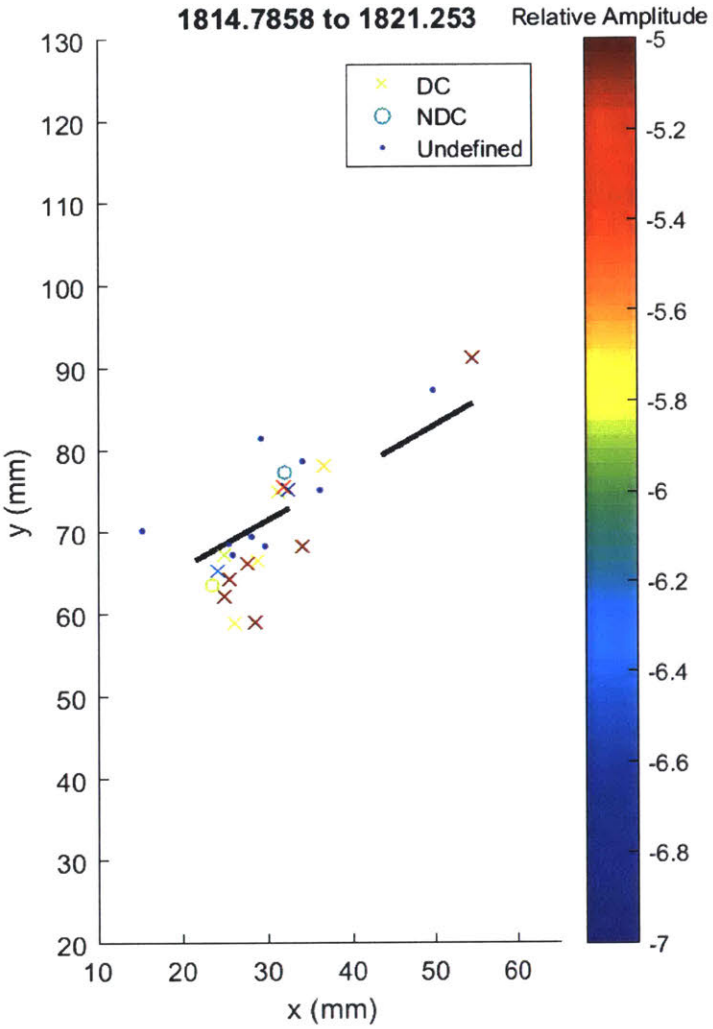

Some tensile events occur, but the largest amplitude events continue to be shear. Locations are mostly around the left flaw, particularly below the outer tip.

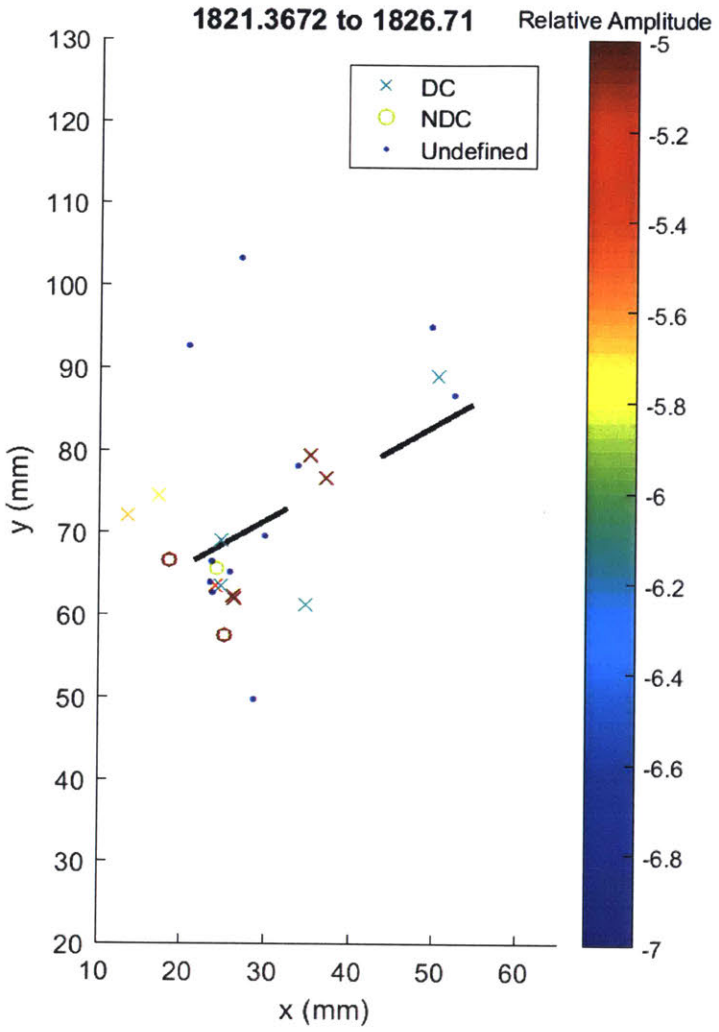

Generally same as previous frame.

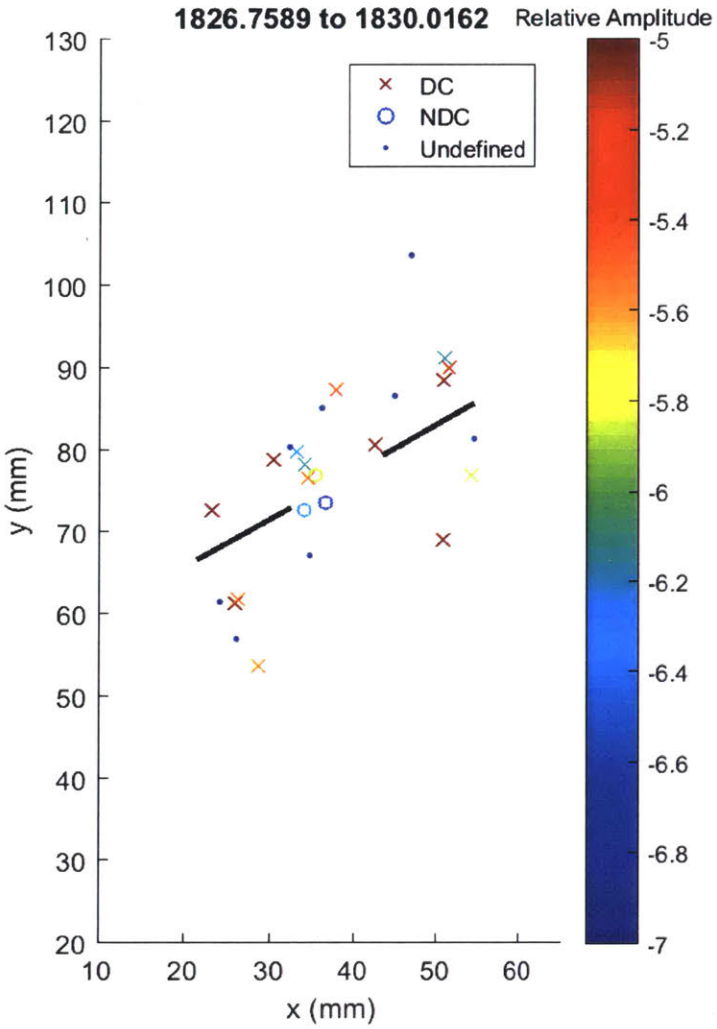

AE events occur around both flaws, with high amplitude events concentrated around wing crack locations. More events in the bridge than previously. Three low amplitude tensile events occur in the bridge, high amplitude events tend to be shear.

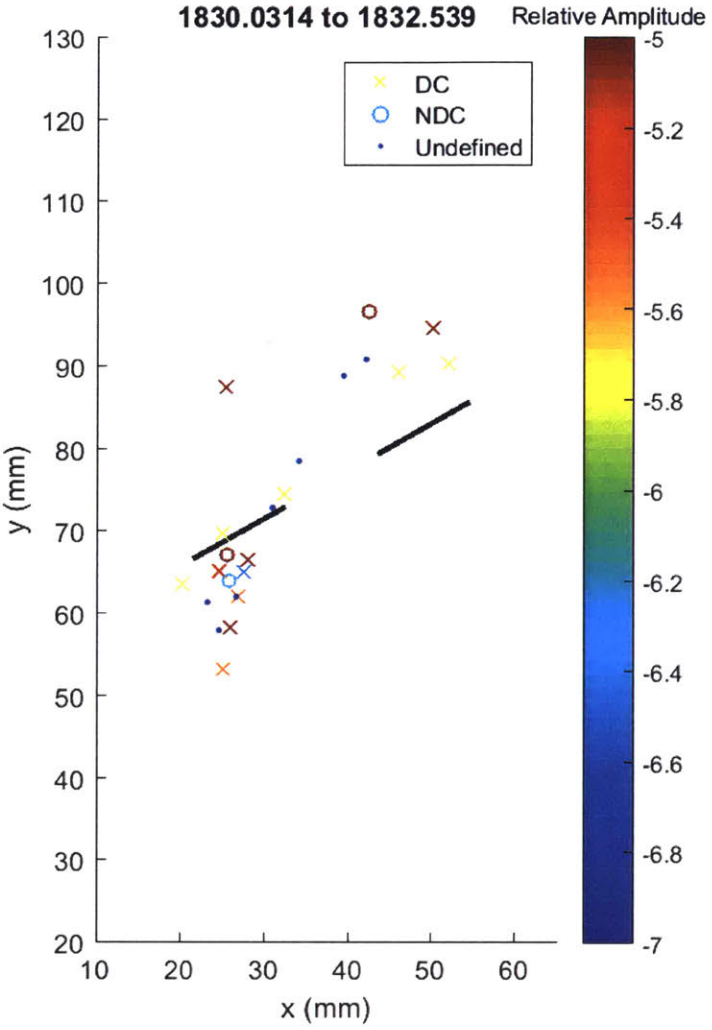

Key frame. Primary cluster of AE events tend to be linearly oriented below the outer tip of the left flaw, the site of crack initiation. One large tensile event occurs immediately at the tip, while shear events (large and small) occur up to 2cm below the flaw tip. This appears to be a coalescence of microcracks, where the tensile events coalesce through a series of shear microcracks. Some diffuse events also occur above the right flaw. Peak pressure occurs around this time.

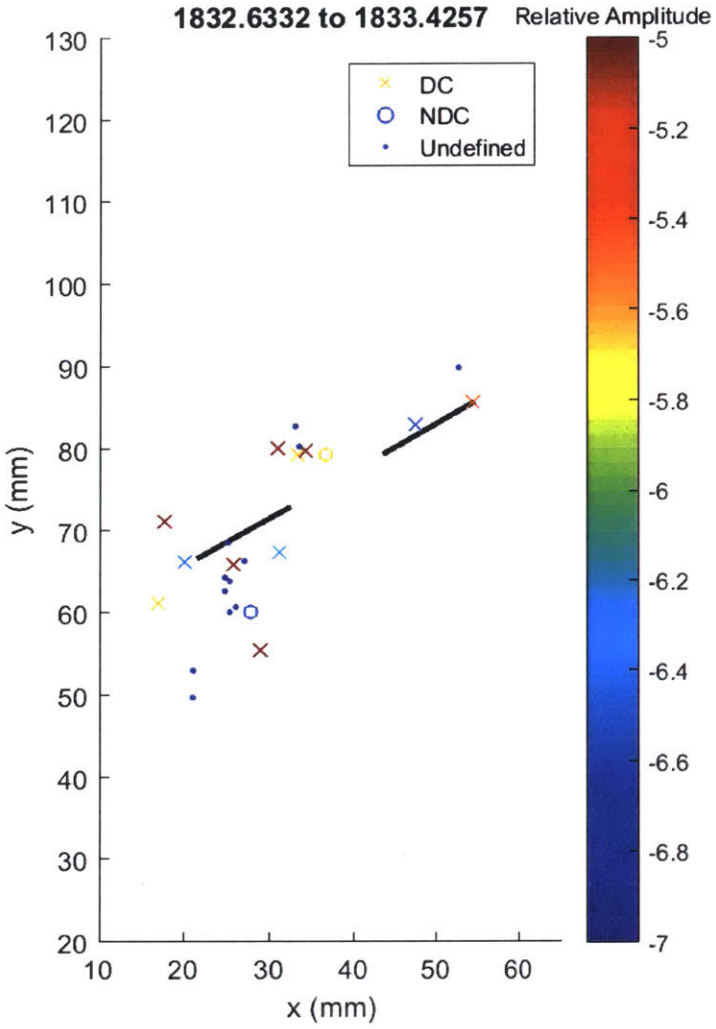

AE events continue to cluster at both tips of the left flaw. Out tip of left flaw consists mainly of low amplitude undefined events.

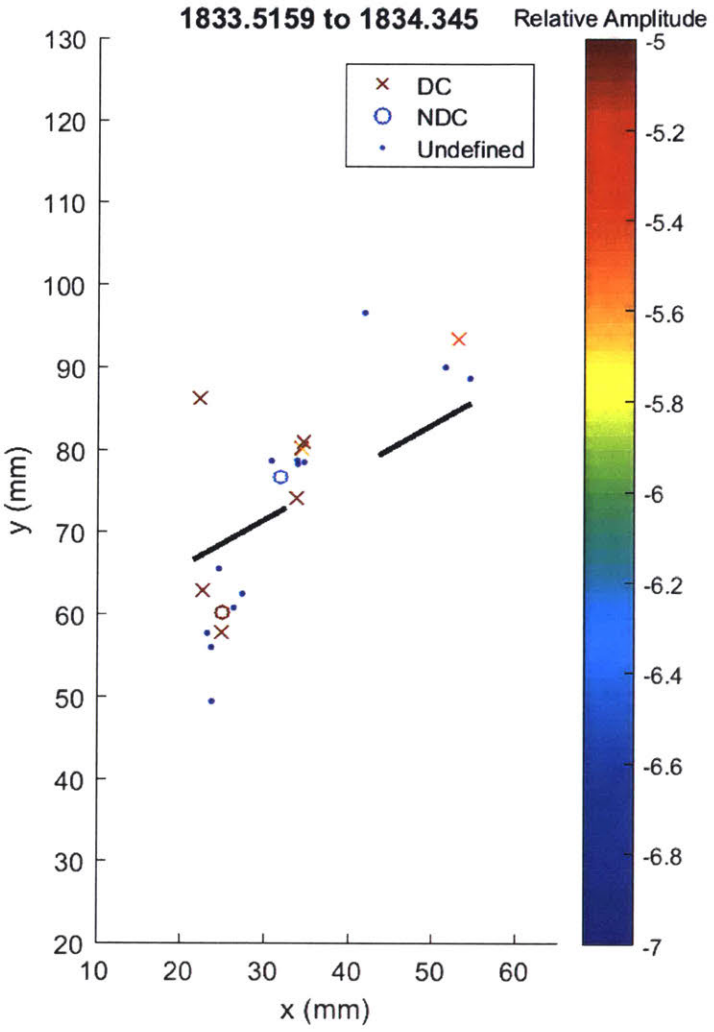

Events continue to occur at both tips of the left flaw, including large amplitude shear and tensile events.

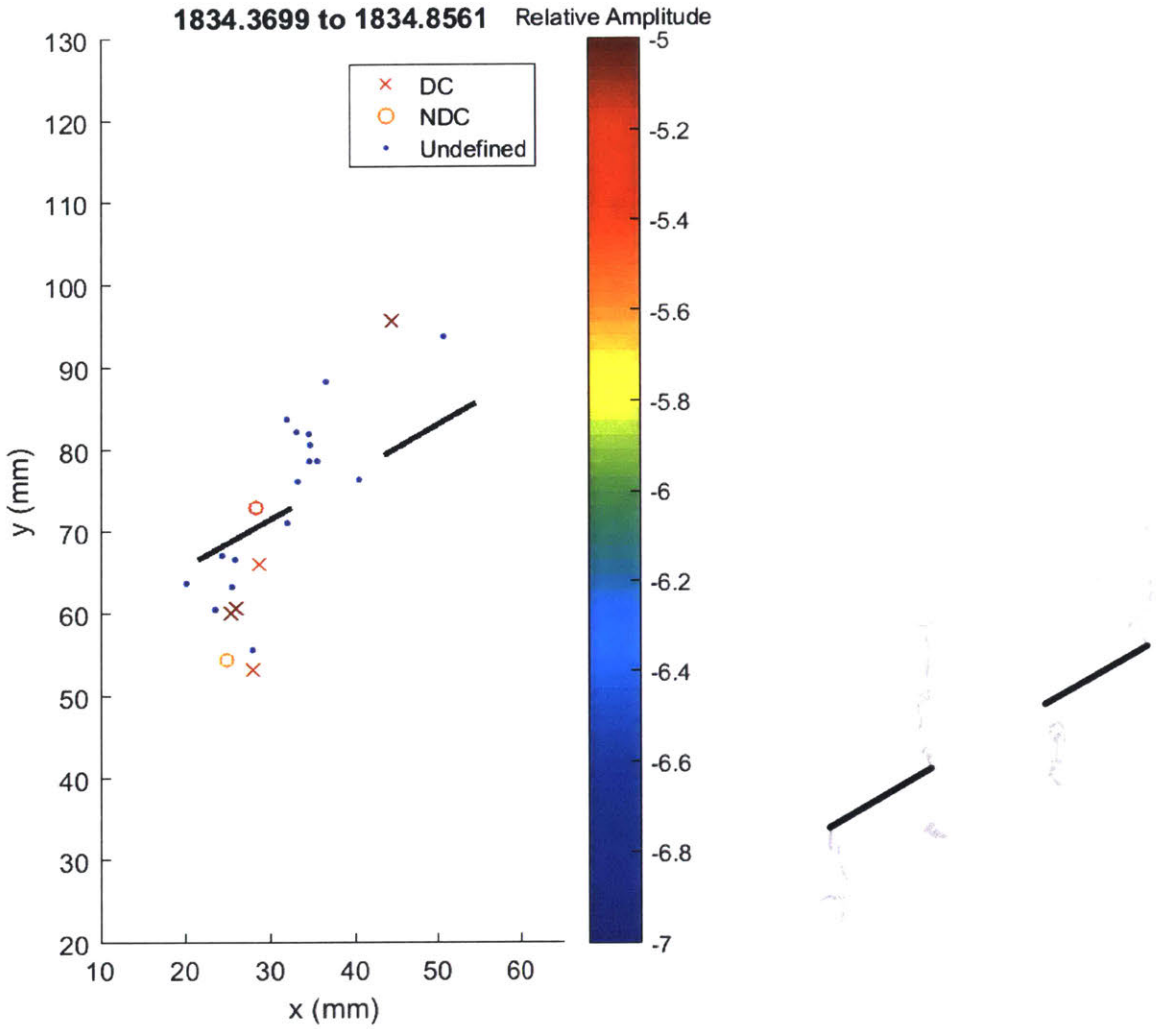

By this point the white patching largely reflects the wing cracks exhibited by the AE and the final crack pattern. Inner tip of left flaw consists only of small amplitude undefined events, while outer tip of left flaw shows a number of high amplitude shear events, and one tensile events 1.5cm below the tip.

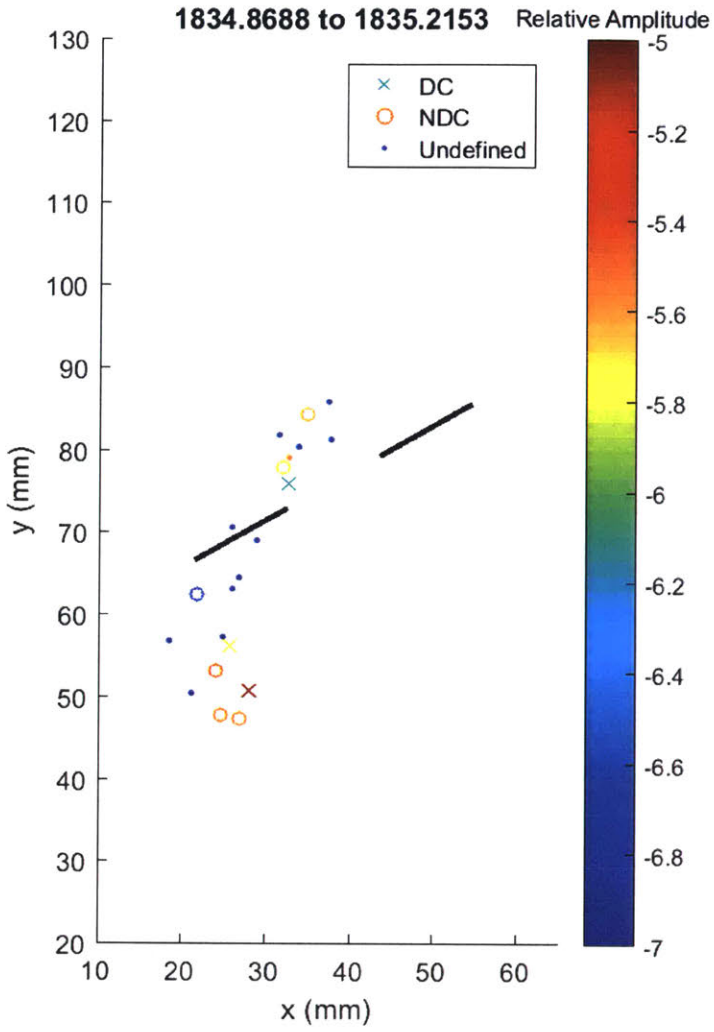

Events at both tips of left flaw, tensile events appear to be moving away from the flaw tips.

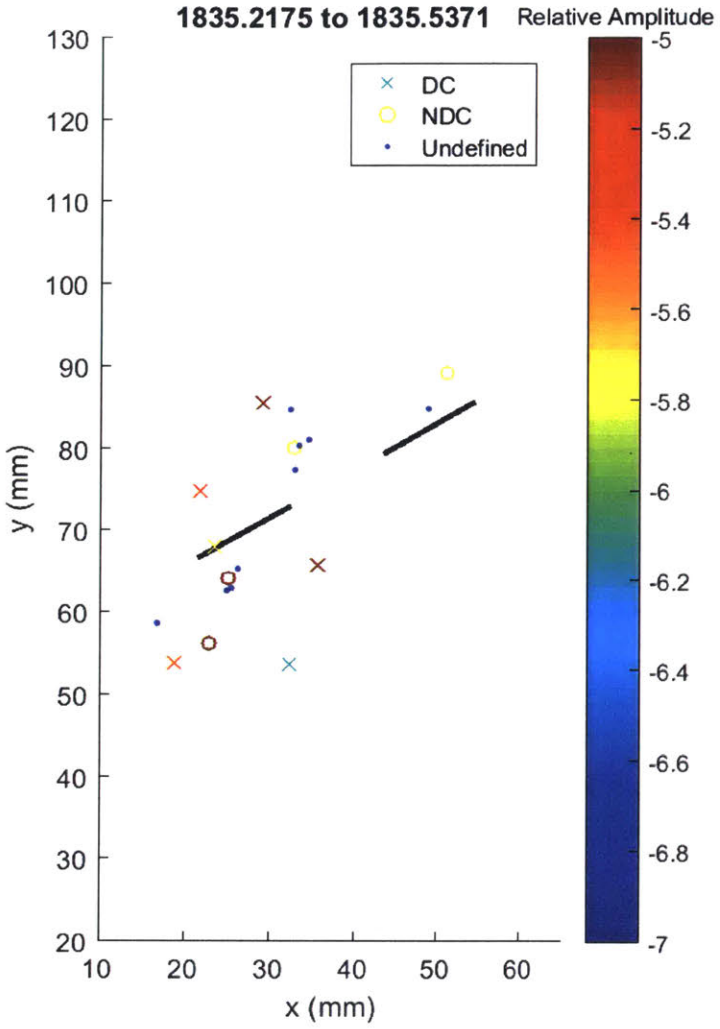

Some clustering of events at inner tip of left flaw, otherwise events are scattered.

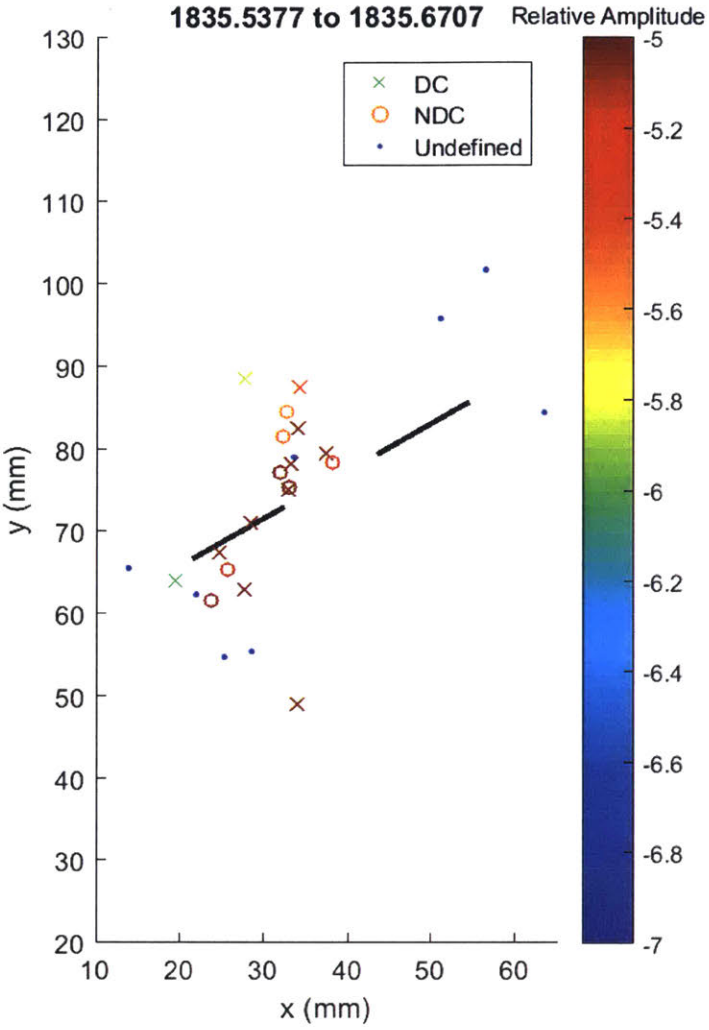

Key frame. Significant linear cluster of high amplitude shear and tensile events at inner tip of left flaw, where the high amplitude events are closest to the flaw tip. This again appears to be a coalescence of microcracks, but different in nature from the outer tip, where the tensile events followed the shear events. Here they appear to be occurring together. Some high amplitude shear and tensile events also occur at the outer tip.

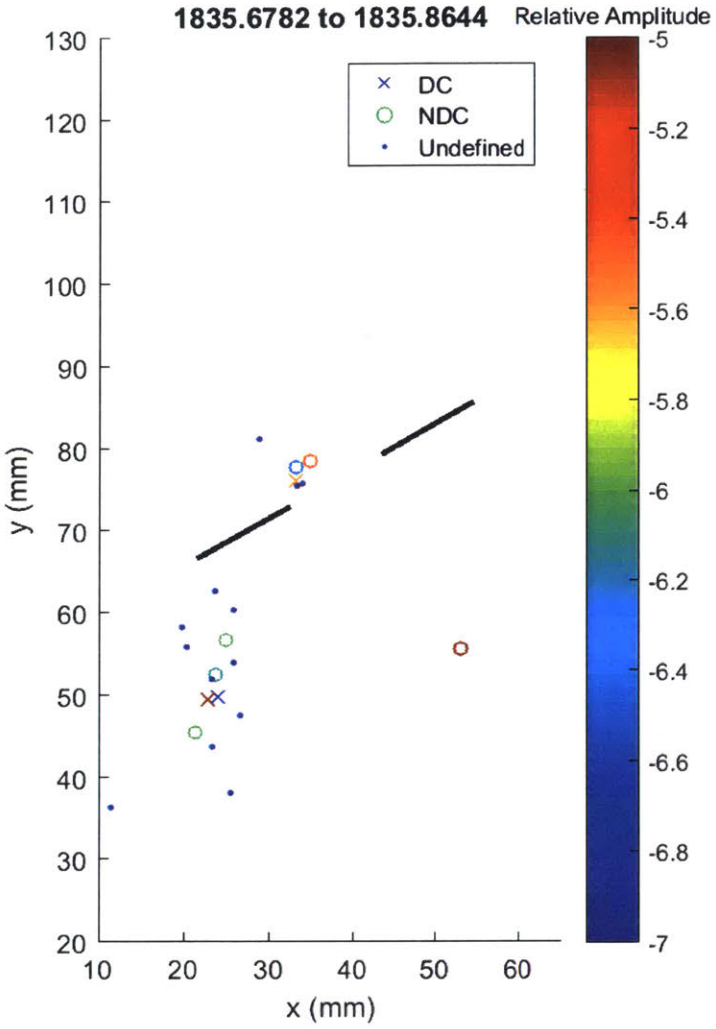

Events on both sides of left flaw. Left side of wing crack consists mainly of low amplitude undefined and tensile events. This may be because the left side has already experienced significant damage. AE events at the inner tip consists of 2 tensile and 1 shear event, some with large amplitude.

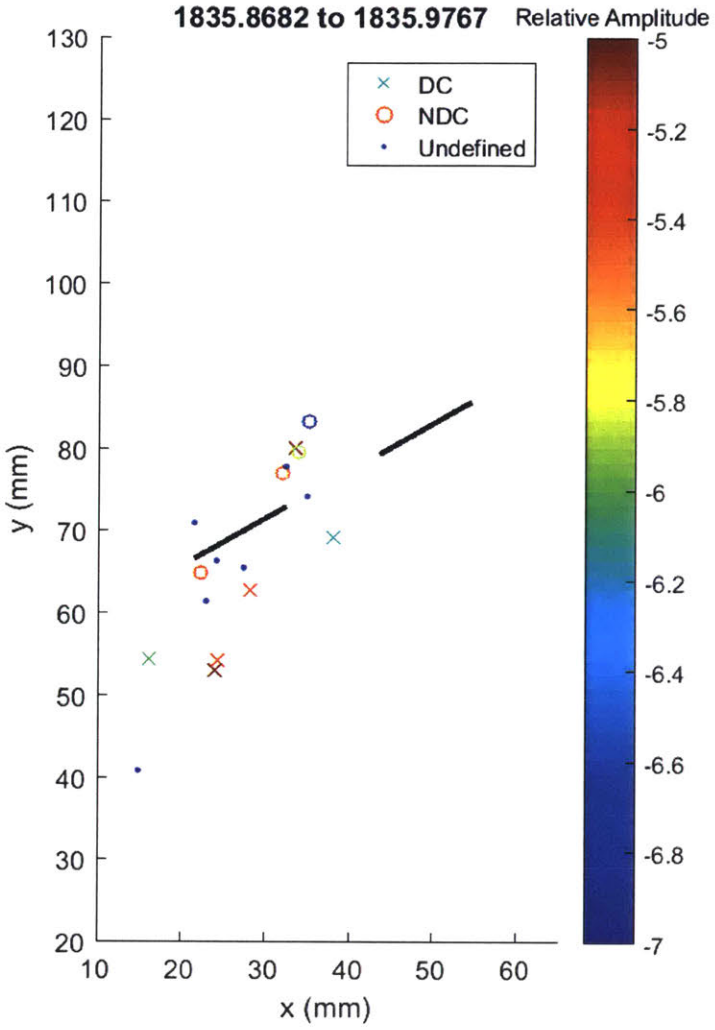

Large tensile events occur at both tips of the left flaw, and large shear events happen 2cm below outer tip of left flaw. Other scattered events happen at both tips of left flaw.

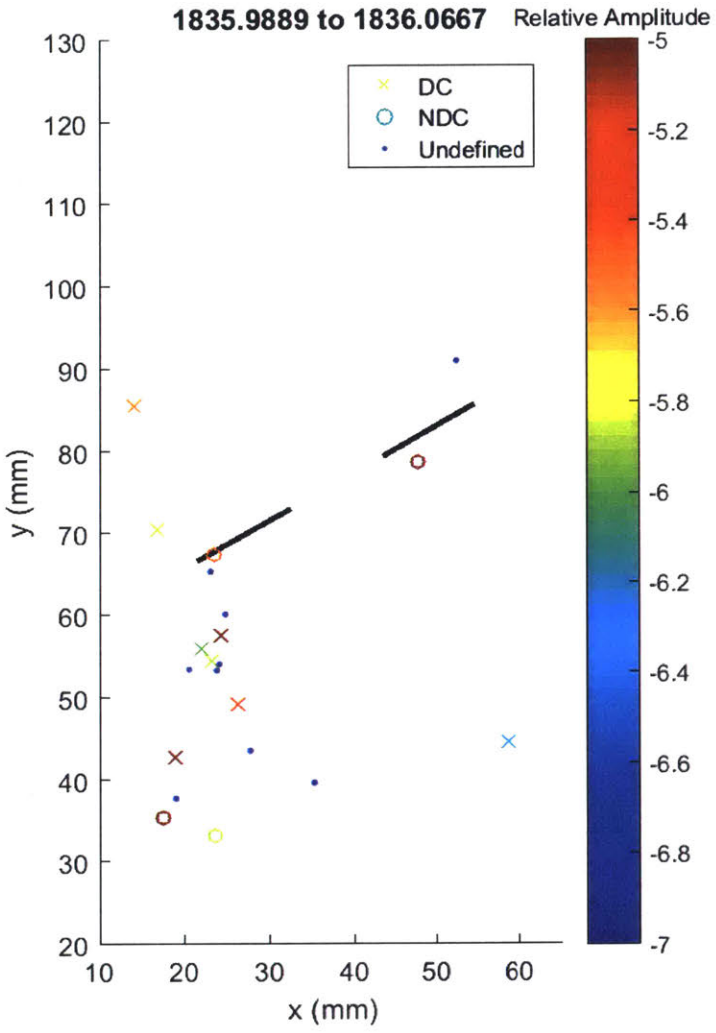

Widely scattered linear pattern of AE hypocenters below outer tip of left flaw. Mainly shear events, but the 2 tensile events are high amplitude. Suggests damage is progressing further from the flaw tip.

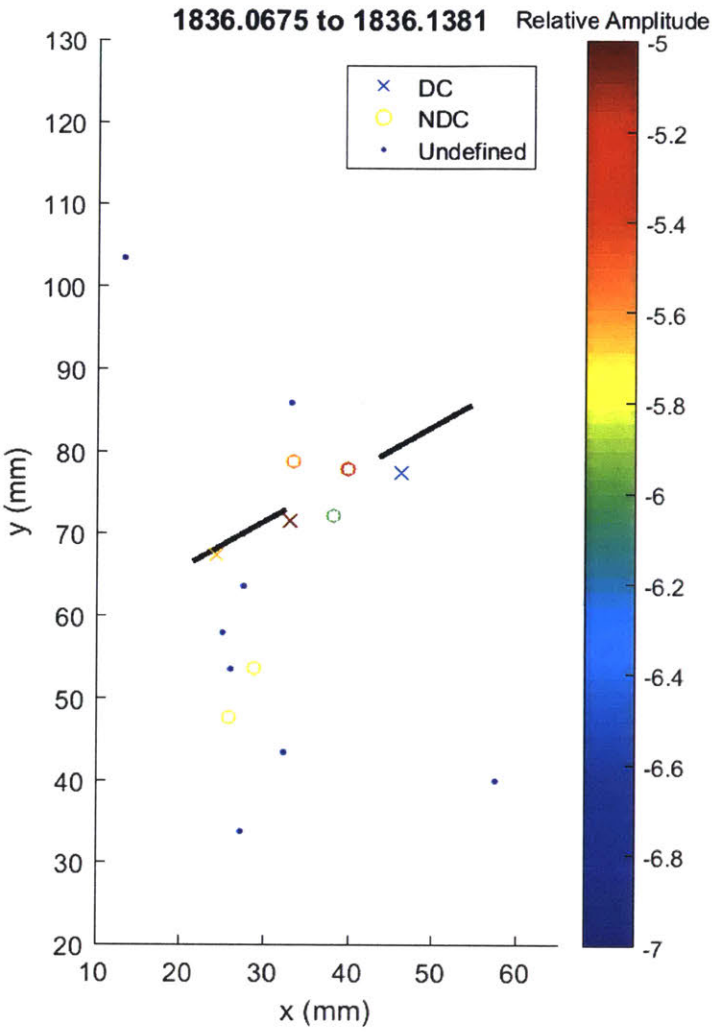

Scattered events. 2 large tensile events and 1 large shear event occur in the bridge.

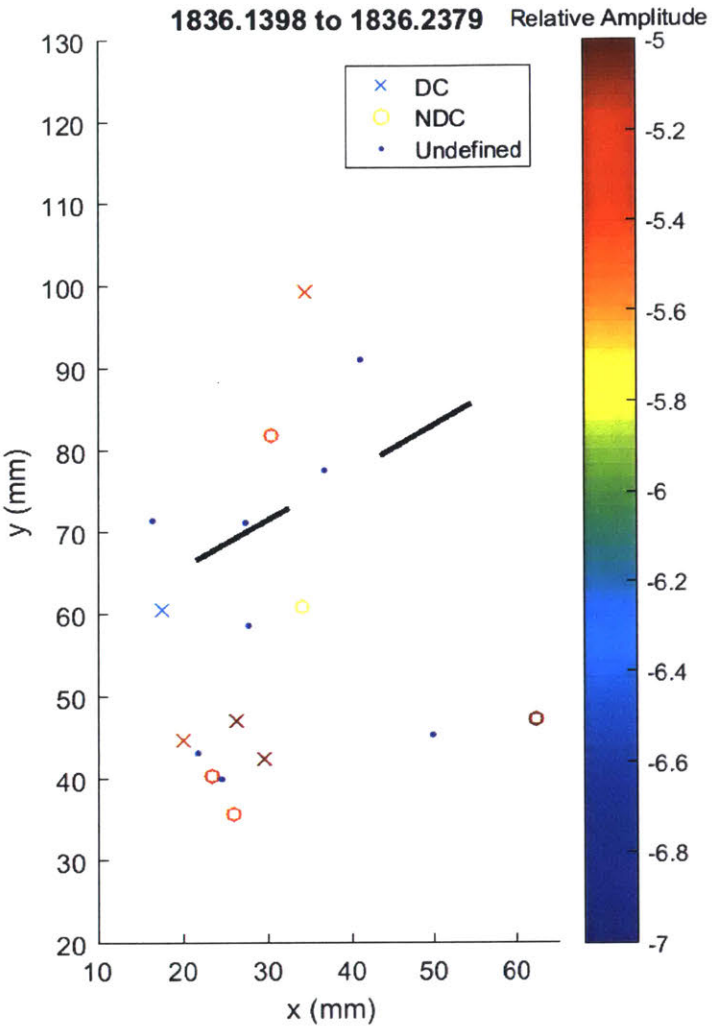

3 large shear and 2 large tensile events occur about 3cm below the outer left flaw tip. This may be the damage zone reaching the O-ring.

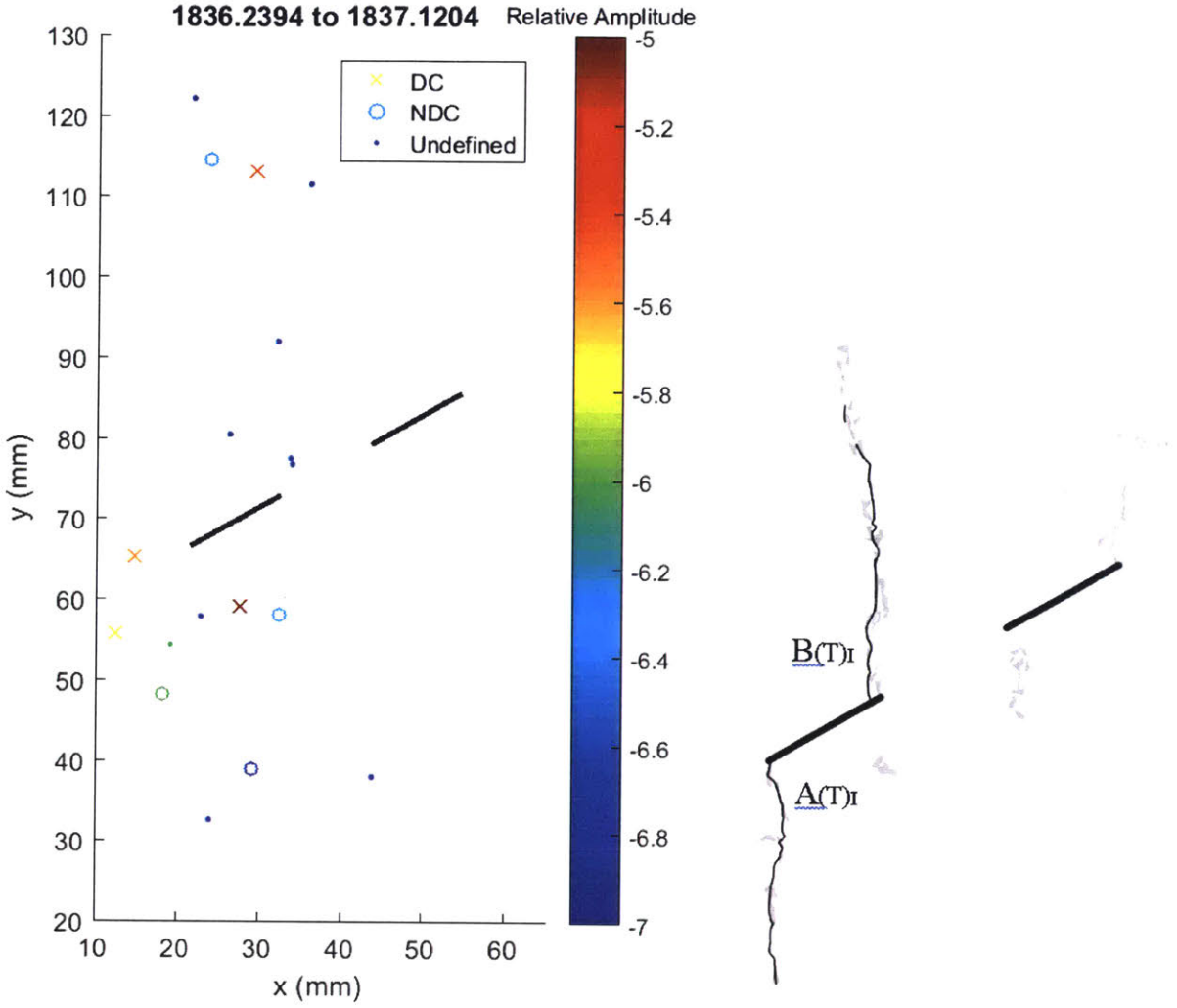

This frame extends after the pressure has decreased and the rock is already cracked, and events are largely scattered.

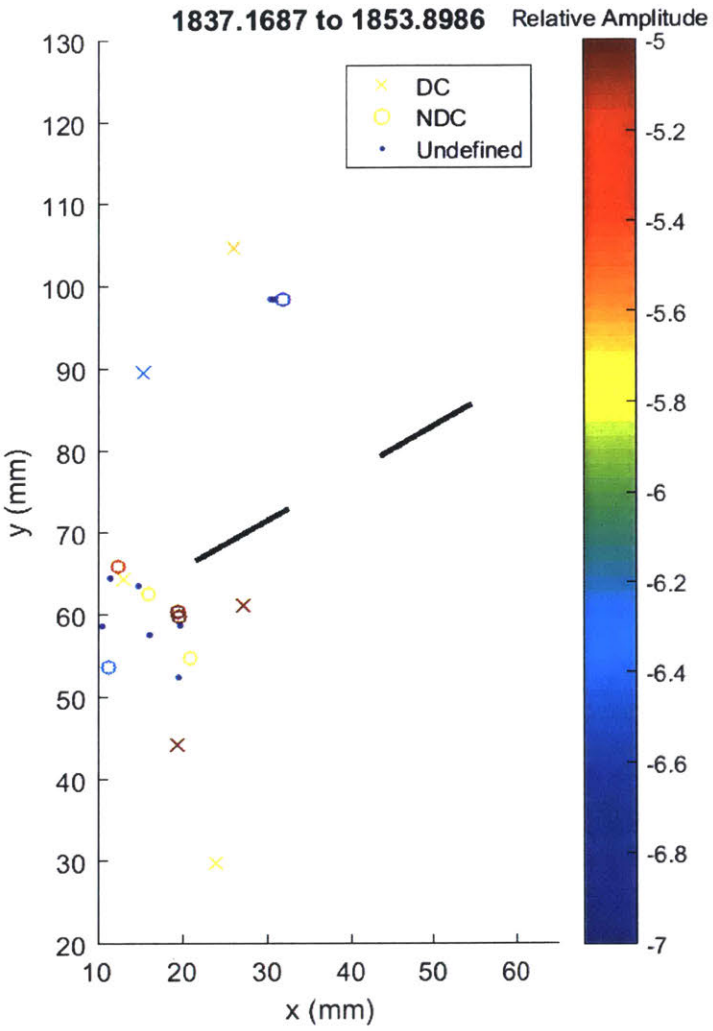

Events largely concentrated to the left of the outer tip of the left flaw.

Summary:

Initially, AE events occur on the outer tips of both flaws. However, by the second frame (after first 5% of events occur, and around 45 seconds before cracking), there appears to be a preference for the left flaw, which is where the crack initiation occurs. This is likely due to heterogeneities in the specimen. Being a VL5 test, there are significantly more shear events than tensile as compared to the VL0 tests. There are also some stages where there appears to be a coalescence of tensile microcracks joining a previous series of shear microcracks. This occurs first for the outer tip where visual cracking initiates, followed by microcrack coalescence on the inner tip. These occur 5 s and 0.8 s before crack propagation respectively.

AE hypocenter analysis for specimen 2a-30-0-VL5-C

Final crack geometry:

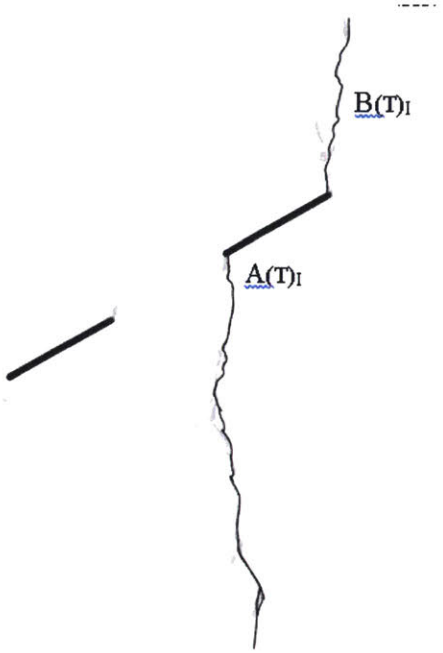

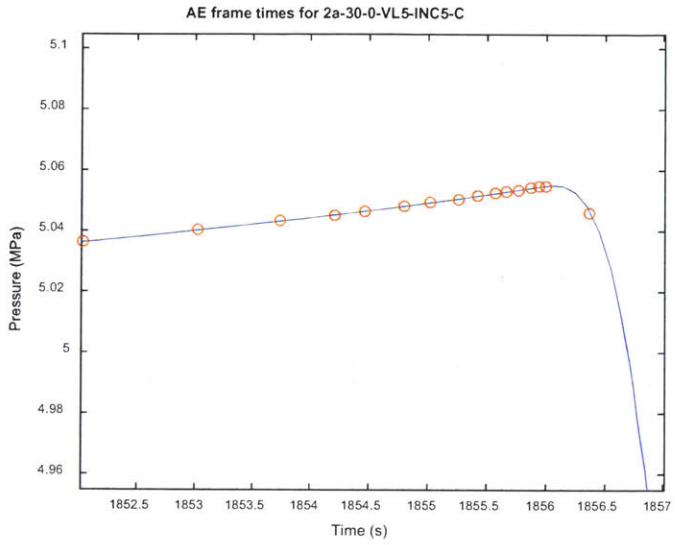

Crack initiates from inner tip of right flaw, followed by tensile crack B from the outer tip of the right flaw in classic wing pattern. Peak pressure occurs immediately prior to pressure breakdown.

Development of AE locations are shown over the 20 frames presented in this analysis, where each frame shows 5% of the total number of events recorded during the test. This means that initially the frames will cover a long time period since few AE occurred at the beginning, while towards failure each frame will only cover fractions of a second since AE occur at a rapid rate.

Events with greater than 50% CLVD (compensated linear vector dipole) are considered shear type events and are marked with an 'x', while events with less than 50% CLVD are considered tensile and marked with 'o'. For those events detected by 4 sensors, it is not possible to invert the moment tensor and so these events are marked as undefined with '.'. The colour of an event indicates its relative magnitude, where red is the largest. Black ellipses are used to highlight areas of interest.

Where possible, AE frames are shown next to the appropriate analysis sketch from Bruno. However, these tend to be few in between and as discussed, the high speed frames tend to occur after the end of detectable AE events.

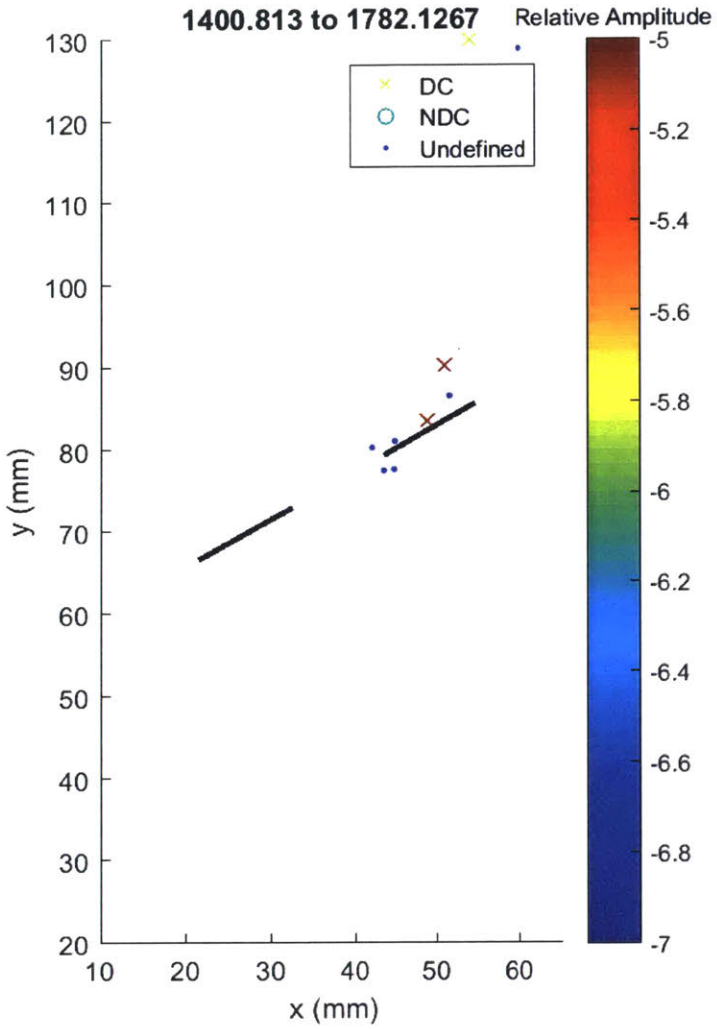

Two large shear events occur above the right flaw, and a four undefined events occur at the inner tip of the right flaw.

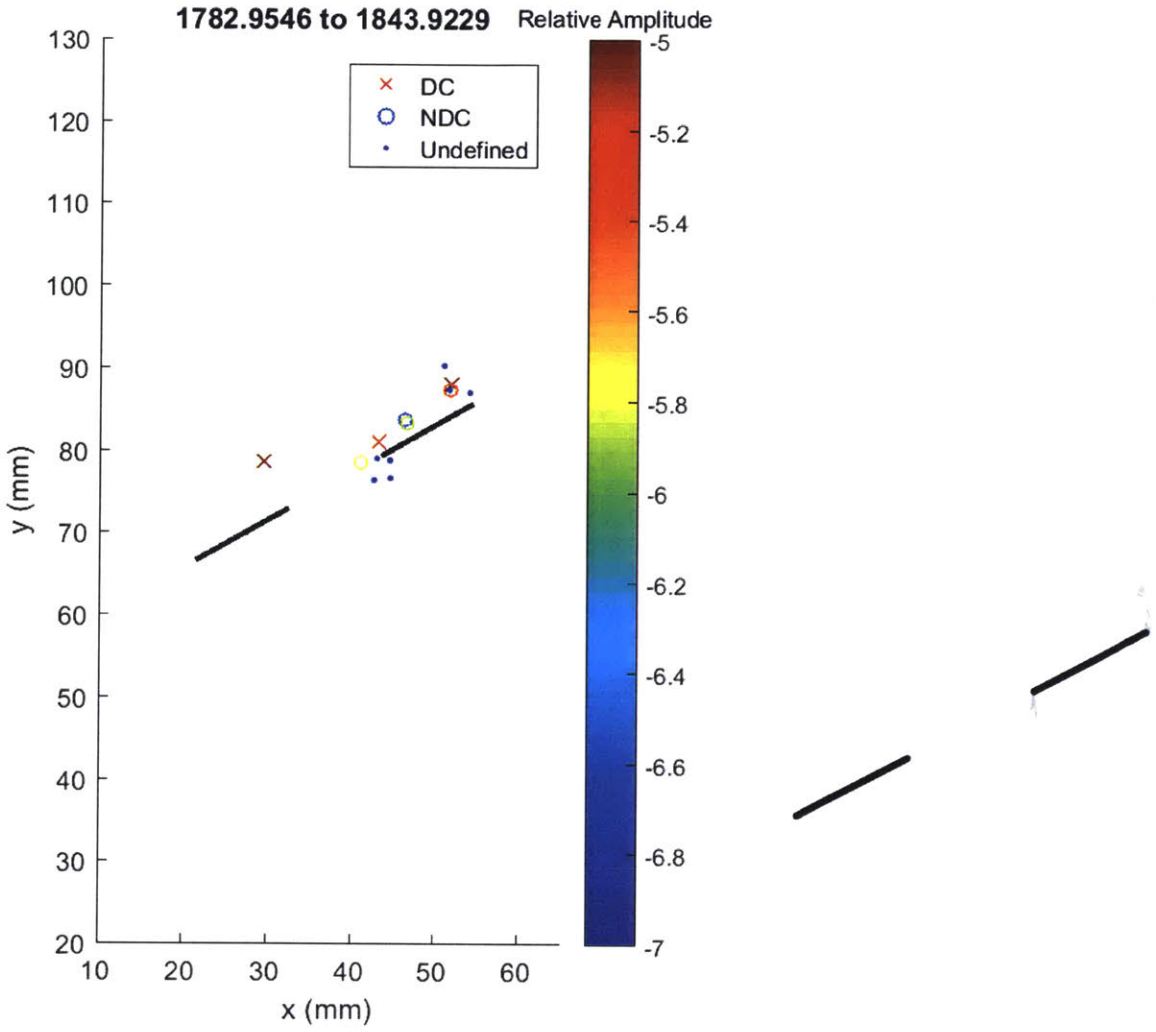

Minor white patching seen at both tips of right flaw. Shear and tensile events occur at both tips of the right flaw. One large shear event occurs above inner tip of left flaw.

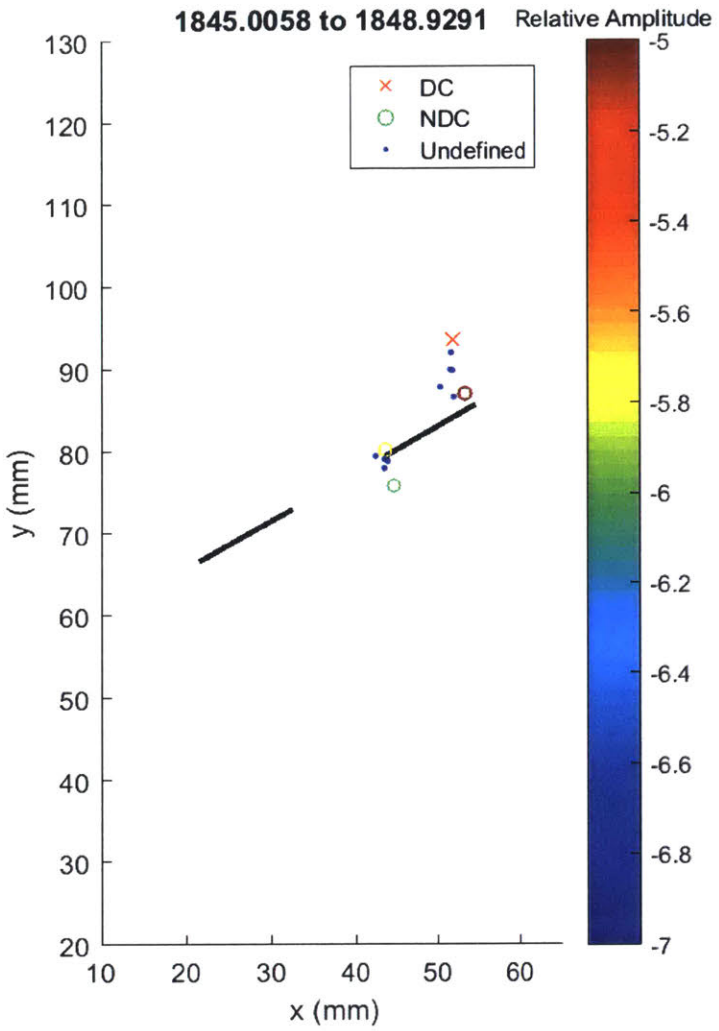

High amplitude shear and tensile events occur at outer tip of right flaw, smaller amplitude tensile events occur at inner tip. Linear pattern of undefined events leading from tensile to shear fracture at outer tip.

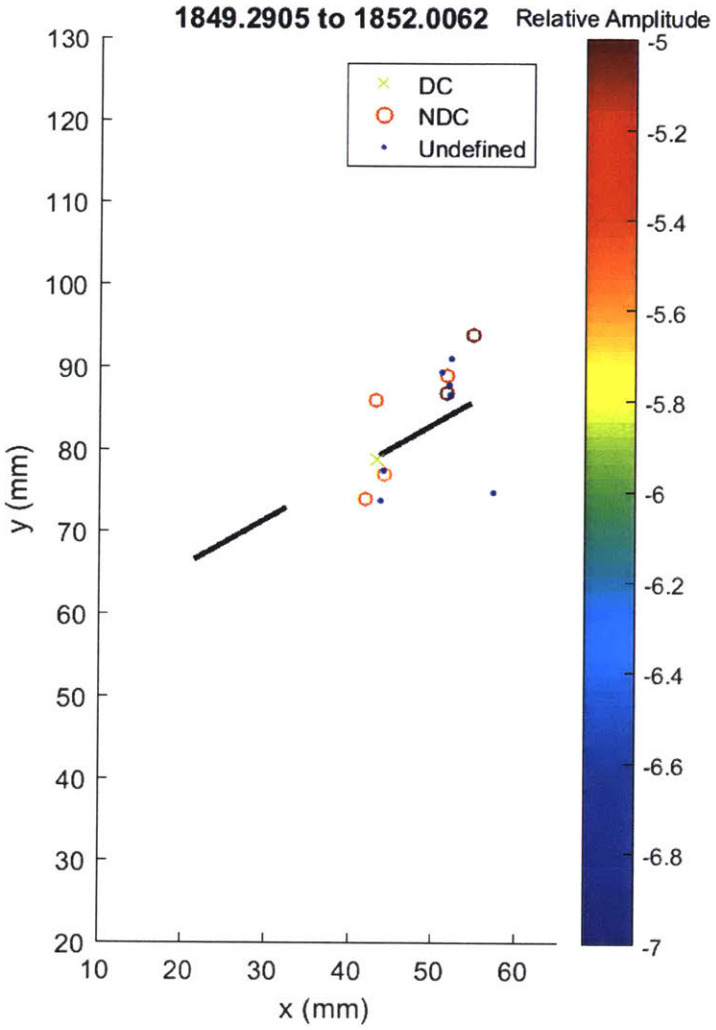

Large amplitude tensile events occur at both flaw tips. Only one small shear event at inner tip of right flaw.

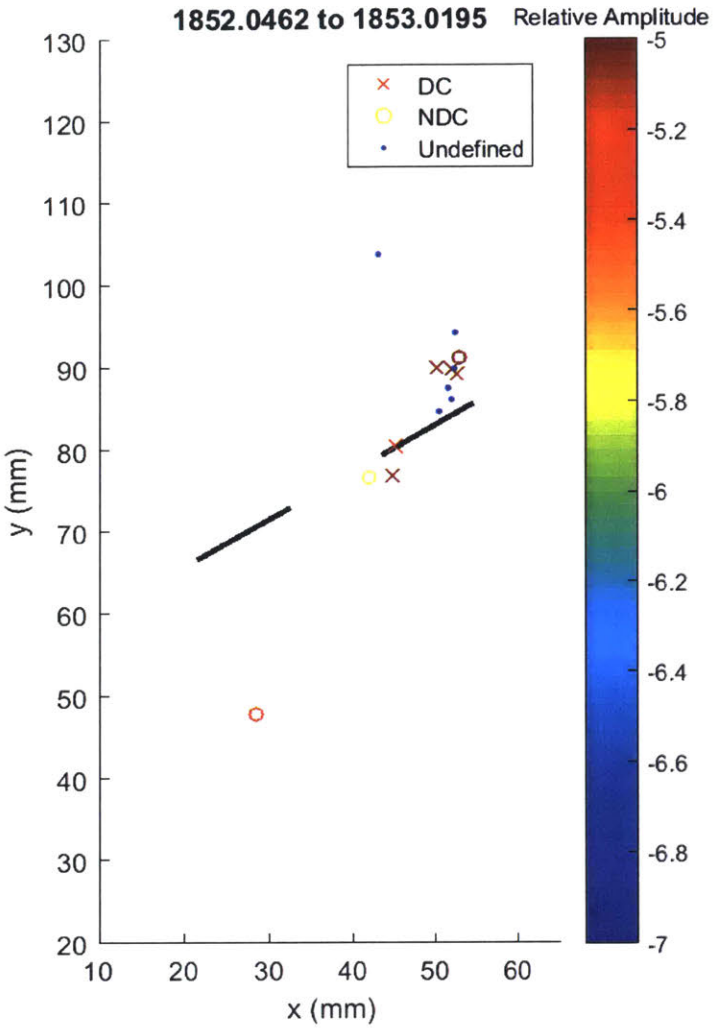

Large amplitude shear and tensile events at both tips. Cluster at outer tip appears to be further from the flaw tip. Outer tip also has a linear pattern of undefined events.

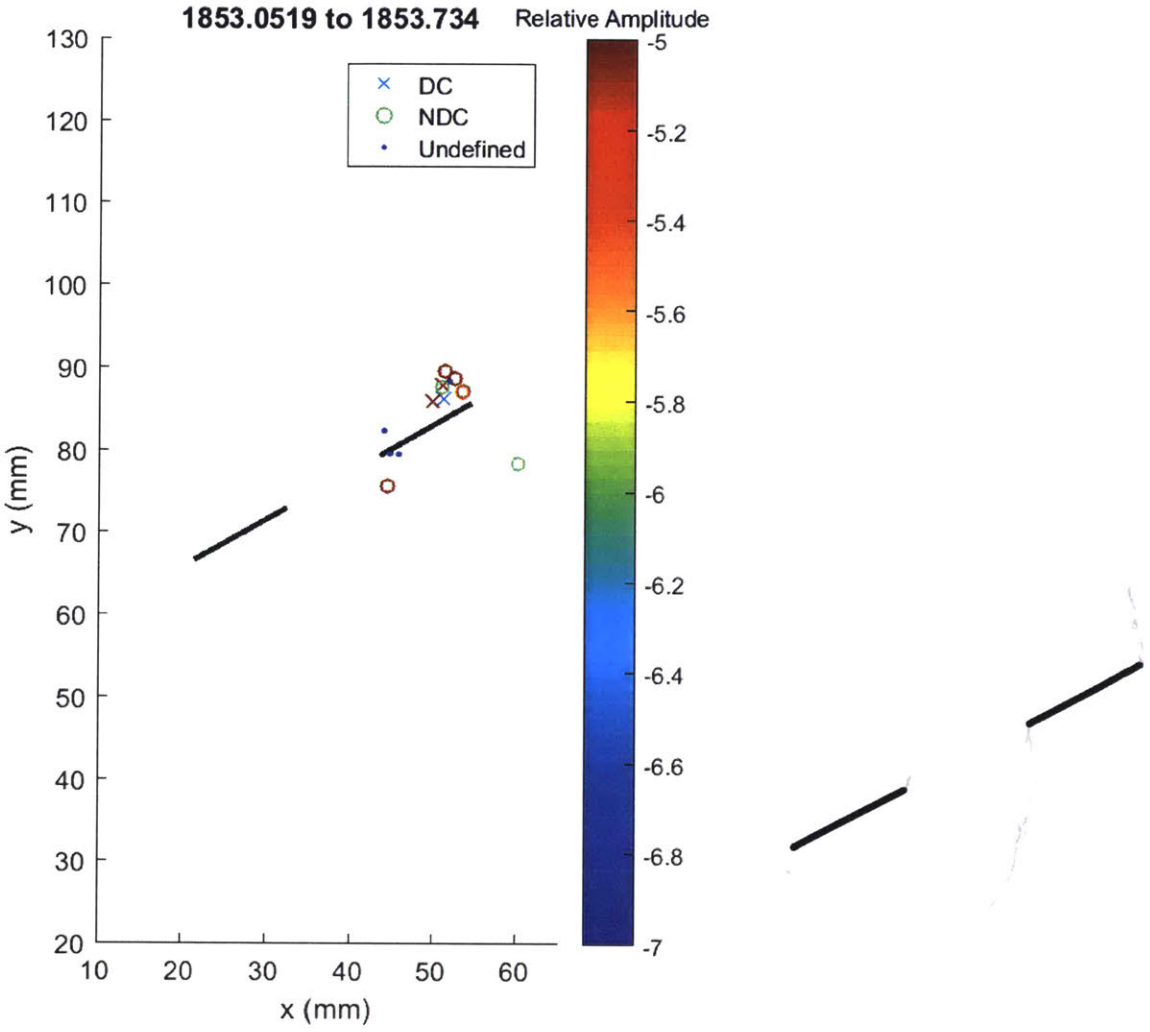

White patching is extensive by this point. High concentration of events at outer tip of right flaw, including 3 large tensile and 2 large shear events. Tensile appears to be linearly oriented from the tip. 3 low amplitude undefined events also occur at inner tip.

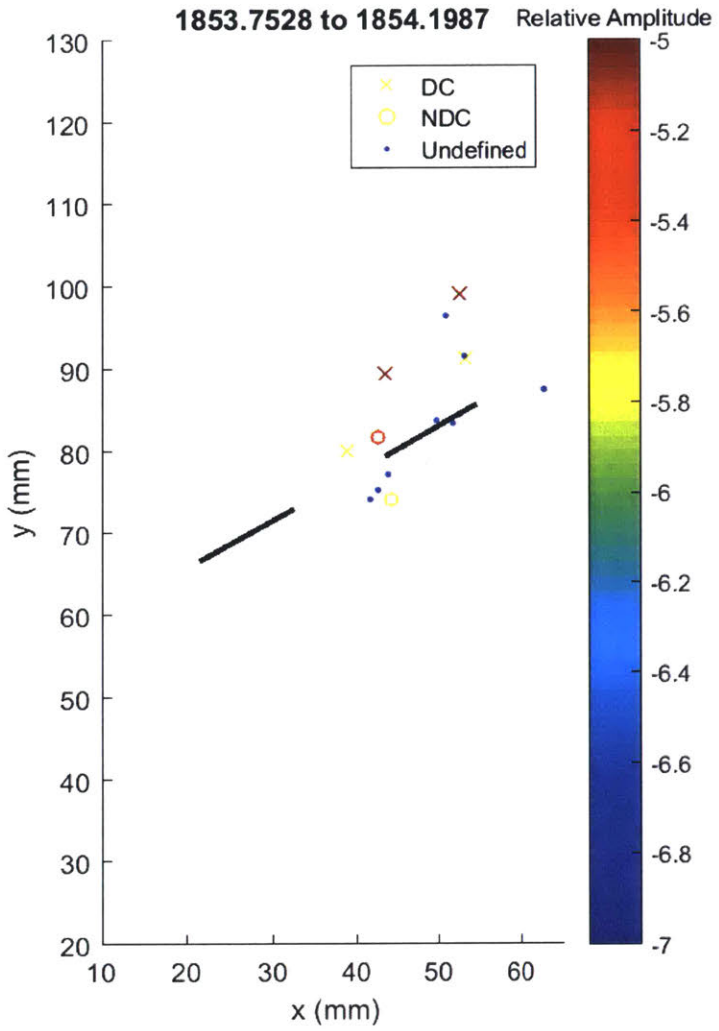

Generally scattered distribution of hypocenter locations.

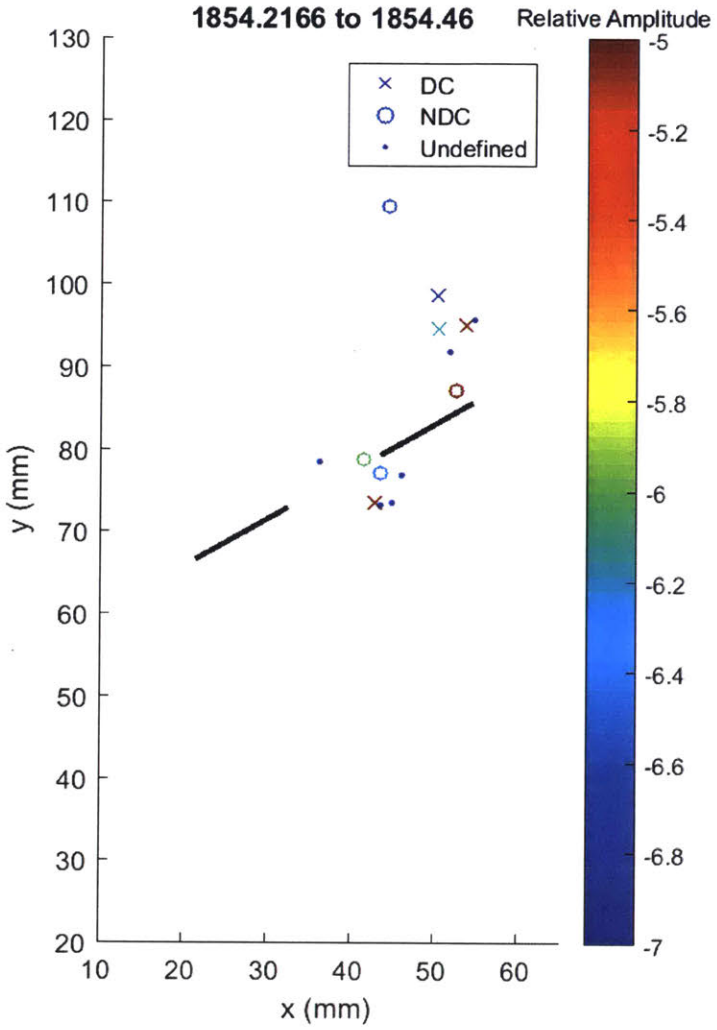

Linear scatter of events at both flaw tips, where the outer flaw shows events extending further away from the flaw tip. Shear events appear to be further from the tips than tensile events.

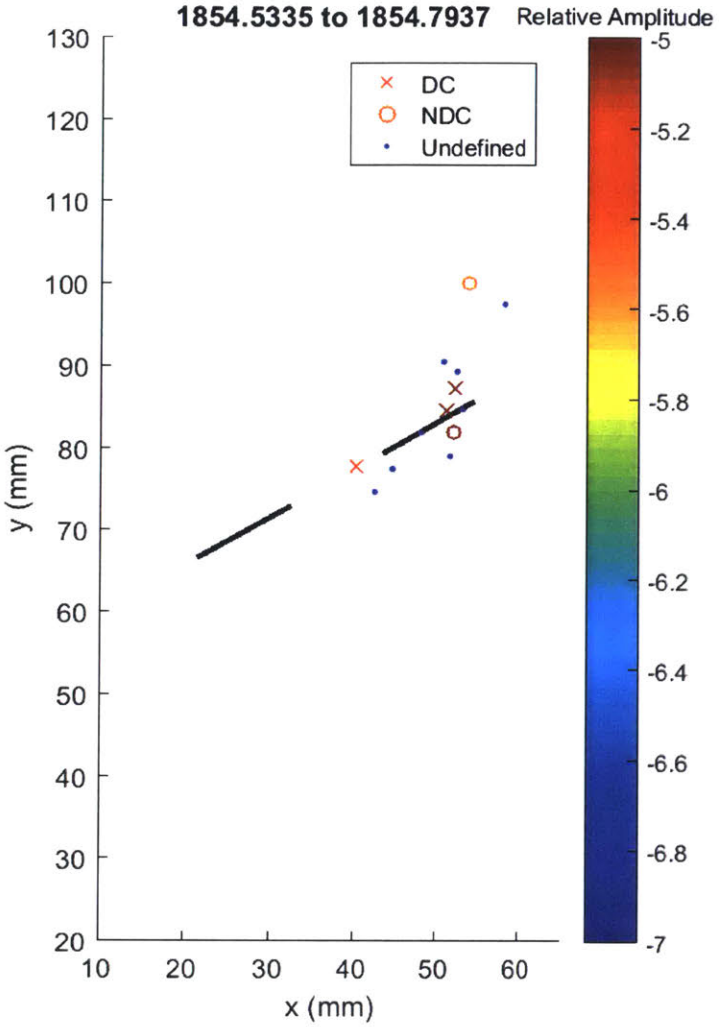

3 shear events and 1 tensile event occur around the flaw.

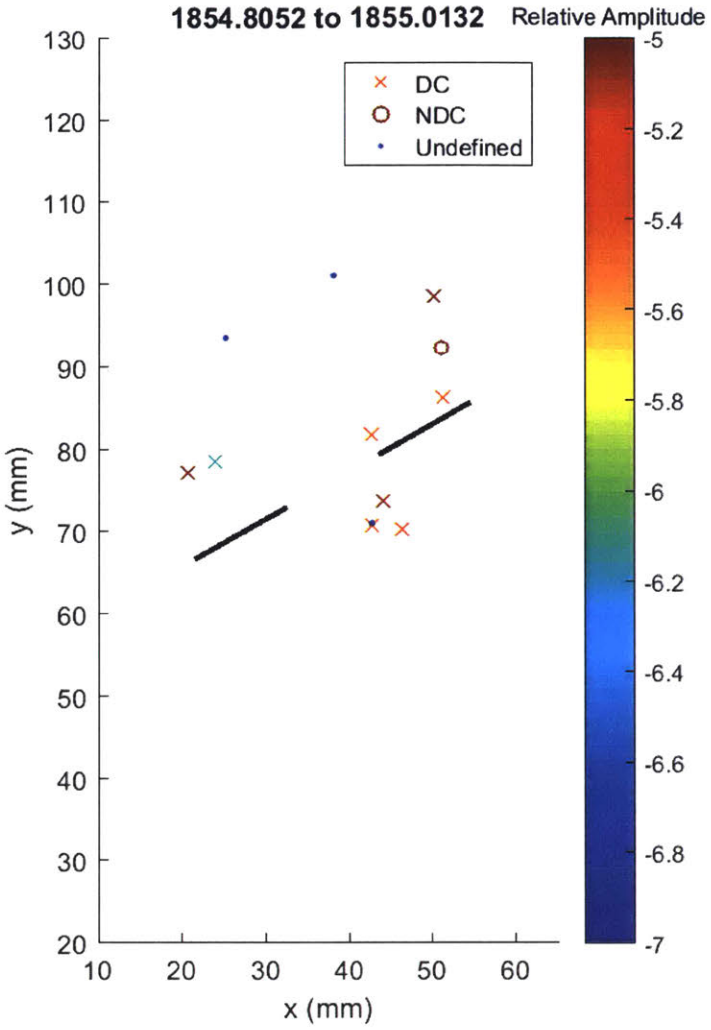

Primarily large amplitude shear events occur at wing crack locations at both flaw tips. 2 shear events occur above left flaw.

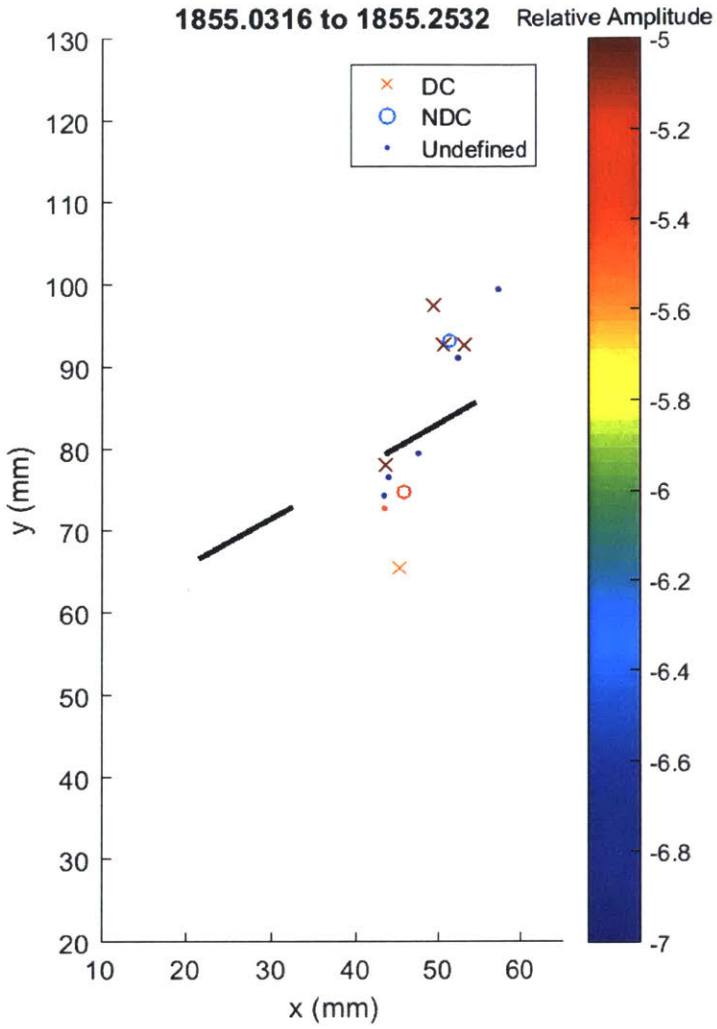

Same as previous frame

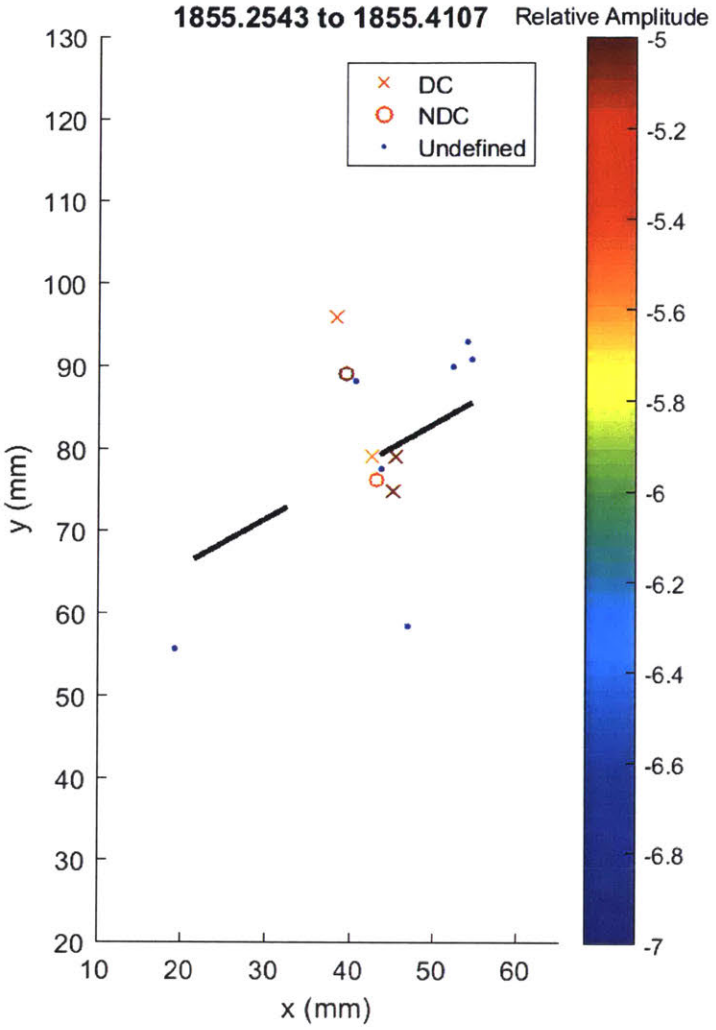

Large amplitude shear and tensile events occur close to the inner tip of the right flaw, while only small undefined events occur at outer tip. Another two events occur at anti-wing crack locations above the left tip of the right flaw.

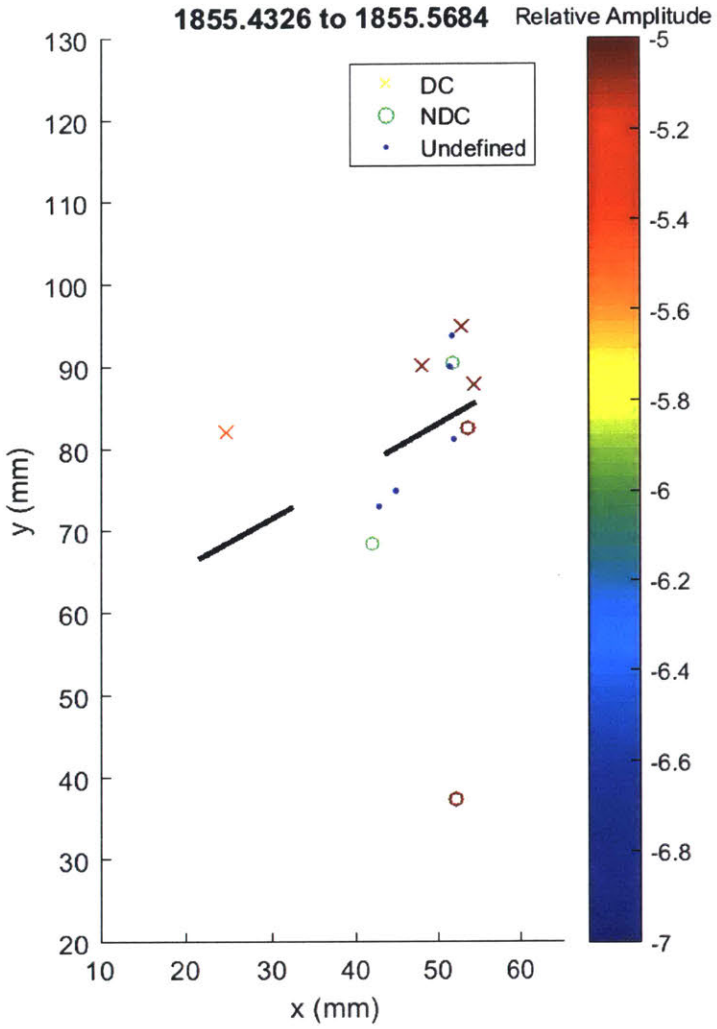

While events in the previous frame were mostly concentrated around the inner tip of the right flaw, in this frame the events occur at the outer tip, again suggesting there may be a cyclical nature to the localisation of damage in the specimen. This cannot be explained by the classic fuse-type theory.

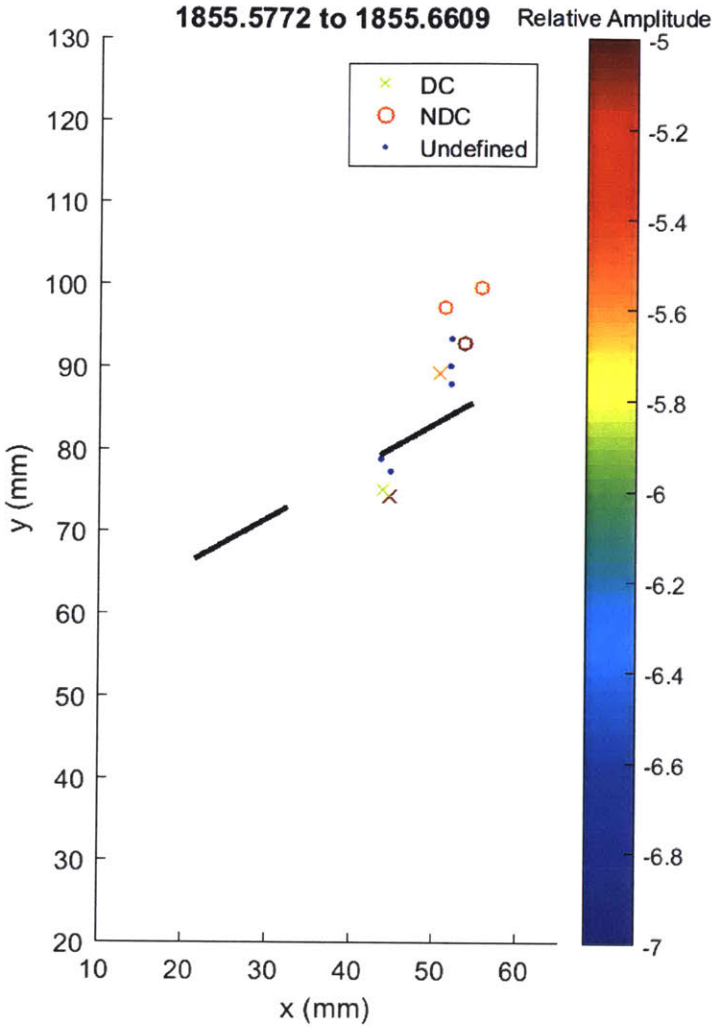

Similarly to the previous frame, damage continues to occur at the outer tip of the right flaw, while only 1 large event occurs at the inner tip.

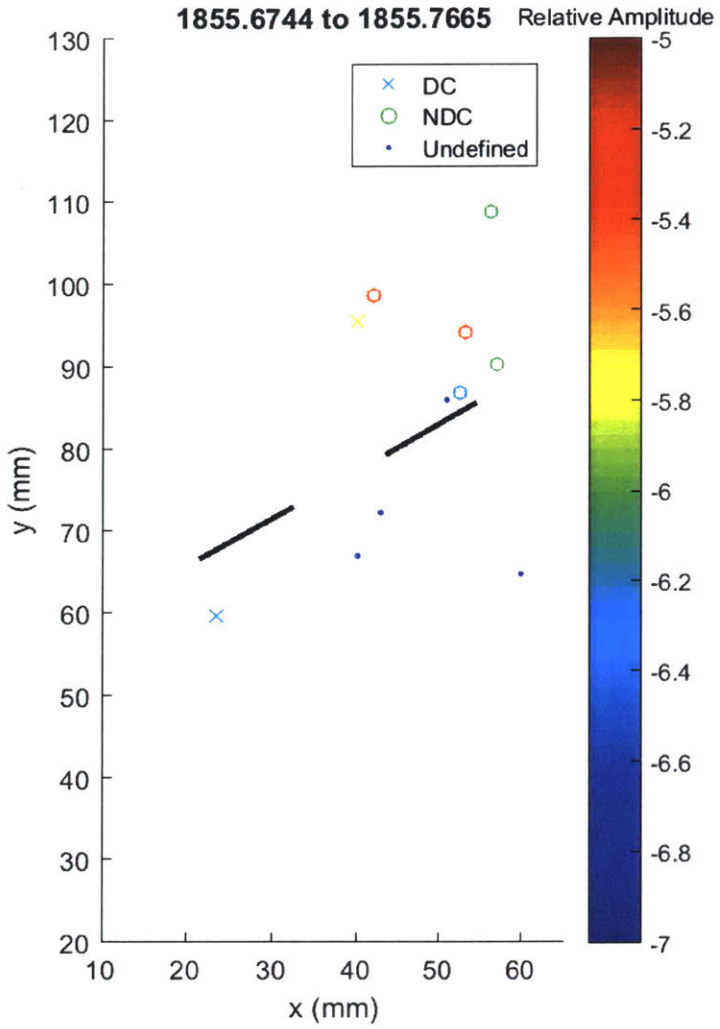

AE events are primarily tensile type, as opposed to previously where they were mostly shear. This indicates that the tensile type events may be related to coalescence of microcracks leading to large level crack propagation. Note, however, that the amplitudes have in fact decreased compared to previous frames.

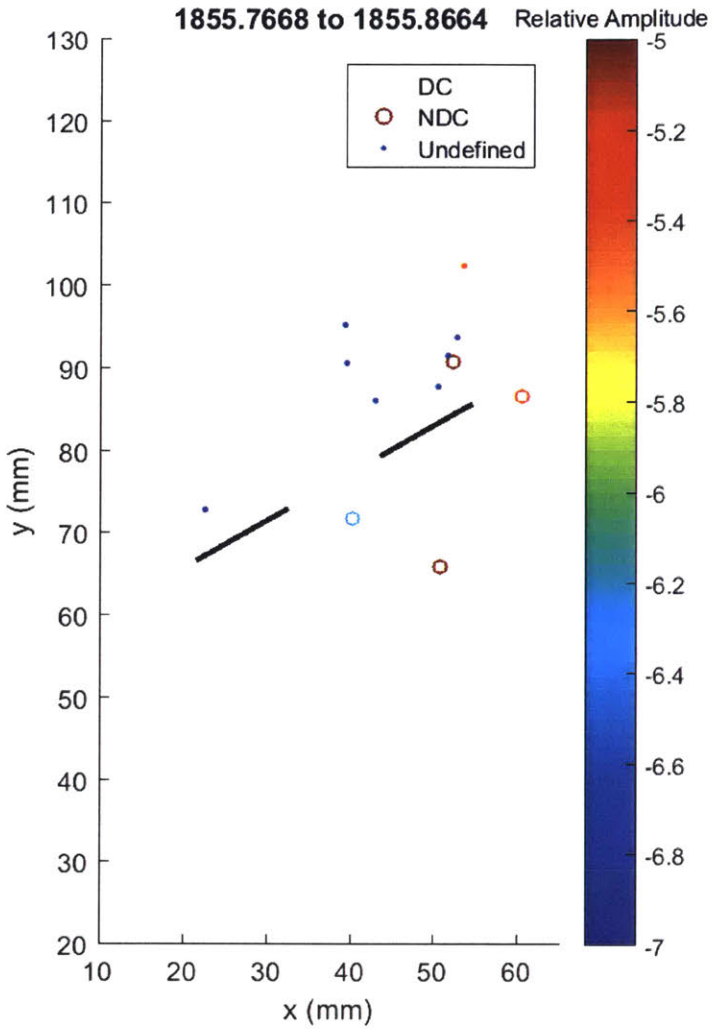

Continued development of scattered tensile and undefined events.

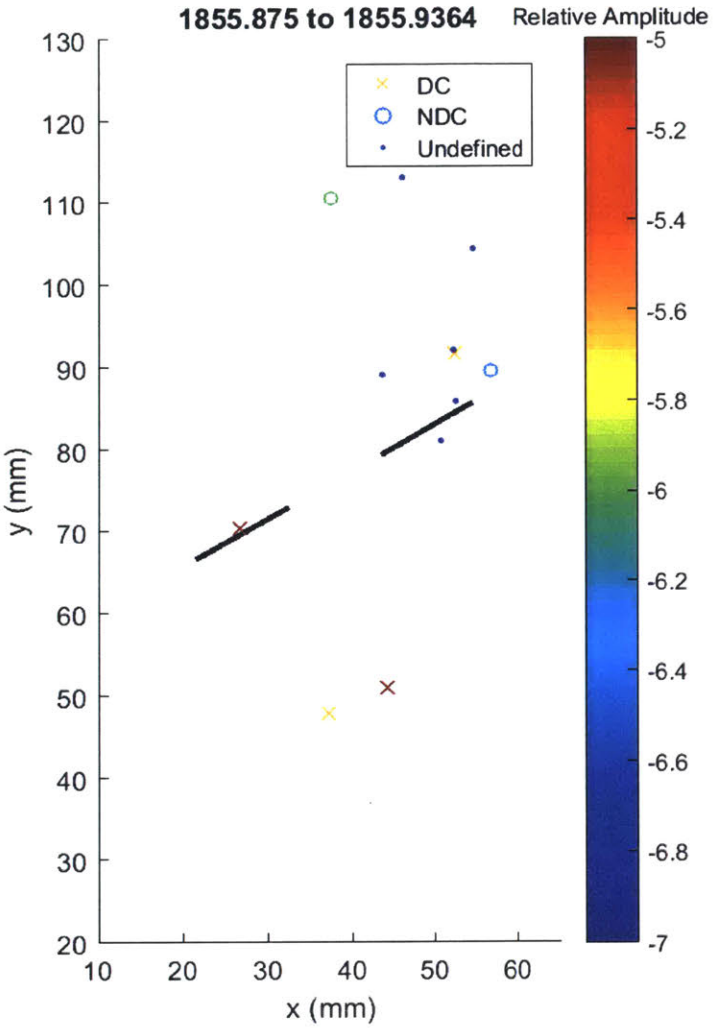

Same as previous frame.

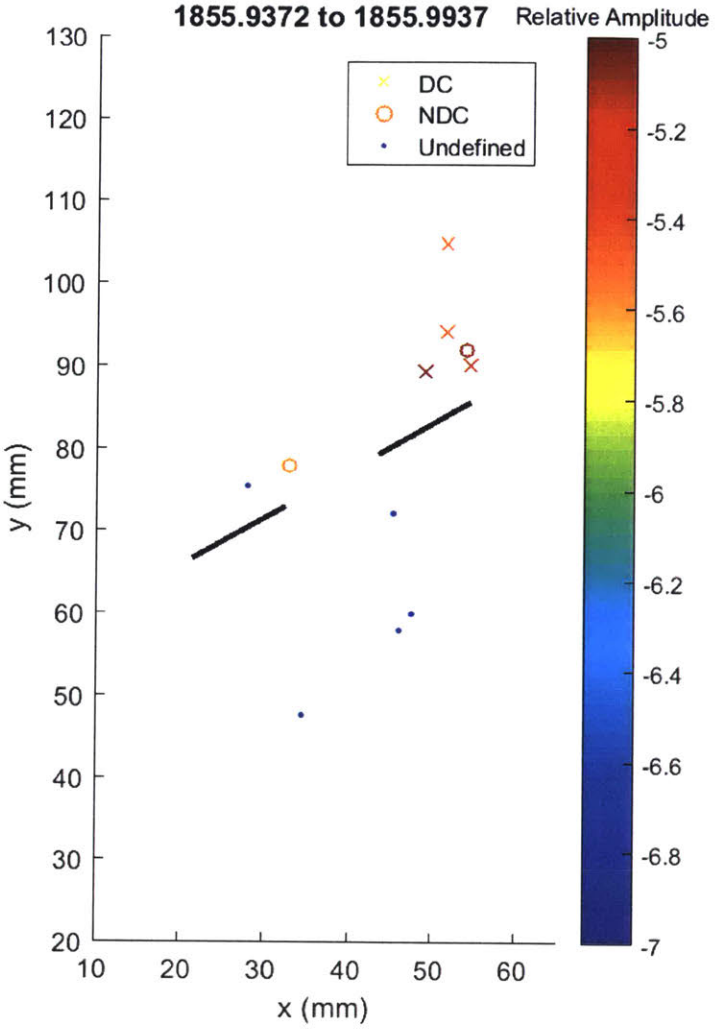

4 large shear and 1 large tensile event occurs above the outer tip of the right flaw, indicating significant further damage along this area of white patching. Peak pressure occurs around this frame.

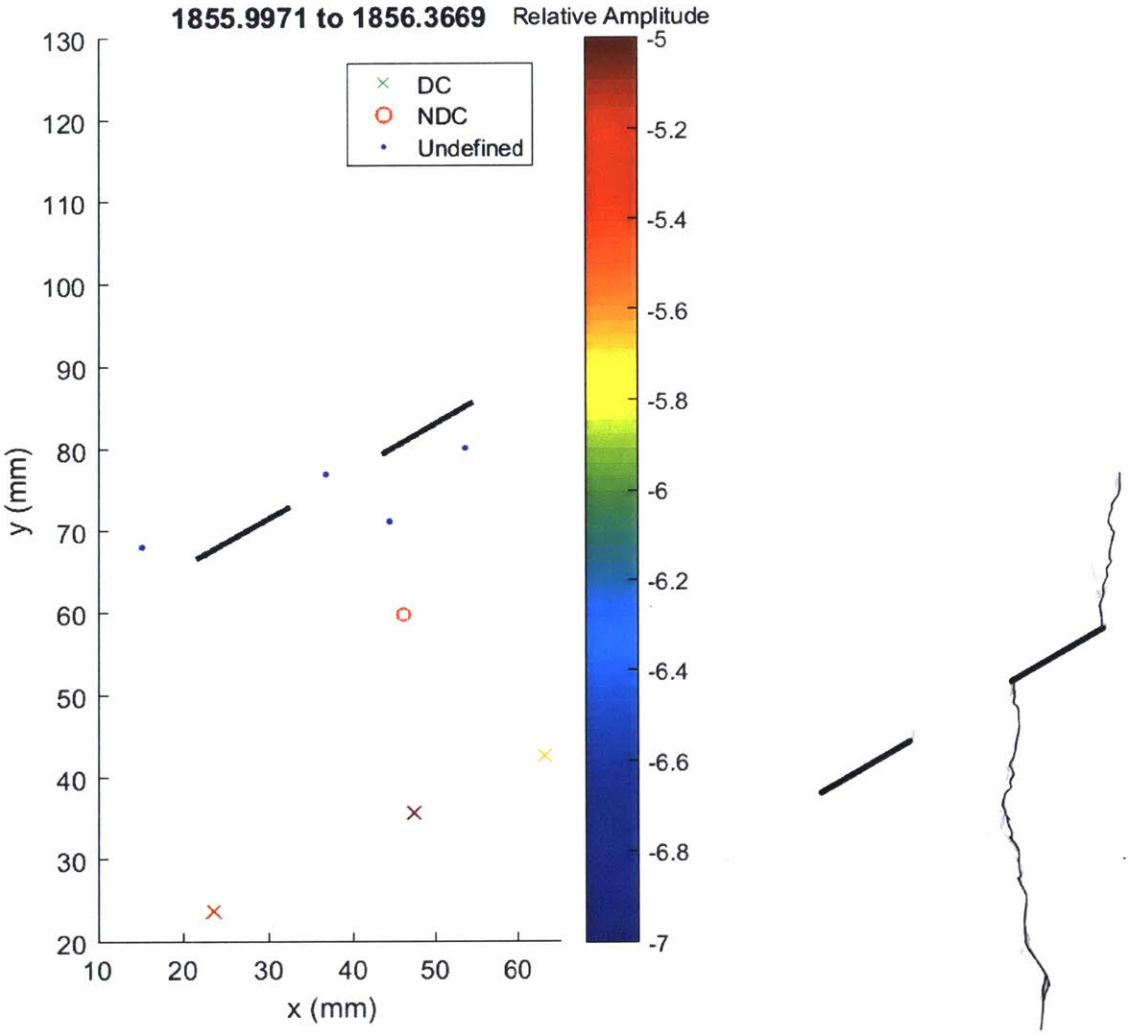

Diffuse AE locations

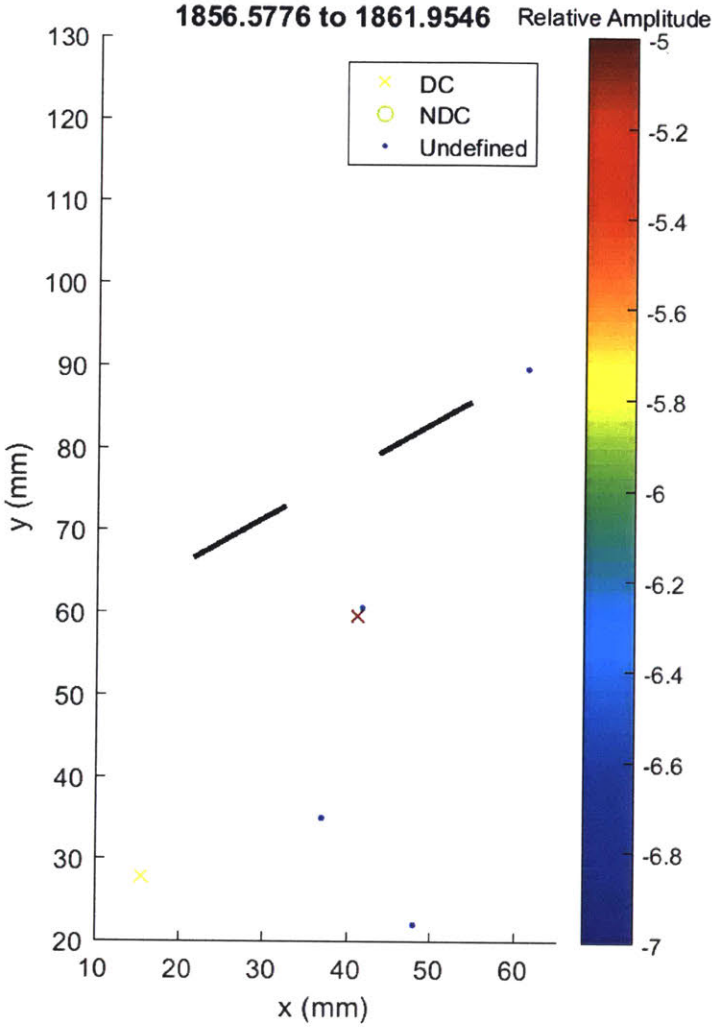

Same as previous frame.

Summary

Similarly to the 2a-30-0-VL5-A specimen, there are more shear events in this test. The hypocenter locations also suggest that more damage occurs earlier at the outer tip of the flaw, which agrees with the 2a-30-0-VL5-A specimen even though in this specimen the visual crack initiates first from the inner tip. Considering the stress field, it is in fact the outer tip that experiences higher stress (?) This specimen also exhibited the cyclical type of behaviour, where damage occurs preferentially at one side of the flaw before shifting to damage occurring at the other side. This does not follow some of the classic "chain reaction" line of thought regarding progression of damage.

AE hypocenter analysis for specimen 2a-30-30-VL0-C

Final crack geometry:

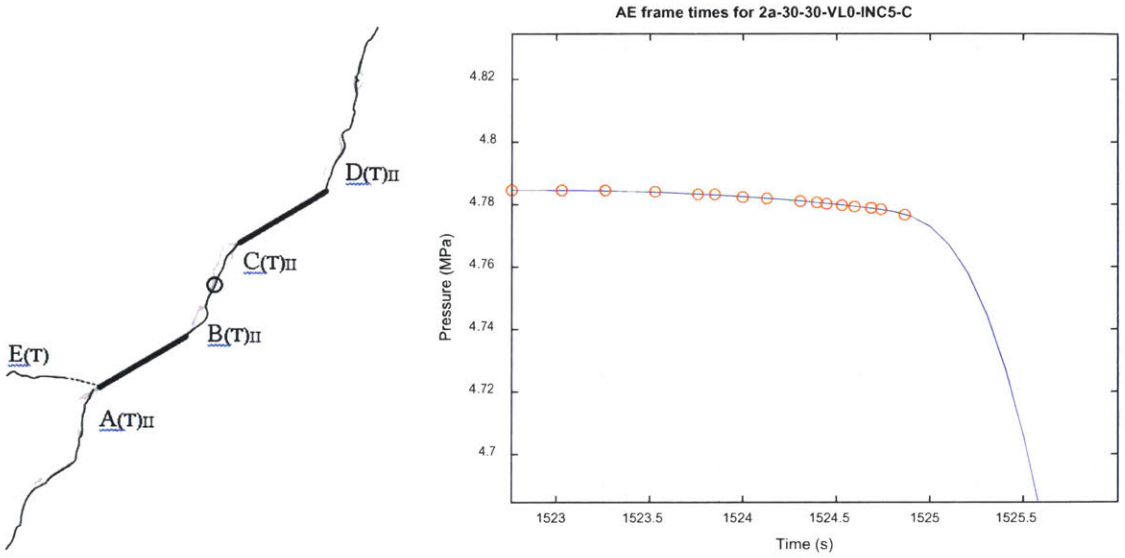

Crack first initiates from outer tip of left flaw, then cracks initiates from both inner tips and coalesce. Finally a crack initiates from the outer tip of the right flaw. Peak pressure occurs significantly before the timing of analysis; pressure begins to decrease faster at approximately 1523.5 s.

Development of AE locations are shown over the 20 frames presented in this analysis, where each frame shows 5% of the total number of events recorded during the test. This means that initially the frames will cover a long time period since few AE occurred at the beginning, while towards failure each frame will only cover fractions of a second since AE occur at a rapid rate.

Events with greater than 50% CLVD (compensated linear vector dipole) are considered shear type events and are marked with an 'x', while events with less than 50% CLVD are considered tensile and marked with 'o'. For those events detected by 4 sensors, it is not possible to invert the moment tensor and so these events are marked as undefined with '.'. The colour of an event indicates its relative magnitude, where red is the largest. Black ellipses are used to highlight areas of interest.

Where possible, AE frames are shown next to the appropriate analysis sketch from Bruno. However, these tend to be few in between and as discussed, the high speed frames tend to occur after the end of detectable AE events.

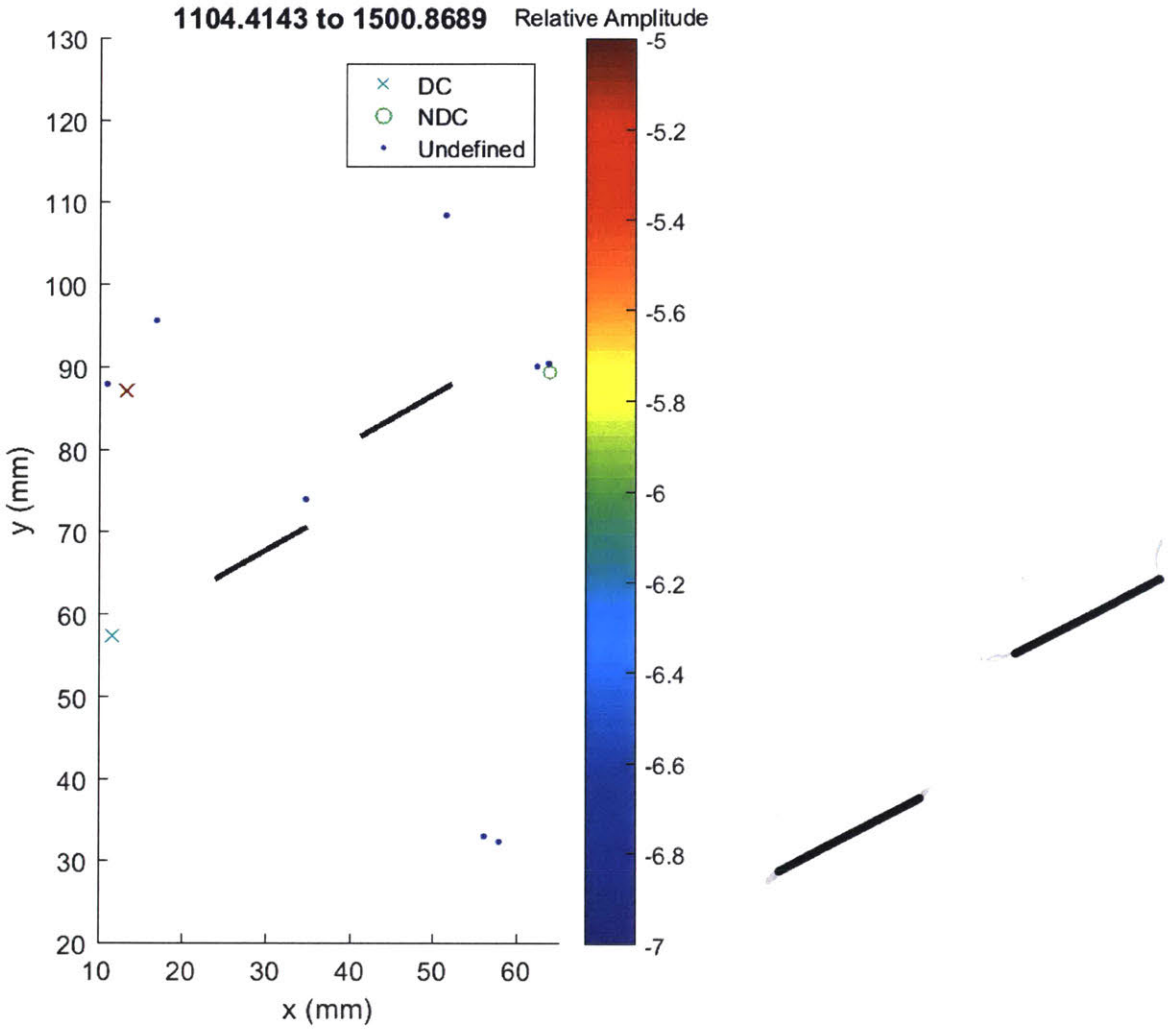

Events scattered throughout specimen. Some white patching occurs at tips of right flaw.

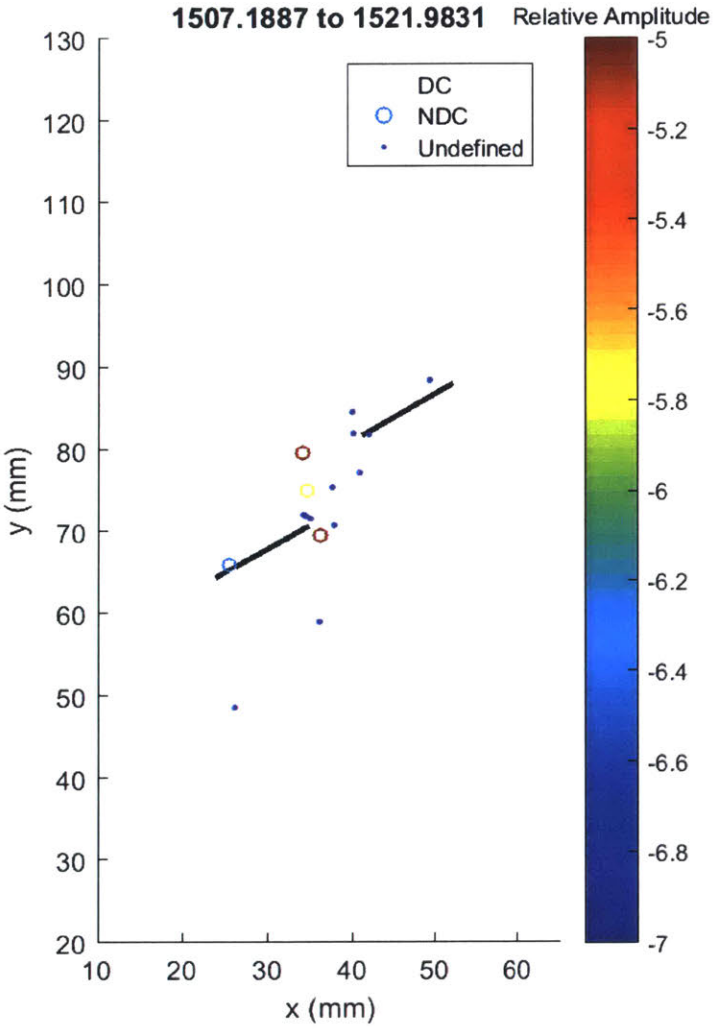

Tensile events occur along a wing crack pattern on the inner tip of the left flaw, undefined events occur throughout the bridge area.

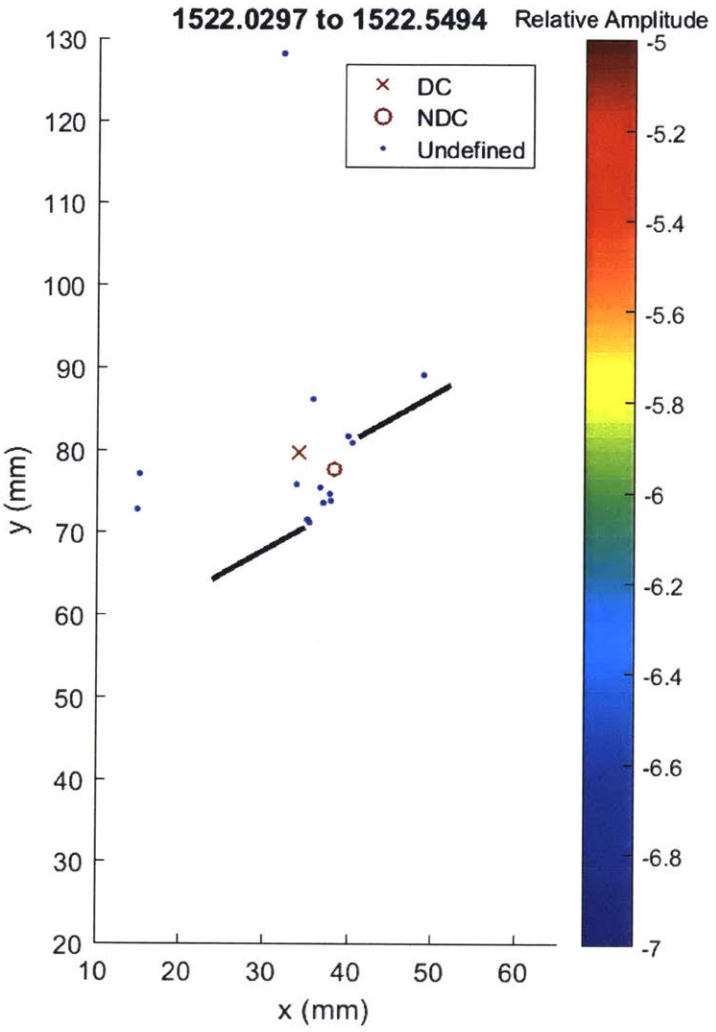

One tensile and one shear event occurs in bridge area, small undefined events mostly occur in bridge area.

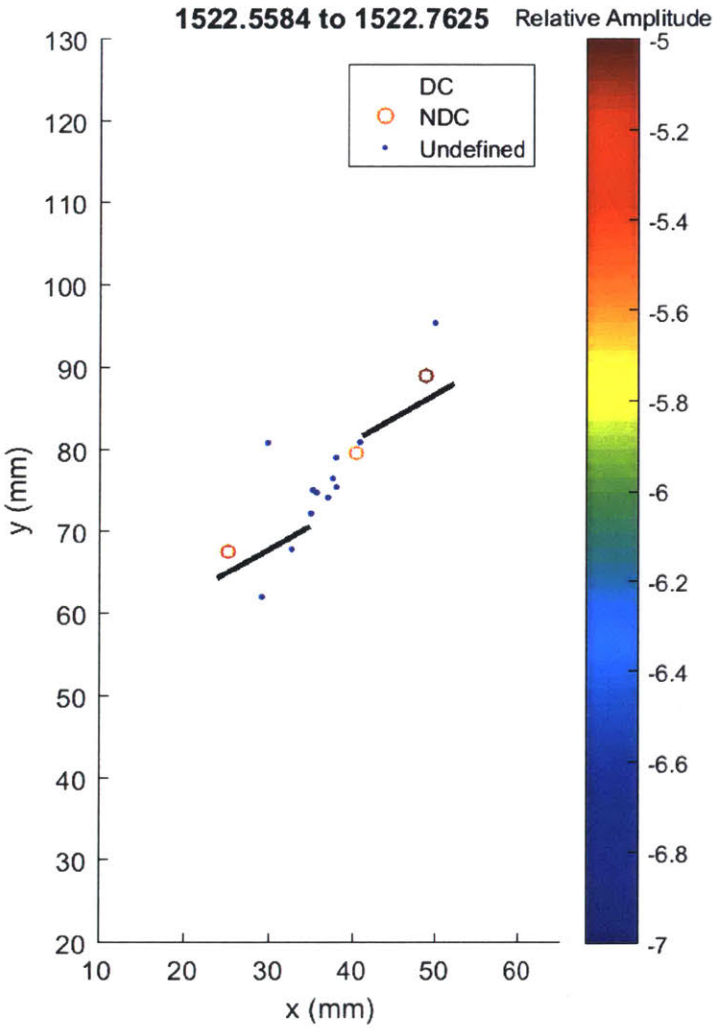

Tensile events occur at both outer flaw tips, and at inner tip of right flaw. Undefined events continue to occur in the bridge.

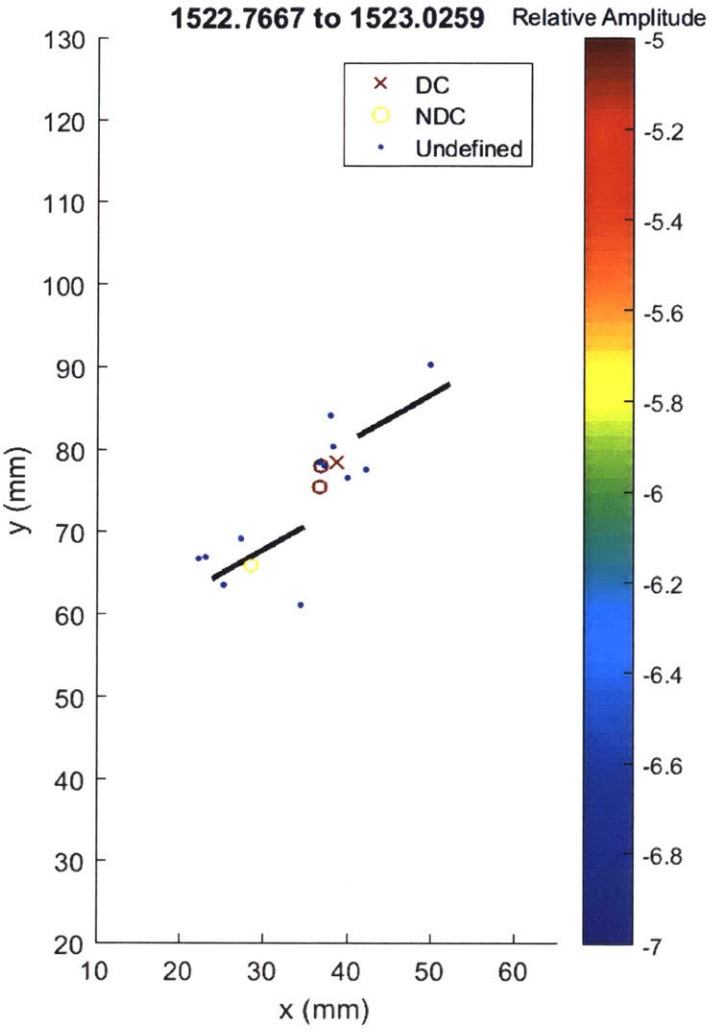

2 large tensile and 1 large shear event occurs in bridge area along with small undefined events. One intermediate amplitude tensile event and some small undefined events occur at outer tip of left flaw.

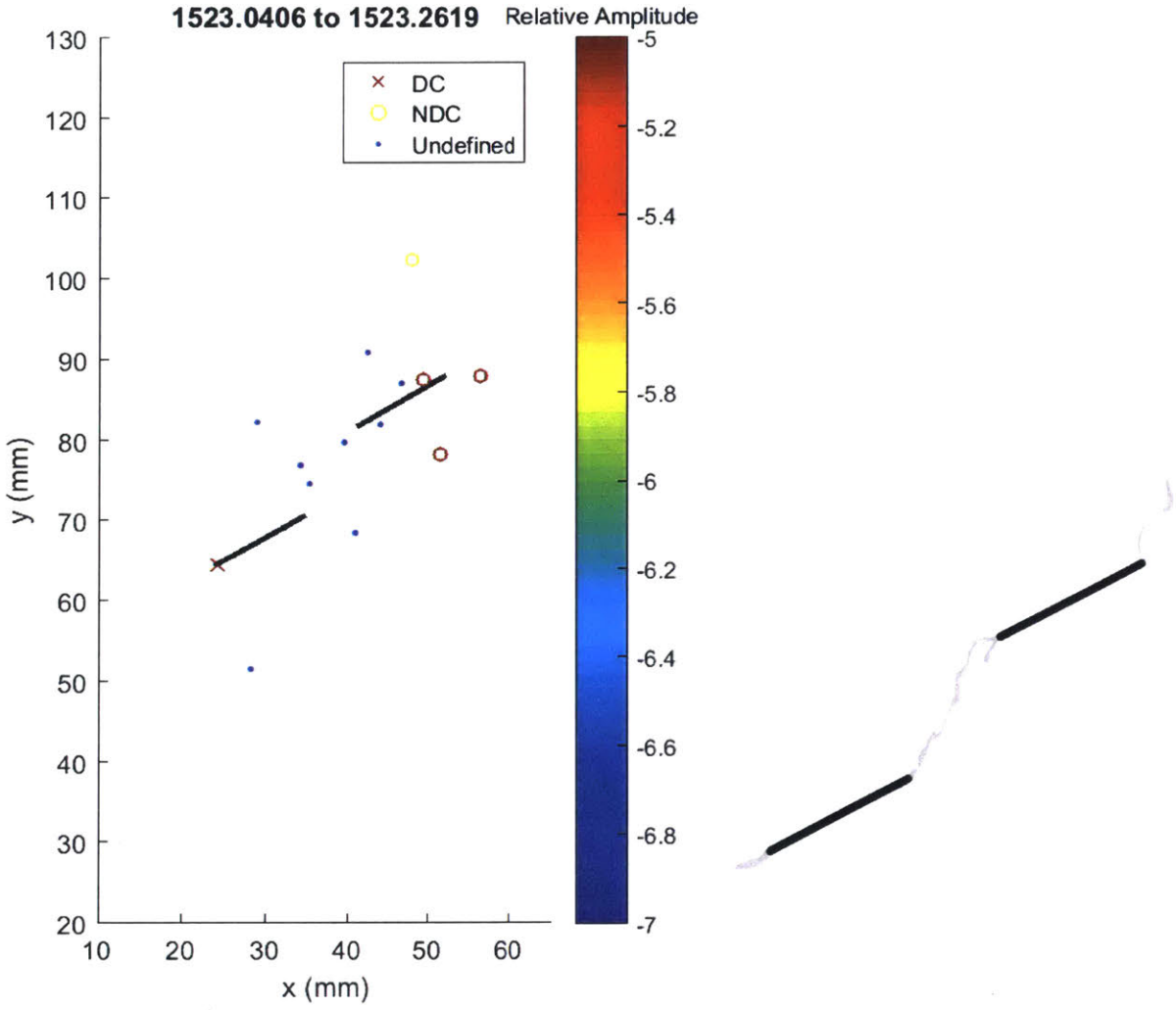

One shear events occurs at outer tip of left flaw. Small undefined events occur in bridge area. Large tensile events occur around outer tip of right flaw. Significant white patching highlights all area of eventual crack.

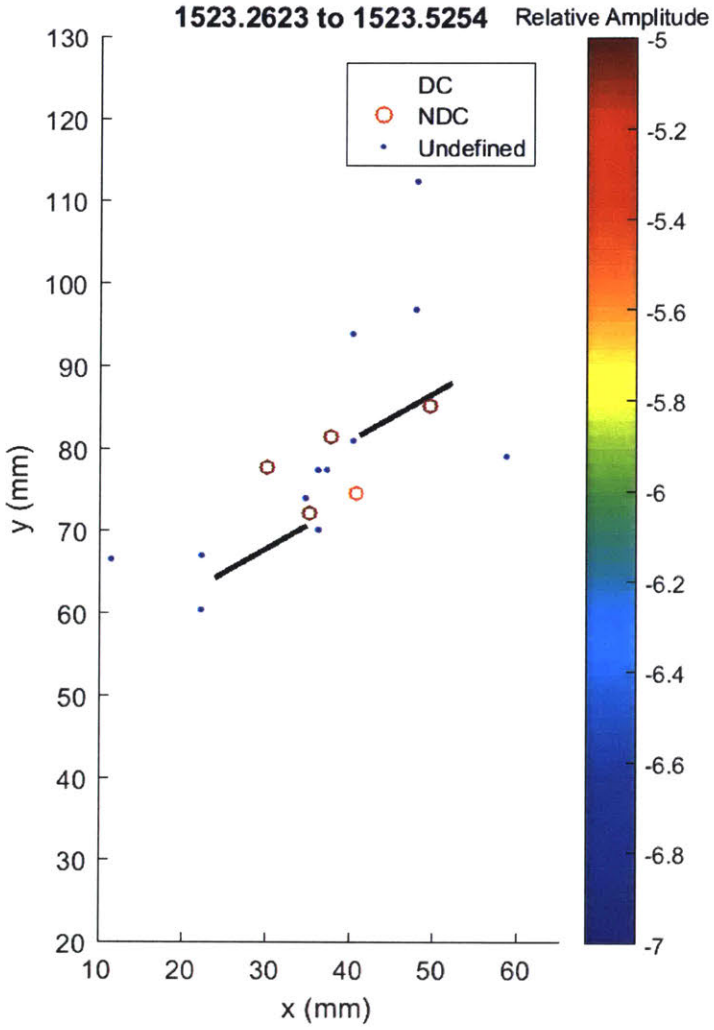

4 tensile events occur in bridge area including at both inner flaw tips. Pressure begins to decrease faster at this time.

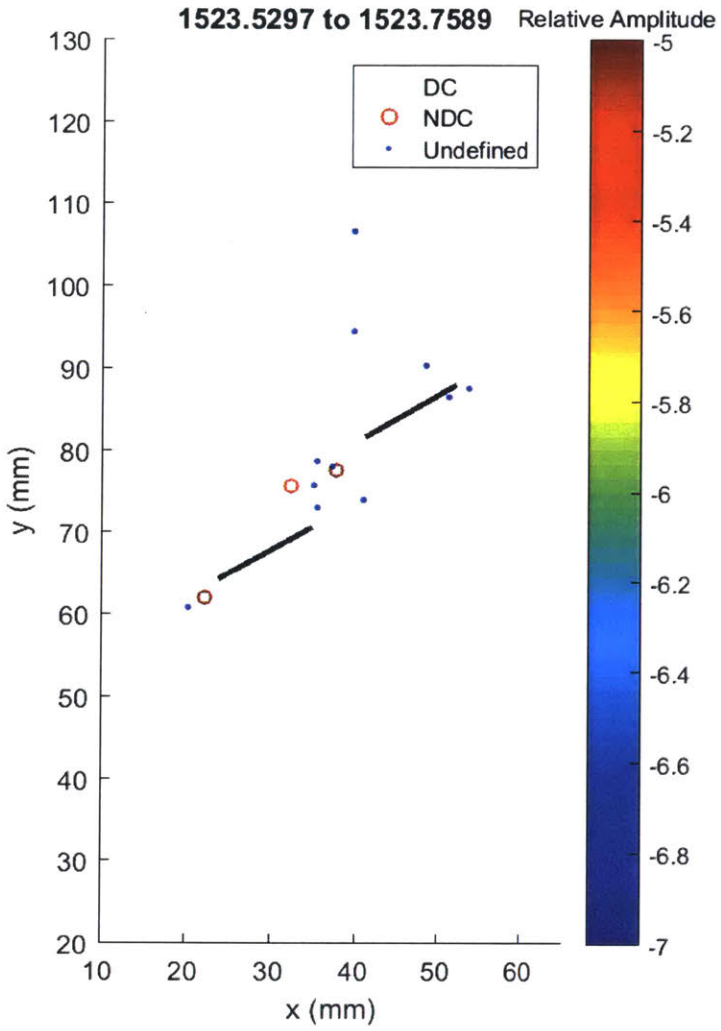

2 large tensile events occur in bridge, another large tensile event at outer tip of left flaw.

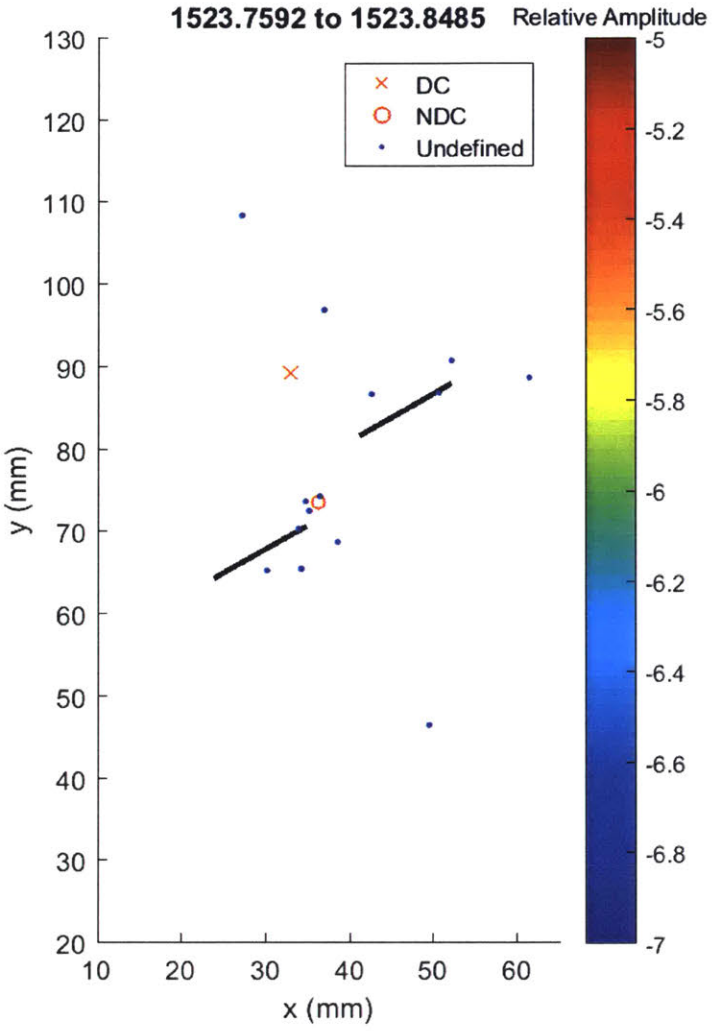

One large tensile event occurs at inner tip of left flaw, along with some small undefined events.

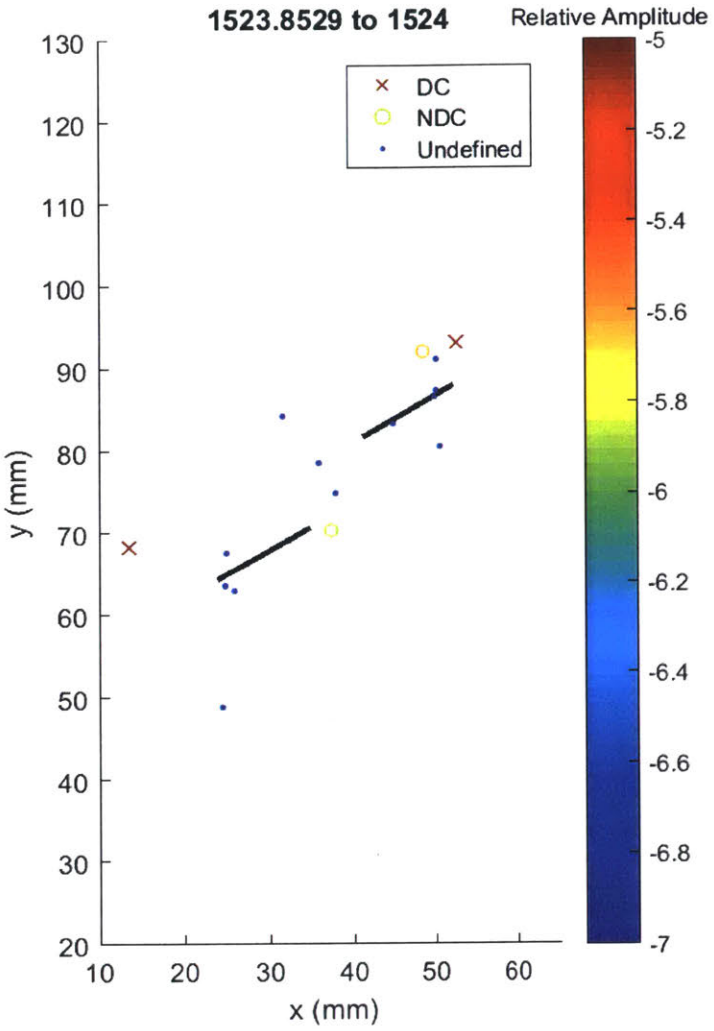

Larger amplitude events occur at the outer tip of the right flaw and the inner tip of the left flaw. Small undefined events occur all around the flaw area.

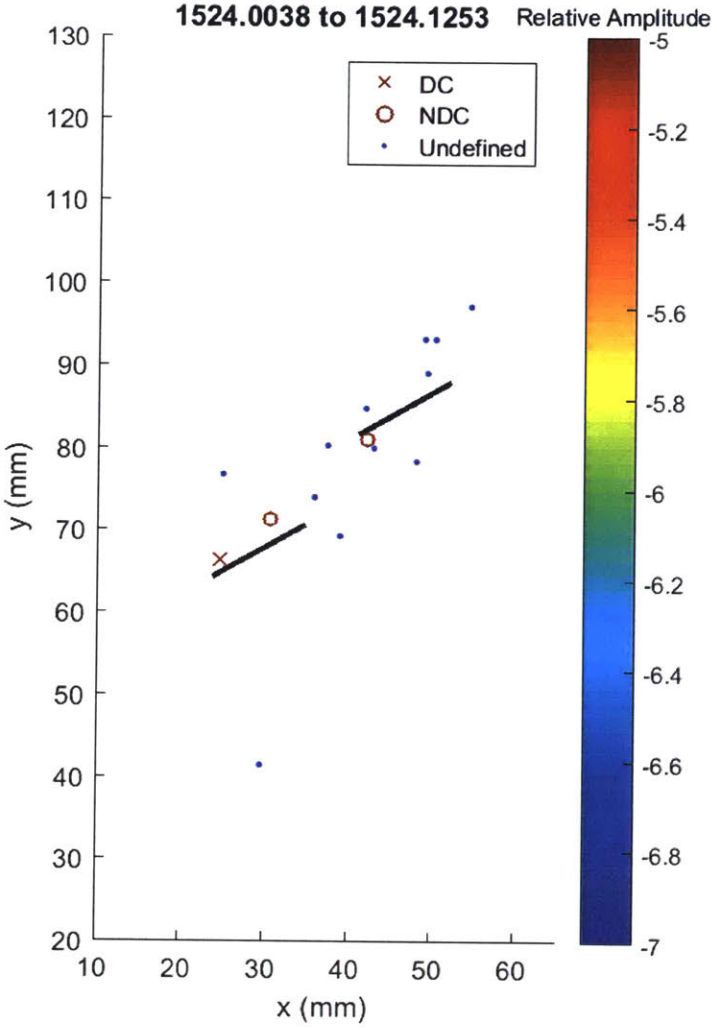

Large amplitude events occur at inner tips and outer tip of left flaw. Smaller events occur all around right flaw.

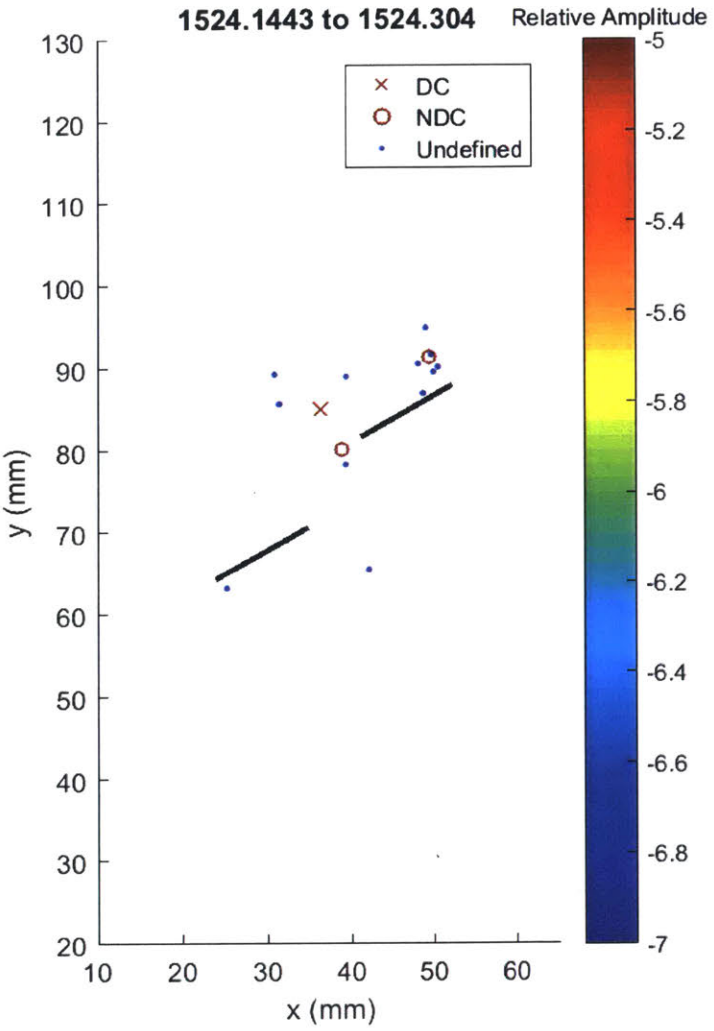

Large events occur at both tips of right flaw. Little AE activity on left flaw.

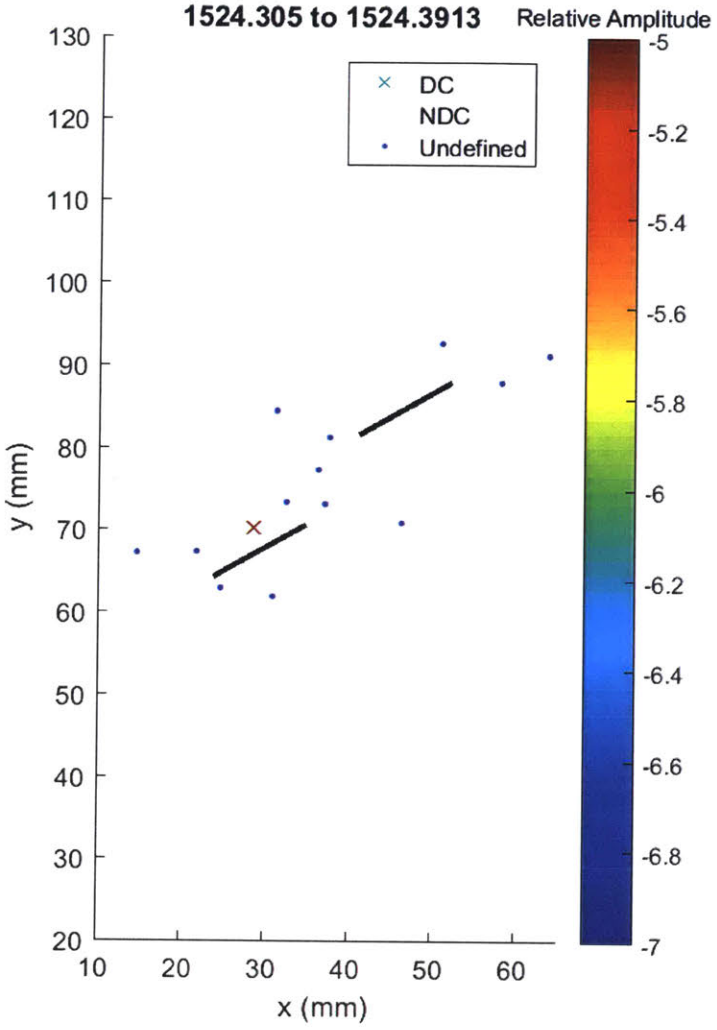

AE activity generally occurs around left flaw, compared to the previous frame where they occurred around the right flaw.

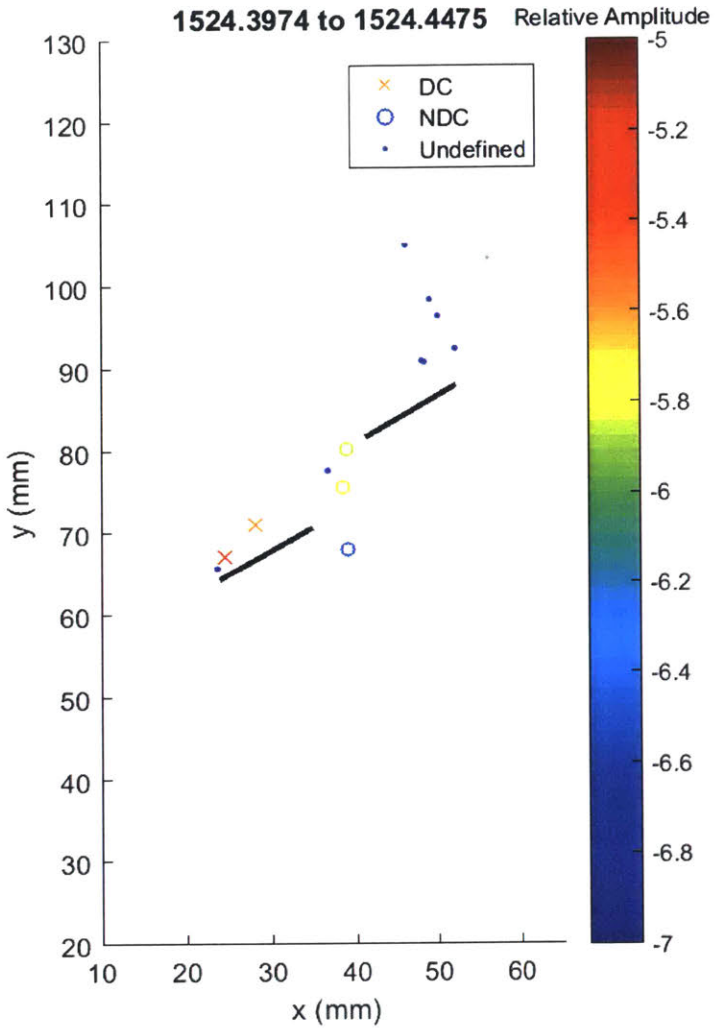

Key frame. Significant separation of mechanisms. Large shear events occur at outer tip of left flaw, intermediate amplitude tensile events occur in the bridge area, and small undefined events form a wing crack shape at outer tip of the right flaw.

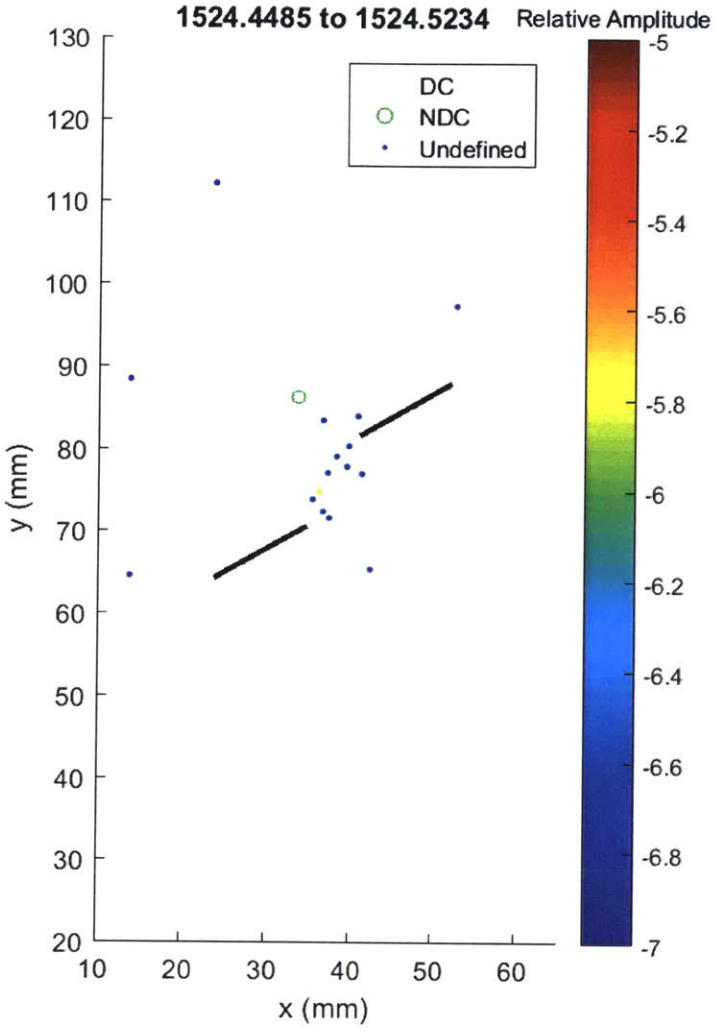

Lots of small undefined events in bridge area.

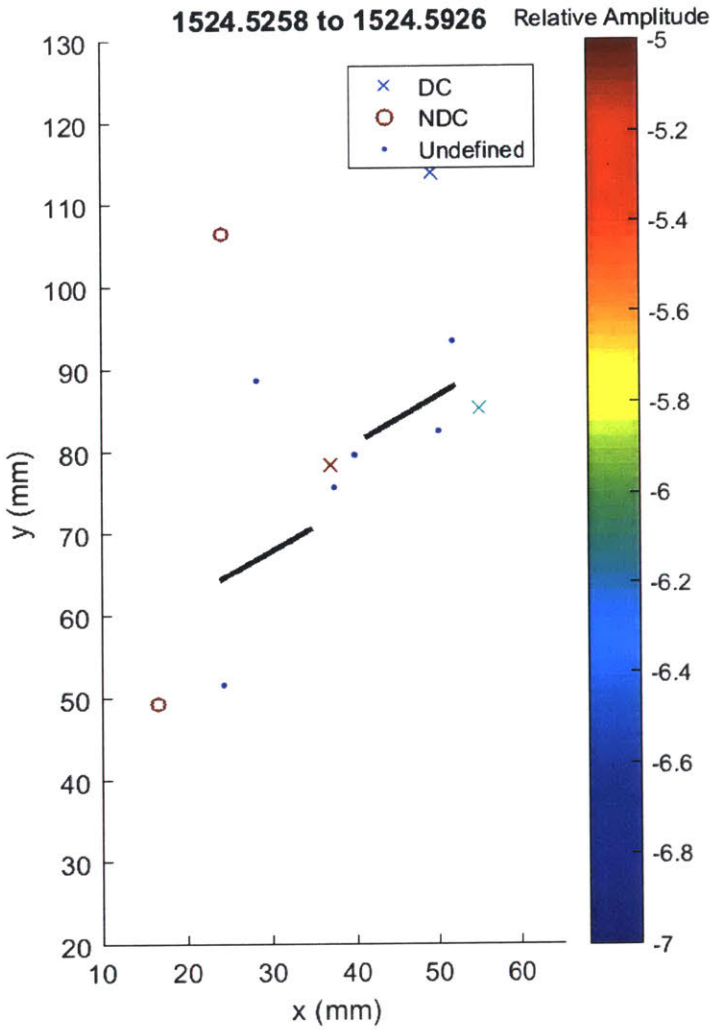

Hypocenter locations are generally scattered.

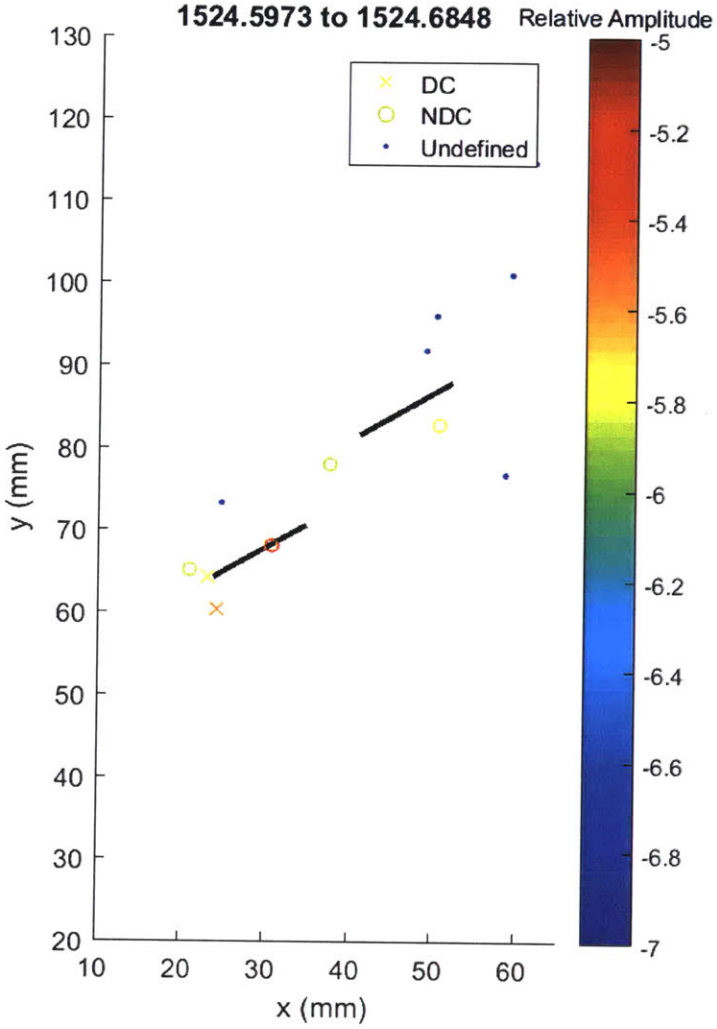

Intermediate amplitude events occur throughout flaw area. 1 large shear and 1 large tensile event occurs around left flaw.

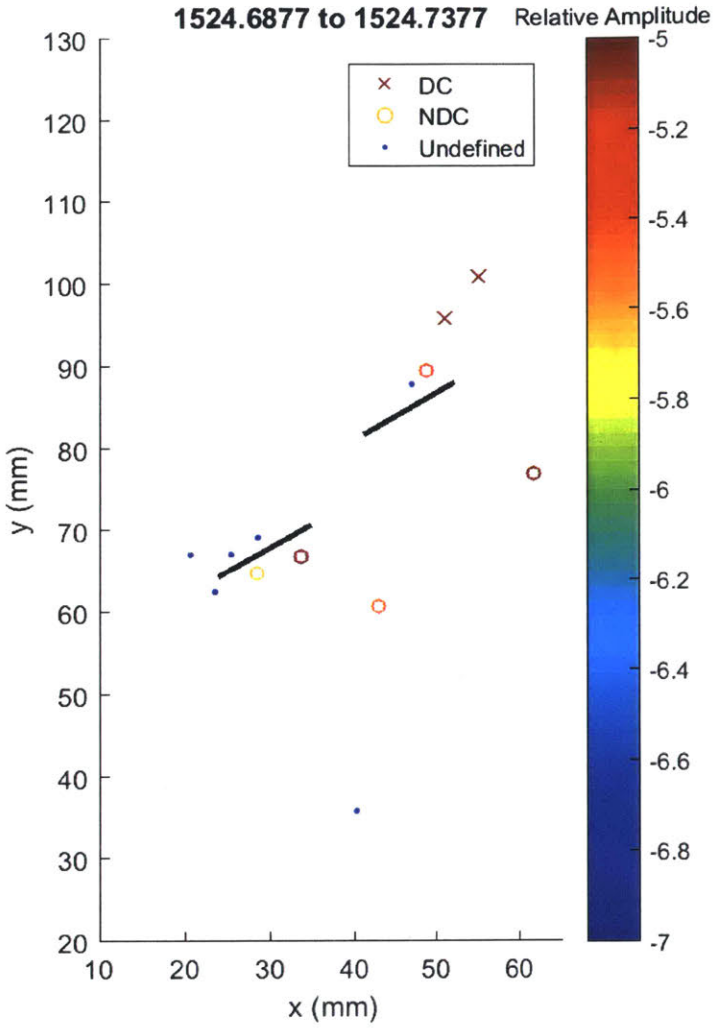

Key frame. Large amplitude tensile events occur around both flaws. 2 shear events occur above outer tip of right flaw.

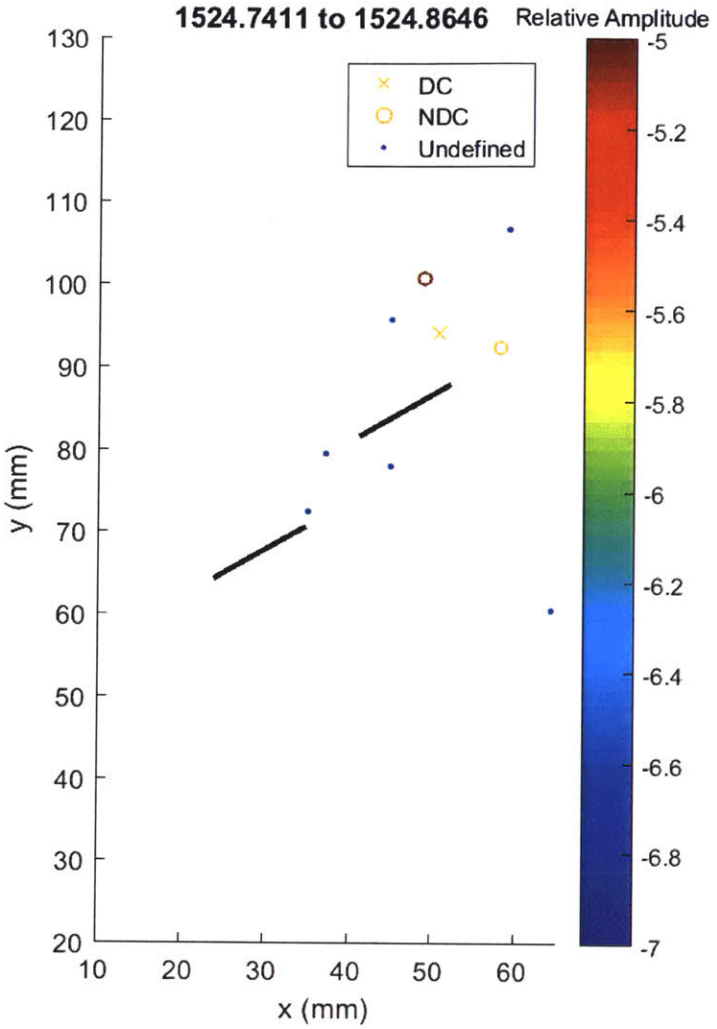

2 tensile and 1 shear event occur above outer tip of right flaw.

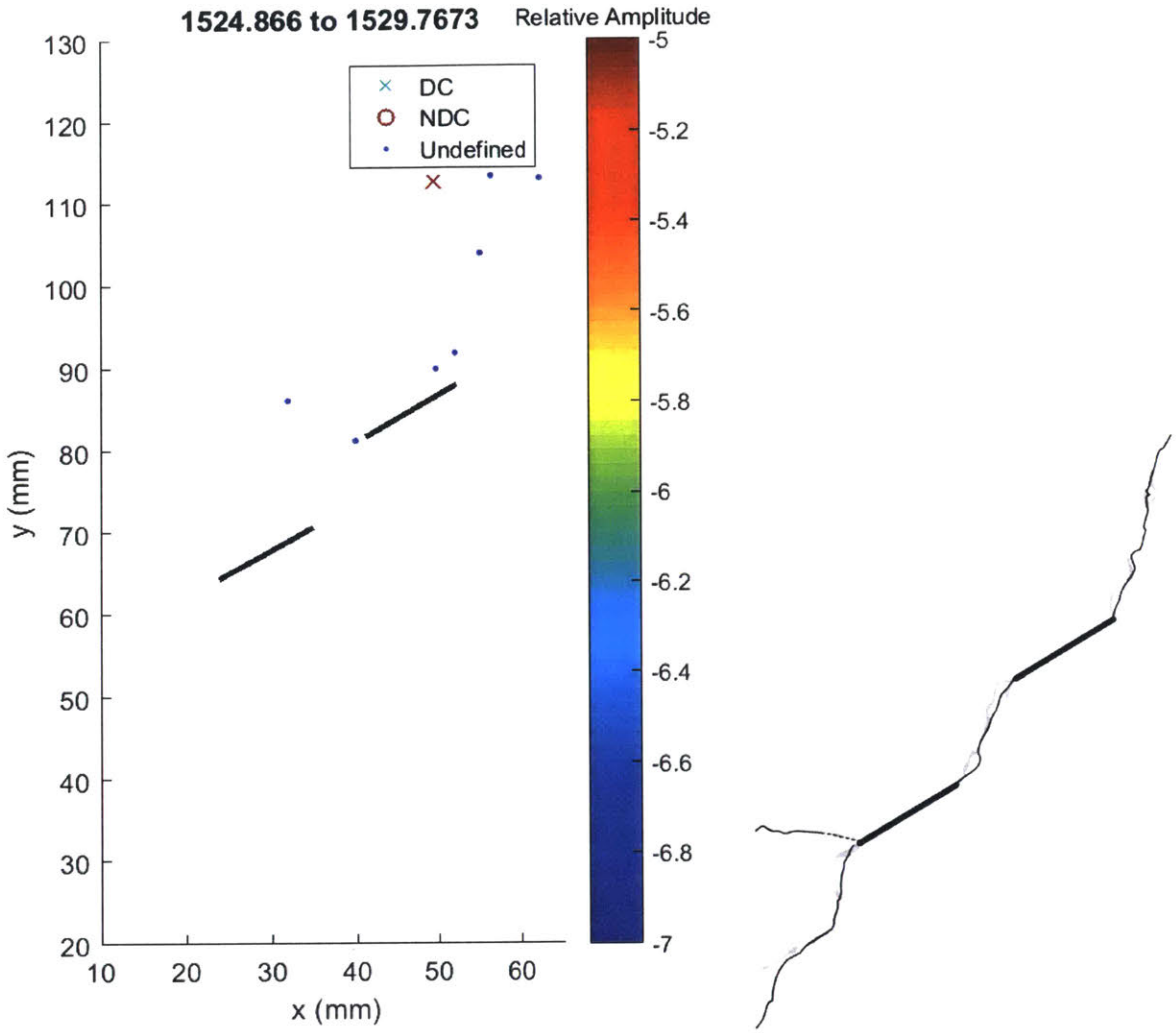

Last frame. Few small undefined events occur around right flaw.

Summary:

Generally more tensile than shear events, as with the previous VL0 tests. This test did not produce a large number of AE, but it appears in general the events initially occur more towards the bridge area. There also appears to be some preference for the right outer tip, even though visible crack initiation occurs at the left outer tip.

AE hypocenter analysis for specimen 2a-30-30-VL5-B

Final crack geometry:

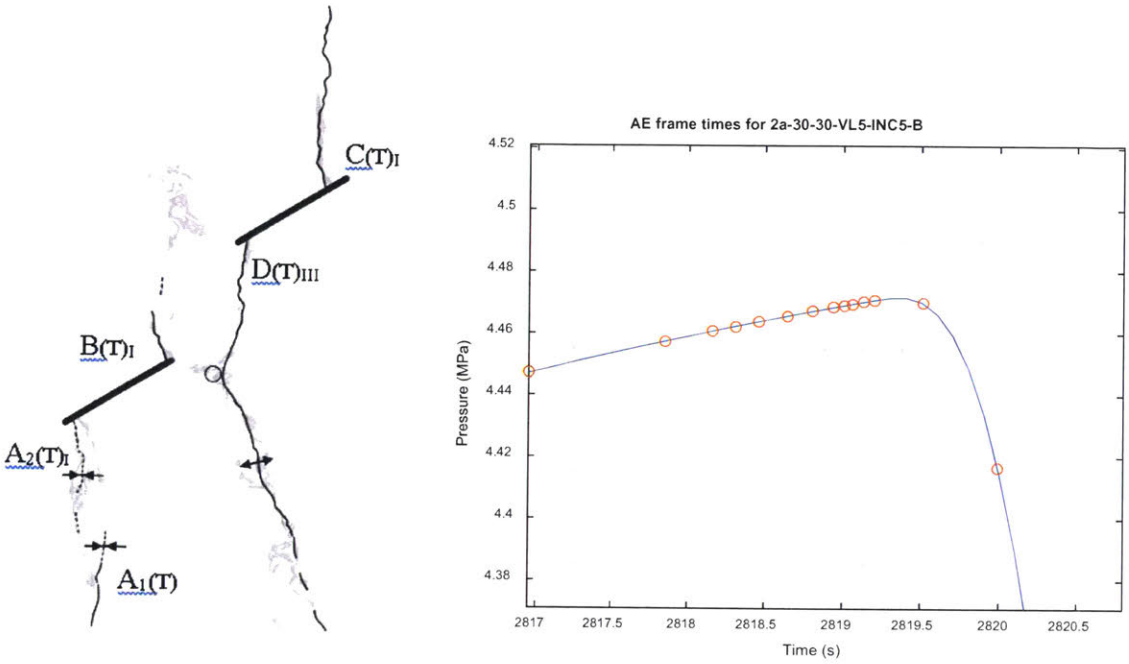

This specimen shows a more complex fracture pattern than the previous specimens. En-echelon cracks A1 and A2 initiate off the outer tip of the left flaw, followed by a wing crack off the inner tip of the left flaw. A crack then initiates from the outer tip of the right flaw, followed by a wing crack on the inner tip of the right flaw which curves towards the anti-wing area of the left flaw. Peak pressure occurs immediately prior to pressure breakdown.

Development of AE locations are shown over the 20 frames presented in this analysis, where each frame shows 5% of the total number of events recorded during the test. This means that initially the frames will cover a long time period since few AE occurred at the beginning, while towards failure each frame will only cover fractions of a second since AE occur at a rapid rate.

Events with greater than 50% CLVD (compensated linear vector dipole) are considered shear type events and are marked with an 'x', while events with less than 50% CLVD are considered tensile and marked with 'o'. For those events detected by 4 sensors, it is not possible to invert the moment tensor and so these events are marked as undefined with '.'. The colour of an event indicates its relative magnitude, where red is the largest. Black ellipses are used to highlight areas of interest.

Where possible, AE frames are shown next to the appropriate analysis sketch from Bruno. However, these tend to be few in between and as discussed, the high speed frames tend to occur after the end of detectable AE events.

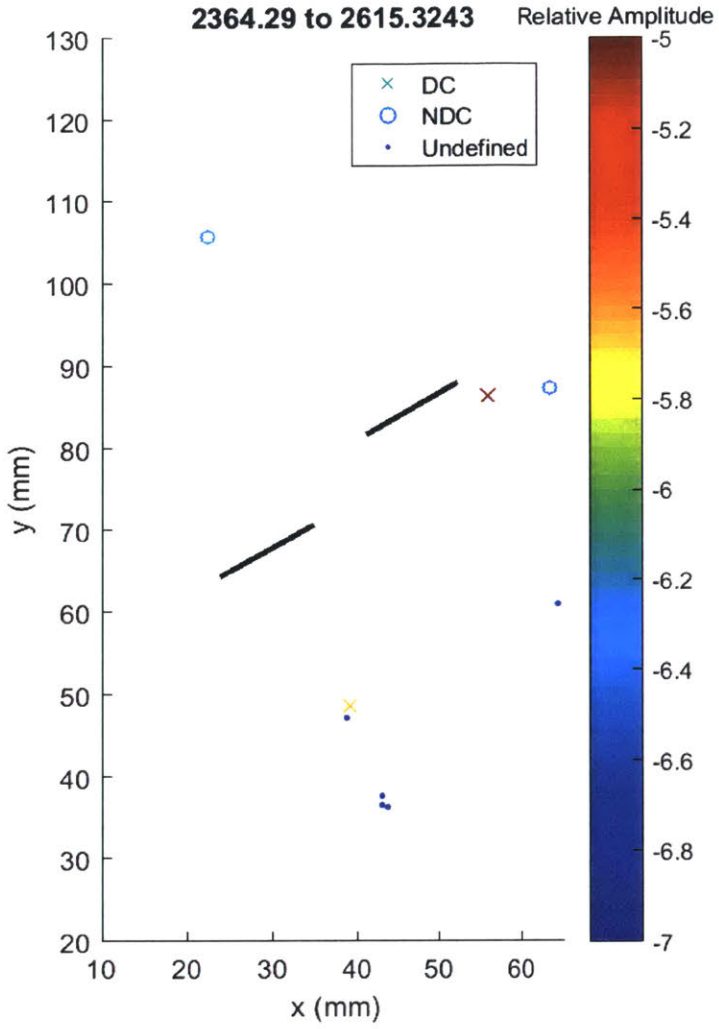

Initially diffuse hypocenter locations. 1 large shear event occurs at outer tip of right flaw.

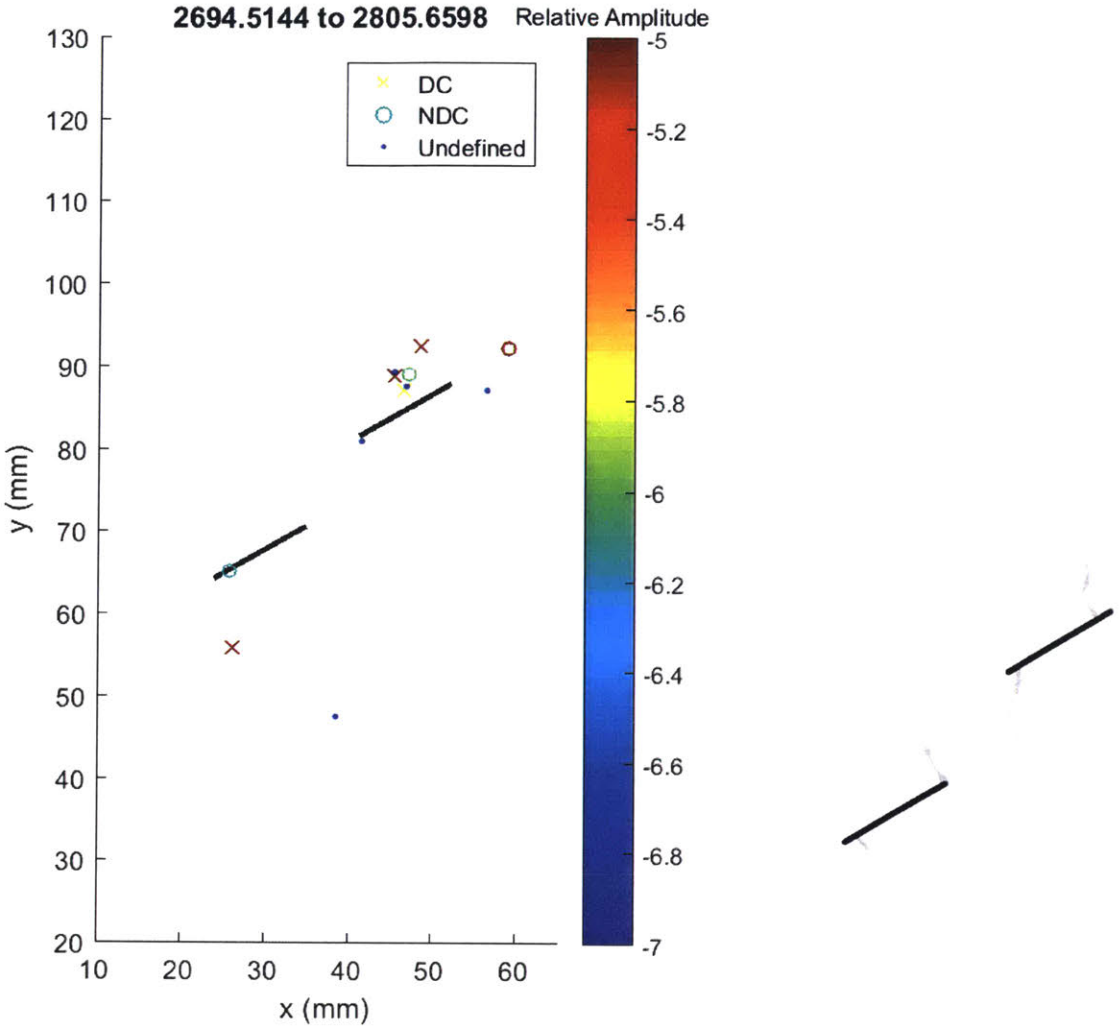

1 large shear event occurs below outer tip of left flaw, 2 large shear events occur above right flaw. Visually, there is some white patching on all flaw tips by this point, even though AE events appear to only have occurred on the outer right flaw tip.

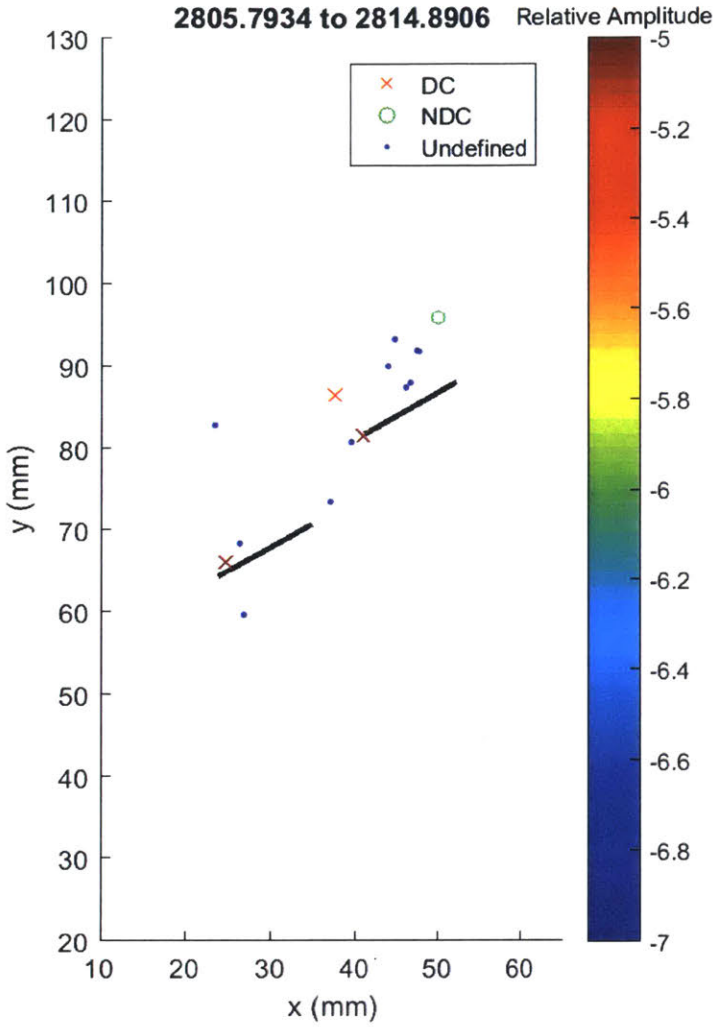

High amplitude shear events occur at outer tip of left flaw and inner tip of right flaw. 6 small undefined events occur above right flaw outer tip, where the large shear events occurred in the previous frame.

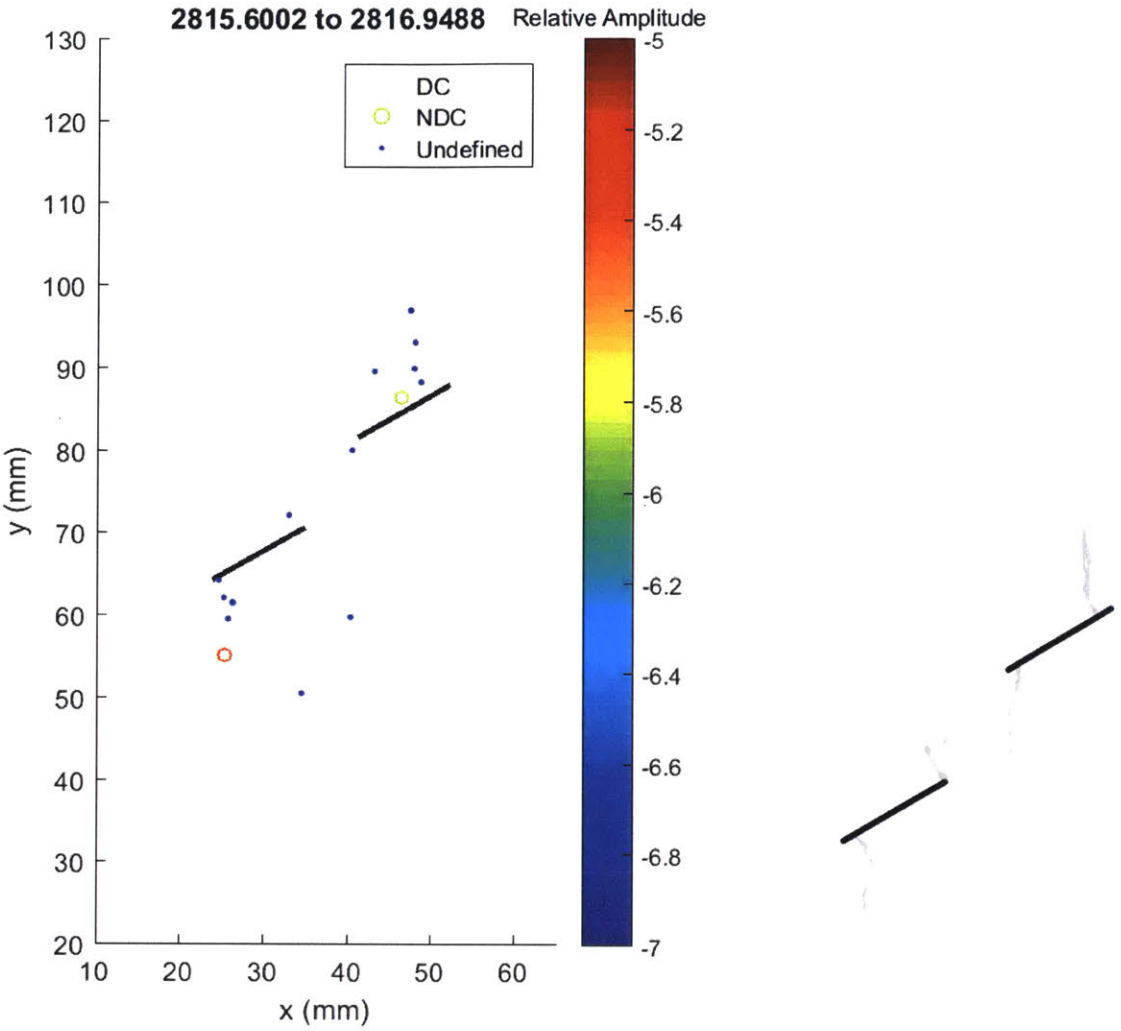

1 tensile event occurs around each outer flaw tip, along with a number of smaller undefined events. Visual white patching is extensive at all flaw tips by this time.

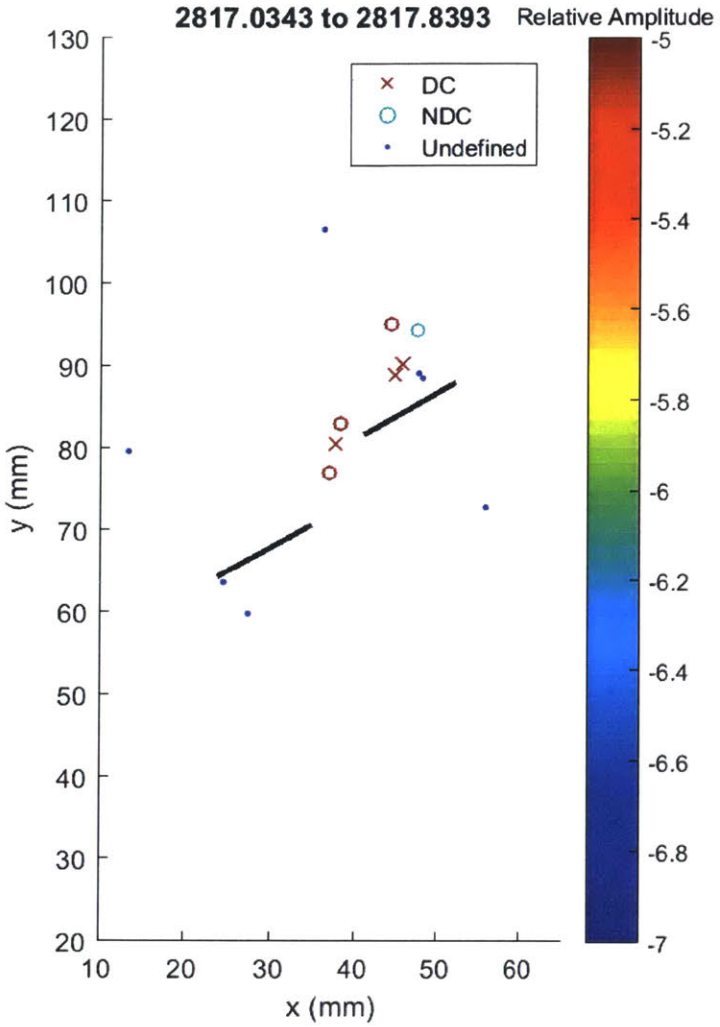

2 large tensile and 1 large shear event occurs in the bridge, while 2 large shear and 1 large tensile event occurs at the outer tip of the right flaw.

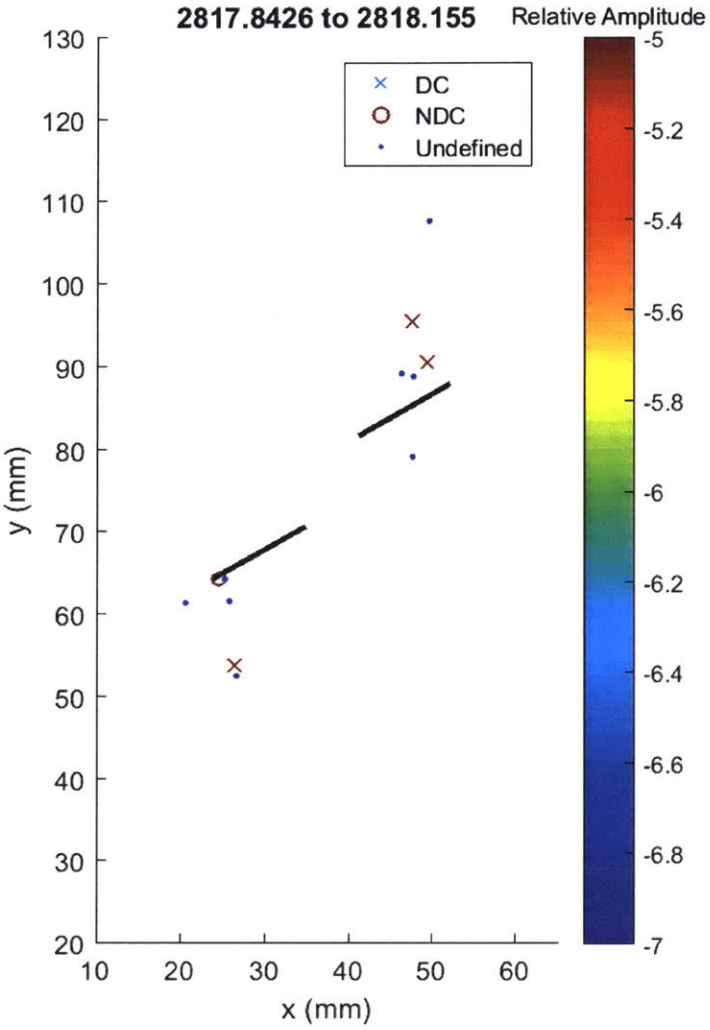

2 large shear event occurs above the outer tip of the right flaw, and 1 large shear and 1 large tensile event occurs at the outer tip of the left flaw.

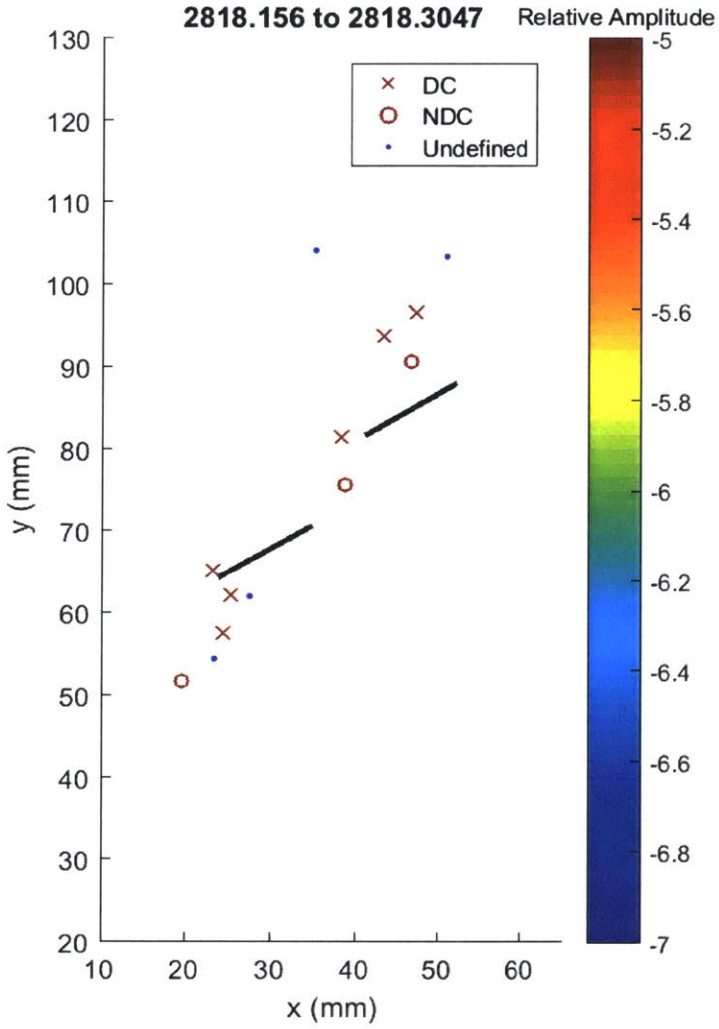

Large amplitude events mark out crack path on both outer flaw tips and in the bridge.

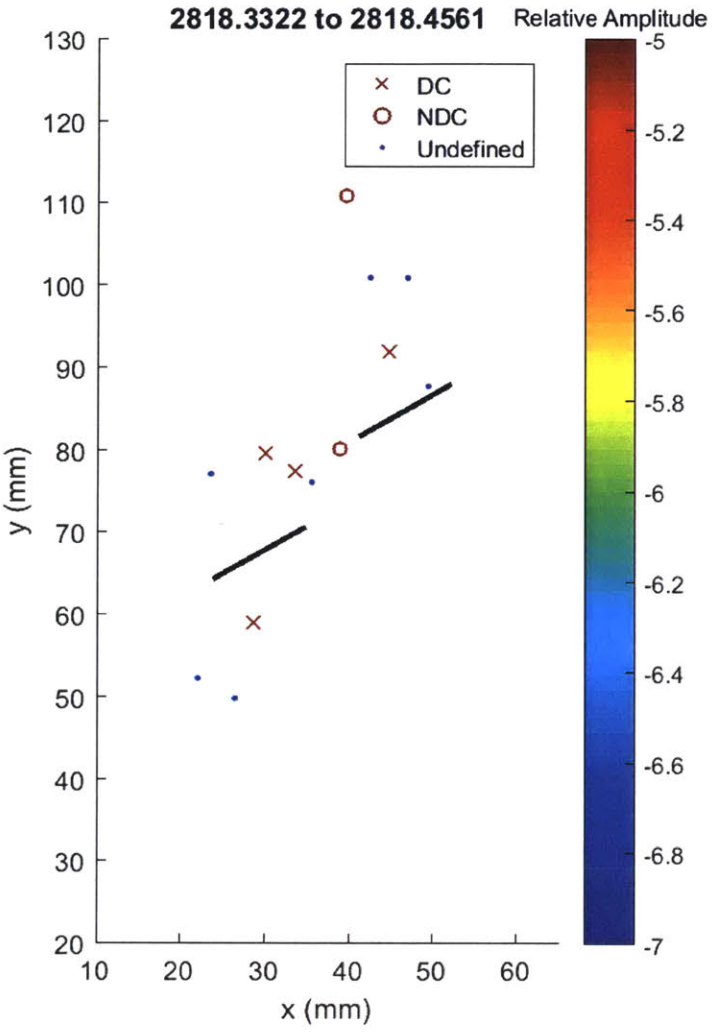

High amplitude events continue to occur, although in this frame their locations are diffused.

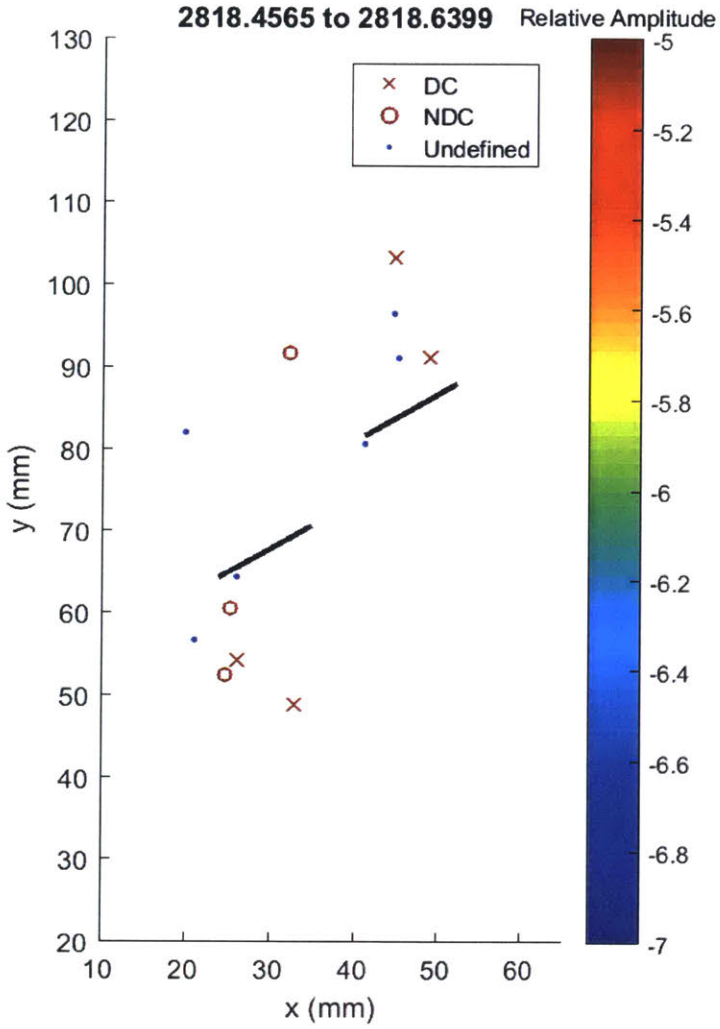

Large amplitude events occur at both outer flaw tips.

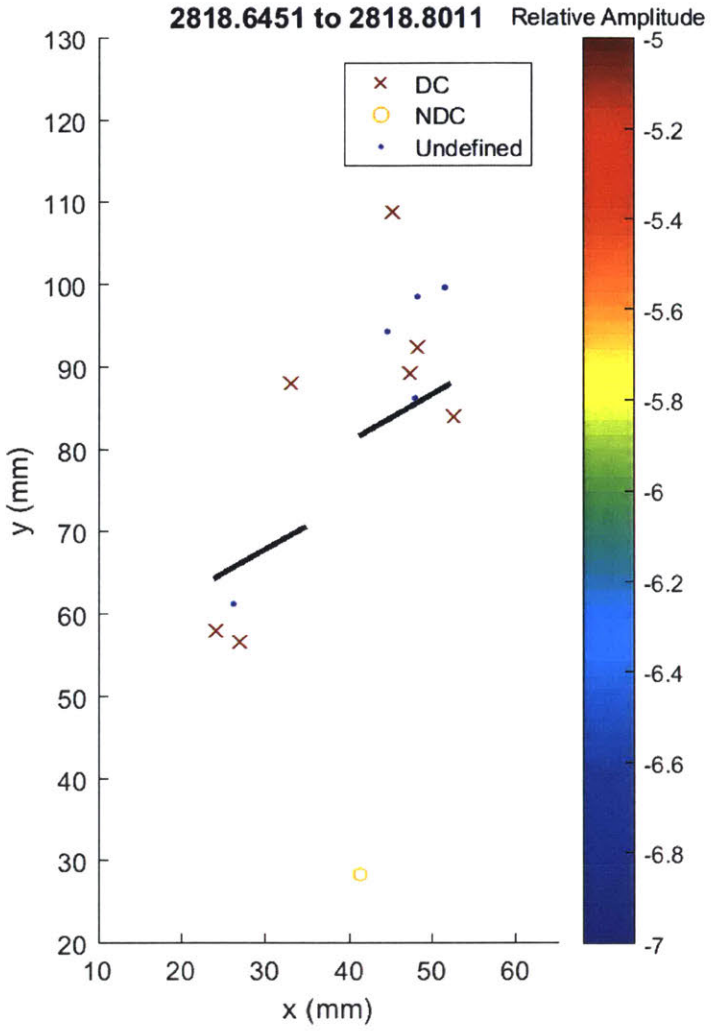

All events are shear type, and occur at both outer flaw tips.

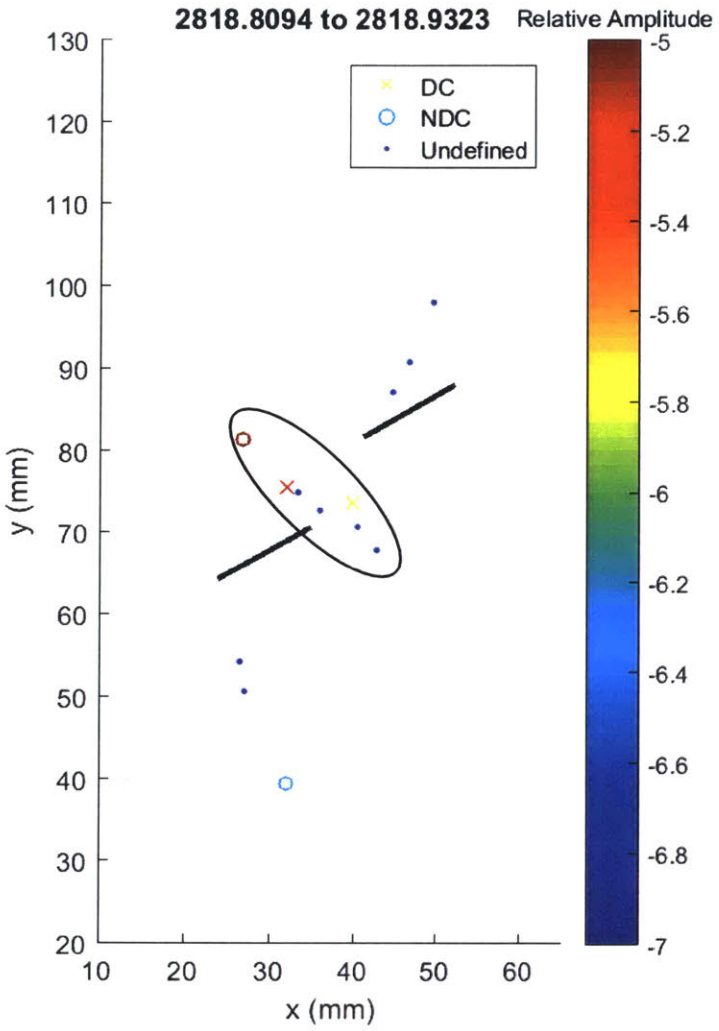

Main cluster of events appears to be oriented about 60 degrees from the orientation of the left flaw.

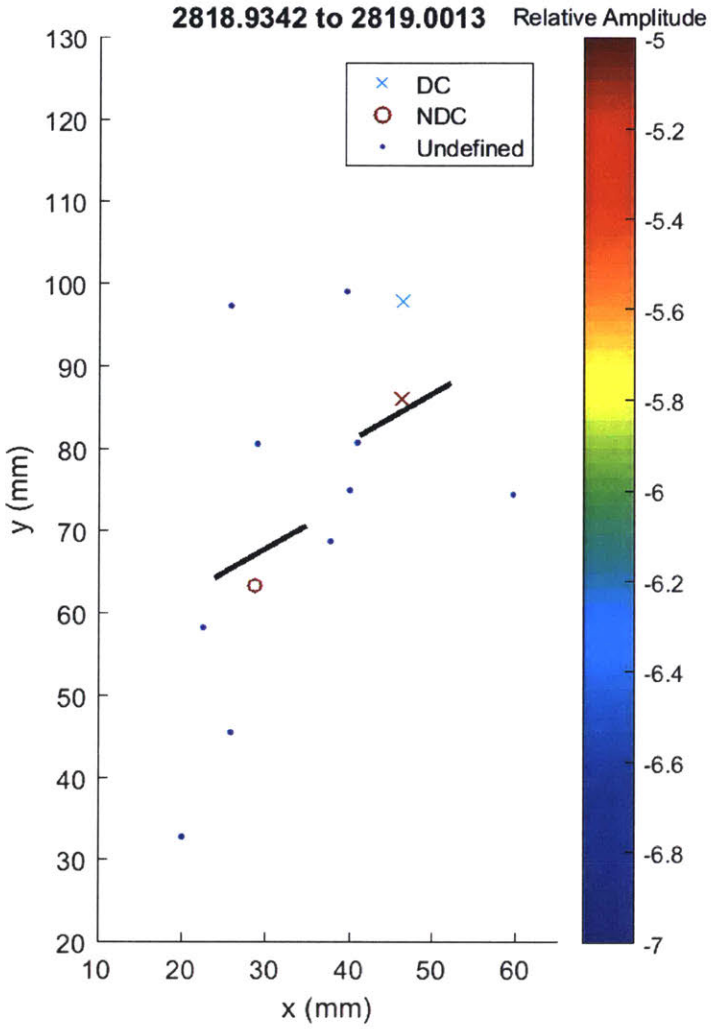

De-clustered event locations.

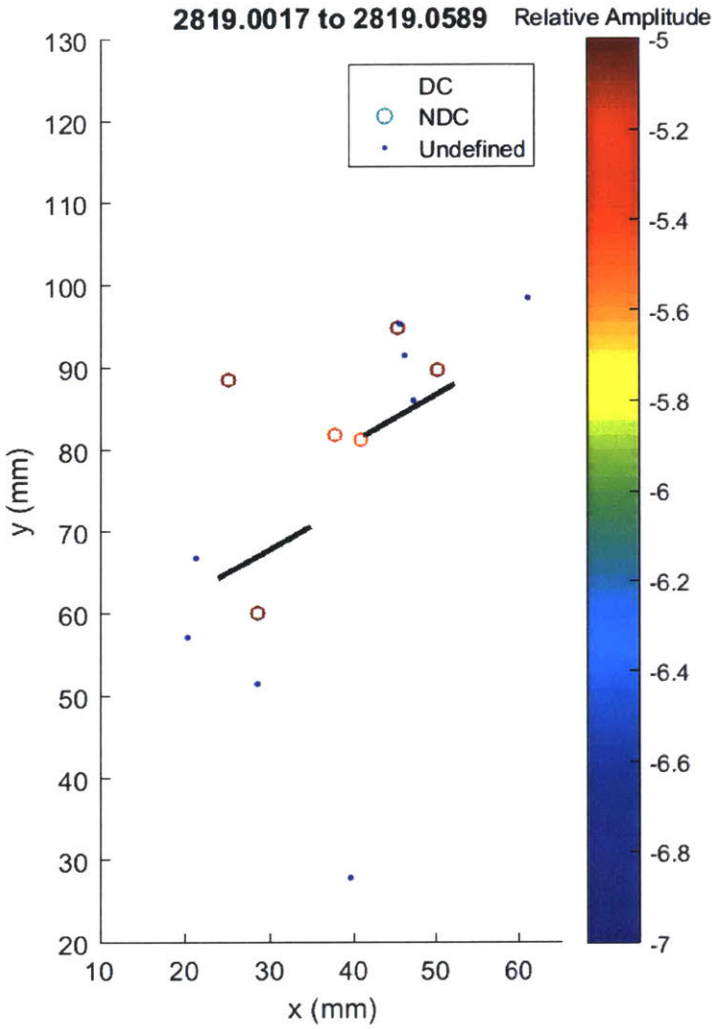

Key frame. All large AE events are shear type, and in this frame appear to be concentrated linearly above both tip of the right flaw.

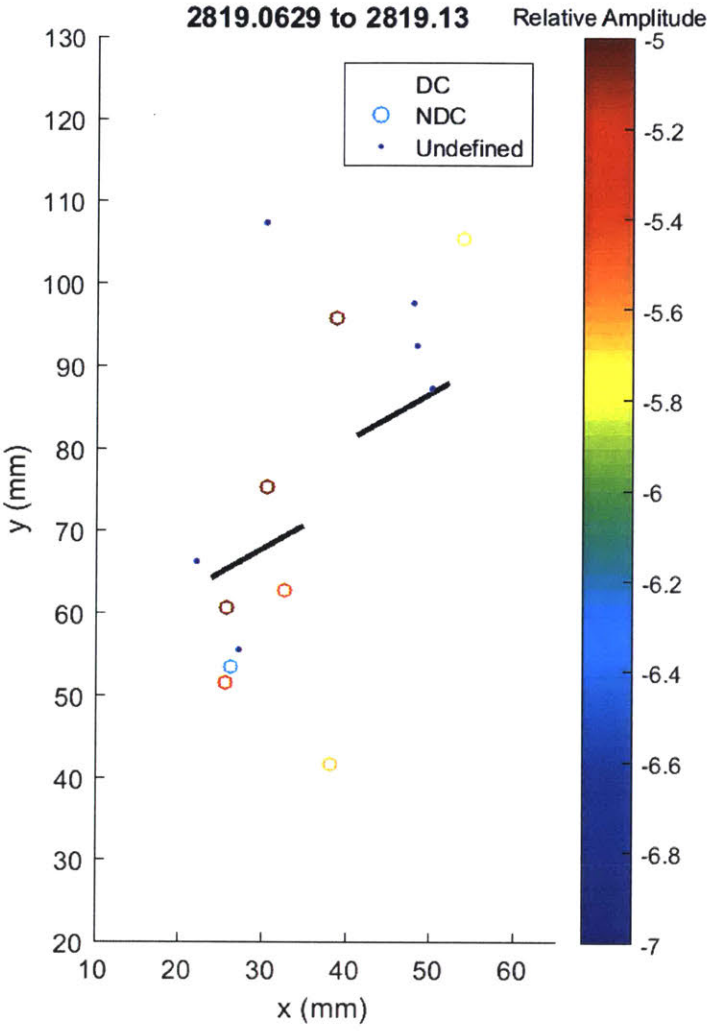

All large events continue to be tensile, but this time concentrated on both tips of the left flaw. This indicates that microcracks coalesced through a tensile mechanism first on the right flaw in the previous frame, and now on the left flaw in this frame.

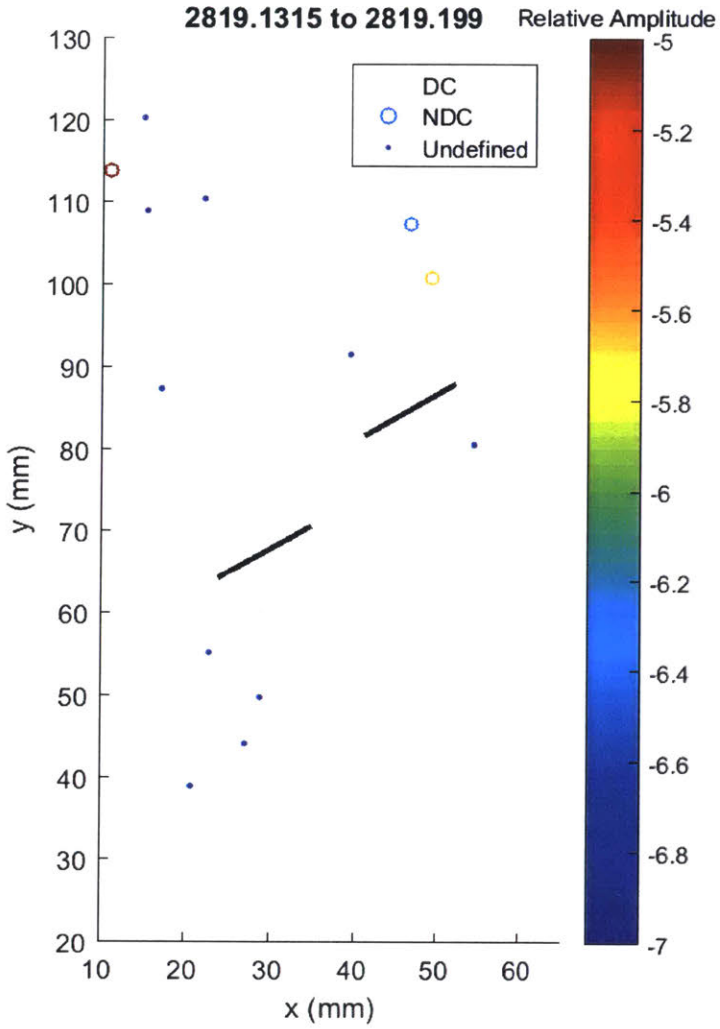

Diffuse AE locations

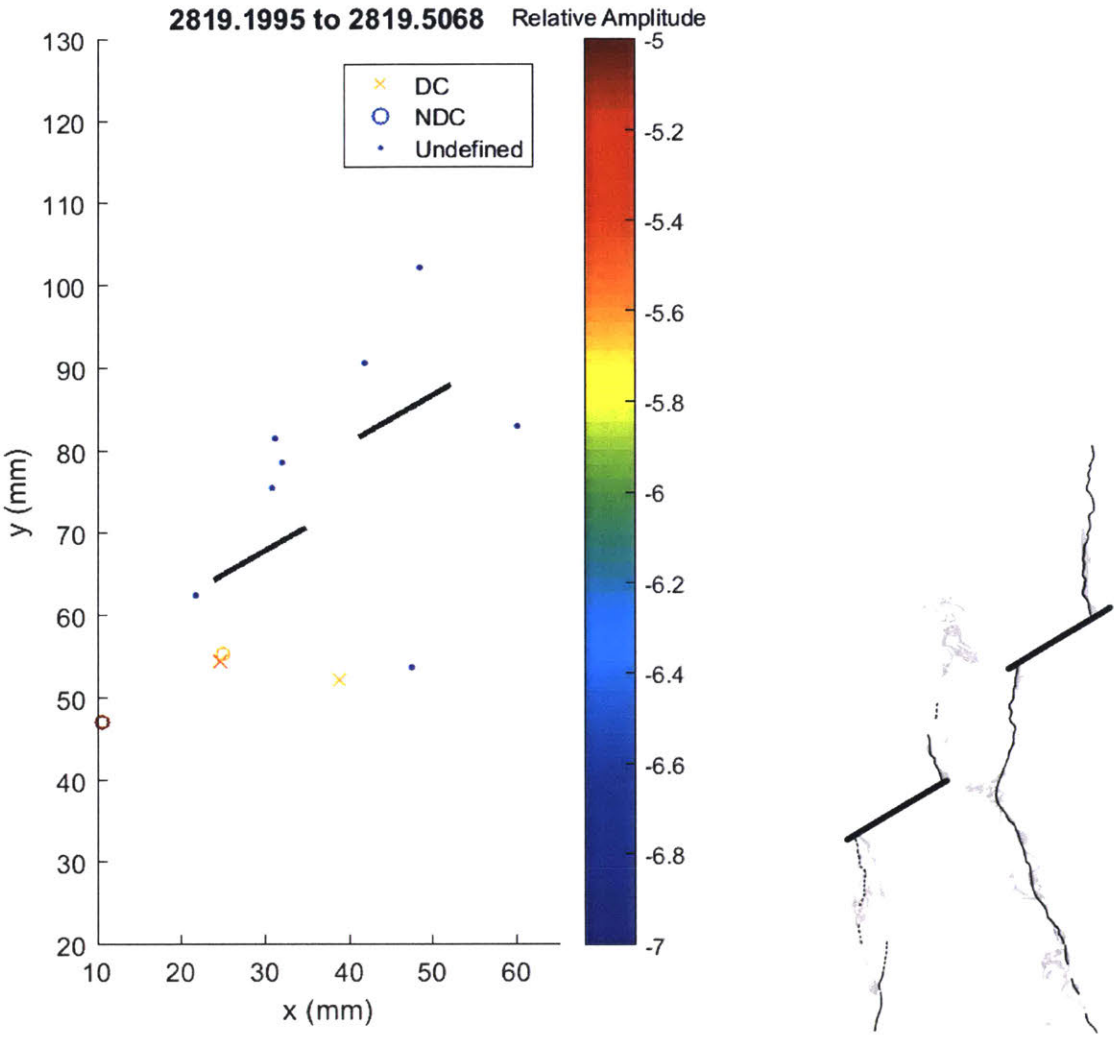

Same as previous frame. Visual crack initiation and propagation occurs within this frame.

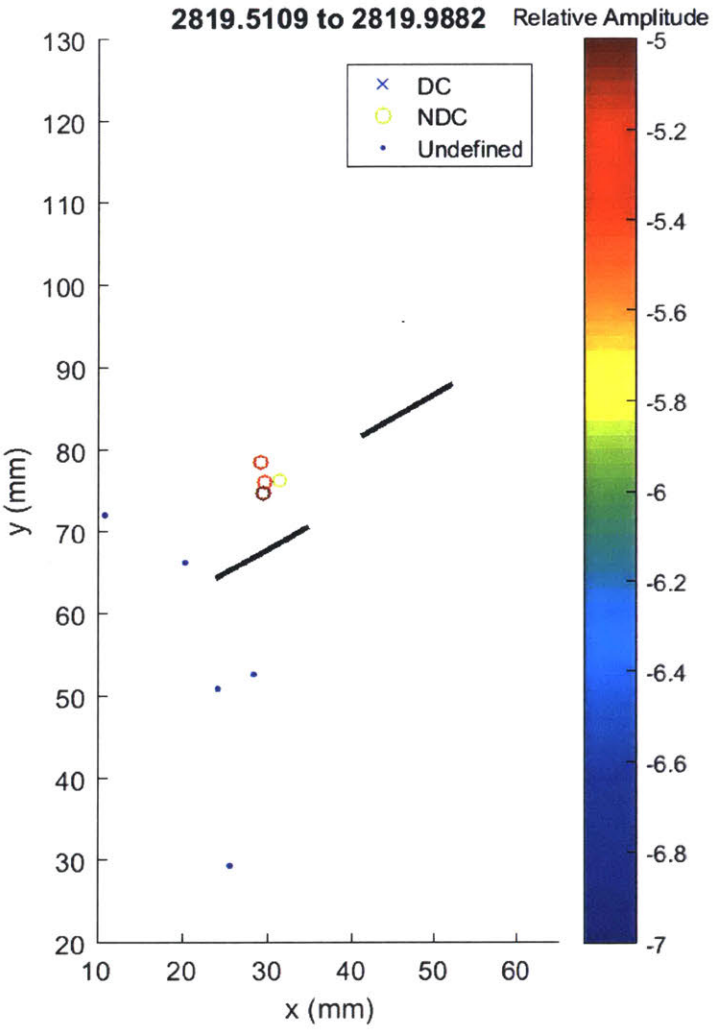

Cluster of 4 tensile events above the inner tip of the left flaw

Summary:

As a VL5 test, there were more shear events. However, in the last few frames before crack initiation, the frames consisted solely of tensile events, indicating microcrack coalescence. This coalescence appears to occur first on the right flaw, then the left flaw, despite the visual showing crack initiation on the outer tip of the left flaw. In terms of locations, the first half of the frames showed AE events occurred in the bridge area, but as the specimen approached crack initiation events tended to be more concentrated in wing/anti-wing locations. There did not appear to be significant evidence from AE regarding the en-echelon cracking A1 and A2 on the outer tip of the left flaw.

AE hypocenter analysis for specimen 2a-30-30-VL5-C

Final crack geometry:

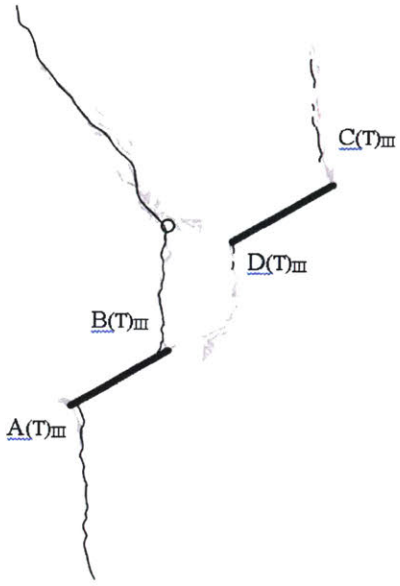

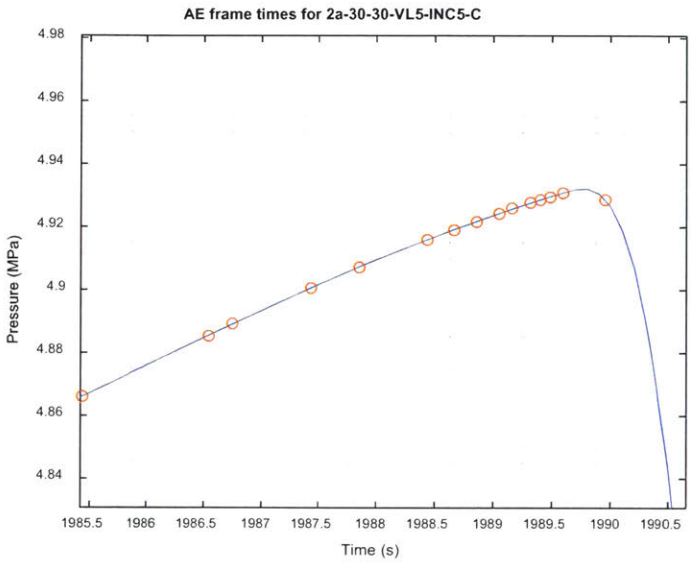

A wing crack forms first on the left flaw, then the right flaw. Peak pressure occurs immediately before pressure breakdown.

Development of AE locations are shown over the 20 frames presented in this analysis, where each frame shows 5% of the total number of events recorded during the test. This means that initially the frames will cover a long time period since few AE occurred at the beginning, while towards failure each frame will only cover fractions of a second since AE occur at a rapid rate.

Events with greater than 50% CLVD (compensated linear vector dipole) are considered shear type events and are marked with an 'x', while events with less than 50% CLVD are considered tensile and marked with 'o'. For those events detected by 4 sensors, it is not possible to invert the moment tensor and so these events are marked as undefined with '.'. The colour of an event indicates its relative magnitude, where red is the largest. Black ellipses are used to highlight areas of interest.

Where possible, AE frames are shown next to the appropriate analysis sketch from Bruno. However, these tend to be few in between and as discussed, the high speed frames tend to occur after the end of detectable AE events.

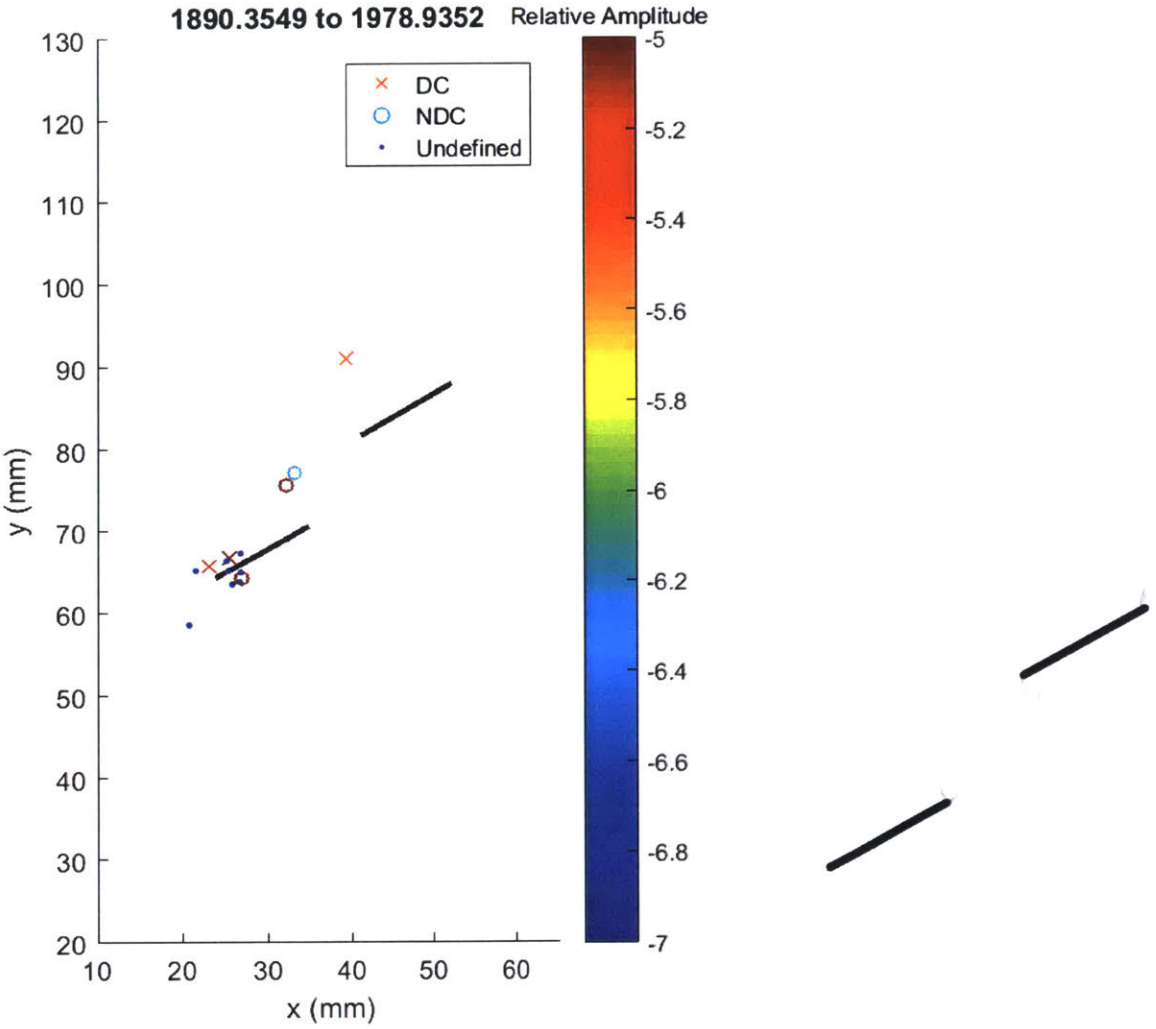

2 shear and 1 tensile events occur at outer tip of left flaw, and 2 tensile events occur at inner tip of left flaw. Visually, there is some slight white patching at the flaw tips.

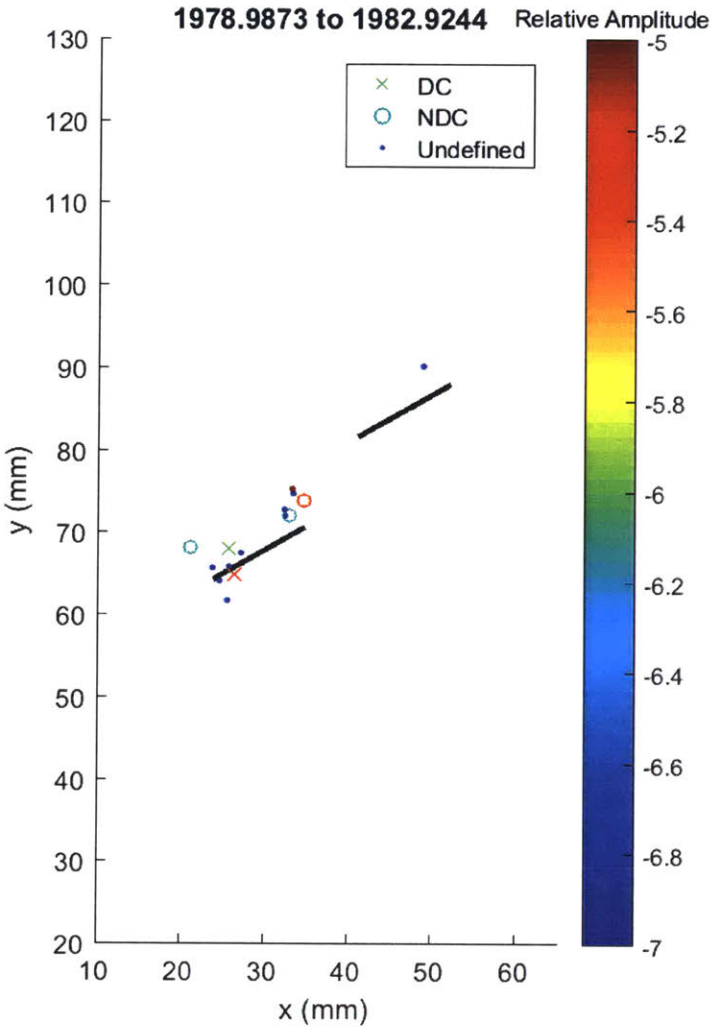

Events occur at both tips of the left flaw, again shear events occur at the outer tip while the inner tip only exhibits tensile events.

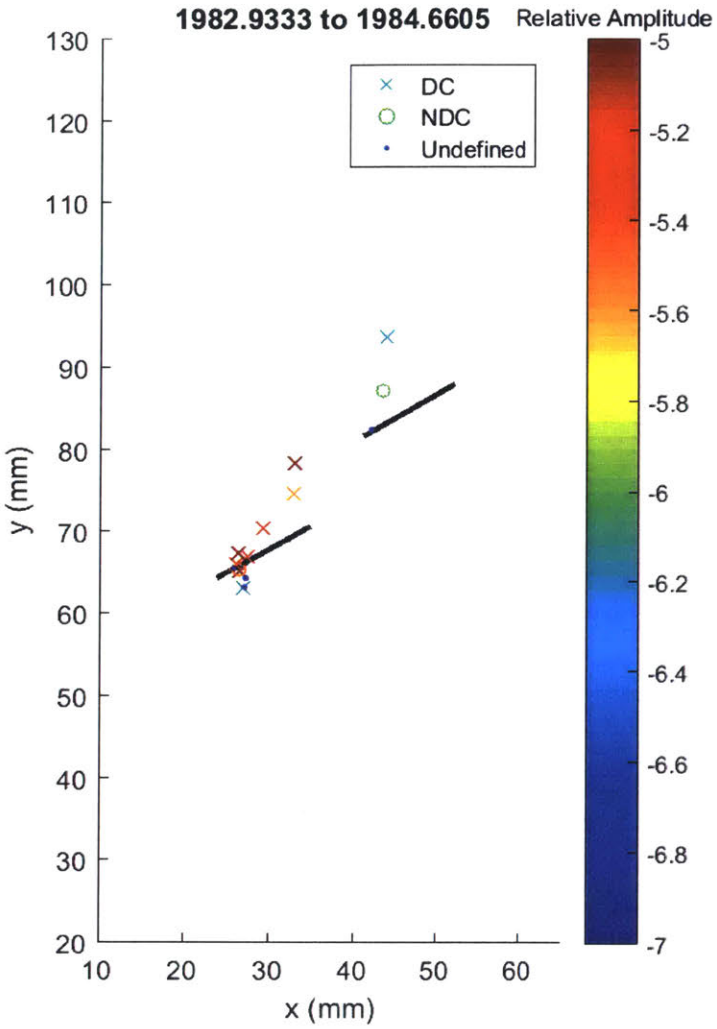

Key frame. Series of high amplitude shear events occur along a wing crack pattern on the left flaw, while 2 small amplitude events occur above right flaw.

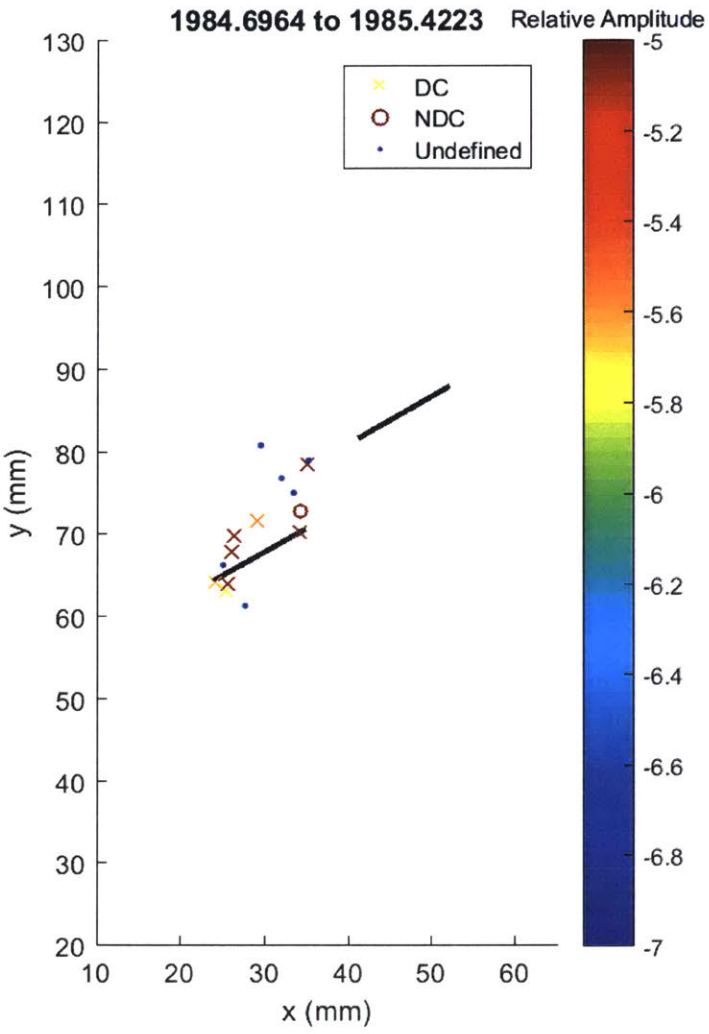

Events continue to mostly be large amplitude shear, occurring above both tips of the left flaw.

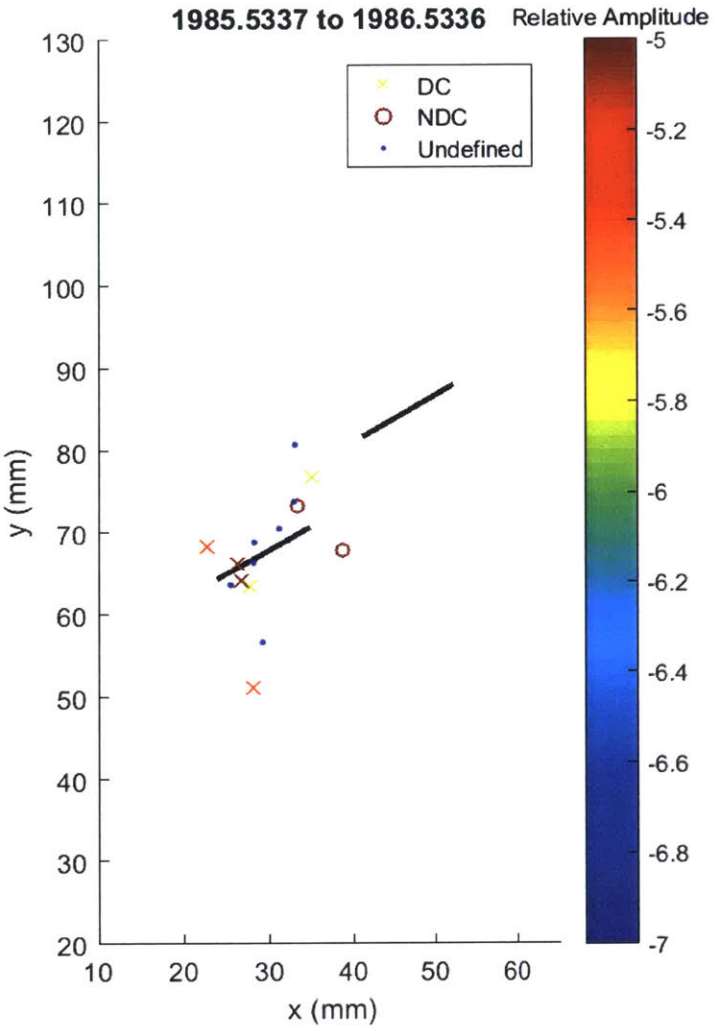

4 shear events occur around the outer tip of left flaw, oriented normal to the flaw, while 2 large tensile events occur on either side of the inner tip of the left flaw, also oriented normal to flaw.

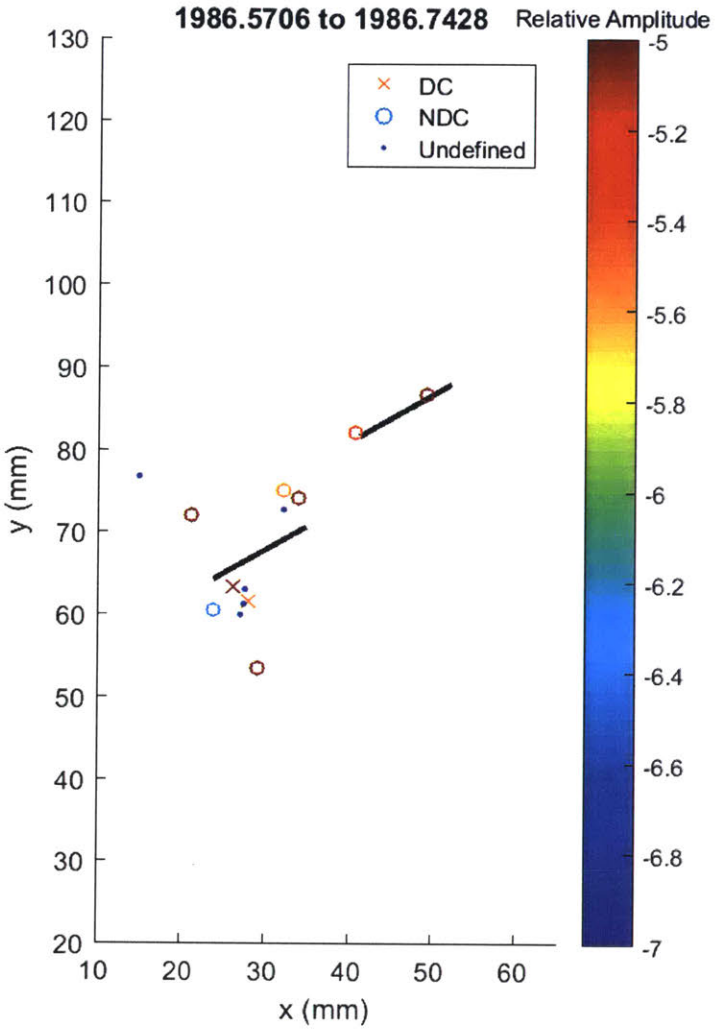

Key frame. Notable transition from shear to tensile type events, which occur at all flaw tips but with a higher concentration at the outer tip of the left flaw. It may be that the occurrence of a some of the tensile events triggered a dynamic stress that caused opening events in other locations.

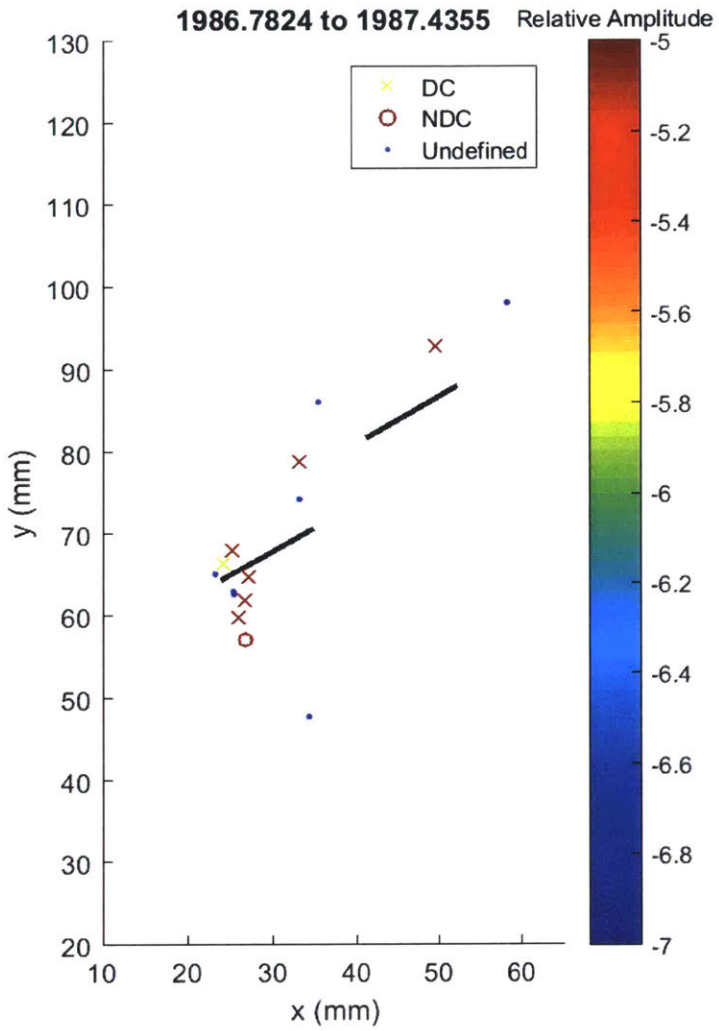

Events transition back to being primarily shear, with the majority occurring below the outer tip of the left flaw. This is also where visual crack initiation occurs.

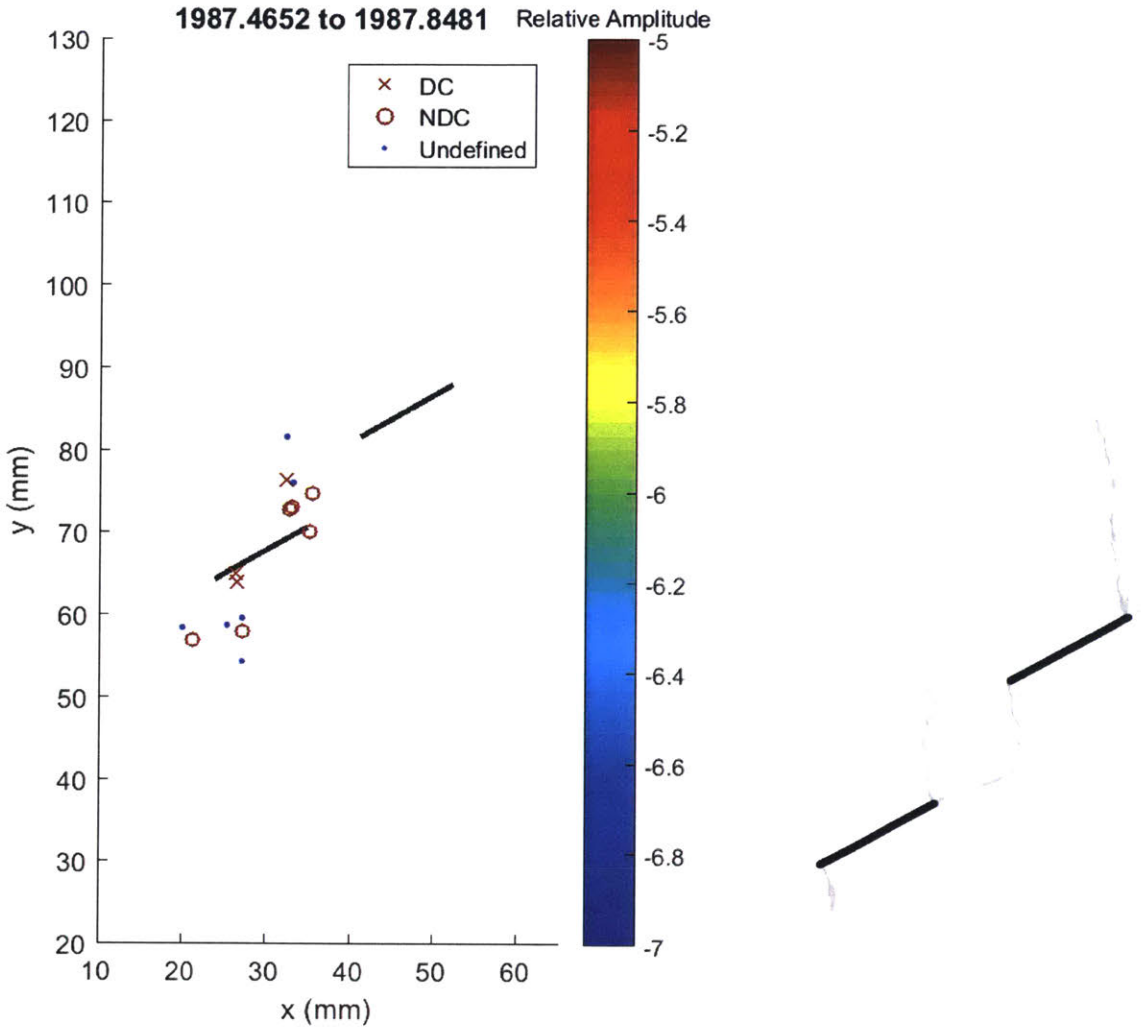

2 shear events occur near to the outer tip of the left flaw, while 4 large tensile events occur very near to the inner tip. This indicates that microcracks are coalescing at the inner tip. Visually, there is extensive white patching from all flaw tips.

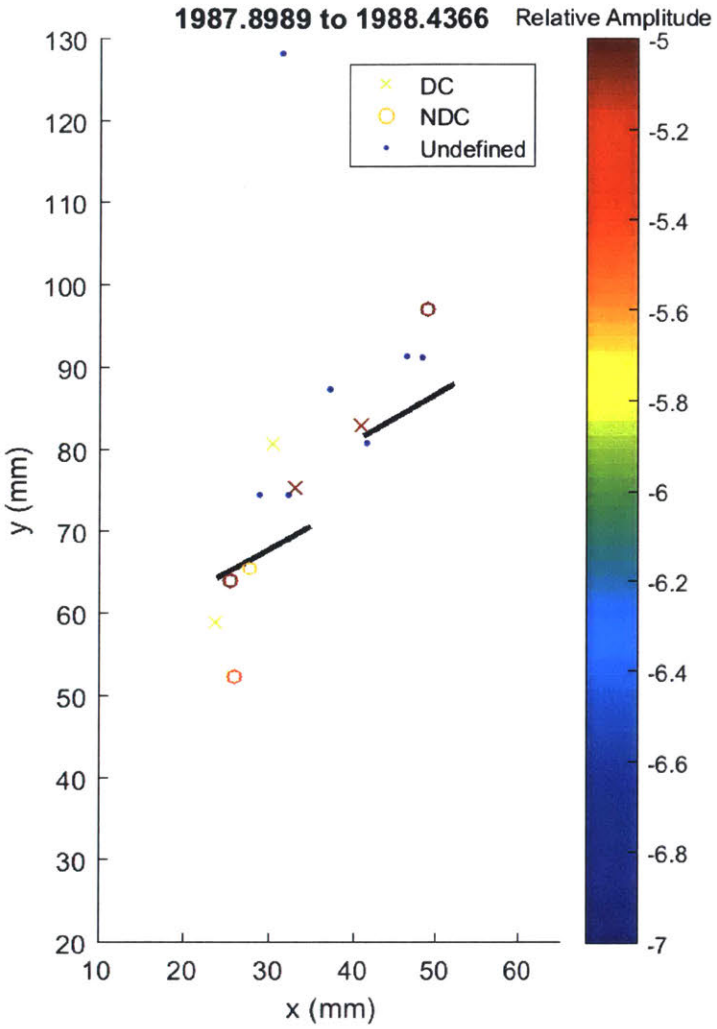

Shear events occur at both inner tips, while tensile events occur at outer tip of the left flaw.

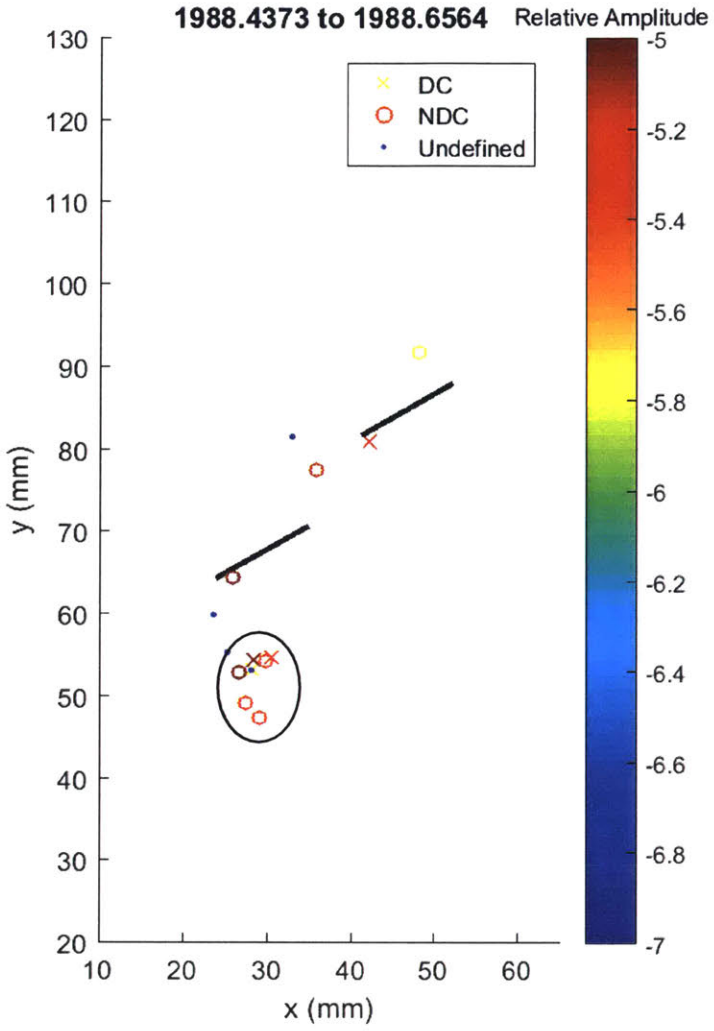

Small number of events occur at all tips, but there is a cluster of 2 large shear and 4 large tensile events that occur 1.5cm below the outer tip of the left flaw, indicating that the process zone "front" has moved significantly beyond the tip of the flaw.

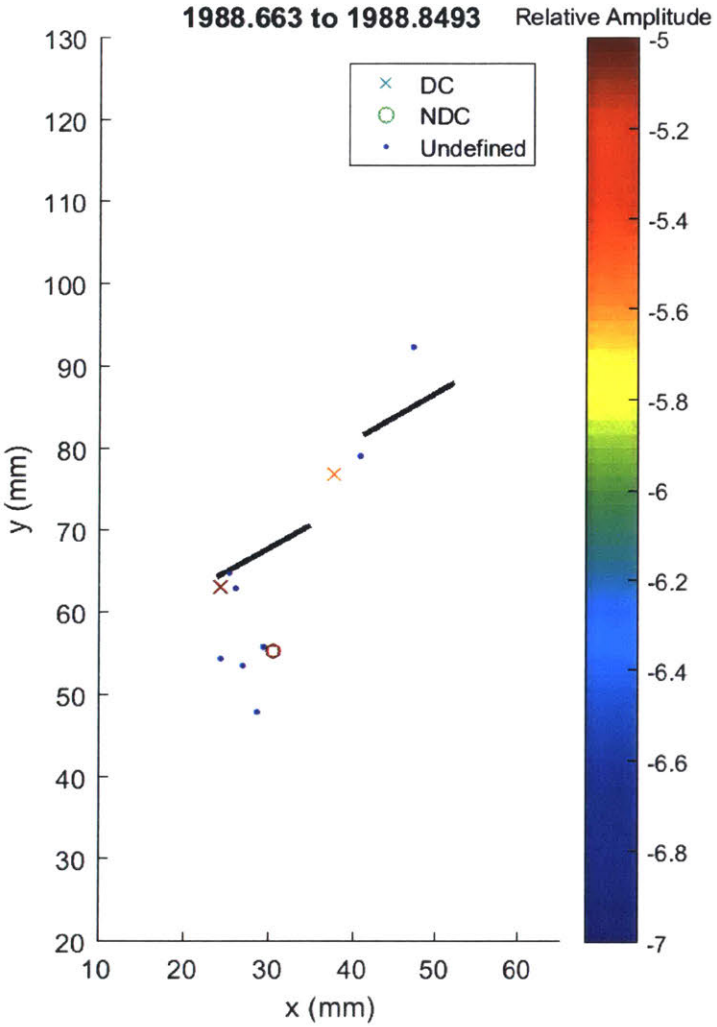

Most events are small and undefined.

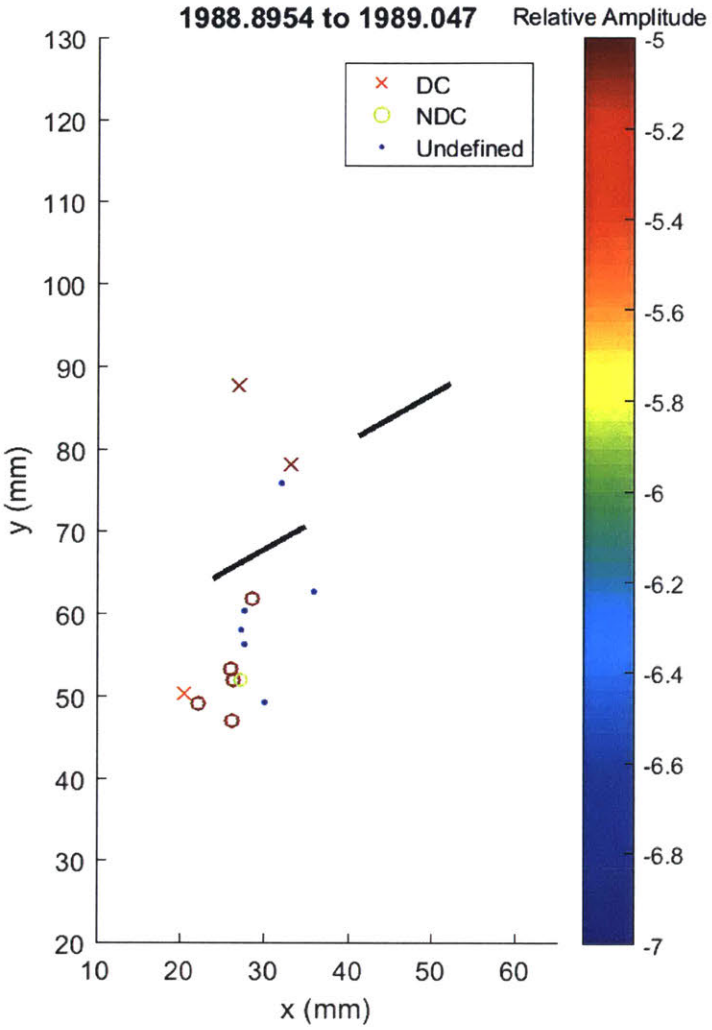

Cluster of 5 large tensile and 1 large shear events continues to occur in a zone approximately 1.5cmbelow the outer tip of the left flaw. 2 large shear events also occur above the inner tip of the left flaw.

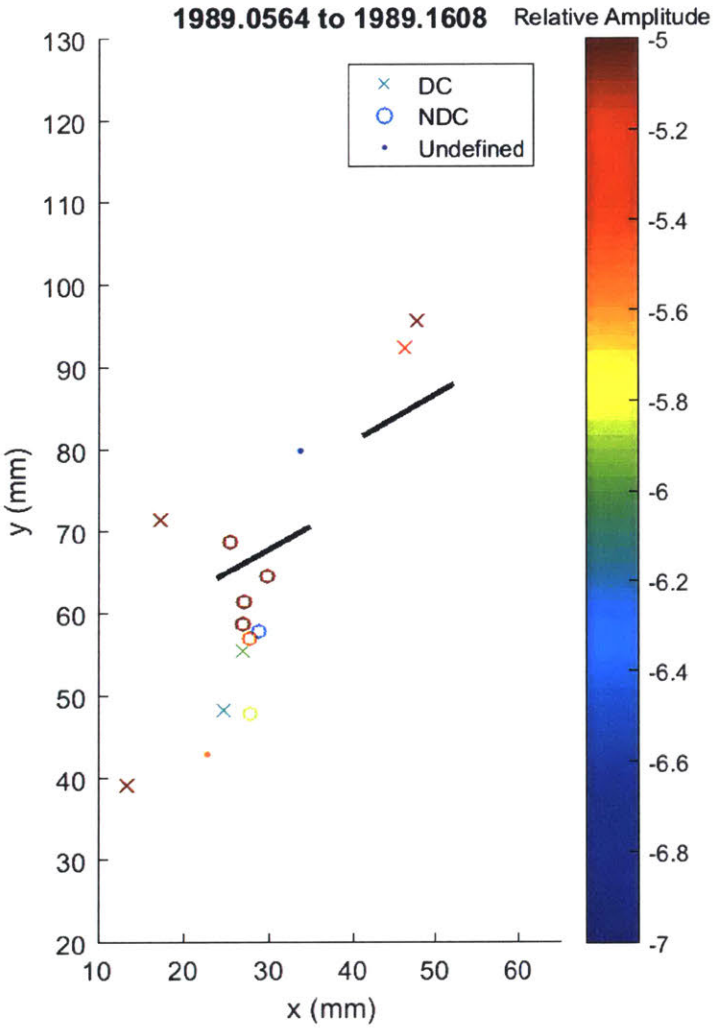

Key frame. 4 large tensile events occur close to the outer tip of the left flaw, while smaller amplitude events occur further from the flaw tip. This may be and indication of further opening of the damaged area near the tip at the specimen approaches visual (macro) crack initiation. 2 large shear events occur above outer tip of right flaw.

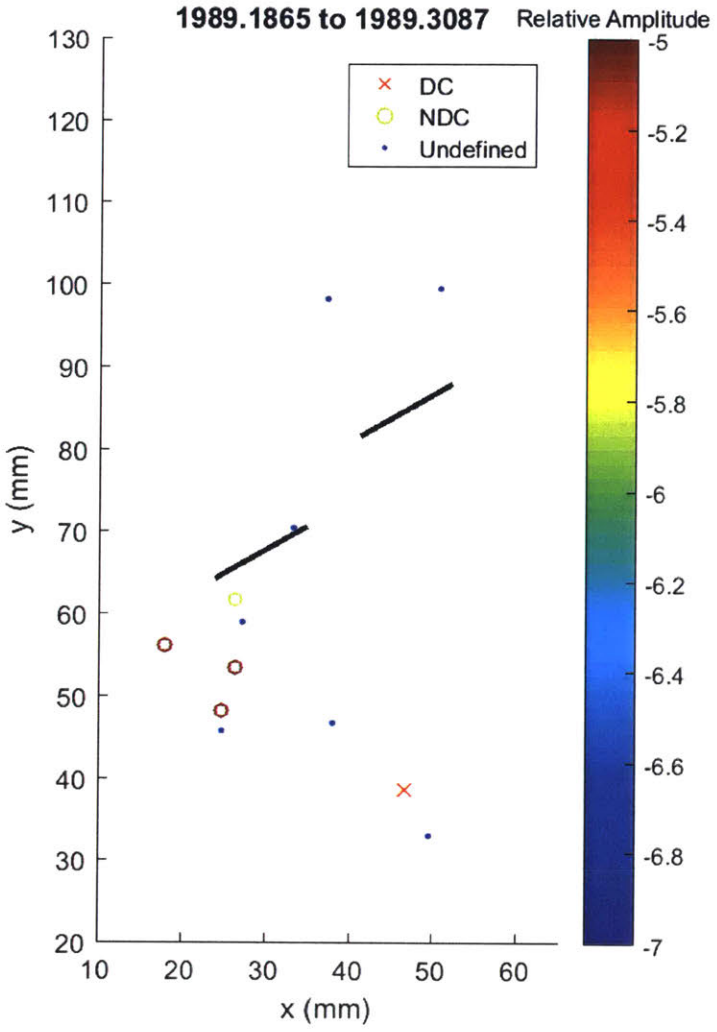

Large tensile events occur below the outer tip of the left flaw.

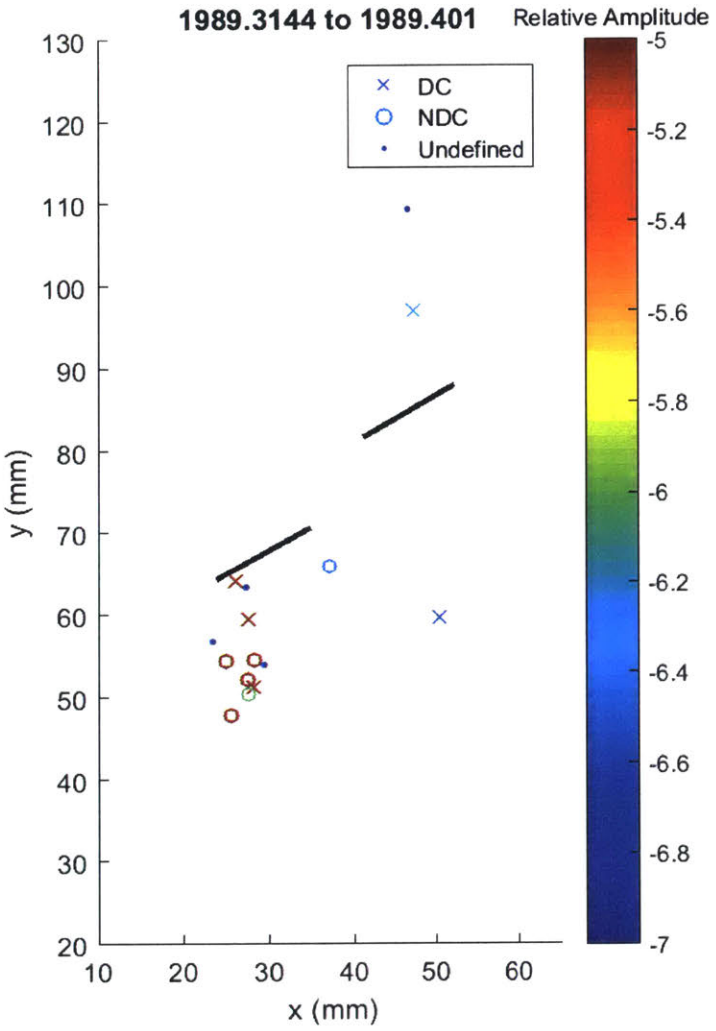

Key frame. Similar to some of the previous frames, there is a cluster of 4 large tensile events approximately 1.5cm below the outer tip of the left flaw, while shear events are closer to the tip.

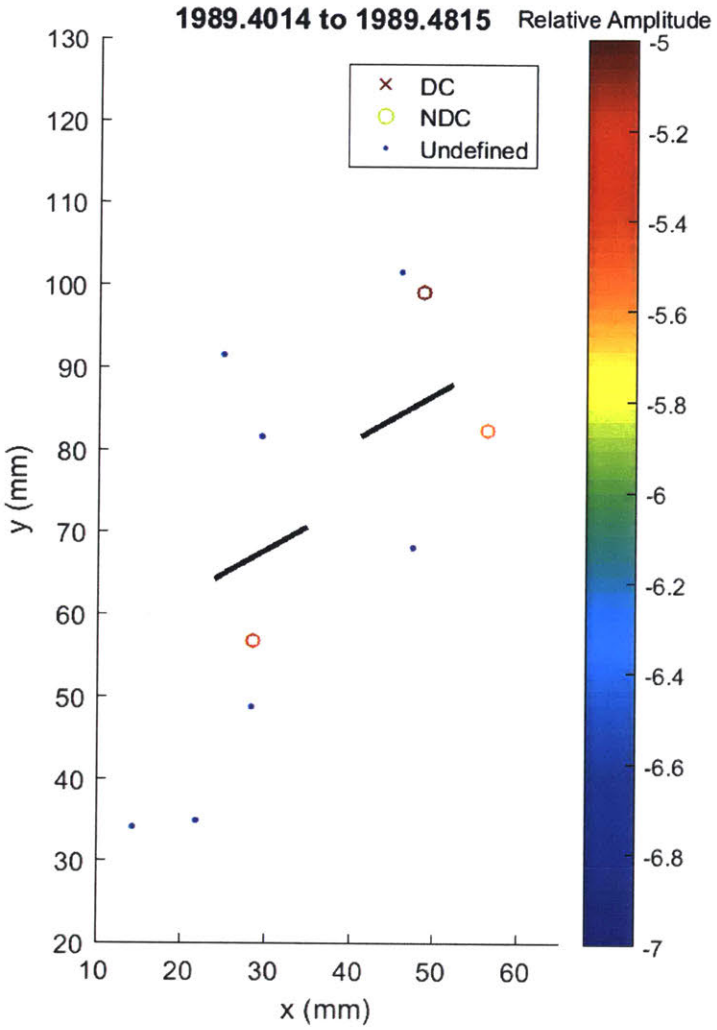

Events are generally diffuse.

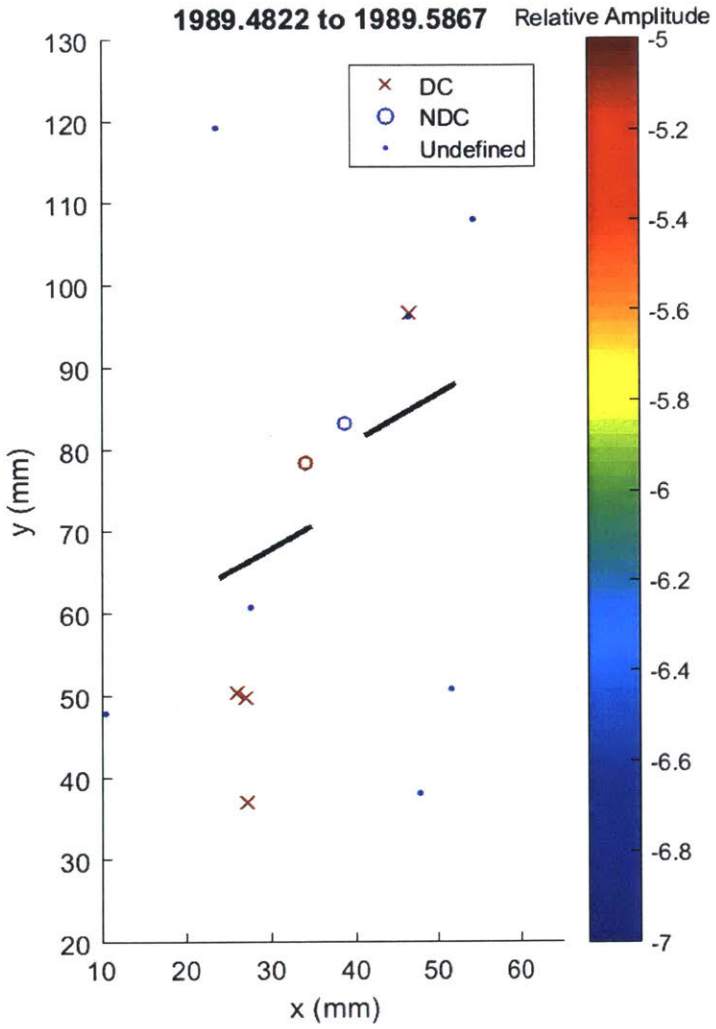

3 large shear events occur below the outer tip of the left flaw.

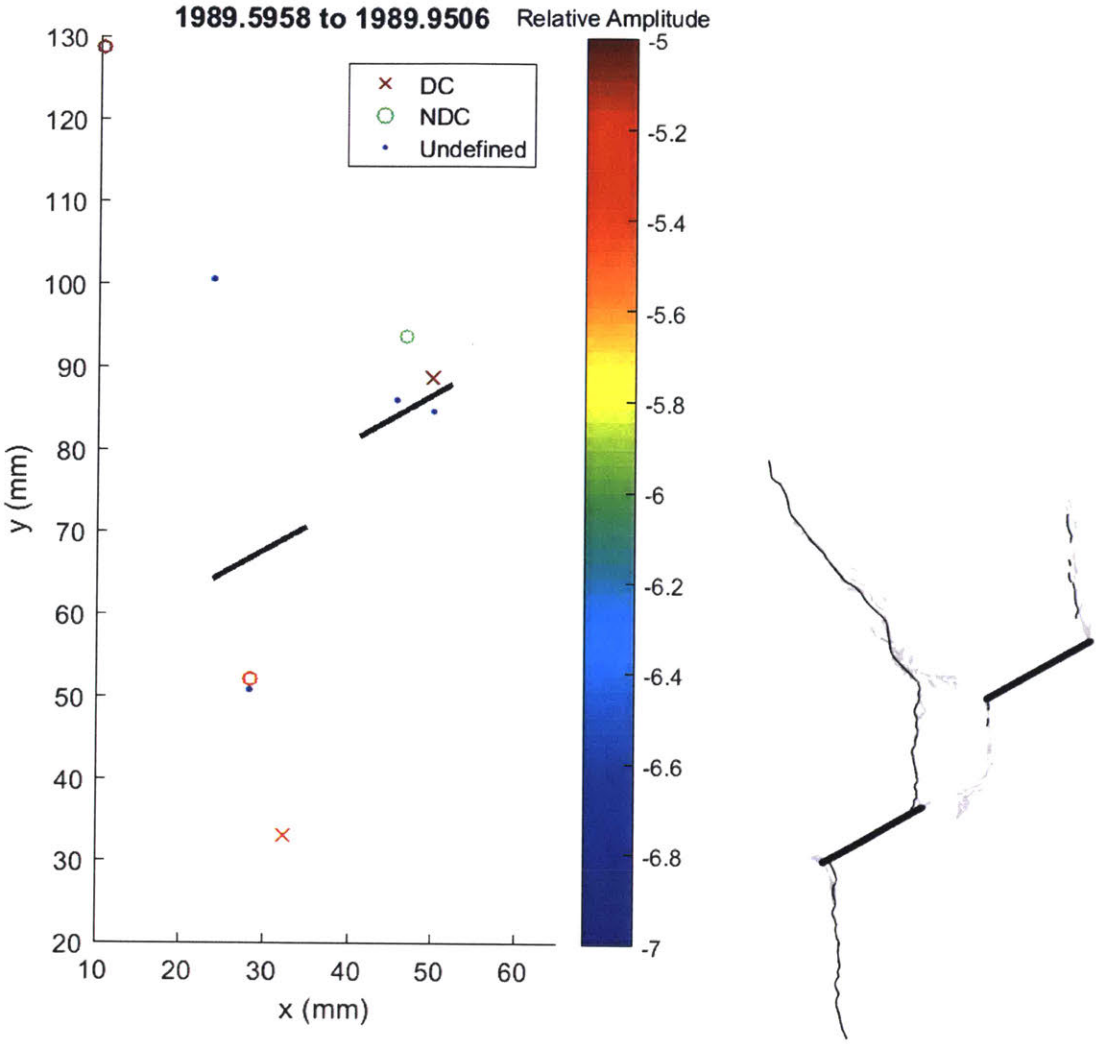

Diffuse series of events, appears to be some migration towards the right flaw. Pressure drops and cracks initiate around the end of this frame. Peak pressure occurs around this frame.

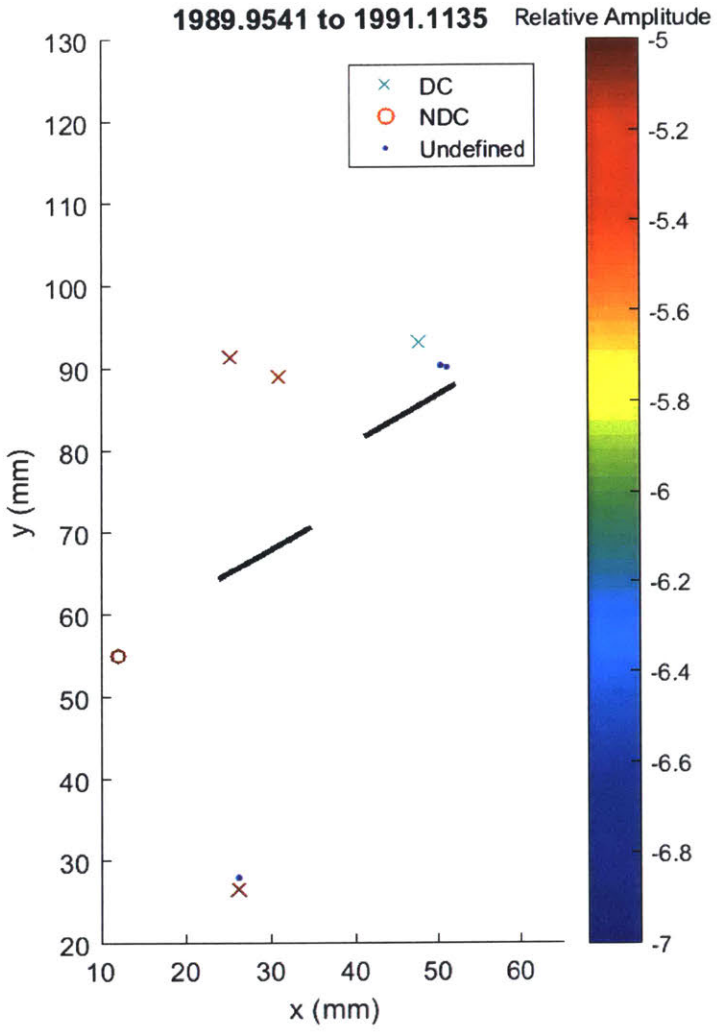

Same as above.

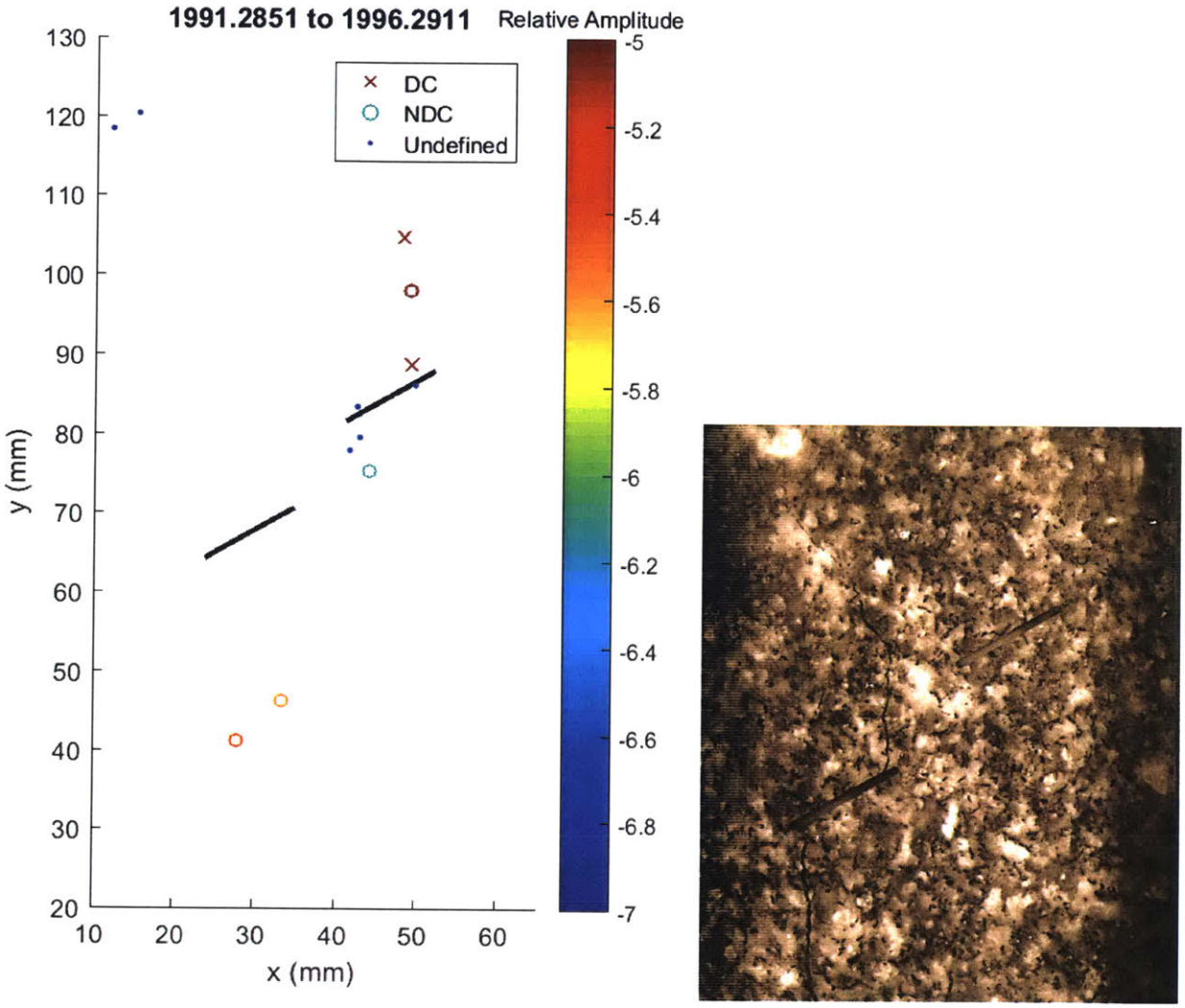

Same as above, where the events above the outer tip of the right flaw are now large amplitude events.

Summary:

In this specimen, there was a clear preference for activity on the left flaw, with a specific concentration of events approximately 1.5cm below the outer tip of the left flaw. If we look at the photo presented above, there does not appear to be a significant grain in that region at the surface. It also appear that tensile events, though somewhat rarer, also tend to occur in groups i.e. we often see tensile events occur closely in time, even if they are separated in space. This may be related to a static or dynamic change in the stress field.

AE hypocenter analysis for specimen 2a-30-90-VL0-B

Final crack geometry:

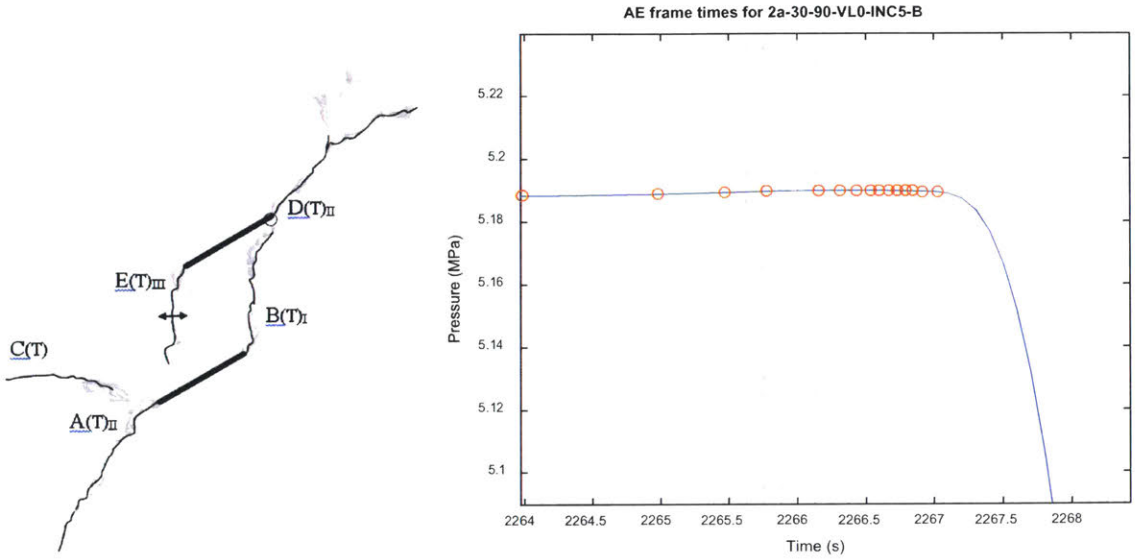

Crack A first initiates from the left tip of the bottom flaw, followed by crack B which initiates from the right tip of the bottom flaw and coalesces with the top flaw. Crack C then opens proximally from the left tip of the bottom flaw, followed by crack D and E from the top flaw. Pressure is relatively stable prior to pressure breakdown.

Development of AE locations are shown over the 20 frames presented in this analysis, where each frame shows 5% of the total number of events recorded during the test. This means that initially the frames will cover a long time period since few AE occurred at the beginning, while towards failure each frame will only cover fractions of a second since AE occur at a rapid rate.

Events with greater than 50% CLVD (compensated linear vector dipole) are considered shear type events and are marked with an 'x', while events with less than 50% CLVD are considered tensile and marked with 'o'. For those events detected by 4 sensors, it is not possible to invert the moment tensor and so these events are marked as undefined with '.'. The colour of an event indicates its relative magnitude, where red is the largest. Black ellipses are used to highlight areas of interest.

Where possible, AE frames are shown next to the appropriate analysis sketch from Bruno. However, these tend to be few in between and as discussed, the high speed frames tend to occur after the end of detectable AE events.

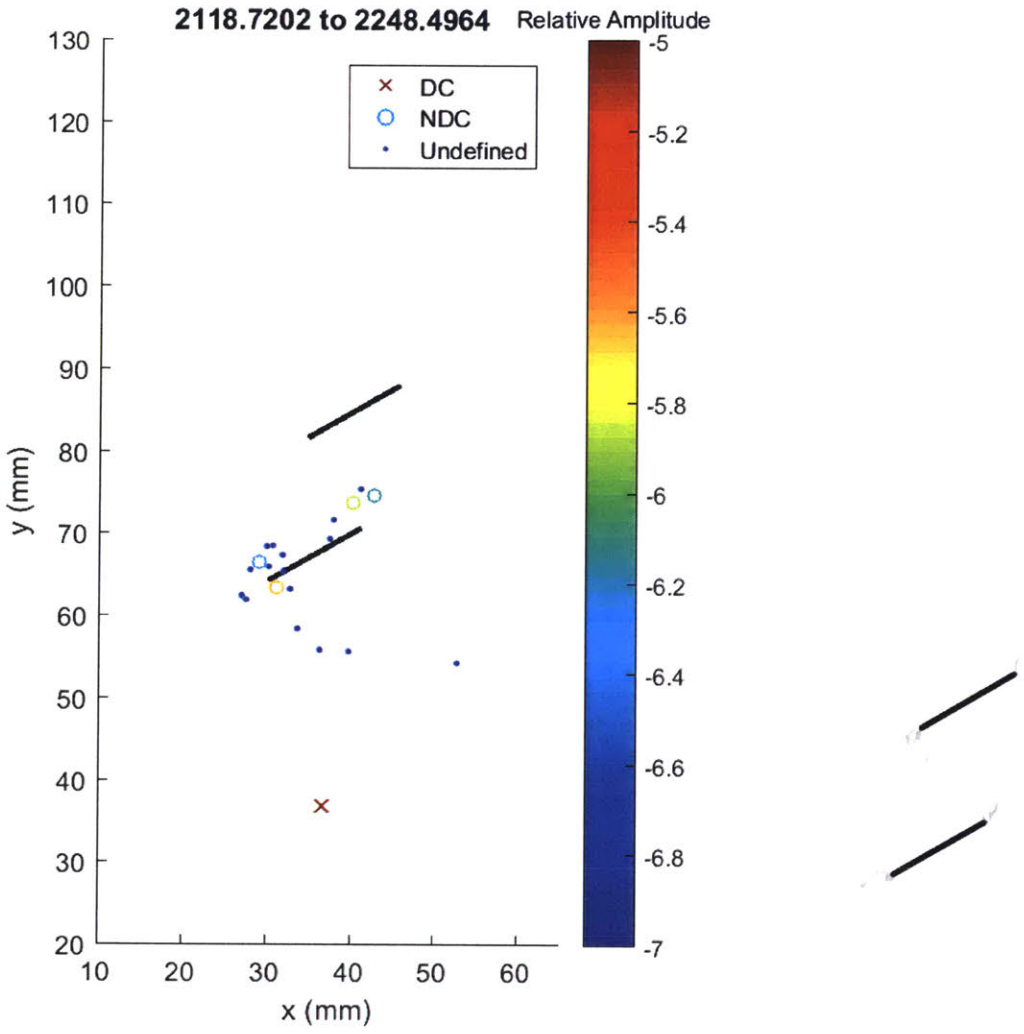

Tensile events occur at both tips of the bottom flaw. Small amplitude undefined events tend to be more concentrated at the left tip of the bottom flaw. Visual analysis shows some damage at flaw tips.

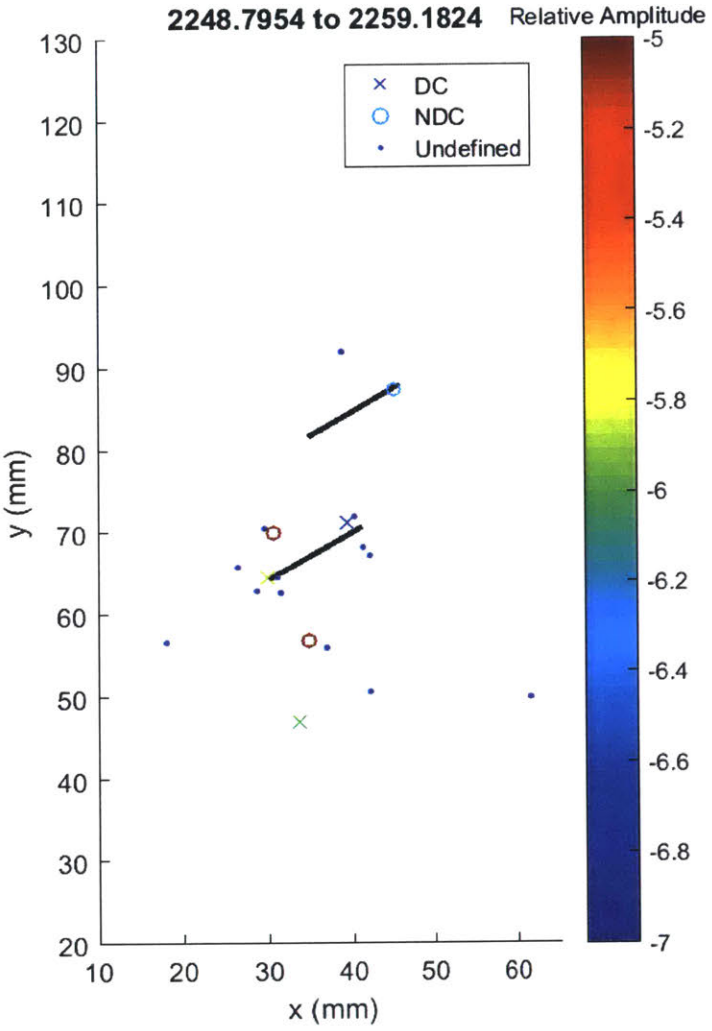

2 large amplitude tensile events occur above and below the left tip of the bottom flaw. Small amplitude shear events occur at both tips of the bottom flaw, and a single small tensile event occurs at the right tip of the top flaw.

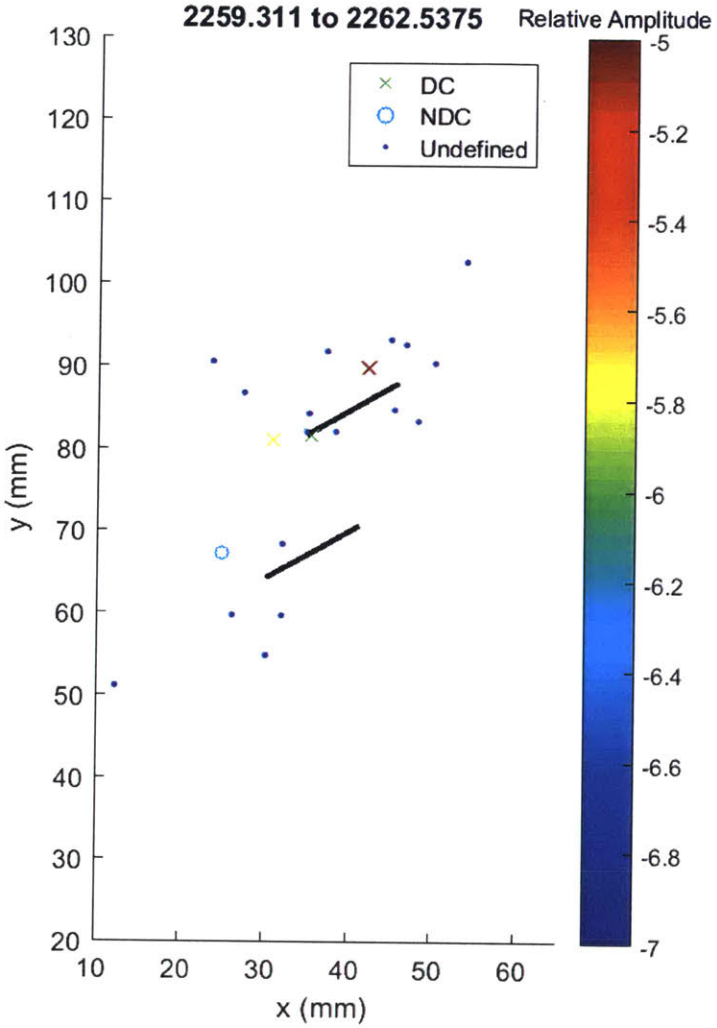

3 shear events occur around the top flaw, along with a number of small undefined events.

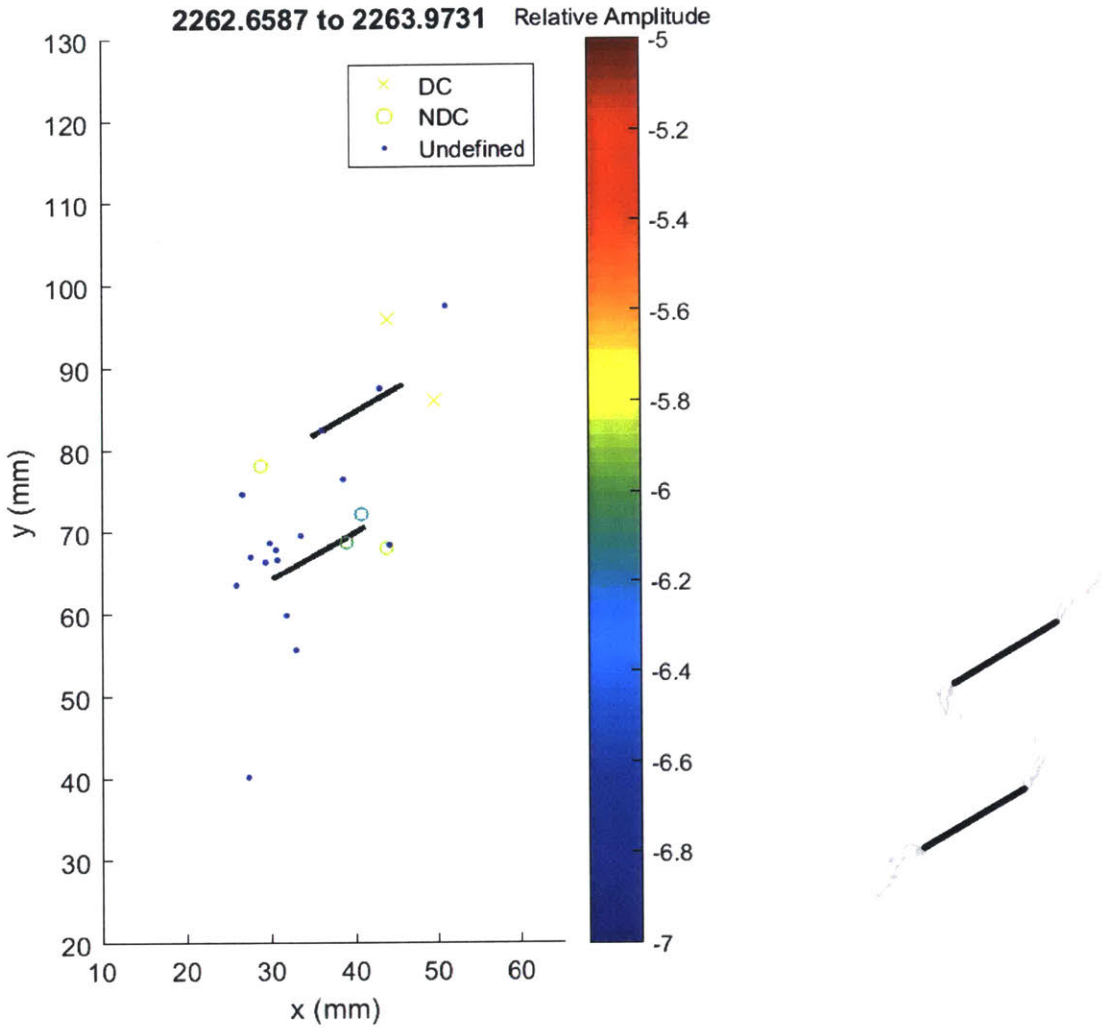

Small tensile and undefined events occur around the bottom flaw, while 2 small shear events occur around the right tip of the top flaw. Visual analysis shows further damage at flaw tips.

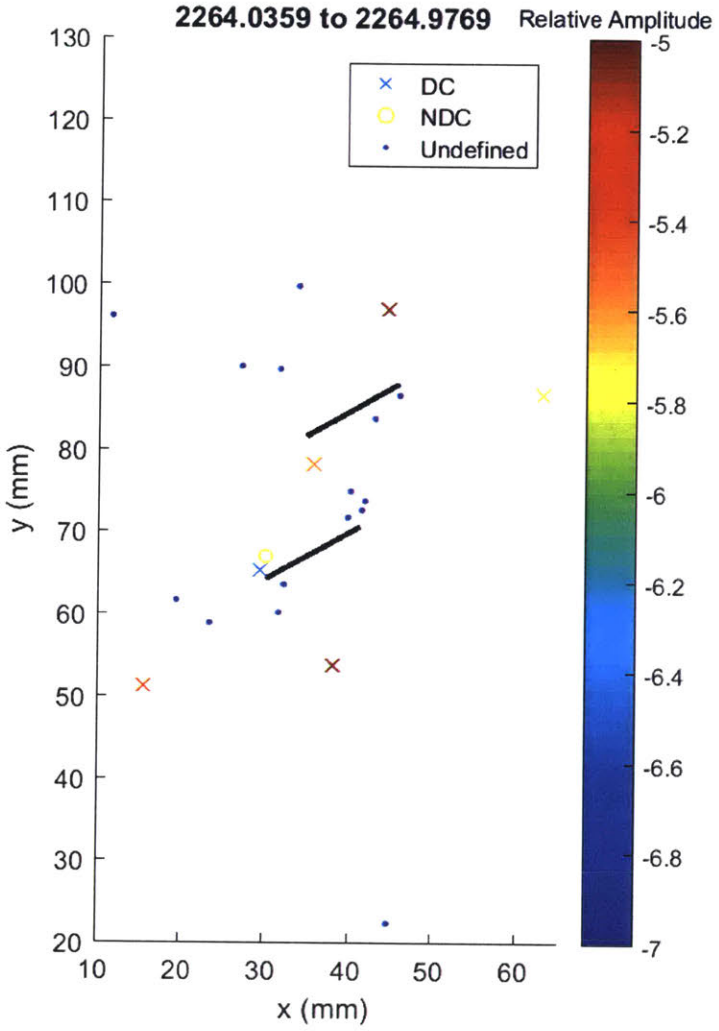

High amplitude shear events occur throughout the specimen, and small undefined events occur at all 4 flaw tips, particularly the right tip of the bottom flaw.

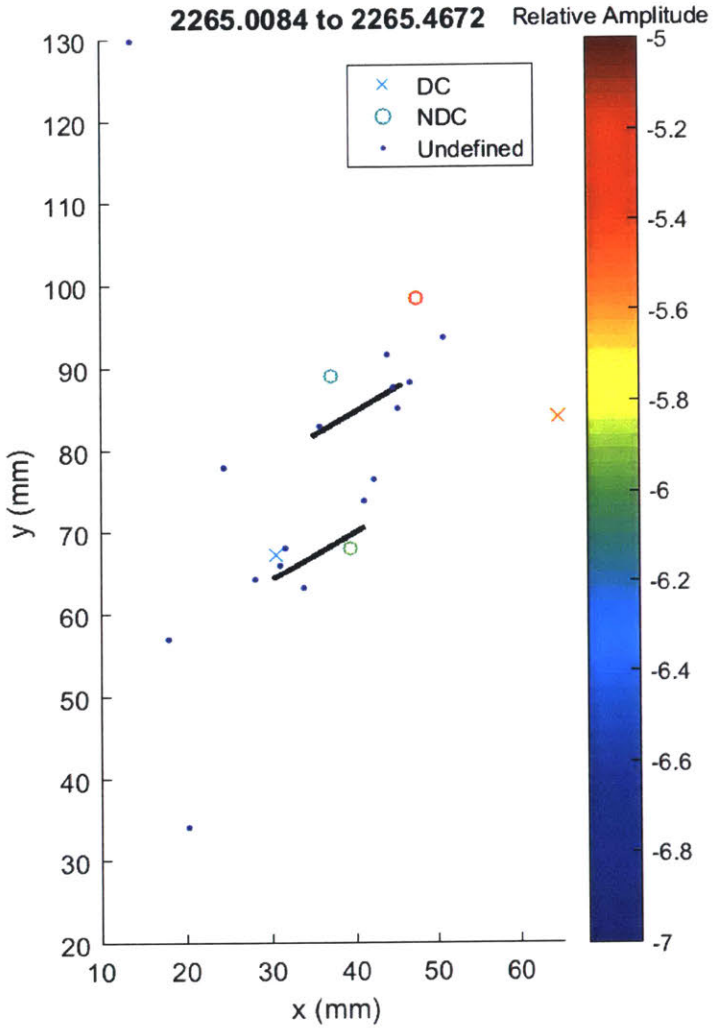

AE events are generally smaller amplitude, and are generally scattered. There is some alignment of events along visually identified crack B, which initiates from the right tip of the bottom flaw and coalesces to the right tip of the top flaw.

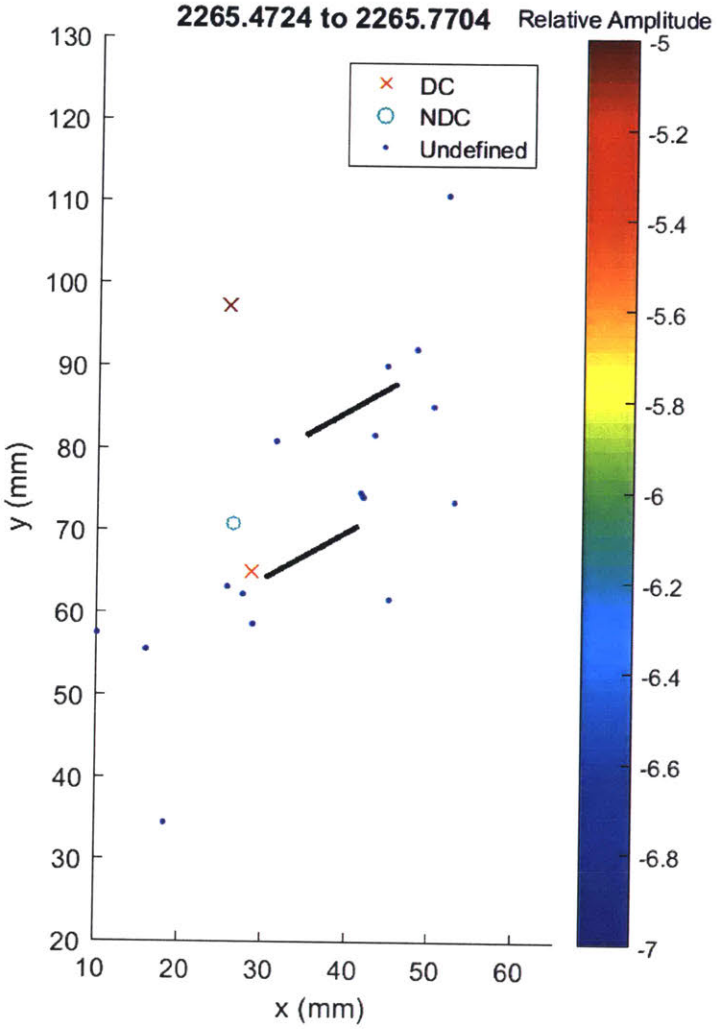

Diffuse event locations.

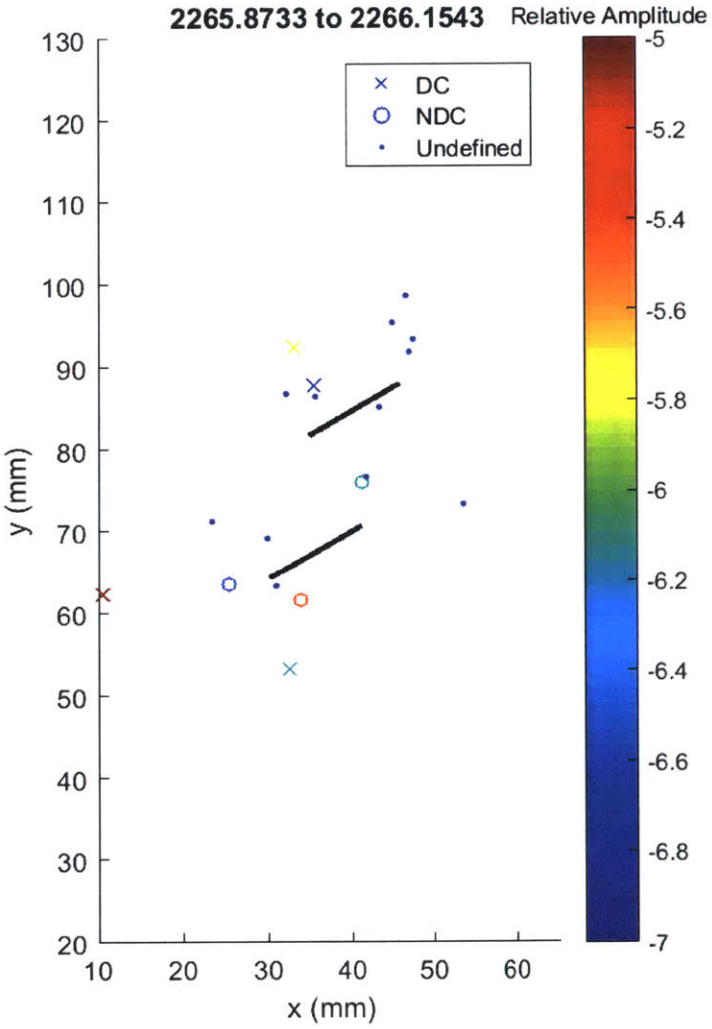

Continuing trend that the shear events tend to occur above the top flaw, and tensile events occur around the bottom flaw.

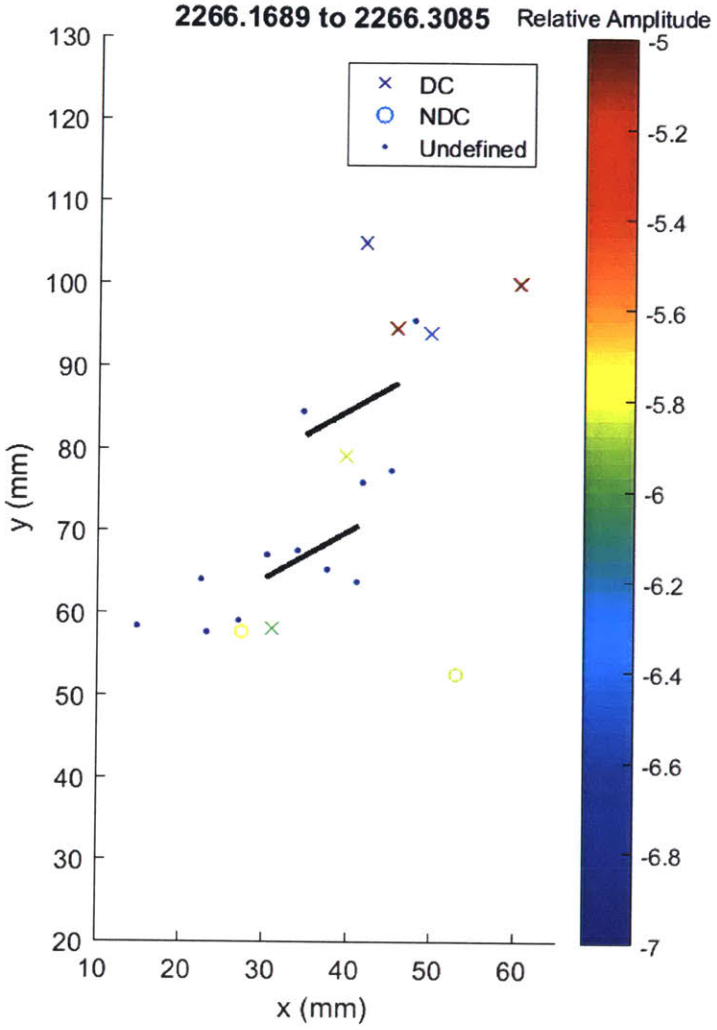

Same as above.

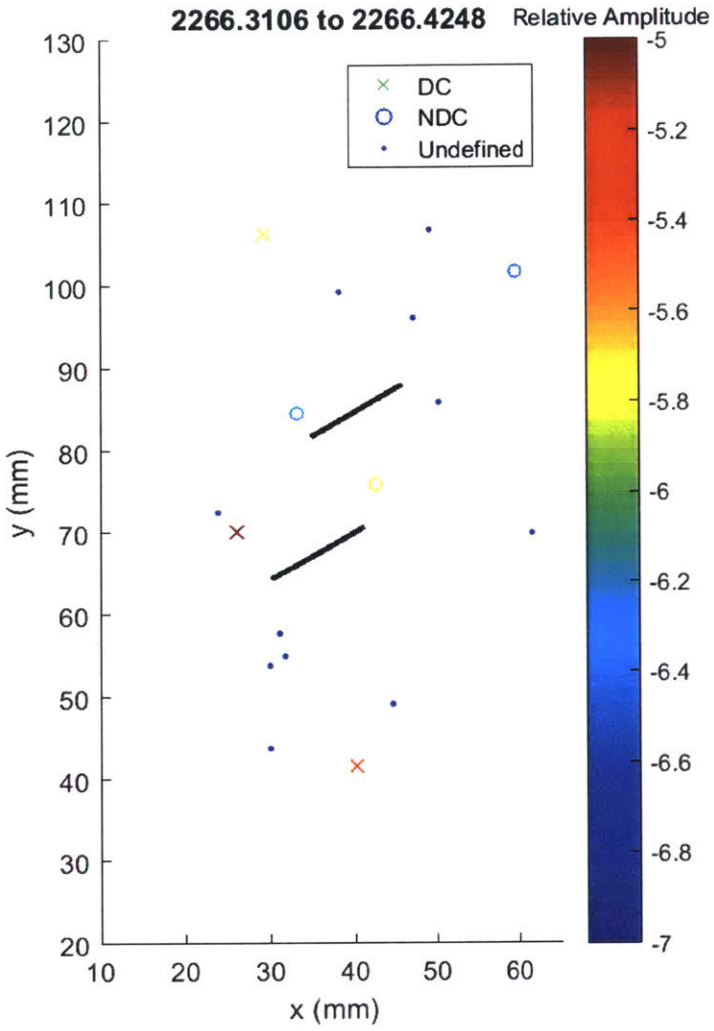

Small to intermediate tensile events occur at right tip of bottom flaw, and left tip of top flaw. A large shear event occurs above the left tip of the bottom flaw.

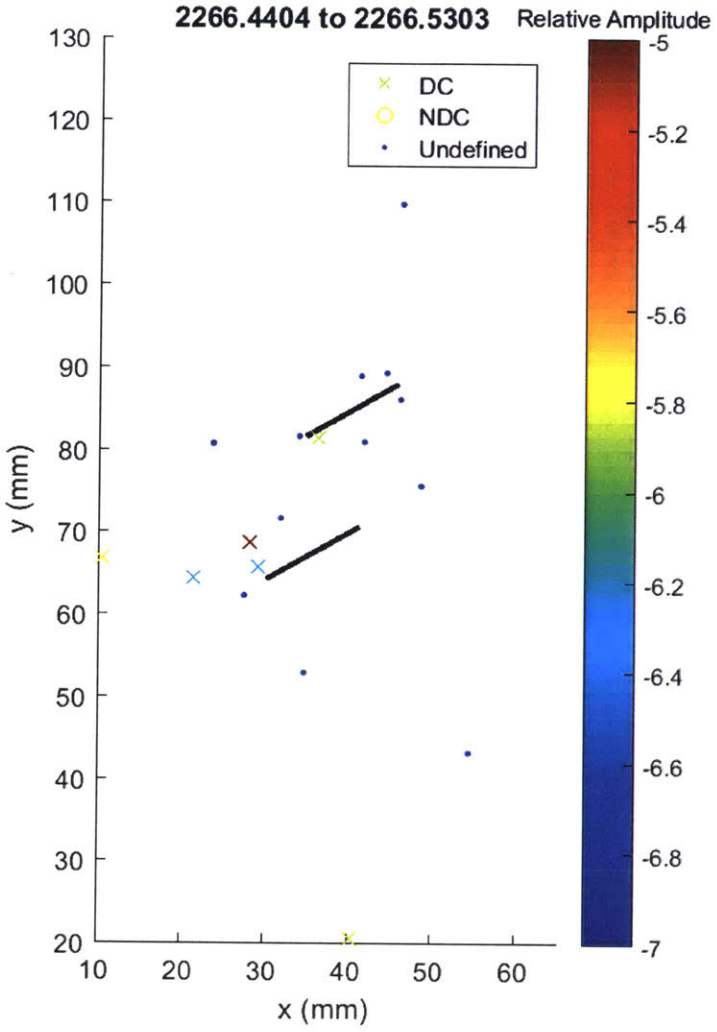

Shear events occur at the left tips of both flaws, and no tensile events are detected. Undefined events concentrated around right tip of top flaw.

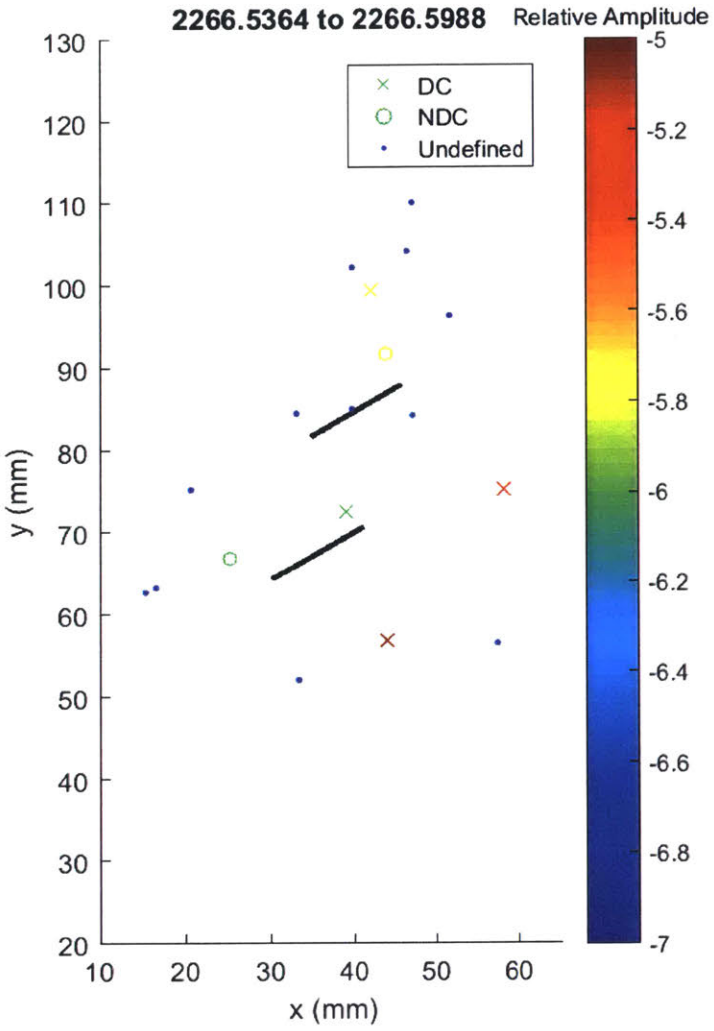

Small to intermediate amplitude tensile and shear events occur near both flaws. 2 large amplitude shear events occur away from the flaw area.

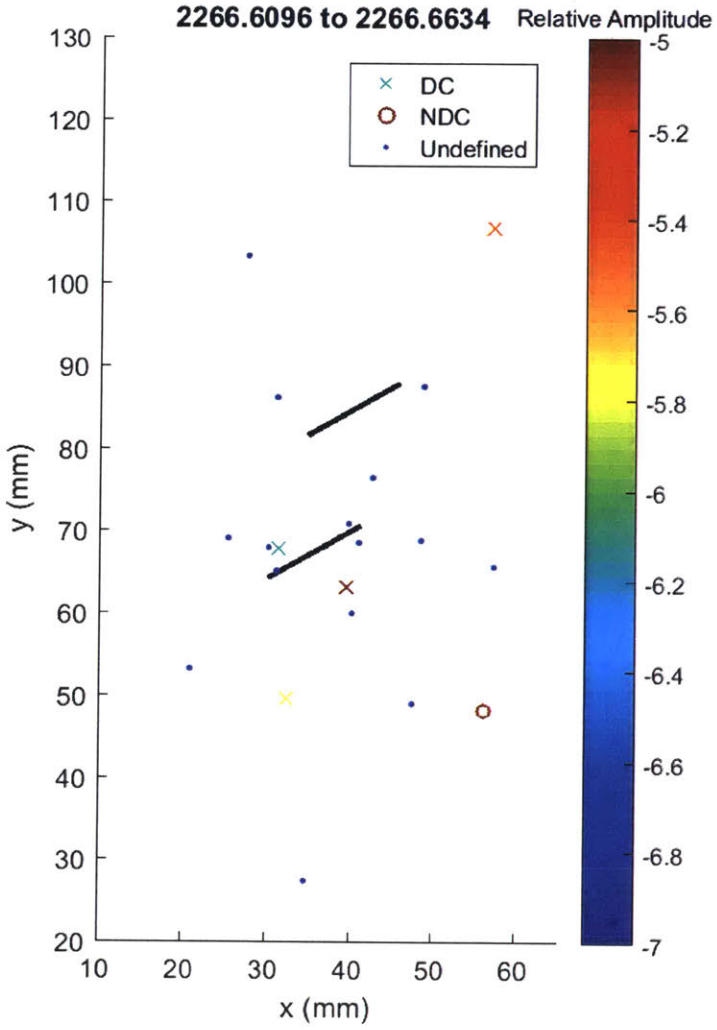

Appears to be some concentration of events around the bottom flaw, but in general locations are quite scattered.

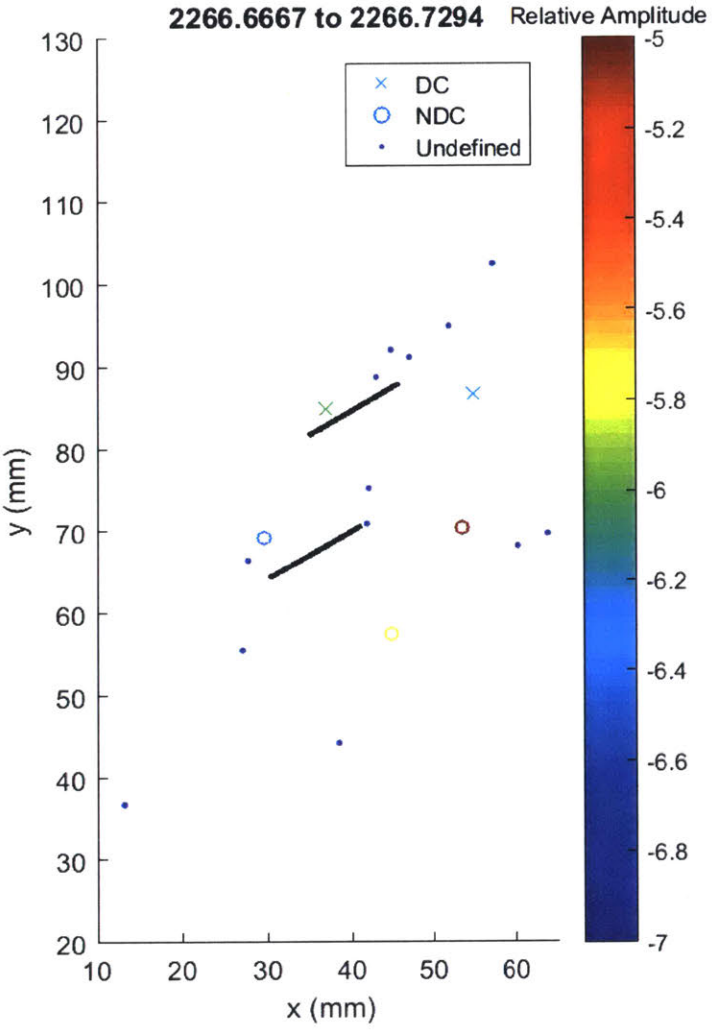

Again see that shear events occur around top flaw, and tensile around bottom. Undefined events appear to track crack D which initiates from the right tip of the top flaw.

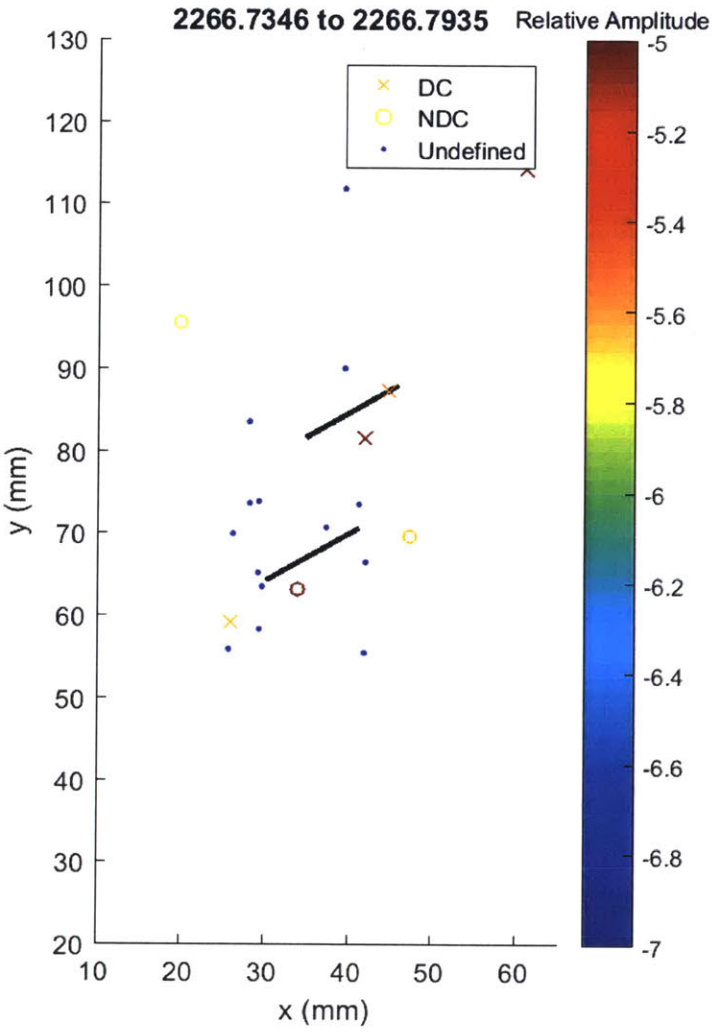

AE locations appear to be more concentrated than previously. 2 large shear events occur below the right tip of the top flaw, and 2 large tensile events occur around the bottom flaw.

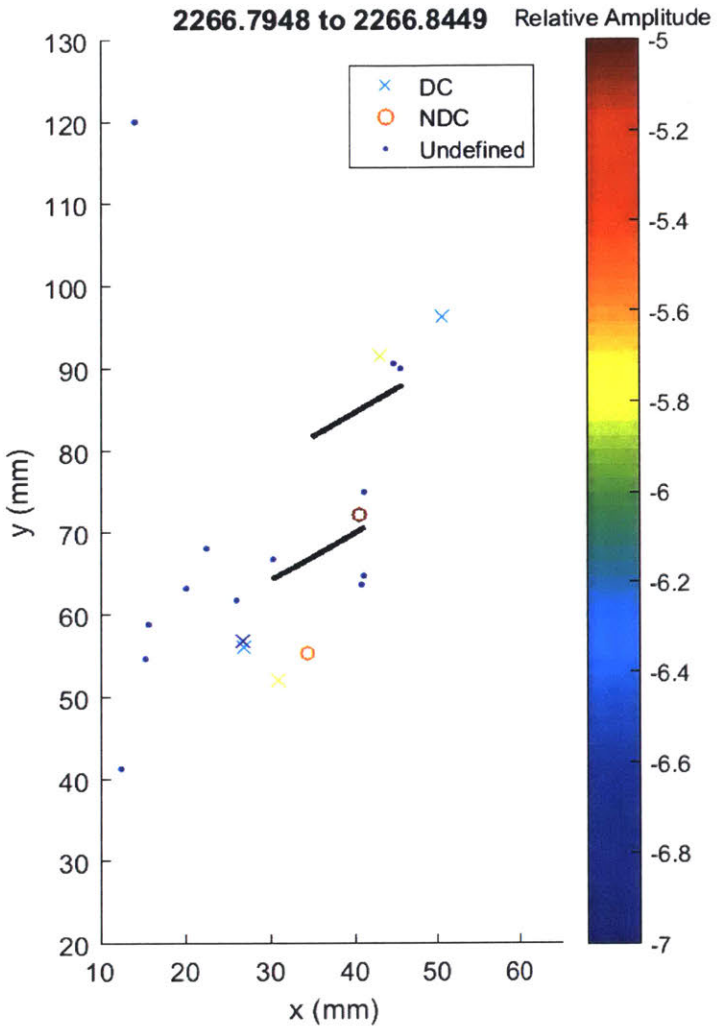

2 small shear events occur around the right tip of the top flaw, and a large tensile event occurs on the right tip of the bottom flaw. 3 intermediate shear and 1 large tensile event occurs below the left tip of the bottom flaw, and undefined events appear to track crack C.

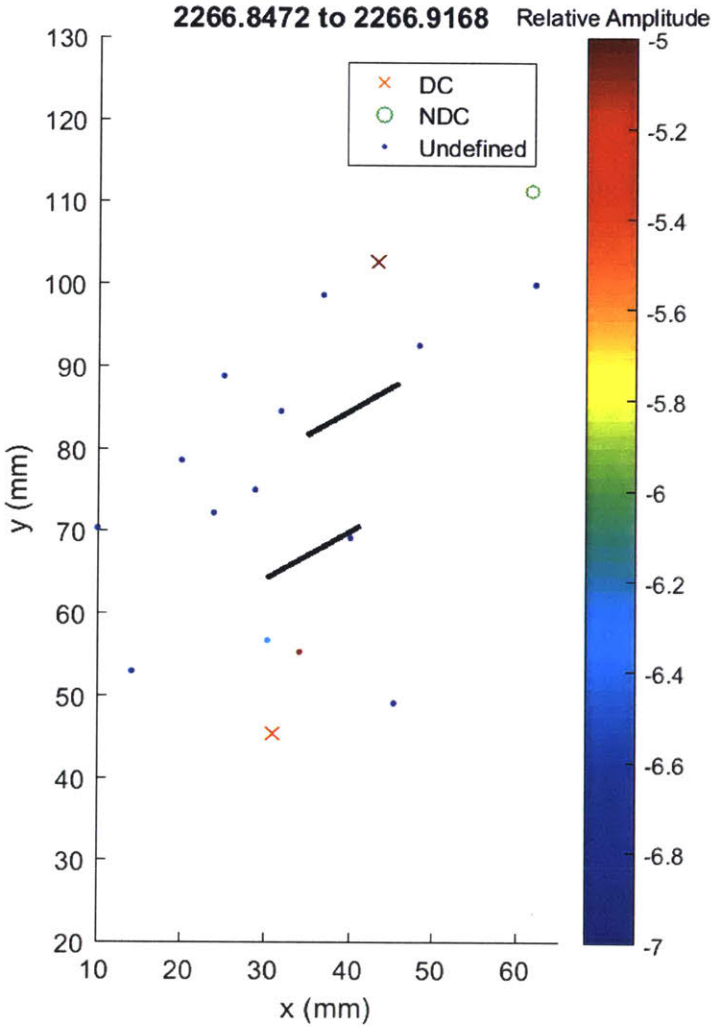

Diffuse locations.

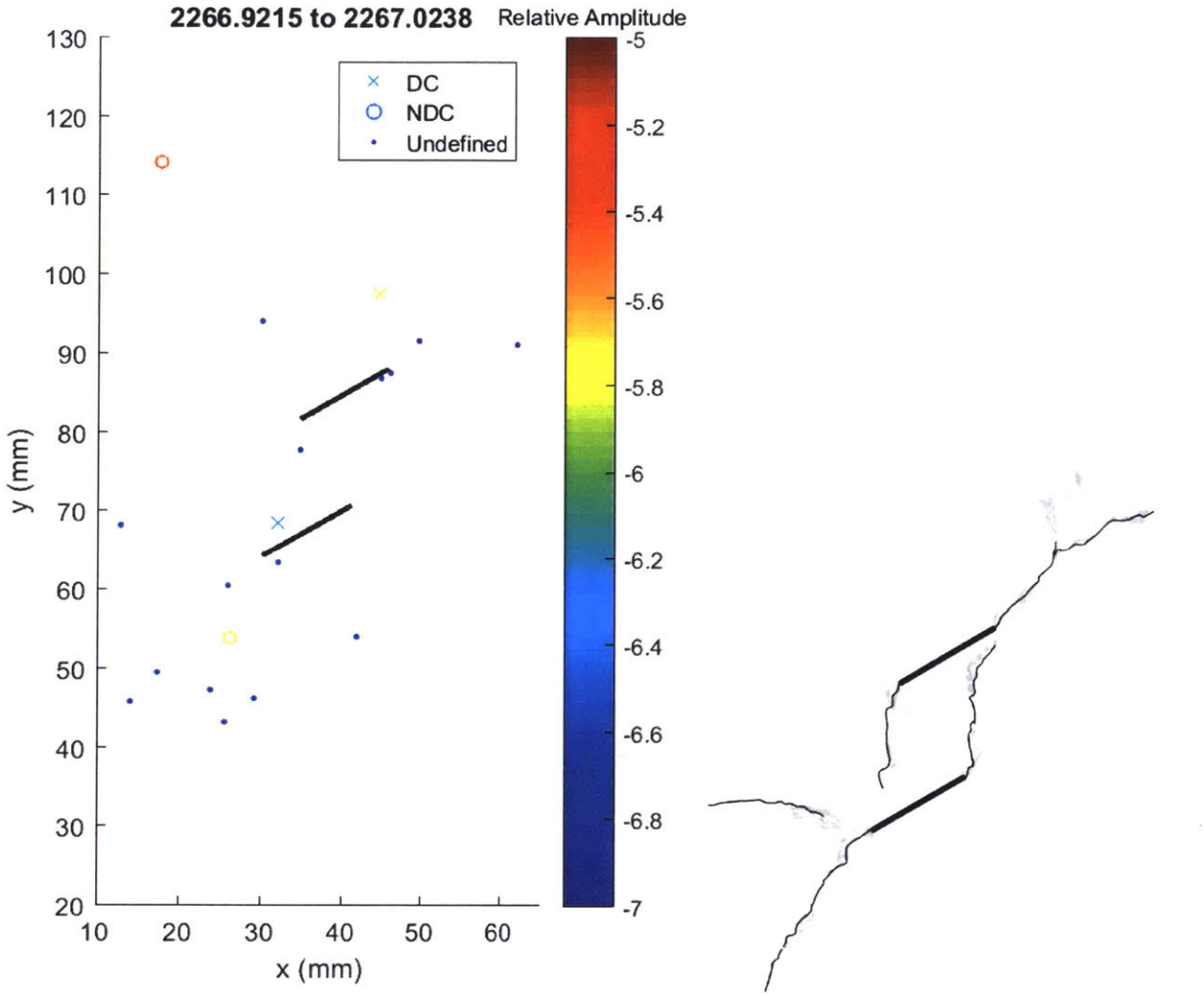

Same as above. Crack initiation and propagation occur around this time.

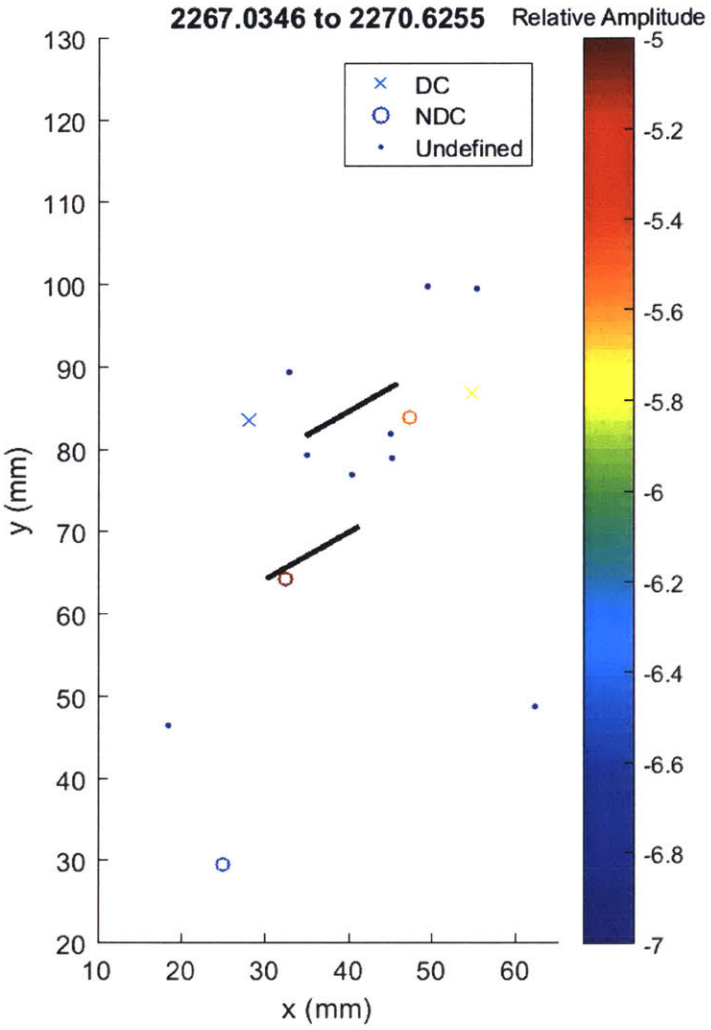

Tensile events occur at left tip of bottom flaw, and right tip of top flaw.

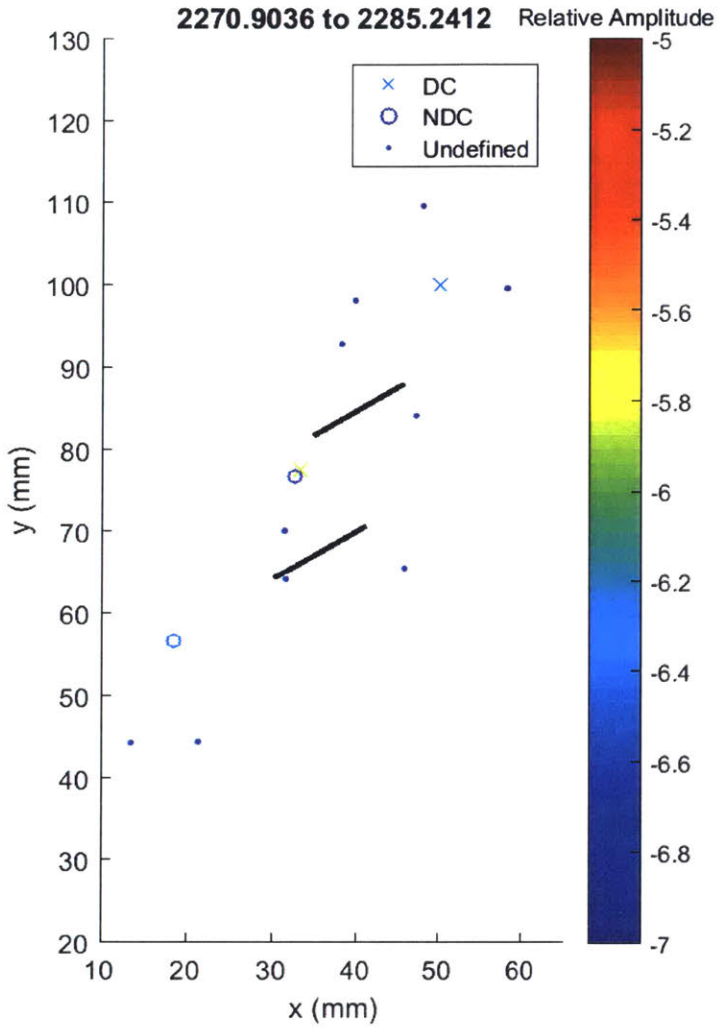

Diffuse events

Summary:

Very few instances of a concentration of events at any location, compared to 2a-30-0 and 2a-30-30 orientations. Locations are generally more scattered. In general, more events occurred around the bottom flaw, and on the right side where crack coalescence occurred. There also seemed to be a trend where more shear events occurred above the top flaw, while tensile events occurred in the bridge and below the bottom flaw.

AE hypocenter analysis for specimen 2a-30-90-VL5-C

Final crack geometry:

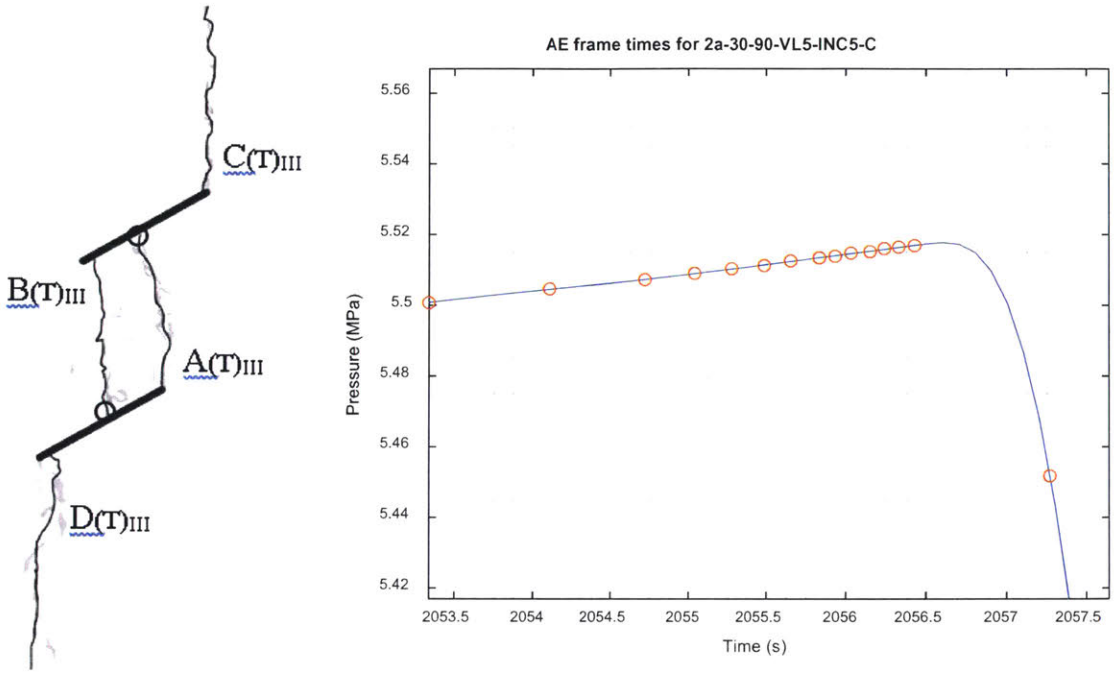

Pattern is largely symmetric. Cracks A and B initiates from the right tip of the bottom and left tip of the top flaws respectively, and coalesce to the middle of the other flaw. Cracks C and D then initiates from the top right and bottom left flaw tips respectively. Peak pressure occurs immediately prior to breakdown.

Development of AE locations are shown over the 20 frames presented in this analysis, where each frame shows 5% of the total number of events recorded during the test. This means that initially the frames will cover a long time period since few AE occurred at the beginning, while towards failure each frame will only cover fractions of a second since AE occur at a rapid rate.

Events with greater than 50% CLVD (compensated linear vector dipole) are considered shear type events and are marked with an 'x', while events with less than 50% CLVD are considered tensile and marked with 'o'. For those events detected by 4 sensors, it is not possible to invert the moment tensor and so these events are marked as undefined with '.'. The colour of an event indicates its relative magnitude, where red is the largest. Black ellipses are used to highlight areas of interest.

Where possible, AE frames are shown next to the appropriate analysis sketch from Bruno. However, these tend to be few in between and as discussed, the high speed frames tend to occur after the end of detectable AE events.

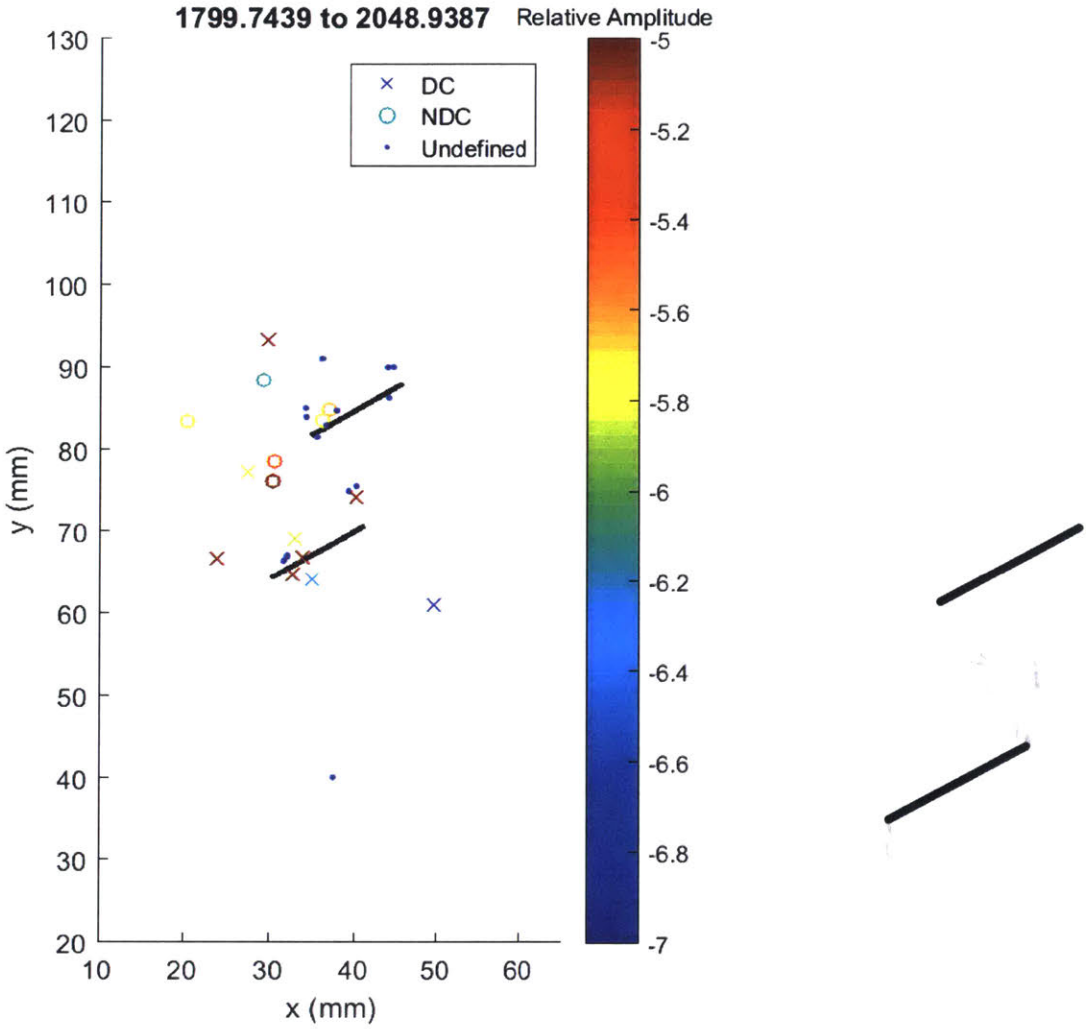

Events occur at all flaw tips, with more shear events occurring around the bottom flaw and more tensile events around the left side of the top flaw. Visual white patching is mostly concentrated above the bottom right flaw tip.

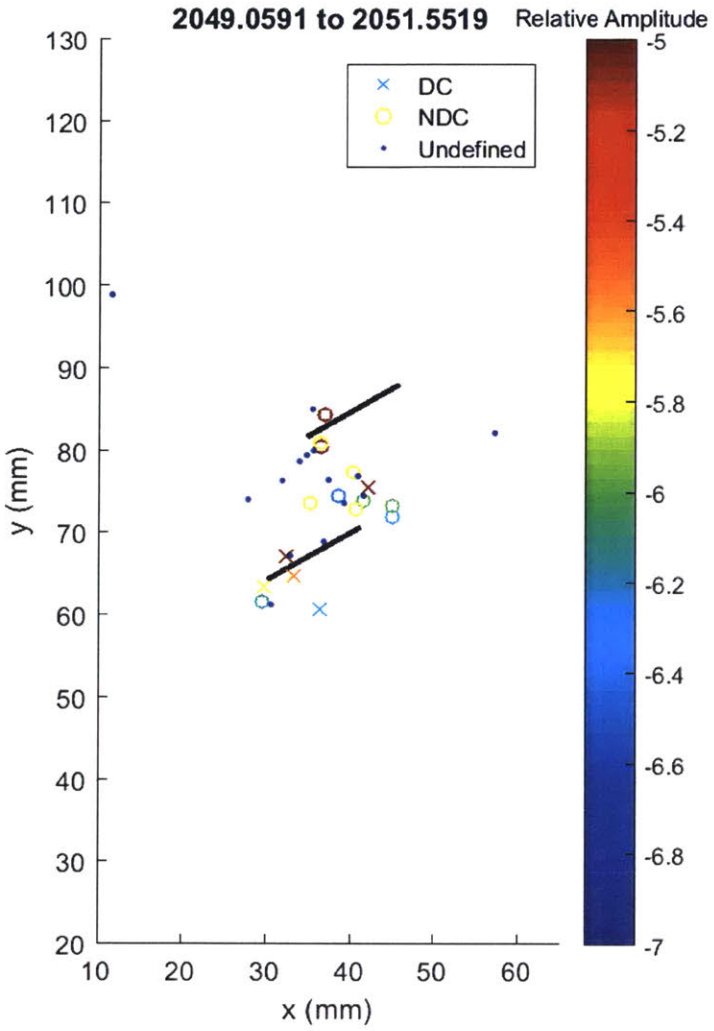

High amplitude shear events occur at both tips of the bottom flaw, and high amplitude tensile events occur at left tip of top flaw. Many low amplitude tensile events occur above the right tip of the bottom flaw.

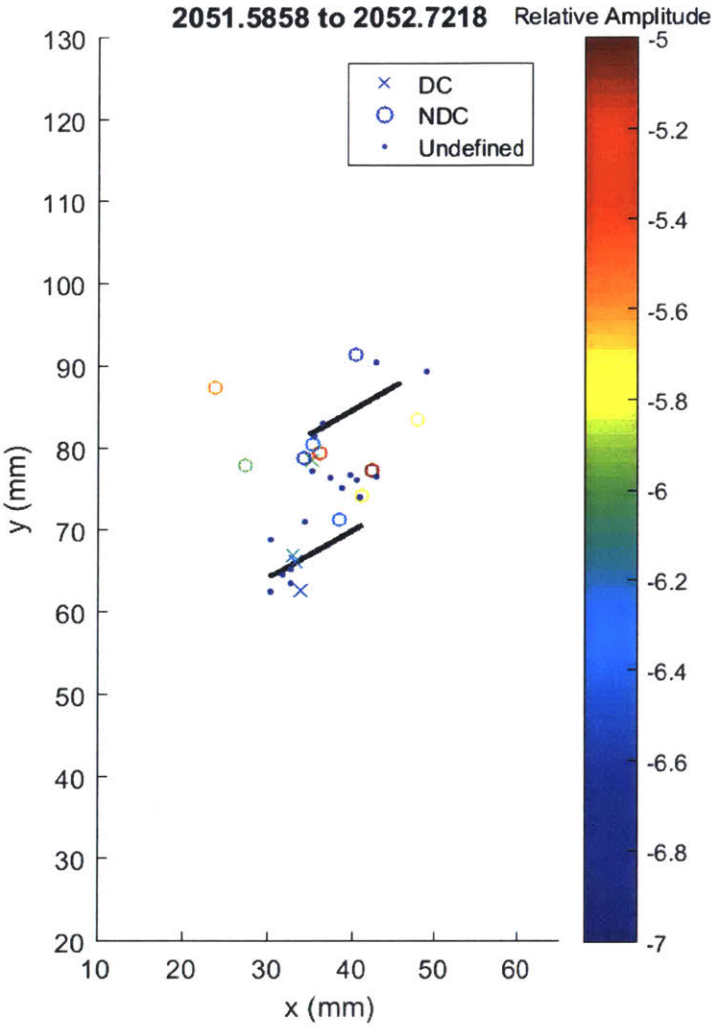

Tensile events occur at left tip of top flaw and right tip of the bottom flaw. Shear events occur at the left tip of the bottom flaw.

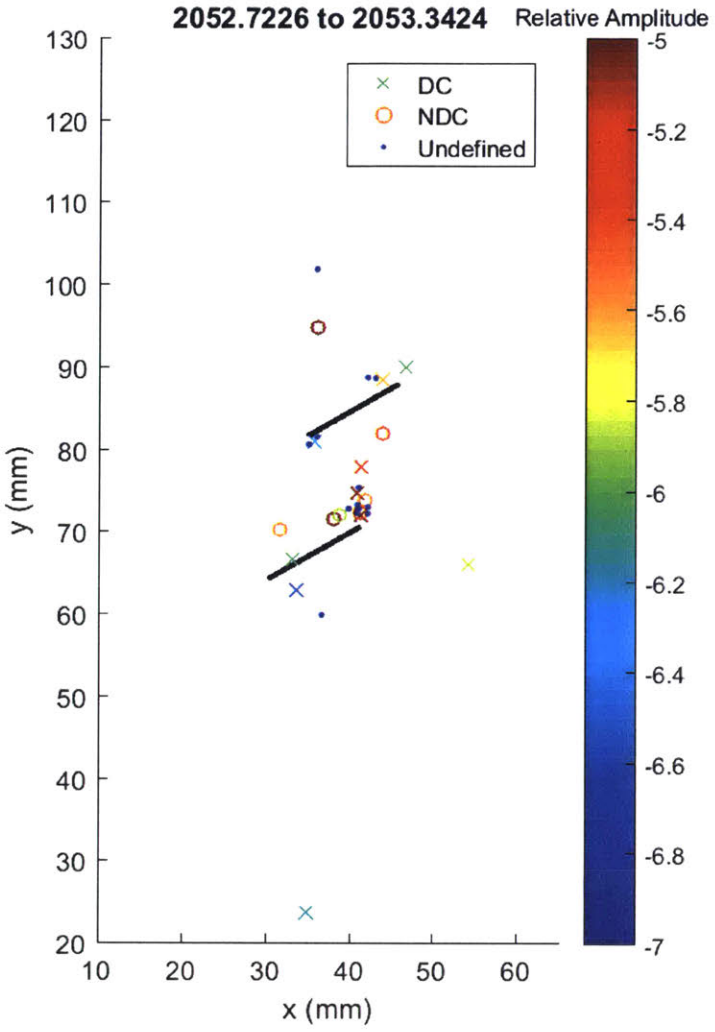

Many high amplitude shear and tensile events occur at the right tip of the bottom flaw, and a few shear events occur at the other flaw tips.

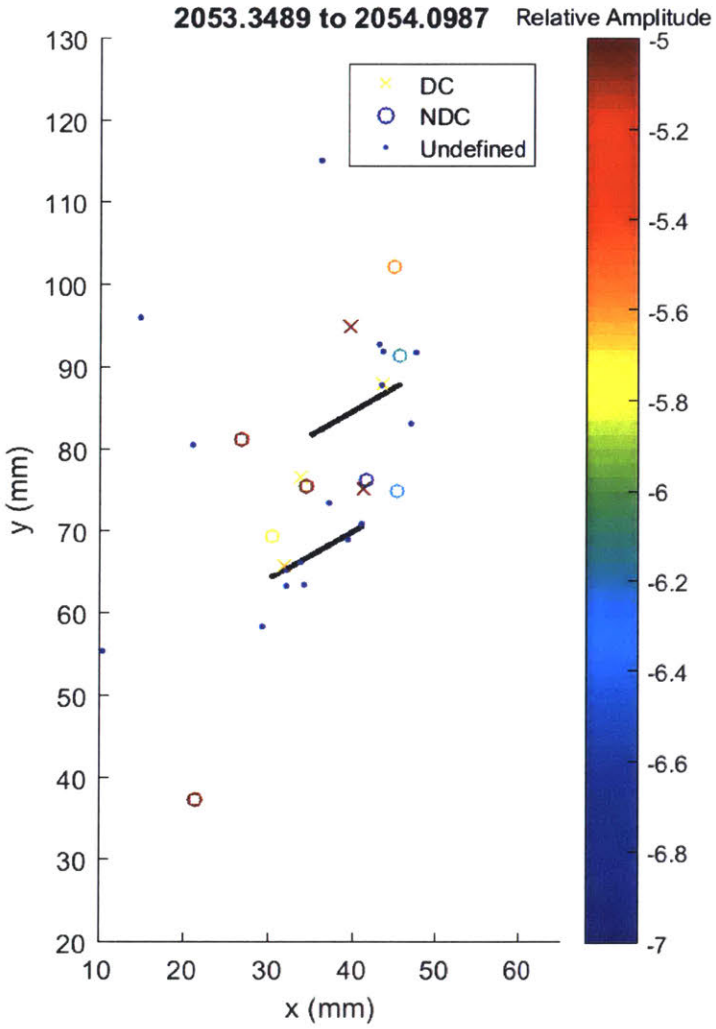

Tensile and shear events occur in the coalescence zone and above the right tip of the top flaw.

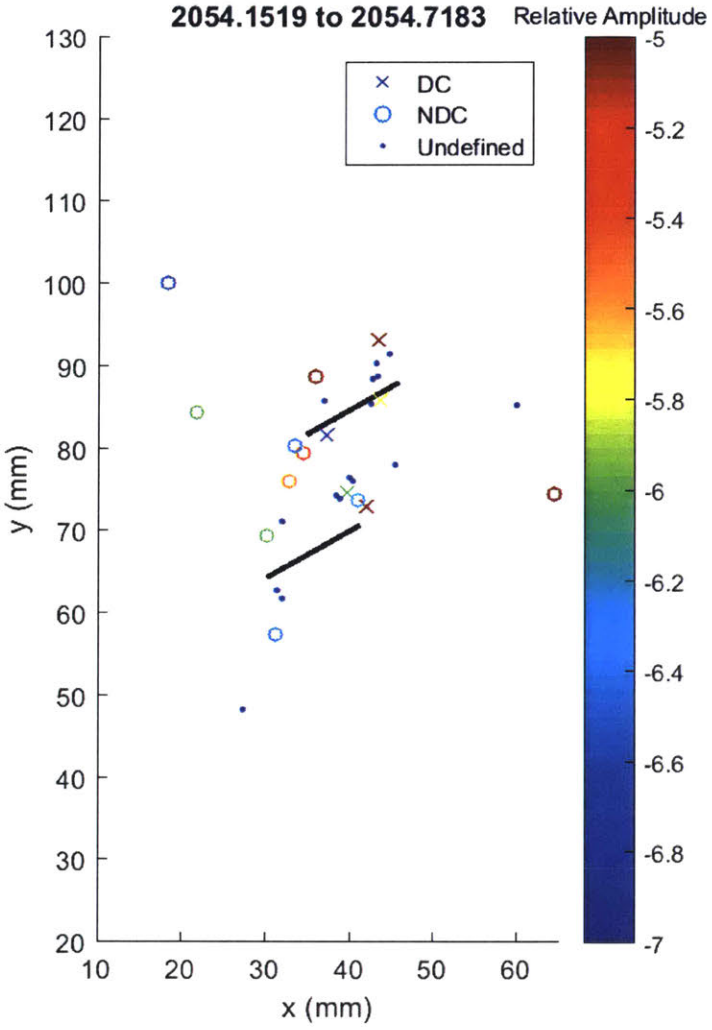

Linear pattern of tensile events occur between the left tips of the top and bottom flaw. High amplitude shear events also occur above the right tips of both flaws.

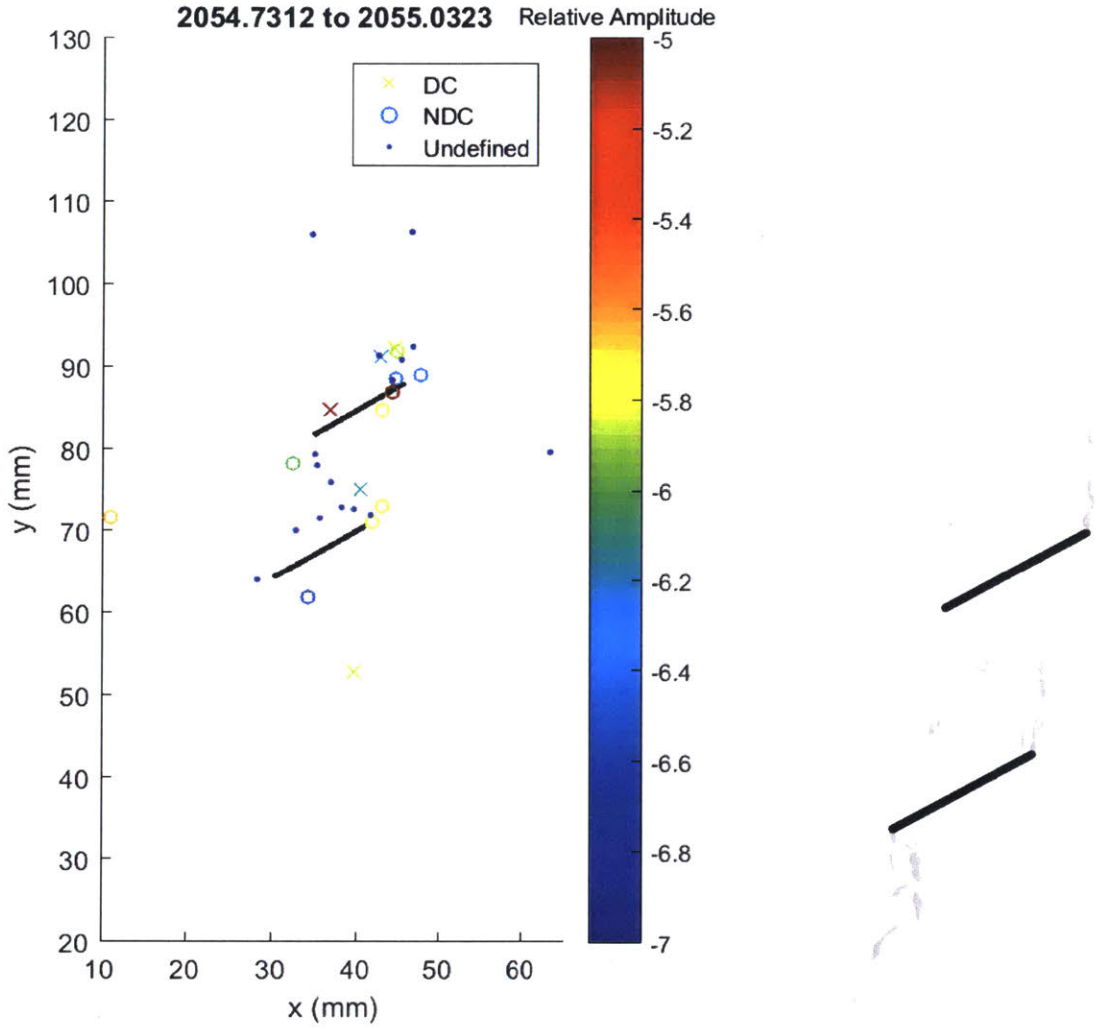

Concentration of tensile events at the right tip of the top flaw, and a lesser concentration on the right tip of the bottom flaw. Small amplitude undefined events occur in a linear pattern between the left tip of the top flaw and the right tip of the bottom flaw. Visual white patching mostly occurs on the bottom left and top right flaw tips,

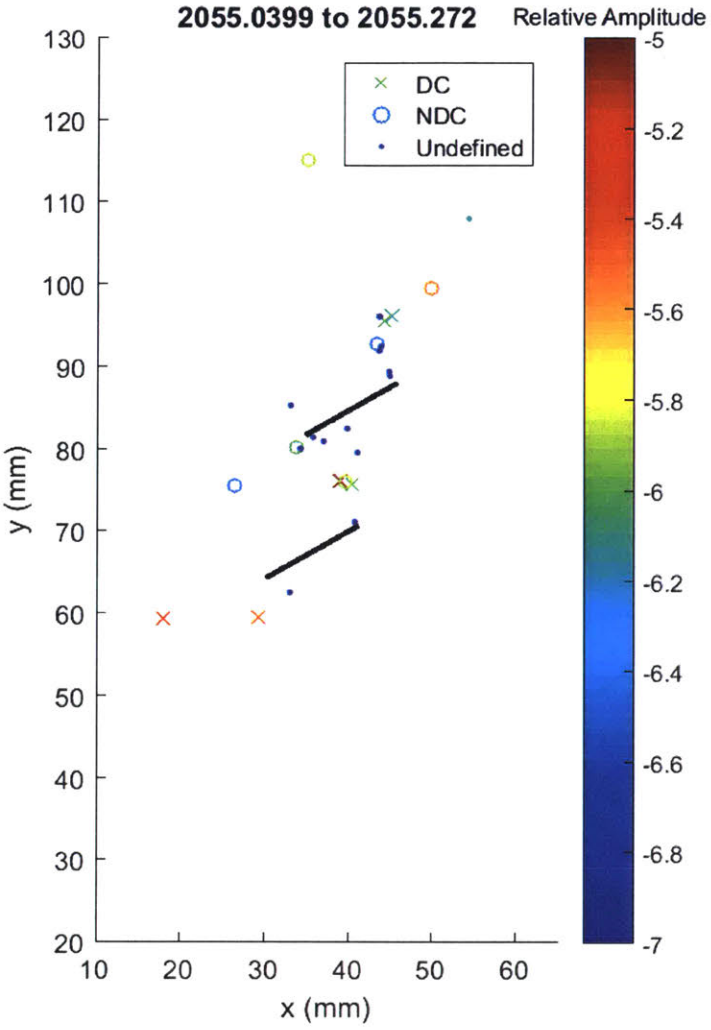

More shear events around the bottom flaw, more tensile towards the top but generally diffuse event locations.

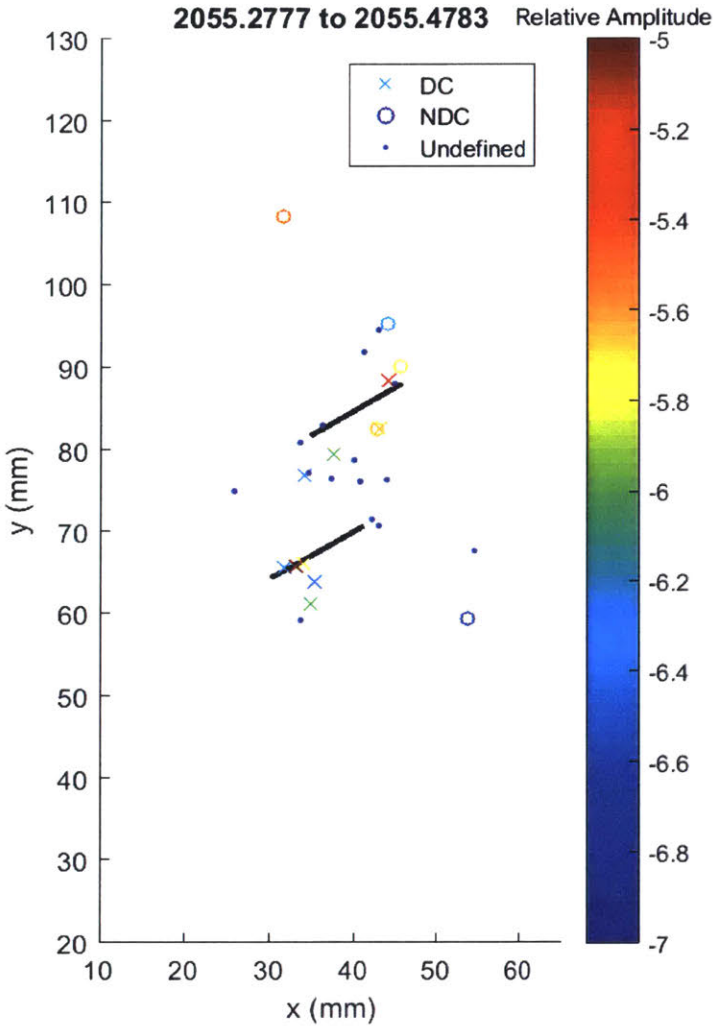

Cluster of shear events below the left tip of the bottom flaw, and along the bottom of the top flaw. A few tensile events occur near the right tip of the top flaw. Undefined events generally occur in coalescence zone.

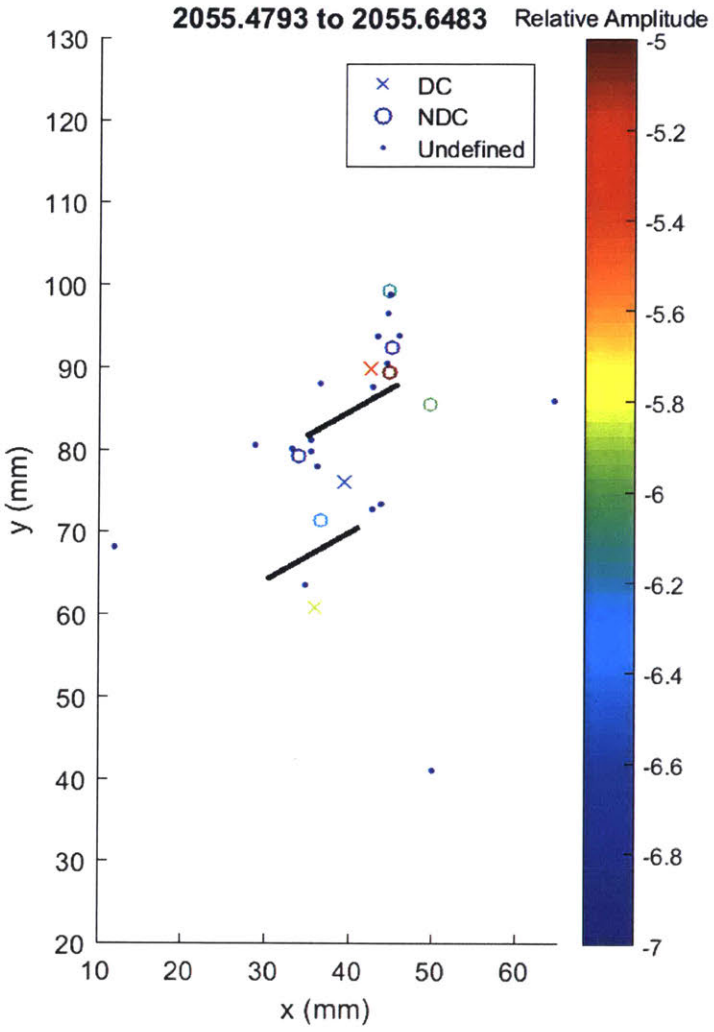

AE events generally occur on the line connecting the left tip of top flaw with right tip of bottom flaw, and above the right tip of the top flaw.

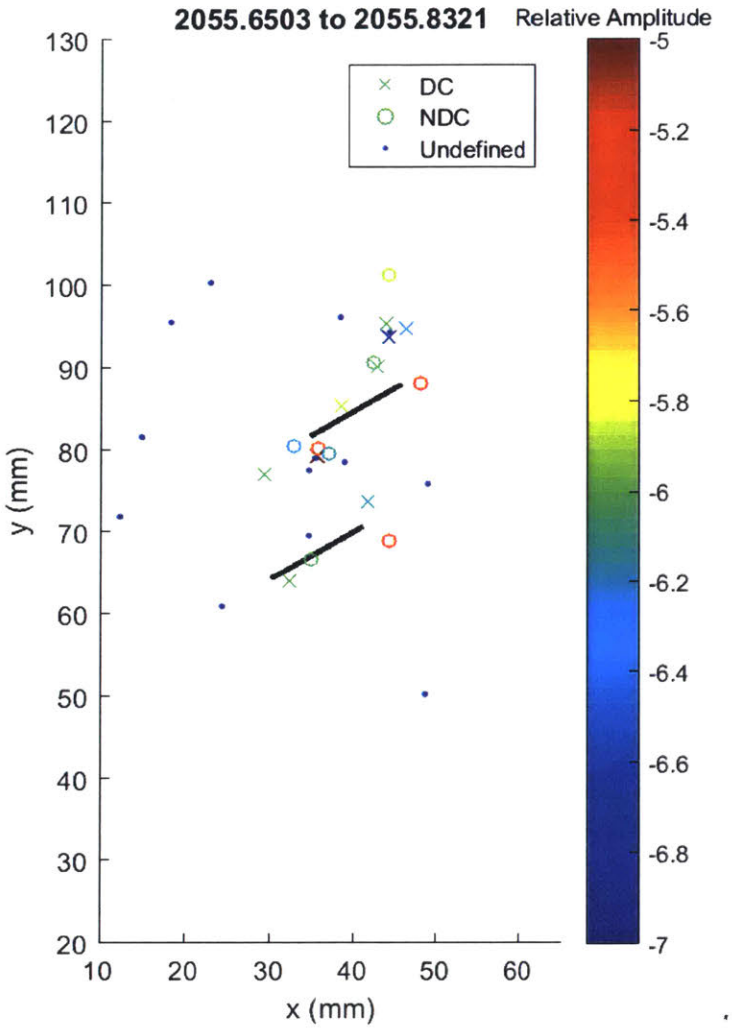

Large tensile event occurs at 3 out of 4 of the flaw tips. Continued concentration of small shear and tensile events above the right tip of the top flaw.

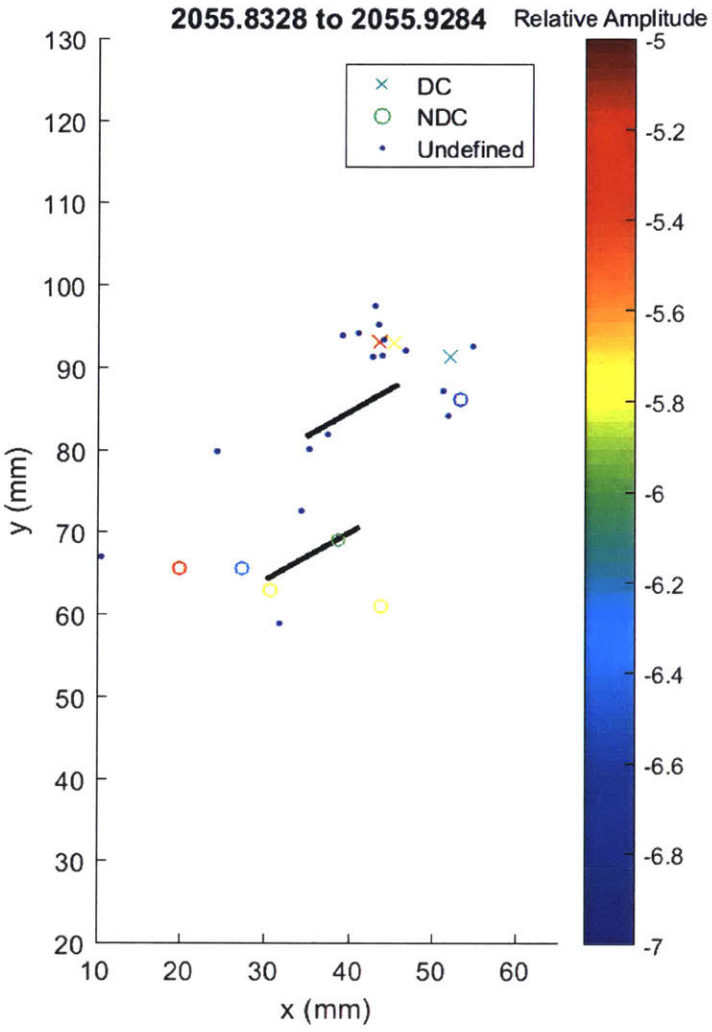

Tensile events occur around the bottom flaw, and undefined events continue to cluster above the right tip of the top flaw.

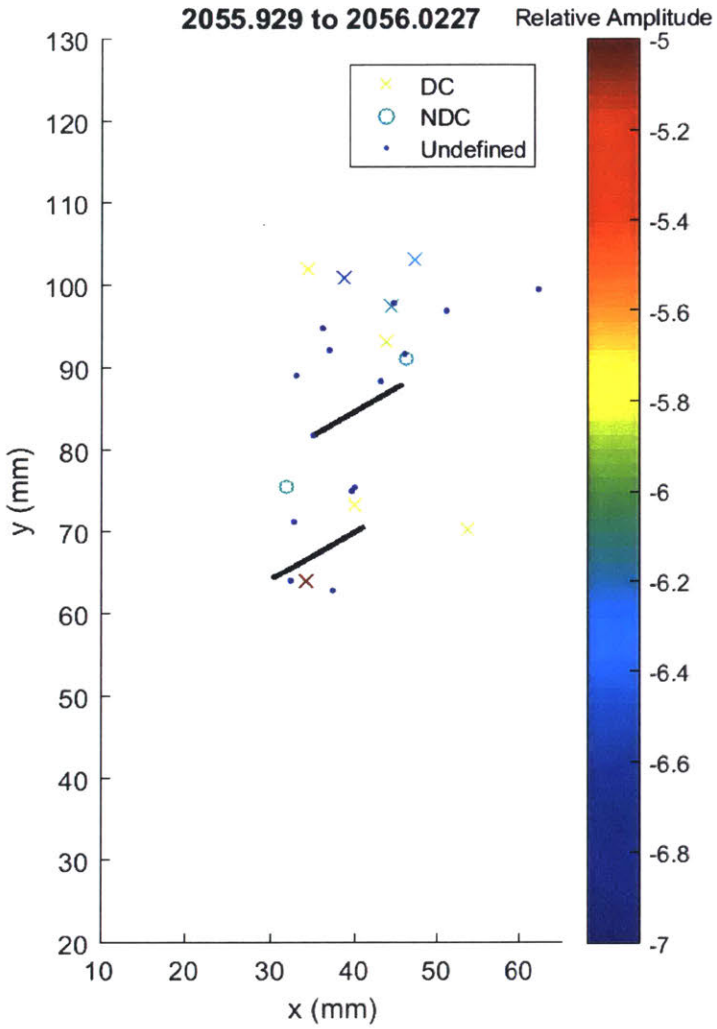

Diffuse events occur above the top flaw.

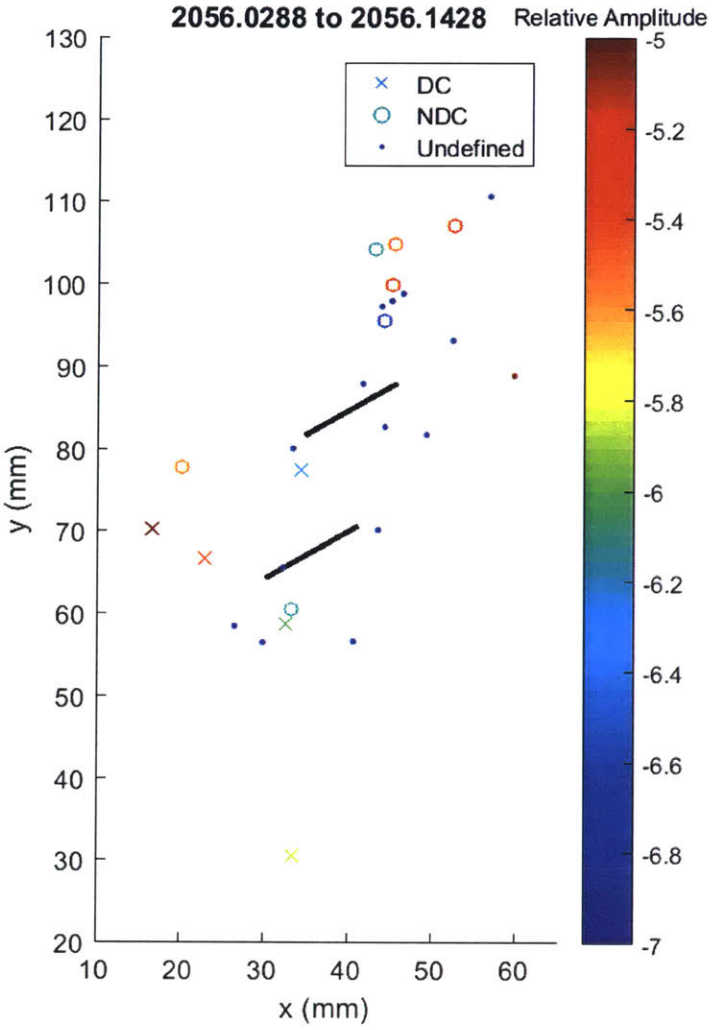

Cloud of tensile events above the right tip of the top flaw continues to move upwards

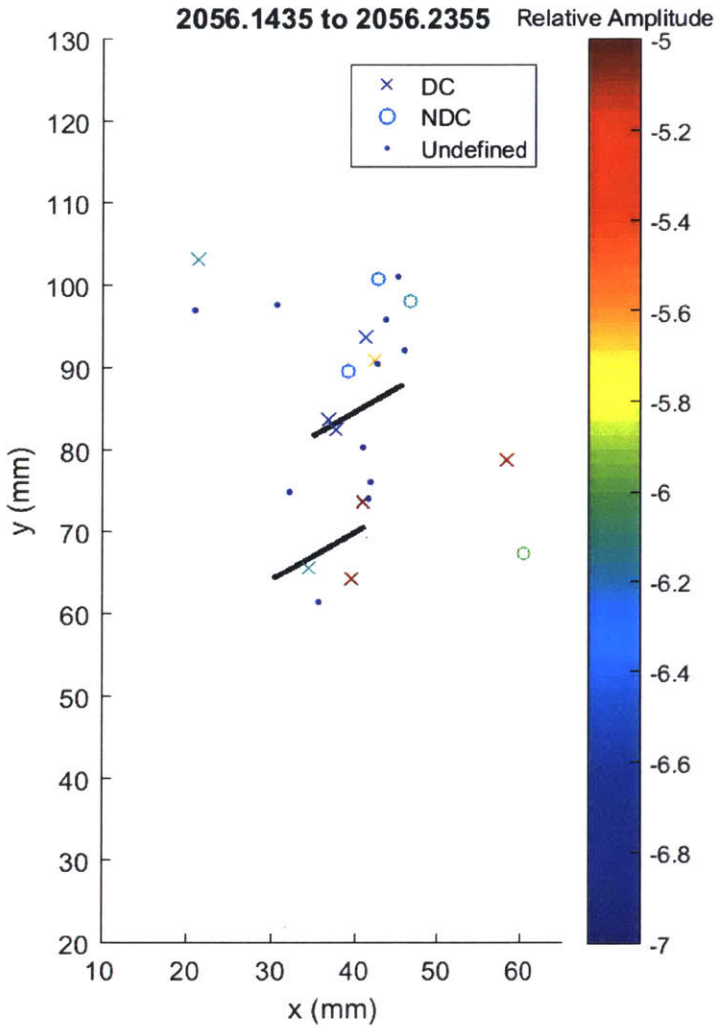

Shear events occur around the right tip of the bottom flaw, while tensile and shear events occur above the top flaw.

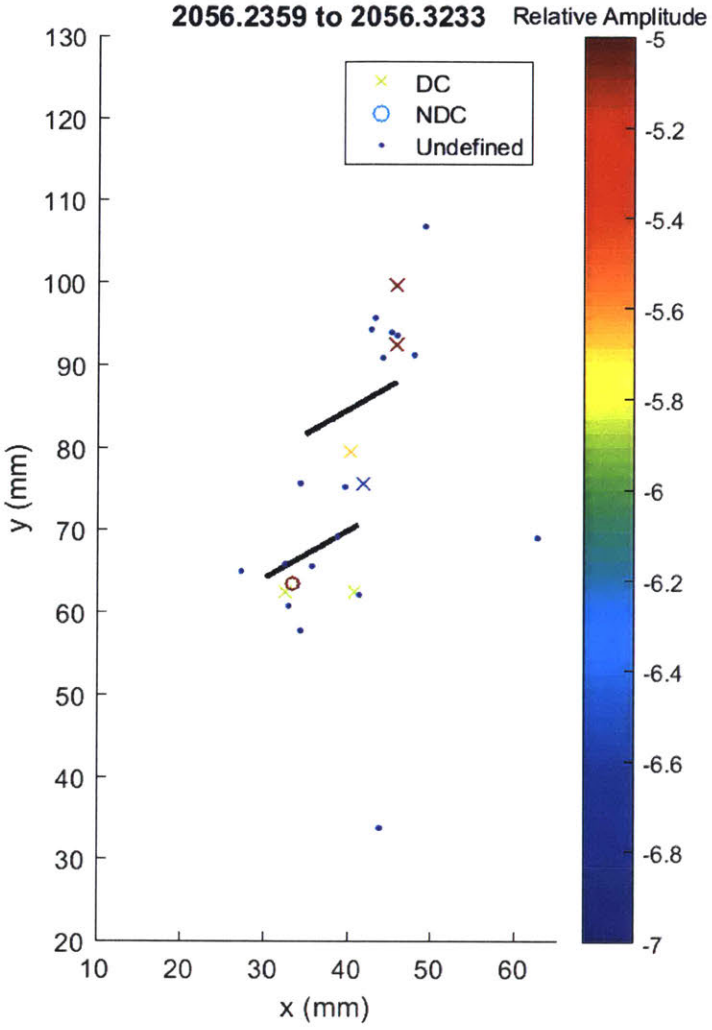

Shear events occur above the right tips of both flaws, while a large tensile event occurs at the left tip of the bottom flaw.

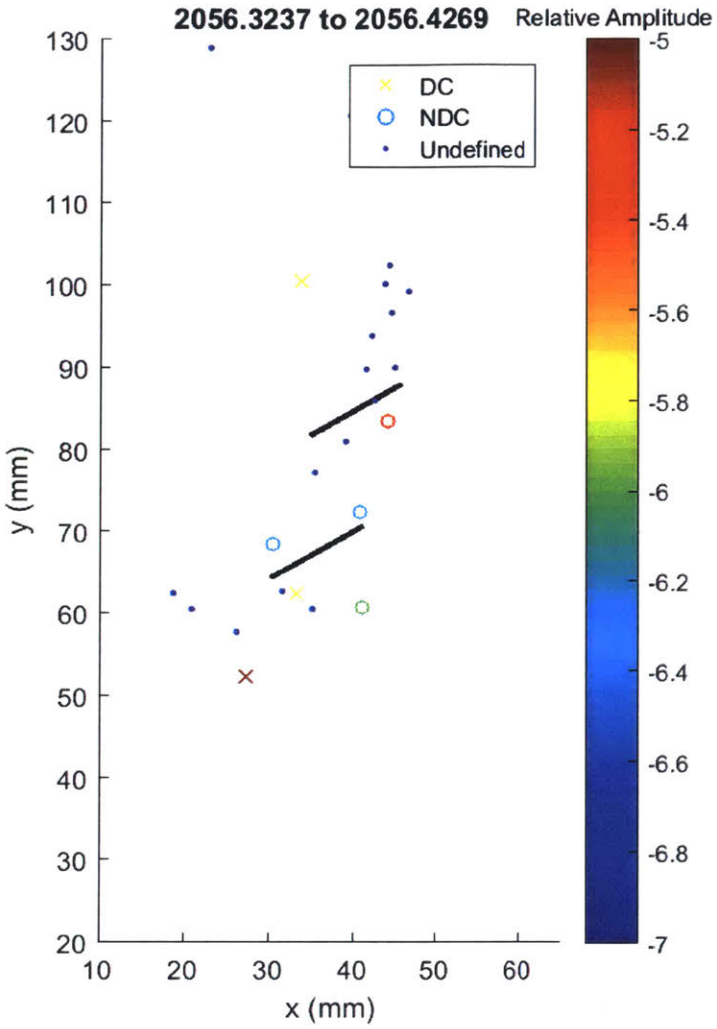

Tensile event occurs around 3 of 4 flaw tips, and cloud of undefined events occurs above right tip of top flaw.

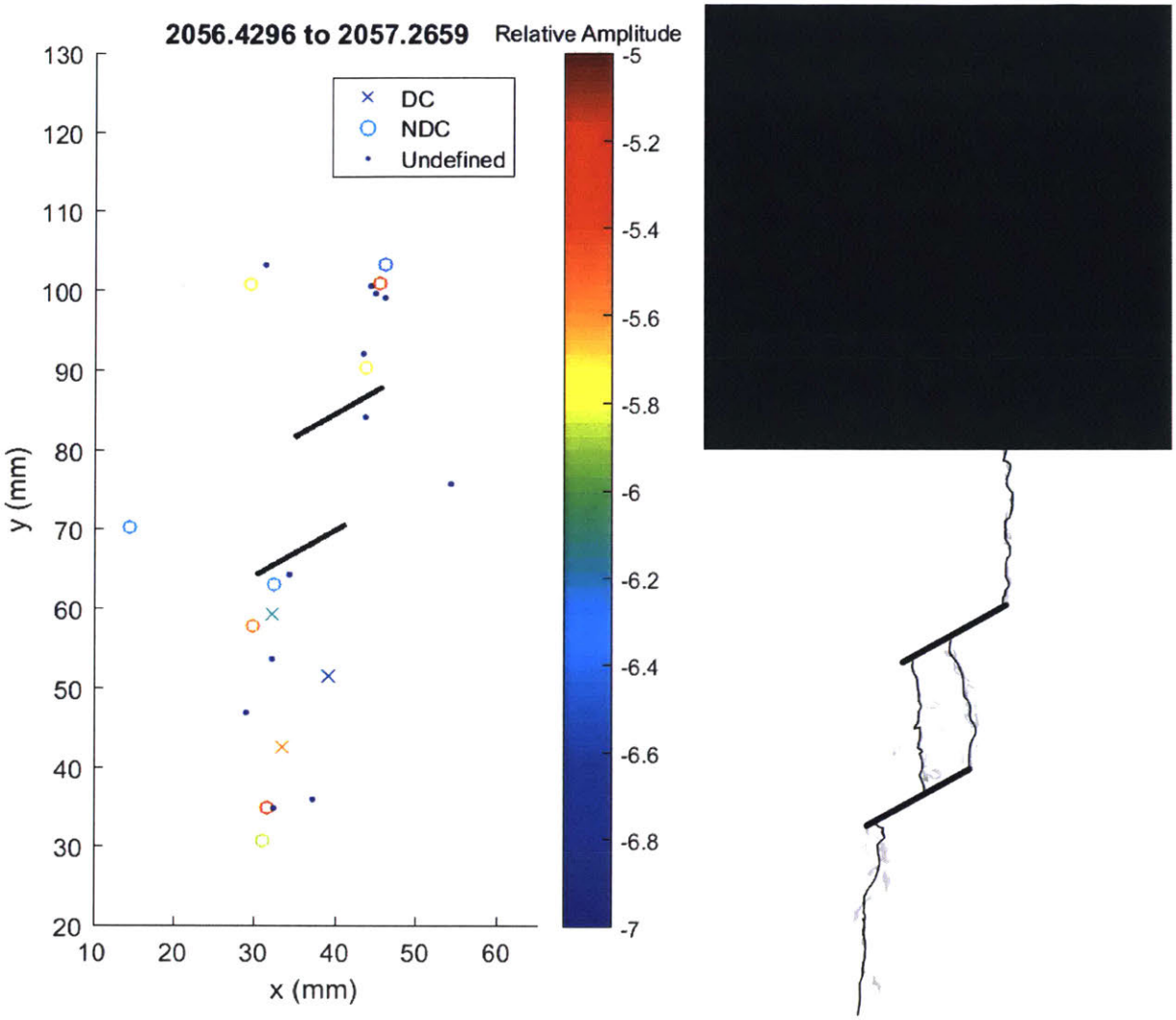

Key frame. Zone above right tip of top flaw continues to see tensile events, while significant AE activity occurs along visually identified crack D, containing shear and tensile events. Visual crack initiation occurs around this time.

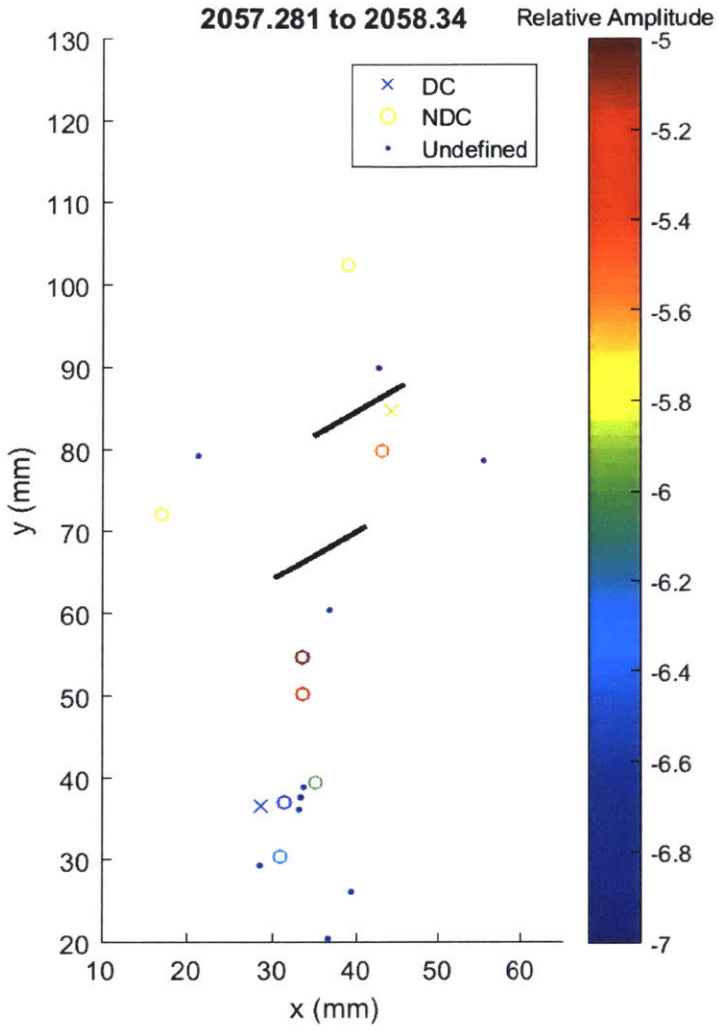

AE activity continues below left tip of bottom flaw. 2 tensile events 1.5cm below the tip suggest the process zone moves downwards.

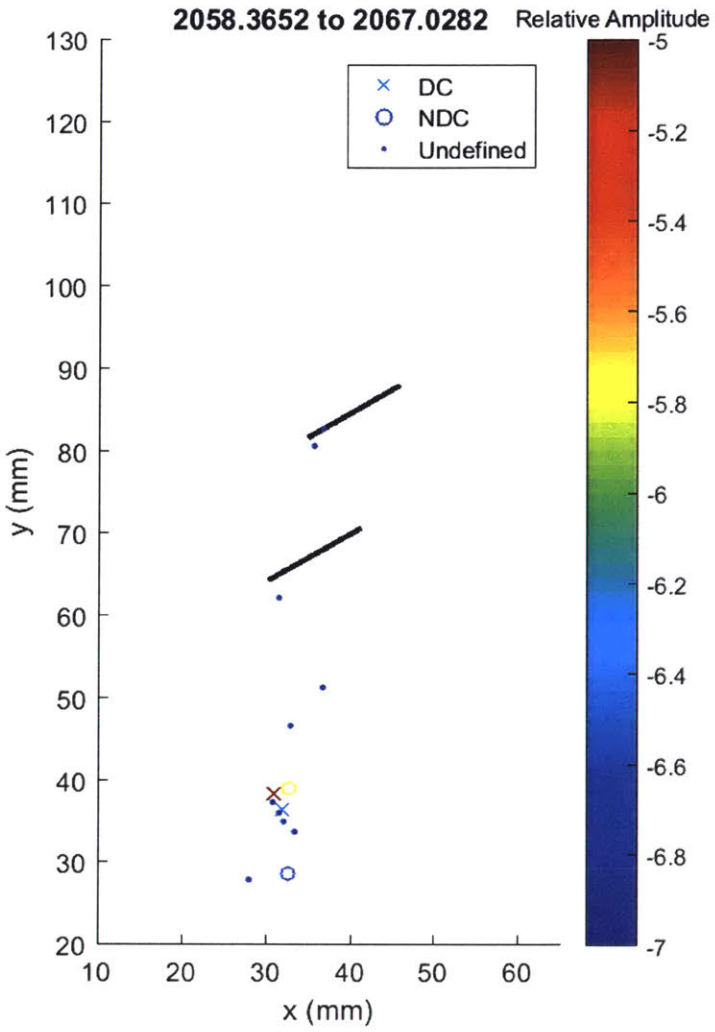

Process zone continues to move away from the flaw tip.

Summary:

This specimen appears to have a significant number of tensile events compared to previously analysed VL5 specimens. Again during the earlier phases we see more shear events on the bottom flaw, and tensile on the top flaw. The patterns made by AE hypocenter locations suggest there is significant damage along a line between the left flaw tips, as well as between the top left flaw tip and the bottom right flaw tip, even though cracks A and B turned out as they did. In general, the AE locations were more concentrated above the top right flaw tip and below the bottom left flaw tip, as opposed to the coalescence zone where events were generally more diffuse and less patterned in time.

AE hypocenter analysis for specimen 2a-30-120-VL0-B

Final crack geometry:

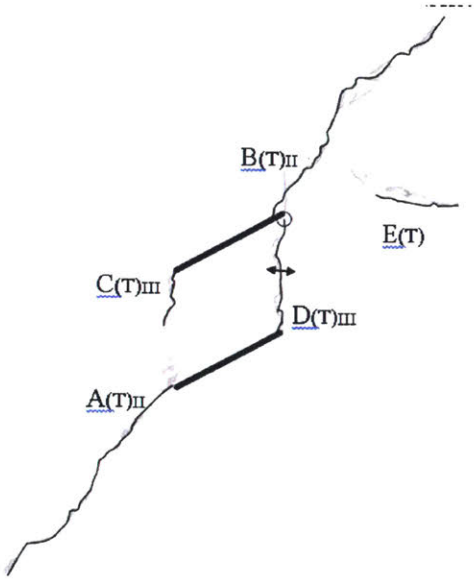

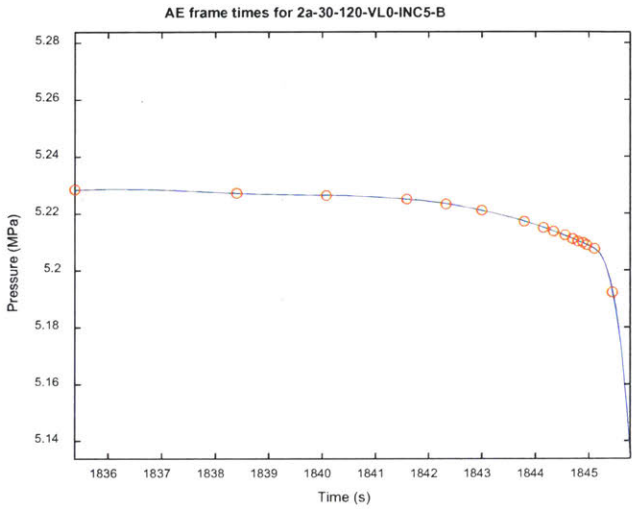

Crack initiates from bottom left flaw tip, then from the top right flaw tip. Crack C then initiates from the top left flaw tip, but does not coalesce while crack D initiates from the bottom right flaw tip and coalesces to the top right flaw tip. Water pressure decreases from the first AE frame, and drops faster starting around 1841.5 s.

Development of AE locations are shown over the 20 frames presented in this analysis, where each frame shows 5% of the total number of events recorded during the test. This means that initially the frames will cover a long time period since few AE occurred at the beginning, while towards failure each frame will only cover fractions of a second since AE occur at a rapid rate.

Events with greater than 50% CLVD (compensated linear vector dipole) are considered shear type events and are marked with an 'x', while events with less than 50% CLVD are considered tensile and marked with 'o'. For those events detected by 4 sensors, it is not possible to invert the moment tensor and so these events are marked as undefined with '.'. The colour of an event indicates its relative magnitude, where red is the largest. Black ellipses are used to highlight areas of interest.

Where possible, AE frames are shown next to the appropriate analysis sketch from Bruno. However, these tend to be few in between and as discussed, the high speed frames tend to occur after the end of detectable AE events.

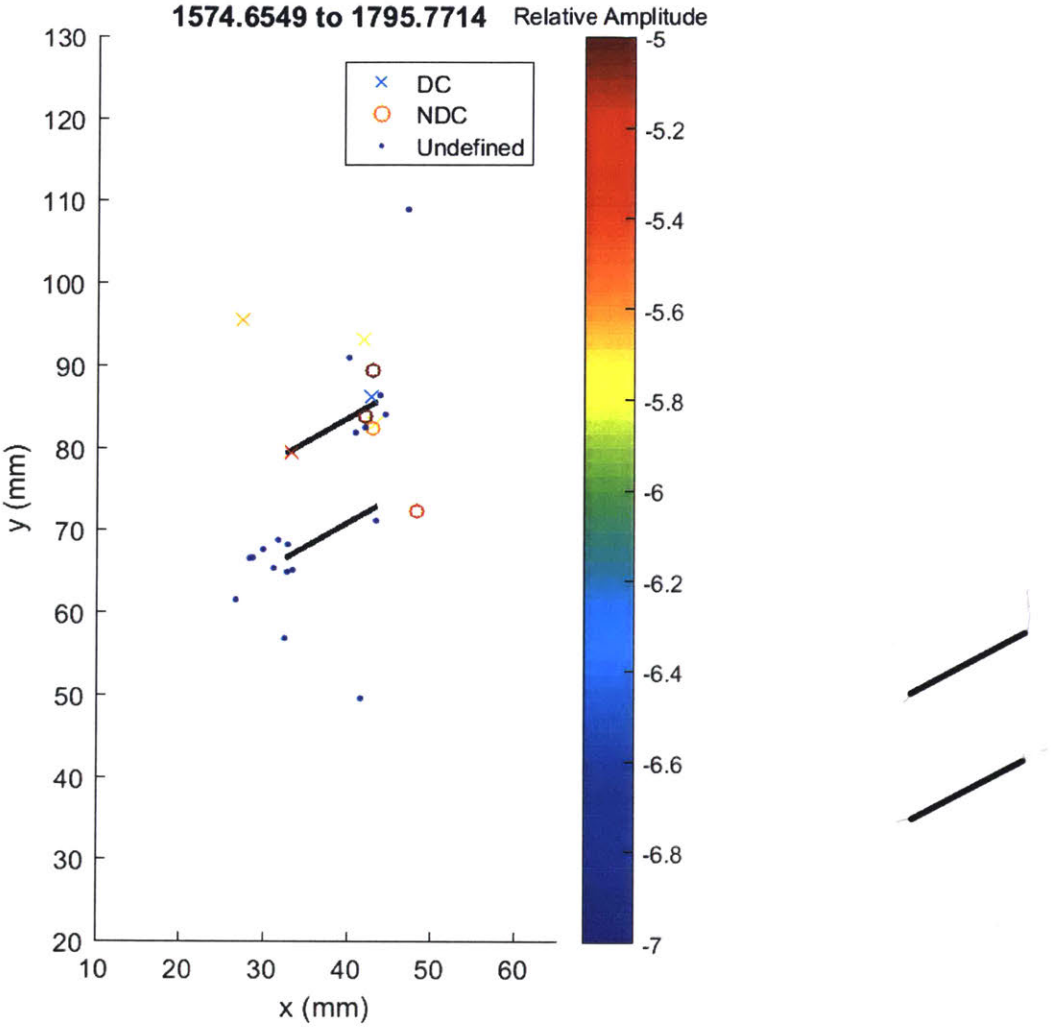

Concentration of tensile events at top right flaw tip, and small undefined events at bottom left flaw tip. Some white patching at all tips, most notably at the top right flaw tip.

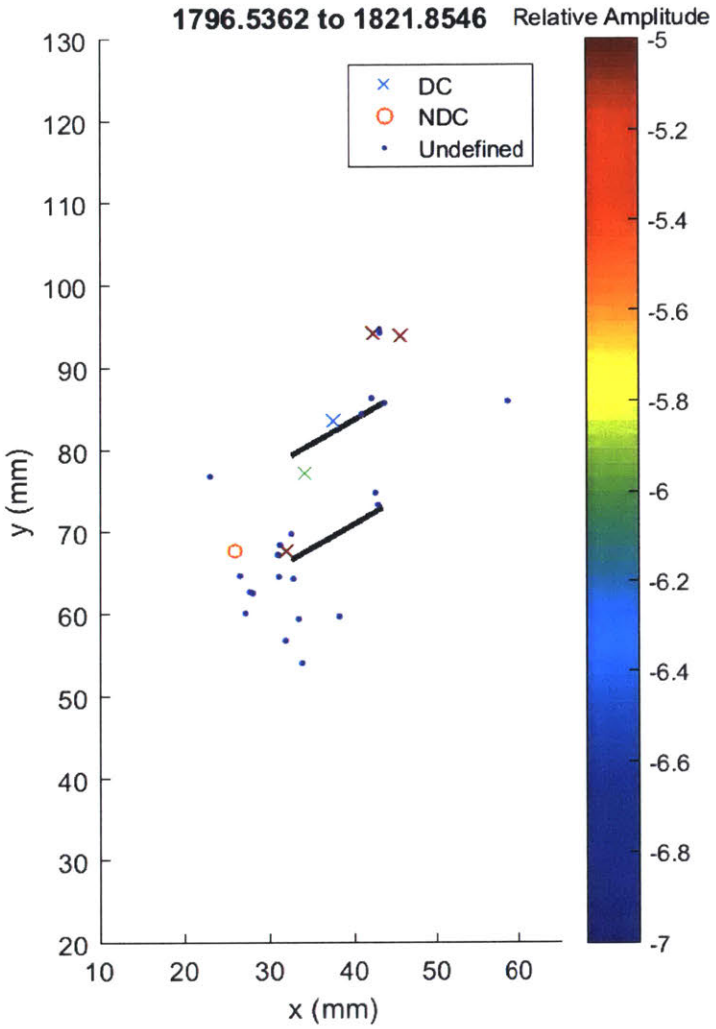

Small undefined events continue to cluster below bottom left flaw tip, while 2 large shear events occur above the top right flaw tip.

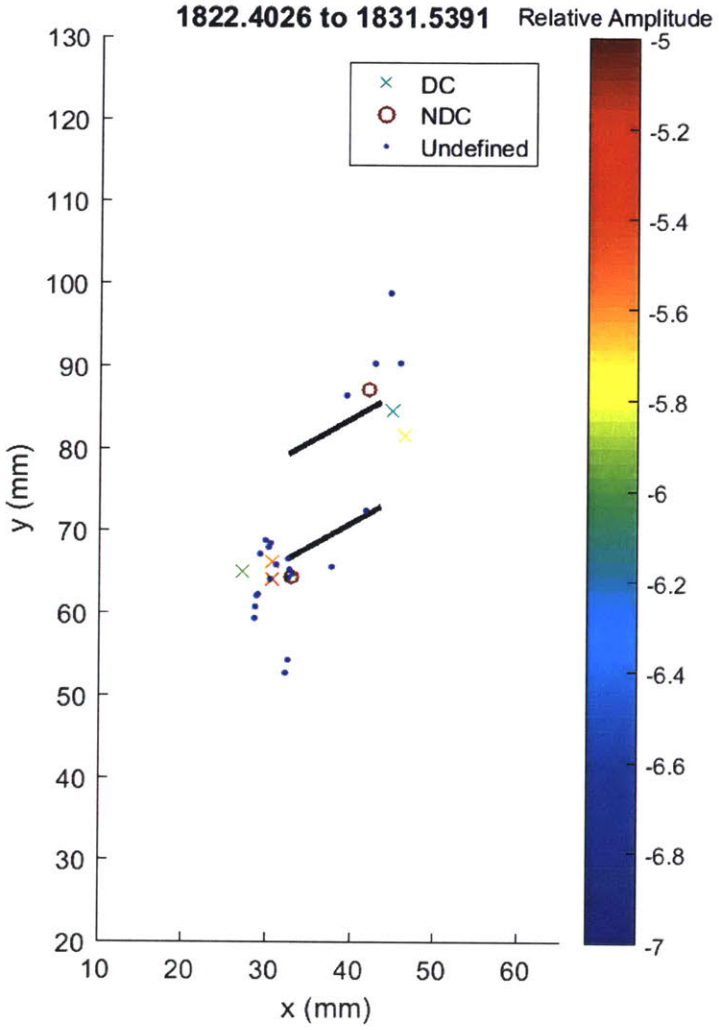

Shear and tensile events occur at bottom left and top right flaw tips.

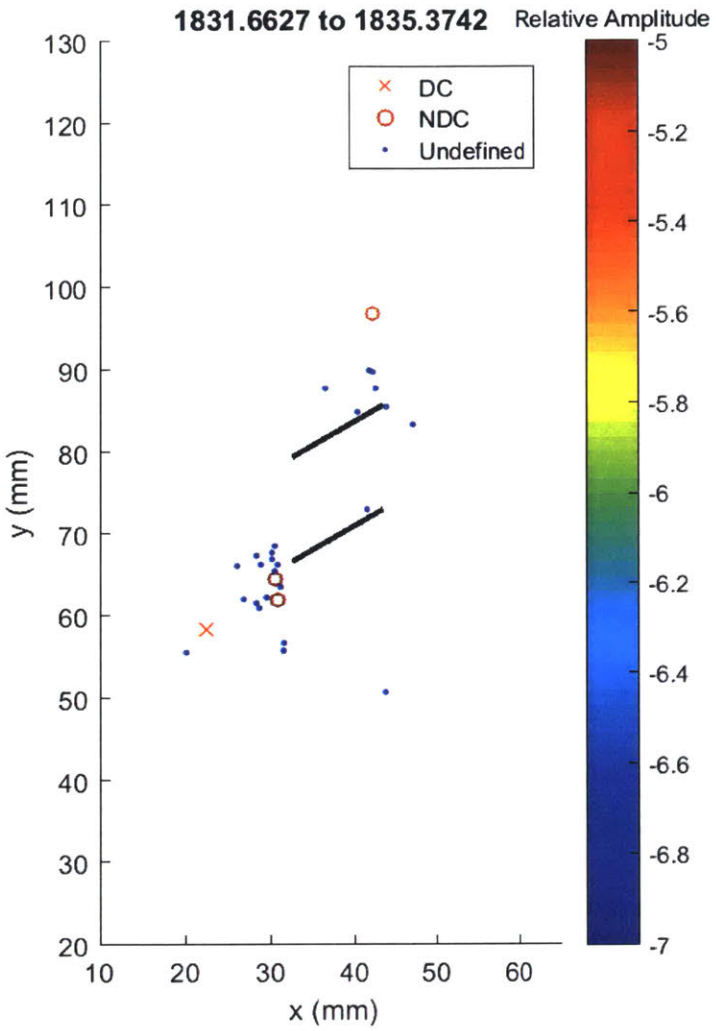

2 tensile events and many small undefined events occur at the bottom left flaw tip. The small events appear to encircle a large grain. A few events also occur above the top right flaw tip.

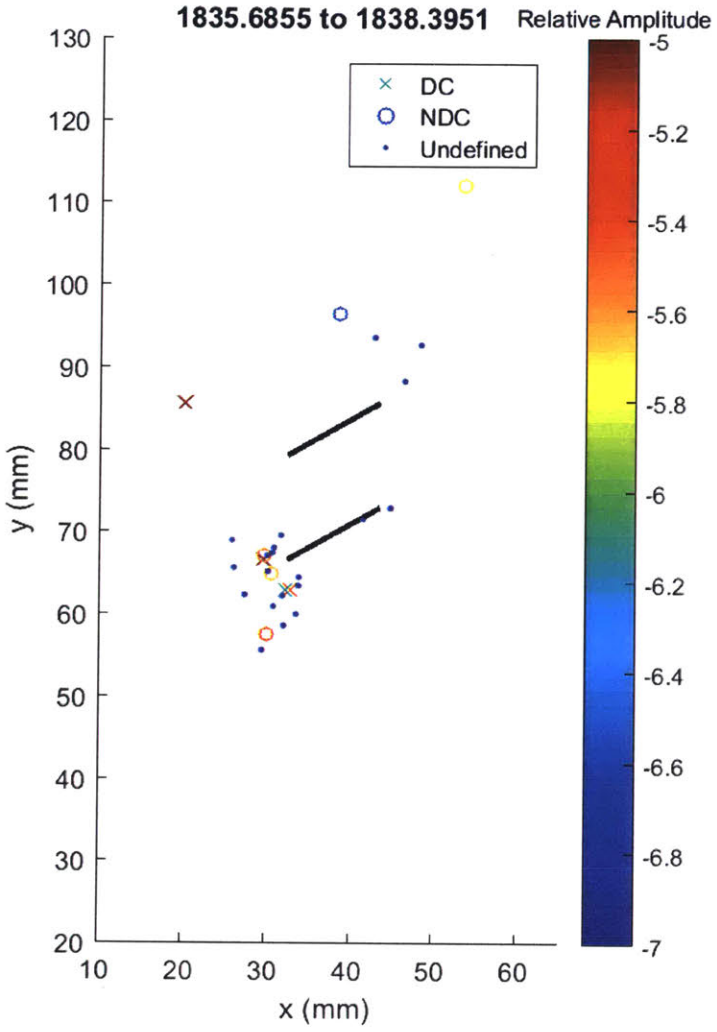

Shear and tensile events occur at the bottom left flaw tip.

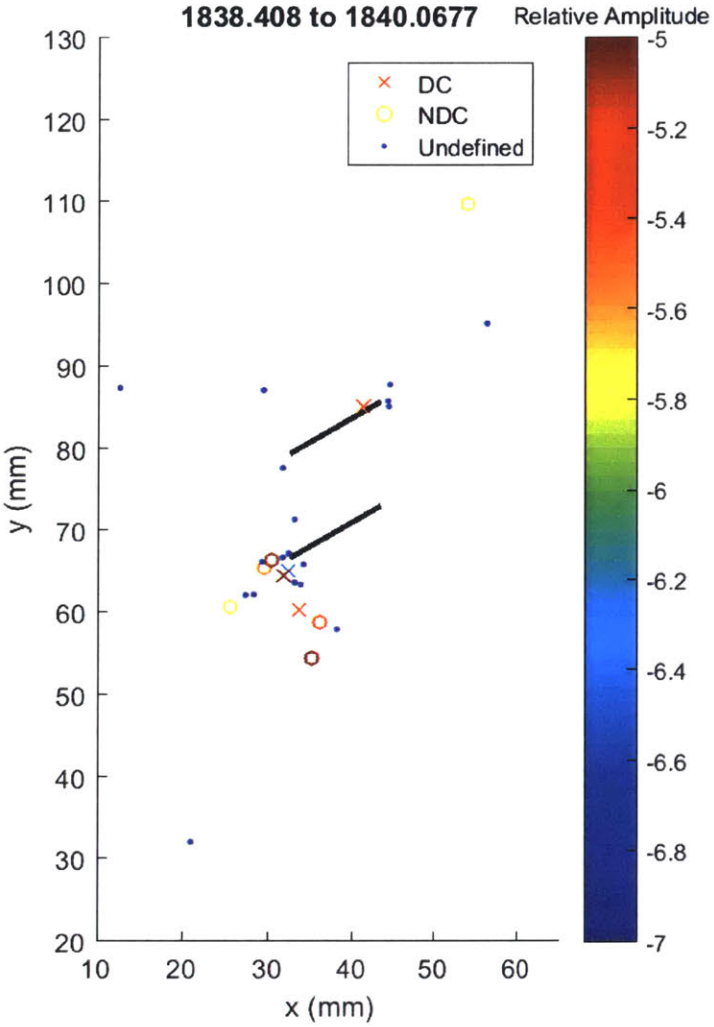

Same as above.

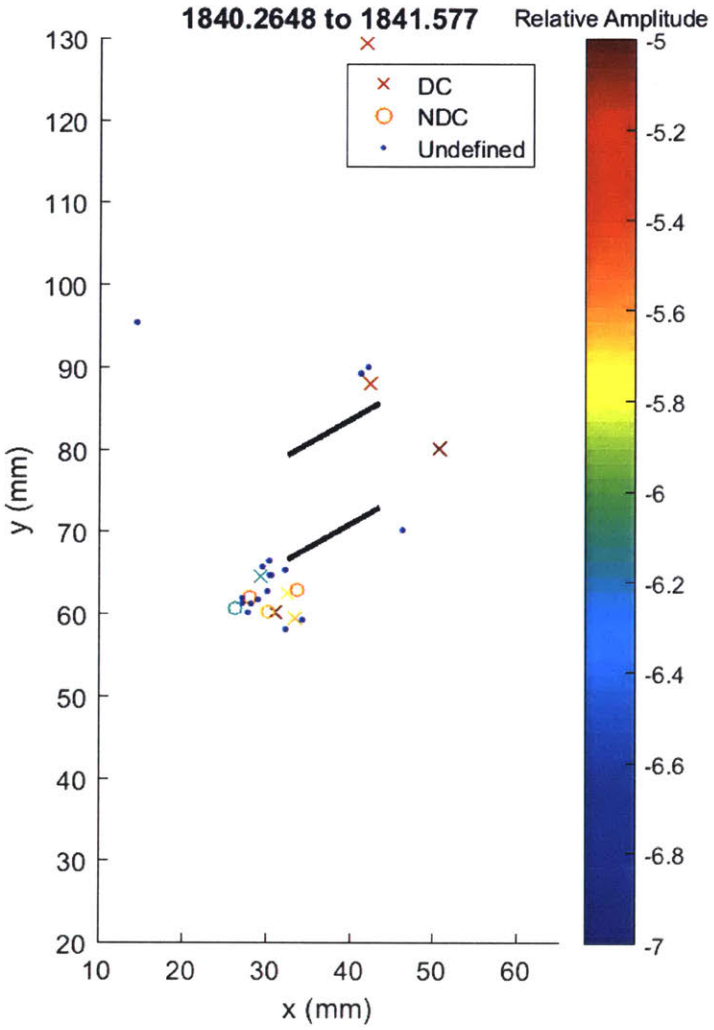

Same as above.

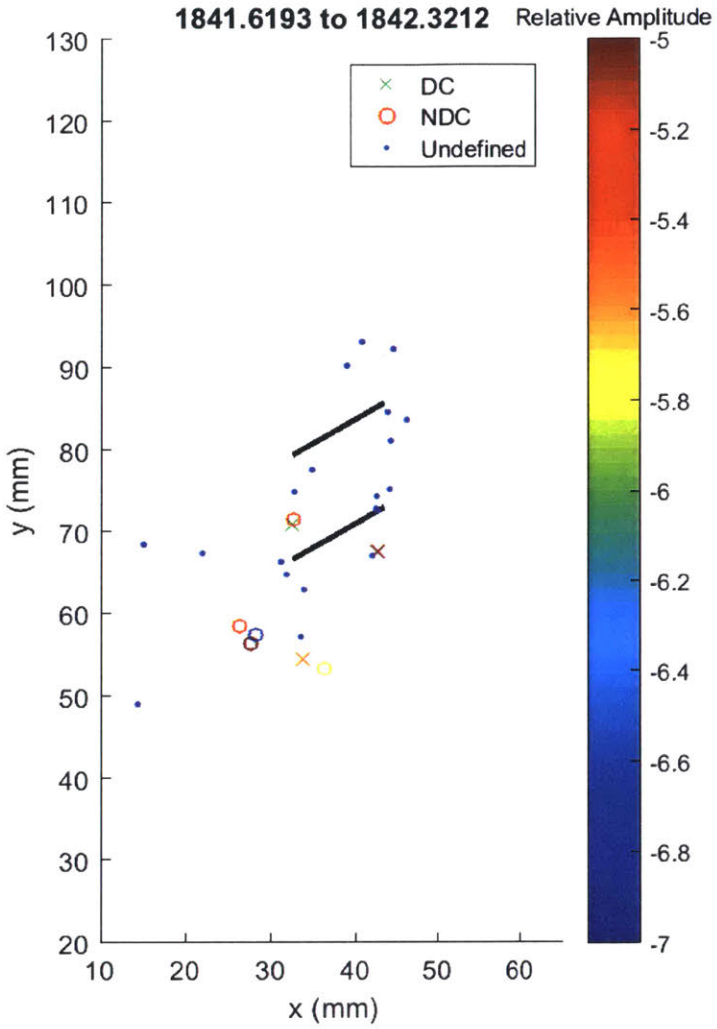

Key frame. Small undefined events map out coalescence between top left and bottom left flaw tips, as well as between top right and bottom right flaw tips. 2 large tensile events occur 1cm below the bottom left flaw tip. **This microcrack coalescence corresponds to the time at which water pressure begins to decrease faster.**

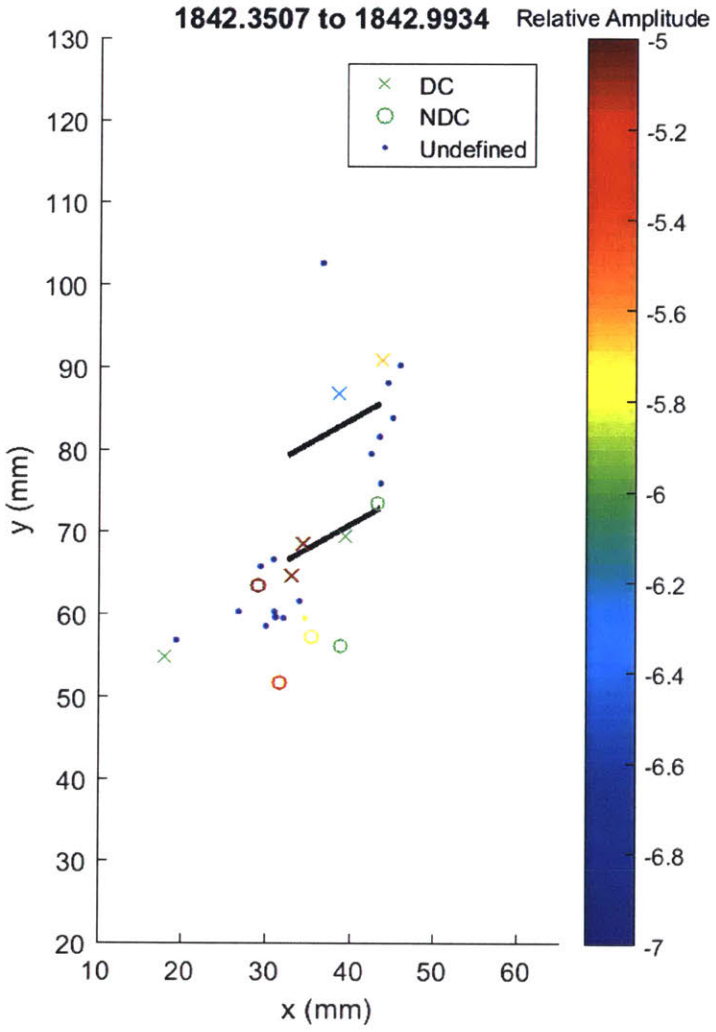

Small undefined events map out coalescence between top right and bottom right flaw tips. 2 large shear and 1 large tensile event occurs near bottom left flaw.

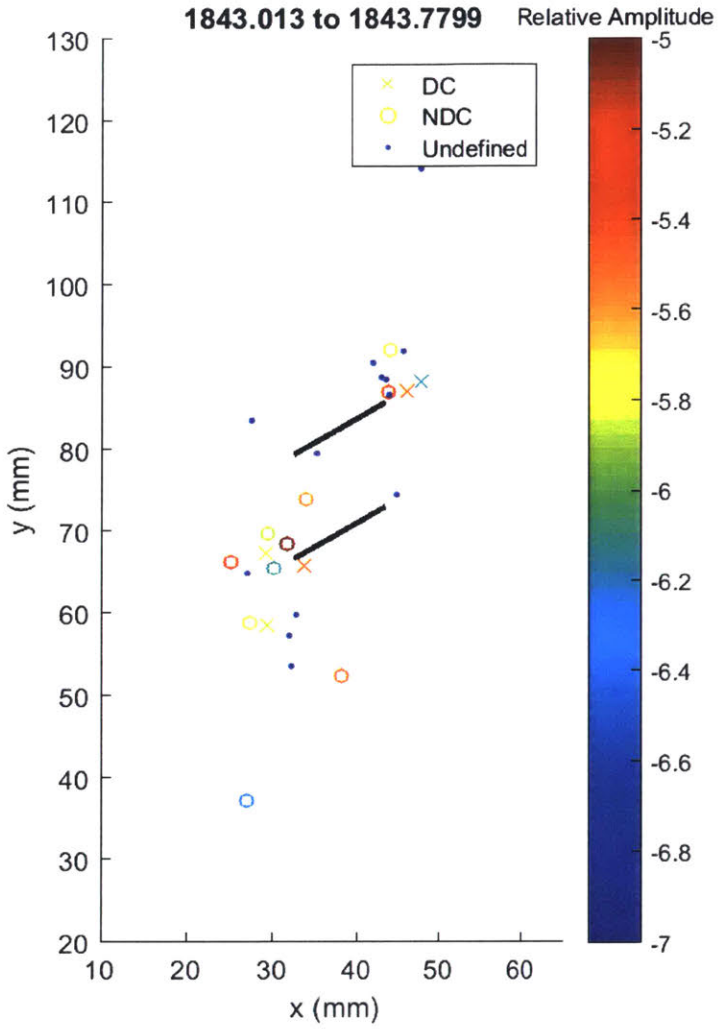

Many tensile events occur near bottom left flaw tip, likely continuing opening of microcracks

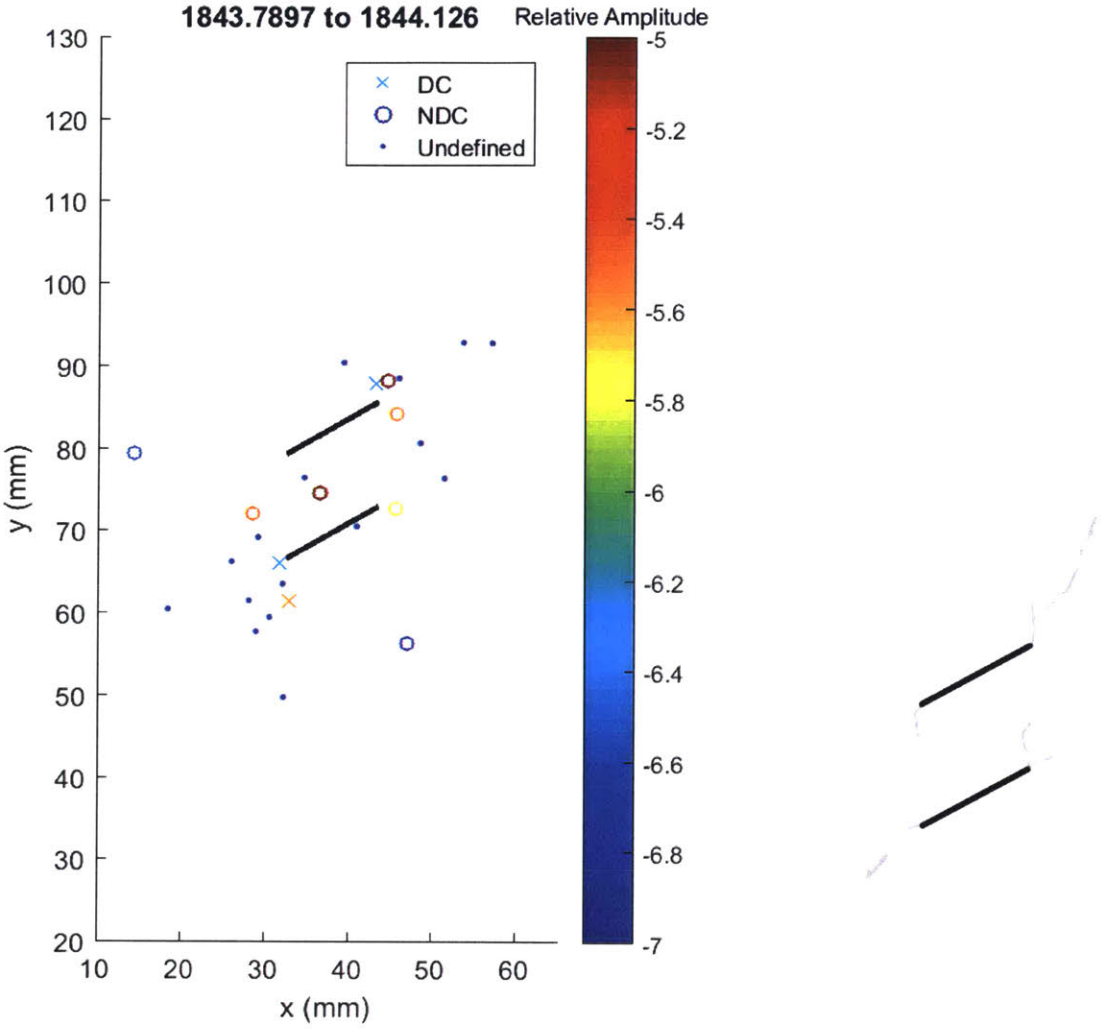

Main tensile events scattered around the specimen. Visually, where is some white patching at all flaw tips, and extensive white patching at the top right flaw tip.

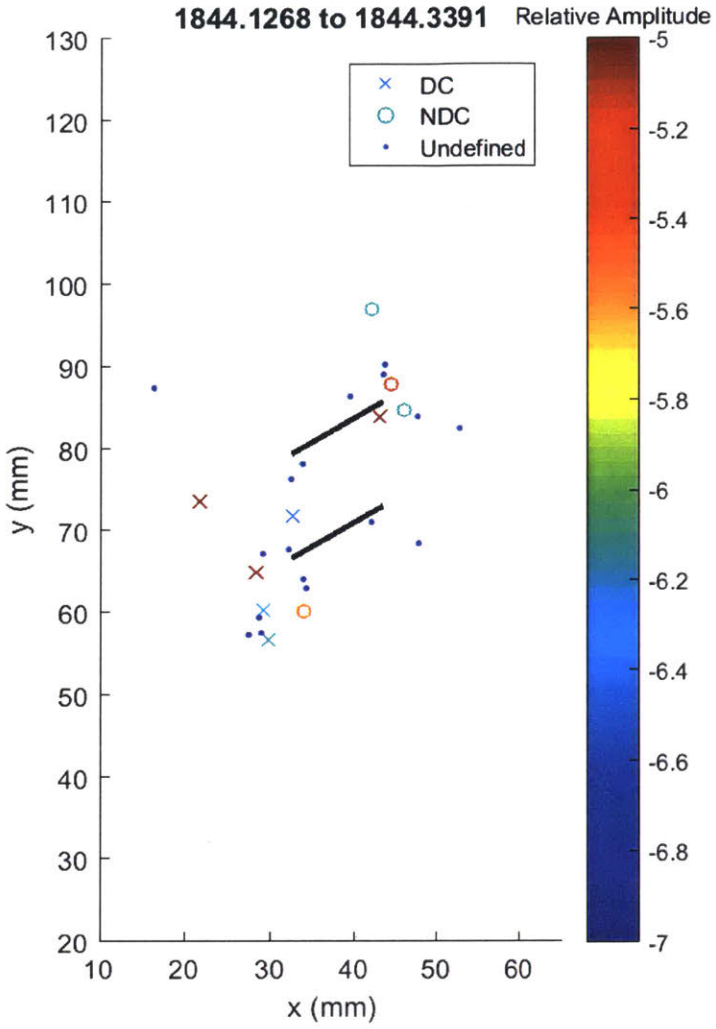

Shear events occur around the bottom left flaw tip, tensile at the top right flaw tip.

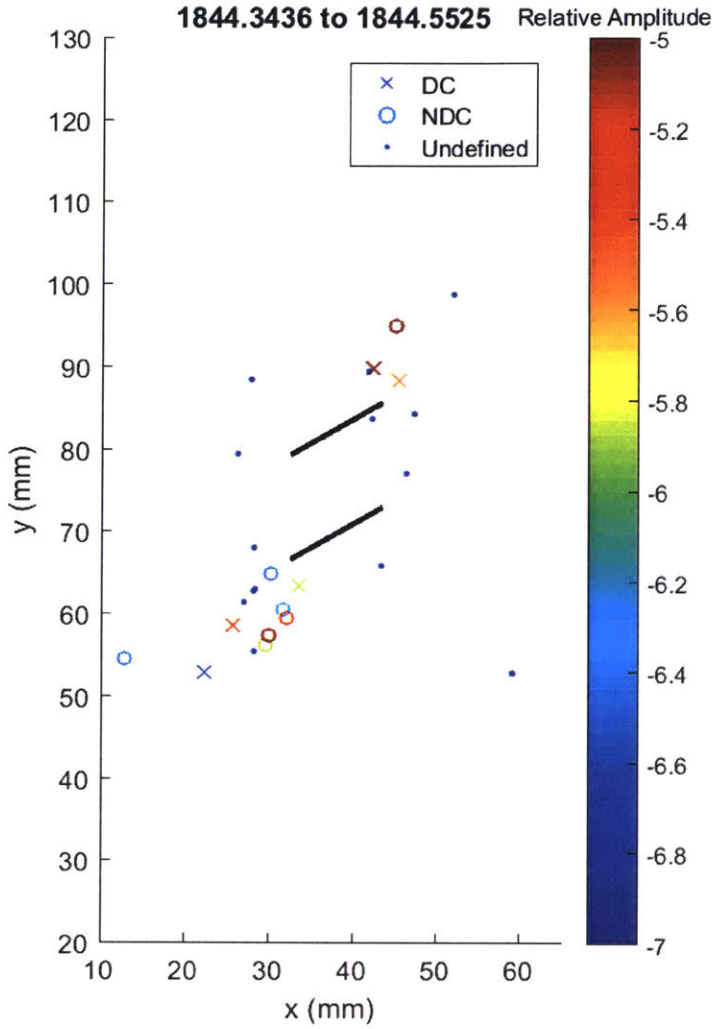

Events continue to cluster at the bottom left and top right flaw tips. More tensile at bottom left, and more shear at top right, opposite to the previous frame.

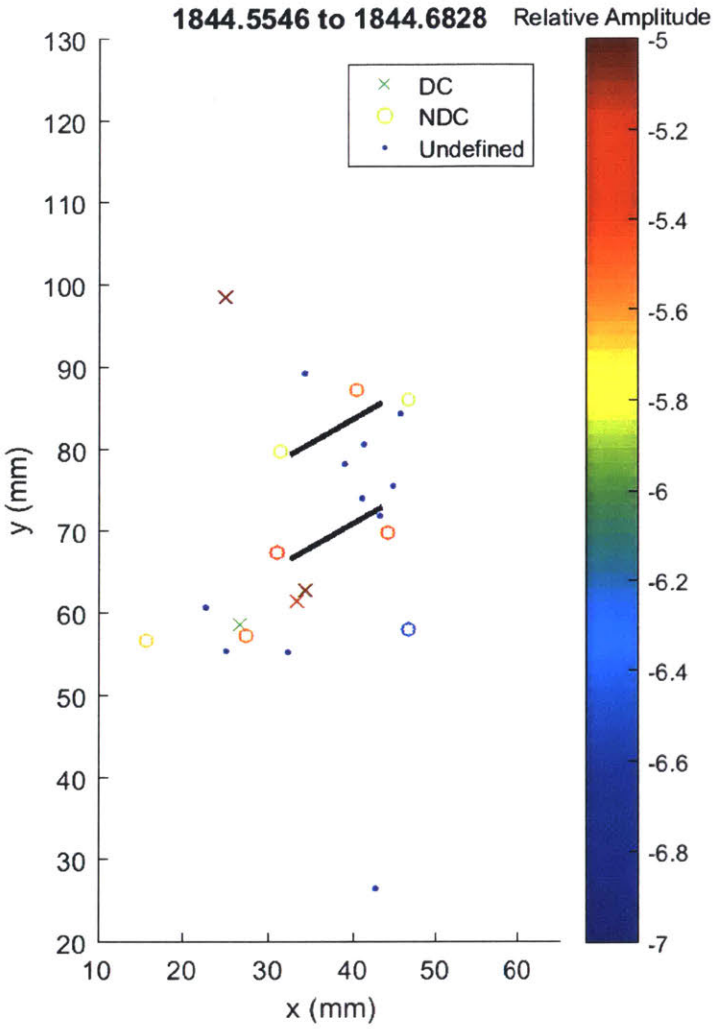

2 large tensile events occur at the bottom flaw tips, and 2 smaller tensile events occur at the top flaw tips. Other events scattered elsewhere.

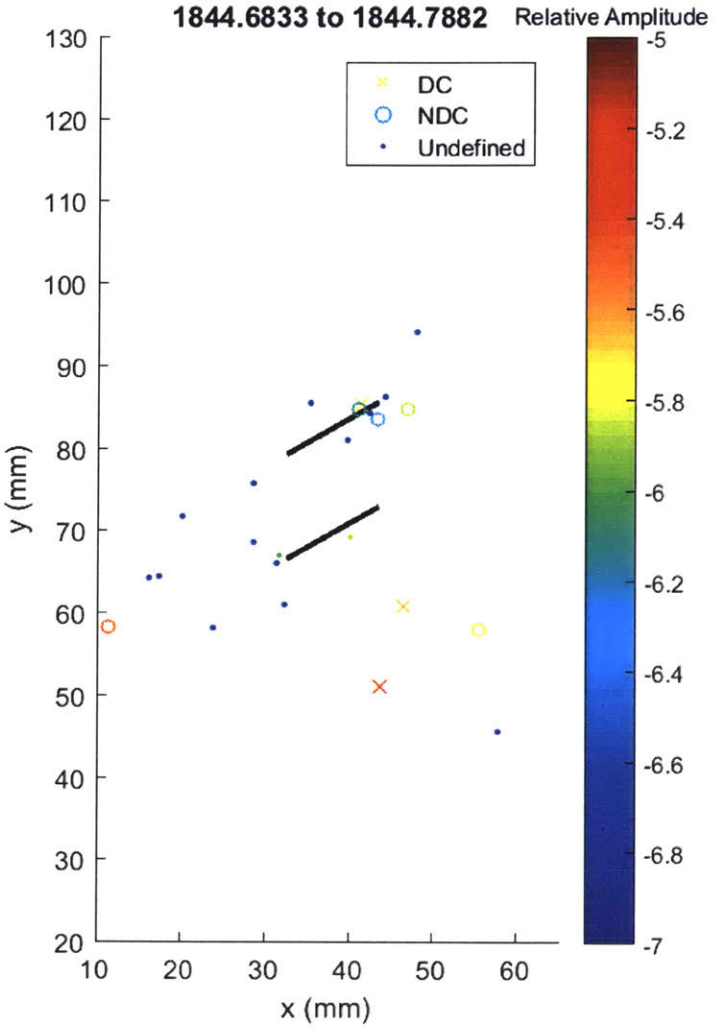

3 tensile events occur at top right flaw tip, scattered events elsewhere.

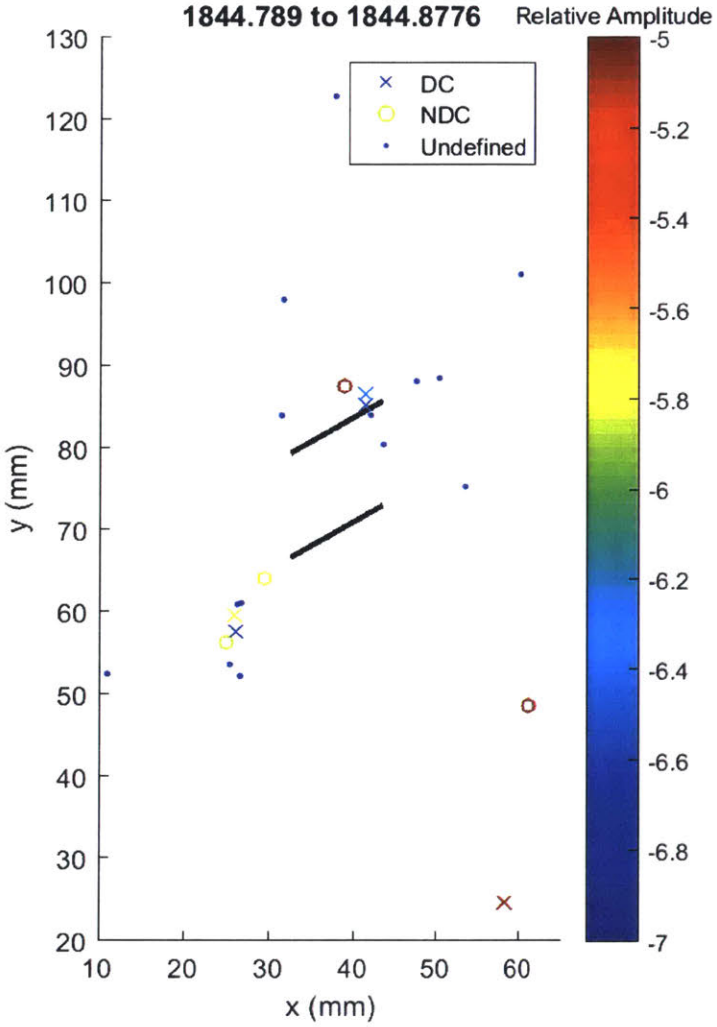

Linear cluster of events 1-2 cm away from the bottom right flaw tip that approximately follows the trajectory of crack A. some events also occur around the top right flaw tip.

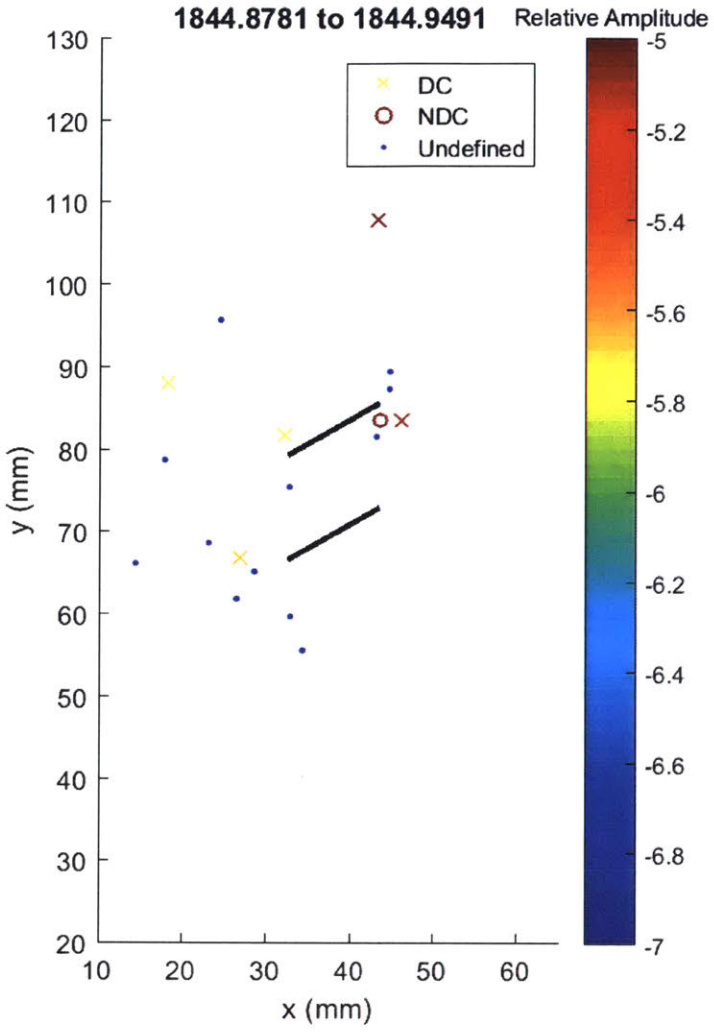

1 large shear and 1 large tensile event occurs near the top right flaw tip.

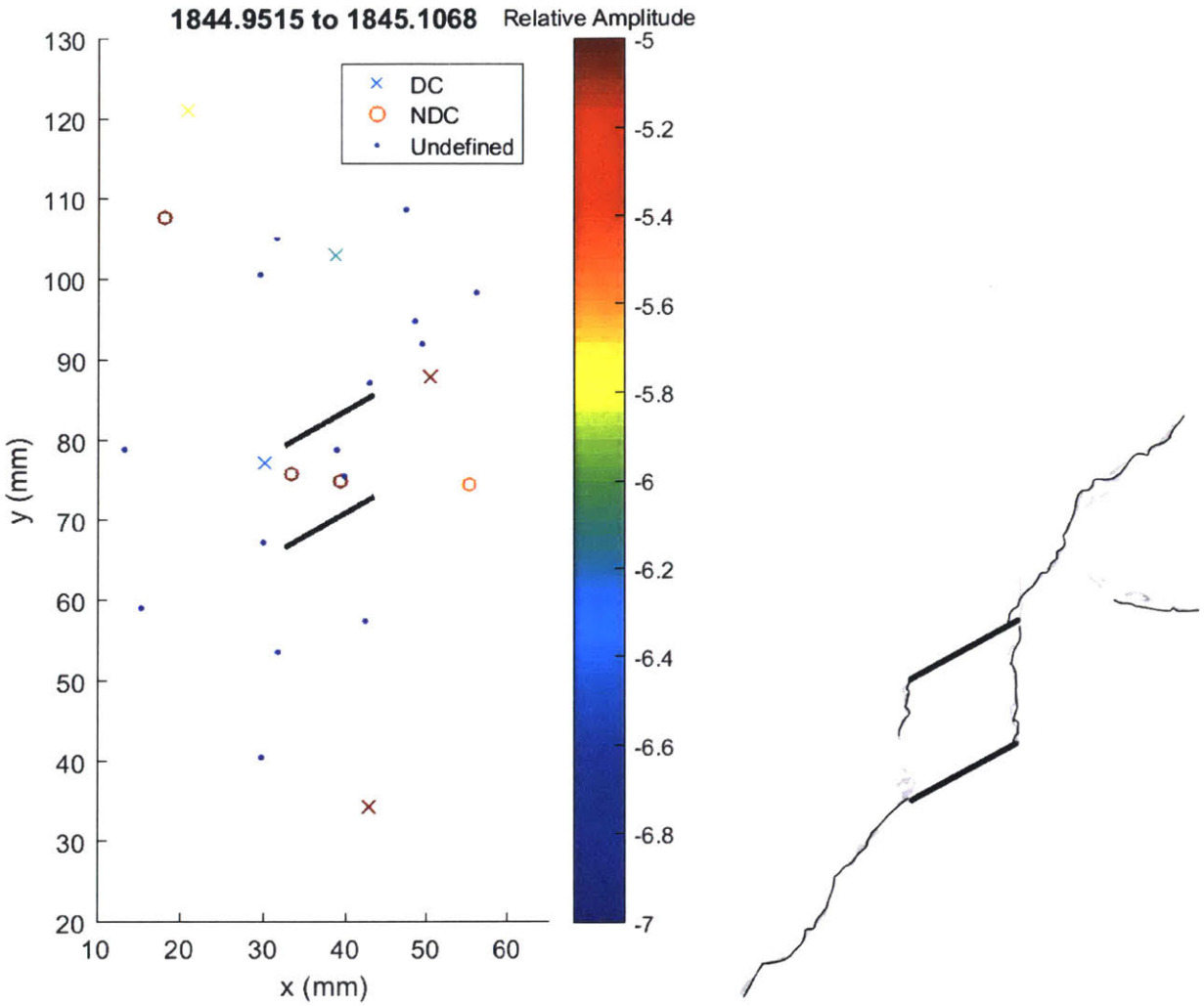

Generally scattered events. Crack initiation and propagation occur in this frame.

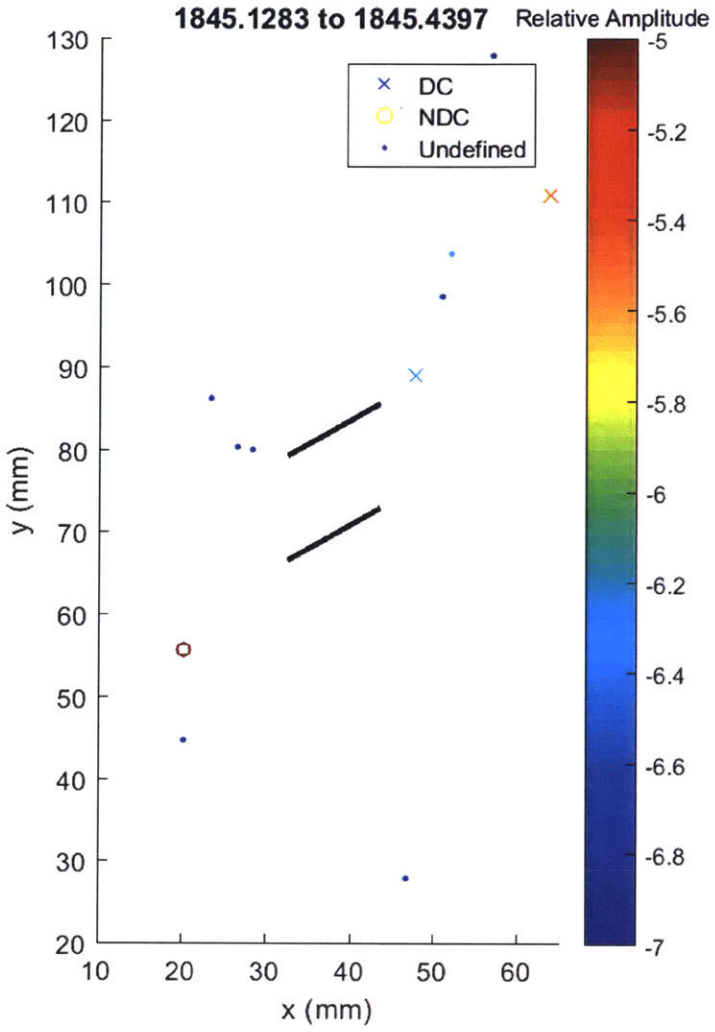

Same as previous.

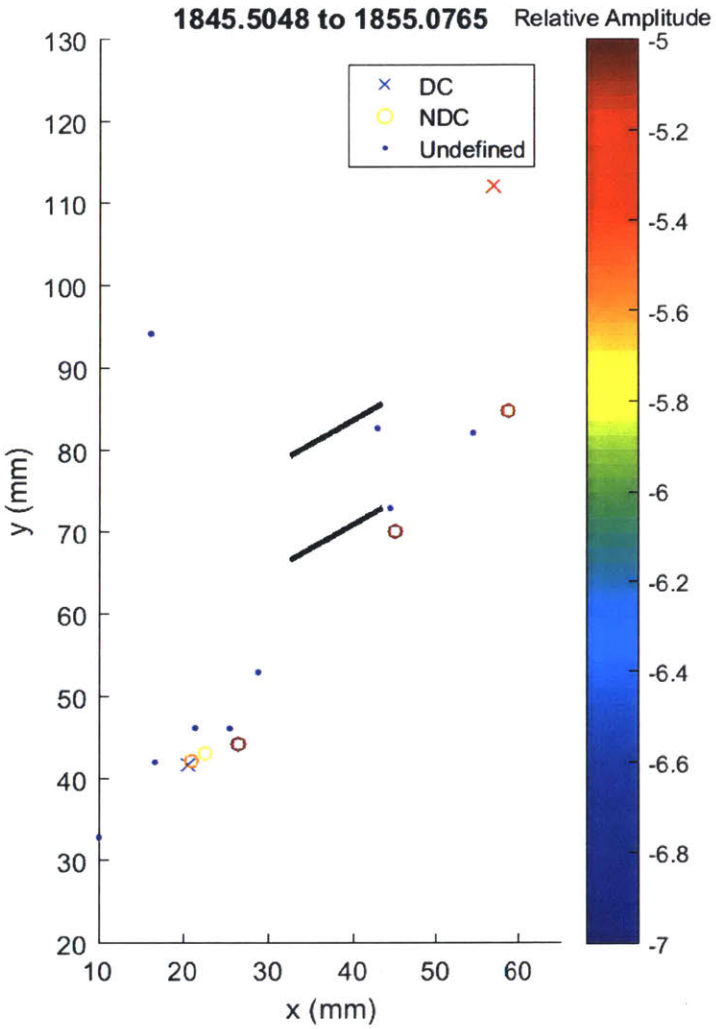

Tensile events well below the bottom left flaw tip, likely a result of the crack reaching the O-ring seal.

Summary:

Generally AE events occurred at the bottom left and top right flaw tips, where first 2 cracks initiated. The visual analysis indicated that more damage was occurring above the top right flaw, but in the AE there was more activity on the bottom left flaw, which is incidentally also where the first crack initiated. This indicates that either the material at the bottom left flaw tip was such that it exhibited less visible damage, or that the damage at the bottom left flaw tip was more severe without being more extensive. It was also noted in this test that the onset of a number of tensile events, which may be related to microcrack coalescence, corresponded to an inflection in the pressure-time curve, whereupon the pressure decreased faster than previously. AE events corresponding to coalescence cracks C and D occurred later than those corresponding to cracks A and B.

AE hypocenter analysis for specimen 2a-30-120-VL5-B

Final crack geometry:

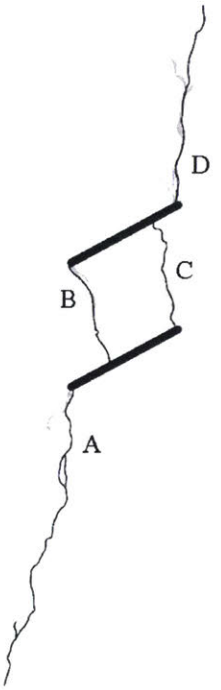

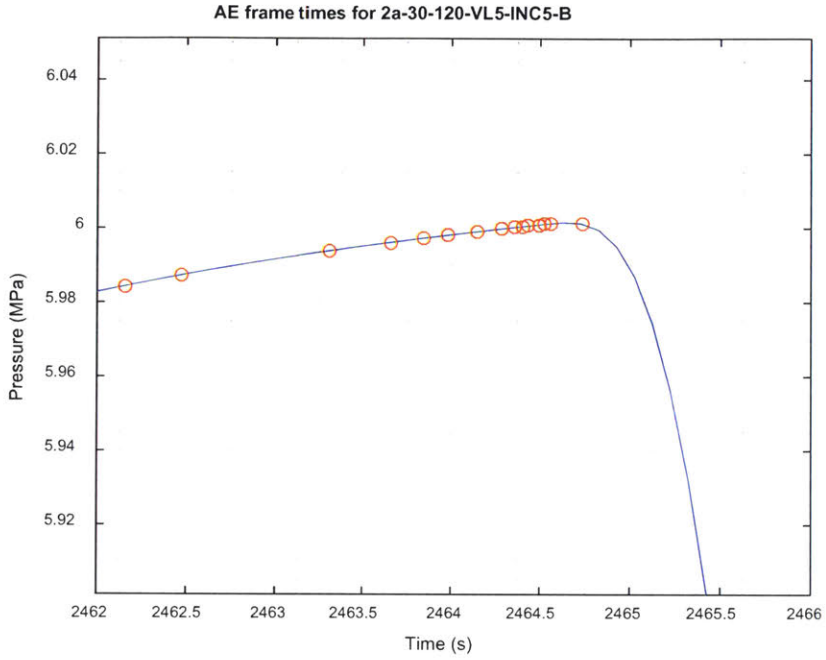

There was no high speed data for this test, but like the 2a-30-120-VL0-B geometry cracks initiate from the bottom left and top right flaw tips., while cracks initiate and propagate towards the other flaw from the top left and bottom right flaw tips. Water pressure is at peak value immediately before crack initiation.

Development of AE locations are shown over the 20 frames presented in this analysis, where each frame shows 5% of the total number of events recorded during the test. This means that initially the frames will cover a long time period since few AE occurred at the beginning, while towards failure each frame will only cover fractions of a second since AE occur at a rapid rate.

Events with greater than 50% CLVD (compensated linear vector dipole) are considered shear type events and are marked with an 'x', while events with less than 50% CLVD are considered tensile and marked with 'o'. For those events detected by 4 sensors, it is not possible to invert the moment tensor and so these events are marked as undefined with '.'. The colour of an event indicates its relative magnitude, where red is the largest. Black ellipses are used to highlight areas of interest.

Where possible, AE frames are shown next to the appropriate analysis sketch from Bruno. However, these tend to be few in between and as discussed, the high speed frames tend to occur after the end of detectable AE events.

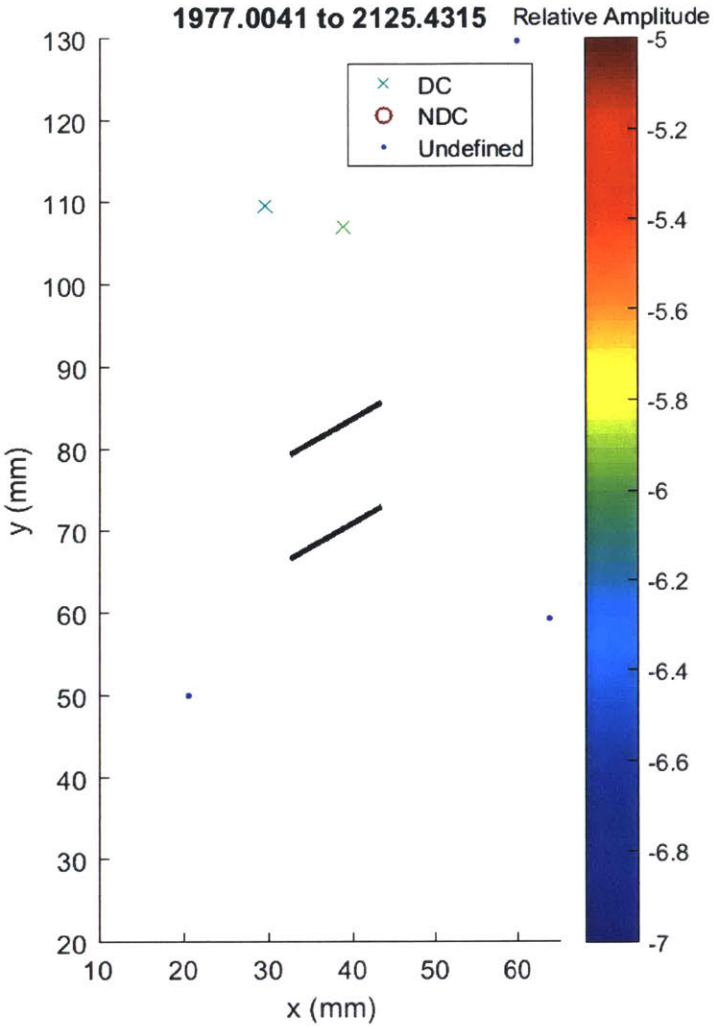

Scattered events.

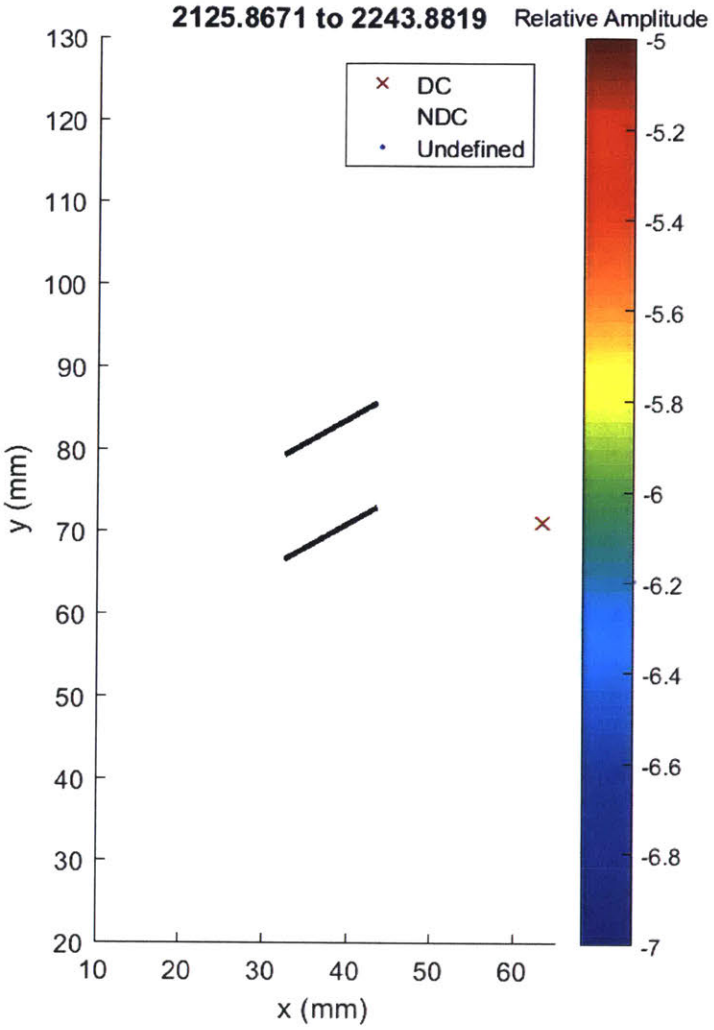

Same as above.

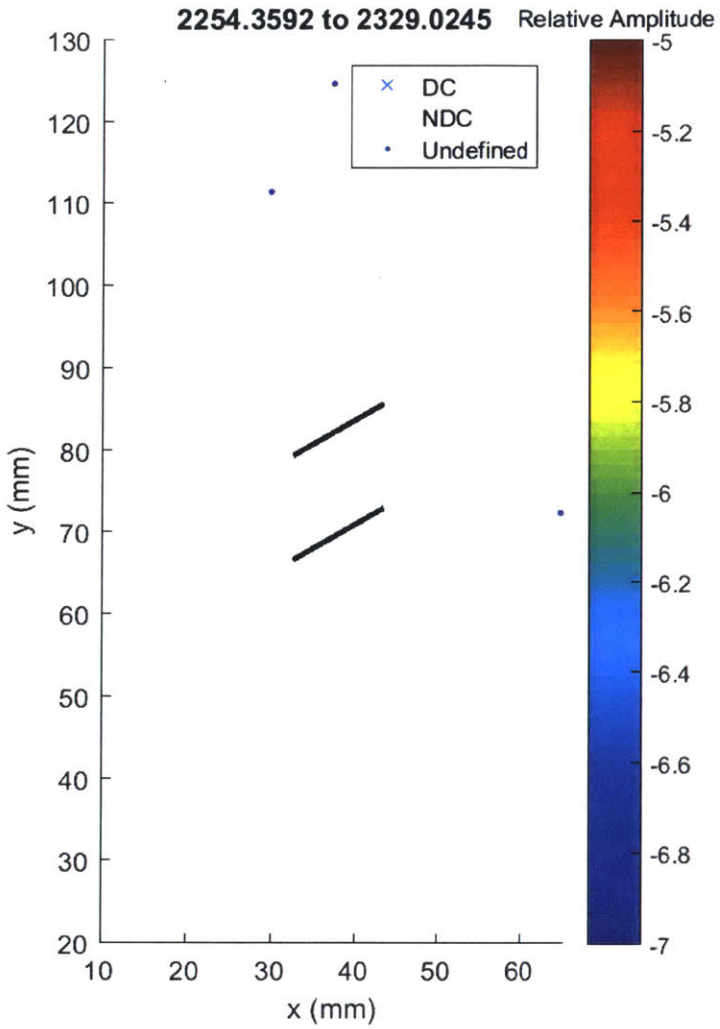

Same as above.

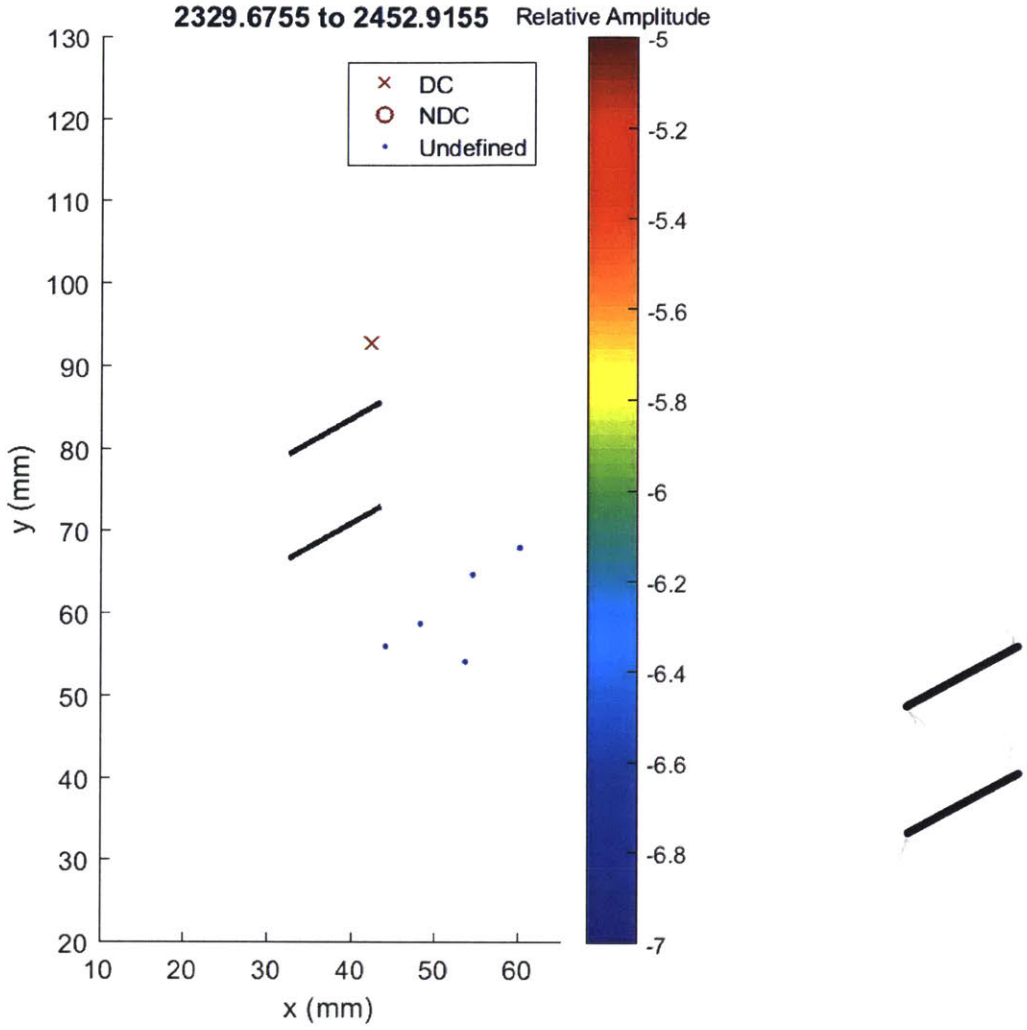

1 large shear event above the top right flaw. Some low amplitude undefined events below the bottom right flaw tip.

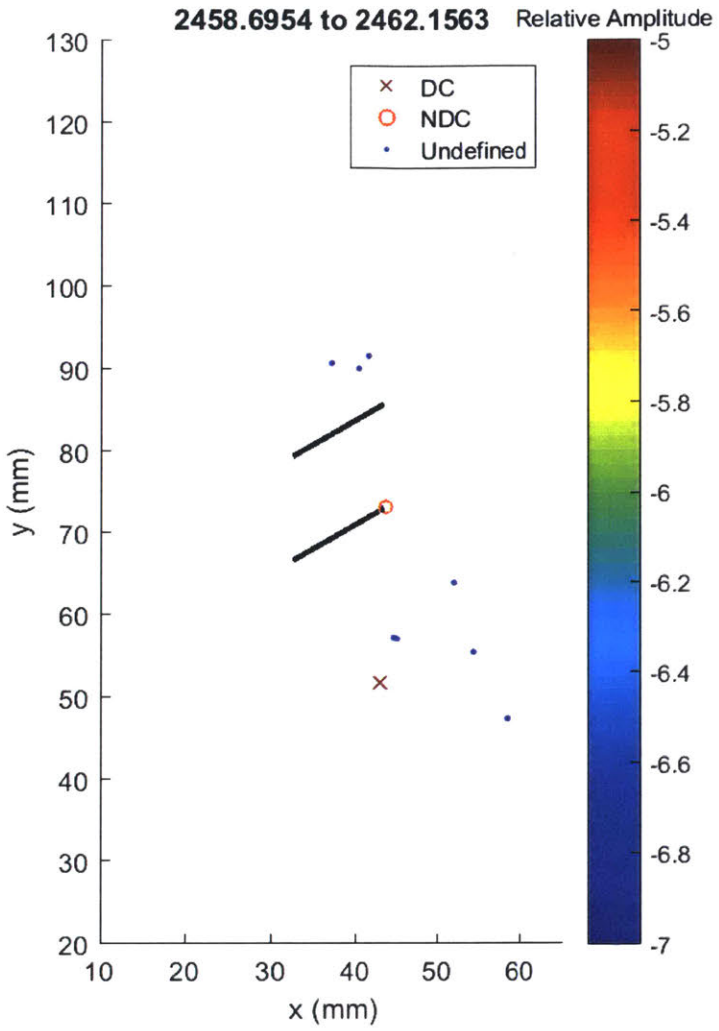

1 large tensile event occurs at the bottom right flaw tip. Some undefined events above the top right and below the bottom right flaw tip. Visual analysis shows there is some damage at all flaw tips, and extensive damage at the top right flaw tip.

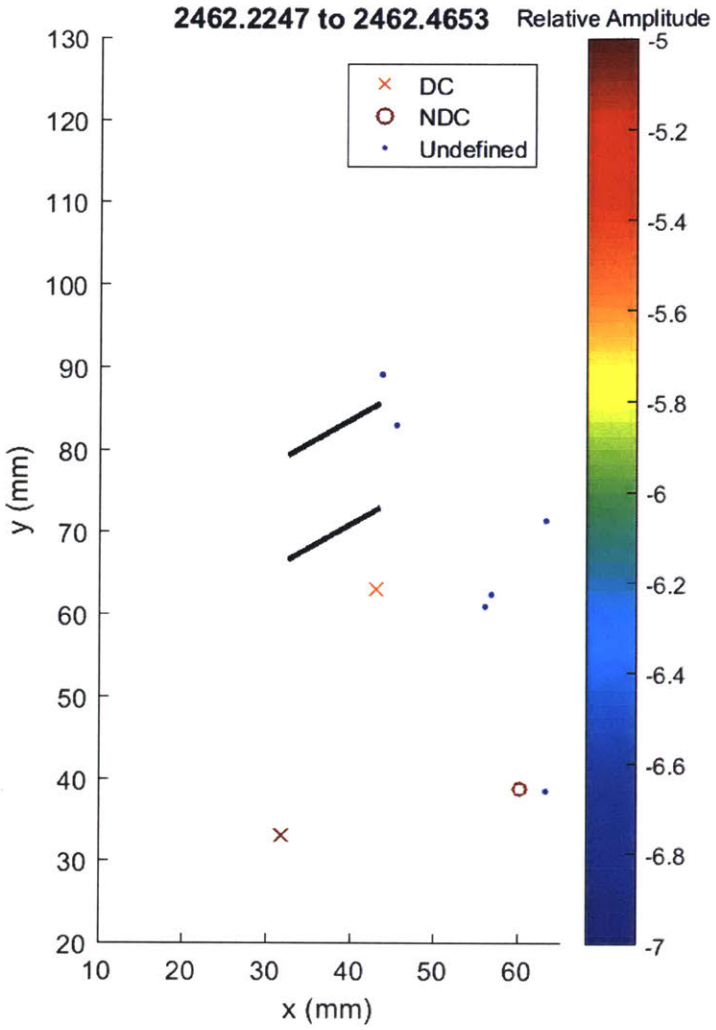

Generally scattered events. 1 large shear event below bottom right flaw tip.

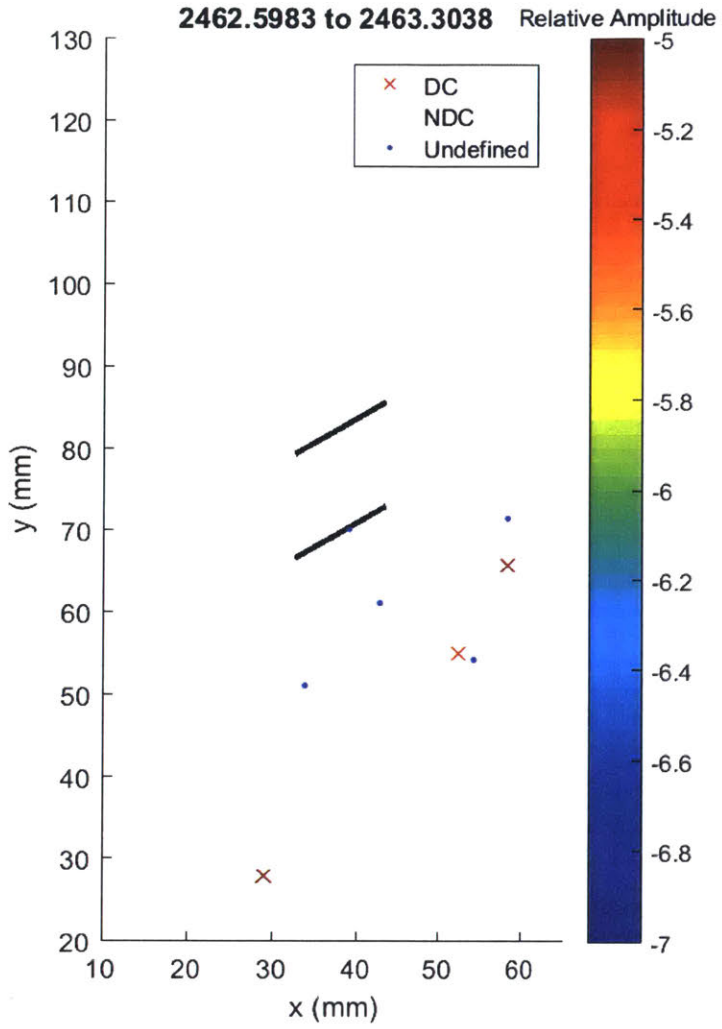

2 large shear events approximately 2cm away from bottom right flaw tip.

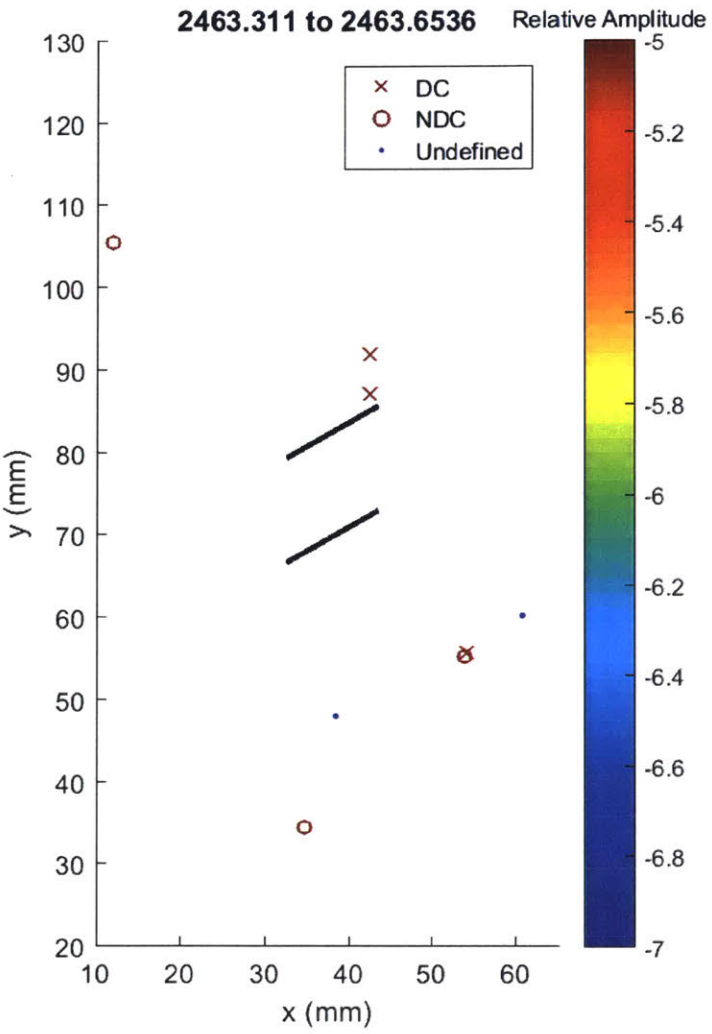

2 large shear events occur at the top right flaw tip. Scattered events otherwise.

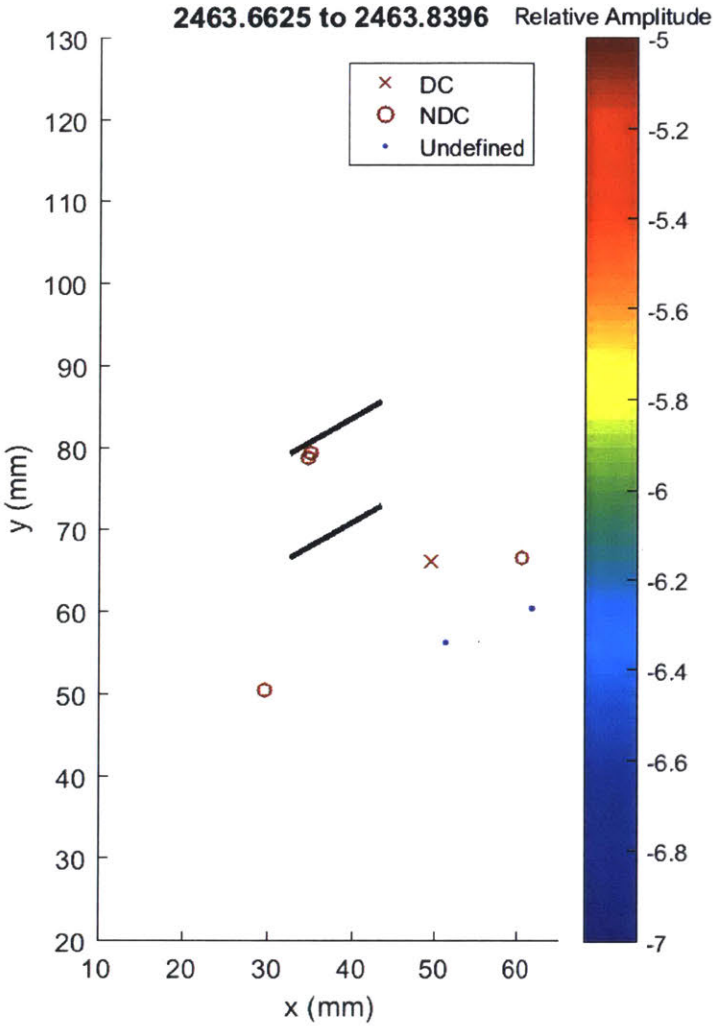

2 large tensile events just below the top left flaw tip. 3 large amplitude events occur below the bottom flaw.

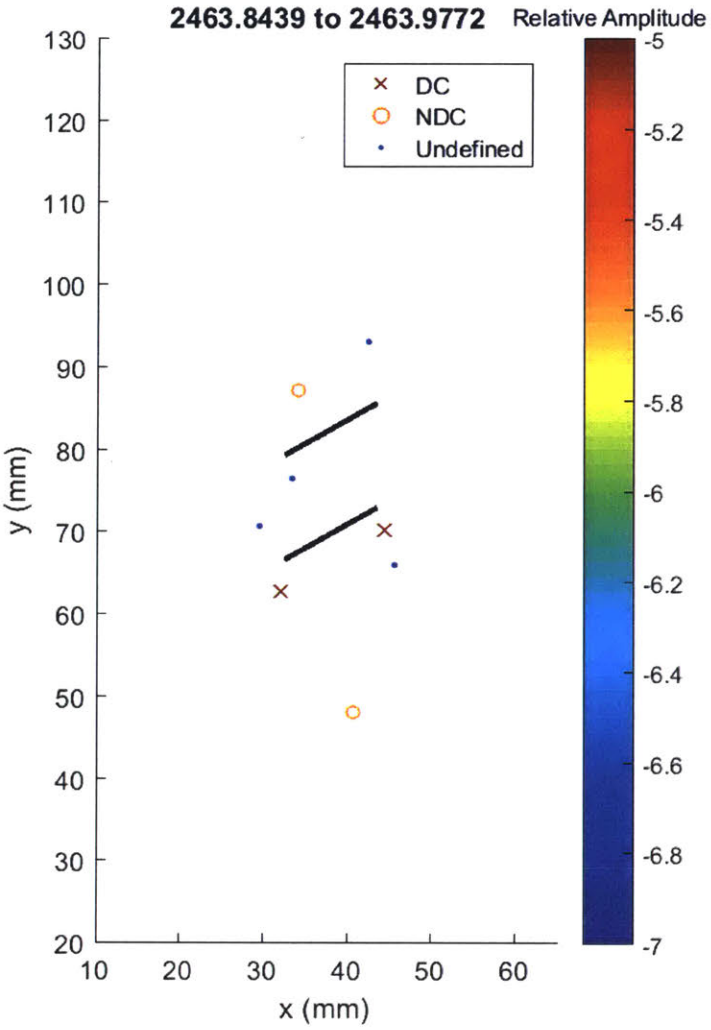

A large shear event occurs at both tips of the bottom flaw.

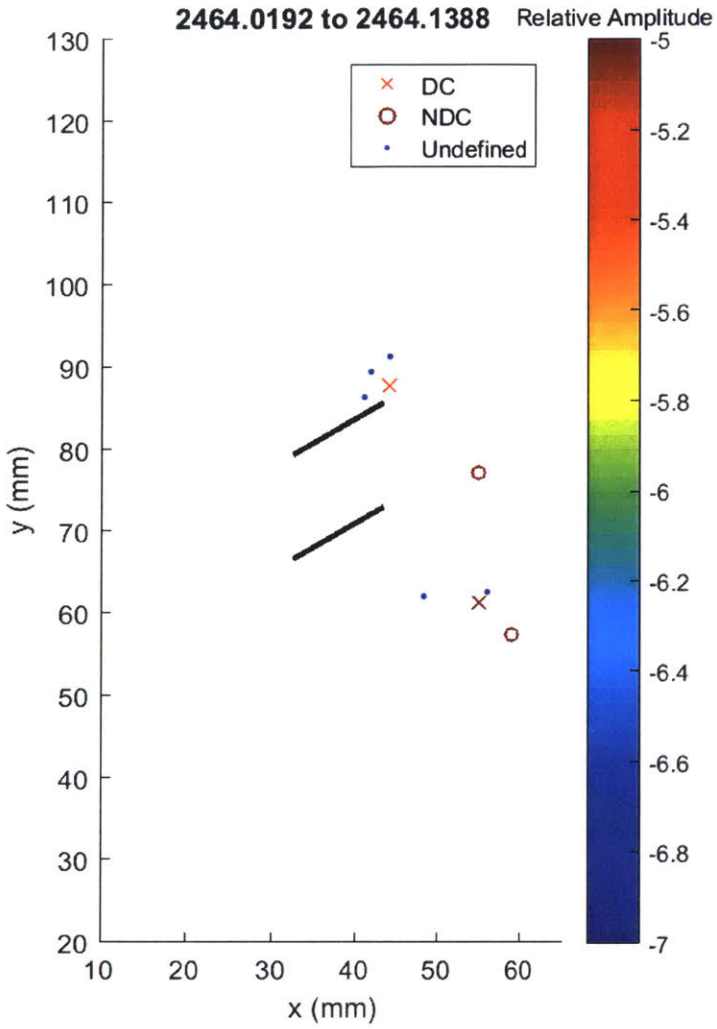

1 large shear event occurs at top right flaw tip. Large amplitude events continue to occur to the lower right of the bottom right flaw tip.

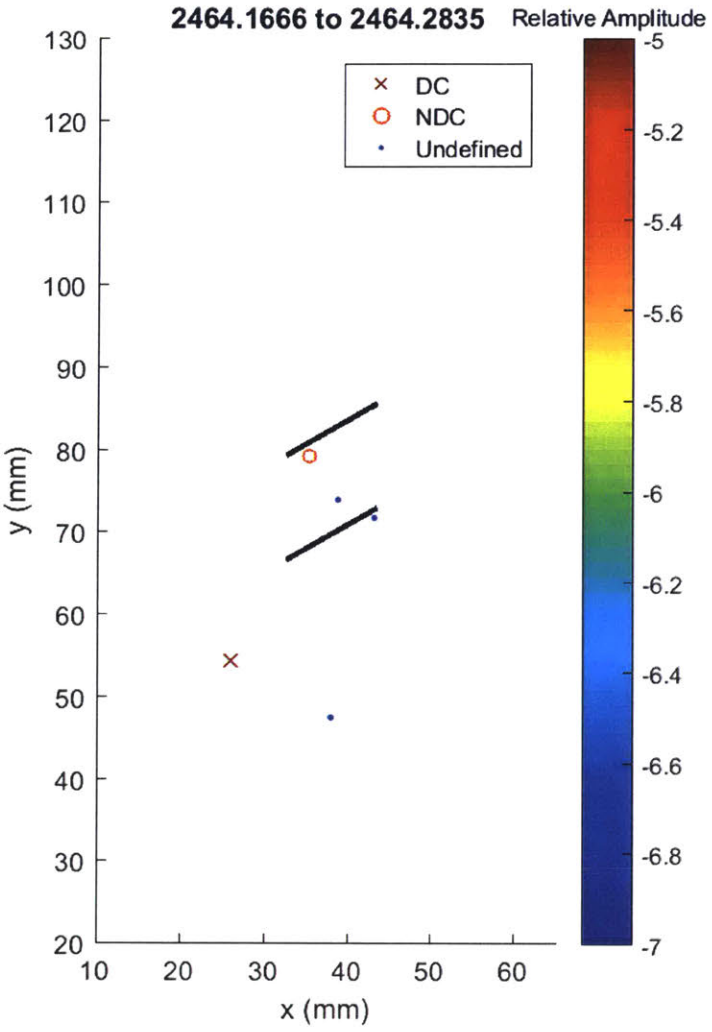

Another tensile event occurs below the top left flaw tip.

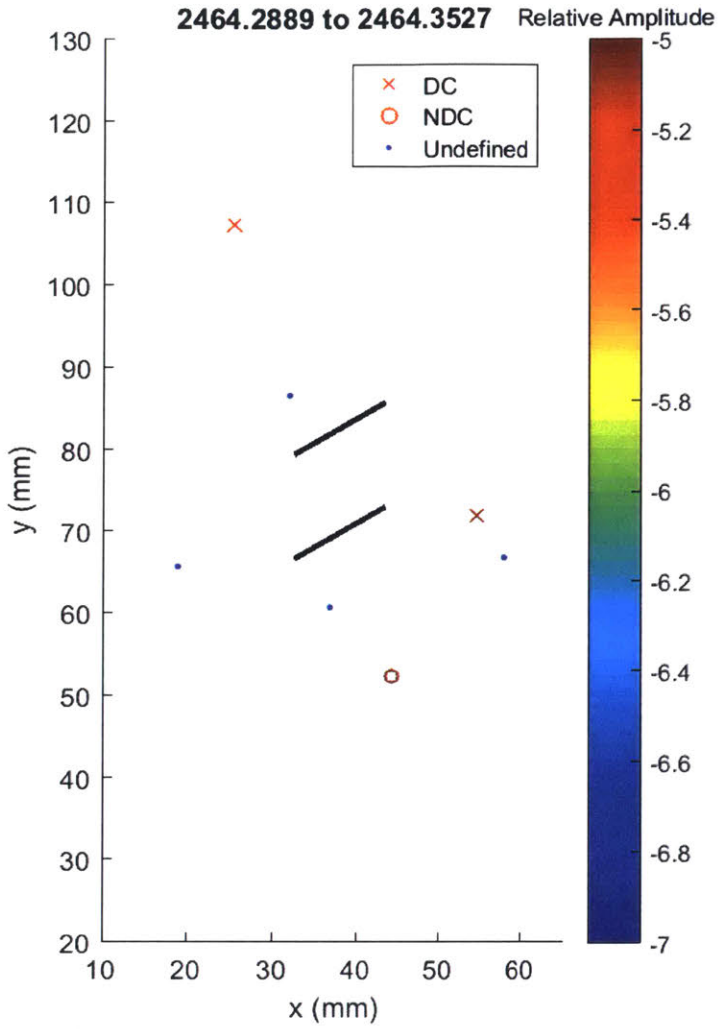

Scattered events.

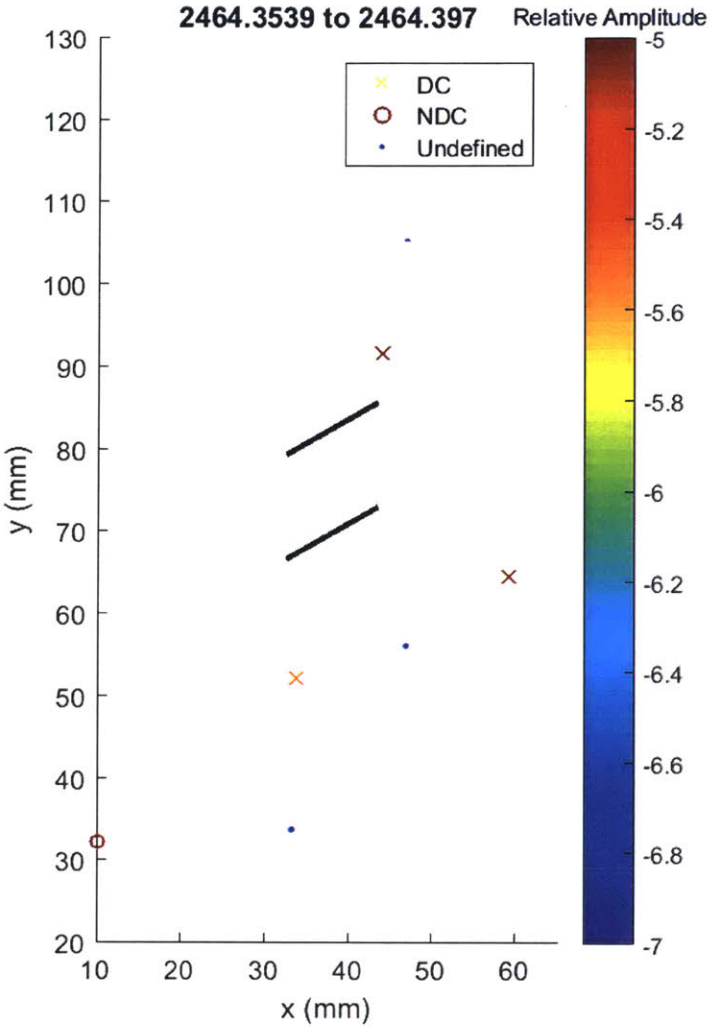

1 large shear event occurs above top right flaw tip.

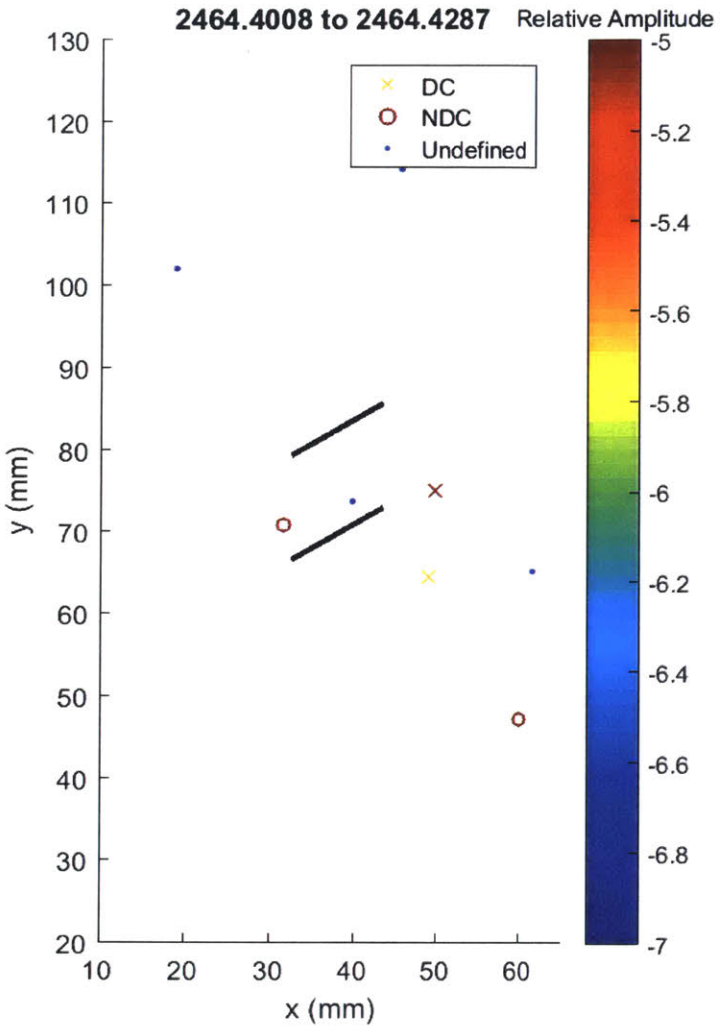

1 large tensile event occurs at bottom left flaw tip, 2 large shear events occur near bottom right flaw tip.

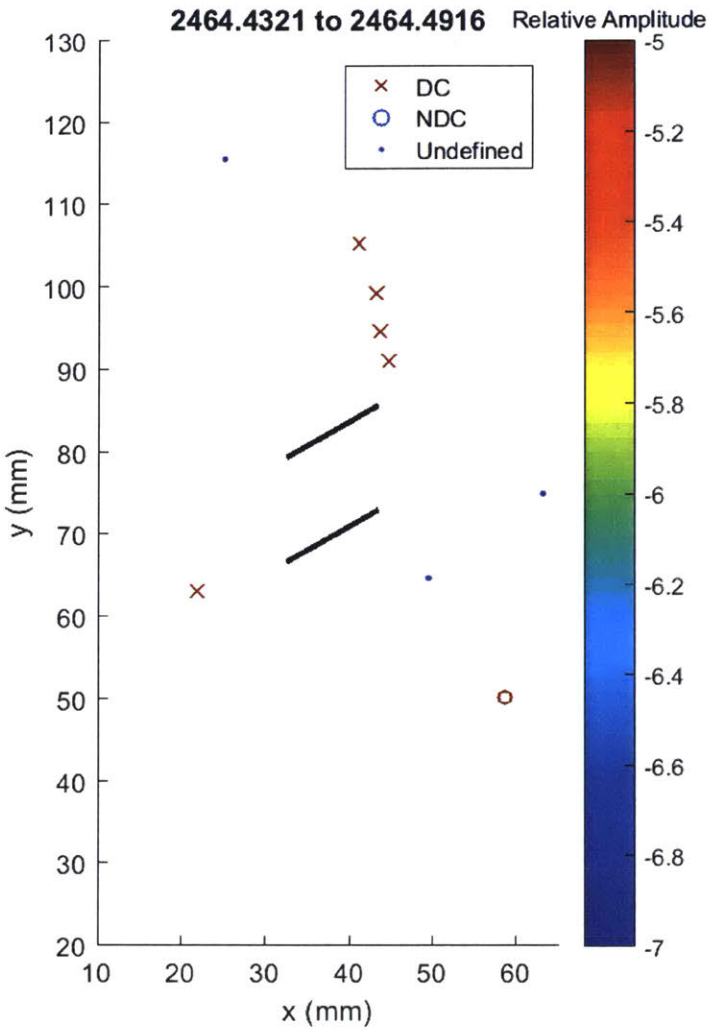

Key frame. 4 linearly patterned large shear events occur above the top right flaw tip.

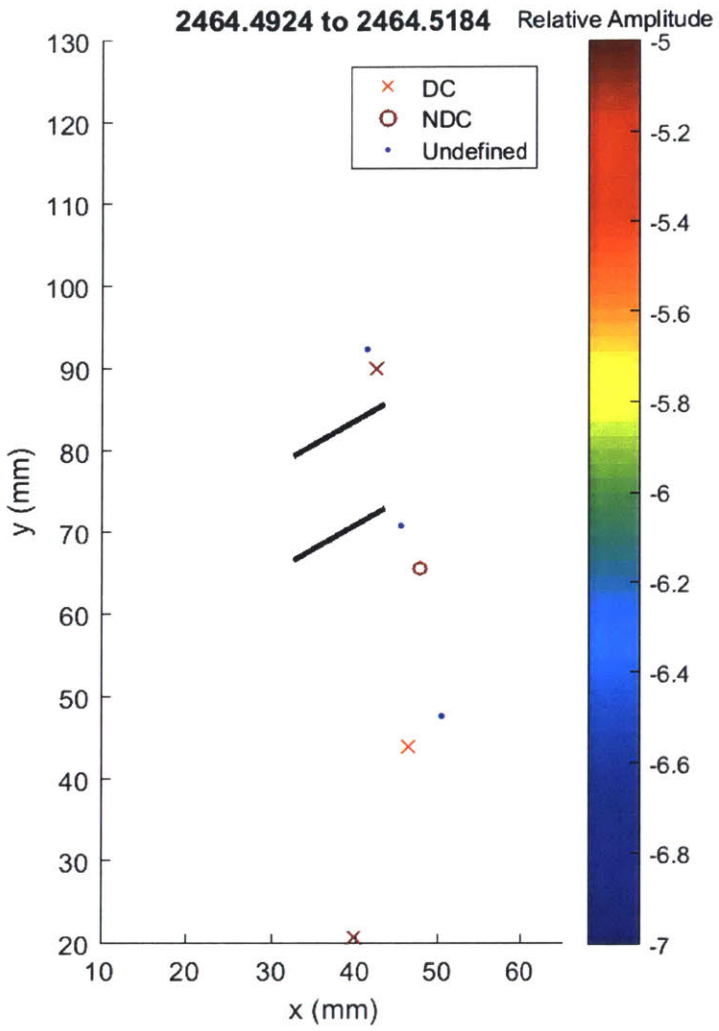

Another shear event occurs at top right flaw tip.

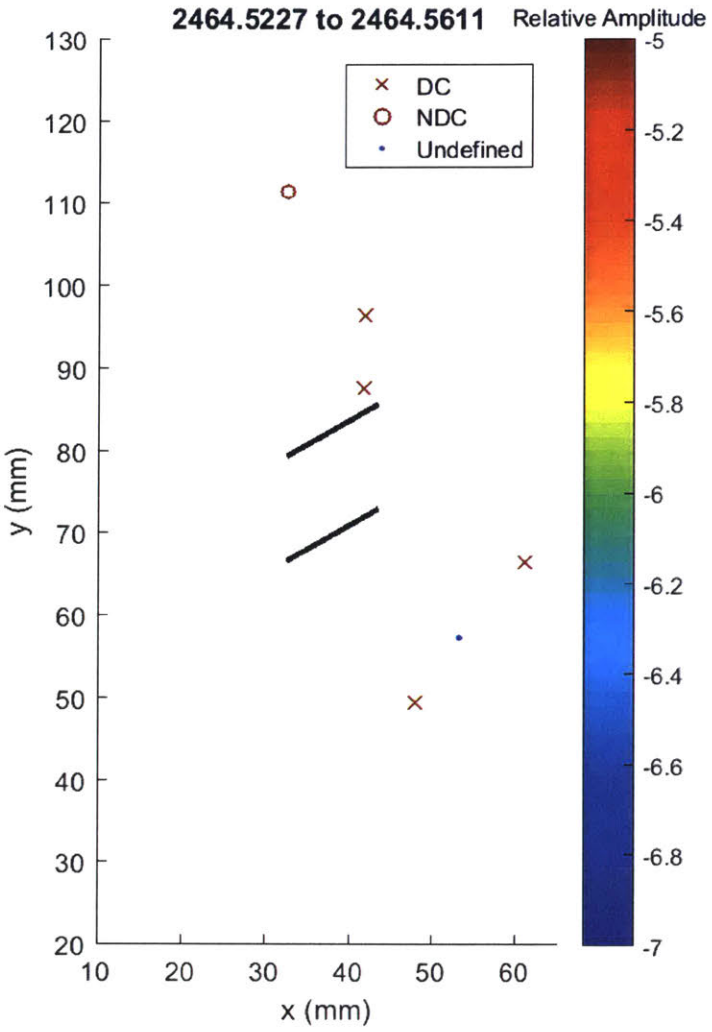

2 more large shear events at top right flaw tip.

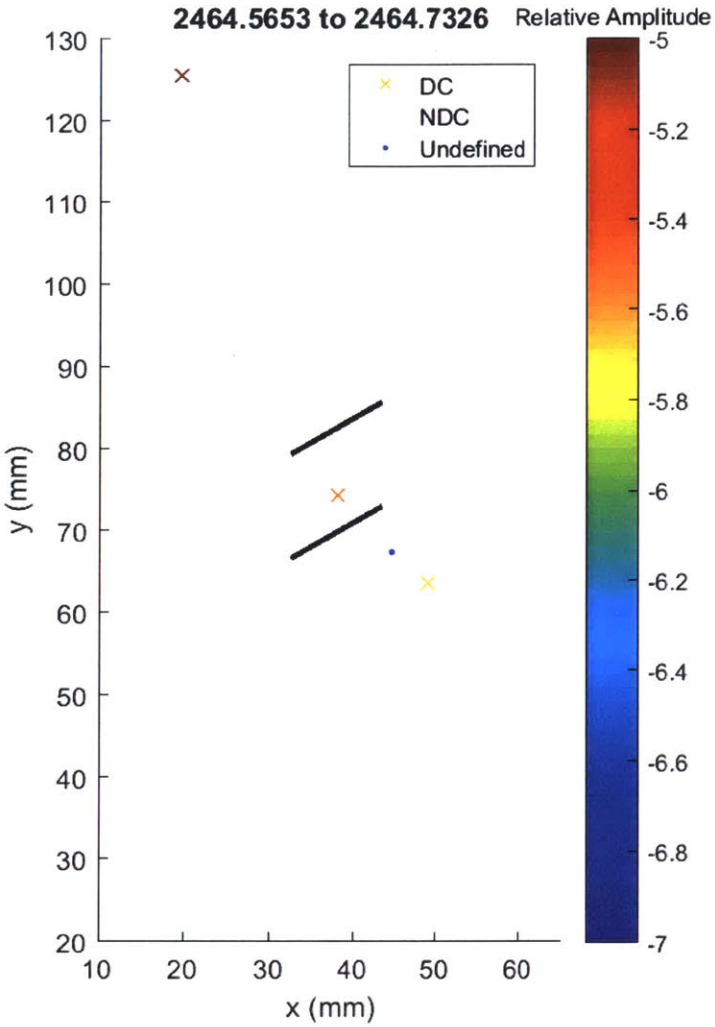

1 shear event occurs in bridge area, another below the bottom right flaw tip.

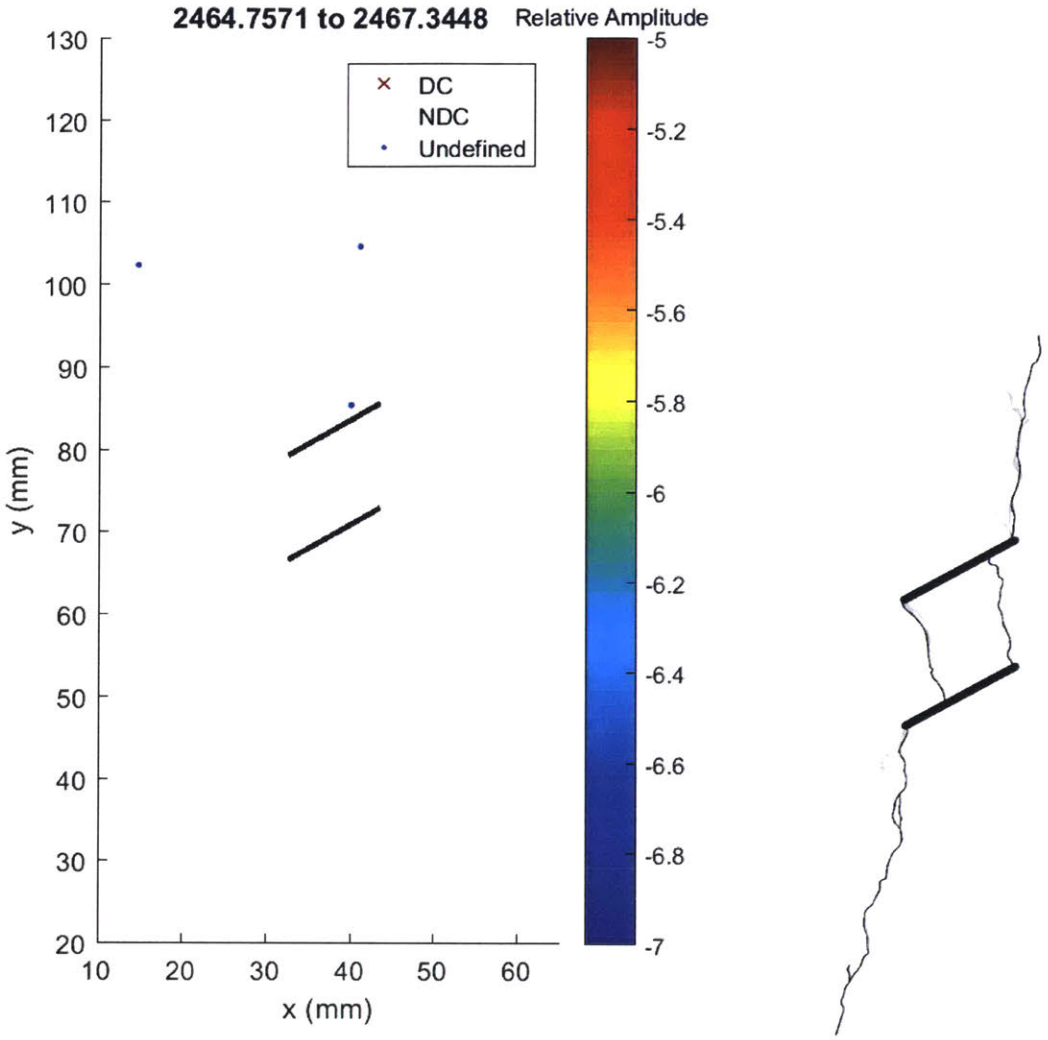

Scattered events. Visual crack initiation and propagation occurs in this time.

Summary:

Few events detected in this test, likely due to a deficiency in the test setup. Generally linearly patterned shear events occurred at the top right flaw tip. This agrees with the observations of white patching, which was significantly more extensive at the top right flaw tip. Some events occur to the lower right of the bottom right flaw tip. There were generally more shear than tensile events.

AE hypocenter analysis for specimen 30-VL5-B

Final crack geometry:

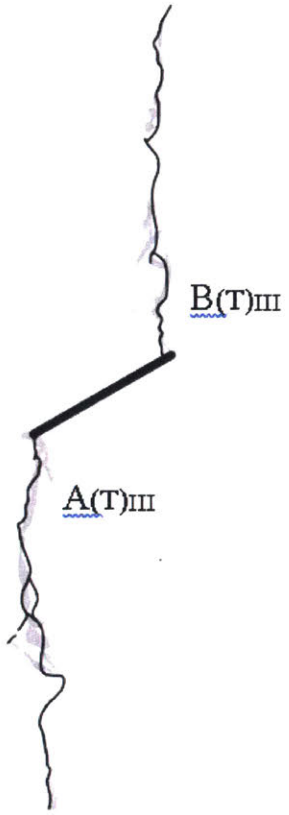

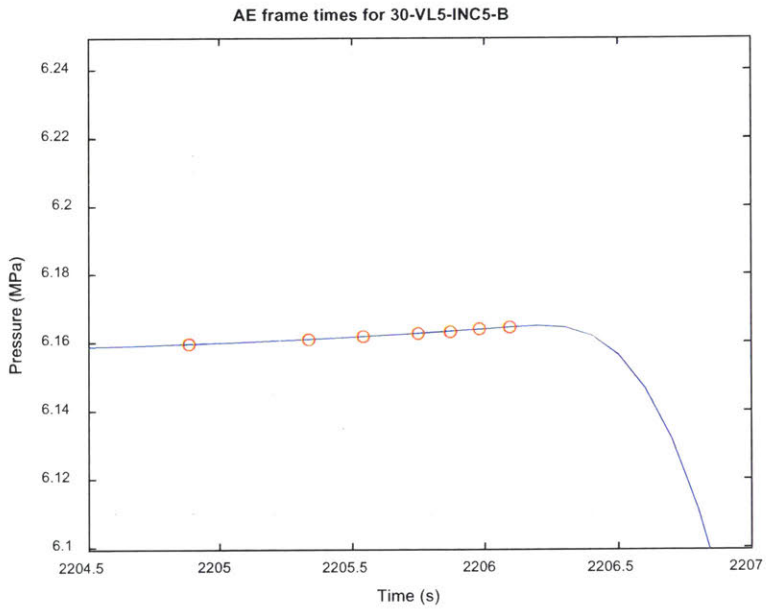

Cracks form the classic wing crack pattern, initiating first from the left tip. Pressure reaches maximum value immediately before fracture initiation.

Development of AE locations are shown over the 20 frames presented in this analysis, where each frame shows 5% of the total number of events recorded during the test. This means that initially the frames will cover a long time period since few AE occurred at the beginning, while towards failure each frame will only cover fractions of a second since AE occur at a rapid rate.

Events with greater than 50% CLVD (compensated linear vector dipole) are considered shear type events and are marked with an 'x', while events with less than 50% CLVD are considered tensile and marked with 'o'. For those events detected by 4 sensors, it is not possible to invert the moment tensor and so these events are marked as undefined with '.'. The colour of an event indicates its relative magnitude, where red is the largest. Black ellipses are used to highlight areas of interest.

Where possible, AE frames are shown next to the appropriate analysis sketch from Bruno. However, these tend to be few in between and as discussed, the high speed frames tend to occur after the end of detectable AE events.

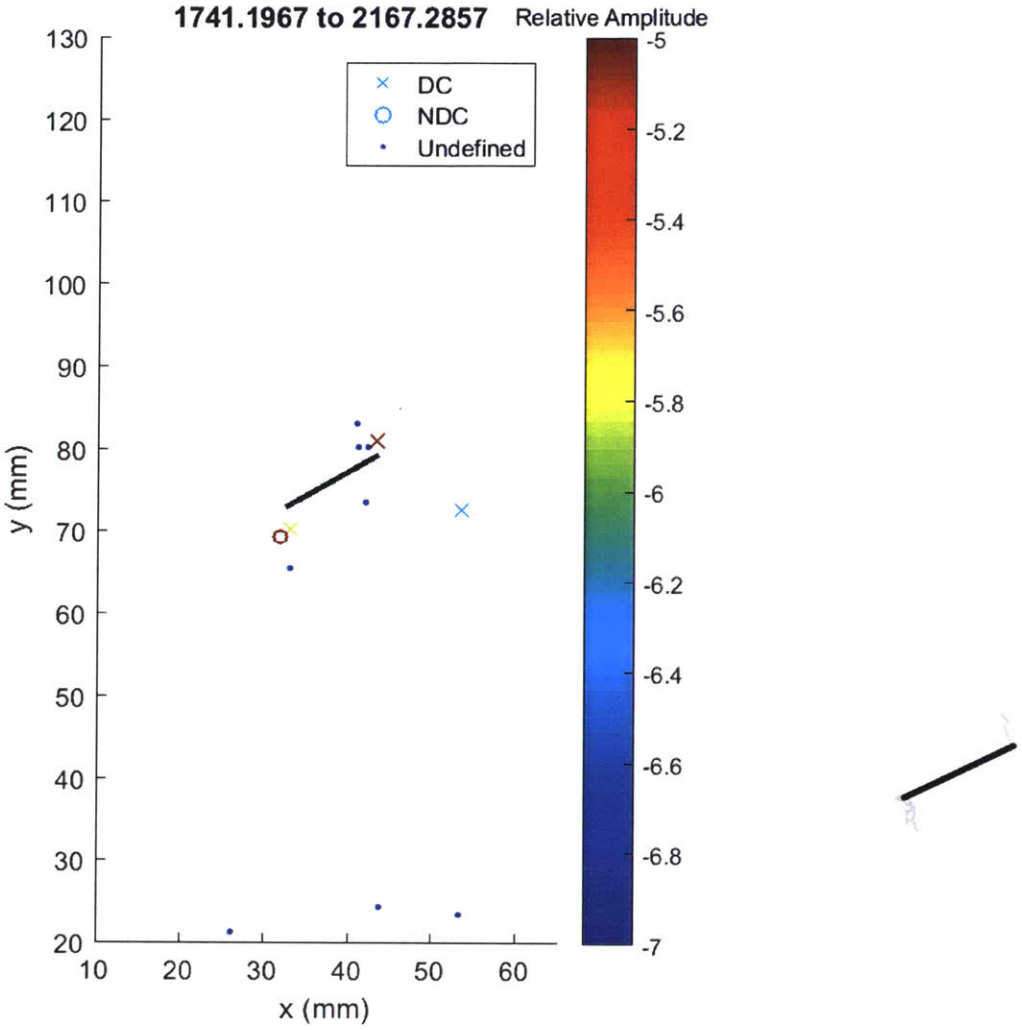

Large shear event occurs at the right tip, and large tensile event at the left tip. Visually there is a small amount of white patching at the flaw tips.

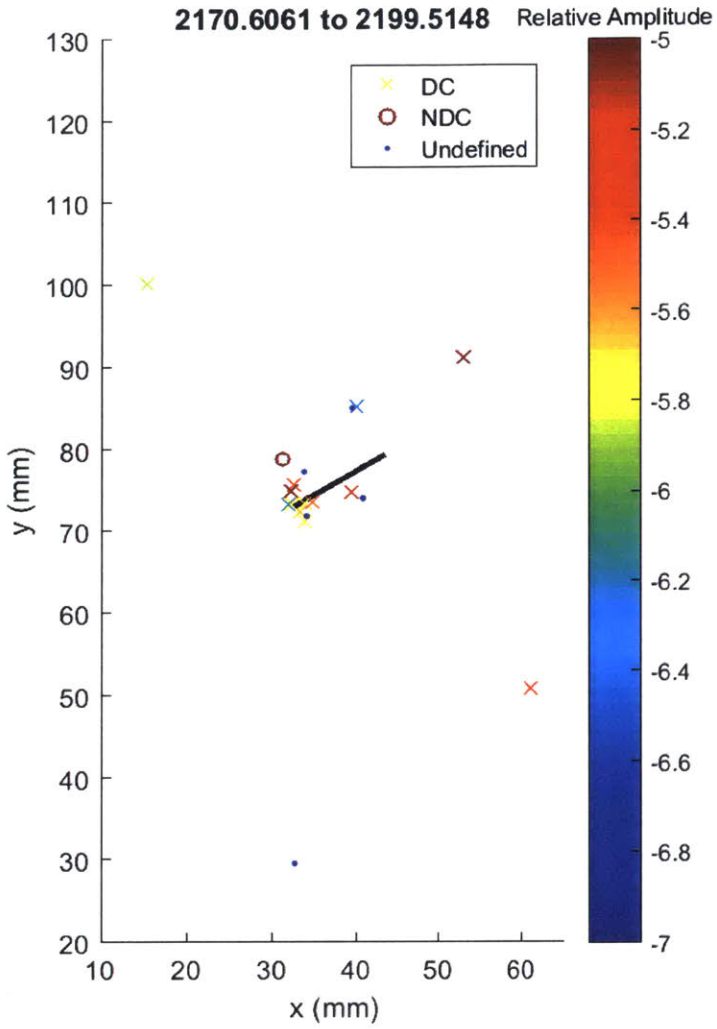

Many shear events concentrated at left tip. 1 large tensile event above the left tip, rather than below as expected by the wing crack pattern.

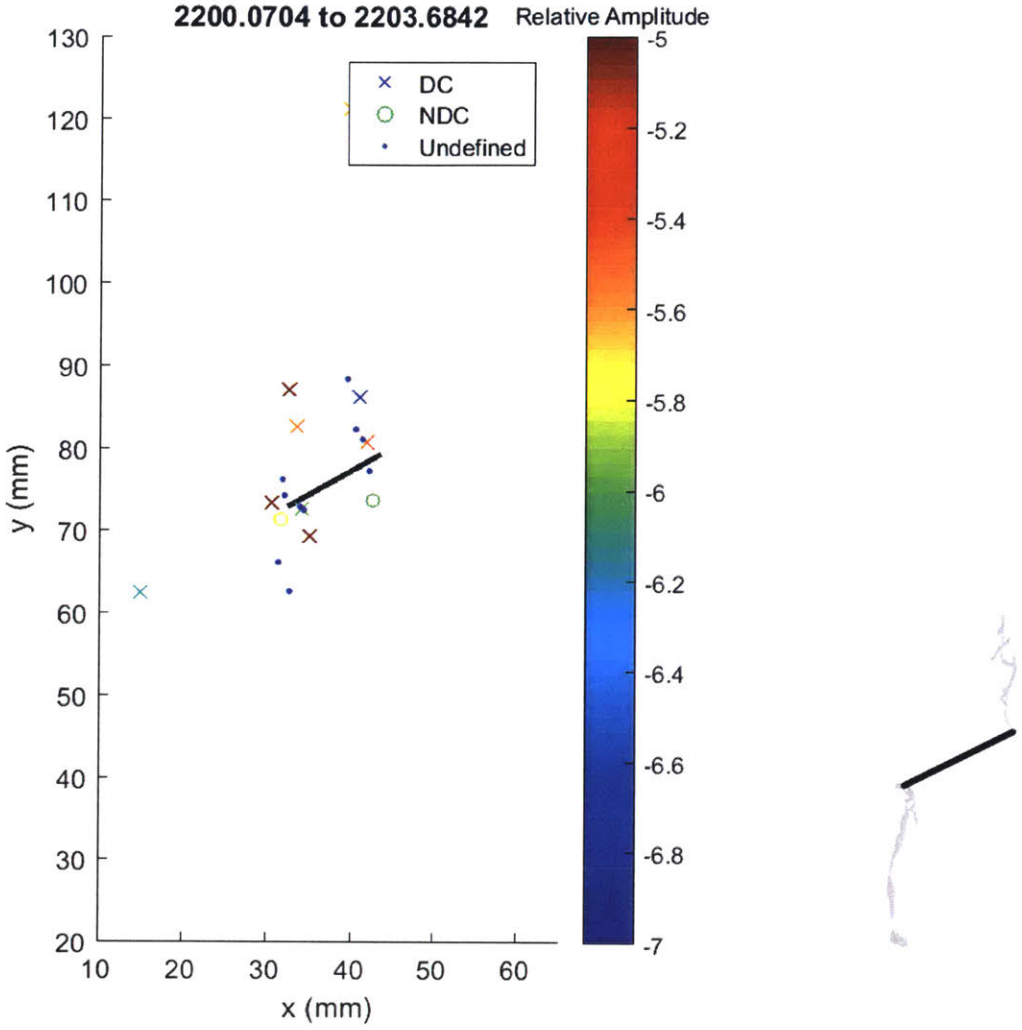

Mostly shear cracks occurring above both tips, again contrary to wing crack pattern which would suggest the left side events would be below the tip. Visually, there is extensive white patching by this point.

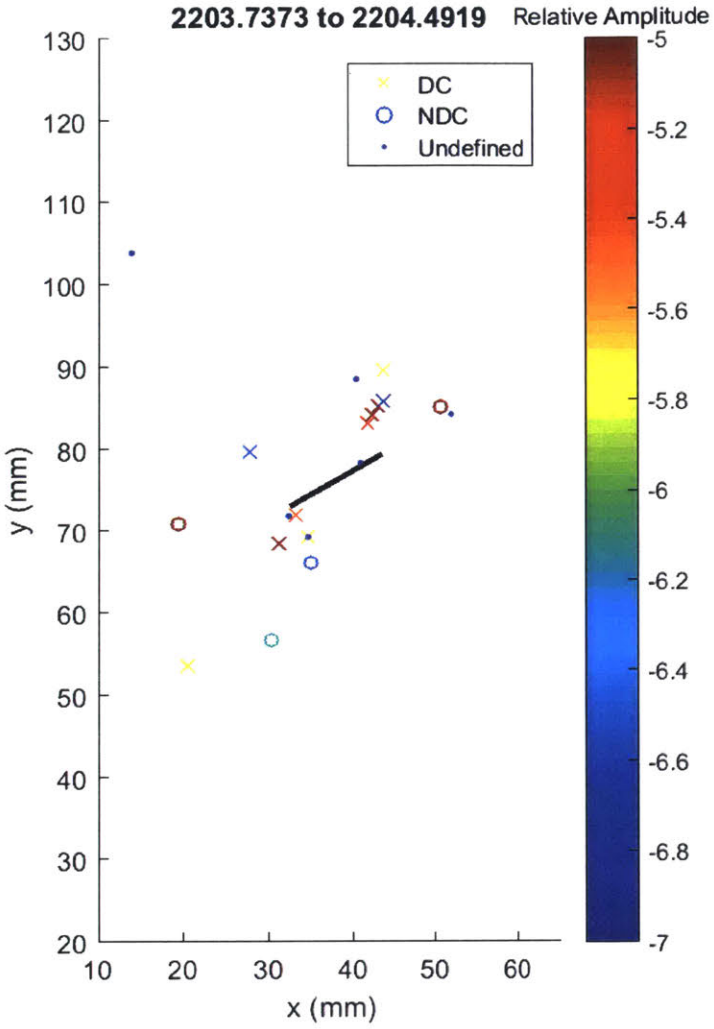

4 closely spaced large shear events occur above the right flaw, few shear events below left flaw. 2 tensile events occur proximally away from each flaw tip.

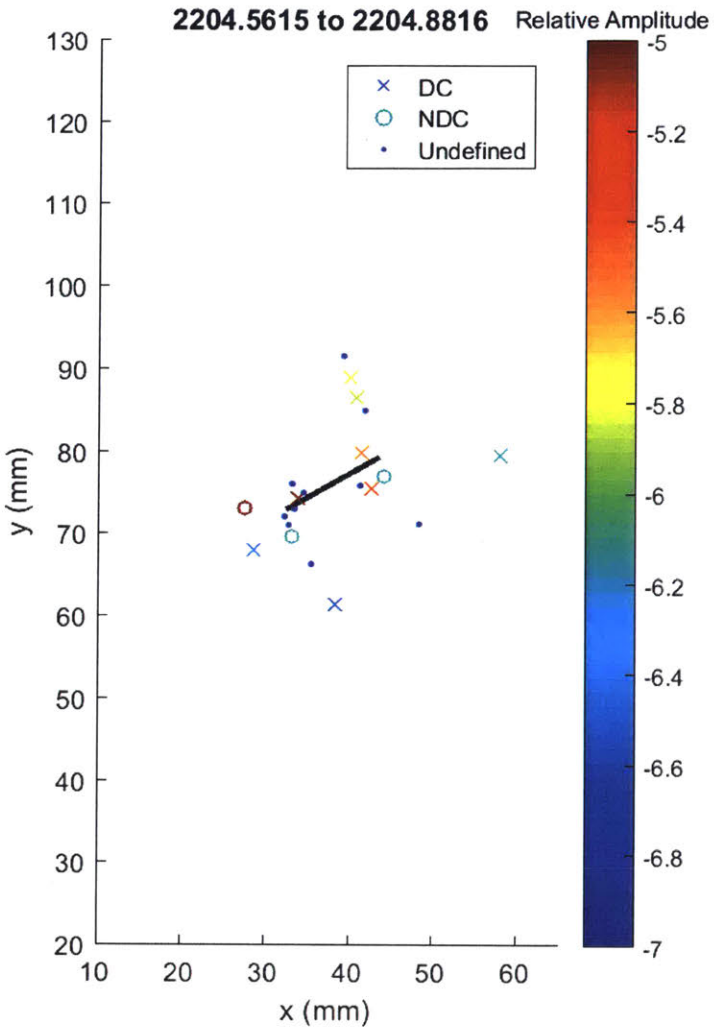

Shear events continue to line up above right tip. 1 large tensile event near left tip.

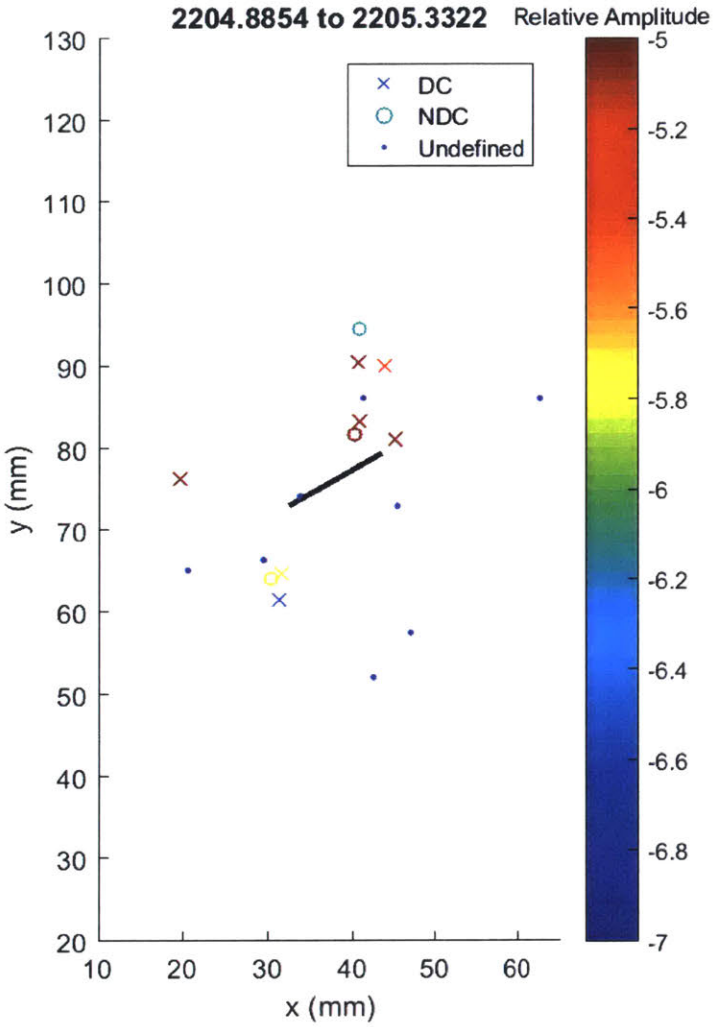

Appearance of 1 large tensile and 4 large shear events above right tip suggests microcrack coalescence.

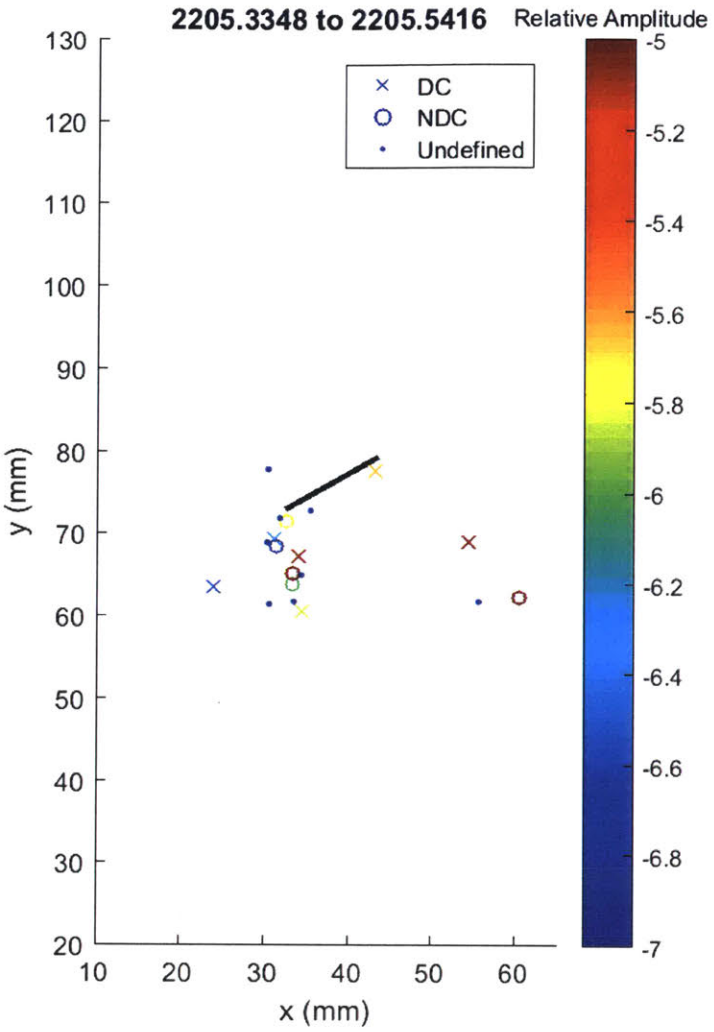

Both tensile and shear events occur below the left tip, suggesting microcrack coalescence on the left side.

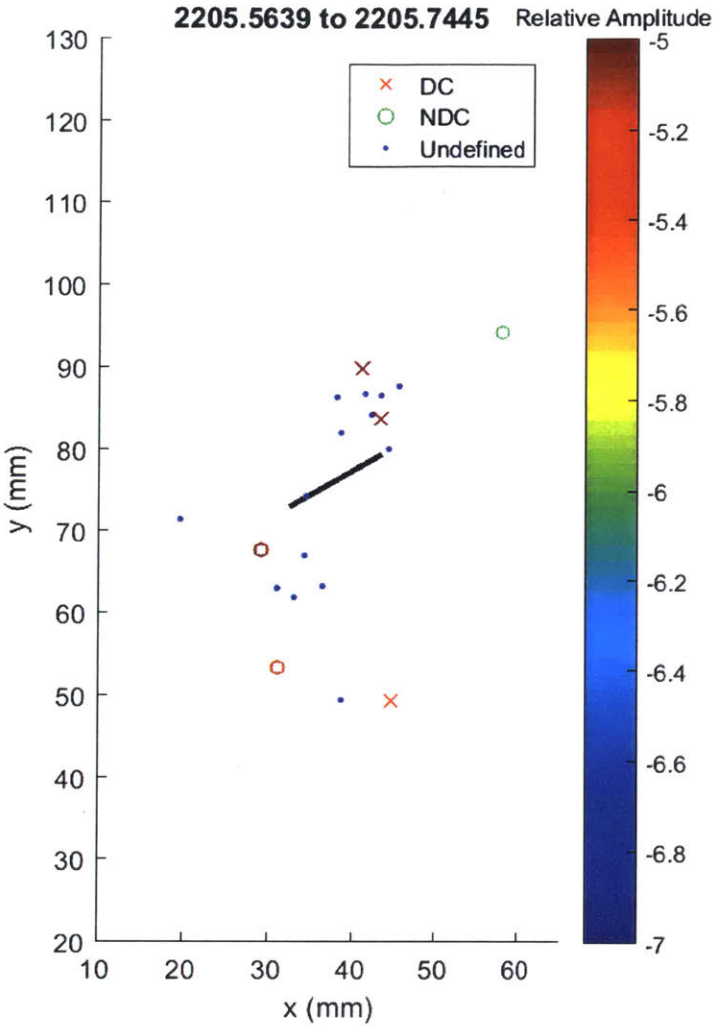

2 large shear events above right tip, and some tensile events far below the left tip. Small undefined events are loosely scattered around each flaw tip.

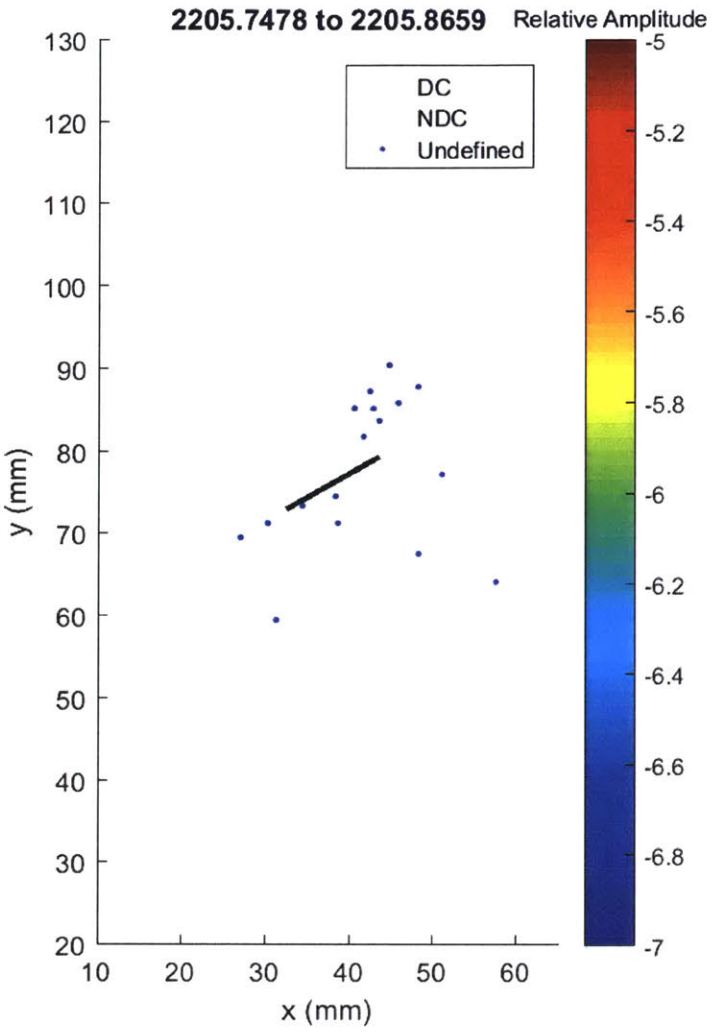

Only small undefined events are detected. They are located most commonly above the right tip.

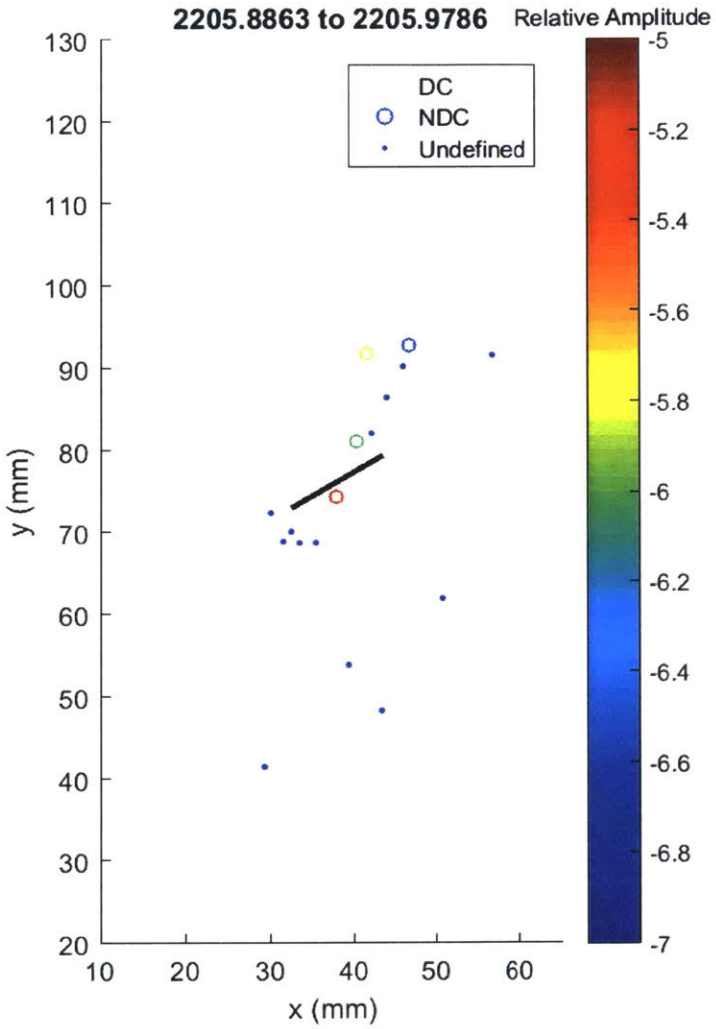

Small tensile events occur above right tip, and some small undefined events cluster close to the left tip.
1 large tensile event occurs at the center of the flaw.

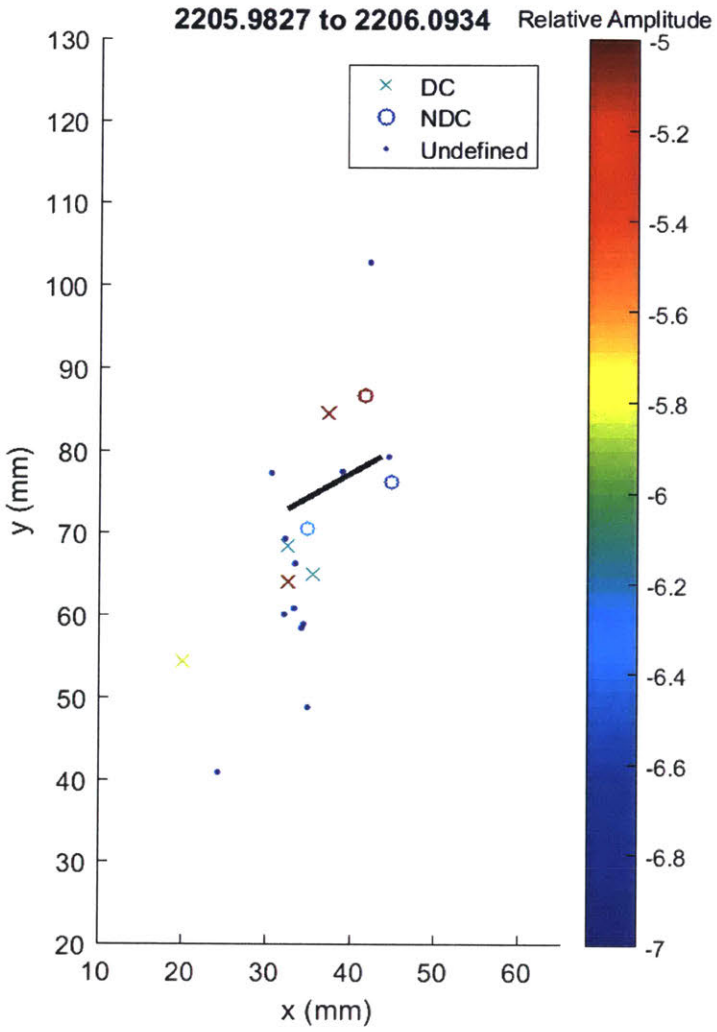

Majority of events clustered at left tip, including 2 small shear, 1 small tensile and 1 large shear. Likely continued creation of microcracks.

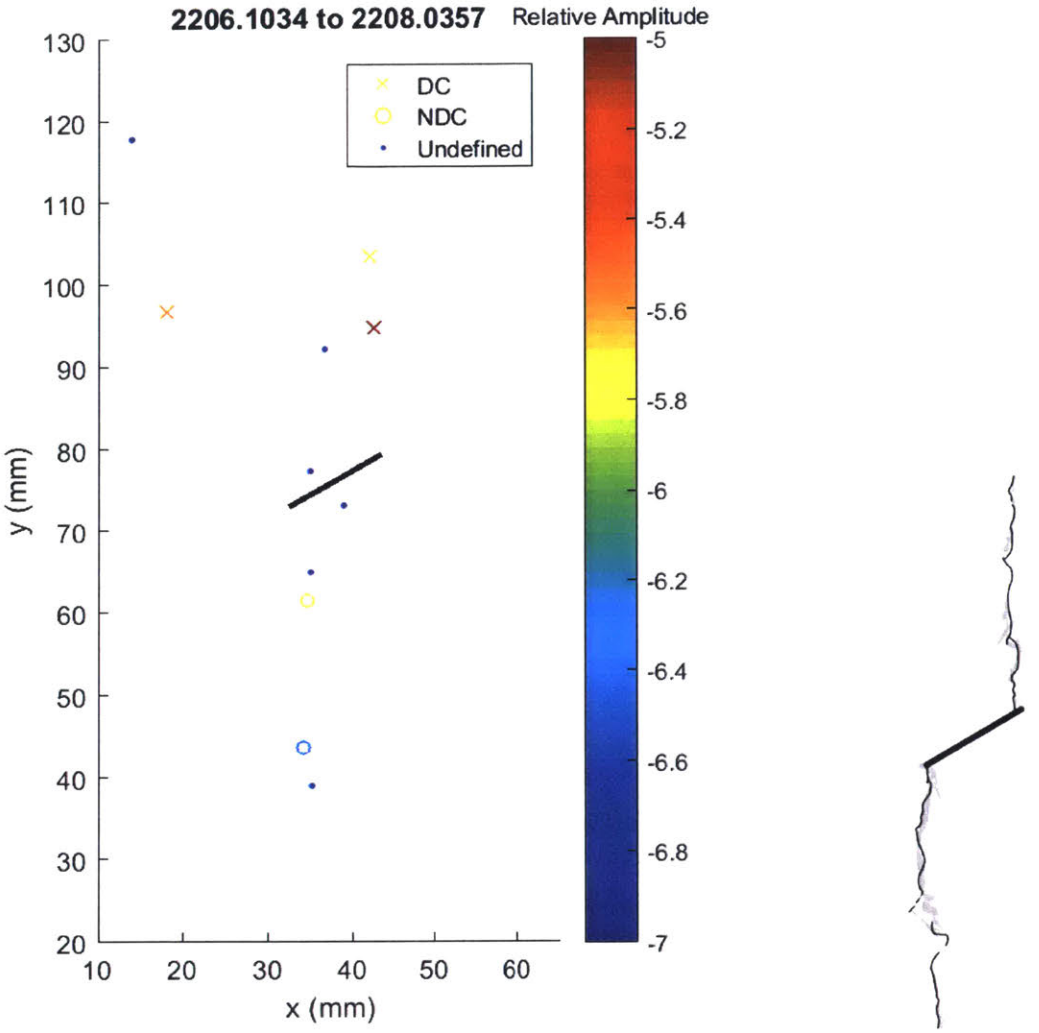

Events become generally scattered. Fracture initiation and propagation occurs at this time.

Summary:

Generally more shear than tensile, but as before more tensile events begin to occur further into the test. Clustering of AE events occurred first on the left tip, but in general there seemed to be more damage at the right tip, which was also where microcrack coalescence occurred first. Visually the left tip showed crack initiation first. During early time, there appeared to be linear patterns of AE events above **both** flaw tips, as opposed to wing crack pattern where the damage is below the left tip. However, towards the end of the test the AE locations occur coincidentally with the white patching.

AE hypocenter analysis for specimen 30-VL5-C

Final crack geometry:

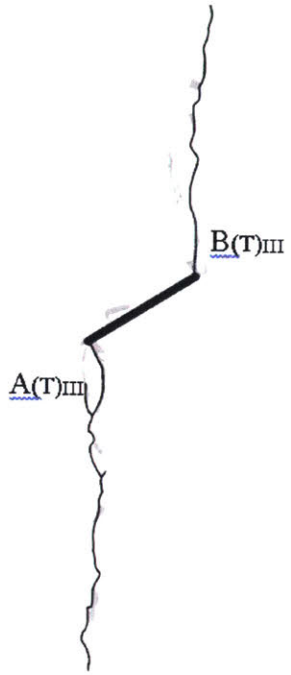

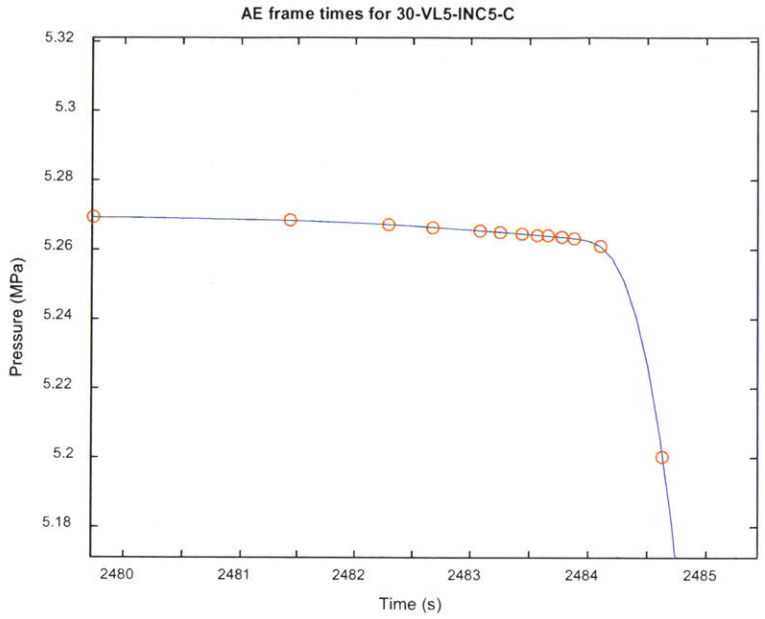

Cracks form the classic wing crack pattern, initiating first from the left tip. Pressure has a slight inflection point around 2482 s.

Development of AE locations are shown over the 20 frames presented in this analysis, where each frame shows 5% of the total number of events recorded during the test. This means that initially the frames will cover a long time period since few AE occurred at the beginning, while towards failure each frame will only cover fractions of a second since AE occur at a rapid rate.

Events with greater than 50% CLVD (compensated linear vector dipole) are considered shear type events and are marked with an 'x', while events with less than 50% CLVD are considered tensile and marked with 'o'. For those events detected by 4 sensors, it is not possible to invert the moment tensor and so these events are marked as undefined with '.'. The colour of an event indicates its relative magnitude, where red is the largest. Black ellipses are used to highlight areas of interest.

Where possible, AE frames are shown next to the appropriate analysis sketch from Bruno. However, these tend to be few in between and as discussed, the high speed frames tend to occur after the end of detectable AE events.

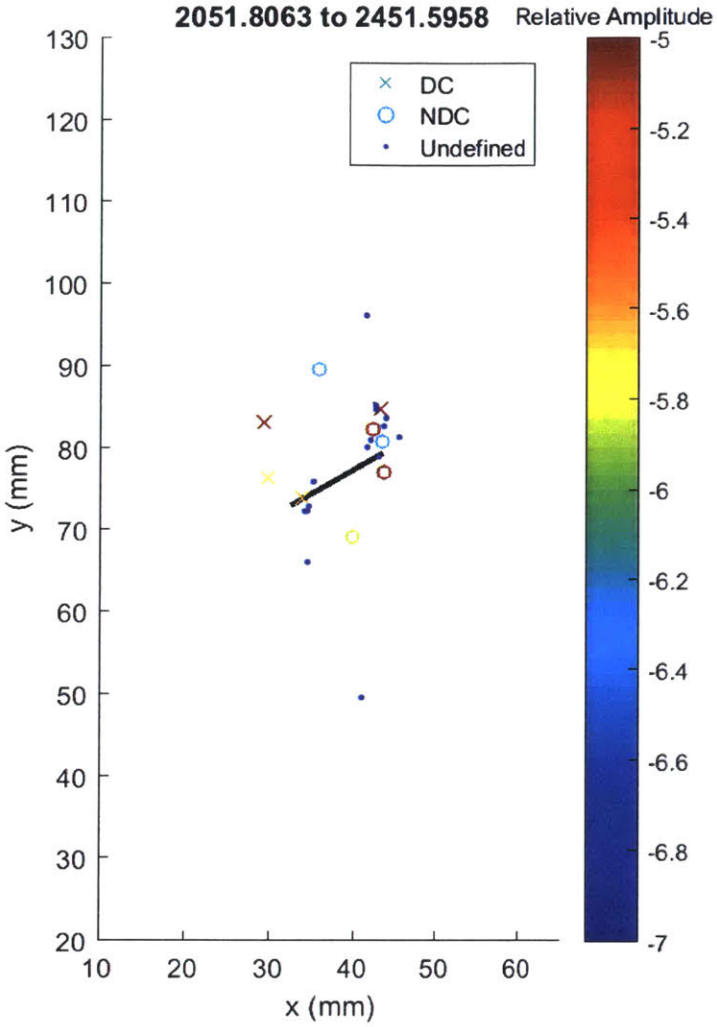

2 large tensile events occur at right tip, and a shear event occurs above each flaw tip. More small events appear to be clustered around the right tip. Visually, there is a small amount of white patching at the tips, and some white patching right of the left tip.

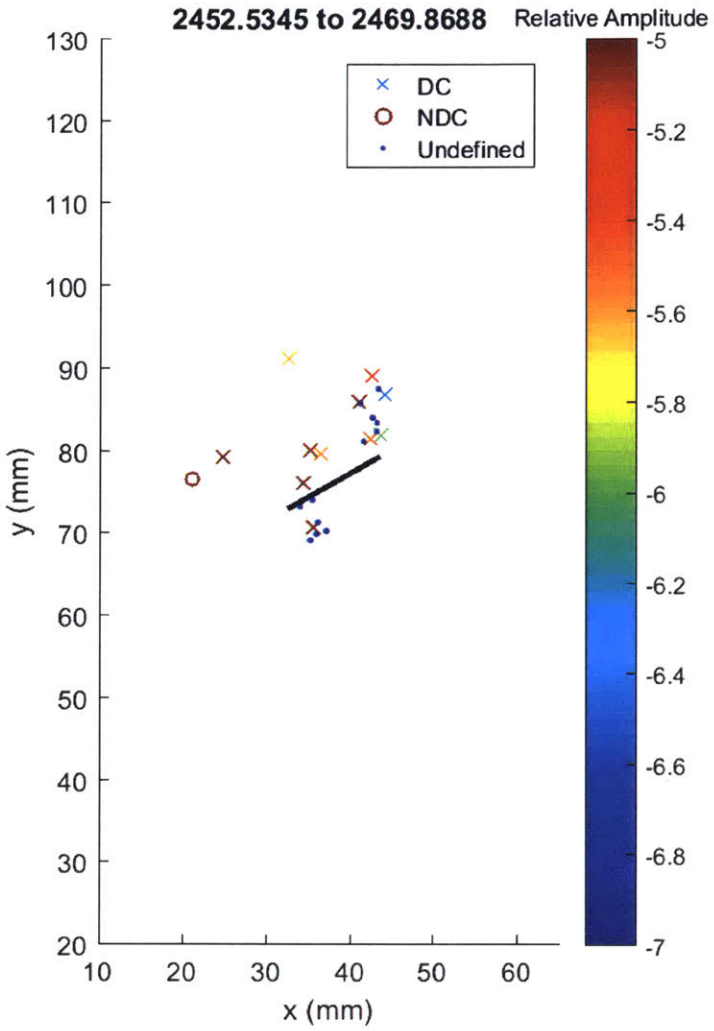

Large amplitude shear events occur above **both** flaw tips, but small undefined events cluster below the left tip, and above the right tip as suggested by fracture mechanics.

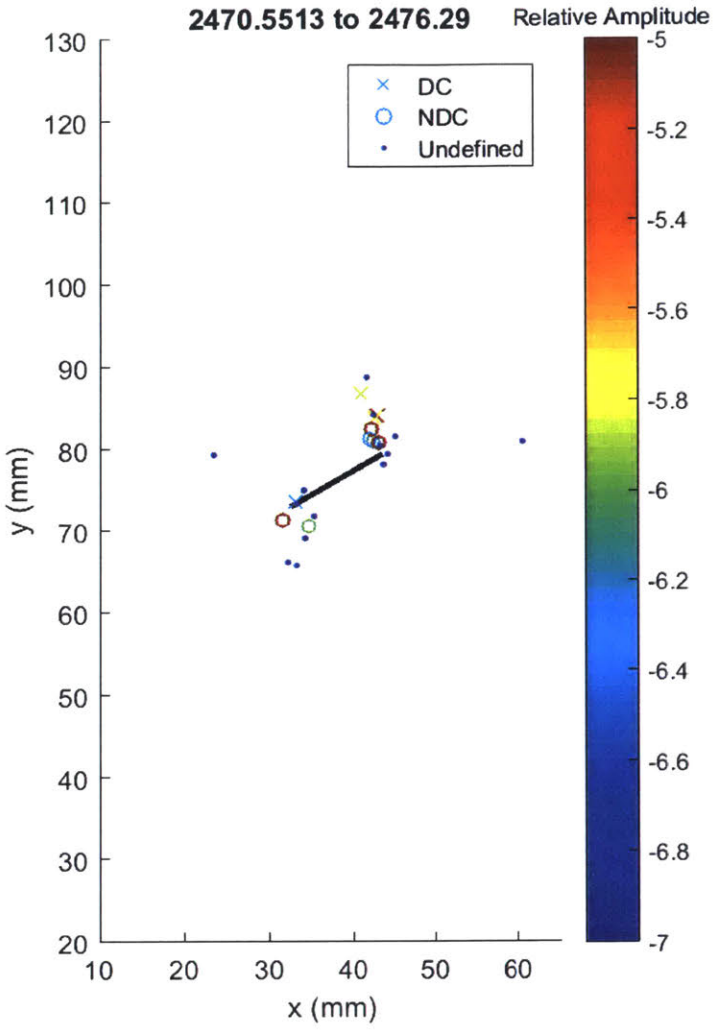

Large tensile events occur at both flaw tips, while shear events appear to be smaller amplitude.

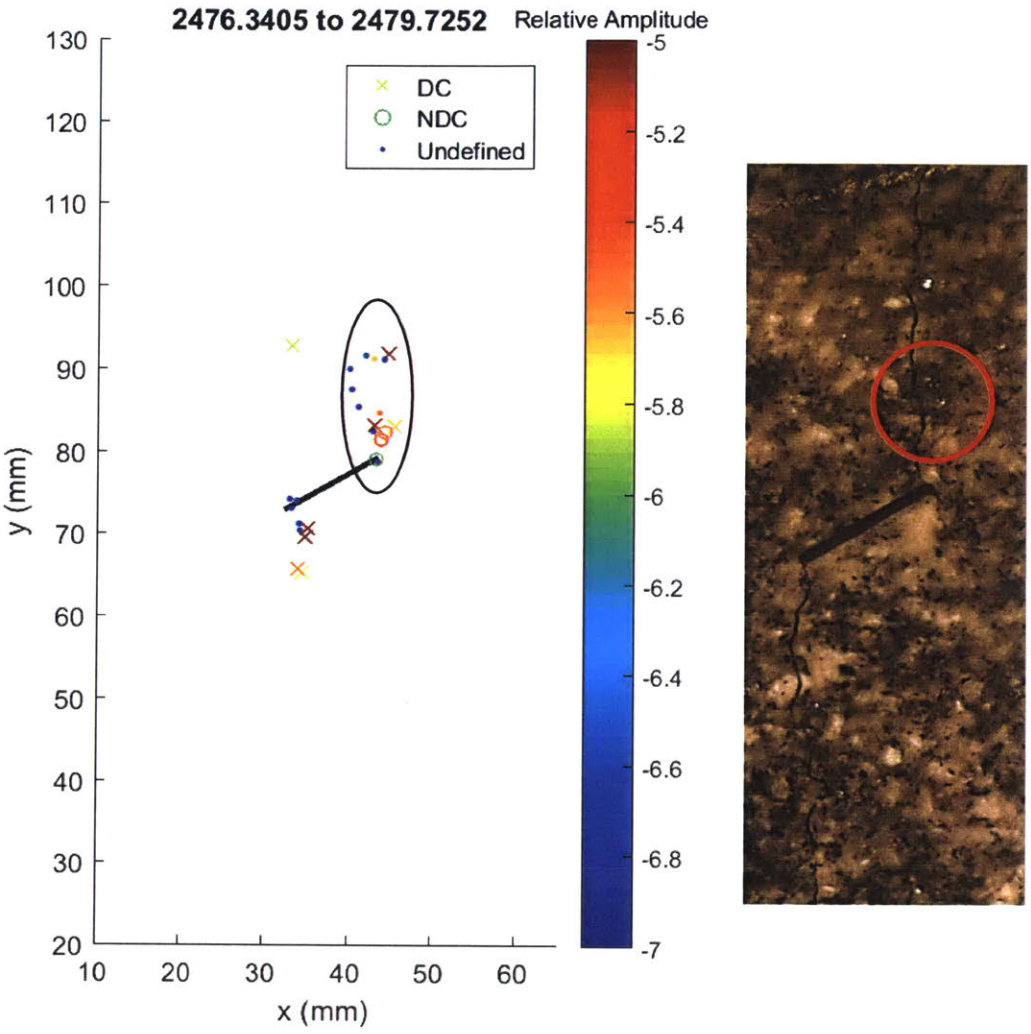

4 large shear events occur below the left tip, while 2 large tensile and 2 large shear events occur at the right tip. **Very curiously,** there is a curved line of small undefined events reaching up to a large shear event approximately 1 cm above the right tip. High resolution photo indicates there is a large grey grain at this location.

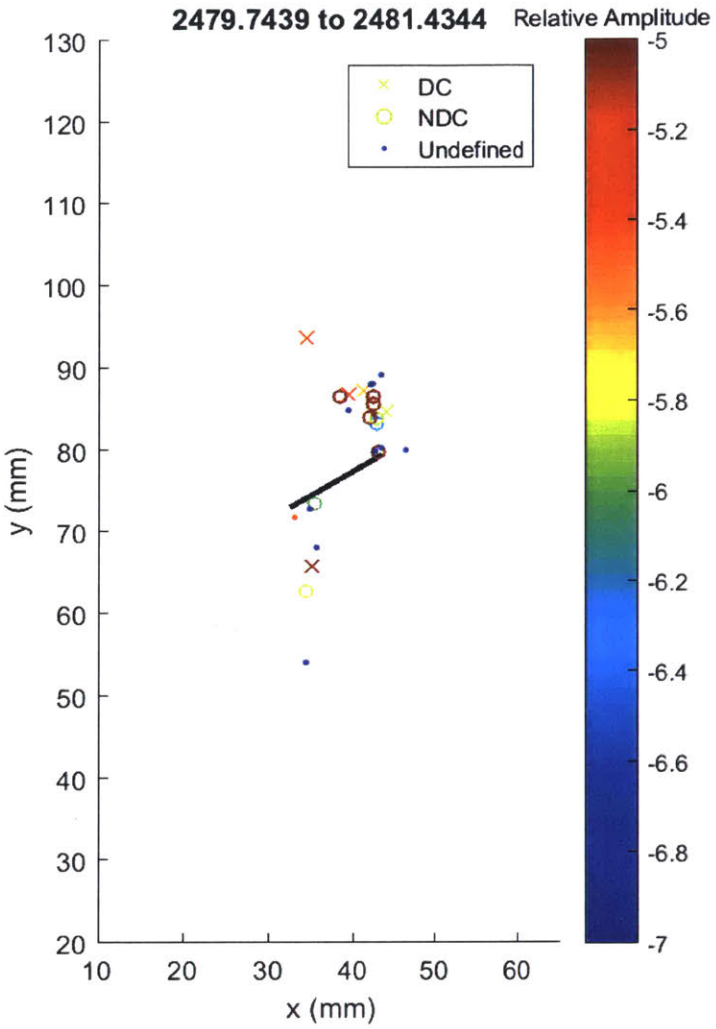

Cluster of large tensile events above right tip where the line of small events occurred in the previous frame, and some large shear events above the tensile events. Few events occur at the left tip.

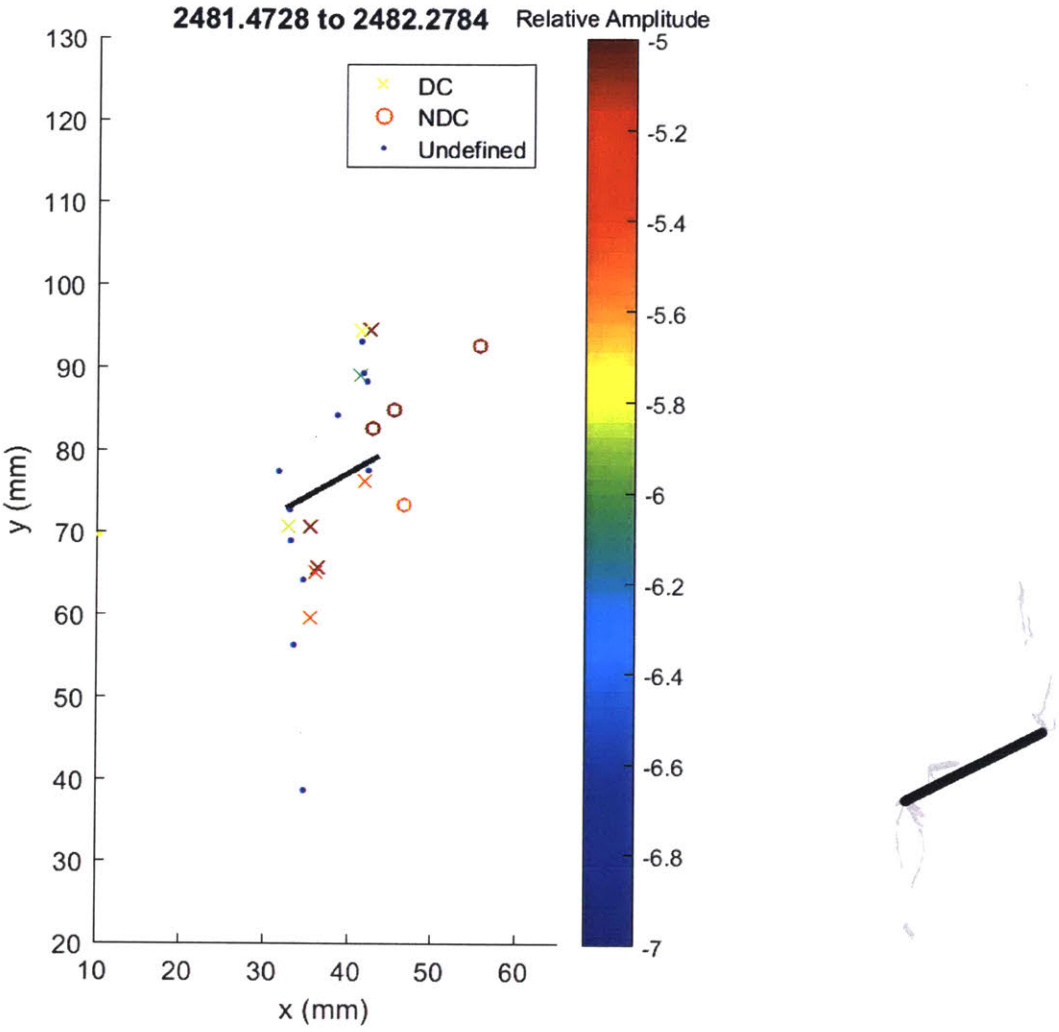

Left tip shows a line of large shear events, while right tip shows a number of large tensile events. White patching develops approximately up to 1-2 cm from each flaw tip. Visual analysis suggests the white patching on the right tip is separated, and the curved line of AE events 2 frame prior supports the idea that damage localised on a grain above the right flaw tip.

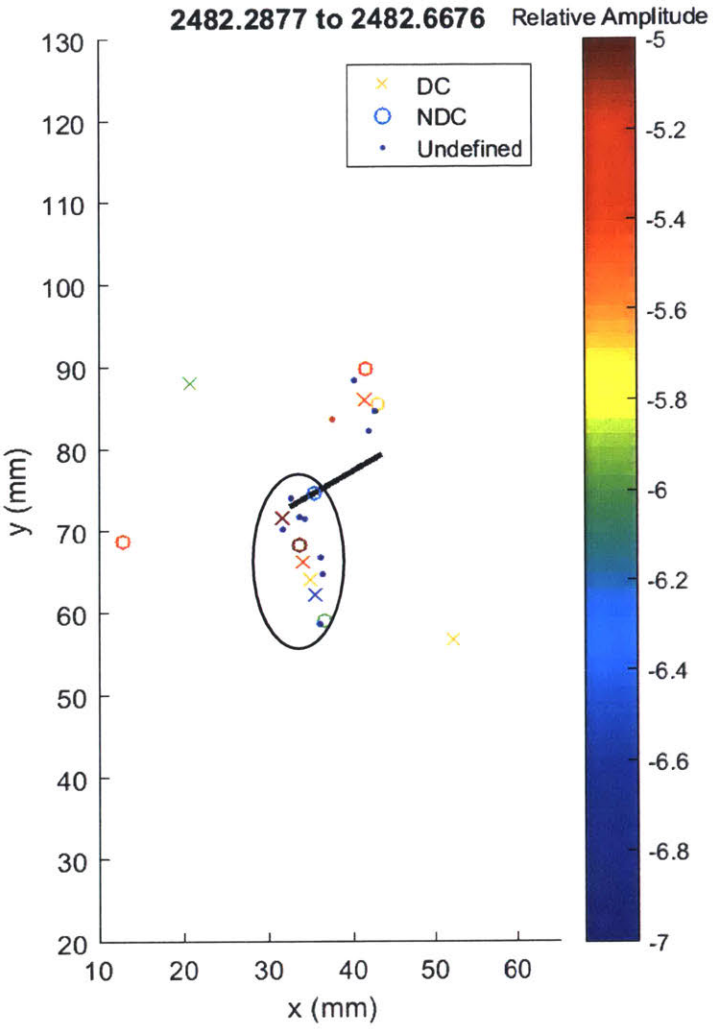

Line of events at left tip maps very well to the theoretical shape of a wing crack. Largest events occur closest to the tip, and amplitude decays with distance from the tip. This frame well illustrates the conceptual model of the growth of damage before a crack tip. 2 shear and 1 tensile event occurs above the right tip.

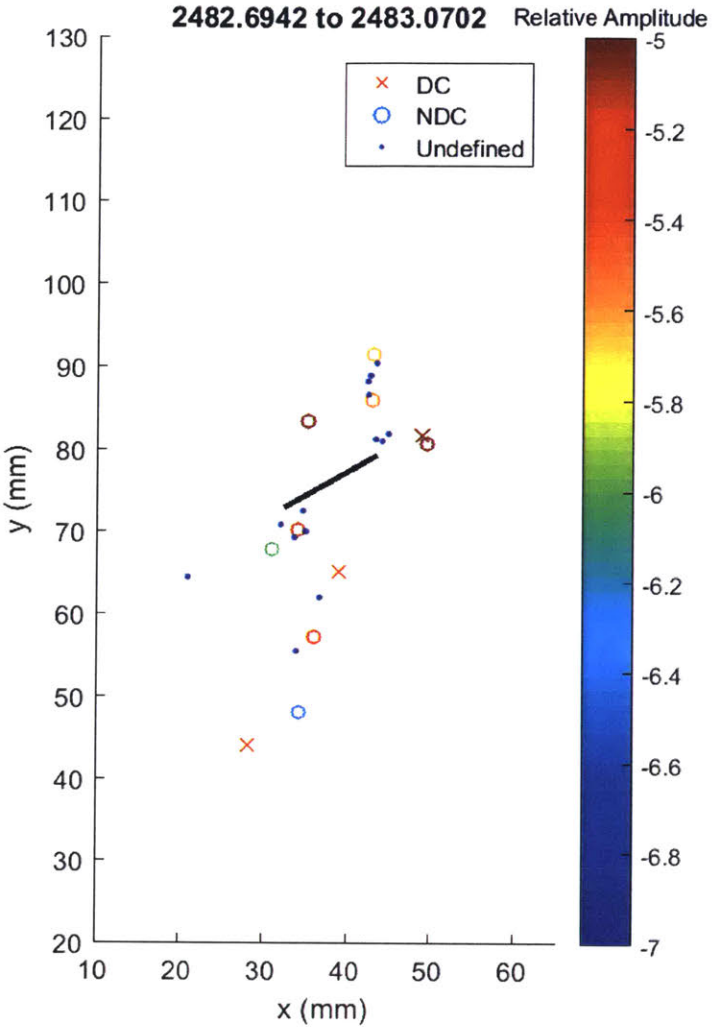

Tensile events occur approximately at wing crack locations on both flaw tips – likely microcrack coalescence.

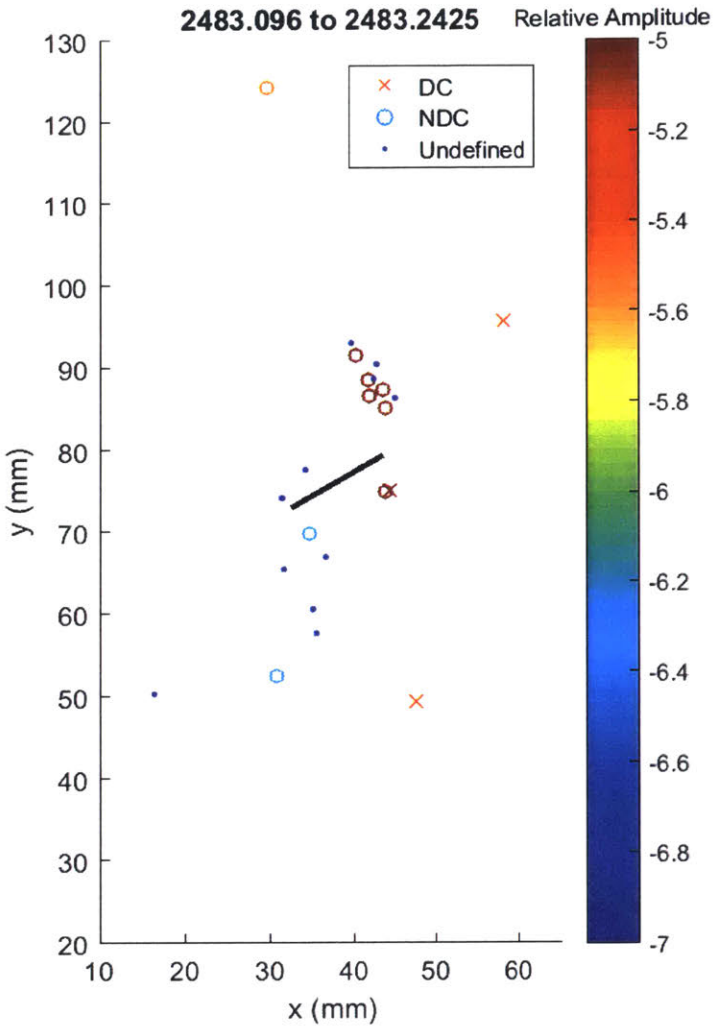

5 large tensile events occur on a line above the right flaw tip – significant growth of the process zone?

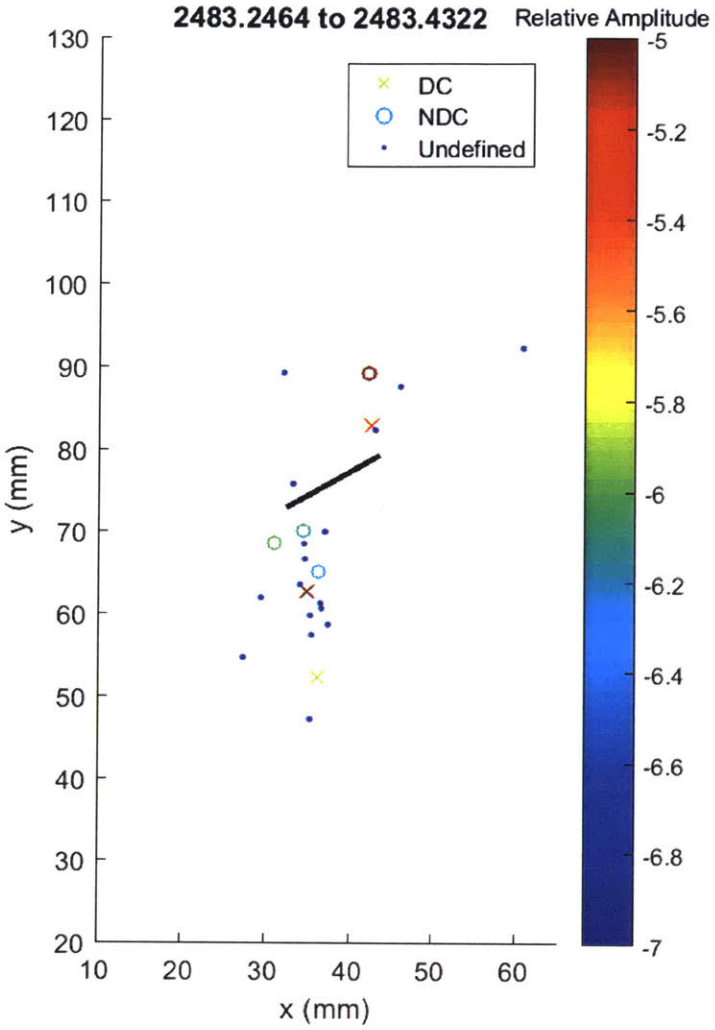

Small tensile events occur at the left tip along with many small undefined events. 1 large shear and 1 large tensile event occurs above right tip.

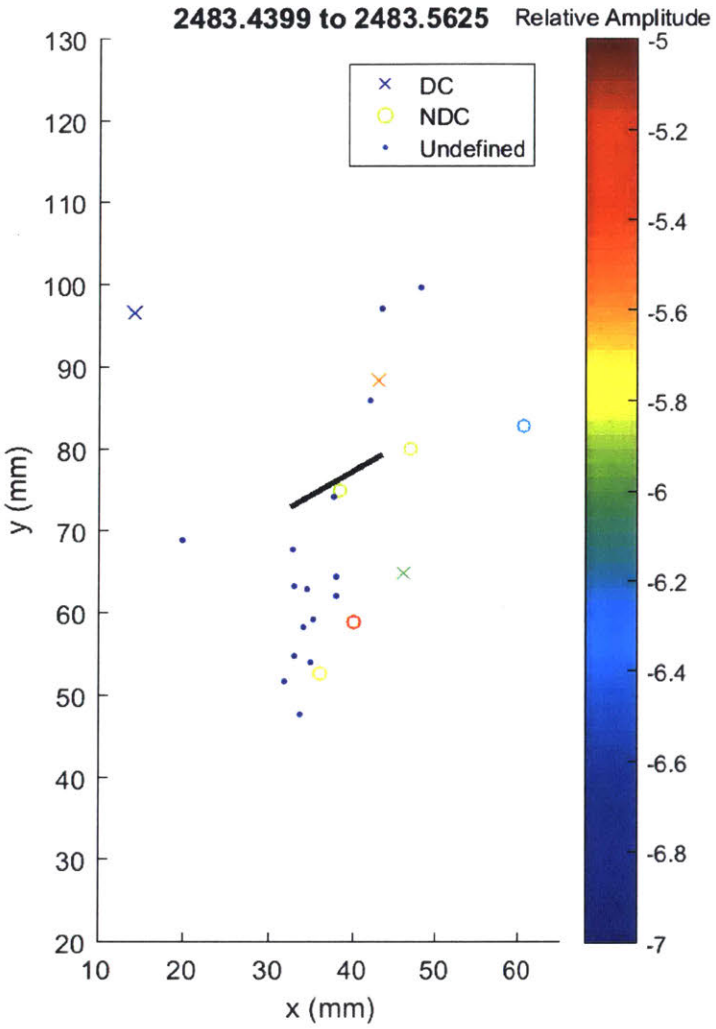

Same as above.

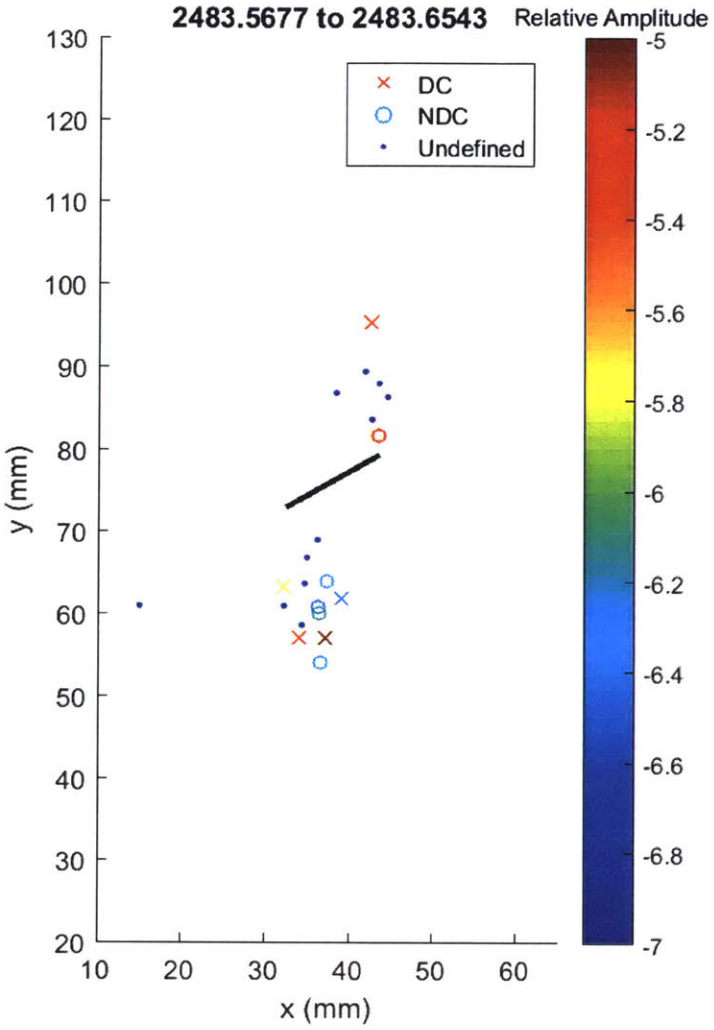

Small tensile and large shear events continue to occur below the left tip, and appear to be moving downwards. This is indicative of the process zone growth. Right tip shows 1 tensile event, with a group of small undefined events above the tensile event, and a shear event above that.

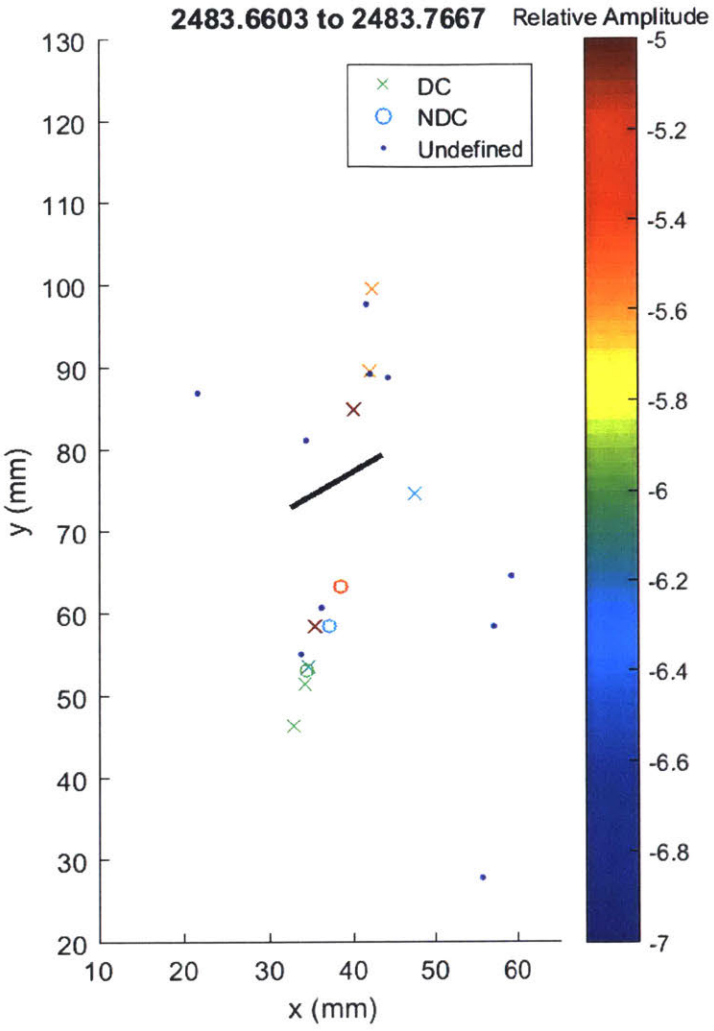

3 shear events occur above the right tip, while 1 large shear and 1 large tensile event occurs below left flaw, and smaller events occur further from the flaw tip.

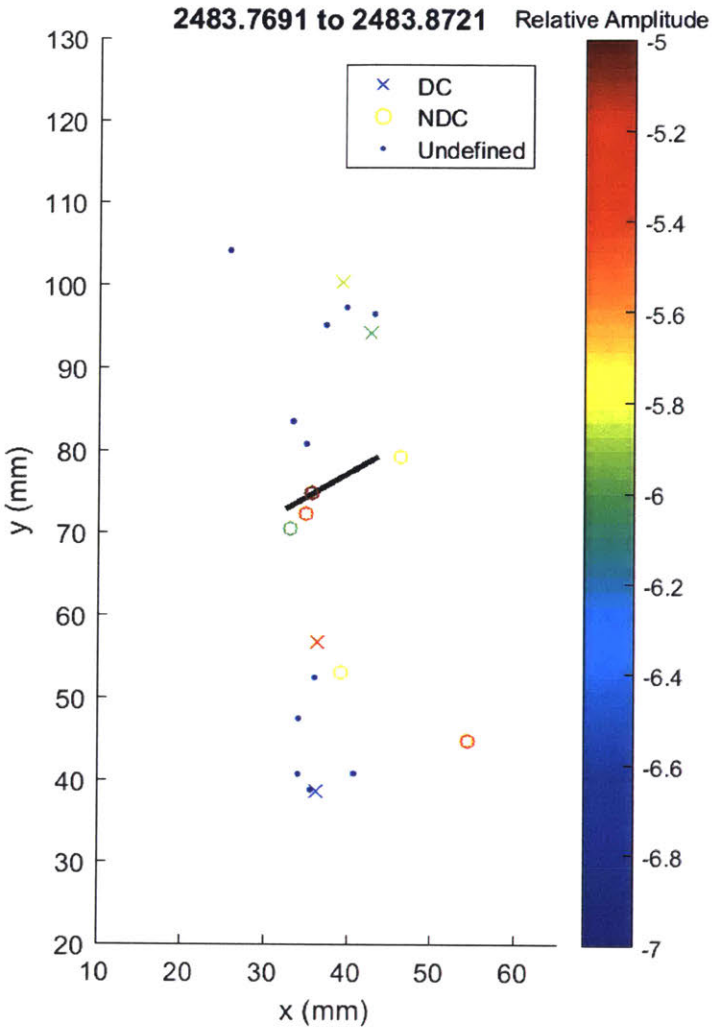

3 tensile events occur at left tip, and groups of events occur approximately 2-3cm away from each flaw tip.

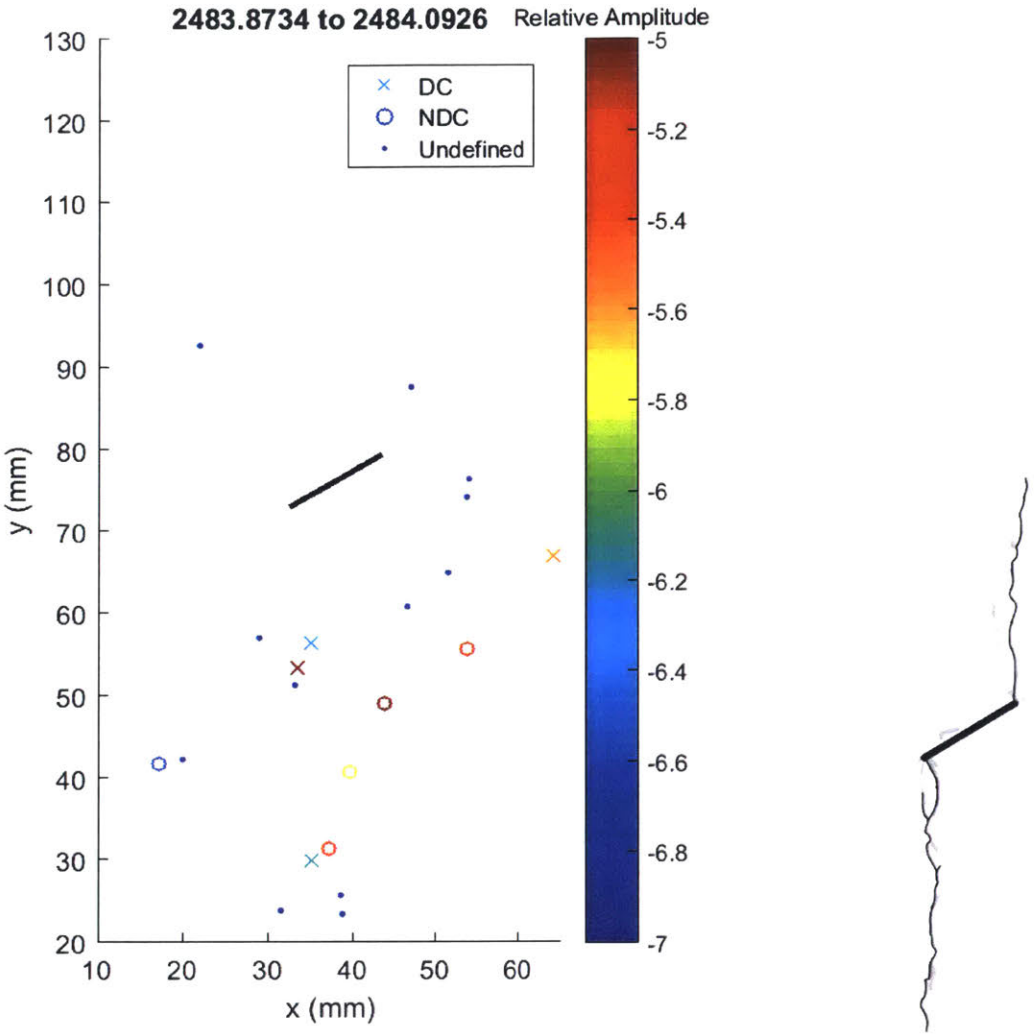

Scattered event locations. Visual crack initiation and propagation occur in this time.

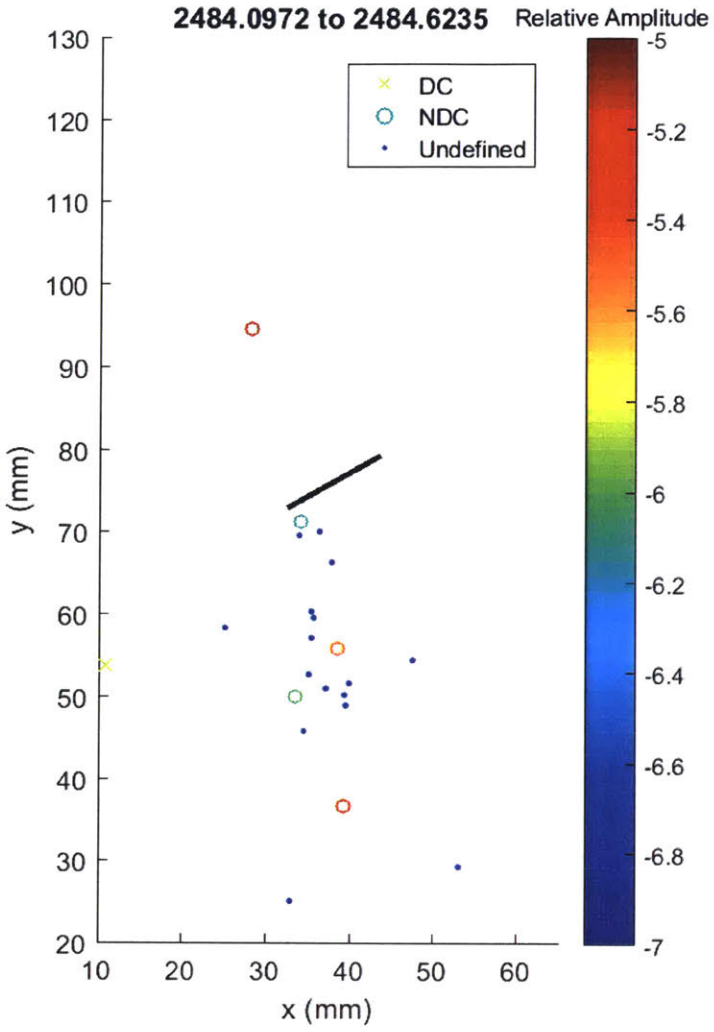

Undefined and tensile events map out the wing crack area below the left tip.

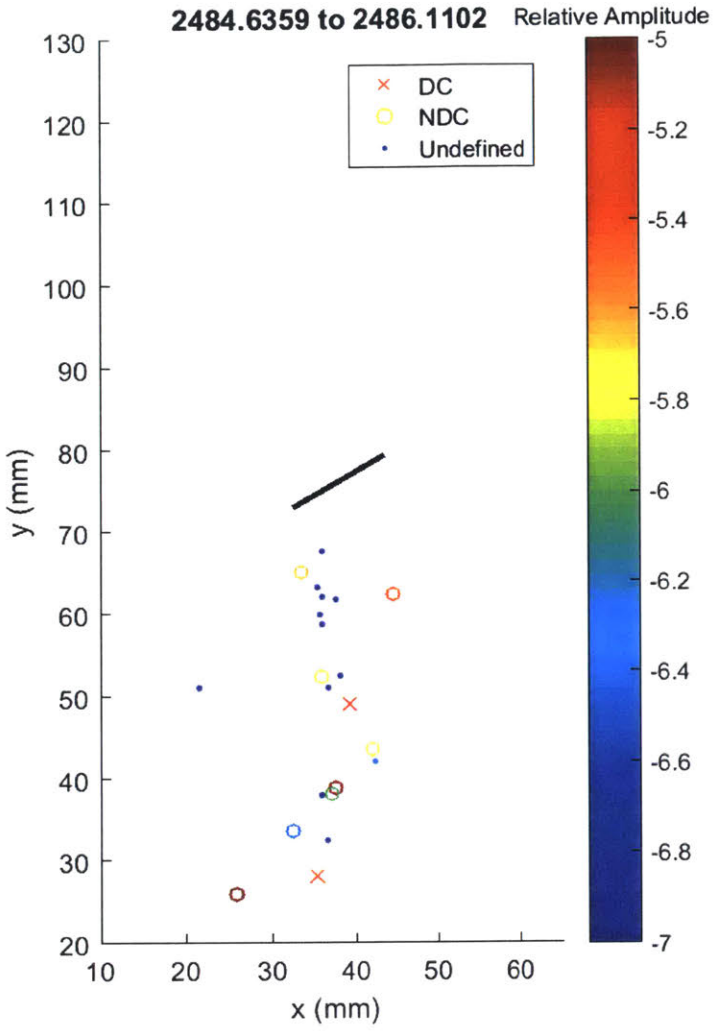

Same as above.

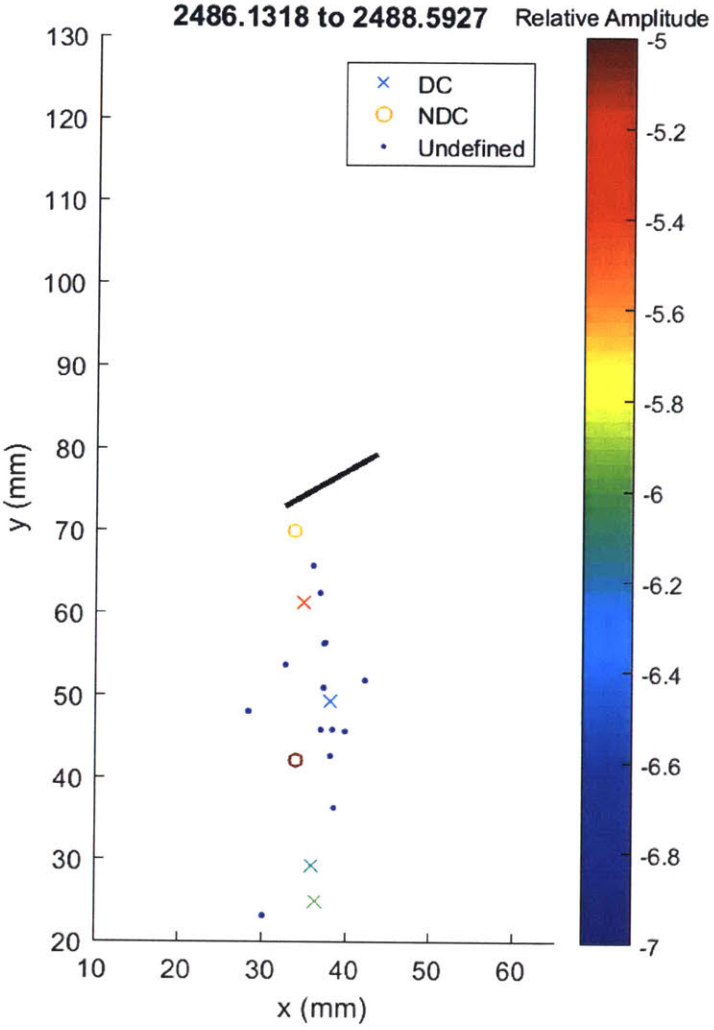

Same as above.

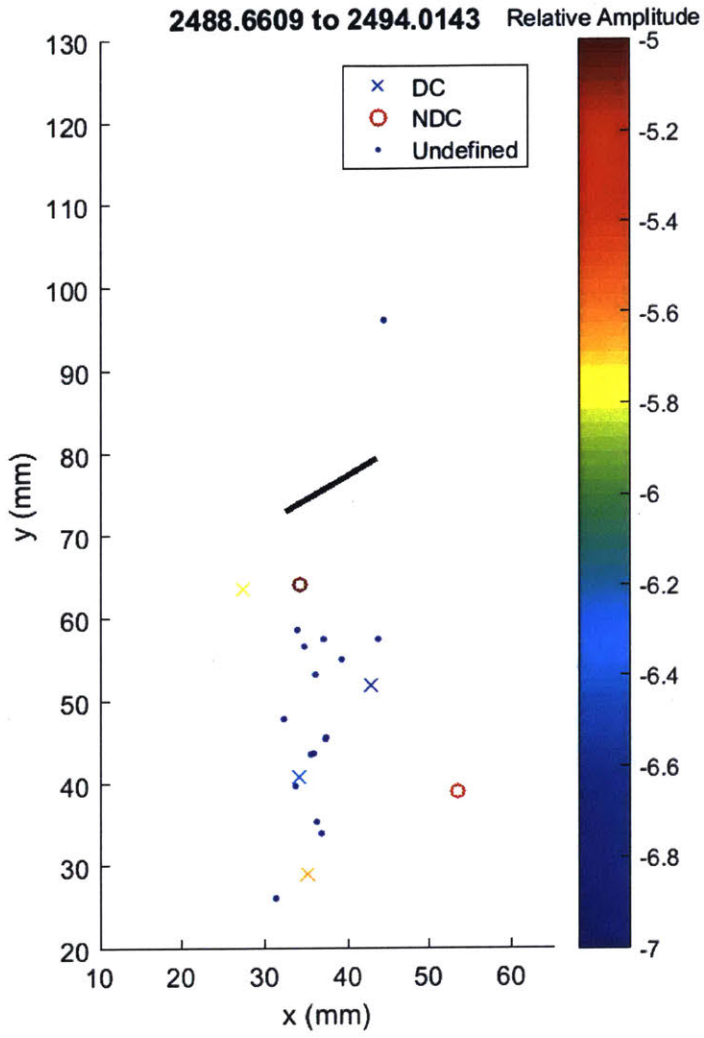

Same as above.

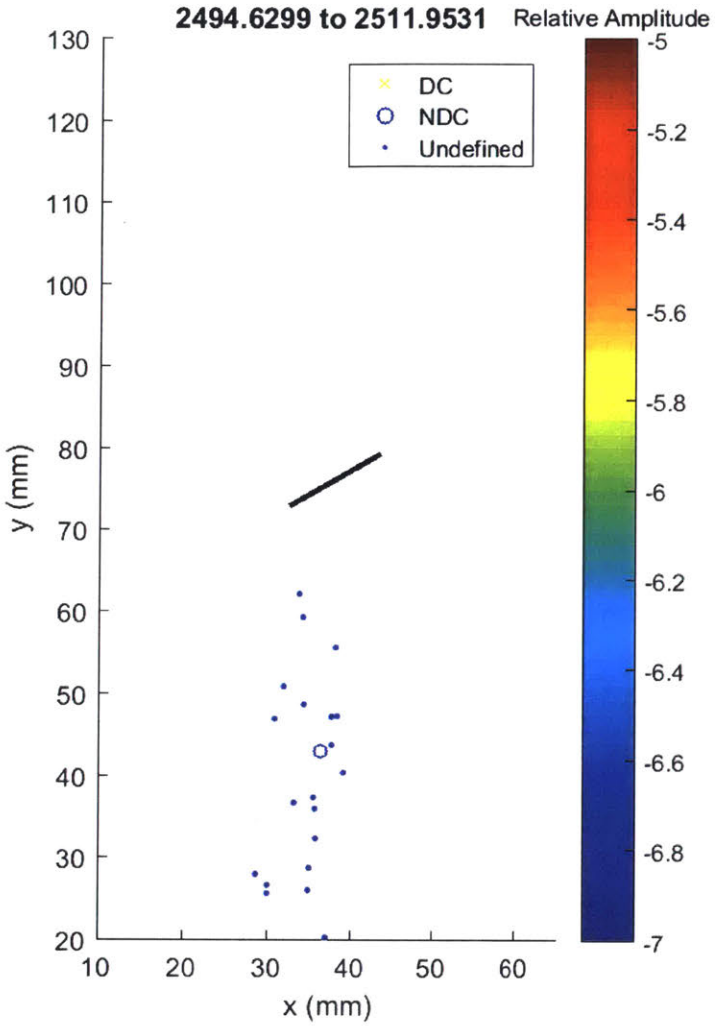

Same as above.

Summary:
There were more tensile events in the beginning compared to the other single flaw test, which was also VL5 and cracked in a very similar way. This test was informative in showing many AE phenomena:

- Clusters of shear events occurring above both flaw tips early during the experiment: not wing pattern
- A line of small events occur in a line leading up to a large shear event at a large grain. Larger tensile events occur along the line of the small events in the next frame. 7 seconds later another group of tensile events occur in close proximity to this large grey grain.
- During early times, the left tip showed mainly shear events, while the right tip showed mainly tensile events. What could cause this?
- in one frame we clearly see a decay in amplitude away from the flaw tip
- during early times we find more evidence that the progression of damage on the flaw tips are related: in some frames the events are mostly clustered on one tip, and the next frame they are clustered on the other tip